Development of new probes based on carbon nanocones for near-field microscopies

Germercy Paredes Guerrero

THÈSE

En vue de l'obtention du

DOCTORAT DE L'UNIVERSITÉ DE TOULOUSE

Délivré par l'Université Toulouse 3 - Paul Sabatier

Présentée et soutenue par

Germercy PAREDES GUERRERO

Le 28 octobre 2020

Development of new probes based on carbon nanocones for near-field microscopies

Ecole doctorale : **SDM - SCIENCES DE LA MATIERE - Toulouse**

Spécialité : **Sciences et Génie des Matériaux**

Unité de recherche :

CEMES - Centre d'Elaboration de Matériaux et d'Etudes Structurales

Thèse dirigée par

Marc MONTHIOUX et Fabrice PIAZZA

Jury

M. Gérard VIGNOLES, Rapporteur
Mme Sophie MARSAUDON, Rapporteure
M. Mauricio TERRONES, Examinateur
Mme Christina VILLENEUVE-FAURE, Examinatrice
M. Marc MONTHIOUX, Directeur de thèse
M. Fabrice PIAZZA, Directeur de thèse
M. Thierry ONDARCUHU, invité

A la hermosa memoria de mis padres, Gregorio & Germania

Estaré por siempre agradecida y orgullosa de su inspiración, confianza, apoyo, enseñanzas y legado.

REMERCIEMENTS

« La reconnaissance est la mémoire du cœur »

Hans Crhistian Andersen

Quisiera agradecer a la Pontificia Universidad Católica Madre y Maestra (PUCMM), particularmente, al "Programa de Formación Disciplinar" por financiar mi proyecto de investigación en el CEMES-CNRS; a la Vicerrectoría de Investigación e innovación, a la Facultad de Ciencias e Ingeniería y a la escuela de Ingeniería Industrial, por su receptividad y cooperación.

Je voudrais aussi remercier le Centre d'Élaboration de Matériaux et d'Études Structurales (CEMES) et le Programme des Investissements d'Avenir (EUR grant NanoX n° ANR-17-EURE-0009) pour le financement partiel à ce projet en me donnant accès aux installations pour accomplir ce travail de recherche dans un cadre d'excellence internationale.

Mes sincères remerciements vont également à mes directeurs de thèse Dr. Marc MONTHIOUX et Dr. Fabrice PIAZZA, pour leur support et la confiance qu'ils m'ont accordés pendant ces années. Merci pour l'inspiration, la compréhension et les encouragements que vous m'avez apportés dans les périodes très difficiles pour moi que ce soit dans le contexte personnel et/ou professionnel.

I would like to thank all the jury members, M. Gérard VIGNOLES, Mme. Sophie MARSAUDON, M. Mauricio TERRONES, Mme. Christina VILLENEUVE-FAURE, and M. Thierry ONDARÇUHU; who have taken a valuable time for evaluating my work. Thanks for sharing your expertise with me and thus strengthening my research knowledge and experience.

Je voudrais aussi remercier toutes les personnes des divers laboratoires de recherche avec qui j'ai eu l'opportunité de collaborer ici à Toulouse :

- pour **le CEMES** : Pascal PUECH (qui parle peu, mais quand il parle, il donne toujours des bons conseils et PAS que sur le Raman !) ; Grégory SEINE (merci pour toute votre aide pour notre travail autour de l'AFM) ; Robin COURS (rebaptisé les "mains de fée". Grand Merci à toi !) ; Laure NOE, David NEUMEYER, Cécile MARCELOT, Béatrice PECASSOU, Patrick, Mathieu DELMAS, Christophe DESHAYES, Renaud PECHOU, Erik DUJARDIN, et Mireille TRUPIN.
  I would like to thank also my "bestiole" Agnieszka, and my carbon gossip girls, Mariem and Divya. Thanks for all the time shared and for your support. But, as all was not "gossip-time" only, I have also to say thanks Mariem for the beautiful SEM images you have taken for this work.

I cannot forget the most disciplined and organized guy I have ever met: Sir Abraao TORRES. Thank you for your patience to answer all my questions, for your help with SEM images, and for all our discussions about Latin-American education and socioeconomics issues.
Gracias al grupo hispano-parlantes del CEMES, por todos los momentos compartidos literalmente alrededor de la mesa: Christophe, Daniela, Silvia, David, Amelia, Vero, Kathrin y tod@s.;

- Pour **le LPCNO-INSA**- Etienne PALLEAU, Laurence RESSIER ;
- Pour **le LCC-** Marine TASSE- et Gabor MOLNAR.

Ainsi que Raúl Arenal de **l'Instituto de Nanociencias de Aragon (INA-Sarragosse, Espagne**) pour sa disponibilité et pour m'avoir accueilli pour les campagnes de caractérisations HRTEM. Gracias Raúl !

Un grand MERCI, à mon ami le Dr. Philippe Ouzilleau ! Merci pour ton écoute et pour tes bons conseils. Merci pour faire partie de mon réseau "graphénique" d' aide.

Quisiera agradecer a toda mi familia, elevo mi agradecimiento a Dios por los padres que me regaló. A mis padres por su amor incondicional y por su visión y ejemplo de vida. ¡Gracias a ellos, hoy por hoy el olor de las páginas de los libros de la biblioteca de la casa siguen siendo mi "*magdalena de Proust*". ¡Ese recuerdo que con nostalgia me hace rememorar mis días de infancia, donde siempre había espacio para ser yo misma y soñar en grande!
Gracias a mis hermanos Grecia, Fátima y Gregorio, por siempre estar. Gracias Grecia por tu optimismo y tu apoyo incondicional. Gracias por ser mi "community manager" ☺.
Fátima, sin ti nada de esto hubiese sido posible, gracias por tu generosidad y entrega para toda la familia.

Je voudrais également remercier mi novio Julien, pour son encouragement, pour son soutien et amour. Merci pour avoir supporté mon caractère, bien qu'il ne soit pas facile de nature, et qui s'est souvent empiré à cause des nuits blanches passées lors de la rédaction de ce manuscrit. Grand merci pour ta compréhension !
Merci également à madame Jacqueline et monsieur Gérard, ainsi qu'à Émilie, Sébastien et Aurore (merci pour tes bisous du haut de tes 2 ans), pour votre intérêt à mon travail et votre encouragement pendant tout ce temps-là.

Agradezco además a mis tías Miledy, Leocadia; a mis primas Dennis, Eléxida, Carmen, Fanny, Karina, Elvia, Jenny, Idalma por entender mi "weirdness" y apoyarme. Así como mis entrañables amigas Miosotis, Melissa y Dayelin, que me han demostrado que los verdaderos amigos no conocen de distancias, y que el cariño y la amistad pueden atravesar el atlántico y a veces un poco más…

Thanks to my super team -supporters, either as my life-coaching, hiking, or sharing some beers: Orlando (love you Orly), Néstor (el españolete), Geoffrey, Yves, Misael, Néstor (le Grec), Dinesh, Anthony, Joanna, Delphine.

Summary

Introduction 1

Chapter 1: Graphene-based carbon (nano)cones: a review 5

1. Introduction 7
2. The various ways to generate carbon conical morphologies 9
2.1 Structure-driven conical forms 9
2.1.1 Wedge disclination (introducing pentagon defects)
2.1.2 Screw dislocation (the "cone-helix" model)
2.1.3 Radial edge dislocation
2.2. Texture-driven conical forms 27
2.2.1. Graphene oblique with respect to the cone axis
2.2.2 Graphenes parallel to the cone axis
2.2.3 Graphene perpendicular with respect to the cone axis:
2.3 Morphology-driven (process-driven) conical forms 37
2.3.1. During growth
2.3.2. Post-growth
3. Property and applications of conical carbon morphologies 43
3.1. Properties 43
3.1.1. Electronic properties
3.1.2. Mechanical properties
3.2. Applications 45
3.2.1. Electron field-emission
3.2.2. Scanning probe microscopies (SPM)
3.2.3. Electrodes
3.2.4. Adsorption-based applications
4. Conclusions 54
References

Chapter 2: Synthesis process and formation mechanisms of carbon nanocones by CVD 65

1. Summary of the previous work (Allouche's thesis) 67
1.1. The basis of synthesis process 67
1.2. Description of the morphologies obtained 70

1.3. Pyrolysis conditions *vs* morphology type 73
1.4. Detailed description of the conical sub-morphology: the Spiky-Bead case (SB) 75
1.5. Growth mechanisms 81
1.6 Questions and remarks 85
2. The synthesis of carbon-cone-bearing morphologies at CEMES 86
2.1. Introduction 86
2.2. Description of the process 87
2.2.1. Furnace description
2.2.2. Preparation of substrate
2.2.3. Process conditions
2.3. Towards the synthesis of Spiky Short-Fibers (SSF) 91
2.3.1 Reference conditions (1390°C, CH_4/H_2 = 1/2, total flow rate = FLOW3)
2.3.2. Decreasing CH_4/H_2 by decreasing CH_4 and leaving H_2 unchanged (hence reducing the total flow rate)
2.3.3. Decreasing CH_4/H_2 by increasing H_2 and leaving CH_4 unchanged (hence increasing the total flow rate)
2.3.4. Defining the conditions for the synthesis of the SSF morphology
2.4. Understanding further the growth mechanisms 100
2.4.1. The deposition process
2.4 2. The cone description (SEM, TEM, Raman) and growth
3. Conclusions 114
References

Chapter 3: Fabrication and mounting process of carbon cones as scanning microscopy probes 121

1. Scanning Probe Microscopy (SPM) techniques 123
2. Fabrication and mounting process of SPM probes 124
2.1. Top-down micromachining process 125
2.2. Bottom up manufacturing process 126
3. Carbon nanocones as SPM probes 129
3.1. SSF carbon nanocone tips: description and characteristics 130
3.2. Mounting process 131
3.2.1. Cantilever specifications
3.2.2. Gluing process
3.2.3. Welding Process
4 Characterization of the carbon nanocone probes 137
4.1. Resonance frequency 137
4.2. Tip geometry 138
4.3. Tip alignment 140
4.4. Structural integrity of the carbon probe once mounted as a probe 142

4.4.1. High Resolution Transmission Electron Microscopy (HRTEM)
4.4.2. Raman spectrometry
5. Conclusions 147
References

Chapter 4: Application tests of nanocone probes for various SPM modes 151

1. Introduction 153
2. Non-electrical modes 153
2.1. Atomic Force Microscopy (AFM) – Topography 154
2.1.1. Principle and notions
2.1.2. Imaging quality and performances
2.1.3. Capability of the carbon nanocones as AFM probes
2.1.4. Sample description and imaging protocol and performances
a) Au nanoparticles deposited on Si wafer
b) Highly-Oriented Pyrolytic Graphite (HOPG)
c) Single silicon crystal surface (wafer)
2.1.5. Durability test: wear resistance of the carbon nanocones
a) Description of the wear resistance test protocol
b) Comparison of probe performances
2.2. Peak Force Quantitative Nano-Mechanical AFM (PFQNM-AFM) 170
2.2.1. PFQNM-AFM mapping - Principle and notions
2.2.2. Mechanical properties of the probes used (both nanocone- and Si-based)
a) Cantilever sensitivity and contact force
b) Spring constant
2.2.3. Comparison of the mechanical properties of the different probes
2.2.4. Capability of the carbon nanocones as PFQNM AFM probes
a) Apparent tip radius
b) Young modulus mapping on a homogeneous sample
c) Young modulus mapping on a heterogeneous sample
2.2.5. Evolution of the measurement parameters as a function of the contact force
3. Electrical modes 184
3.1. Conductive-AFM (C-AFM) 187
3.1.1. Principle and notions
3.1.2. Capability of the carbon nanocones as C-AFM probes
a) Sample description, imaging protocol and performances
b) Current-voltage (I-V) curves and current mapping
3.2. Scanning Tunneling Microscopy (STM) 196
3.2.1. Principle and notions
3.2.2. Capabilities of the carbon nanocones as STM probes
a) Sample description, imaging protocol and performances
b) Au substrate

c) ITO substrate
d) HOPG substrate
3.3. Kelvin Force Microscopy (KFM) 203
3.3.1. Principle and notions
3.3.2. KFM signal, contrast, and resolution parameters
3.3.3. Capability of carbon nanocones probes for KFM
a) Samples and measurement imaging protocol
b) Charge injection test
c) KFM - Negatively-charged latex nanoparticles assembled by nanoxerography onto a PMMA substrate
d) KFM - Aluminum alloy A2024 sample
4. Conclusions 213
References

Conclusions & perspectives 217

Annexes 225

Résumé en français 231

Abstracts 257

Introduction

« Caminante, son tus huellas
el camino y nada más;
Caminante, no hay camino,
se hace camino al andar.
Al andar se hace el camino… »

Antonio Machado

Carbon materials are suitable for many applications since they may exhibit exceptional and versatile physical (electrical, thermal, and mechanical) properties. Those were found to be particularly enhanced in carbon nanoforms, i.e., carbon morphologies for which at least one dimension is below 100 nm. The emblematic representatives of such carbon nanoforms are typically nanotubes and graphenes, which both have generated a huge amount of work and publications worldwide, the latter having been the subject of a Nobel Prize in 2010, whereas it was once considered earlier to dedicate a Nobel Prize to the former as well. However, another carbon nanoform is worth considering while it has not been the focus of the same worldwide attention, i.e., carbon conical forms (carbon nanocones). Carbon nanocones may exhibit specific geometric characteristics such as needle-like shape, high aspect ratio, various cone angles, and micron-size bases along with nanosized apex at the tips. They may also exhibit the same variety in the number of walls, texture and nanotexture as carbon nanotubes. Correspondingly, they are expected to exhibit better mechanical stability than the narrow cylinder morphology which is typical of their carbon nanotube counterparts. They also show interesting thermal and electrical properties providing graphene layers are perfectly aligned with respect to the cone axis. All of this can make conical forms excellent candidates for a variety of applications spanning from nanoelectrodes, high surface area adsorbing materials electron emitters, and probes for near-field microscopies (so-called scanning probe microscopies - SPM).

CEMES has been studying for several years the formation of a variety of carbon nanocones based on the deposition of pyrolytic carbon onto individual carbon nanotubes as support. Although the formation mechanisms may still be debated, they were successfully tested as electron emitters in a previous work, actually allowing designing a cold-field emission electron source with the best performances ever. This background was an excellent motivation to investigate the same carbon nanocones for another promising application, namely as probes for SPM. For SPM, which aims at acquiring high resolution images of three-dimensional features at nanoscale and measuring the local properties of a surface, sharp carbon conical morphologies as probes can combine the mechanical stability of a cone and the high aspect ratio of a narrow diameter cylinder, which make them potentially superior to the commonly used carbon nanotubes and commercial silicon probes. However, unlike carbon nanotubes, which have been extensively studied for this application, only few works concerning the potential of carbon nanocones for SPM probes are reported in the literature. This can be due to many factors related to the synthesis processes and subsequent technical issues. Indeed, few studies are reported about the synthesis, properties and applications of conical carbon forms. Needle-like conical forms can be produced by many methods such as CVD, plasma, etc. Most of these processes are limited either in yield, density, control of the geometric shape, control on the material structure, and respect of the structural integrity, as in the case of plasma-assisted techniques. On the other hand, the handling of the cone morphologies as individual objects so that to mount them onto SPM-specific supports such as cantilevers is not straightforward and comes with numerous technical issues. Likewise, attempts for directly growing conical tips onto cantilevers by various means have also been conducted, but none of these techniques allowed an individual growth and control of the conical forms to be obtained. Therefore, preparing SPM probes based on individual carbon cones by means of robust and easy processes appeared as a

promising perspective but also as a challenge to meet. Additionally, the literature is quite limited regarding the variety of the SPM modes which conical carbon probes were tested for.

In this work, the feasibility of using CVD-prepared carbon nanocones as SPM probes is evaluated from the synthesis of the carbon cones to their testing for different SPM modes. The study is reported as follows:

- In **Chapter 1**, an exhaustive bibliography study describing the main carbon conical forms reported in the literature in all aspects from their synthesis process, physical characteristics, and tested applications is presented.
- **Chapter 2** depicts the original CVD-growth process used for the high yield synthesis of unique carbon cone-bearing morphologies with controlled geometry and dimensions, named Spiky Bead (SB) and Spiky Short Fibers (SSF). The carbon cone inner structure, texture, and nanotexture is studied by scanning electron microscopy (SEM), transmission electron microscopy (TEM) and Raman spectroscopy, and the formation mechanisms are discussed so that to bring, we believe, a new insight on the overall mechanisms of pyrolytic carbon deposition.
- **Chapter 3** presents different technical approaches for mounting the SSF morphologies as SPM probes. The carbon cones once mounted as probes are characterized by different techniques (SEM, TEM, Raman).
- in **Chapter 4**, the nanocone morphologies mounted as SPM probes are evaluated for diverse electrical and non-electrical SPM modes, by considering a variety of criteria such as performance, durability and versatility of the probes. All along these tests, comparisons with metal or commercial silicon probes are also performed.
- Finally, a section dedicated to the **conclusions and perspectives** highlights the main findings concerning, on the one hand, the synthesis mechanisms of the conical forms presented in this work, and on the other hand, their performances as tips for each of the tested SPM modes. Possible improvements are also identified and advices are given to implement them in forthcoming works.

-Chapter 1 -

Graphene-based carbon (nano)cones: a review

« Douter est le début de la sagesse.
Douter nous amène à nous interroger, et
éventuellement à découvrir la vérité »

Pierre ABÉLARD

Chapter 1: Graphene-based carbon (nano)cones: a review

1. Introduction

Carbon is an outstanding material with interesting physical and mechanical properties. The first evidences of carbon forms were related to either so-called "amorphous" carbon (later-on actually discovered to often be graphenic and turbostratic, instead of really amorphous), or diamond, or graphite [*1Delhaes2011*, *2Inagaki2014*]. Graphite is based on sp^2-hybridized carbon atoms and consists of a three-dimensional crystal made of graphene sheets, piled-up in an ordered way so that to generate a hexagonal crystallographic structure, and because of this tends to adopt planar forms, where "planar" may apply to large scale (e.g., microsized flakes) as well as to local scale (e.g., nanopore walls). Diamond is based on sp^3-hybridized carbon atoms and results from the ordered stacking of carbon tetrahedra in all directions of space so that to generate a face centered cubic structure, and because of this tends to adopt isometric forms. Later on, *sp*-hybridized carbon atoms were found to adopt linear [*3Hu2009*] or loop [*4Fang2019*] forms, although specific conditions have to be fulfilled for their synthesis and observation due to the high instability of the configuration. All of these are carbon forms with distinctive features and properties, because of the unique carbon atomic structure and subsequent hybridization versatility. Indeed, the ability of carbon atoms to create covalent bonds with other carbon atoms in various ways allows the formation of diverse morphologies with a wide structural and/or textural versatility. Graphenic materials, in particular, due to the high anisotropy of the building element (the aromatic ring), can adopt many forms in addition to planar ones, with respect to the three directions of space:

- "0D": solid spheres (onions) [*5Ugarte92*, *6Harris1994*], hollow spheres either with single-graphene (fullerenes [*7Kroto1985*]) or multigraphene (shells [*8Saito1995*]) walls, which carbon blacks could also somehow belong to [*9Donnet1993*],
- 1D: chains of nanoparticles (as for some carbon blacks [*9Donnet1993*]), filaments (e.g. nanotubes, either single-walled [*10Endo1976*, *11Iijima1993*, *12Bethune1993*] or multi-walled [[*13Radushkevich1952*, *14Iijima1991*] and nanofibers [*15Rodriguez1995*])
- 2D: flakes, e.g. graphene (either single layered [*16Geim2010*], or multi-layered whatever the structure (i.e., either turbostratic or graphitic [*17Monthioux2017*]), nanoribbons [*18Terrones2010*], etc.
- 3D: "trees" [*19Ajayan2000*], foam [*20Wu2015*], glassy carbons" [*21Harris2004*], etc.

Among this large typology are also conical graphenic forms, which can occur in nature [*22Jaszczak2003*, *23Glad2014*] or result from various synthesis processes [*24Eksioglu2006*, *25Dumpala2008*]. The texture (i.e., the way graphene layers display in the morphology [*17Monthioux2017*, *26Allouche2005*]) of carbon cones depend mainly on the “layer-to-layer” interaction energy between the different graphene sheets. Indeed, their texture and stacking

arrangement can influence the nucleation, growth, and properties of the conical morphologies [*22Jaszczak2003*, *27Dimovski2017*]. The different conical forms can then be defined by the orientation of the graphene layers with respect to their axis, even though the axis can be solid or hollow, hence forming a central channel in the latter case. According to the inclination angle (from 0 to 180°) of the layers with respect to the axis, different conical shapes with a variety of apex angles can be formed. Of course, some particular carbon deposition conditions (e.g. precursors, growth rate, temperature, carbon concentration, etc.) during the growth process can play a key role. However, the related growth mechanisms and the reasons why graphene layers adopt a particular configuration with respect to the cone axis remain not clearly understood.

The first evidence of the synthesis of conical forms was reported by Bacon in the sixties [*28Bacon1960*, and earlier references within]. Since then, other conical carbon morphologies were produced and published in the literature, again based on a large variety of crystallographic structures (either related to graphite, or diamond, or amorphous) and also able to exhibit a large versatility in texture.

In addition to the intrinsic interest of understanding why and how such amazing morphologies may form, carbon cones may exhibit a specific interest for some applications over other carbon morphologies, e.g. carbon nanotubes in first place. In spite of this, from our knowledge, review papers attempting to categorize carbon conical forms with respect to their growth mechanisms, and/or synthesis processes, and/or structures/textures, and/or potential applications are only few and partly unsatisfactory, although they are quite useful bibliographical sources: [*27Dimovski2017*] is not exhaustive; some hints about structural models are given in [*24Eksioglu2006*] but this publication was published more than 10 years ago and may need updating, it also proposes too many categories which make the landscape confusing, and we believe that a simplification is possible; a book chapter about carbon microtubes and cones [*25Dumpala2008*] focuses mainly on synthesis process aspects; then finally, the most recent review paper on conical carbon forms mainly concerns nanohorns and their chemical applications [*29Karousis2016*].

We therefore propose in this *Chapter* an updated, tentatively exhaustive review on the typology of carbon conical forms, the various ways for generating them, and their potential applications. However, a key issue to solve prior to start the work was to determine what criterion the various cones dug out from the literature should be sorted by. After considering chronology, process types, and growth mechanisms, we have decided to categorize them according to the causes, whatever they are, that drive the morphology towards adopting the conical shape preferably to any other, and to investigate the literature from this standpoint. We thereby believe our contribution to the field to be original.

The present *Chapter* is focused on carbon conical morphologies, hence it will not include a thorough report on carbon filamentous morphologies, which is plethoric in the literature, unless there are similarities in texture and growth mechanisms which are worth mentioning. It will not review on diamond cones either, as they barely compare to the kind of all-graphene carbon cones this thesis work is dealing with, from structural, textural, and nanotextural points of view.

2. The various ways to generate carbon conical morphologies

After carefully analyzing the various conical morphologies reported in the literature, it came out that the overall conical shape is due to three main causes: *(i)* structural, mostly by means of the introduction of disclinations and/or dislocations in the graphene lattice [*30Harris1977*, *31Rozhkov2018*]; *(ii)* textural, i.e. related to the overall relative orientation of the graphene stacks with respect to the cone axis with no relation with any structural defect; and (iii) process-related, i.e., the conical shape is enforced by the synthesis process regardless of the two previous causes, either during the formation step, or as a post-formation step, for instance by means of shaping, trimming, etching, etc.

2.1 Structure-driven conical forms

A detailed analysis of the aspects that have to be considered in this *Section* was reported in a recent review paper [*29Karousis2016*], yet it is focused on conical carbon forms so-called "nano-horns" (see below). It is useless to rephrase this excellent work; hence we will just provide the information on what seems to be the most important. Readers specifically interested in this *Section* are invited to also read this paper to collect more information.

The geometrical shape of all conical morphologies is determined exclusively by their size and cone angle. Considering mere geometrical aspects, a cone curvature in a graphene sheet can be achieved in three different ways (**Fig.1**).

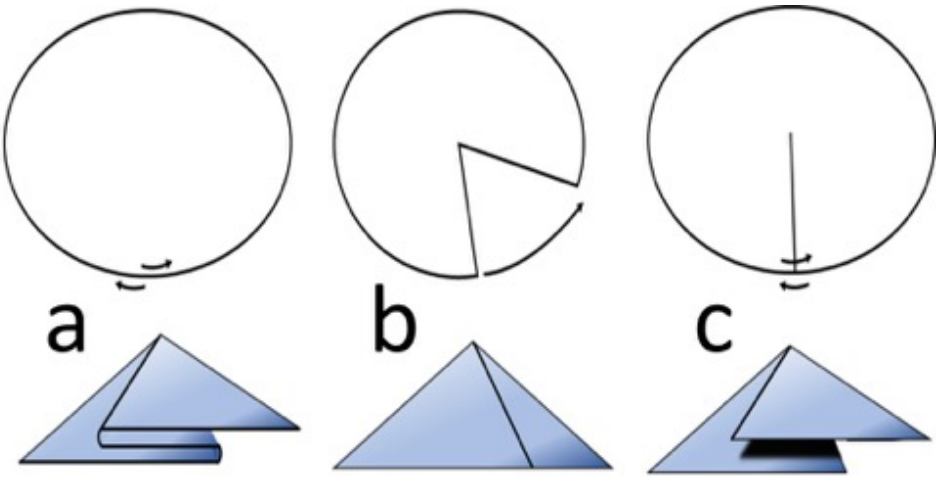

Figure 1: *The various geometrical ways of forming a conical shape from a flat sheet. Adapted from [*29Karousis2016*]* ***(a)*** *making a pair of folds as for generating a funnel.* ***(b)*** *removing a triangular segment from the graphene sheet and reconnecting the edges.* ***(c)*** *creating a cut on the graphene sheet but overlapping the edges, in order to form a helix.*

The cone angles generated can be different for each geometrical model as changing the cone angle changes the curvature, and in addition, the cone helicity varies along the cone axis, as the curvature of the cone surface gradually changes [*32Ge1994*, *33Sattler1995*]. So, understanding the geometrical parameters that can determine the way and degree of curvature of conical shapes is important, e.g. for the development of potential applications. When considering a

graphene surface, no example corresponding to case (a) in **Fig.1** (obtainable by coupling a screw and a wedge dislocations) has been found yet. On the other hand, cases (b) and (c) in **Fig.1** appear to be quite common in the literature, and correspond to the introduction of a wedge disclination, and to the coupling of a wedge disclination and a screw dislocation, respectively. The former (case (b)) may also be described as the "pentagon model" whereas the latter (case (c)) may also be described as what is often referred to as the "cone-helix model" in the literature, after the designation proposed by [*34Double1974*].

2.1.1 Wedge disclination (introducing pentagon defects)

The "pentagon model" describes most of the seamless conical geometries having a cap and large apex angles in the range ~19° to ~113° [*32Ge1994*], *35Ihara1996*, *36Krishnan1997*]. Such apex angles are indeed formed by the incorporation of pentagons within the graphene lattice because of the creation of a wedge disclination. This disclination corresponds to topological defects, constrained by the periodic structure of the crystal, here the graphene lattice [*30Harris1977*]. Considering the hexagonal periodicity of the graphene lattice (six-fold symmetry), the only way of creating this disclination without altering the lattice is by removing a wedge portion from the graphene sheet, the wedge angle being a multiple of the sixth of a circle, i.e. 60°. As a consequence, and according to the Euler theorem [*37Ebessen1998*], pentagons are incorporated within the hexagonal graphene lattice (**Fig.2a**).

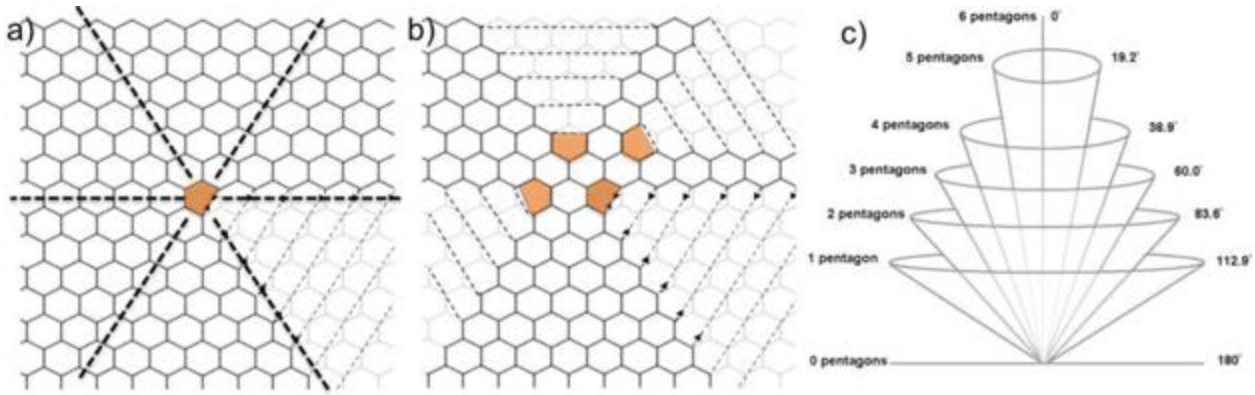

Figure 2: *Illustration of the creation of conical morphologies by the incorporation of pentagons within a graphene lattice.* ***(a)*** *graphene sheet with one pentagon in the lattice.* ***(b)*** *graphene sheet with 4 pentagons in the lattice.* ***(c)*** *Relationship between the number of pentagons incorporated in the graphene lattice and the corresponding apex angle value of the cone formed. From [*29Karousis2016*].*

This spontaneously creates a conical morphology with an apex angle related to the number of pentagons and to the disclination angle as [*36Krishnan1997*]:

$$\alpha = 2.sin^{-1}\left(1 - \frac{n}{6}\right) \qquad (1)$$

where α is the cone apex angle, and n corresponds to the number of pentagons (hence n x 60° is the disclination angle).

In consequence, a discrete number (from 1 to 5) of pentagons is introduced in the graphene lattice without creating noticeable constrains elsewhere than at the bond angles involving the carbon atoms at the location of the pentagon(s) (**Fig 2**). Of course, the bond angles between the atoms from the graphene layer are also slightly constrained because of the curvature of the cone surface thus created, and the constrain decreases as carbon atoms farer from the apex are considered, due to the continuously decreasing graphene curvature. This is important as the graphene surface reactivity increases as the curvature increases. As a geometrical consequence, wedge disclination-driven cones will present just only five possible apex angles corresponding to the increasing possible, discrete number of pentagons, up to five (**Fig.2c**). For six and twelve pentagons, half a sphere and a full sphere will be created, respectively. For a number of pentagons in-between (7 to 11), a curved surface will be created with no chance for it to close.

There have been several attempts in the literature to classify such a family of single graphene cones by discriminating between the various possibilities of combining the pentagons and other geometrical considerations [*38Balaban1994*, *39Klein2006*]. However, they are pure geometrical works which do not relate necessarily with real cases, as it is likely that some configurations will be preferred to others because of energetic reasons.

Wedge disclination-based single-graphene cones were not actually found isolated before 1994 [*6Harris1994*], but a lot of work was carried-out after the discovery of fullerenes [*7Kroto1985*] from which researchers started to play with the amazing geometry rules that govern the construction of curved surfaces from the combination of hexagons, pentagons, and heptagons. The fullerene era has put under the spotlight the Euler's theorem which we have already referred to above, and which became very popular in the field despite it is purely geometric and had nothing to do with carbon and material crystallographic structure in first place. Few years later, the effect of pentagons (and heptagons) on the graphene topography was investigated thoroughly when studying how multiwall nanotube ends may close, starting right after Iijima published his landmark paper [*14Iijima1991*].

In 1994, then, the occurrence of nanosized single-graphene cones was reported by Harris [*6Harris1994*] (**Fig.3c**). They were found in a microporous carbon "soot" synthetized from the evaporation of a graphite electrode via arc discharge and then subjected to toluene extraction, mild oxidation conditions (CO_2 flow, 850°C), and finally very high-temperature treatment (2500-3500 K) by electron bombardment under vacuum. It is likely that the oxidation step has little to do with the formation of the single-graphene nanocones since the damages it has induced to the graphenic walls of the microporous carbon were probably closed back by the final heat-treatment. On the other hand, what is the relative part, in the nanocone formation mechanisms, of the electron bombardment effect with respect to the high-temperature effect in the uncommon heat-treatment process used is not clear. Indeed, such a process may have induced re-evaporation of the soot material and subsequent carbon redeposition [*40Klabunde1994*] as the observed nanocones. It is worth noting that the graphenic nature of those nanocones was actually not demonstrated at that time, but was just presumed from the high-resolution transmission electron microscopy (HRTEM) images, basically based on the guessing that the conical nanomorphologies could not be otherwise than graphene-based, once the chemical nature of the starting material and the characteristics of the other phases produced from it were considered. The guessing was right. However, they were no further

studied until they were rediscovered and named as "nanohorns" by Iijima *et al*., who reported about them at the Boston MRS meeting in 1998, and then published their observations in 1999 while demonstrating that such morphologies could be produced in significant quantities [*41Iijima1999*]. The paper reported results from electron diffraction and electron energy loss spectroscopy (EELS), although no diffraction pattern nor EELS spectrum were actually shown. Although the comment on the diffraction patterns was partly wrong (the patterns could definitely not be that of "polycrystalline graphite"), the graphenic nature of the morphologies was ascertained.

In both Harris's and Iijima's experiments, nanohorns were obtained roughly following similar conditions, from the evaporation (by arc or laser) of graphite (or HOPG) in reduced pressure (of Ar or He), i.e., conditions similar to that used to produce fullerenes. Due to their single-graphene nature, nanohorns aggregate in order to tentatively share their π electrons, i.e. the cohesive forces are van der Waals ones, the same way as single wall carbon nanotubes (SWCNTs) aggregate into bundles. However, unlike SWCNTs, nanohorns have a much lower aspect ratio and are geometrically all different from each other, with a surface including both positive and negative curvatures, hence they gather into aperiodic ball-like nanoparticles (**Figs.3a-3b**), as opposed to SWCNTs, which are able to gather into bundles presenting crystallographic periodicities.

In [*41Iijima1999*], a typical nanohorn was described as a 2-3 nm cylindrical tube with a length of 30-50 nm and a terminal conical shape with a cone angle of ~20° (revealing the presence of 5 pentagons). However, if nanohorns were really all alike, they would aggregate differently, i.e., according to somehow periodic assemblies. In fact, nanohorns have to be seen as carbon atoms condensing into a graphene lattice while attempting to curve into a close surface in order to eliminate dangling bonds as quick as possible, but which failed becoming nanotubes because no catalyst was there to help. Therefore, they exhibit a whole variety of morphologies, which may include any of the whole range of cone angles [*42SuarezMartinez2013*] hypothesized in **Fig.2c**, as well as heptagons [*6Harris1994*]. Of course, this observation may vary with the synthesis conditions.

Because they always gather and overlap into ball-like nanoparticles, making observing both nanohorn ends difficult, it was questioned whether they were fully closed surfaces or might possibly be opened at the end opposed to the sharpest conical end. The latter option was ruled out once BET measurements have provided specific surface areas in the range of 300 m^2/g [*43Murata2000*], which can be expanded by a factor of 3 to 4 upon oxidation [*44Murata2001*, *45Bekyarova2003*, *46Utsumi2005*], obviously due to the opening of the graphene lattice giving access to the inner surface. From **Fig.3c** and many others alike published in the literature, it is clear that nanohorns do not correspond to a single morphology or molecular structure.

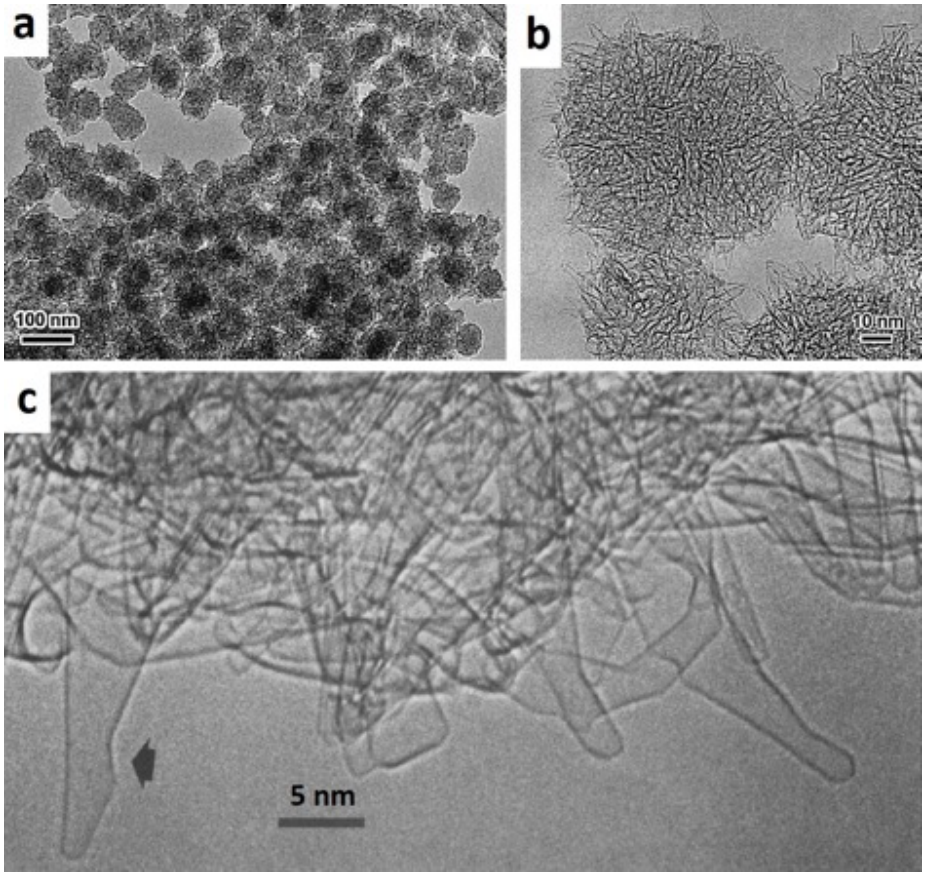

Figure 3: (a) *low magnification image of the ball-like nanoparticles made from aggregated nanohorns.* ***(b)*** *higher magnification image of ball-like nanoparticles such as imaged in (a).* ***(c)*** *The first nanohorns ever imaged. The arrow indicates the location of a heptagon. (a) and (b) are from [*41Iijima1999*], (c) is from [*6Harris1994*].*

Models for nanohorn assemblies have been proposed due to the need for simplification required when attempting property modelling and prediction, however, because of the actual aperiodic structure and asymmetrical morphology of nanohorns, all are wrong and misleading. Indeed, they suggest cylindrical main bodies, hollow aggregate core, covalent bonding between nanohorn ends, uniform cone angles, and a radial display, which all are irrelevant features, statistically speaking (**Fig.4**).

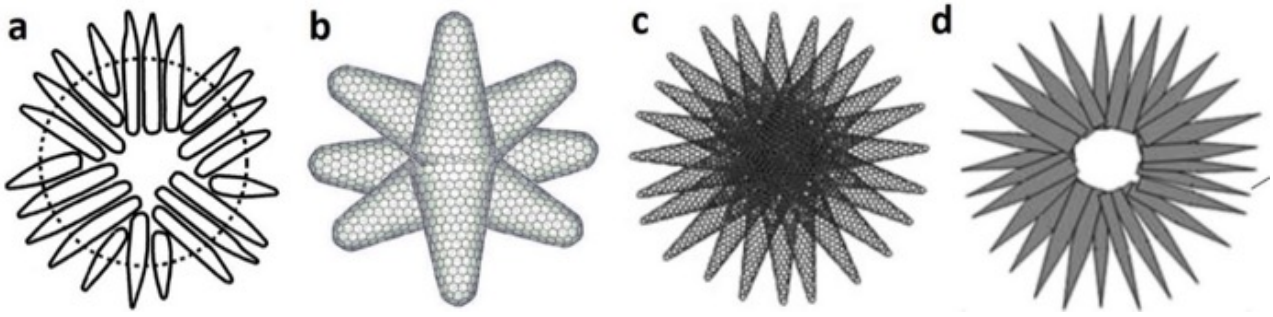

Figure 4: *Various models from the literature proposed for a ball-like nanoparticle made from aggregated nanohorns such as that imaged in* ***Fig.3****.* ***(a)*** *from [*41Iijima1999*];* ***(b)*** *from [*47Pagona2007*];* ***(c)*** *from NEC website;* ***(d)*** *From [*48Shi2017*].*

Beside CO_2 laser ablation of a graphite target, nanohorns were shown to be obtained by various other ways, such as a torch arc in open air [*49Takikawa2002*], an electric arc immersed in liquid nitrogen [*50Wang2004*], the pulsed arc-discharge in air [*51Yamaguchi2004*], and the heating of a graphite substrate by electromagnetic induction giving rise to Joule heating up to 3200°C, although a significant amount of graphene veils seems to be produced concomitantly, in close association with the nanohorns [*52Pagura2010*].

Due to their single-graphene nature which makes them likely to exhibit specific properties different from that of regular nanosized objects, nanohorns were extensively studied for about 10-15 years, generating an abundant literature. This literature has been already gathered and thoroughly commented in review papers [*29Karousis2013*] and book *Chapters* [*53Yudasaka2008*] which the readers are invited to read for further details.

Also in 1994 was reported for the first time the formation of disclination-driven multi-graphene nanocones [*32Ge1994*]. They were prepared via the condensation of carbon vapor (obtained by resistively heating a carbon foil) onto a cooled-down (-30°C) HOPG substrate maintained at low pressure (in the range of 10^{-8} Torr). These cones, whose typical dimensions were of ~20 nm in length and ~5-10 nm at the base, were described as presenting a fullerene-type cap apex, and cone angles of ~19° (the smallest angle possible for this kind of cones, **Fig.2c**). However, it is worth noting that neither the graphenic nature nor the graphene orientation were demonstrated. The description was merely based on the presumable carbon nature because of the carbon source on the one hand, and on the systematic cone angle value of 19° which was compatible with the occurrence of 5 pentagons at the cone apex on the other hand. The cone surface is smooth at nanoscale, suggesting it is actually made of a graphene layer. Of course, the assumption appears likely nowadays, thanks to what was learnt from the study of nanohorns, and moreover thanks to the subsequent large-scale synthesis of conical morphologies with similar textures exhibiting the whole distribution of discrete cone angle values of **Fig.2c** that was reported few years later by [*36Krishnan97*].

In Krishnan *et al.*'s material, prepared through the pyrolysis of a mixture of liquid hydrocarbons in an arc-generated plasma torch process, the cones indeed showed apex angles of 123.6°, 86.6°, 60.0°, 38.9°, 19° corresponding to 1-5 pentagons incorporated in the graphene sheet as allowed by the pentagon model as predicted in [*32Ge1994*]. The objects are amazing regarding their geometrical perfection and dimension uniformity, in the micrometer range in diameter, but usually below 50 nm in thickness (**Figs.5a** to **5e**). Surprisingly, the distribution of the cone angles within the material did not follow what is requested by energetic considerations [*35Ihara1996*], i.e., the occurrence frequency should increase as the number of pentagons decreases, because corresponding to a decreasingly stressed structure, namely 180° (no pentagon), then 123.6° (1 pentagon), then 86° (2 pentagons), etc. Instead, the most frequent were observed to be 180°, then 60° (3 pentagons), and then 38.9° (4 pentagons). Treacy and Kilian [*55Treacy2001*] have tentatively explained this by proposing that the "pentagon road" (meaning that the pentagons are at the origin of the conical form) is preceded by a so-called "designability mechanism" (in which early carbon seeds do not contain pentagon(s) yet) whose possible existence is supported by molecular-dynamics simulation [*56Kawai2002*]. While the former only consider the enthalpy minimization, hence resulting in the highest number of pentagons being the less frequent, combining with the latter also allows considering entropy,

which is likely to modify the ranking in the frequency of occurrence. Zhang *et al.* [*57Zhang2006*] however, by considering the competition between entropy and free energy, obtained an opposite result where the 5-pentagon cone came out as the most stable case, which they said to be consistent with experimental observations, but it is not right [*35Ihara1996*].

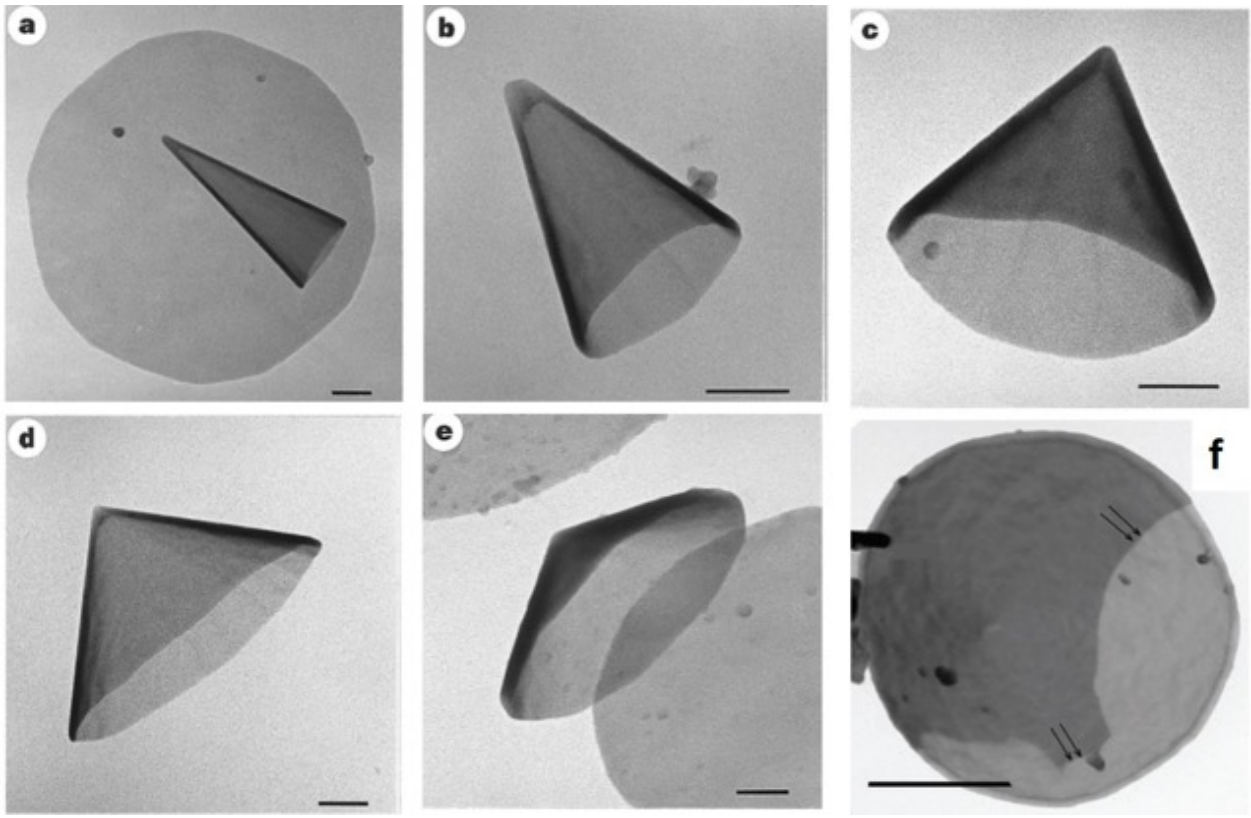

Figure 5: *From* ***(a)*** *to* ***(e)*** *examples of the type of carbon nanocones obtained in [*36Krishnan1997*] exhibiting the five possible cone angles as predicted by [*32Ge1994*]. Nanodiscs are also shown in (a) and (e). Scale bars = 200 nm.* ***(f)*** *Evidence for a partly completed layer (edge indicated by the double arrows) covering a nanocone surface. Bar = 500 nm [*54Naess2009*].*

From the texture point of view, each cone can be described by a stack of similar single graphene cones, such as a pile of more or less pointy cones (**Fig.6a**). However, a close examination of the morphologies in **Fig.5** and further studies [*54Naess2009*] showed that the edge line of the open base of the cones tends to polygonize, hence suggesting a tendency of the cone wall to form facets, more frequently on large angle cones according to [*54Naess2009*]. From the structural point of view, it seems that both nanodiscs [*61Garberg2008*] and nanocones [*54Naess2009*] are a mixture of extended graphene layers stacked according to the graphitic (Bernal) structure, and short graphene layers with the turbostratic structure, the latter phase supposedly embedding the former. This is somehow consistent with the observation of facets, which are a way to allow building the 3D periodicity with stacked graphenes. Upon a very high temperature treatment (2700°C), the whole cones are said to become graphitic, yet not as single crystals [*54Naess2009*]. However, this would require to be ascertained further, as neutron and electron diffraction results were inconsistent (presence of the *101* or *112* diffraction spots in the former, which were absent in the latter).

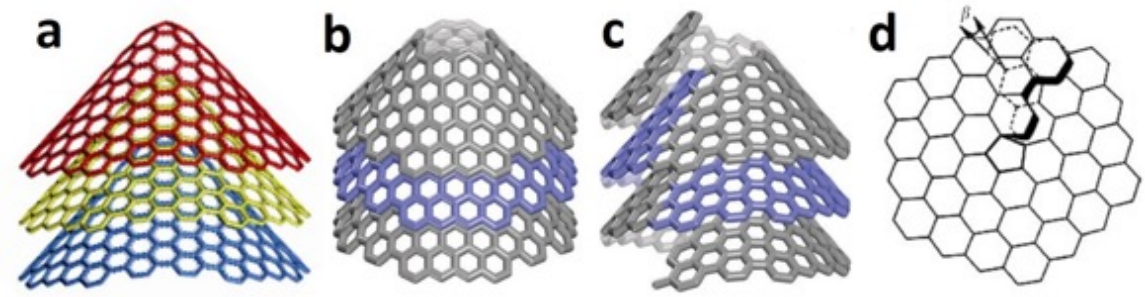

Figure 6: (a) *sketch of a stack of wedge-disclination-generated graphene cones, corresponding to the cone-stack configuration (model taken from [*58Cheng2012*]).* ***(b)*** *sketch of a stack of wedge-disclination-generated truncated graphene cones, corresponding to the lampshade-stack configuration. Cone angle is 83.6°, corresponding to a wedge angle of 120°.* ***(c)*** *The equivalent of (b) with a cone-helix configuration, here with a hollow core (see Section 2.1.2). ((b) and (c) models taken from [*59Zhu2017*].* ***(d)*** *top view of a model proposed by [*60Amelinckx1992*] for explaining the possible existence of cone-helix configuration with solid core: the same graphene disc is cut along a line of bonds and then made start to overlap on itself so that to generate a pentagon at the center, which becomes an apex, and make the overlapped layers to be rotated from the angle β.*

Some studies have suggested that nanohorns might form from the closing of single graphene layers previously formed in the process [*56Kawai2002*, *62Kasuya2002*]. It is unlikely, because it is intuitively understandable that the conditions (high temperature and reduced pressure) for the synthesis of single-graphene nanohorns in both [*6Harris1994*] and [*41Iijima1999*] experiments may rapidly generate pentagon-rich closed graphene structures. Indeed, because of the lack of other alternatives (carbon atoms are the only ones available, and in low concentration), it is also a matter of energy minimization that the solid that is being built as a graphene try to form a closed surface as fast as possible, which also makes that nanohorns and morphologies alike cannot be otherwise than nanosized. In comparison, it may appear counter-intuitive that the formation of pentagons is favored in the conditions (high temperature, enhanced pressure, H-rich atmosphere) to grow nanocones and nanodiscs in [*36Krishnan1997*] experiments. However, all the experiments, including others such as the induction heating used by [*52Pagura2010*] to produce nanohorns share the use of high temperatures (several thousand degrees), and steep temperature gradients, which therefore appear as the key parameters to promote the occurrence of wedge disclinations in the building graphene material. Indeed, such conditions allow atomizing the either solid or liquid carbon source, and enforcing the rapid condensation of carbon atoms, dimers, and trimers into a solid, graphenic product, meanwhile forming pentagons in the course of the process.

It is noteworthy that there is no doubt that the multiwalled nanocones described by [*36Krishnan1997*] obey the "cone-stack" model, i.e. they definitely cannot be a single graphene sheet coiled around the axis as a helix (the "cone-helix" model, see next *Section*) for the following reasons: *(i)* the cone angle values experimentally observed are discrete, and correspond to that predicted for an increasing number of pentagons from 1 to 5; *(ii)* cone surfaces do not exhibit any step line; *(iii)* The conical wrapping of a graphene disk over itself as exampled by **Fig.6d** by forming one pentagon at the center [*60Amelinckx1992*] is unlikely because inducing too much stress to the C-C bonds involved in the pentagon. Therefore, the central part would have to show some hole*; (iv)* there are evidences (**Fig.5f**) for the occurrence

of partly completed outer layers covering the cones [*54Naess2009*] and the disks [*61Garberg2008*].

Item (iv) above is important as it demonstrates that carbon atoms somehow add to the graphene faces first, which is in contradiction with what is usually considered in the literature since the early studies of so-called carbon whiskers and even pyrolytic carbon deposition [*63Sears1959*, *64Gillot1968*, *65Fitzer1991*], which assume that the growth direction is favored parallel to the graphene face (i.e., carbon atoms add on the graphene edge). This is particularly true in conditions of fast growing. Actually, edge growth probably occurs meanwhile for nanocones and nanodiscs as well, as it is a way an additional layer may complete, after the first seed of it has formed (see **Fig.5f**).

An embodiment from the cone-stack model accounting for the morphologies in **Fig.5** is the same configuration, however with the central part of the starting graphene disk removed, so that to form a corona. Then a sector is removed as for the plain disks, and then the cut edges are put back in contact so that to generate a truncated cone, looking like a lampshade (**Fig.6b**). This has the advantage to remove a source of stress (the pentagons) but, on the other hand, it creates dangling bonds. Hence, there is a competition between both solutions, and the energy of a whole conical system will account for this when building up. Ideally, even though there is no longer any pentagon added to the lattice since the central part is removed, the sector angle to be removed has to be a multiple of 60° as for wedge disclinations in order for the cut edges to close back seamlessly and make possible the continuity of the graphene lattice all over the conical surface. Truncated cones can then be piled-up (**Fig.6b**). However, no individual conical morphology of any size similar to that of [*36Krishnan98*] but exhibiting an empty core has ever been evidenced. The reason can be that, for a limited number of graphenes, the energetic cost of forming pentagons during growth is less than leaving dangling bonds. On the contrary, for a large number of graphenes piled up, the situation could be reversed [*58Cheng2012*, *66Monthioux2007*] and the configuration with a central channel as in **Fig.6b** may be possible.

As a matter of fact, when the number of piled-up cones is high, a filamentous morphology is formed, which prevails over the conical morphology. This is one of the ways herringbone-type (or "fishbone-type") carbon nanotubes are formed, the other one being the cone-helix configuration that will be discussed in the next *Section 2.1.2*. Such herringbone nanotube morphologies, hence built-up from the lampshade-stack configuration, are actually largely reported in the literature, often also designated as obeying a "cup-stack" configuration [*66Monthioux2007*, *67Kiselev1998*, *68Terrones2001*, *69Endo2002*, *70Endo2003*, *71Zhao2012*]. However, most of the claims for a cone-stack configuration are not experimentally supported in the above-mentioned papers, but in [*66Monthioux2007*, *71Zhao2012*] where it was shown that their herringbone CNT materials happened to be dismantled by gentle mechanical stresses applied for, e.g., dispersing the material in order to prepare them for TEM investigation. This is actually the behavior expected for morphologies built-up from graphenic entities that are held together by van der Waals forces only, as for genuine graphite or platelet nanofibers [*66Monthioux2007*]. Even more, as all the morphologies in [*67Kiselev1998*, *68Terrones2001*, *69Endo2002*, *70Endo2003*] were prepared for TEM once, it is likely that they were subjected to a sonication procedure as mentioned in [*67Kiselev1998*], which they withstood remarkably.

Therefore, a cone-helix instead of cone-stack configuration could be suspected for many papers against the claim by the authors such as in the literature above mentioned but [*66Monthioux2007*, *71Zhao2012*].

A second disturbing observation with respect to the cone-stack hypothesis for herringbone CNTs of the papers cited is that the cone angles, yet truncated, should obey the pentagon-rule, i.e., they should exhibit values selected among the five shown in **Fig.2c**, which they do not. This, also, is presumably in favor of a cone-helix stacking model, as it enables any cone angle value from >0° to <180°. However, it is quite possible that, specifically for truncated cones with large diameters, this condition (i.e., the cone angle is related to the virtual presence of pentagon(s)) may be relaxed due to the ability of graphene to accommodate strain by allowing angle deformations [*72Després1995*, *73Després2002*]. This is supported by the fact that herringbone CNTs that were demonstrated to be cone-stacked (based on their mechanical behavior) were however found not to obey the pentagon rule [*66Monthioux2007*]. We will come back to this.

2.1.2 Screw dislocation (the "cone-helix" model)

Other typologies of cones with a wide variability of apex angles that cannot be explained by the incorporation of pentagons in the graphene lattice can be produced through the propagation of a screw dislocation. This is a growth mode that started being popular in the fifties to account for the growth of metallic whiskers [*74Peach1952*], which correspond to a catalyst-free, rapid growth of a crystalline phase in conditions of low supersaturation of the medium (although adding a catalyst may change the latter condition). A similar growth mechanism was then suspected for carbon as soon as whisker-like morphologies were found, as early as in 1957 (referring to the work presented by Tsusuku at the 3rd International Carbon Conference in Buffalo[1], mentioned in subsequent papers). According to Tsusuku, and subsequently to [*22Jaszczak2003*, *34Double1974*, *64Gillot1968*, *75Haanstra1972*] in first place, and then many others [*76Dong2002*[2], *27Dimovski2017*, *59Zhu2017*, *78Kulitskiy2019*], conical morphologies (most of them nanotubes) of this type could be explained by a helical model in which a single, continuous, ribbon-like graphene layer is helically wrapped around the elongation axis of the morphology (sketched in **Fig.7c**). This rotation generates overlapping angles within a continuous range of possible angle values that depend on the extent of overlapping. This induces the formation of conical entities with a variety of apex angle values (0°-180°), i.e., not limited to the five angle values generated by the incorporation of an increasing number of pentagons (**Fig.2c**), although a higher occurrence of specific overlapping angles corresponding to some commensurability configuration between the superimposed layers was sometimes observed [*34Double1974*]. The relationship between the cone apex angle and the overlapping angle is as follows:

[1] The related Proceedings were edited by the American Carbon Society, which has not made them available to literature search engines.

[2] It is worth noting that Dong et al. first claimed for a different, catalyst-free growth mechanisms [*77Dong2001*], and then agreed for the cone-helix mechanism once they found out that the whisker occurrence was related to the presence of ZrC crystals originating from the carburation of ZrO_2 nanoparticles providing from the ZrO2 balls used in the planetary mill [*76Dong2002*].

$$\alpha = 2 \times sin^{-1}[1 - (\theta_{sector} + \theta_{overlap})/360] \qquad (2)$$

where α, θ_{sector}, and $\theta_{overlap}$ represent the apex, sector, and overlap angles, respectively.

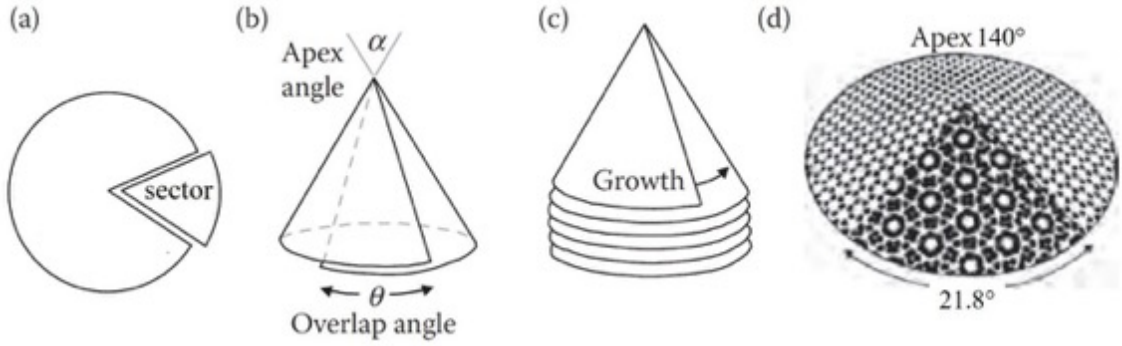

Figure 7: *Sketch of the cone-helix mode:* ***(a)*** *from removing a sector with an angle noted θ_{sector} from a graphene disc,* ***(b-c)*** *the cone is formed by an overlapping of the graphene layer.* ***(d)*** *the overlapping angle noted $\theta_{overlap}$ will impact the apex angle of the cone noted α. modified from [*27Dimovski2017*] and [*34Double1974*].*

Two important comments have to be made about **Fig.7**:

(1) Removing a sector from the graphene disk as in **Fig.7a** is not compulsory for making a cone. Cutting the lattice along a radius and then making both free edges overlap is enough. Therefore, θ_{sector} = 0 is possible, as well as any other angle value (although, in practice, a graphene portion large enough for allowing overlapping should be left). Likewise, if a sector is removed, the overlapping is not necessary. It is enough to put the free edges in contact and then shift the two edges vertically away from each other, and then start the overlapping second coil from the free edge. Hence $\theta_{overlap}$ = 0 is also possible (of course, θ_{sector} = $\theta_{overlap}$ = 0 would result in a screw configuration with no conical angle and then similar to a parking ramp where the graphene remains perpendicular to the elongation axis). Therefore, the variability in both θ_{sector} and $\theta_{overlap}$ enables a continuous variety of cone angles. However, when the sum of the sector and overlapping angles equals some specific values the overlapping graphenes may adopt specific stacking displays [*24Eksioglu2006*]. For instance, for $\theta_{overlap}$ = 0 and θ_{sector} = one of the five possible wedge disclination angles (n x 60°, with n = 1-5), superimposed graphenes follow the AA stacking sequence. For other [θ_{sector} + $\theta_{overlap}$] values, the superimposed graphenes can be in position of commensurability giving rise to supercells and moirés (see the example in **Fig.7d**, for θ_{sector} = 0 and $\theta_{overlap}$ = 21.8°), or the graphite basal stacking AB could even be restored [*24Eksioglu2006*, *58Cheng2012*, *79SuarezMartinez2020*]. However, not all [θ_{sector} + $\theta_{overlap}$] values are energetically equivalent, and some may be preferred to others [*22Jaszczak2003*]. A thorough, systematic investigation of these aspects is lacking.

(2) As already pointed out in the previous *Section*, the conical wrapping of a graphene ribbon with a solid core as sketched by **Fig.7c** in very unlikely. Taking the example of the model proposed by [*60Amelinckx1992*] as reproduced in **Fig.6d** for a helical overlapping of a graphene disk on itself to form a cone while leaving a pentagon at the center, it is clear that

such a structure would induce too much stress to the C-C bonds involved in the central pentagon. Therefore, the central part has to be empty, in an extent that depends on the cone angle (the smaller the angle, the larger the hollow core [*59Zhu2017*]).

An important statement is that the occurrence of the cone-helix configuration does exist, as it was definitely and beautifully demonstrated by Vera-Agullo *et al.* [*80VeraAgullo2007*], who were able to grab the extremity of the coil of a catalytically-grown herringbone type nanotube and then to pull it out and unwrap it as a several-micrometer-long single graphene ribbon (**Fig.8**).

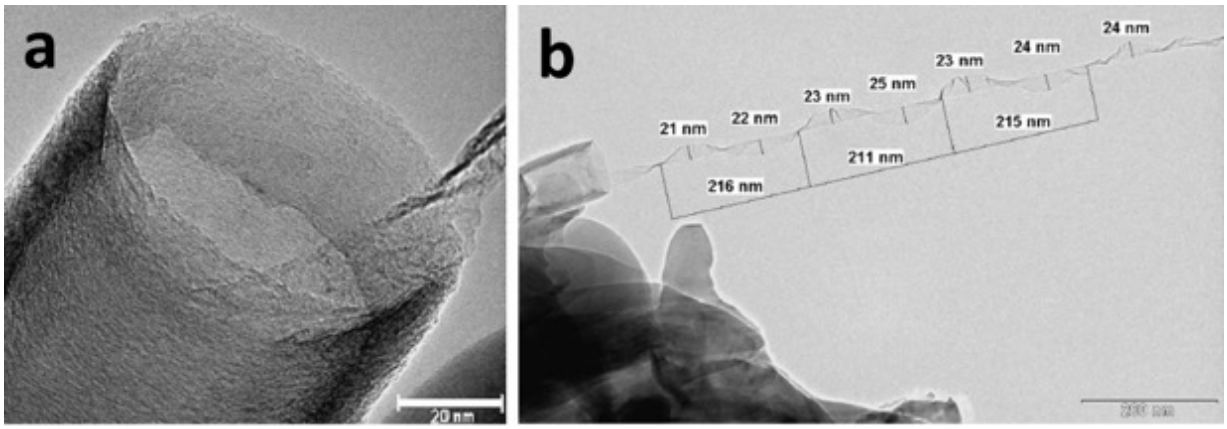

Figure 8: (a) *TEM image of the open end of a herringbone-type carbon nanotube whose first coil has been grabbed and then started to be pulled out.* ***(b)*** *Low magnification image showing that the nanotube wall is actually made from a single graphene ribbon that can be continuously unwrapped over a length of several micrometers [*80VeraAgullo2007*].*

What is possible for nanotubes should be possible for cones as well. We note that **Fig.8b** suggests that the ribbon is a single graphene, but it can also be multilayered [*81Motojima1995*]. Whatever, it is then ascertained that both the cone-stack (*Section 2.1.1*) and the helically-wrapped-ribbon (cone-helix) configurations exist. One way to discriminate between both, when possible, is to check for the mechanical behavior of the morphologies upon gentle grinding or sonication. Filaments with cone-stack (or lampshade-stack) configuration happen to lose the filamentous morphology [*66Monthioux2007*], whereas filaments with the helically-wrapped-ribbon configuration are able to maintain it.

Apart from the mechanical behavior already mentioned in the previous Section, and as also pointed out in [*24Eksioglu2006*, *59Zhu2017*], it is quite difficult to discriminate between individually stacked conical graphenes (e.g., the cone-stack configuration of the multiwalled carbon nanocones discussed in previous *Section 2.1.1*) and the helically-wrapped graphene-ribbon configuration (unless a clear demonstration as in **Fig.8** is made), as they both generate the herringbone texture in projection. It is the same whether the core of the morphology (along the elongation axis) is solid (as in so-called herringbone nanofibers, **Figs.6a** and **7c**), or empty (as in so-called herringbone nanotubes **Figs.6b** and **6c**). The reason is because the main observation tool for this is TEM, which provides 2D-projected images of 3D objects. This means that, in most of the articles from the literature, the cone-helix model is merely assumed instead

of demonstrated, usually based on a previous work who had also assumed the same (and the situation is actually the same for the cone-stack/lampshade-stack models, which were often merely claimed despite the lack of experimental evidences). Of course, the conical-helix model could account for almost all the existing conical morphologies. Sometimes, there are enough evidences for that indeed. For example, in the naturally-formed carbon cones described in [*22Jaszczak2003*], many cone angle values were found, i.e., far beyond the only five values reported in **Fig.3c**, and the cone surface may happen to exhibit a step line, marking the edge of the terminal turn, hence ascertaining the cone-helix configuration (**Figs.9a** and **9b**).

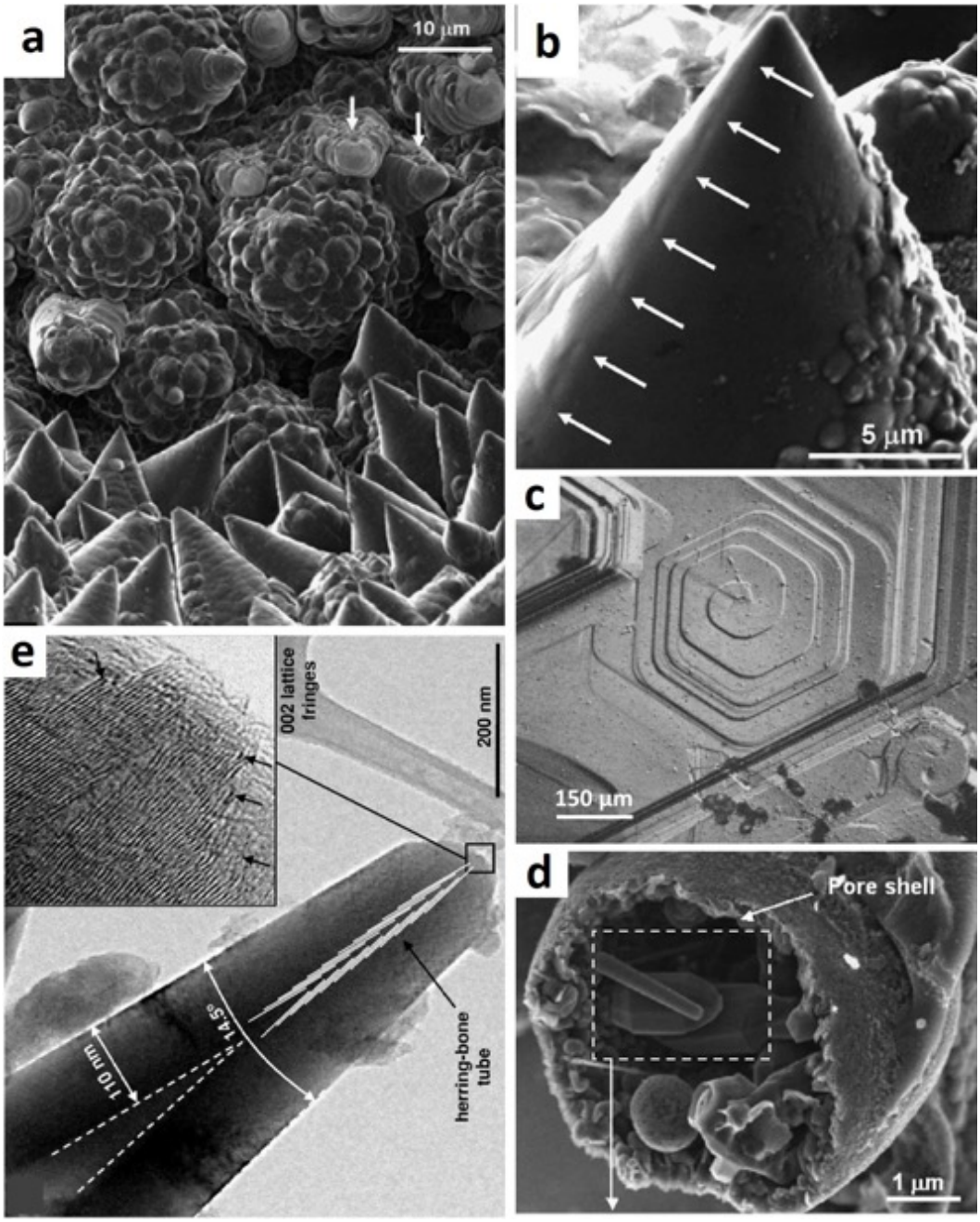

Figure 9: (a) *and* ***(b)*** *SEM images of the naturally-formed cones discovered by [*22Jaszczak2003*]. Arrows in (b) indicate the occurrence of a step-like feature on the cone surface, as a strong support to the cone-helix configuration hypothesis.* ***(c)*** *spiral growth of a graphite crystal as found in [*82Roscoe1973*].* ***(d)*** *and* ***(e)*** *conical carbon forms found in the pores of a 2000°C-heat-treated phenolic resin [*87Gogotsi2002*].*

The early work by Roscoe *et al.* [*82Roscoe1973*] is interesting because it provides a unique example of a conical morphology based on a non-basal screw-dislocation (**Fig.9c**) for which the graphenes are perpendicular to the cone axis instead of oblique, as it is the case for all the morphologies mentioned in this *Section 2.1.2*. This allows the structure to be really graphitic. They were obtained during attempts to grow graphite crystals from hypereutectic solutions of carbon and iron. However, even among the experiments reported, this perfect case has rarely occurred.

On the other hand, the assumption for this configuration in the literature may be questioned in several instances, and the same way as the screw-dislocation-based growth theory for metallic whiskers proposed in the early days [*74Peach1952*] has more recently been largely proven incorrect [*83Smetana2007*], it might be necessary to revisit part of the so-far well-admitted mechanisms for growing carbon whiskers. A striking example is the cone-helix configuration that was claimed for the cone-based filaments (or "columns") that were prepared and studied in [*34Double1974*, *60Amelinckx1992*, *75Haanstra1972*, *84Lin2007a*]. Despite they were prepared following different conditions (solid carbon source + Fe traces + 2800°C for [*64Gillot1968*], CO + SiC + 1800°C for [*60Amelinckx1992*, *75Haanstra1972*], pitch + porous template + 2500°C post-treatment for [*84Lin2007a*]), the morphologies obtained are amazingly alike (**Fig.10**). Conical morphologies observed in [*85Saito2007*] could be similar, but whether they were easily dismantled was not shown.

The way the morphologies in **Fig.10** mechanically behave indicates that they should actually obey the cone-stack model instead of the cone-helix model that was claimed in all the papers above-mentioned. Moreover, the thin disk-like entities obtained (e.g., **Figs.10f** and **10g**) fairly look alike the nanocones shown in **Fig.5**. They are individual disks or cones, and do not exhibit any step at their surface nor empty core. Is it possible that the same features would be obtained if the morphologies were obeying the cone-helix model? **Fig.8** shows that cone-helix morphologies should dismantle – assuming that they would - as a ribbon-like morphology, but nothing alike was found in the papers cited. Therefore, it is more likely that these morphologies are of the cone-stack model and should have better been placed in previous *Section 2.1.1*. However, on the other hand, two observations could support the cone-helix model indeed: *(i)* cone apex angles are in the range 135-155°[3], i.e. larger than the largest value allowed for a cone-stack configuration (113° for a single pentagon); *(ii)* the diffraction patterns may show periodically dotted *hk0* diffraction rings (**Fig.10h**), as a very plausible result of a spiral pitch [*60Amelinckx1992*, *75Haanstra1972*].

However, as already pointed-out at the end of *Section 2.1.1*., it might be possible that the "pentagon-rule" is not so strict, and that ascertaining the cone-helix configuration only based on the statement that the cone angles are different from the only five pentagon-driven allowed-values (**Fig.2c**) mistakenly neglects the ability of C-C bonds in graphene to accommodate strains [*72Després1995*, *73Després2002*], specifically when truncated cones (with empty core)

[3]This angle range does not necessarily indicate a variability from a conical rod to another. A more recent study has shown that the cone angle within a same carbon rod actually increases significantly from the bottom to the top, from ~60° to ~180° [*86Lin2007b*]. Therefore, considering how easily the carbon rods may dismantle, the range of apex angles observed may just depend on at which height the rod pieces observed have broken.

are considered. Likewise, obtaining regularly dotted *hk0* diffraction rings as in **Fig.10h** might not be specific of a cone-helix configuration as, in the cone-stack model, stacked cones with a given rotation of one cone with respect to the cone underneath could display according to a configuration of minimal energy, thereby also providing dotted *hk0* diffraction rings.

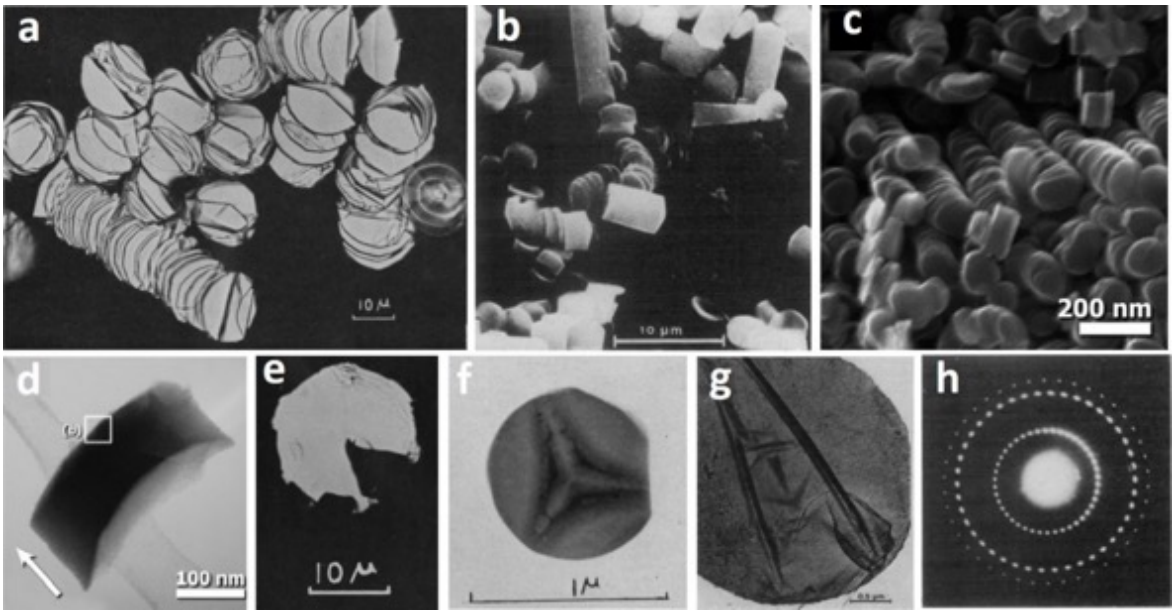

Figure 10: *Images from various kinds of microscopies of columnar morphologies with very similar features obtained by different authors.* ***(a)*** *to* ***(c)*** *the morphologies exhibit conical ends and easily dismantle into disk-like entities, also with conical features;* ***(d)*** *a side view of a thick entity exhibiting a dome-shape whose conical origin is likely;* ***(e)*** *to* ***(f)*** *top views of thin disk-like entities;* ***(e)*** *results from squeezing a large entity against a surface, resulting in the disc-like with a ~60°-wedge as shown. This demonstrates the mechanical behavior of a former conical morphology that was enforced to flatten and then broke following a rupture line according to a radius;* ***(f)*** *a conical entity that was thin enough for most of its surface to be able to flatten upon the interaction with the substrate. The three folds that converge to the center are a witness of the conical shape;* ***(g)*** *Another large disk-like entity showing folds. Folds do not converge probably because the conical morphology is too thin and is able to accommodate the strain;* ***(h)*** *electron diffraction pattern obtained for entities such as in (e), (f), or (g), with the electron beam perpendicular to the main graphene surface. (a) (e) (f) are from [*64Gillot1968*], (b) (g) (h) are from [*75Haanstra1972*], (c) (d) are from [*84Lin2007a*].*

Overall, it comes out that the discrimination between the cone-stack and the cone-helix configurations is still not clear, and that further studies are still needed to understand more about the rules driving the occurrence of conical forms. Therefore, as already stated for the cone-stack model, one of the most reliable tests for ascertaining one stacking configuration over the other is to subject the material to mechanical stresses such grinding or sonication. This is what was carried-out for the sharp cones with very narrow apex angles incidentally found by [*87Gogotsi2002*]. These conical morphologies (that they improperly named "graphite conical crystals" since electron diffraction patterns did not show any evidence of the 3D graphite structure) consist of cones with apex angles in the range 3-15°, up to 3 µm in diameter at their base and up to 15 µm in length (**Fig.9d**). The nanotexture is close to perfection. They have grown without catalyst within glassy carbon pores that develop by the carbonization of phenolic resin at 2000°C in N_2 atmosphere at a pressure of 10 Torr (**Fig.9d**). It is however

assumed that the gas composition and pressure that develop in the pores is totally different, including significant amounts of hydrocarbons and O_2 (subsequently converted in CO). The conical shape is supposed to be formed by the addition of atoms to the graphene planes terminating at the outer surface of a primarily-grown herringbone nanotube. As usual, the cone-helix configuration was presumed, based on the cone angles that do not obey the pentagon-rule. However, a good support for this is that the conical morphologies survived the grinding of the material without shattering in pieces. Regardless of the stacking configuration (**Fig.9e**), the projected textural (longitudinal) model is that of **Fig.12b-left**. Despite no catalyst was deliberated added, the authors acknowledged that the traces of Fe, among other elements, found in the material may play a role, for instance in promoting the growth of the primary herringbone MWCNTs. However, the latter is unlikely, because the inner cavity of the conical morphologies is conical as well, which is very uncommon for MWCNTs. The morphology is interesting, but the yield is low and the formation is poorly controlled.

The insufficient understanding concerning the carbon cone growth mechanism is also caused by the wide variability in the synthesis conditions able to induce conical morphologies, specifically with the cone-helix configuration, which is most often related to the presence of a catalyst, or conditions of low supersaturation [*75Haanstra1972*]. Thus, the control of their shape and their properties is very difficult in order to produce well-defined conical morphologies with desired characteristics, as it may depend on the structure of the seed at the beginning of the catalytic nucleation [*55Treacy2001*, *56Kawai2002*], the catalyst state (liquid or solid), size, and morphology [*66Monthioux2007*], as well as the synthesis conditions (temperature, gradients, maturation, gas concentration and composition, pressure).

To summarize, should a key difference be given between the formation conditions for conical morphologies that are generated by the incorporation of pentagons (*Section 2.1.1*) and that generated by a cone-helix configuration (this *Section 2.1.2*), we may refer to catalysts, whose presence is required for a vast majority of the latter but may be not for the former, and whose geometrical characteristics and activity play a determining role in the resulting graphene texture and final conical shape.

2.1.3 Radial edge dislocation

The previous *Section* described an edge-dislocation-based spiral-growth mechanism with graphenes being oblique with respect to the growth direction and cone axis, but another spiral growth may occur through a radial edge dislocation, which keep the graphenes parallel to the cone axis [*63Sears1959*] (**Fig.11a**). It involves the preferred nucleation of vertical graphene seeds promoted by conditions of low supersaturation occurring during the condensation process [*63Sears1959*]. This is the case for the carbon whiskers first reported by Bacon ([*28Bacon1960*], and earlier references within) along with other whiskers, ribbon-like instead of scroll-like, which attracted much less attention and for which little information was provided, probably because they were seldom. They both were obtained by subjecting graphite electrodes to an arc-generated plasma of ~3650°K under a pressure of 92 atmospheres of argon. They were named "graphite whiskers" because they showed some evidences that the Bernal stacking of graphite was present, although possibly not involving an individual whisker

as a whole, making that one whisker could not be considered as a single crystal, as far as crystallography is concerned. First, the concentric display of the graphenes around the whisker axis was demonstrated by X-ray diffraction. A scrolled nature of the whiskers was suspected from their overall morphology, which was somewhat similar to that of **Fig.11c** and then sketched in **Fig.11a**.

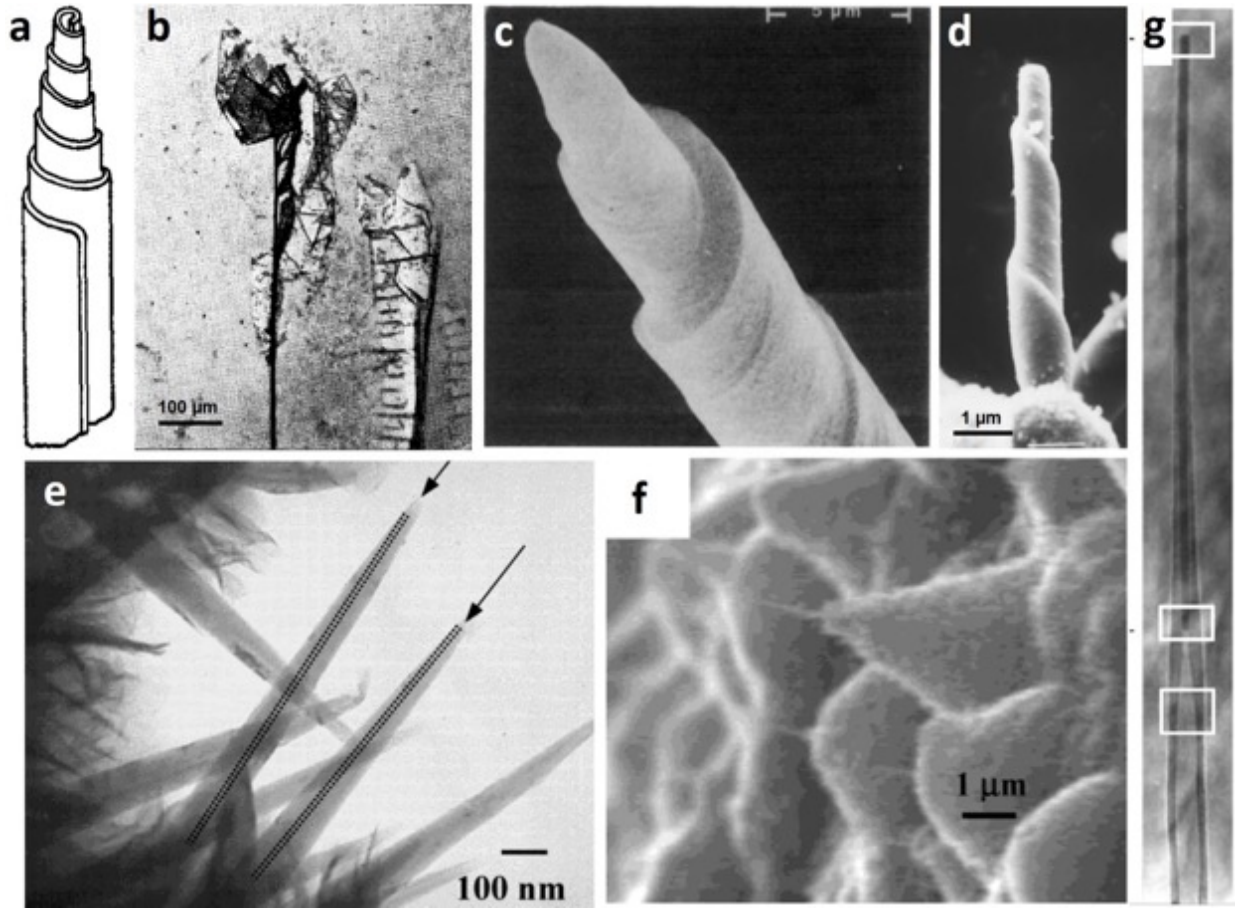

Figure 11: (a) *Sketch of the carbon whisker morphology proposed by Bacon. Length can be as high as 3 cm.* ***(b)*** *optical micrograph showing the result of passing a current through a whisker [*26Bacon1960*].* ***(c)*** *SEM image of a carbon whisker possibly similar to that of Bacon [*75Haanstra1974*].* ***(d)*** *SEM image of a carbon whisker looking like that of Bacon, but actually demonstrated exhibiting a different texture [*77Dong2001*].* ***(e)*** *and* ***(f)*** *Conical morphologies formed by a microwave plasma enhanced CVD process. (f) corresponds to different local conditions allowing the primarily-grown carbon nanotube making the core of the overall conical morphologies to be evidenced [*89Mani2003*].* ***(g)*** *Conical nanotube resulting from a change in the physical state of the catalyst during the growth: solid for the cylindric part, and liquid for the conical part. The inner diameter at the bottom is 40 nm [*93Sun2007*].*

Quite interestingly, this was confirmed by passing a high current through them, inducing the whiskers to unwrap, resulting in more or less crumpled multigraphene layers observable by optical microcopy, whose sizes (see **Fig.11b**) were much larger than that of the whisker diameters. Such an unwrapping effect on scrolled graphene morphologies by charge injection was subsequently supported by calculation [*88Braga2004*].

No other example of carbon whiskers similar to Bacon's ones was claimed to be synthetized since then, although referring to them was made several times. However, some whiskers from the literature look alike. For instance, when growing by pyrolysis of CO above 1800°C on SiC

the columnar carbons discussed in the previous *Section*, [*75Haanstra1972*] also produced the morphology shown in **Fig.11c**. They described it as deriving from a cone-helix whisker whose lateral growth was promoted by abrupt changes in temperature, but the actual characterization of the inner texture was actually not made. **Fig.11d** provides another example, but the graphenes were demonstrated not to be parallel but oblique with respect to the whisker axis [*77Dong2001*].

Another case is that of carbon conical morphologies for which both the orientation of graphenes parallel to the elongation axis and their scroll-like wrapping were determined from electron diffraction, without any other morphological or textural evidence [*89Mani2003*], although the outer morphology does not look like that of Bacon's whiskers (**Fig.11e**). [*89Mani2003*] and subsequent studies [*90Lowe2006*, *91Chernomordik2008*] reported the formation of what they called "nanopipettes", a designation that has become popular but was improper, as only based on the statement that the morphology included a uniform hollow core of diameter 1-3 nm, without any further demonstration that it could actually behave as a pipette (i.e., able to suck-in a liquid, and then to release it). A Pt wire was used as a catalytic substrate and a flow of CH_4 highly diluted (1-2%) in H_2 in a microwave-plasma-enhanced CVD set-up. These tapered whiskers with typical diameter at base of 200-700 nm and 6 µm in length were shown to start with the growth of a primary MWCNT (**Fig.11f**), and then were presumed to be created from a competition between the radial growth (through a scroll-like mechanism) and axial growths of the cone on the one hand, and the etching of the deposited carbon by the plasma on the other hand. Consistently with the overall uncertainty regarding the actual texture of conical carbon morphologies which is revealed and discussed in the present work, it is worth noting that, in a subsequent paper [*92Dumpala2011*], part of the co-authors of the Mani *et al.*'s paper no longer mentioned a scroll configuration such as that of Bacon's whiskers but a purely concentric, telescope-like configuration as sketched in **Fig.12c-right**.

Finally, the conical morphology reported by Sun *et al.* [*93Sun2007*], which basically consists of a several-micrometer-long pointy nanotube (**Fig.11g**), is a unique example where the tapering of the MWCNT comes from a change in its growth mode, making it switching from a cylindric, herringbone, cone-helix (supposedly) configuration to a conical, concentric and scrolled configuration somewhat similar to that of Bacon's whiskers. The change is induced by the change in the physical state of the catalyst, which switches from solid and facetted to liquid during the course of the tip-growth, because of the time taken by the crystal to thermalize in very fast heating conditions (850°C/s). The morphologies have withstand peeling off actions without being morphologically affected in any sense, which ascertains the cone-helix configuration of the herringbone, bottom part and a structural relationship between the latter and the upper, concentric part, hence suggesting that the wrapping of the graphene keep going all along the tube, inducing a continuity between the cone-helix growth and the scroll growth.

Such examples illustrate that observing the outer morphology is not enough, carrying-out a careful investigation of the inner texture is a key-point. This said, it is likely that some morphologies described in the literature as resulting from another growth mode or textural model may actually be related to Bacon's one instead because, as for discriminating between the cone-stack and the cone-helix textures (see previous *Section*), it is quite difficult to

discriminate in projected HRTEM images between the scroll-concentric texture (**Fig.11a**) and the regular concentric texture (**Fig.12c**). Examples of these will be provided in *Section 2.2.2*.

2.2. Texture-driven conical forms

Some of the possible conical morphologies already discovered or yet to find may not relate to a structural defect as discussed in the previous *Section* but to the specific arrangement of the graphene layers (with respect to the cone axis), caused by other mechanisms. Therefore, we can classify conical morphologies in three main groups according to their texture, as depicted in **Fig.12**:

- Graphene sheets oblique to the cone axis (**Figs.12a** and **12b**);
- Graphene sheets parallel (concentric) to the cone axis (**Fig.12c**);
- Graphene sheets perpendicular to the cone axis (**Fig.12d**);

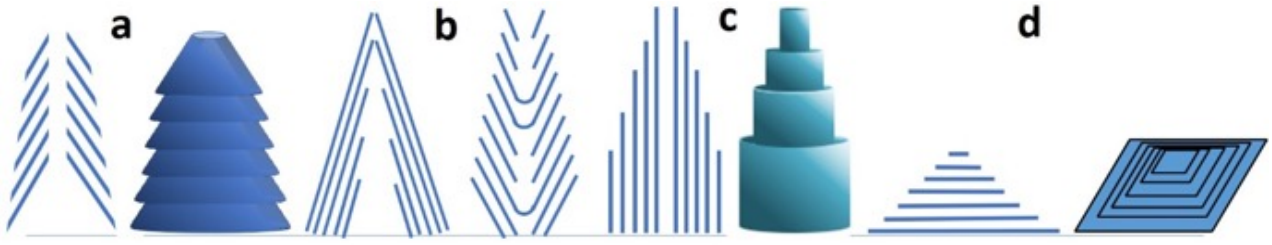

Figure 12: *Sketch of the three ways to generate graphenic morphologies whose conical forms are driven by the texture, i.e., the orientation of the graphene layers with respect to the cone axis.* ***(a)*** *and* ***(b)*** *three different textures for graphene sheets oblique to the cone axis.;* ***(c)*** *graphene sheets parallel to the cone axis;* ***(d)*** *graphene sheets perpendicular to the cone axis. The line-drawings aside the 3D models sketch the way the inner texture of overall conical morphologies may look like when seen as projected images such as obtained by HRTEM. Although the 3D models in (a), (c), (d) hypothesize a stack configuration, the projected textures would look the same in case of a cone-helix configuration.*

2.2.1. Graphene oblique with respect to the cone axis

All elongated carbon morphologies (nanotubes, nanofibers, or cones) showing graphenes oriented obliquely with respect to the elongation axis, hence exhibiting the so-called herringbone texture in longitudinal section, pertain to one of the following three categories:

- Those exhibiting one of the five possible angles generated by the incorporation of pentagons, thereby generating the herringbone texture, in longitudinal section, can be described as resulting from a wedge disclination, and therefore pertain to the structure-driven conical form category discussed in *Section 2.1.1*.
- Those based on a cone-helix model can be described as resulting from a screw dislocation, and therefore pertain to the structure-driven conical form category discussed in *Section 2.1.2*.
- The third category, therefore texture-driven since not structure-driven, is for the elongated carbon morphologies that do not belong to the two previous ones, and they are the ones to be discussed now.

Unless very seldom exception, morphologies from the last two categories are generated by a catalyst-driven process, with the graphene faces generated parallel to the catalyst surface (when any) being a very frequent configuration. However, in principle, the third category above-mentioned (i.e., texture -driven) should not exist because, although it cannot be based on a cone-helix configuration, it cannot be based on a cone-stack or lampshade-stack configuration either, whether the locus of the elongation axis is solid or hollow, because of the need to close the conical graphene surface seamlessly which, theoretically, requires a wedge dislocation. However, we already mentioned in *Section 2.1.1* that this condition is very likely to be able to relax for large diameter truncated cones. This is certainly responsible for many misinterpretations in the literature, and exampled in *Sections 2.1.1. and 2.1.2*.

Examples of genuine herringbone conical morphologies (i.e., not CNT) that were demonstrated to be built from piled-up truncated cones (lampshade-like, as sketched in **Fig.12a**) do not exist in the literature. But several were demonstrated to exhibit one of the models sketched in **Fig.12b** in projected, longitudinal sections. It is clear that they could belong to either the cone-helix or the cone-stack configurations, but considering the uncertainty revealed in the previous *Sections* regarding the determination of the stacking model, they are reported here.

Okuno *et al.* [*94Okuno2005*] have obtained amazing micrometer-sized, polygonized conical objects (**Fig.13**) which somehow relate to that of Gogotsi *et al.* [*87Gogotsi2002*] (**Figs.9d** and **9e**). They were obtained in large amount by a combustion flame technique using an oxy-acetylenic torch, hence involving a significant amount of oxygen (O_2/C_2H_2 = 0.9 vol.). Although the growth is said catalyst-free, the role of the ~1200°C-heated molybdenum plate used as a substrate may be questioned. The authors claim to have obtained two kinds of morphologies, so-called "rod-like" (**Fig.13a** and **13b**) and "pin-like" (**Fig.13c** and **13d**). The latter exhibits the same texture as that of **Fig.9e**, i.e. graphenes are parallel to the cone surface but oblique to the cone axis (**Fig.13d**), hence again corresponding to the sketch of **Fig.12b-left**. On the other hand, the authors claim that the texture of the rod-like morphologies is different, with the graphenes parallel to both the surface and the elongation axis, thereby meaning that the conical shape cannot be otherwise than that sketched as **Fig.12c**. But they might be wrong, because the large thickness, the long length, and the very small cone angle of the morphologies make this impossible to ascertain. What is real is that both the rod-like and the pin-like morphologies exhibit a perfect nanotexture and both also exhibit a twisted, facetted surface (**Figs.13a** to **13c**), suggesting that they might grow following the same mechanisms, making likely that they exhibit the same texture. In such a case, the pitch of the twist seems to relate to the cone angle: the smaller the cone angle, the slighter the twist pitch. The authors actually only discussed the formation mechanisms of the rod-like morphologies, and suggested the leading role of thermal fluctuations occurring in the graphenes primarily deposited onto the Mo substrate, which could subsequently promote the growing graphenes to orientate vertically, helped by the steep thermal gradient. This an original, interesting hypothesis, yet never suggested or confirmed anywhere since then. On the other hand, they have observed that a carbon nanofilament can be found to protrude from the rod-like cone tip (**Fig.13b**). Also, in subsequent experiments where they deliberately grew carbon nanofilaments by introducing catalysts, they observed that rod-like morphologies started to form around the nanofilaments. Therefore, a simpler growth

mechanism would be that the conical morphologies grow onto primarily formed carbon nanofilaments acting as supports, for which the Mo substrate or nanoparticles as impurities might play a catalytic role. Other morphologies were also found which pertain to *Section 2.2.2*.

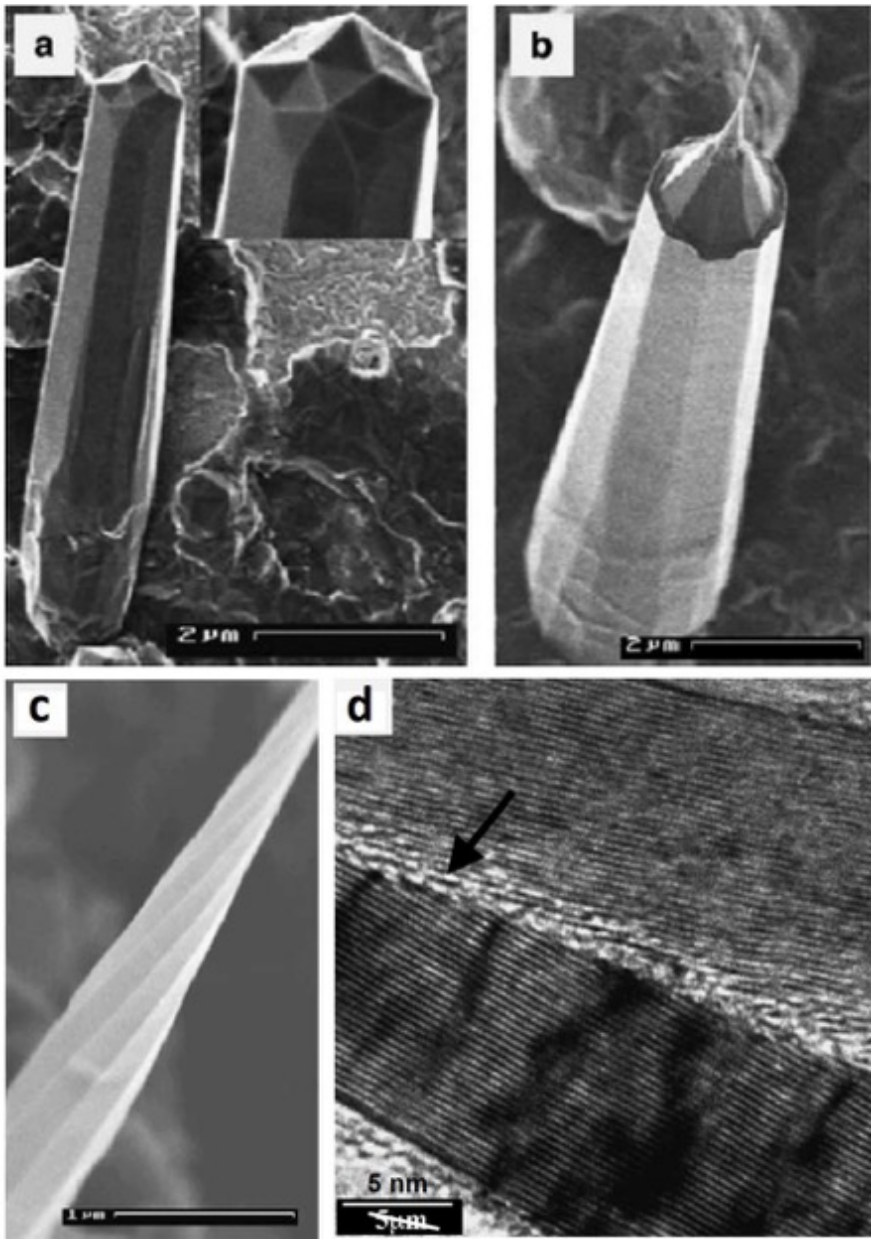

;

Figure 13: *Conical carbon morphologies found as the products from a combustion flame technique using an oxy-acetylenic torch onto a Mo substrate [*94Okuno2005*]. **(a)** and **(b)** were designated as "rod-like" morphologies, whereas **(c)** and **(d)** pertain to a so-called "pin-like" morphology. It is not clear whether both are independent, or whether the pin-like morphology is that sometimes found at the tip of rod-like morphologies as in (b). Original scale in (d) was obviously wrong, and then is corrected here as what is believed the actual scale.*

[*95Liu2004*] obtained conical morphologies of about 1 μm in length whose graphenes, as guessed by the direction of Bragg fringes in the TEM images (**Fig.14b**), are oblique to the cone axis while being parallel to the cone surface. The overall projected texture is therefore somewhat similar to that of [*87Gogotsi2002*] and [*94Okuno2005*] (**Fig.12b-left**). They were obtained in fairly large quantity (**Fig.14a**) as a failed attempt to produce CNTs in a stainless-

steel autoclave at 500°C with metallic Mg while replacing ethanol by butyl alcohol. The nanotexture is surprisingly high with respect to the low temperature used. They are however quite different objects, as they are easily individualized, and with an open end at the base, accessible to filling. Unfortunately, the characterization was not sufficient and poorly explained. In particular, low magnification images (**Fig.14a**) show that the cone surface is rough, which is not consistent with what is shown in the high magnification image of a single cone provided as **Fig.14b**.

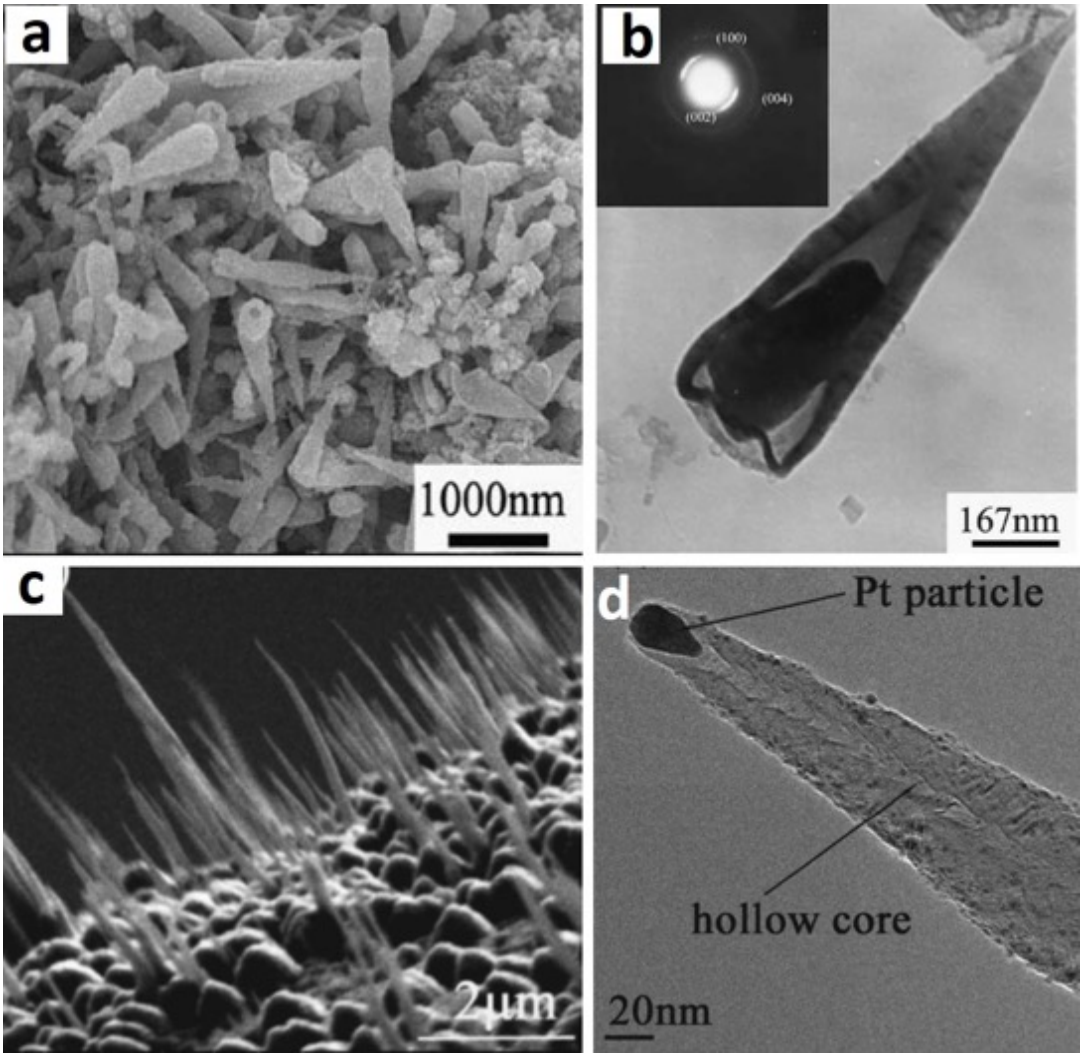

Figure 14: *Some conical carbon morphologies found:* ***(a)*** *and* ***(b)*** *as a result from the Mg-catalyzed carbonization of butyl alcohol at 500°C in autoclave [*95Liu2004*].* ***(c)*** *and* ***(d)*** *as a result from the Pt-catalyzed cracking and carbonization of H_2+CH_4 in a PE-HF-CVD process on Au [96Li2005].*

[*96Li2005*, *97Li2007*] describe several-μm-long conical morphologies that they named "tubular carbon cones". They were built from graphene sheets displayed obliquely along a herringbone-bamboo hollow core, with nanometric tips (5-10 nm) and apex angles of about 10° (**Fig.14c** and **d**). The overall projected texture is sketched as **Fig.12b-right**, with the catalyst located at the apex. As seen from the HRTEM image [*97Li2007*], the nanotexture quality is much less than for the previous cases. The carbon cones were obtained by a Hot Filament (Ta), plasma-enhanced Chemical Vapor Deposition process which generates a plasma at high temperature under a

10:50 H_2/CH_4 flow ratio in presence of Pt in the hot zone. Gold wires were used as substrate. Such processes exhibit huge thermal gradients, typically from 1800°C (Ta filament) down to 750°C (Au wire) over a 1 cm distance. Cones grow as a forest perpendicular to the substrate (**Fig.14c**). The growth mechanism was explained as a competition between an axial Pt-catalyzed growth of a primary carbon nanotube and its radial growth by addition of carbon species while a continuous etching of the side-carbon by hydrogen species is responsible for the conical shape. Although the etching effect on deposited carbon as responsible for the cone morphology was considered and studied by multiscale Monte Carlo/surface diffusion numerical simulation [*98Levchenko2008*], a simpler and more plausible mechanism suggested by images such as **Fig.14d** could be that the growth of a herringbone CNT starts from the carbon-containing atmosphere thanks to the catalytic action of a Pt particle. The Pt particle is large enough for not being able to physisorb onto the Au surface, making the growth mechanism be of tip-growth type. Because of the huge temperature gradient, part of the catalyst gradually vaporized as it lifts-up, unless it is plasma-etched as suggested later-on [*97Li2007*], making that the tube diameter decreases as it grows, thereby forming a cone. This simpler mechanism is also consistent with very similar morphologies that were obtained previously by Merkulov *et al* [*99Merkulov2001a*], again based on a plasma-enhanced CVD process. In this paper, the authors claimed for a constant tip size over the increasing length and explained their morphology by the primary tip-growth of a herringbone MWCNT followed by a preferred thickening at the base by subsequent carbon deposition, but this is not consistent with the observation that the inner channel becomes as narrower as it is closer to the tip. As a matter of fact, the same authors stated that the catalyst size actually decreases at the cone grows in a parallel paper [*100Merkulov2001b*].

2.2.2 Graphenes parallel to the cone axis

These conical morphologies correspond to graphene layers growing parallel with respect to the cone axis. As opposed to conical morphologies with oblique graphenes (herringbone texture), only one type of texture with graphenes parallel to the elongation axis, the concentric texture (**Fig.12c**), was found to be able to form conical morphologies in the literature. Many different examples are reported in the literature, which mostly differ from their synthesis process (and growth mechanisms) (**Fig.15**).

Basically, there are two: (i) Chemical Vapor Deposition (CVD), either hot-wall [*26Allouche2005*, *101Jacobsen1997*, *102Allouche2003*, *103Monthioux2006*, *104Xia2005*] or cold-wall [*105Muradov2002*, *106Zhang2007*, *107Zhang2009*], and (ii) Microwave Assisted Plasma Chemical Vapor Deposition (MPCVD) [*92Dumpala2011*, *108Zhang2003*, *109Zhang2005*, *110Tan2007*, *111Shang2005*, *112Shang2007*, *113Shang2008*, *114Shang2011*, *115Lee2011*, *116Zhuang2015*]. There are few other miscellaneous synthesis processes such as that reported by Gogotsi *et al.* which merely involved 2000°C-carbonization of a glassy carbon polymeric precursor [*87Gogotsi2002*, *117Gogotsi2000*], and that used by Okuno *et al.* who used an oxy-acetylenic torch [*94Okuno2005*]. For all of the papers cited so far in this *Section 2.2.2* but by Muradov and Schwitter [*105Muradov2002*] and Gogotsi *et al.* [*87Gogotsi2002*, *117Gogotsi2000*], the growth was reported with some catalytic particles added and, correlatively, for all the same

papers but [*105Muradov2002*], the conical morphologies include a nanofilament as the central core (a carbon nanofilament for all, but in [*115Lee2011*] for which the filament was SiO_2-based). However, the claim for a catalyst-free - and therefore nanotube-free - process by [*105Muradov2002*] is certainly wrong, because vapor-grown carbon fibers (VGCFs) are formed in the early steps of the process, and it is well-known for long that VGCFs grow around a primary carbon nanotube [*118Endo1995*]. Likewise, because Gogotsi *et al.* [*117Gogotsi2000*] did find a carbon nanotube at the central core around which their conically-tipped whiskers grew, their claim for a catalyst-free process might be wrong. Indeed, to grow spontaneously as a filament without a catalyst, carbon requires the occurrence of some gradient, e.g., the electrical field in the electric arc process [*14Iijima1991*], otherwise the catalyst-free growth of carbon nanotube should always be questioned.

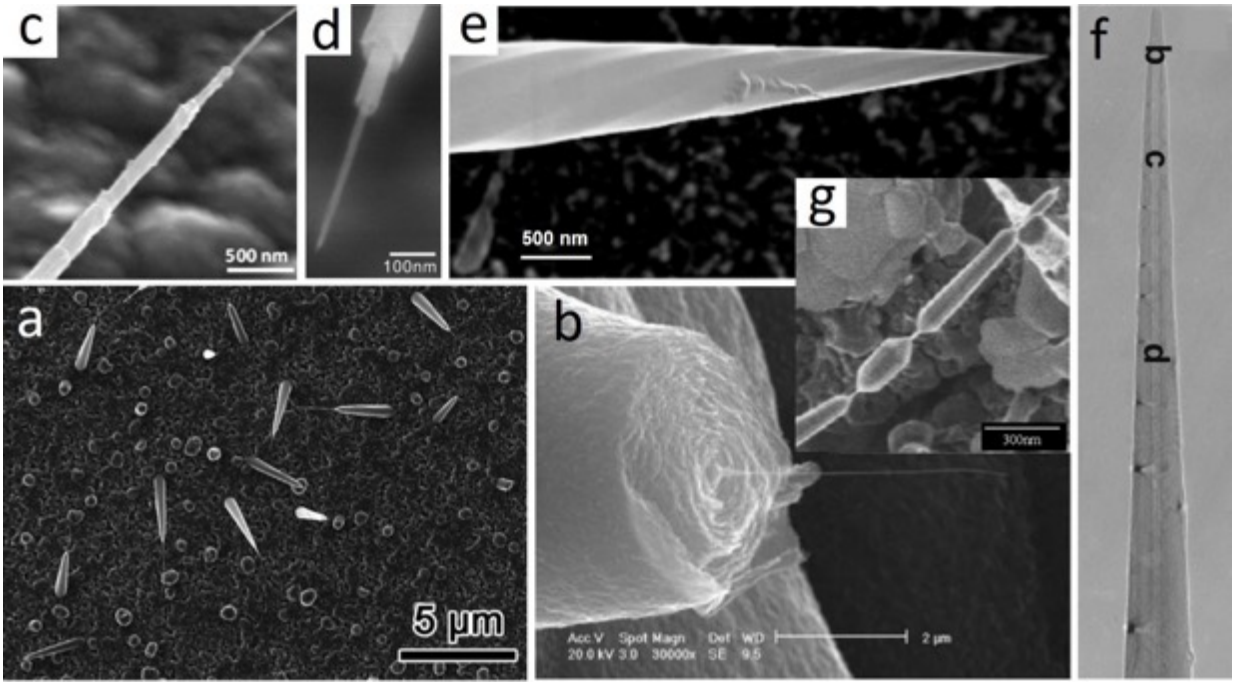

Figure 15: (a) *Example of carbon conical morphologies growing somewhat perpendicular to the substrate. CNTs protruding from the cone apices are seen [*116Zhuang2015*]. **(b)** Broken cross-section of a cone showing the relative roughness of the cone surface, the presence of the inner primary MWCNT, and the concentric display of the subsequent deposit making the cone [*106Zhang2007*]. **(c)** and **(d)** Examples of the telescope-like morphology demonstrating the concentric, nested texture of the graphene layers, from [*92Dumpala2011*] and [*112Shang2007*] respectively. **(e)** and **(f)** Examples of the outer and inner aspects of the conical carbon morphology, from [*108Zhang2003*] and [*109Zhang2005*] respectively. The inner diameter in (f) is 5-10 nm; note the similarity with **Fig.13c**; letters b, c, d in the image refer to the original text. **(g)** cone-tipped cylindrical morphologies displayed along a primarily-grown carbon nanofilament [*94Okuno2005*]. All morphologies were obtained from microwave-plasma-assisted CVD but in (b) (cold-wall CVD) and (g) (oxy-acetylenic torch).*

Most of the conical morphologies reported in this category have micrometric bases and lengths, a few-degree cone angle (< 10°), and a nanosized apex, of which **Fig.15** provides some examples. The fact that they all grow based on a multiwalled carbon nanotube (making a cylindrical hollow core) serving as the main axis excludes a nucleation of the cones from a

structural defect at the center of the morphology [*104Xia2005*] such as that reported in *Sections 2.1.1 and 2.1.2*.

There are mostly two ways the conical morphologies are proposed to grow from this central nanotube. According to several authors, one way is the result of a simultaneous axial/radial growth competition process [*92Dumpala2011*, *104Xia2005*, *109Zhang2005*, *111Shang2005*, *112Shang2007*, *113Shang2008*] occurring over the primarily-grown CNT onto which the radial growth happens from the subsequent deposit of carbon species onto the CNT surface. In such a case, the conical shape comes either from the preferred carbon deposition closer to the CNT base helped by the catalyst or some gradient (e.g., thermal) [*92Dumpala2011*, *108Zhang2005*, *111Shang2005*, *112Shang2007*], or from the preferred etching of the post-deposited carbon closer to the CNT tip due the etching species (e.g., hydrogen radicals) generated by the plasma [*106Zhang2007*]. The other main way is to consider two independent and successive steps in which the CNT grows first thanks to the catalyst, and then the conical morphology forms onto it according to a catalyst-free process [*26Allouche2005*, *101Jacobsen1997*, *102Allouche2003*, *103Monthioux2006*, *115Lee2011*, *116Zhuang2015*]. The work by Lee *et al* is specifically important here, since they grew conical carbon morphologies by a MPCVD process based on the primary growth of a silicon oxide based nanofilament, which demonstrates that the subsequent formation of the cone is actually independent from the nature (chemical composition texture) of the supporting filament [*115Lee2011*]. This growth mechanism as proposed with strong experimental support in [*101Jacobsen1997*] and the subsequent papers is worth being detailed.

The cones grow at high temperature (1300°-1500°C) using methane and hydrogen as feedstock (radial growth, or thickening step) which follows a catalytic CVD process at lower temperature during which the axial nanotube (~5nm in diameter) growth takes place (lengthening). The radial growth is conducted by the increase of the outer shells via the deposition of carbon species during the second step. The cones formed have micrometer sizes (7-10 µm), apices with a 5-10 nm diameter, and a smooth surface (**Fig.16**) [*101Jacobsen1997*, *102Allouche2003*]. The cones are strongly attached to larger carbon beads or fibre segments with rough surface which are also formed onto the primary CNT. HRTEM revealed that (i) both the beads or fiber segments and the cones exhibit a concentric texture and a perfect nanotexture for the cones, whereas the nanotexture is distorted for the bead or fiber parts. Interestingly, the structure of the beads or fiber segments is turbostratic whereas the cone structure is turbostratic when the radius of curvature is small (i.e., for the inner shells and at the apex) and graphitic when the radius of curvature is large (i.e., for the outer shells). This shows that all the graphene cylinders building the cones are of the same chirality [*26Allouche2005*]. It is proposed [*103Monthioux2006*], with both the support of the literature and of experimental observations, that the long times of flight of species enabled by the furnace used not only promote the primary cracking of the feedstock but also multiple recombination of the species resulting from the primary and secondary cracking reactions. Therefore, both radical species and liquid poly-aromatic hydrocarbons (PAH)-rich droplets are formed and may co-exist. PAHs may physisorb on any surface, typically the primary CNTs or the carbon layers previously deposited onto them, whereas the radicals only chemisorb onto the available nucleation sites, typically the graphene edges covering the cone surface. As a broad picture, the

PAH mostly contribute to depositing the primary cone seeds periodically along the primary MWCNTs (hence independently from any surface defect) and then to growing the rough parts (the beads or fiber segments), whereas the radicals mostly contribute to growing the smooth parts, i.e., the cones. The PAHs/radicals ratio governs whether the cone fully develop (**Figs.16a, 16b, 16d**) or not (**Figs.16a** and **16b**), and whether the rough surface parts develop as beads (**Fig.16a**) or fiber segments (**Figs.16b** and **16d**).

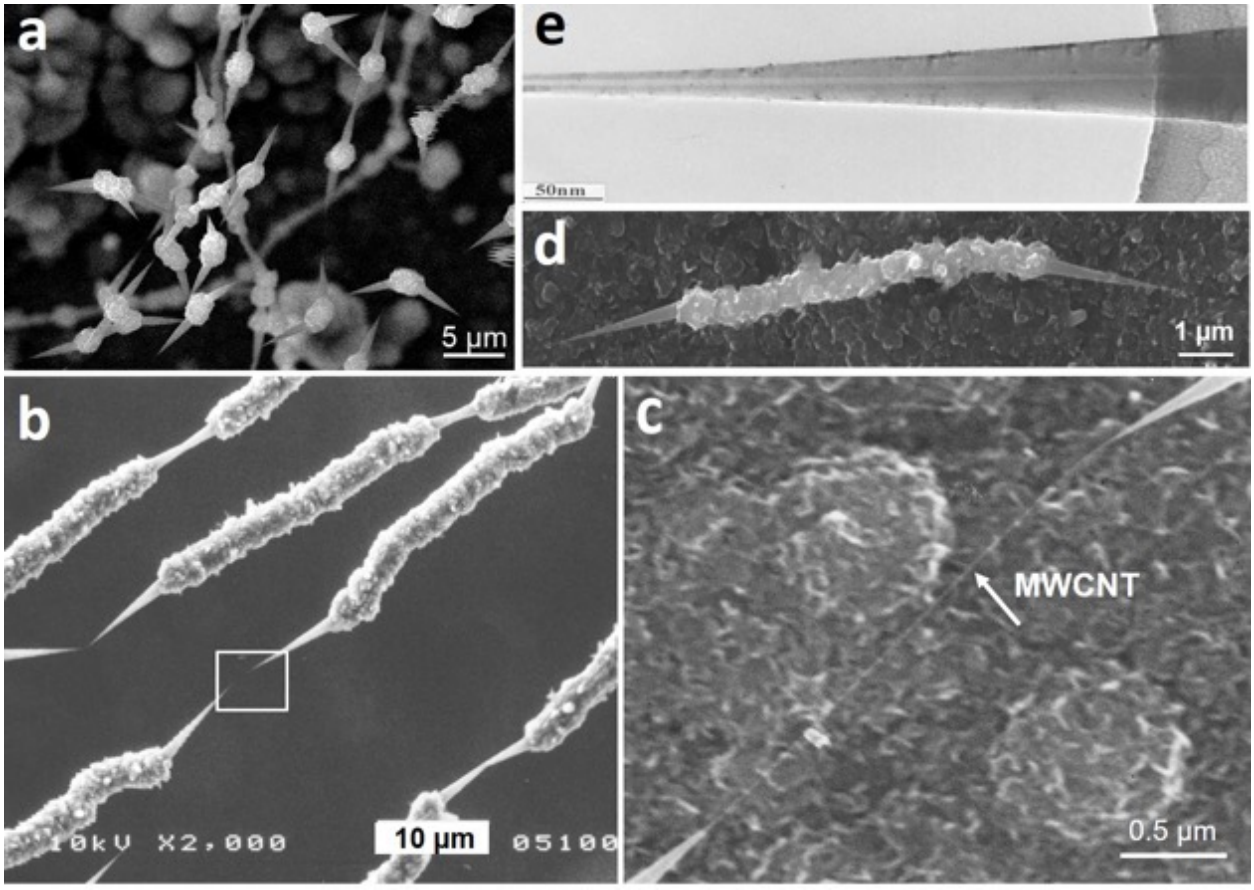

Figure 16: *Conical carbon morphologies obtained by long time-of-flight CVD [*26Allouche2005, 101Jacobsen1997, 102Allouche2003, 103Monthioux2006*]:* ***(a)*** *the so-called "spiky-bead" morphology. The image provides examples of fully developed and partially-developed cones.* ***(b)*** *example of another morphology where the beads are elongated as fiber-segments. The image provides examples of fully developed and partially-developed cones.* ***(c)*** *Magnification of the area framed in (b) showing the naked primary MWCNT joining two opposed cones.* ***(d)*** *example of the so-called "spiky-short-fiber" morphology.* ***(e)*** *Low magnification image of a cone close to the tip showing the central hollow core of the primary MWCNT. HRTEM images demonstrated that graphenes are displayed concentrically, according to the sketch of* ***Fig.12c-left*** *[*26Allouche2005*]. Note the overall similarity of (e) with* ***Fig.15f****, but also the difference regarding the cone angles: constant in* ***Fig.15f*** *(the projection of the cone surface follows straight lines) and meniscus-like in (e) (the projection of the cone surface follows negatively curved lines) [*103Monthioux2006*].*

Interestingly, applying the principle of the co-existence of radicals and PAHs proposed in the above-mentioned work in proportions driven by the temperature and pressure conditions proper to the each of synthesis processes used could allow accounting for all the other conical morphologies described in the present *Section*, including regarding textural and morphological details: (i) the occurrence of a protruding, uncoated CNT at the cone apex [*106Zhang2007*, *107Zhang2009*, *111Shang2005*, *112Shang2007*, *113Shang2008*, *116Zhuang2015*]; (ii) the

occurrence of a structurally independent filament at the core of the morphology [*106Zhang2007*, *107Zhang2009*, *112Shang2007*, *113Shang2008*, *115Lee2011*]; (iii) the crenulated aspect and/or rough surface of the main body supporting the cone [*103Xia2005*, *105Muradov2002*, *106Zhang2007*, *113Shang2008*, *115Lee2011*] opposed to the smooth surface of the conical part [*105Muradov2002*, *108Zhang2003*, *109Zhang2005*, *111Shang2005*, *113Shang2008*]. The observations also fully relate to what looks like failed attempts [*119Ting2000*, *120Ting2001*] to duplicate the early work reported in [*101Jacobsen1997*], from which Ting *et al.* wrongly hypothesized that surface defects might play a leading role, in contradiction with the PAH model. Moreover, it may also be consistent with features found during experiments devoted to grown VGCFs and which remained unexplained, consisting of nanosized cone-like deposits onto carbon nanofilaments [*10Endo1976*, *118Endo1995*[4]]. Finally, it also may account for morphologies found in non-CVD conditions by Gogotsi *et al* [*117Gogotsi2000*] and Okuno *et al* [*94Okuno2005*]. Indeed, both experiments involved very high temperatures (1800-2000°C), which are conditions during which recombination reactions to generate PAHs are unfavored. Therefore, the prevalent species are radicals. As a matter of fact, the cone-terminated morphologies formed exhibit a perfectly smooth surface, a concentric texture, and a perfect nanotexture, as for the cones described in [*26Allouche2005*, *101Jacobsen1997*, *102Allouche2003*, *103Monthioux2006*].

2.2.3 Graphene perpendicular with respect to the cone axis:

Very few works in the literature report the formation of conical morphologies from graphene layers perpendicular to axis, whose configuration can be sketched as **Fig.12d**. Among the first works reported is probably the work by Krajnovich *et al.* [*121Krajnovich1993*] who reported the formation of conical morphologies whose bases and heights are in the range of several tens micrometers as the result of the irradiation of HOPG by a UV laser (**Fig.17a**). As it was observed that every cone is topped with a few-micrometer large transition metal particle (initially present as impurities in the HOPG), the authors proposed that the metal particle help shunting heat from the surface graphenes down to the thousands of lower graphenes that the metal particle is in contact with, which the very low thermal conductivity of HOPG in the c axis direction would not allow otherwise. The heat shunting lowers the surface temperature, which slows down the sputtering rate as more as the surface is closer to the particle, thereby generating a cone. However, as no structural study was carried out, the display of graphenes was merely assumed from the circular edges seen in the SEM images of the cone surface (**Fig.17a**).

Beautiful hexa-pyramidal objects (**Fig.17b**), in the range of 1 µm high and 0.5 µm large at the base, were obtained by etching either HOPG or so-called flexible graphite (heated at 650°C) with an argon plasma generated by radio-frequency, without any CVD step as the only gas injected was Ar [*23Glad2014*]. Well-conducted characterizations demonstrated the morphologies to be single crystal graphite, with the graphenes perpendicular to the pyramid elongation axis able to easily exfoliate (**Fig.17c**). As the conditions used unfavored carbon

[4] This implies that the model hypothesized as Fig.12 in [*118Endo1995*] to account for the conical deposit observed is not appropriate.

redeposition, the authors propose two well-supported possible formation mechanisms, which may combine. One is the same mask-based mechanism as that above-mentioned, where the masks are impurities embedded in the starting material. Another one is a mask-free etching promoted by the presence of terrace edges at the substrate surface. Amazingly, they found similar morphologies in natural samples.

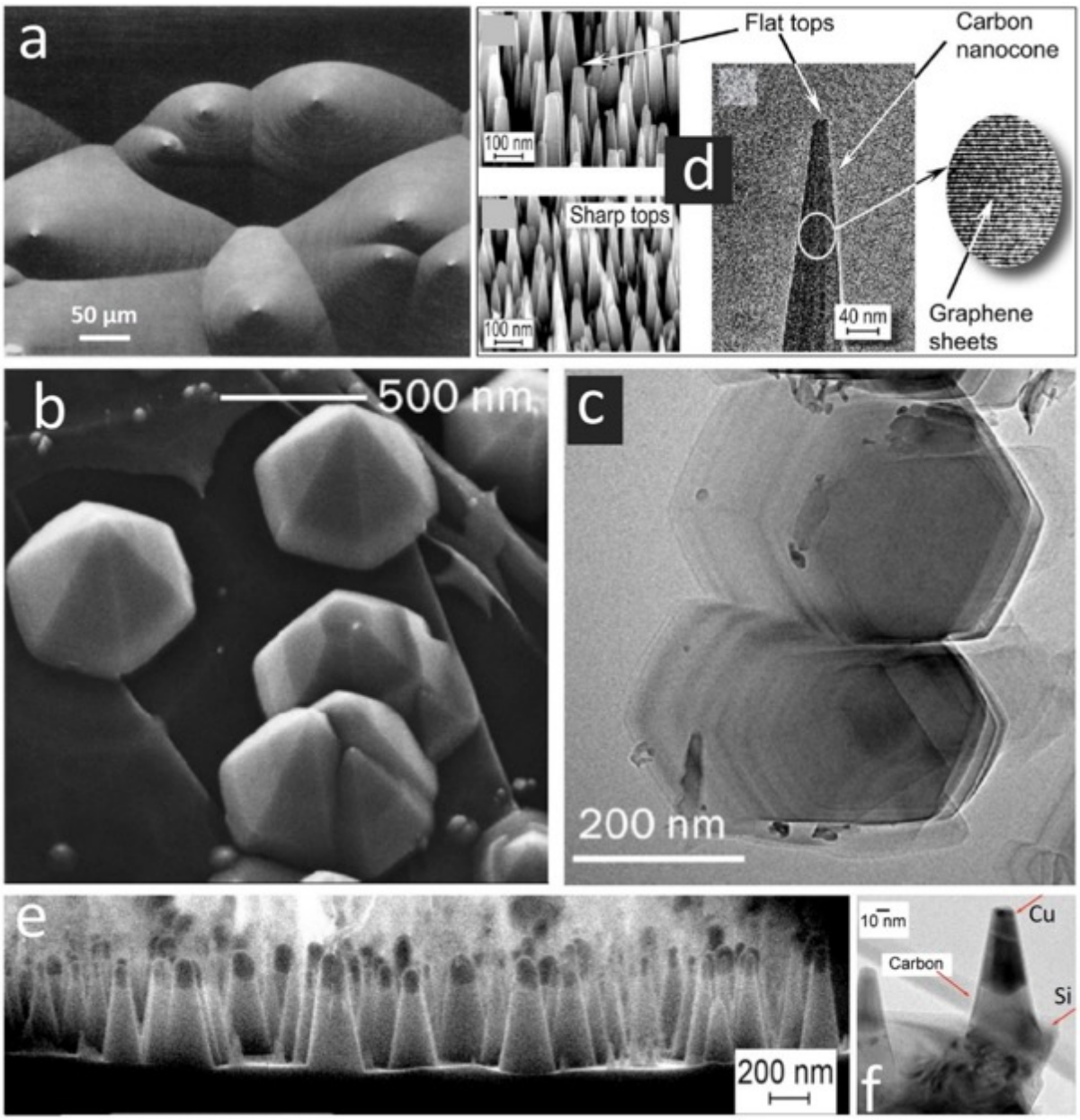

Figure 17: (a) *Conical carbon morphologies obtained by UV-laser etching of HOPG [*121Krajnovich1993*]. **(b)** and **(c)** hexa-pyramidal morphologies obtained by argon plasma etching of HOPG or flexible graphite [*23Glad2014*]. (c) demonstrates the easy delamination between layers upon mechanical stresses induced by the preparation for TEM examination. **(d)** example of array of conical morphologies and evidence for the inner platelet texture as obtained by PE-CVD [*128Levchenko2007*]. **(e)** and **(f)** array of conical morphologies, supposedly with platelet texture, each of them capped with a copper crystal [*129Kumar2010*].*

Finally, a whole series of papers by Ostrikov and coworkers [*98Levchenko2008*, *122Tsakadze2004*, *123Denysenko2004*, *124Tsakadze2005*, *125Ostrikov2005*, *126Ostrikov2006*,

127Xu2006, *128Levchenko2007*, *129Kumar2010*] has thoroughly investigated the possibility to grow carbon cones by means of RF plasma enhanced CVD from CH_4 + H_2 +Ar over Ni particles onto a Si substrate. The method is interesting as it is quite successful and allows growing a more or less dense array of carbon cones onto a substrate only heated at temperature as low as 300°C. The cones were demonstrated to be graphenic, turbostratic carbon by Raman, but no textural characterization was ever carried-out but by Levchenko *et al.* [*128Levchenko2007*], who reported the synthesis of platelet cones (i.e., graphenes are piled up perpendicular to the elongation axis) of 1 µm height, 15 nm apex radius, via a plasma-assisted process (**Fig.17d**). They were called " single-crystalline" but no structural study has ascertained the structure to be otherwise than turbostratic, although the nanotexture seemed to be excellent.

The growth mechanism of these morphologies was described through a three-step process, though purely hypothetic: (i) graphenes form parallel to the surface of the catalyst nanoparticles of nickel according to cylindrical morphologies of constant diameter; (ii) the cone forms as radial growth occurs by the attachment of carbon atoms to borders of the hydrogen-terminated graphene sheets while axial growth keeps going by the formation of new layers generated at the base in contact with the catalyst; (iii) once the catalyst nanoparticle is entirely covered, the radial growth keeps going the same way, but the axial growth can only continue by the formation of new layers at the top of the nanocones, which is flat first, but become sharp with time. It cannot be ascertained whether all the conical morphologies described in Ostrikov's group papers [*98Levchenko2008*, *122Tsakadze2004*, *123Denysenko2004*, *124Tsakadze2005*, *125Ostrikov2005*, *126Ostrikov2006*, *127Xu2006*, *128Levchenko2007*, *129Kumar2010*] are all the same and similar to that described in [*128Levchenko2007*], but it is likely, as synthesis conditions were close, except in [*127Xu2006*] where two RF plasma sources were coupled. It is worth noting that the method is versatile enough for allowing the growth of carbon cones each topped with a Cu crystal (**Fig.17e-17f**) [*129Kumar2010*].

2.3 Morphology-driven (process-driven) conical forms

2.3.1. During growth

Of course, in most of the cases, conical forms are obtained during growth. However, this sub-*Section* is devoted to works for which it is impossible to assign the conical shape to the texture, i.e. the way graphenes are displayed relative to each other, because it was not described (neither the structure, in most of the cases, i.e. whether it was diamond-related or graphenic). For the works described here, the reasons for the conical shape is mostly morphological.

An early work by Messier *et al.* [*130Messier1982*] using argon plasma etching of various carbon targets resulted in covering the carbon substrates with more or less packed conical morphologies (somewhat alike to what is shown in **Fig.17d** regarding the overall morphology). Carbon texture and structure from the cone were unidentified. Nothing as well-ordered as what was obtained also by argon plasma etching by Glad *et al* [*23Glad2014*] (described in *Section 2.2.3*) was obtained. However, conditions were quite different, starting with a 15 times lower RF power in [*130Messier1982*].

Argon etching was also used by Tanemura *et al.*, however also involving a metal (Mo, Si, Ni), unusual ultra-high vacuum conditions (10^{-6}-10^{-2} Pa), a tilted (45-55°) ion beam (known for promoting surface texturization, as opposed to a normal incidence), and a mostly unheated substrate [*131Tanemura2004*, *132Tanemura2005a*, *133Tanemura2005b*, *134Tanemura2006*, *135Zamri2011*]. Probably because of the metallic element added, the conical morphologies obtained cannot result from etching processes only. As opposed to Glad *et al.* [*23Glad2014*] they admitted that carbon re-deposition was possible and partly responsible for the cone formation. The main difference with the work by Messier *et al.* [*130Messier1982*] is the occurrence of a carbon nanofilament protruding from each cone apex (**Fig.18a**). Considering the widespread occurrence of a primarily grown CNT as the core of many conical morphologies as described in the previous *Sections*, whether the carbon nanofilament grew at the cone apex or pre-existed was questionable. They beautifully demonstrated the former hypothesis by growing a carbon nanofilament at the apex of a Si probe for scanning probe microscopy by using the same method [*134Tanemura2006*]. Surprisingly, although the authorship of the paper is partly shared with that of Tanemura's papers, Zamri *et al.* [*135Zamri2011*] claimed for the non-catalytic growth of the CNT. However, as the etched substrate was a commercial graphite plate, the presence of impurities was likely.

A unique example of etching a pure carbon target (flexible graphite) by means of a pulsed, powerful (~1 mJ) laser probe instead of argon ions was reported by Zhao *et al.* [*136Zhao2009*]. A dense array of carbon conical forms is created, possibly over large surfaces by scanning the laser probe. Interestingly, the polarization direction of the incoming light was found to determine the growth direction of the cones, which aligned perpendicularly to it. Again, the characterization is poor as the resulting carbon hybridization type (sp^2 or sp^3) and structure (amorphous or crystallized) of the cones was not investigated. Yet an easily implemented one, the process has the inconvenient to create craters in the graphite surface, which make that the orientation of the cone axes is not uniform all over the irradiated surface (see **Fig.20d**).

Chen *et al.* [*137Chen2004*] reported the formation of micrometer-sized carbon cones with various geometrical characteristics diameter, and a 5° cone angle. They were produced by a Ni catalyst-driven growth by an electric field-guided PE-CVD process. The growth of the carbon nanocone was carried out at 700 °C using a mixture of C_2H_2 + NH_3 gases at 3 Torr, which are conditions very similar to that used in [*99Merkulov2001*]. As the conical shape was obtained by adjusting the dc bias to be higher than 550V, whereas lower dc bias only generated tip-grown herringbone nanotubes, its formation was convincingly explained by an etching plasma effect, which caused the reduction of the diameter of the catalytic particle as it moves up until its complete elimination leading consequently to a sharp cone and the stop of the growth, as also proposed in [*97Li2007*, *100Merkulov2001b*]. The conical morphology is enhanced by the concomitant carbon deposition at the cone base, as more efficient as it occurs closer to the base (hence to the heated substrate). This mechanism is the same as that proposed by [*96Li2005*, *97Li2007*, *99Merkulov2001*] (see *Section 2.2.1*), however it is more convincing here as they succeeded to grow a CNT at the tip of the cones by switching the dc bias from high to low values. Although the texture of the CNTs grown was somewhat evidenced as being herringbone, there was not such characterization of the texture (nor the structure or nanotexture) for the cones. But the fact that they do not exhibit any central hollow channel, and contain some Ni

nanoparticles and some Si, suggests that, instead of "crystalline" as claimed by the authors, they might be poorly organized or amorphous, possibly due to the severe etching that opposes or destroys a good structuration.

Very similar process conditions were used in [*138Lee2017*] to grow an array of carbon conical morphologies of 60 nm tip size, 3 μm diameter base, and 47 μm length. The authors claimed them to be single carbon nanotubes but this was obviously not the case. The cone characterization is very poor in terms of texture, nanotexture, structure, and even chemical composition. Related conditions were used by [*139Zhong2004*], yet different because their synthesis procedure combines dc bias-enhanced plasma with a microwave generator to assist the catalyst-promoted (Fe instead on Ni) CVD formation of carbon cone array. They also used H_2 + CH_4 instead of NH_3 + CH_4 as feedstock, and the substrate temperature (< 600°C) was only due to the interaction with the plasma. [*139Zhong2004*] mentioned the same tip-growth as in [*137Chen2004*] although they did not evidence any catalyst particle at the cone tips, and pointed-out that the sub-micrometer conical morphologies are formed because the electric-field strength is self-enhanced by the growth of the carbon cones, an effect that should be common to many plasma-based CVD processes [*98Levchenko2008*]. Consequently, this electric field increases the directional movement of ionic carbon species towards the carbon nanotube nuclei, allowing carbon to nucleate also at the roots of the nanotubes, hence contributing to generate, by this manner, conical shapes by lateral growth. Therefore, Zhong *et al.* mentioned the formation of carbon nanofibers, but they did not show any evidence for that, although they designated each cone as being a single nanofiber. Also, importantly, most of the cones were said to be amorphous, which is barely compatible with the principle of catalytic growth of carbon morphologies, which generally comes along with some structuration. Again, this might be the result of the etching effect by the plasma. Poorly organised graphenic carbon cone arrays of unidentified texture were also grown using a related approach as above, yet only combining microwave plasma and Co-assisted CVD [*140Wang2005*]. Feedstock was CH_4+H_2 (5-15:80), and the bias was varied from 0 to 300 V. It was observed that the aspect ratio of the cones was increased by increasing the bias and decreasing the carbon species concentration, thereby supporting the well-spread idea that the former parameter prevails on driving axial growth while the latter parameter drives radial growth.

A quite peculiar morphology was obtained by Chen *et al* as early as in 2000 [*141Chen2000*], which resembles a tree, i.e. with trunk and branches (**Fig.18c** and **d**). They were grown on Ni dots from C_2H_2 + N_2 (3:97) by means of DC-plasma (450 V bias) combined with HF-CVD (Fe-Co alloy substrate at 800°C, 20 Torr). Morphologies obtained were described by the authors as a series of inverted lampshade-type carbon protrusions stacked over each other which grow at the surface of a central nanotube while it grows, which gives the overall morphology the appearance of an elongated cone (**Fig.18c** and **d**). Therefore, the morphology is supposed to somehow follow the model in **Fig.12a-right**, yet including a nanotube in the central part. But such a configuration does not appear right from the SEM or TEM images, and a spiral growth of graphene layers oriented more or less perpendicular to the tube surface appears more likely from short-duration growth experiment (**Fig.18b**), and also from a quite similar morphology grown later on by Dumpala *et al.* [*92Dumpala2011*] (**Fig.18e**). Intriguingly, it was observed that the conical morphology was produced only if the catalyst-coated substrate (Ni dots patterned

onto a Fe + Co layer coating a Si wafer) was pre-treated with H_2 in the HF-CVD reactor. Without this step, only regular CNTs were formed. This remains unexplained.

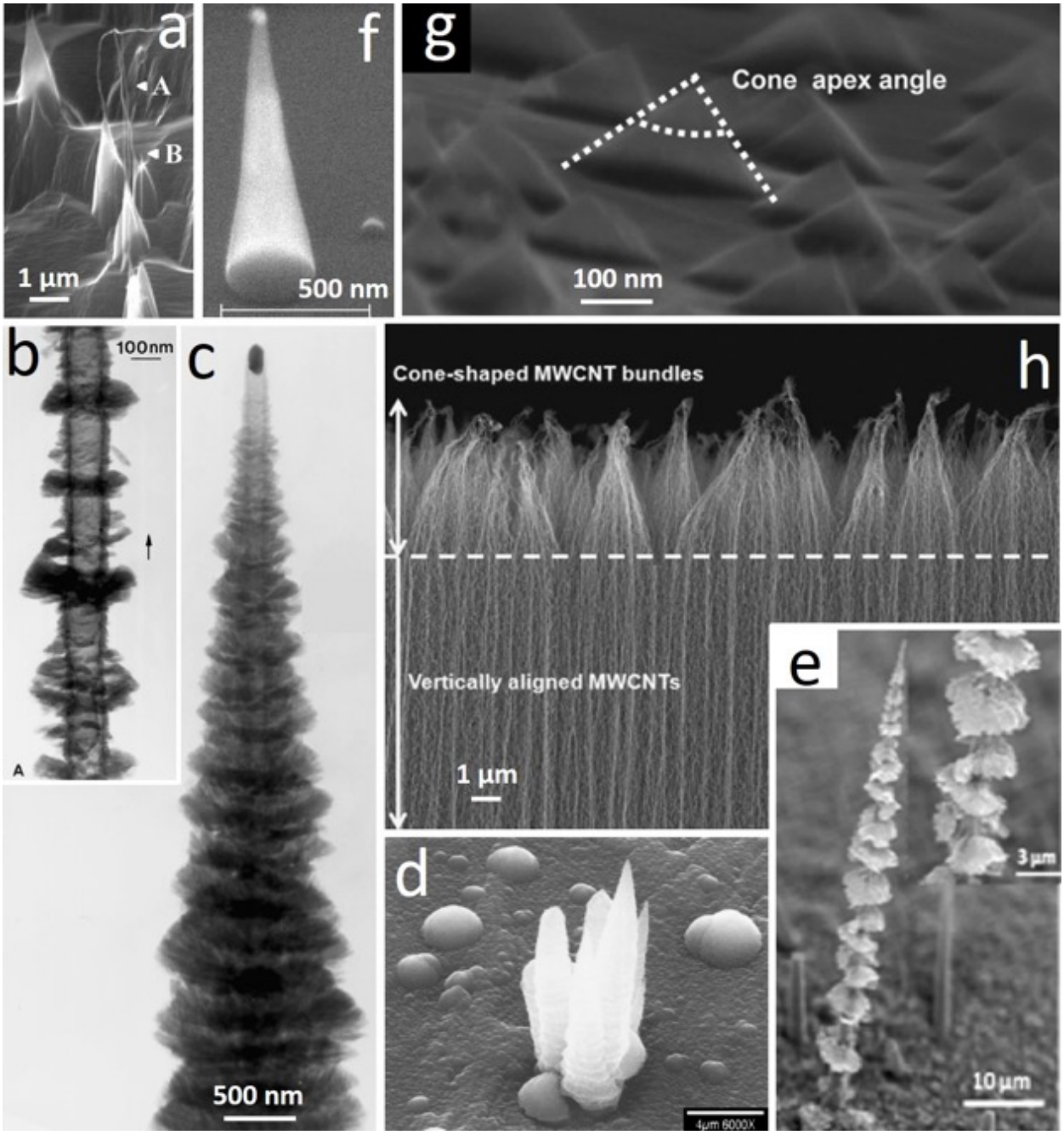

Figure 18: (a) *conical morphology with a carbon nanofilament growing at the apex as obtained from the ion bombardment of glassy carbon in presence of Mo [*131Tanemura2004*]; letters A and B in the image refer to the original text.* ***(b)*** *to* ***(d)*** *Conical carbon morphology obtained by a combined DC-plasma + HF-CVD method onto Ni dots [*141Chen2000*];* ***(c)*** *results from a short duration experiments to see the early steps of the occurrence of the branches;* ***(d)*** *they grow as islands onto each Ni dot.* ***(e)*** *A similar morphology as in (b) grown in [*92Dumpala2011*].* ***(f)*** *A conical CNT bundle as obtained by a combined DC-plasma + thermal (hot wall) CVD method onto Ni dots [*143Tan2005*]; the actual presence of CNTs does not appear but was demonstrated by TEM.* ***(g)*** *Conically shaped CNT bundle terminations as obtained by a plasma-free HF-CVD process onto pre-etched Cu substrate [*144Mata2011*].* ***(h)*** *Conical CNT bundles obtained from a two-step process involving the formation of vertically aligned CNTs first, subsequently subjected to an oxygen-containing plasma [*147Lim2010*].*

DC-plasma combined with HF-CVD was also used by Lu *et al.* [*142Lu2006*] who obtained dense arrays of carbon nanocones whose structure (diamond-related, graphenic, or a mix of both) was able to be tailored by adjusting the surface roughness, the Si substrate and the H_2/CH_4 ratio of the gaseous feedstock, and the timing at which turning the plasma on. The nature of the feedstock and the absence of any catalyst made the main differences with the previous work by Chen *et al.* [*141Chen2000*].

A work combining CVD (thermal, C_2H_2 + NH_3, cold-wall furnace with 700°C-heated Ni-coated Si substrate) and plasma conditions (glow discharge, -500 V bias) was carried out by Tan *et al.* [*143Tan2005*], resulting in a quite different conical morphology than above, i.e., conical CNT bundles (**Fig.18f**).

In order to explain the conical shape of the bundles, the authors proposed a mechanism of differential growth between the inner CNTs and outer CNTs. Based on considering that the diffusion route of the carbon species is quenched by the successive rings of growing CNTs around the primary one, the growth of the CNTs is presumed to be as lower as the CNTs are outer. However, this is barely convincing. Because the CNT growth is of the tip-based type, hence such a mechanism should result in having catalyst nanoparticles to be present at various heights in the cone. This is not what is observed, as the catalyst was only evidenced at the cone tip instead (**Fig.18f**). Also, it is questionable why outer CNTs would start to grow after the primary CNT as to a second CNT ring, then as a third CNT ring, etc., instead of all growing in the same time. Whatever, it is worth noting that the reality of the conical morphologies as made up from CNTs does not appear in the SEM image (**Fig.18f**) although it was demonstrated by TEM. This makes the work reported in *Section 2.3.1* able to be reconsidered, i.e., it is possible that some of the poorly characterized carbon cones reported in Tanemura *et al.*'s papers and in [*137Chen2004*, *138Lee2017*, *139Zhong2004*] are actually conical carbon nanofilament bundles.

Finally, a unique example of plasma-free synthesis of carbon nanofilaments that spontaneously arrange into conical bundles (**Fig.18g**) while they grow was reported in [*144Mata2011*]. They used the HF-CVD process to grow poorly organized carbon nanofibers from CH_4/H_2/Ar onto a Cu substrate. Because of a chemical pre-etching of the Cu substrate, the Cu surface becomes nano-texturized and exhibits catalytically active nano-bumps. A complex multilayer carbon deposit is formed, which includes a layer of cone-shaped CNF bundles. As the CNFs grow from bumps instead of individual nanoparticles, the latter could not lift-off and the base-growth mechanism was enforced. Why the CNFs gather together by their tips so that to form cones was tentatively explained by the authors as an effect of attractive van der Waals forces. But this is poorly convincing as the same effect should then apply to any vertically-aligned CNFs or CNTs grown as a forest, making that conically shaped bundles should be very common in the literature, which is not the case (unless plasma shaping is used, see next *Section 2.3.2*).

2.3.2. Post-growth

Conical carbon morphologies were also obtained from pure etching of prefabricated carbon morphologies such as carbon fibers or pristine nanotubes. The main idea of these post-growth

processes is to create sharper morphologies. In that case, the starting carbon material to be etched is selected so that to exhibit graphenes somewhat oriented in the direction of the future cone axis mostly because the application envisaged is electron emission. Original works are those based on an assembly of carbon sub-morphologies, typically carbon nanotubes, as reported in [*145Liu2004*, *146Huang2006*, *147Lim2010*]. As opposed to the work by Mata *et al.* and Tan *et al.* above [*143Tan2005*, *144Mata2011*], regular vertically-aligned carbon nanotubes were first grown by regular catalyzed-CVD and then subsequently subjected to a plasma etching process which induced the nanotubes to gather into conical bundles (**Fig.18h**). They both observed that the conical shaping was only obtained with a plasma involving O_2, as compared to Ar only. Based both on this statement and on XPS results, Lim *et al.* proposed that oxygenated functions are created at the edge of the opened tube tips, creating dipoles that generate attractive forces between neighboring CNT tips, hereby forming the conical bundle terminations. This explanation could then be valid for the results by Liu *et al*. as well [*145Liu2004*], who did not provide any.

In order to obtain carbon cones to be used as SPM probes or voltammetric sensors, a totally different route was used by Mousa [*148Mousa1996*], Castellanos-Gomez *et al.* [*149CastellanoGomez2010*] and then Sripirom *et al.* [*150Sripirom2011*], who basically adapted to carbon fibers the well-known electrochemical etching process used to taper metal filaments. NaOH was used, and the carbon fiber was actually tapered at its end, exhibiting a conical morphology whose apex is however not so sharp. In the case of [*150Sripirom2011*], the apex radius of curvature is ~25 nm (**Fig.19**). Little information only was given on the type of carbon fiber used to start with[5], and no characterization was made of the possible alteration of the graphene structure and nanotexture by the etching.

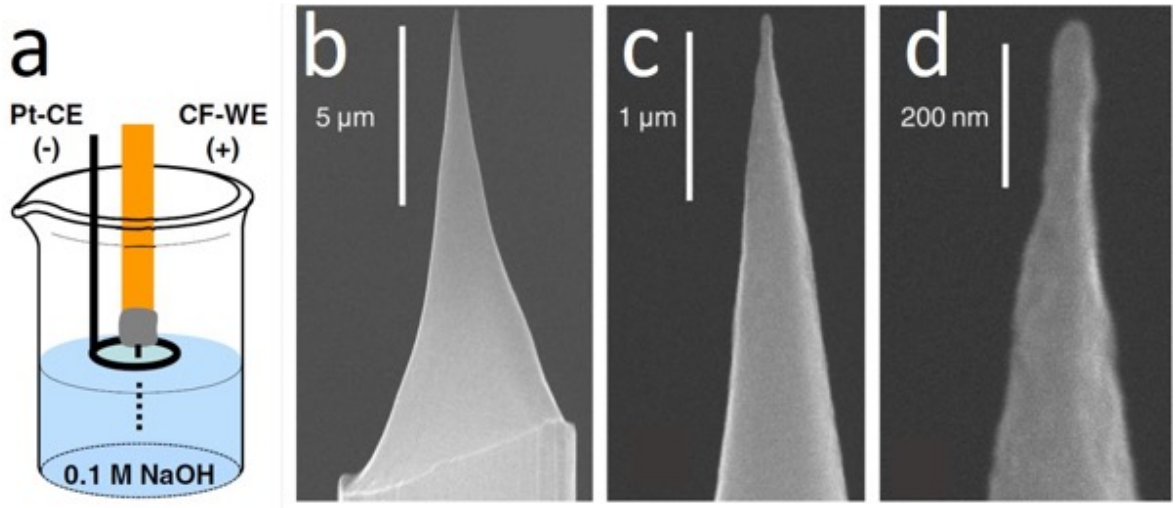

Figure 19: *Electrochemical etching of a regular carbon fiber [*150Sripirom2011*]. **(a)** Principle; the carbon fiber is glued by a carbon paste (grey color) to a tungsten wire (orange color), and then soaked into the etchant solution. A DC voltage between the anode (the carbon fiber) and the cathode (a Pt wire loop) adjusted so that to run a current of 30-40 µA is applied, while the carbon fiber is slowly retracted upward. **(b)** to **(d)** images of the apex obtained at increasing magnification.*

[5] It is described as "high-modulus" in [*148Mousa1996*], but the small diameter – 7 µm - is rather that of a PAN-based instead of pitch -based carbon fibre, which might be an important choice because the latter exhibit higher conductivity and Young modulus.

Finally, the dynamic oxidation in air at increasing temperature was used in [*151Huang2016*] to tentatively enhance the sharpness of the apex of the carbon nanocones shown in **Fig.5**. The nanocone material was bought from the company named n-Tec AS and subsequently subjected to a 2700 °C annealing in order to make the nanotexture perfect prior to oxidation. Valuable observations on the oxidation mechanism were made, and statistics showed an actual sharpening of the cone apices, from a majority above 20 nm in the starting material down to a majority below 10-20 nm in the oxidized material. The poor control of the cone apex aspect at all scale (atomic, textural, nanotextural) due to the variability of the behavior of cone apices upon oxidation is a probable limitation for subsequent applications.

3. Property and applications of conical carbon morphologies

3.1. Properties

3.1.1. Electronic properties

Because of the huge variability of the texture, nanotexture, and even structure in conical carbon forms which overpasses that of carbon nanotubes, very few works have dealt with investigating the properties of carbon cones from a theoretical point of view, using methods such as *sp* tight-binding Hamiltonian and *ab initio* calculations [*152Lammerts2000*, *153Charlier2001*, *154Lammert2004*, *155Munoz2005*, *156Pincak2015*]. They all concern the electronic properties, and exclusively the case – no wonder, as it is the easiest to model - of the ideal single-graphene molecular structures obeying the pentagon rule depicted in **Fig.2c**. The role of the number and location of pentagons was investigated [*152Lammerts2000*, *156Pincak2015*], eventually combined with heptagons [*155Munoz2005*]. Closed and opened cone apices were compared, showing the importance of the atomic configuration (armchair or zigzag) of the opening edge [*155Munoz2005*], as well as hypothetical cone combinations [*157Shenderova2001*]. The existence of dipole moments and their interaction with H_2 molecules was investigated [*158Heiberg2008*], and their behavior as thermal rectifier as well [*159Yang2008*]. STM images of cone apices were calculated, which match actual images [*160Kobayashi2000*]. Electronic properties were also calculated for nanohorns considering the only 5-pentagon cone tip, which is supposed to best account for the nanohorn configuration [*161Berber2000*]. All these calculations are about too ideal objects (e.g., single graphene cones have not been isolated yet, and single graphene nanohorns are far from the ideal sketch as depicted in **Fig.4** for being really useful in property predictions of the actual objects). However, as opposed to ideal single-graphene cones, nanohorns do exist, and therefore were experimentally measured for their magnetic properties [*162Garaj2000*, *163Bandow2001*, *164Imai2006*], and behavior to charge transfer through doping with Li, K, and Br [*165Bandow2000*] or functionalization [*166Cioffi2007*], or gas adsorption [*167Urita2006*]. Detailed comments on these aspects can be found in [*52Yudasaka2008*].

3.1.2. Mechanical properties

Alike electronic properties, experimental works dealing with the mechanical properties of carbon cones are scarce in the literature. As a matter of fact, we did not find any. The issue was addressed theoretically, mostly based on molecular dynamics, and again mostly focused on single-graphene, pentagon-driven conical forms as sketched in **Fig.2c**. The behavior of such cones was investigated under axial compression [*168Jordan2004*, *169Liew2007*, *170Tsai2007*, *171Liao2007*], axial tension [*171Liao2007*, *172Wei2007*], and subjected to free vibration (mostly transverse) [*173Hu2012*, *174FirouzAbadi2012*, *175Yan2014*, *176Narjabadifam2015*]. The conical objects were considered either as such [*168Jordan2004*, *172Wei2007*, *170Tsai2007*, *174FirouzAbadi2012*, *176Narjabadifam2015*], or uncapped [*169Liew2007*, *171Liao2007*, *173Hu2012*, *175Yan2014*]. Parameters that were varied were the cone height, the cone angle, and the radius of the tip opening (when uncapped). Some interesting conclusions were obtained, for instance: tensile Young moduli are in the range 290-730 GPa [*172Wei2007*]; the tensile strength-to-failure increases and the tensile strain-to-failure decreases as the cone angle increases from 0° (CNT) to 19.2° (5 pentagons) to 38.2° (4 pentagons) [*172Wei2007*]; For a 19.2° cone (base fixed, uncapped cone, 0.34 nm top radius, 4.33 nm height), the fundamental transverse vibration frequency is in the range of 0.4 THz [*173Hu2012*, 175Yan2014]; the effects of cone angle and tip radius somehow compensate in transverse vibration, and the same fundamental frequency is obtained with appropriate combinations of both [*175Yan2014*]; it was even possible to deduce that, when starting from a preformed graphene, rolling it into a conical structure is preferred over a tubular structure [*170Tsai2007*]. The work by [*177Raj2018*] is a single example of a modelling work by means of MD and molecular mechanics that did consider stacked cones (up to three, instead of single-graphene cones) with various angles. The study investigated the behavior of single cone being axially pulled-out from a cone stack, and then being axially pushed-in back onto the stack top. The axial compression of the whole cone stack was also studied. In this landscape, the work by Liu *et al.* [*178Liu2004*] appears quite original as it is the only one studying the bending behavior of multi-wall cones with a concentric texture, i.e. as sketched in **Fig.12c**.

However, despite the reason given as a motivation for such studies are generally to bring support to the use of carbon cones for applications as SPM probes and electron emitters where anticipating their mechanical stability and behavior is required, they are of little practical interest. Indeed, the cones modelled are unrealistic with respect to those that will actually be used on the one hand (single graphene cones do not exist, and the cones are too much nanosized (few nm high) anyway), and many of the conclusions reached are merely common-sense results, for instance: smaller cone angle induces higher strain energy in compression, cones exhibit lower cohesive energy than flat graphene, cones with smaller angles exhibit lower melting temperatures [*170Tsai2007*]; rigidity to axial compression decreases as the cone angle increases [*171Liao2007*]; in-plane compression induces higher strain energy than axial compression [*169Liew2007*]; transverse vibration frequency decreases as the cone length increases [173Hu-*2012*, *174FirouzAbadi2012*, *175Yan2014*, *176Narjabdifam2015*].

Therefore, the field of the experimental study of the mechanical properties of carbon cones of various kinds is still unexplored.

3.2. Applications

Carbon conical morphologies, particularly those having needle-like shapes with a high aspect ratio (length over diameter ratio) at their tips, are expected to show better mechanical stability than narrow cylinder morphologies [*99Merkulov2001*, *101Jacobsen1997*]. In addition to this, they can also show excellent thermal and electrical properties when both the alignment and the nanotexture of graphene sheets are perfect, as well as a good chemical stability because of the carbon nature, although it may depend on the graphene orientation and the possible presence of reactive graphene edges at the cone surface. All of these characteristics make these structures very promising for several fields of potential applications.

3.2.1. Electron field-emission

The electron field-emission capabilities of carbon nanocones were the very first electronic property to be tested, as early as in 2000, with targeted applications such as screen displays, or X-ray generators, for which an array of emitters is required. More rarely, applications requiring a single emitting tip were also targeted, such as for cold-field emission electron guns (CFEG) that equip high-performance electron microscopes. Electron emission properties are assessed by parameters such as the emission current density (in A/cm^2, generally measured at the maximum value obtainable before the emitter structural integrity is affected), the turn-on electric field (i.e. the electric field to be applied from which the emission starts), the threshold electric field (i.e., the electric field needed to obtain a reference value of the emission current density), the brightness (i.e., the emission current density per angle solid unit, in $A/m^2.sr$) or the reduced brightness (same as previously, however divided by the acceleration voltage, hence in $A/m^2.sr.V$), the field enhancement factor (as the ratio of the local electric field value at the emitter tip over the overall electric field applied between the cathode – i.e., the emitter - and the anode), and the current stability over time. Depending on the applications, parameters to prioritize may be different. For instance, for screen displays, low work function, low threshold electric field, and low turn-on electric field are desired for limiting the energy consumption. On the other hand, for high performance electron sources for electron microscopes, high brightness, high electron wave coherence, and low energy spread are required, which is helped by limiting the emitting apex down to few nanometers. Because some of the parameters depend on others that are not standardized (surrounding gas pressure, anode-cathode distance, etc.), values are not always easy to compare from a paper to another. The number of emitting tips per surface unit is also quite different from a work to another, also resulting in large variations. Those variations are not easy to interpret and compare as they are not linear. For instance, increasing the emitter density (the number of emitting tips per surface unit) may increase the emission current density until a current saturation may occur (the well-known shielding effect) when the emitting tips are too much packed. However, we may assume that authors have presented the best and highest performances of their devices.

Reference (chronological order)	Synthesis process	Emitter type	Threshold electric field (for a current density of 1 µA/cm²)* Reduced brightness	Turn-on electric field (for a current density of 1 nA/cm²)*	Field enhance-ment factor	Max current or current density measured	Current stability over time
Emitter array							
Chen-2000 [141]	DCP-HFCVD	few pine-like graphenic cones	5 V/µm			30 µA at 8 V/µm	
Bonard-2002 [179]	Film transfert	Nanohorn-layer film	*7 V/µm for 10 mA/cm²*	*3.9 V/µm for 10 µA/cm²*	930	Damages above 1 mA/cm²	
Liu-2004 [145]	CVD + O_2-plasma etching	Dense array of conical CNT bundles				107 mA/cm² at 5.5 V/µm	
Tsakadze-2004 [122]	ICP-CVD	Dense array of high AR graphenic cones	6.4 V/µm			3 mA/cm² at 20 V/µm	
Li-2005 [96] Li-2007 [97]	DCP-HFCVD	Mediumly dense array of conical CNTs	0.27 V/µm		88-135	1 mA/cm² at 0.5 V/µm	1.9 mA/cm² at 0.6 V/µm over 6 h
Tanemura-2005 [132]	Ar+-irradiated graphite	Dense array of cones with protruding CNFs	1.8 V/µm	1.5 V/µm	1951		
Tanemura-2005 [133]	Ar+-irradiated graphite	Dense array of cones with protruding CNFs	3.05 V/µm		2860	1 mA/cm² at 13 V/µm	0.17-0.3 mA/cm² at 10 V/µm over 40 h
Wang-2005 [140]	MWP-CVD	Dense array of graphenic cones	7 V/µm	5 V/µm		173 mA/cm² at 10 V/µm	10 µA at 900 V over 6 h for the least.
Xu-2006 [127]	ICP+RFP-CVD	Dense array of high AR cones				3 mA/cm² at 6.5 V /µm	
Huang-2006 [146]	MWP-CVD	Dense array of conical CNT bundles		*2.5 V/µm for 10 µA/cm²*		4.5 mA/cm² at 6 V/µm	
Lu-2006 [142]	DCP-HFCVD	Dense array of graphenic cones		*4 V/µm for 10 µA/cm²*	2000	1.1x10¹² mA/cm² at 13 V/µm	77% decay at 6 V/µm over 50 min
Shang-2008 [113]	MWP-CVD	Low density array of high AR concentric-texture cones			3700	0.65 mA/cm² at 4 V/µm	
Dumpala-2009 [180]	MWP-CVD	Low density array of high AR concentric-texture cones		0.7 V/µm	7600	520 µA at 3.6 V/µm	
Zhao-2009 136]	Laser-irradiated flexible graphite	Dense array of cones		*3.2 V/µm for (current density)?*	3365	108 µA/cm² at 5.8 V/µm	
Gosh-2010 [181]		Dense array of cones coated with a gold film	*9.5 V/µm for 10 µA/cm²*	*6.1 V/µm for 10 nA/cm²*	1020		
Lee-2017 [138] Kang-2017 [182]	DCP-CVD	Low density array of high AR cones				14 µA at 5 kV (anode) and 5.9 V/µm (gate)	1 µA at 5.3% at 1520 V over 100 h
Individual, single emitter							
Mousa-1996 [148]	Electrohemical etching of carbon µfibre	Tapered single carbon microfibre				0.1 nA at 350 V 2.5 µA at 650 V	
Baylor-2002 [183]	DCP-CVD	Isolated conical CNTs		12-60 V/µm			10 nA at 20-30 V/µm, with a 20% decrease in needed field over 175 h
Zhang-2007 [106]	Cold-wall CVD	Concentric-texture graphenic cone with central CNF				103 µA at 169 V	
Zamri-2011 [135]	Ar+-irradiated graphite	Cone with protruding CNF		70-80 V/µm			0.5 µA at 150 V with large fluctuations over 0.5 h
Lee-2017 [138]	DCP-CVD	High AR cone	1.7 10^7 A/m².sr.V		2620	10 µA at 1.2 kV (4.5 V/µm), 3.5 10^5 A/cm²	
Houdellier-2012 [184] deKnoop-2014 [185] deKnoop-2015 [186] Houdellier-2015 [187] Mamishin-2017 [188]	ToF-CVD	High AR concentric-texture high-nanotexture cone	1.6 10^9 A/m².sr.V		15000	30 µA at 1;5 kV extraction voltage	5 µA with 10 nA fluctuations at 408 V over 1 h 2 nA at 1.3 kV extraction voltage over 9 h
*Unless indicated otherwise							

Table 1: *Summary of the electron emission performances of carbon cones either as arrays (upper part) or as single emitter (lower part) as reported in the references provided in the first column. Abbreviations: CVD = chemical vapor deposition; HF = hot-filament; DCP = direct current plasma; ICP = inductively coupled plasma; MWP = microwave plasma; RFP = radio-frequency plasma; ToF = Time of Flight. Turn-on electric field values from arrays cannot compare with that of single tips due to the difference in the number of tips to emit the same current value.*

Table1 gathers the results reported in the literature regarding the field emission properties of both carbon-cone-based emitter arrays and single emitters. **Fig.20** illustrates some of the emitters tested. For all of them, the plots of the logarithm of the emission current density versus the electric field, were shown to follow a linear dependence, thereby confirming that the emission current is caused by the quantum tunneling effect predicted by the Fowler-Nordheim model [*189Fowler1928*].

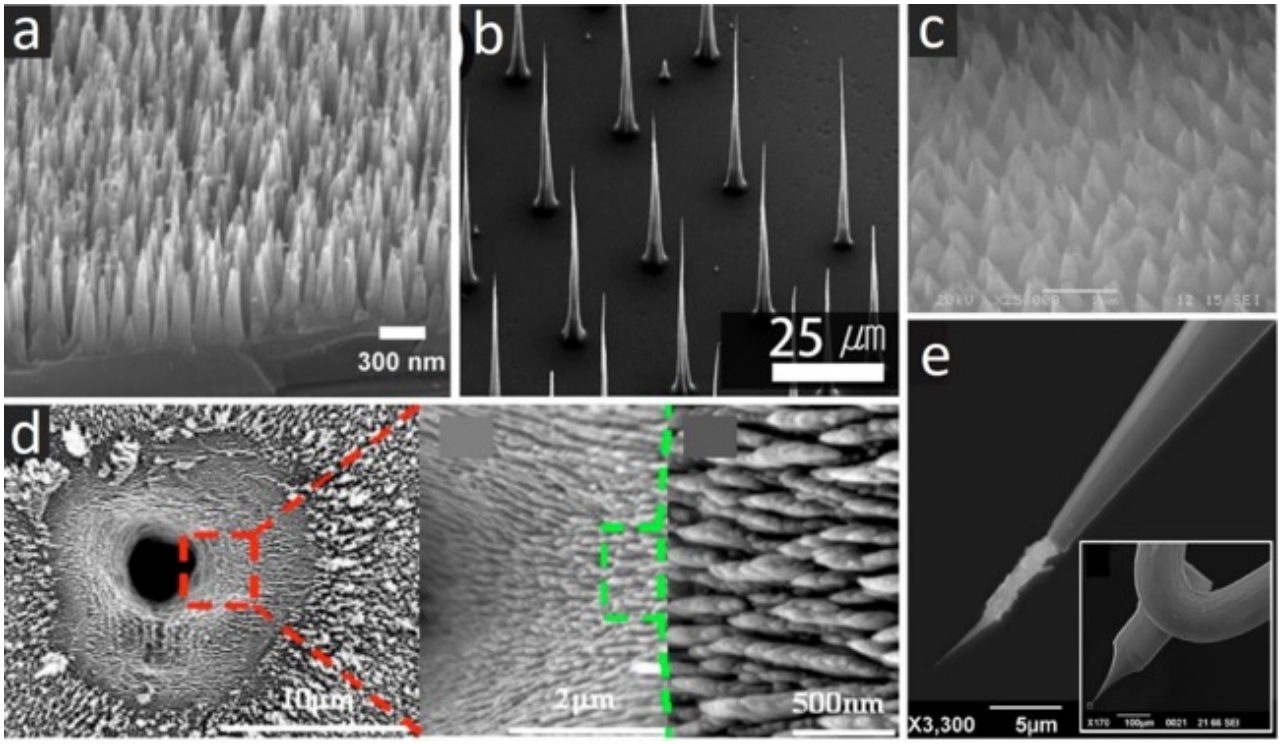

Figure 20: *Various examples of conical carbon morphologies tested for their electron emission properties.* ***(a)*** *Example of a dense array of carbon cones, here prepared by MWP-CVD [*140Wang2005*].* ***(b)*** *Example of a low-density array of carbon cones, here prepared by DCP-CVD [*182Kang2017*].* ***(c)*** *A unique carbon cone array obtained by Ar+ ion irradiation of a Nafion polymer film, subsequently coated with an ultrathin film of gold [*181Ghosh2010*].* ***(d)*** *Array of carbon cones prepared by the laser irradiation of flexible graphite; the hole is due to the laser impact [*136Zhao2009*].* ***(e)*** *ToF-CVD-prepared carbon cone welded onto a W tip; in inset, low magnification view of the W tip welded onto the V-shape W filament subsequently put into the CFEG source of a Hitachi 2000 TEM [*184Houdellier2012*].*

As previously said, comparing works is difficult due to the lack of a common parameter to do so. However, trends can be found. Most of the authors stated that the emission performances obtained with carbon cones are better than with carbon nanotubes [*96Li2005*, *97Li2007*, *136Zhao2009*, *145Liu2004*, *146Huang2006*, *184Houdellier2012*], or equal for the least [*133Tanemura2005*, *180Dumpala2009*]. As an example, Liu *et al.* [*145Liu2004*] reported a current density of 45 mA/cm^2 for a regular, forest-like CNT array which increased up to 107 mA/cm^2 for the same array after shaping the CNT bundles into cones. As another example, Li *et al.* [*96Li2005*] calculated a work function of 0.12 eV, to be compared to 5.3 eV for CNTs. However, this value is doubtful as surprisingly very low, considering that, for graphenic carbon, the work function was everywhere else found to fall in the range of 4-5 eV for various examples of CNTs as well as high aspect ratio nanocones [*185deKnoop2014*] and graphite

[*190Mathur1953*]. Another surprising result is the ability of the single conical tip reported by Baylor *et al.* [*183Baylor2002*], which relates to the conical morphology described in [*99Merkulov2001*, *100Merkulov2001*], to maintain a 10 nA emission current over 175 h provided the applied electric field is gradually decreased by 20%. Such a behavior implies that the current would have increased if the applied electric field would have been maintained constant instead, which is in contradiction with the overall behavior of electron emitters, specifically at a chamber pressure of 13.10^{-5} Pa which is the highest used among **Table1**, except for [*133Tanemura2005*] (10^{-4} Pa). Finally, another surprising value is the huge emission current density of 1.1 10^{12} mA/cm^2 reported by [*142Lu2006*] which exceeds by far any other one.
Two experiments are worth being commented a bit further. One is the work by Bonard *et al.* [*179Bonard2002*], which is specific as the emitting material is not cone-based but is a dense coating of nanohorns instead. In spite of this, the resulting performances are in the same range as for the other materials. The other work is that by Gosh *et al.* [*181Ghosh2010*], which is the only one having obtained a cone array from the irradiation of a polymer target instead of graphite (**Fig.20c**). No information about the cone structure and chemical composition is provided, but it does not matter much because the cone array is subsequently coated with gold, which is the actual emitting material then. Hence it does not compare with the others, but on the other hand, it is the only example of an electron emitting material while remaining flexible and photo-transparent.

When the comparison is available, the best performances in terms of threshold electric field (0.27 V/µm) and turn-on electric field (0.7 V/µm) are respectively obtained in [*96Li2005*, *97Li2007*] (who compared to 1-2 V/µm for CNTs) and [*180Dumpala2009*] (who compared to ~0.7 V/µm for CNTs), i.e. for processes in which the etching effect of plasma is limited and where the conical morphology is mostly obtained from catalytic growth, thereby allowing the graphenic nature of the carbon cones to develop and leaving the nanotexture unaffected, as opposed to other cone synthesis methodologies involving plasma-etching. In all the papers but in [*122Tsakadze2004*], the interest of high aspect ratio needle-like morphologies for gaining in performances is emphasized. The contradictory loss in performance observed in [*122Tsakadze2004*] upon the plasma-driven formation of cones is possibly due to the alteration of the carbon structure due to the etching by the plasma. Considering what was just stated, the best performances are then expected when combining a plasma-free synthesis process, a very high aspect ratio (along with a nanosized apex), and perfect graphenes aligned with the cone axis.

Indeed, this corresponds to the carbon nanocones with a concentric texture synthesized by Allouche *et al.* [*26Allouche2005*, *102Allouche2003*] (**Fig.16**), which were successfully tested as the cathode (i.e., the emitting tip) for CFEG application in both a scanning electron microscope [*187Houdellier2015*, *188Mamishin2017*]. and a transmission electron microscope [*184Houdellier2012*, *187Houdellier2015*] (**Fig.20e**). As a probable consequence of their atom-size surface roughness and low reactivity of graphene basal plane, the adsorption or residual molecules from the surrounding atmosphere is very limited. Carbon nanocones showed a very good current stability with no current decay for hours [*184Houdellier2012*, *188Mamishin2017*] in ultra-high vacuum conditions (10^{-9} Pa, as opposed to 10^{-5} Pa in all other papers). It is worth noting that this is the only work for which the emitting cones were tested in "real-life"

conditions, i.e. put in commercial equipment (electron microscopes), and compared to the best CFEG on market. This was not done in any other study, and could not be possible with CNT, because the particular morphology of the cones used (conical shape and large micrometric base), minimizes the vibration effects previously observed for carbon nanotube emitters when emitting. Vibrations make the emitter no longer behave as a few-nanometer-large electron source, and the phase coherence of the beam is killed [*184Houdellier2012*, *187Houdellier2015*]. As a matter of fact, when comparing to regular tungsten cathode, the same carbon nanocones allow a five-time better reduced brightness, the highest field enhancement factor ever (15 000), a fairly narrow 0.32 eV energy spread, and an excellent current stability of 2 nA over 9 hours compared to a 90% decay for tungsten in the same conditions. Also, the same cone has withstood a one-year-long operation without enduring any alteration. The laser-induced electron field-emission was also reported from the same carbon cones, but they did not withstand the laser beam energy [*191Bionta2015*].

3.2.2. Scanning probe microscopies (SPM)

Few applications of conical carbon forms as probes for near field microscopies are reported in the literature. This is surprising because carbon cones have been thought as suitable SPM probes quite early [*101Jacobsen1997*, *100Merkulov2001*]. Indeed, for these kinds of applications requiring high resolution images of three-dimensional features and deep trenches, the ideal tip should have a conical body (instead of pyramidal, as it is usual for current ceramic tips, which generates imaging artifacts), small diameters, high aspect ratio, and a nanosized (ideally a single atom) apex. Conical carbon tips combine the mechanical stability of the cone and the high aspect ratio of the narrow-diameter quasi-cylinder form which make them potentially superior over CNTs for such an application. Based on their previous work on growing carbon cones by a DCP-CVD process [*137Chen2004*] combined with a specific masking process allowing a single catalyst dot to be formed by electron-beam-induced deposition (EBID), Chen *et al.* [*192Chen2006a*, *193Chen2006b*] were able to grow a single, high aspect ratio carbon cone onto a tipless SPM cantilever with a controlled tilt angle of ~13° with respect to the cantilever surface (**Fig.21a**). The whole process seems to be suitable to upscaling. The cone was ~2.5 µm high, with a 200 nm base diameter a cone angle of 3-5°, and a few-nanometer apex size, yet with an undetermined structure. Such tips were tested as probes for obtaining AFM images (tapping mode) of various substrates, including a Cu film with ~5nm grains, a 500 nm deep PMMA pattern, a template-stripped Au film on mica immersed in deionized water, and a silicon nitride film on Si. They compared with a regular Si tip from the market. Of course, with the PMMA pattern, they evidenced the better imaging obtained with the carbon cone in terms of lateral and depth resolution, and also artifact-free profiles, thanks to the difference in aspect ratio and geometries (conical angle of 3° compared to a pyramidal angle of ~35°). On the other hand, in spite of their claim for improved imaging performances, the resolution of the Cu grains obtained with the C-probed image does not appear much better than with the Si-probed image (**Fig.21b**). Contours are actually less blurred, but the average grain size seems to be equal or even smaller with the Si tip, questioning the sharpness of the carbon cone apex. The superiority of the carbon probe over the silicon probe is more obvious with liquid medium imaging. Finally,

it is worth noting that the authors tested the mechanical durability of the carbon cone probe, and it was convincingly shown that the lateral resolution of the probe did not change for 7 hours of operation.

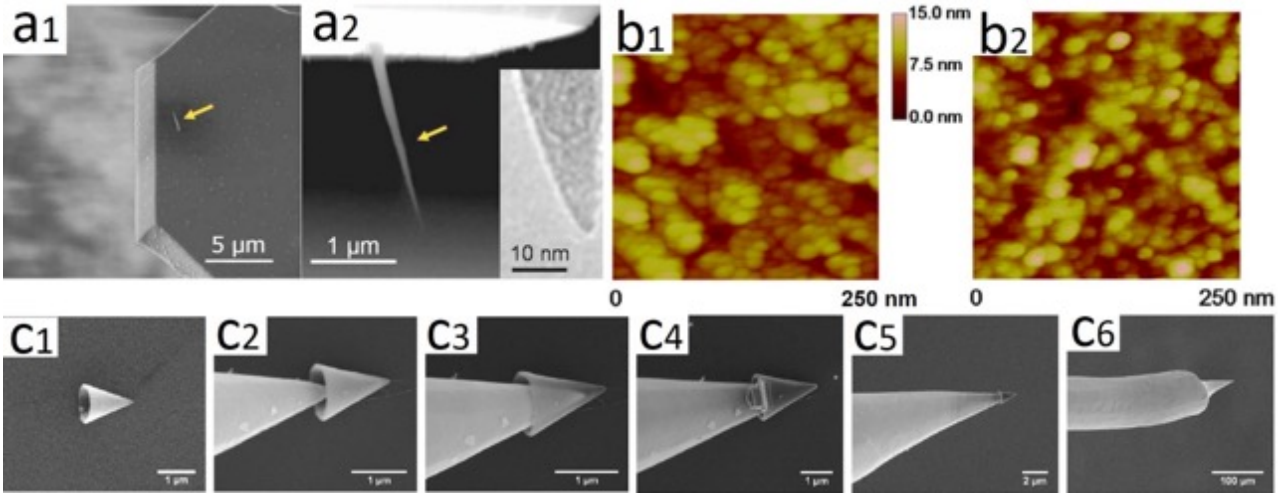

Figure 21: (a1) *and* ***(a2)*** *low and then high magnification SEM image of the carbon cone tip (yellow arrow) grown onto a tipless Si cantilever. Inset in (a2): TEM image of a typical cone apex (from [*192Chen2006a*]).* ***(b1)*** *AFM image (tapping mode) of a Cu film surface as probed by a carbon cone tip;* ***(b2)*** *the same (different area), probed with a regular Si tip (from [*193Chen2006b*]).* ***(c1)*** *to* ***(c6)*** *step by step SEM image sequence of the encapsulation of an Au nanotip into a carbon cone. The Au tip is moved by a micromanipulator; in (C4), the cone is welded with platinum to the Au tip (from [*195CanoMarquez2015*].*

The same conical carbon tips were used for magnetic force imaging [*194Chen2008*]. For doing so, the carbon tip was coated by a sputtering and then a 650°C annealing process with the tetragonal phase of a iron/platinum alloy known for its high coercivity (which ensures that the magnetization of the probe remains stable even when scanning a strongly magnetic material) and high saturation magnetization (which ensures that the probe has enough magnetic moment in spite of its nanosized). The performances were tested onto a high density CoCrPt:SiO/Ru perpendicular magnetic recording medium, and compared with the regular Si tips coated the same way. The high aspect ratio of the carbon tip support is able to reduce the probing magnetic volume, allowing an increase in the lateral image resolution of magnetic domains[6], in the range of 20 nm.

A very elegant and simple way to coat gold nanotips with graphene using carbon cones was reported by Cano-Marquez *et al.* [*195CanoMarquez2015*]. The motivation of the work was to enhance the mechanical resistance of the gold tip, but the process could be adapted to any tip with the suitable geometry. The type of cones used is that of **Fig.5**. The gold tip was prepared by chemical etching and then introduced by a micromanipulator into a carbon cone with the appropriate cone angle, and then welded (**Fig.21c**). The gain in mechanical resistance was supported by fully atomistic reactive MD simulations. However, again, the MD modelling

[6] It is worth noting that the authors have mistakenly inverted the compared phase images from the Si-based probe and the C-based probe in their figures 3 and 4, respectively. The comments provided here are based on the statement that the images inverted are presumably that of their figure 3.

considered a single-graphene cone only, whereas we know that this type of cones includes many stacked cones (see *Section 2.1.1*).
Finally, conical carbon tips obtained from the electrochemical etching of highly oriented graphenic microfibers as illustrated in **Fig.19** was tested as STM probes [*150Sripirom2011*]. The image of an Au grating with 2.5 grooves/μm was well resolved in air but no comparison with a regular STM probe was provided. Noise-free atomic resolution in UHV was also successfully obtained on the surface of a Si(*111*) substrate, and was said comparable to that of a standard W tip. [*149CastellanosGomez2010*] were also quite successful with testing the same kind of tapered carbon fibers (sub-100 nm apex radius) as tips for combined STM/AFM studies based on quartz tuning fork force sensors. This was due to their light weight (which made them not to degrade the starting Quality Factor of the sensor significantly: -2% only, as opposed to -40% with regular PtIr tips), high modulus (ensuring high resonance frequencies), and good electrical conductivity.

3.2.3. Electrodes

Arrays of the high aspect ratio carbon cones with concentric texture and high nanotexture prepared in [*89Mani2003*] were tested as nanoelectrodes by [*90Lowe2006*]. Nanoelectrodes are interesting devices which possess many advantages over macro-sized electrodes, as well stated in Lowe *et al.*'s paper introduction. However, carbon nanotubes are nanosized as well, hence they can suit the need too. However, it was expected that the scroll-like graphene wrapping that was assumed for those nanocones make them exhibit a large density of graphene edges at the cone surface, which is favorable for fast electron transfer rates for instance. The dispersed array of nanocones was embedded into an insulating polymer so that only the cone tips protrude. This way, the conical forms have an inter-electrode distance (3-4 μm) suitable for preventing the diffusion boundary layers to overlap, and for the array to behave as a single nanoelectrode. Such nanoelectrode ensembles were tested as working electrode in cyclic voltammetry with model analytes. They were shown to ensure a rapid steady state current and high sensitivity for electrochemical sensing applications in a reproducible manner, and with long-term stability (800 CV scans over 35 days).

The use of single ultramicroelectrodes with tapered tips prepared from the electrochemical etching of carbon microfibers for cyclic voltammetry was reported in [*150Spirom2011*]. Such electrodes revealed to exhibit a small effective tip radius of ~1μm, and a wide practical potential window in acidic and alkaline electrolytes.

Finally, nanohorns were also tested as electrode components in electrochemical systems such as supercapacitors and batteries. For supercapacitors [*196Yang2006*], nanohorns were previously opened by oxidation in order to allow the solvated ions to access the inner porosity. A specific capacitance of 144 F/g was reached with an aqueous electrolyte providing small solvated ions (0.53 nm). This is not bad, but still low compared to values such as ~500 F/g reachable with other carbon materials (for instance [*197Sankar2015*]). The authors then explained that the capacitance could be improved by using organic electrolytes and increasing the opening size in the nanohorn structure so that the larger solvated organic ions (1.16-1.40

nm) may access the inner nanohorn cavity. However, considering the actual dimension of nanohorns, about few nm long, it is likely that oxidizing them further so that to increase the opening size will reduce too much the graphene surface to the detriment of the electrical conductivity and molecule trapping ability. Finally, [*198Wu2014*] used pristine nanohorns (i.e., not opened by oxidation) to prepare a carbon-sulfur composite material as the sulfur-based cathode for S-Li batteries, to compensate for the low electrical conductivity of sulfur. Indeed, S-Li-based batteries are of great interest because of their high theoretical energy density (2567 W.h/kg), and the abundance and low-toxicity of sulfur. The resulting battery system exhibited good performances, with an initial capacity of 1200 mA.h/g which was maintained at 693 mA.h/g after 100 cycles, that are in the average of what is obtained with other carbon-based S-Li batteries [*199Liang2016*]. But it is still below the expectations, and no route was proposed (what about using opened nanohorns?) to improve the performances of such a material regarding improving the capacity and lowering significantly the capacity decay over cycling.

3.2.4. Adsorption-based applications

Mostly nanohorns have been tested for a variety of applications dealing with the adsorption of a variety of species, from single atoms to nanoparticles. As for the energy storage applications just mentioned at the end of the previous *Section*, such applications are mostly based on the high surface area and high micropore volume of the material, which are both suitable features in this regard. Therefore, because their use for these applications actually have nothing to do with their conical shape, they will only be briefly commented. Hence, the literature cited is not exhaustive either, and further related references can be found in [*29Karousis2016*, *53Yudasaka2008*].

Because the specific surface area can reach ~1200 m^2/g by opening the nanohorn molecular structure [*44Murata2001*, *45Bekyarova2003*, *46Utsumi2005*], almost all the applications cited below have been using nanohorns subjected to various degrees of oxidation. The latter were demonstrated a sieving capability by adjusting the size of the entry ports to the size of the molecules to trap [*200Murata*-2002]. Gas storage was then envisaged, and subsequently confirmed by modelling using theoretical cones whose sizes are compatible with that of nanohorns [*201Adisa2011*]. Experimental attempts started with methane. A specific volume storage capacity of 160 cm^3/cm^3 of nanohorn material was achieved at room temperature and 3.5 MPa (35 bars) [*202Bekyarova2003b*], and a specific mass storage capacity of 110 mg/g (11 wt%) was achieved at room temperature and 6.3 MPa once the microporosity was tailored by the treatment and intercalation of HNO_3 molecules [*203Yang2005*]. Unfortunately, no comparison with any other storage material was provided for the performance level to be assessed. As opposed to CH_4, the storage of H_2 was found very limited at room temperature (0.55 wt% at 10 MPa) [*204Xu2007*], even though the nanohorns are combined with catalyst nanoparticles such as Pd [*205Giasafaki2015*] or Pt, Pd-Ni, etc. Despite it revealed to be useless for H_2 storage, physisorbing metal nanoparticles on large specific area carbon substrate such as nanohorns could be quite interesting as a chemically inert, nanosized catalyst support, as it was demonstrated with 2 nm-large Pt particles [*206Yoshitake2002*]. However, in such an application, depending on the strength of the physisorption forces, the catalyst can be gradually

lost and the durability of the Pt-C material during repeated use could be limited. An interesting strategy, using opened nanohorns, was to use the latter as nanocrucibles to construct and then trap nanosized metal particles by admitting metal atoms (Gd) one by one into the nanohorn cavities (**Fig.22a**) from which the subsequent nanoparticles could not escape [*207Hashimoto2004*].

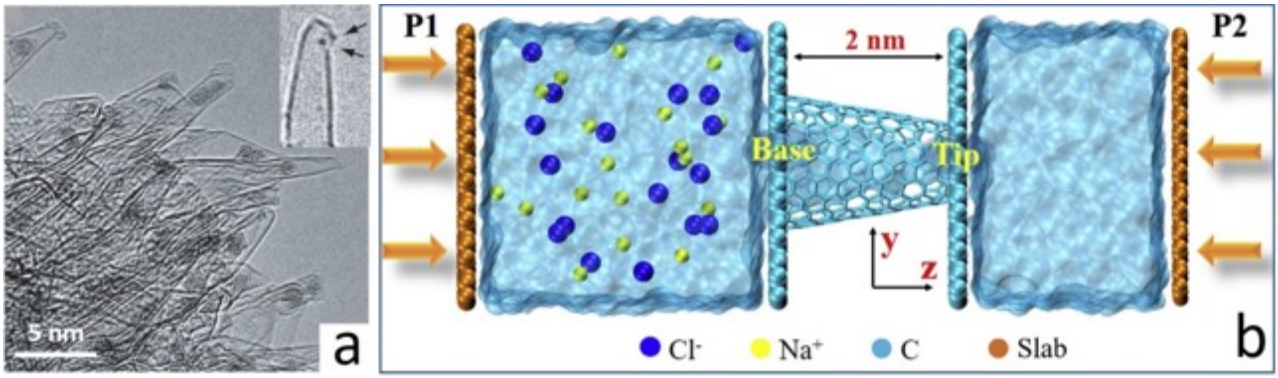

Figure 22: (a) *Gd-clusters built atom-by-atom within the cavity of nanohorns; inset: two Gd atoms (arrows) entering a nanohorn through a narrow entry port [*207Hashimoto2004*].* ***(b)*** *the desalination device model studied in [*211Li2018*]: an uncapped carbon cone is fixed between two graphene sheets (light blue) poked with openings whose diameters match that of the cone base and tip respectively; two rigid graphene slabs(brown) are used to applied constant pressures at the left (high pressure) and right (low pressure) parts of the device; salty water is put in the left part; once the desalination is over, water with 0.5 mol/l of NaCl is left on the left while only pure water is present on the right.*

Finally, nanohorns were investigated as carriers in drug delivery systems. Various molecules with therapeutic functions were tested for their adsorption and then desorption ability, such as glucocorticoid dexamethasone (anti-inflammatory) [*208Murakami2004*], and cisplatin (anticancer) [*209Ajima2005*], among others. The results have validated the concept. It was checked that the loaded nanohorns can cross different physiological barriers, either non-polarized (as for macrophage cells) or polarized (as for gastrointestinal tract) [*48Shi2017*].

In this field of application, very few examples only are dealing with conical carbon forms other than nanohorns. One is experimental, and has assessed the ability of the multiwall pentagon-driven cones shown in **Fig.5** in retaining various molecules present in water (chlorophenols in that case), for titration and/or depollution purposes [*210JimenezSoto2009*]. The authors pointed out that "*the physical and chemical properties of such a material would make them appropriate for this application*", but which properties are targeted is not clear, and unfortunately, they did not mention any. The applicability of the carbon cones as sorbent materials was stated, but their performance was not compared with regular sorbent materials. Finally, an original work was carried-out to assess the ability of the same carbon cones for water desalination [*211Li2018*]. The motivation was inspired by the expected combination, in such nanocones, of the nearly frictionless water flow in CNTs, and of the highly permeable and selective water flow in aquaporins (biocomponents of cell membranes with a conical, channel structure). The work was based on MD modelling only, but the device tested was proven to be efficient (**Fig.22b**). Uncapped cones with 3 different cone angles were used, and the 19.2° one demonstrated to be the most efficient, with performances (calculated) overpassing by two

orders of magnitude that of commercial membranes in terms of water permeability for the same ion rejection rate.

4. Conclusions

There is a large variety of conical carbon morphologies, single-walled or multi-walled, from nanometric to micro-nanometric sizes. The world of carbon (nano)cones is as vast as that of carbon nanotubes, and possibly vaster, as they need the same parameters as CNTs to be described (diameter, number of walls, helicity angle, nanotexture, texture, structure) but with additional specific parameters such as the cone angle, disclination angle, and, generally speaking, the type of structural defect (disclination, dislocation) they can be born from. Therefore, carbon cones exhibit distinctive characteristics, which fully depend on their growth mechanism and synthesis process. Unfortunately, the related knowledge is far less advanced than that for nanotubes, in all possible aspects:

Designation: graphite/graphitic/graphenic/graphene cones, hexagonal-pyramidal graphite hillocks, nanohorns, fullerene cones, carbon nanocones, graphite whiskers, carbon nanopipettes, cone-shaped graphitic whiskers, Conical crystals of graphite, conical carbon nanotube, conical carbon tubular structures, pointed carbon nanotubes, tubular carbon cones, hollow carbon cones, conical carbon (nano)fibers, tubular graphite cones, conical carbon protrusions… Throughout the articles published, the nomenclature is highly imaginative and figurative, abusively diverse, and sometimes inappropriate, hence generally misleading.

Growth mechanisms: most of the reasons why conical forms are generated have been identified (either structural, through wedge disclination, screw dislocation, radial wedge dislocation, or textural). However, because of the overall poor, insufficient characterization, the easiness of referring to previously published models yet not firmly demonstrated, and the dogmatic respect of certain geometric rules (e.g., the pentagon rule) that may apply to molecular forms (structurally perfect, nanosized single graphene cones) but not to larger, multilayered, faulted conical forms, there is little certainty regarding the actual display of graphenes and growth mechanisms of carbon cones in a majority of articles. There are good reasons for this; one is that TEM would be a key method, but discriminating between various graphene displays (e.g., scrolled vs concentric, or stacked lampshades vs helically wrapped single graphene ribbon) is made difficult because what TEM reveals is a projected volume; another reason is that the number of atoms becomes rapidly too high, preventing many modelling principles to be used.

A full understanding of the mechanisms driving the formation of graphene-based conical morphologies of various kinds is therefore yet to achieve.

Process conditions *vs* cone characteristic relationships: Carbon cones based on sp^3-carbon, which were not covered by this, are certainly better understood and controlled, because of the isotropy and low versatility of the building unit (the carbon tetrahedron, as opposed to graphene), and also because of the lack of structural defects (e.g., disclination, dislocation) able

to easily affect the diamond structure and the overall outer morphology. Hence, the variety in sp^3-carbon-based conical morphologies is certainly low.

This is obviously not true for graphenic cones for which the textural versatility is fairly high, even unique. Of course, trends can be found. For instance, generating individual carbon atoms or small carbon moieties (e.g., dimers) in vacuum conditions will result in forming cones in which the creation of pentagons will have a driving role. Also, using genuine CVD conditions (i.e., not plasma-assisted) may result in cone formation conditions resembling that of other known processes such as the formation of CNTs or the deposition of pyrolytic carbon. Unfortunately, the lack of thorough characterization of the carbon cones formed still prevents, in a large extent, a determinist approach of the formation of carbon cones, able to propose and predict the right conditions for synthesizing conical forms with the desired textural, nanotextural, and structural features. This is particularly true for plasma-assisted processes. Even though the statement made by Chen *et al*. [*137Chen2004*] regarding CNTs (i.e., DC-plasma-enhanced CVD tends to induce a herringbone texture whereas MW-plasma-enhanced CVD tends to induce a concentric texture) seems to also be true for cones, there are too many examples of cone synthesis that were not followed by the needed cone characterization for this statement to be statistically ascertained. On the other hand, plasma-assisted or irradiation methods cannot provide the best structural and nanotextural quality.

Applications: As seen, only few papers concerning the potential applications of conical graphene-based morphologies are reported in the literature. No commercial application has been generated, even in the field where graphenic cones seem the most promising such as electron emission and SPM probes. This can be explained by several causes: (i) synthesis issues: for some of them, it is still difficult to control the shape, yield, and reproducibility of conical forms. For processes that enable good yield and reproducibility such as the plasma-assisted ones, the material is poorly controlled or limited in terms of structural quality, hence not providing the best of the possible performances; (ii) technical issues: For individual uses, there is an intrinsic difficulty to control the accurate location and manipulation and a single cone. Either the cones have to grow at the very place of the device they have to be when in use, for instance on a tip of an AFM cantilever, or they have to be subsequently grabbed and manipulated to be positioned at the right place. The ways and dimensions with which many of the cones actually grow prevent their manipulation as single objects. Even if Chen *et al.* [*192Chen2006*, *193Chen2006b*, *194Chen2008*] succeeded in the *in-situ* growth of a single carbon cone onto a tipless cantilever, the process involves many steps, costly and is time consuming. (iii) Cost issue: designing and running the adequate synthesis, then characterizing, and then ensuring the quality control in the cone fabrication process chain is expensive and time consuming.

From this review, which was tried to be thorough and comprehensive, it comes out that the research field of carbon (nano)cones is promising the same way as CNTs were, and could actually solve some issues that CNTs are facing in their use for some applications. However, the carbon cone field is unfairly neglected as there still are many investigations to carry-out and a lot of understanding to achieve in all aspects, from synthesis to applications. The following *Chapters* aim at contribute to this.

References

1. Delhaes P. ***Carbon-based solids and materials***. ISTE (London, UK), Wiley and Sons (Hoboken, NJ, USA). 2011.
2. Inagaki M., Kang F., Toyoda M., Konno H. ***Advanced Materials science and Engineering of carbon***. Elsevier & Tsinghua University Press (2014).
3. Shi L., Rohringer P., Suenaga K., Niimi Y., Kotakoski J., Meyer J. C., Peterlik H., Wanko M., Cahangirov S., Rubio A., Lapin Z. J., Novotny L., Ayala P., Pichler T. *Confined linear carbon chains as a route to bulk carbyne*. **Nature Mater.** 15 (2016) 634-640.
4. Kaiser K., Scriven L. M., Schulz F., Gawel P., Gross L., Anderson H. L. *An* sp*-hybridized molecular carbon allotrope, cyclo [18] carbon*. **Science** 365 (2019) 1299-1301.
5. Ugarte D. *Curling and closure of graphitic networks under electron-beam irradiation.* **Nature** 359 (1992) 707-709.
6. Harris P. J. F. *High-resolution electron microscopy studies of a microporous carbon produced by arc-evaporation*. **J. Chem. Soc. Farad. Trans.** 90 (1994) 2799-2802.
7. Kroto H., Heath J.R., O'Brien S.C., Curl R.F., Smalley R.E. *C_{60}: Buckminsterfullerene*. Nature 318 (1985) 162-163.
8. Saito Y. *Nanoparticles and filled nanocapsules*. **Carbon** 33 (1995) 979-988.
9. Donnet J.-B. ***Carbon black science and technology***. 2nd edition (Donnet J.-B., Bansal R. C., Wang M.-J., eds). Marcel Dekker (New York, USA). 1993.
10. Endo M., Oberlin A., Koyama T. *Filamentous growth of carbon through benzene decomposition*. **J. Cryst. Growth** 32 (1976) 335-349.
11. Iijima S., Ichihashi T. *Single-shell carbon nanotubes of 1-nm diameter*. **Nature** 363 (1993) 603-605.
12. Bethune D. S., Klang C. H., de Vries M. S., Gorman G., Savoy R., Vazquez J., Beyers R. *Cobalt-catalysed growth of carbon nanotubes with single-atomic-layer walls*. **Nature** 363 (1993) 605-607.
13. Radushkevich LV, Lukyanovich VM. *O strukture ugleroda, obrazujucegosja pri termiceskom razlozenii okisi ugleroda na zeleznom kontakte*. Zurn Fisic Chim 26 (1952) 88–95.
14. Iijima S. *Helical microtubules of graphitic carbon*. **Nature** 354 (1991) 56-58.
15. Rodriguez N. M., Chambers A., Baker T. K. *Catalytic engineering of carbon nanostructures*. **Langmuir** 11 (1995) 3862-3866.
16. Novoselov, K. S., Geim, A. K., Morozov,S. V., Jiang, D., Zhang, Y., Dubonos, S. V., Grigorieva, I. V., Firsov, A. A. *Electric field effect in atomically thin carbon films*. **Science** 306 (2004) 666–669.
17. Monthioux M., Noé L., Kobylko M., Wang Y., Cazares-Huerta T. C., Pénicaud A. *Determining the structure of graphene-based flakes from their morphotype*. **Carbon** 115 (2017) 128-133.
18. Terrones M., Botello-Méndez A. R., Campos-Delgado J., López-Urías F., Vega-Cantú Y. I., Rodríguez-Macías F. J., Elías A. L., Muñoz-Sandoval E., Cano-Márquez A. G., Charlier J.-C., Terrones H. *Graphene and graphite nanoribbons: Morphology, properties, synthesis, defects and applications*. **NanoToday** 5 (2010) 351-372.
19. Ajayan P. M., Nugent J. M., Siegel R. W., Wei B., Kohler-Redlich P. *Growth of carbon micro-trees*. **Nature** 404 (2000) 243.
20. Wu X., Jiang L., Long C., Fan Z. *From flour to honeycomb-like carbon foam: Carbon makes room for high energy density supercapacitors*. **Nano Energy** 13 (2015) 527-536.
21. Harris P. J. F. *Fullerene-related structure of commercial glassy carbons*. **Phil. Mag.** 84 (2004) 3159-3167.
22. Jaszczak J. A., Robinson G. W., Dimovski S., Gogotsi Y. *Naturally occurring graphite cones.* **Carbon** 41 (2003) 2085-2092.
23. Glad X., de Poucques L., Jaszczak J. A., Belmahi M., Ghanbaja J., Bougdira J. *Plasma synthesis of hexagonal-pyramidal graphite hillocks*. **Carbon** 76 (2014) 330-340.
24. Eksioglu B., Nadarajah A. *Structural analysis of conical carbon nanofibers*. Carbon 44 (2006) 360–373
25. Dumpala S., Bhimarasetti G., Gubbala S., Meduri P., Kona S., Sunkara M. K. *Carbon microtubes and conical carbon nanotubes*. In: ***Small Materials*** (Schwartz M., ed), CRC Press (2008). Ch.22.
26. Allouche H., Monthioux M. *Chemical vapor deposition of pyrolytic carbon on carbon nanotubes. Part 2. Texture and structure*. **Carbon** 43 (2005) 1265–1278.

27. Dimovski S. Gogotsi Y. *Graphite Whiskers, Cones, and Polyhedral Crystals*. In ***Carbon Nanomaterials*** (Gogotsi Y., Presser V., eds), 2nd edition, CRC Press (2017), pp. 89-114.
28. Bacon R. *Growth, structure, and properties of graphite whiskers*. **J. Appl. Phys.** 31 (1960) 283-290.
29. Karousis N., Suarez-Martinez I., Ewels C. P., Tagmatarchis N. *Structure, properties, functionalization, and applications of carbons nanohorns*. **Chem. Rev.** 116 (2016) 4850-4883.
30. Harris W. F. *Disclinations*. **Scient. Amer.** 237 (1977) 130-145.
31. Rozhkov M. A., Kolesnikova A. L., Yasnikov I. S., Romanov A. E. *Disclination ensembles in graphene.* **Low Temp. Phys.** 44 (2018) 918-924.
32. Ge M., Sattler K. *Observation of fullerene cones*. **Chem. Phys. Lett.** 220 (1994) 192-196.
33. Sattler K. *Scanning tunnelling microscopy of carbon nanotubes and nanocones*. **Carbon** Vol.33 (1995) 915-920.
34. Double D.D., Hellawell A. *Cone-helix growth forms of graphite*. **Acta Metall.** 22 (1974) 481-487.
35. Ihara S., Itoh S. *Structure of polygonal defects in graphitic carbon sheets*. **Phys. Rev. B** 54 (1996) 14713-14719.
36. Krishnan A., Dujardin E., Treacy M.M.J., Hugdahl J., Lynum S., Ebbesen T. W. *Graphitic cones and the nucleation of curved carbon surfaces*. **Nature**, Vol. 388 (1997) 451-454.
37. Ebbesen T. W. *Cones and tubes: Geometry in the chemistry of carbon*. **Acc. Chem. Res.** 31 (1998) 558-566.
38. Balaban A. T., Klein D. J., Liu X. *Graphitic cones*. **Carbon** 32 (1994) 357-359.
39. Klein D. J., Balaban A.T. *The eight classes of positive-curvature graphitic nanocones*. **J. Chem. Inf. Model.** 46 (2006) 307-320.
40. Klabunde K. J. ***Free atoms, clusters, and nanoscale particles***. Academic Press (1994).
41. Iijima S., Yudasaka M., Yamada R., Bandow S., Suenaga K., Kokai F., Takahashi K. *Nano-aggregates of single-walled graphitic carbon nano-horns*. **Chem. Phys. Lett.** 309 (1999) 165-170.
42. Suarez-Martinez I., Mittal J., Allouche H., Pacheco M., Monthioux M., Razafinimanana M., Ewels C. P. *Fullerene attachment to sharp-angle nanocones mediated by covalent oxygen bridging*. **Carbon** 54 (2013) 149-154.
43. Murata K., Kaneko K., Kokai F., Takahashi K., Yudasaka M., Iijima S. *Pore structure of single-wall carbon nanohorn aggregates.* **Chem. Phys. Lett.** 331 (2000) 14-20.
44. Murata K., Kaneko K., Steele W. A., Kokai F., Takahashi K., Kasuya D., Hirahara K., Yudasaka M., Iijima S. *Molecular potential structures of heat-treated single-wall carbon nanohorn assemblies*. **J. Phys. Chem. B** 105 (2001) 10210-10216.
45. Bekyarova E., Kaneko K., Yudasaka M., Kasuya D., Iijima S., Huidobro A., Rodriguez-Reinoso F. *Controlled opening of single-wall carbon nanohorns by heat treatment in carbon dioxide*. **J. Phys. Chem. B** 107 (2003) 4479-4484.
46. Utsumi S., Miyawaki J., Tanaka H., Hattori Y., Itoi T., Ichikuni N., Kanoh H., Yudasaka M., Iijima S., Kaneko K. *Opening mechanism of internal nanoporosity of single-wall carbon nanohorn*. **J. Phys. Chem. B** 109 (2005) 14319−14324.
47. Pagona G., Sandanayaka A. S. D., Araki Y., Fan J., Tagmatarchis N., Charalambidis G., Coutsolelos A. G., Boitrel B., Yudasaka M., Iijima S, Ito O. *Covalent functionalization of carbon nanohorns with porphyrins: nanohybrid formation and photoinduced electron and energy transfer*. **Adv. Funct. Mater.** 17 (2007) 1705-1711.
48. Shi Y., Shi Z., Li S., Zhang Y., He B., Peng D., Tian J., Zhao M., Wang X., Zhang Q. *The interactions of single-wall carbon nanohorns with polar epithelium*. **Intern. J. Nanomed.** 12 (2017) 4177-4194.
49. Takikawa H., Ikeda M., Hirahara K., Hibi Y., Tao Y., Ruiz Jr. P.A., Sakakibara T., Itoh S., Iijima S. *Fabrication of single-walled carbon nanotubes and nanohorns by means of a torch arc in open air*. **Physica** B 323 (2002) 277–279.
50. Wang H., Chhowalla M., Sano N., Jia S., Amaratunga G. A. J. *Large-scale synthesis of single-walled carbon nanohorns by submerged arc*. **Nanotechnol**. 15 (2004) 546–550.
51. Yamaguchi T., Bandow S., Iijima S. *Synthesis of carbon nanohorn particles by simple pulsed arc discharge ignited between pre-heated carbon rods*. **Chem. Phys. Lett.** 389 (2004) 181–185.
52. Pagura C., Barison S., Battiston S., Schiavon M. *Synthesis and characterization of single wall carbon nanohorns produced by direct vaporization of graphite*. In: **Technical Proceedings of the 2010 NSTI Nanotechnology Conference and Expo** "Nanotech 2010", Vol. 1.
53. Yudasaka M. Iijima S., Crespi V. H. *Single-wall carbon nanohorns and nanocones*. In *Carbon Nanotubes* (Jorio A., Dresselhaus G., Dresselhaus M. S., eds.), **Topics Appl. Physics** 111, Springer-Verlag (2008) 605–629.

54. Naess S. N., Elgsaeter A., Helgesen G., Knudsen K. D. *Carbon nanocones: wall structure and morphology*. Sci. Technol. **Adv. Mater.** 10 (2009) 065002.
55. Treacy M. M. J., Kilian J. *Designability of graphitic cones*. In *Nanotubes, Fullerenes, Nanostructured and Disordered Carbon* Conference, San Francisco, April 17-20, **Mat. Res. Soc. Symp. Proc.** 675 (2001) W2.6.1-W2.6.6.
56. Kawai T., Miyamoto Y., Sugino O., Koga, Y. *Nanotube and nanohorn nucleation from graphitic patches: Tight-Binding Molecular-Dynamics simulations*. **Phys. Rev.** B 66 (2002) 033404.
57. Zhang S., Yao Z., Zhao S., Zhang E. *Buckling and competition of energy and entropy lead conformation of single-walled carbon nanocones*. **Appl. Phys. Lett.** 89 (2006) 131923.
58. Cheng H.-Y., Zhu Y.-A., Sui Z.-J., Zhou X.-G., Chen D. *Modeling of fishbone-type carbon nanofibers with cone-helix structures*. **Carbon** 50 (2012) 4359-4372.
59. Zhu Y.-A., Wang Z.-J., Cheng H.-Y., Yang Q.-M., Sui Z.-J., Zhou X.-G., Chen D. *Decoding structural complexity in conical carbon nanofibers*. Phys. **Chem. Chem. Phys.** 19 (2017) 14555-14565.
60. Amelinckx S., Luyten W., Krekels T., Van Tendeloo G., Van Landuyt J. *Conical, helically wound, graphite whiskers: a limiting member of the "fullerenes"?* **J. Cryst. Growth** 121 (1992) 543-558.
61. Garberg T., Naess S. N., Helgesen G., Knudsen K. D., Kopstad G., Elgsaeter A. *A transmission electron microscope and electron diffraction study of carbon nanodiscs*. **Carbon** 46 (2008) 1535-1543.
62. Kasuya D., Yudasaka M., Takahashi K., Kokai F., Iijima S. *Selective production of single-wall carbon nanohorn aggregates and their formation mechanism*. **J. Phys. Chem. B** 106 (2002) 4947-4951.
63. Sears G. W. *Growth mechanisms for graphite whiskers*. **J. Chem. Phys.** 31 (1959) 358-360.
64. Gillot J., Bollmann W., Lux B. *Cristaux de graphite en forme de cigare et à structure conique*. **Carbon** 6 (1968) 381-387.
65. Fitzer E. *Chemical vapour deposition. A review of 25 years experience*. **J. Phys. IV, Colloquium C2, Suppl. J. Phys. II**, vol.1 (1991) C2.509-C2.537.
66. Monthioux M., Noé L., Dussault L., Dupin J.-C., Latorre N., Ubieto T., Romeo E., Royo C., Monzon A., Guimon C. *Texturising and structurising mechanisms of carbon nanofilaments during growth.* **J. Mater. Chem.** 17 (2007) 4611–4618.
67. Kiselev N. A., Sloan J., Zakharov D. N., Kukovitskii E. F., Hutchison J. L., Hammer J., Kotosonov A. S. *Carbon nanotubes from polyethylene precursors: structure and structural changes caused by thermal and chemical treatment revealed by HREM*. **Carbon** 76 (1998) 1149-1157.
68. Terrones H., Hayashi T., Munoz-Navia M., Terrones M., Kim Y. A., Grobert N., Kamalaraman R., Dorante-Davila J., Escudero R., Dresselhaus M. S., Endo M. *Graphitic cones in palladium catalysed carbon nanofibers*. **Chem. Phys. Lett.** 343 (2001) 241-250.
69. Endo M., Kim Y. A., Hayashi T., Fukai Y., Oshida K., Terrones M., Yanagisawa T., Higaki S., Dresselhaus M. S. *Structural characterization of cup-stacked-type nanofibers with an entirely hollow core*. **Appl. Phys. Lett.** 80 (2002) 1267-1269.
70. Endo M., Kim Y. A., Hayashi T., Yanagisawa T., Muramatsu H., Ezaka M., Terrones H., Terrones M., Dresselhaus M. S. *Microstructural changes induced in "stacked cup" carbon nanofibers by heat treatment*. **Carbon** 41 (2003) 1941–1947.
71. Zhao Y., Tang Y., Chen Y., Star A. *Corking carbon nanotube cups with gold nanoparticles*. **ACS nano** 6 (2012) 6912-6921.
72. Després J.-F., Daguerre E., Lafdi K. *Flexibility of graphene layers in carbon nanotubes*. Carbon 33 (1995) 87-92.
73. Després J.-F., Daguerre E., Lafdi K. *Dynamic bond length as an explanation for the flexibility of graphene layers*. **Carbon** 40 (2002) 445–467.
74. Peach M.O. *Mechanism of growth of whiskers on cadmium*. **J. Appl. Phys.** 23(1952) 1401-1403.
75. Haanstra H. B., Knippenberg W. F., Verspui G. *Columnar growth of carbon*. **J. Cryst. Growth** 16 (1972) 71-79.
76. Dong J., Shen W., Kang F., Tatarchuk B. *Whiskers with apex angle 135° growing by a disclination growth mechanism*. **J. Cryst. Growth** 245 (2002) 77–83.
77. Dong J., Shen W., Zhang B., Liu X., Kang F., Gu J., Li D., Chen N.P. *New origin of spirals and new growth process of carbon whiskers*. **Carbon** 39(2001) 2325–2333.
78. Kulnitskiy B., Karaeva A., Mordkovich V., Urvanov S., Bredikhina A. *TEM studies of conical scroll carbon nanotubes formed by aerosol synthesis*. IOP Conference Series: **Mater. Sci. Eng.** 693 (2019) 012017.

79. Suarez-Martinez I., Ewels C. *Discussion on the staking sequence in conical carbon forms*. **Private communication** (2020) unpublished results.
80. Vera-Agullo J., Varela-Rizo H., Conesa J. A., Almansa C., Merino C., Martin-Gullon I. *Evidence for growth mechanism and helix spiral cone structure of stacked-cup carbon nanofibers*. **Carbon** 45 (2007) 2751-2758.
81. Motojima S. Itoh Y., Asakura S., Iwagana H. *Preparation of micro-coiled carbon fibres by metal powder-activated pyrolysis of acetylene containing a small amount of sulphur compounds*. **J. Mater. Sci.** 30 (1995) 5049-5055.
82. Roscoe C., Nagle D., Austerman S. B. *Growth of graphite single crystals from iron-carbon solutions*. **J. Mater. Sci.** 6 (1971) 998-1006.
83. Smetana J. *Theory of tin whisker growth: "the end game"*. **IEEE Trans. Electron. Pack. Manufact**. 30 (2007) 11-22.
84. Lin C.-T., Lee C.-Y, Chiu H.-T., Chin T.-S. *Graphene structure in carbon nanocones and nanodiscs*. **Langmuir** 23 (2007) 12806-12810.
85. Saito Y., Arima T. *Features of vapor-grown cone-shaped graphitic whiskers deposited in the cavities of wood cells*. **Carbon** 45 (2007) 248–255.
86. Lin C.-T., Chen W.-C., Yen M.-Y., Wang L.-S., Lee C.-Y., Chin T.-S., Chiu H.-T. *Cone-stacked carbon nanofibers with cone angle increasing along the longitudinal axis*. **Carbon** 45 (2007) 411–415.
87. Gogotsi Y., Dimovski S., Libera J. A. *Conical crystals of graphite*. **Carbon** 40 (2002) 2263-2284.
88. Braga S. F., Coluci V. R., Legoas S. B., Giro R., Galvão D. S., Baughman R. H. *Structure and dynamics of carbon nanoscrolls*. **Nanolett**. 4 (2004) 881-884.
89. Mani R. C., Li X., Sunkara M. K., Rajan K. *Carbon nanopipettes*. **NanoLett**. 3 (2003) 671-673.
90. Lowe R. D., Mani R. C., Baldwin R. P., Sunkara M. K. *Nanoelectrode ensembles using carbon nanopipettes*. Electrochem. **Solid State Lett.** 9 (2006) H43-H47.
91. Chernomordik B., Dumpala S., Chen Z. Q., and Sunkara M. K. *Nanodiamond tipped and coated conical carbon tubular structures*. **Chem. Vap. Dep.** 14 (2008) 256-262.
92. Dumpala S., Jasinski J. B., Sumanasekera G. U., Sunkara. M. K. *Large area synthesis of conical carbon nanotube arrays on graphite and tungsten foil substrates*. **Carbon** 49 (2011) 2725-2734.
93. Sun X., Li R., Stansfield B., Dodelet J.-P., Ménard G., Désilets S. *Controlled synthesis of pointed carbon nanotubes*. **Carbon** 45 (2007) 732–737.
94. Okuno H., Palnichenko A., Després J.-F., Issi J.-P., Charlier J.-C. *Synthesis of graphite polyhedral crystals using a combustion flame method*. **Carbon** 43 (2005) 692–697.
95. Liu J., Lin W., Chen X., Zhang S., Li F., Qian Y. *Fabrication of hollow carbon cones*. **Carbon** 42 (2004) 667–691.
96. Li J. J., Gu C. Z., Wang Q., Xu P., Wang Z. L., Xu Z., D. Bai X. *Field emission from high aspect ratio tubular carbon cones grown on gold wire*. **Appl. Phys. Lett.** 87 (2005) 143107.
97. Li J. J., Wang Q., Gu C. Z. *Growth and field emission properties of tubular carbon cones*. **Ultramicrosc**. 107 (2007) 861-864.
98. Levchenko I., Ostrikov K., Vladimirov S. V. *Growth of carbon nanocone arrays on a metal catalyst: The effect of carbon flux ionization*. **Phys. Plasmas** 15 (2008) 103501.
99. Merkulov V. I., Guillorn M. A., Lowndes D. H., Simpson M. L., Voelkl E. *Shaping carbon nanostructures by controlling the synthesis process*. **Appl. Phys. Lett.** 79 (2001) 1178-1180.
100. Merkulov V. I., Melechko A. V., Guillorn M. A., Lowndes D. H., Simpson M. L. *Sharpening of carbon nanocone tips during plasma-enhanced chemical vapor growth*. **Chem. Phys. Lett.** 350 (2001) 381-385.
101. Jacobsen R. L., Monthioux M. *Carbon beads with protruding cones*. **Nature** 385 (1997) 211-212.
102. Allouche H., Monthioux M. Jacobsen R. L. *Chemical vapor deposition of pyrolytic carbon on carbon nanotubes. Part 1. Synthesis and morphology*. **Carbon** 41 (2003) 2897–2912.
103. Monthioux M., Allouche H., Jacobsen R. L. *Chemical vapor deposition of pyrolytic carbon on carbon nanotubes. Part 3. Growth mechanisms.* **Carbon** 44 (2006) 3183–3194.
104. Xia W., Su D., Schlögl R., Birkner A., Mulher M. *Conical carbon filaments with axial cylindrical channels and open tips*. **Adv. Mater.** 17 (2005) 1677-1679.
105. Muradov N., Schwitter A. *Formation of conical carbon structures on vapor-grown carbon filaments*. **NanoLett**. 2 (2002) 673-676.
106. Zhang W., Xi Z. H., Zhang G. M., Wang S., Wang S. M., Wang J. Y., Xue Z. Q. *Carbon nanotube as the core of conical carbon fiber: fabrication, characterization and field emission property*. **Appl. Phys. A** 86 (2007) 171–175.

107. Zhang W., Xi Z., Bai X., Zhang G. *Pyrolytic synthesis of conical carbon fibers with carbon nanotube tips on carbon substrates*. **J. Phys. Chem. C** 113 (2009) 7629–7632.
108. Zhang G., Jiang X., Wang E. *Tubular graphite cones*. **Science** 300 (2003) 472-474.
109. Zhang G. Y., Bai X. D., Wang E. G., Guo Y., Guo W. *Monochiral tubular graphite cones formed by radial layer-by-layer growth*. **Phys. Rev. B** 71 (2005) 113411.
110. Tan P. H., Zhang J., Wang X. C., Zhang G. Y., Wang E. G. *Raman scattering from an individual tubular graphite cone*. **Carbon** 45 (2007) 1105-1136.
111. Shang N. G., Jiang X. *Large-sized tubular graphite cones with nanotube tips*. **Appl. Phys. Lett.** 87 (2005) 163102.
112. Shang N., Milne W. I., Jiang X. *Tubular graphite cones with single-crystal nanotips and their antioxygenic properties*. **J. Amer. Chem. Soc.** 129 (2007) 8907-8911.
113. Shang N. G., Papakonstantinou P., McLaughlin J., Chen W. C., Chen L. C., Chu M., Stamboulis A. *Fe catalytic growth, microstructure, and lowthreshold field emission properties of open ended tubular graphite cones*. **J. Appl. Phys.** 103 (2008) 124308.
114. Shang N. G., Silva S. R. P., Jiang X., Papakonstantinou P. *Directly observable G band splitting in Raman spectra from individual tubular graphite cones*. **Carbon** 49 (2011) 3048-3054.
115. Lee W. J., Li C., Burke N., Trimm D., Patel J. *The growth and morphology of core/shell heterostructured conical carbon fibers*. **Carbon** 49 (2011) 2735-2741.
116. Zhuang H., Yang B., Zhang L., Heuser S., Jiang X. *SiC-assisted growth of tubular graphenic cones with carbon nanotube tips*. **Carbon** 95 (2015) 824-832.
117. Gogotsi Y., Libera J. A.,1 Kalashnikov N., Yoshimura M. *Graphite polyhedral crystals*. **Science** 290 (2000) 317-320.
118. Endo M., Takeuchi K., Kobori K., Takahashi K. Kroto H. W., Sarkar A. *Pyrolytic carbon nanotubes from vapor-grown carbon fibers*. **Carbon** 33 (1995) 873-881.
119. Ting J.-M., Lan B. C. *Formation of nodulated vapor grown carbon fiber*. **Carbon** 38 (2000) 1917-1923.
120. Ting J.-M., Chen Y. M. *Growth of tubular carbon from vapor phase*. **Mater. Chem. Phys.** 72 (2001) 228–231.
121. Krajnovich D. J., Vasquez J. E., Savoy R. J. *Impurity-driven cone formation during laser sputtering of graphite*. **Science** 259 (1993) 1590-1592.
122. Tsakadze Z. L., Ostrikov K., Long J. D., Xu S. *Self-assembly of uniform carbon nanotip structures in chemically active inductively coupled plasmas*. **Diam. Relat. Mater.** 13 (2004) 1923–1929.
123. Denysenko I. B., Xu S., Long J. D., Rutkevych P. P., Azarenkov N. A., Ostrikov K. *Inductively coupled $Ar/CH_4/H_2$ plasmas for low-temperature deposition of ordered carbon nanostructures*. **J. Appl. Phys.** 95 (2004) 2713-2724.
124. Tsakadze Z. L., Ostrikov K., Xu S. *Low-temperature assembly of ordered carbon nanotip arrays in low-frequency, high-density inductively coupled plasmas*. **Surf. Coat. Technol.** 191 (2005) 49-53.
125. Ostrikov K. *Reactive plasmas as a versatile nanofabrication tool*. Re. Mod. Phys. 77 (2005) 489-511.
126. Ostrikov K., Long J. D., Rutkevych P. P., Xu S. *Synthesis of functional nanoassemblies in reactive plasmas*. **Vacuum** 80 (2006) 1126–1131.
127. Xu S., Ostrikov K., Long J. D., Huang S. Y. *Integrated plasma-aided nanofabrication facility: Operation, parameters, and assembly of quantum structures and functional nanomaterials*. **Vacuum** 80 (2006) 621–630
128. Levchenko I., Ostrikov K., Long J. D., Xu S. *Plasma-assisted self-sharpening of platelet-structured single-crystalline carbon nanocones*. **Appl. Phys. Lett.** 91 (2007) 113115.
129. Kumar S., Levchenko I., Keidar M., Ostrikov K. *Plasma-enabled growth of separated, vertically aligned copper-capped carbon nanocones on silicon*. **Appl. Phys. Lett.** 97 (2010) 151503.
130. Messier R., Krishnaswamy S. V., Walker P. L. Jr. *Ion bombardment induced cone formation on glassy carbon and graphite surfaces*. **Carbon** 20 (1982) 29-33.
131. Tanemura M, Okita T., Yamauchi H., Tanemura S. *Room-temperature growth of a carbon nanofiber on the tip of conical carbon protrusions*. **Appl. Phys. Lett**. 84 (2004) 3831-3833.
132. Tanemura M., Tanaka J., Itoh K., Fujimoto Y., Agawa Y., Miao L., Tanemura S. *Field electron emission from sputter-induced carbon nanofibers grown at room temperature*. **Appl. Phys. Lett.** 86 (2005) 113107.
133. Tanemura M., Tanaka J., Itoh K., Okita T., Miao L., Tanemura S., Lau S. P., Huang L., Agawa Y., Kitazawa M. *Self-regenerative field emission source*. **Appl. Phys. Lett.** 87 (2005) 193102.

134. Tanemura M., Okita T., Tanaka J., Kitazawa M., Itoh K., Miao L., Tanemura S., Lau S. P., Yang H. Y., Huang L. *Room-temperature growth and applications of carbon nanofibers: a review*. **IEEE Trans. Nanotechnol.** 5 (2006) 587-594.
135. Zamri M., Ghosh P., Hayashi A., Hayashi Y., Tanemura M., Sasase M. *Structural change of ion-induced carbon nanofibers by electron current flow*. **J. Vac. Sci. Technol. B** 29 (2011) 04E103.
136. Zhao Q. Z., Ciobanu F., Wang L. J. *Self-organized regular arrays of carbon nanocones induced by ultrashort laser pulses and their field emission properties*. **J. Appl. Phys.** 105 (2009) 083103.
137. Chen L.-H., AuBuchon J. F., Gapin A., Daraio C., Bandaru P., Jin S., Kim D. W., Yoo I. K., Wang C. M. *Control of carbon nanotube morphology by change of applied bias field during growth*. **Appl. Phys. Lett.** 85 (2004) 5373-5375.
138. Lee H. R., Yang H. H., Park K. C. *Fabrication of a high-resolution electron beam with a carbon nanotube cold-cathode*. **J. Vac. Sci. Technol. B** 35 (2017) 06G804.
139. Zhong G., Iwasaki T., Kawarada H., Ohdomari I. *Synthesis of highly oriented and dense conical carbon nanofibers by a DC bias-enhanced microwave plasma CVD method*. **Thin solid films** 464-465 (2004) 315-318.
140. Wang W. H., Lin Y. T., Kuo C. T. *Nanofabrication and properties of the highly oriented carbon nanocones*. **Diam. Relat. Mater.** 14 (2005) 907-912.
141. Chen Y., Guo L., Patel S., Shaw D. T. *Aligned conical carbon nanotubes*. J. Mater. Sci. 35 (2000) 5517-5521.
142. Lu X., Yang Q., Xiao C. Hirose A. *Field electron emission of carbon-based nanocone films*. **Appl. Phys. A** 82 (2006) 293-296.
143. Tan C. K., Loh K. P., Thong J. T. L., Sow C. H., Zhang H. *Plasma synthesis of well-aligned carbon nanocones*. **Diam. Relat. Mater.** 14 (2005) 902–906.
144. Mata D., Amaral M., Fernandes A. J. S., Oliveira F. J., Costa P. M. F. J., Silva R. F. *Self-assembled cones of aligned carbon nanofibers grown on wet-etched Cu foils*. **Carbon** 49 (2011) 2181-2196.
145. Liu Y., Liu L., Liu P., Sheng L., Fan S. *Plasma etching carbon nanotube arrays and the field emission properties*. **Diam. Relat. Mater.** 13 (2004) 1609-1613.
146. Huang C. J., Yeh C. M., Chen M. Y., Hwang J., Kou C. S. *Field emission from a carbon nanofiber/carbon nanocone composite structure fabricated by a two-step growth process*. **J. Electrochem. Soc.** 153 (2006) H15-H17.
147. Lim S.-T., Cho J.-H., Huh S.-R., Jeong G.-H., Kim G.-H. *Mechanism of cone-shaped carbon nanotube bundle formation by plasma treatment*. **Carbon** 48 (2010) 3864-3873.
148. Mousa M. S. *Electron emission from carbon nanotips*. **Appl. Surf. Sci.** 94/95 (1996) 129-135.
149. Castellanos-Gomez A., Agraït N., Rubio-Bollinger G. *Carbon fibre tips for scanning probe microscopy based on quartz tuning fork force sensors*. **Nanotechnol**. 21 (2010) 145702.
150. Sripirom J., Noor S., Kohler U., Schulte A. *Easily made and handled carbon nanocones for scanning tunneling microscopy and electroanalysis*. **Carbon** 49 (2011) 2402-2412.
151. Huang W., Xu J., Lu X. *Tapered carbon nanocone tips obtained by dynamic oxidation in air*. **Roy. Soc. Chem. Adv.** 6 (2016) 25541-25548.
152. Lammert P. E., Crespi V. H. *Topological phases in graphitic cones*. **Phys. Rev. Lett.** 85 (2000) 5190-5193.
153. Charlier J.-C., Rignanese G.-M. *Electronic structure of carbon nanocones*. **Phys. Rev. Lett.** 86 (2001) 5970-5973.
154. Lammert P. E., Crespi V. H. *Graphene cones: classification by fictitious flux and electronic properties*. **Phys. Rev. B** 69 (2004) 035406.
155. Muñoz-Navia M., Dorantes-Davila J., Terrones M., Terrones H. *Ground-state electronic structure of nanoscale carbon cones*. **Phys. Rev. B** 72 (2005) 235403.
156. Pincak R., Smotlacha J., Pudlak M. *Spin-orbit interaction in the graphitic nanocone*. **Eur. Phys. J. B** 88 (2015) 17.
157. Shenderova O. A., Lawson B. L., Areshkin D., Brenner D. W. *Predicted structure and electronic properties of individual carbon nanocones and nanostructures assembled from nanocones*. **Nanotechnol**. 12 (2001) 191–197.
158. Heiberg-Andersen H., Skjeltorp A. T., Sattler K. *Carbon nanocones: A variety of non-crystalline graphite*. **J. Non-Cryst. Sol.** 354 (2008) 5247–5249.
159. Yang N., Zhang G. Li B. *Carbon nanocone: A promising thermal rectifier*. **Appl. Phys. Lett.** 93 (2008) 243111.
160. Kobayashi K. *Superstructure induced by a topological defect in graphitic cones*. **Phys. Rev. B** 61 (2000) 8496-9500.
161. Berber S., Kwon Y.-K., Tomanek D. *Electronic and structural properties of carbon nanohorns*. **Phys. Rev. B** 62 (2000) R2291.

162. Garaj S., Thien-Nga L., Gaal R., Forro L., Takahashi K., Kokai F., Yudasaka M., Iijima S. *Electronic properties of carbon nanohorns studied by ESR*. **Phys. Rev. B** 62 (2000)17115-17119.
163. Bandow S., Kokai F., Takahashi K., Yudasaka M., Iijima S. *Unique magnetism observed in single-wall carbon nanohorns*. **Appl. Phys. A** 73 (2001) 281–285.
164. Imai H., Babu P. K., Oldfield E., Wieckowski A., Kasuya D., Azami T., Shimakawa Y., Yudasaka M., Kubo Y., Iijima S. *^{13}C NMR spectroscopy of carbon nanohorns*. **Phys. Rev. B** 73 (2006) 125405.
165. Bandow S., Rao A. M., Sumanasekera G. U., Eklund P. C., Kokai F., Takahashi K., Yudasaka M., Iijima S. *Evidence for anomalously small charge transfer in doped single-wall carbon nanohorn aggregates with Li,K and Br*. **Appl. Phys. A** 71 (2000) 561–564.
166. Cioffi C., Campidelli S., Sooambar C., Marcaccio M., Marcolongo G., Meneghetti M., Paolucci D., Paolucci F., Ehli C., Aminur Rahman G. M., Sgobba V., Guldi D. M., Prato M. *Synthesis, characterization, and photoinduced electron transfer in functionalized single wall carbon nanohorns*. **J. Amer. Chem. Soc.** 129 (2007) 3938-3945.
167. Urita K., Seki S., Utsumi S., Noguchi D., Kanoh H., Tanaka H., Hattori Y., Ochiai Y., Aoki N., Yudasaka M., Iijima S., Kaneko K*. Effects of gas adsorption on the electrical conductivity of single-wall carbon nanohorns*. **Nanolett**. 6 (2006) 1325-1328.
168. Jordan S. P., Crespi V. H. *Theory of carbon nanocones: Mechanical chiral inversion of a micron-scale three-dimensional object*. **Phys. Rev. Lett.** 93 (2004) 255504.
169. Liew K. M., Wei J. X., He X. Q. *Carbon nanocones under compression: Buckling and post-buckling behaviors*. **Phys. Rev. B** 75 (2007) 195435.
170. Tsai P.-C., Fang T.-H. *A molecular dynamics study of the nucleation, thermal stability and nanomechanics of carbon nanocones*. **Nanotechnol**. 18 (2007) 105702.
171. Liao M.-L., Cheng C.-H., Lin Y.-P. *Tensile and compressive behaviors of open-tip carbon nanocones under axial strains*. **J. Mater. Res.** 26 (2011) 1577-1584.
172. Wei J. X., Liew K. M., He X. Q. *Mechanical properties of carbon nanocones*. **Appl. Phys. Lett.** 91 (2007) 261906.
173. Hu Y.-G., Liew K. M., He X. Q., Li Z., Han J. *Free transverse vibration of single-walled carbon nanocones*. **Carbon** 52 (2012) 4418-4423.
174. Firouz-Abadi R. D., Amini H., Hosseinian A. R. *Assessment of the resonance frequency of cantilever carbon nanocones using molecular dynamics simulation*. **Appl. Phys. Lett.** 100 (2012) 173108.
175. Yan J. W., Zhang L. W., Liew K. M., He L. H. *A higher-order gradient theory for modeling of the vibration behavior of single-wall carbon nanocones*. **Appl. Mathem. Model.** 38 (2014) 2946-2960.
176. Narjabadifam A., Vakili-Tahami F., Zehsaz M., Fakhrabadi M. M. S. *Three-dimensional modal analysis of carbon nanocones using molecular dynamics simulation*. **J. Vac. Sci. Technol. B** 33 (2015) 051805.
177. Raj A., Mokhalingam A., Gupta S. S. *Instabilities in carbon nanocone stacks*. Carbon 127 (2018) 404-411.
178. Liu P., Zhang Y. W., Lu C. *Molecular dynamics simulations of bending behavior of tubular graphite cones*. **Appl. Phys. Lett.** 85 (2004) 1778-1780.
179. Bonard J.-M., Gaál R., Garaj S., Thien-Nga L., Forró L., Takahashi K., Kokai F., Yudasaka M., Iijima S. *Field emission properties of carbon nanohorn films*. **Appl. Phys.** 91 (2002) 10107-10109.
180. Dumpala S., Safir A., Mudd D., Cohn R. W., Sunkara M. K., Sumanasekera G. U. *Controlled synthesis and enhanced field emission characteristics of conical carbon nanotubular arrays*. **Diam. Relat. Mater.** 18 (2009) 1262-1266.
181. Ghosh P., Yusop M. Z., Satoh S., Subramanian M., Hayashi A., Hayashi Y., Tanemura M. *Transparent and flexible field electron emitters based on the conical nanocarbon structures*. **J. Amer. Chem. Soc.** 132 (2010) 4034-4035.
182. Kang J. S., Park K. C. *Electron extraction electrode for a high-performance electron beam from carbon nanotube cold cathodes*. **J. Vac. Sci. Technol. B** 35 (2017) 02C109.
183. Baylor L. R., Merkulov V. I., Ellis E. D., Guillorn M. A., Lowndes D. H., Melechko A. V., Simpson M. L., Whealton J. H. *Field emission from isolated individual vertically aligned carbon nanocones*. **J. Appl. Phys.** 91 (2002) 4602-4606.
184. Houdellier F. Masseboeuf A., Monthioux M., Hÿtch M. J. *New carbon cone nanotip for use in a highly coherent cold field emission electron microscope*. **Carbon** 50 (2012) 2037-2044.
185. de Knoop L., Houdellier F., Gatel C., Masseboeuf A., Monthioux M., Hÿtch M. J. *Determining the work function of a carbon-cone cold-field emitter by* in situ *electron holography*. **Micron** 63 (2014) 2-8.

186. de Knoop L., Gatel C., Houdellier F., Monthioux M., Masseboeuf A., Snoeck E., Hÿtch M. J. *Low-noise cold-field emission current obtained between two opposed carbon cone nanotips during in situ transmission electron microscope biasing*. **Appl. Phys. Lett.** 106 (2015) 263101.
187. Houdellier F., de Knoop L., Gatel C., Masseboeuf A., Mamishin S., Taniguchi Y., Delmas M., Monthioux M., Hÿtch M. J., Snoeck E. *Development of TEM and SEM high brightness electron guns using cold-field emission from a carbon nanotip*. **Ultramicrosc**. 151 (2015) 107-115.
188. Mamishin S., Kubo Y., Cours R., Monthioux M., Houdellier F. *200 keV cold field emission source using carbon cone nanotip: Application to scanning transmission electron microscopy*. Ultramicrosc. 182 (2017) 303-307.
189. Fowler R. H., Nordheim L. *Electron emission in intense electric fields*. **Proc. Roy. Soc. Lond.** A 119 (1928) 173-181.
190. Mathur S. B. L. *The thermionic work function of graphite-III*. **Proc. Nat. Acad. Sci.** 19 (1953) 169-171.
191. Bionta M. R., Chalopin B., Masseboeuf A., Chatel B. *First results on laser-induced field emission from a CNT-based nanotip*. **Ultramicrosc**.159 (2015) 152–155.
192. Chen I.-C., Chen L.-H., Ye X.-R., Daraio C., Jin S., Orme C. A., Quist A., Lal R. *Extremely sharp carbon nanocone probes for atomic force microscopy imaging*, **Appl. Phys. Lett.** 88 (2006) 153102.
193. Chen I.-C., Chen L.-H., Orme C., Quist A., Lal R., Jin S. *Fabrication of high-aspect-ratio carbon nanocone probes by electron beam induced deposition patterning*. **Nanotechnol**. 17 (2006) 4322–4326.
194. Chen I.-C., Chen L.-H., Gapin A., Jin S., Yuan L., Liou S.-H. *Iron–platinum-coated carbon nanocone probes on tipless cantilevers for high resolution magnetic force imaging*. **Nanotechnol**. 19 (2008) 075501.
195. Cano-Marquez A. G., Schmidt W. G., Ribeiro-Soares J., Cançado L. G., Rodrigues W. N., Santos A. P., Furtado C. A., Autreto P. A. S., Paupitz R., Galvão D. S., Jorio A. *Enhanced mechanical stability of gold nanotips through carbon nanocone encapsulation*. **Scient. Rep.** 5 (2015) 10408.
196. Yang C.-M., Kim Y.-J., Endo M., Kanoh H., Yudasaka M., Iijima S., Kaneko K. *Nanowindow-regulated specific capacitance of supercapacitor electrodes of single-wall carbon nanohorns*. **J. Amer. Chem. Soc.** 129 (2007) 20-21.
197. Sankar K. V., Selvan R. K. *Improved electrochemical performances of reduced graphene oxide based supercapacitor using redox additive electrolyte*. **Carbon** 90 (2015) 260-273.
198. Wu W., Zhao Y., Wua C., Guan L. *Single-walled carbon nanohorns with unique hornshaped structures as a scaffold for lithium–sulfur batteries*. **Roy. Soc. Chem. Adv.** 4 (2014) 28636–28639.
199. Liang J., Sun Z.-H., Li F., Cheng H.-M. *Carbon materials for Li–S batteries: Functional evolution and performance improvement*. **Energ. Stor. Mater.** 2 (2016) 76–106.
200. Murata K., Hirahara K., Yudasaka M., Iijima S., Kasuya D., Kaneko K. *Nanowindow-induced molecular sieving effect in a single-wall carbon nanohorn*. **J. Phys. Chem. B** 106 (2002) 12668-12669.
201. Adisa O. O., Cox B. J., Hill J. M. *Open carbon nanocones as candidates for gas storage*. **J. Phys. Chem. C** 115 (2011) 24528–24533.
202. Bekyarova E., Murata K., Yudasaka M., Kasuya D., Iijima S., Tanaka H., Kahoh H., Kaneko K. *Single-wall nanostructured carbon for methane storage*. **J. Phys. Chem. B** 107 (2003) 4681-4684.
203. Yang C.-M., Noguchi H., Murata K., Yudasaka M., Hashimoto A., Iijima S., Kaneko K. *Highly ultramicroporous single-walled carbon nanohorn assemblies*. **Adv. Mater.** 17 (2005) 866-870.
204. Xu W.-C., Takahashi K., Matsuo Y., Hattori Y., Kumagai M., Ishiyama S., Kaneko K., Iijima S. *Investigation of hydrogen storage capacity of various carbon materials*. **Inter. J. Hydrog. Ener.** 32 (2007) 2504-2512.
205. Giasafaki D., Charalambopoulou G., Tampaxis C., Mirabile Gattia D., Montone A., Barucca G., Steriotis T. *Hydrogen storage properties of Pd-doped thermally oxidized single wall carbon nanohorns*. **J. Alloys Comp.** 645 (2015) S485–S489.
206. Yoshitake T., Shimakawa Y., Kuroshima S., Kimura H., Ichihashi T., Kubo Y., Kasuya D., Takahashi K., Kokai F., Yudasaka M., Iijima S. *Preparation of fine platinum catalyst supported on single-wall carbon nanohorns for fuel cell application*. **Physica B** 323 (2002) 124–126.
207. Hashimoto A., Yorimitsu H., Ajima K., Suenaga K., Isobe H., Miyawaki J., Yudasaka M., Iijima S., Nakamura E. *Selective deposition of a gadolinium (III) cluster in a hole opening of single-wall carbon nanohorn*. **Proc. Nat. Acad. Sci.** 101 (2004) 8527-8730.
208. Murakami T., Ajima K., Miyawaki J., Yudasaka M., Iijima S., Shiba K. *Drug-loaded carbon nanohorns: adsorption and release of dexamethasone in vitro*. **Molec. Pharm.** 1 (2004) 399-405.

209. Ajima K., Yudasaka M., Murakami T., Maigné A., Shiba K., Iijima S. *Carbon nanohorns as anticancer drug carriers*. Molec. Pharm. 2 (2005) 475-480.
210. Jiménez-Soto J. M., Cárdenas S., Valcárcel M. *Evaluation of carbon nanocones/disks as sorbent material for solid-phase extraction*. J. Chromat. A 1216 (2009) 5626-5633.
211. Li W., Wang W., Zhang Y., Yan Y., Kral P., Zhang J. *Highly efficient water desalination in carbon nanocones*. **Carbon** 129 (2018) 374-379.

-Chapter 2 -

Synthesis process and formation mechanisms of carbon nanocones by CVD

(

« Me parece haber sido sólo un niño jugando en la orilla del mar, divirtiéndose y buscando una piedra más lisa o una concha más bonita de lo normal, mientras el gran océano de la verdad yacía ante mis ojos con todo por descubrir »

Isaac Newton

Chapter 2: Synthesis process and formation mechanisms of carbon nanocones by CVD

1. Summary of the previous work (Allouche's thesis)

1.1. The basis of synthesis process

Chemical Vapor Deposition (CVD) is a widely used method for thin film coating. It allows the growth of high quality and scalable crystals, fibers and powder materials [*1Carlsson 2010*]. Carbon materials can be obtained by different CVD types, such as microwave plasma CVD, plasma enhanced CVD, thermal catalytic CVD, hot filament CVD etc. (see in *Chapter 1* for the example of conical carbon forms). Thermal catalytic CVD (C-CVD) is being used for years for the deposition of pyrolytic carbon as Vapor Grown Carbon Fibers (VGCF) [*2Tibbets1989*]. Pyrolytic carbon (PyC) consists of graphenic carbon deposit, usually of the turbostratic structure, resulting from the thermal cracking of gaseous or vaporized organic precursors, and then nucleation, and then growth, involving either homogeneous (within the gas phase) or heterogeneous processes [*3Delhaes2002*]. Homogeneous nucleation refers to the reactions (association of atoms or molecule fragments, producing heavier species from the precursor gas, e.g. methane conversion) directly within the gas phase [*3Delhaes2002*]. On the other hand, heterogeneous nucleation supposes a more favorable thermodynamic process, where chemical reactions of dehydrogenation and polyaromatization can take place [*4Huttinger1998*]. The latter implies condensation reactions and absorption and desorption of species [*3Delhaes2002*]. According to where nucleation takes place (onto the substrate or within the gas phase), PyC can exhibit different morphological and textural characteristics. Heterogeneous nucleation tends to form more or less anisotropic (laminar) textures whereas PyC resulting from homogeneous nucleation shows overall isotropic textures [*3Delhaes2002*, *5Oberlin2002*].

As results of the hydrocarbon cracking, two main types of carbon species can be distinguished: radicals, and after secondary reactions, polyaromatic hydrocarbons (PAHs) [*3Delhaes2002*]. For some authors [*6Grisdale1953, 7Tesner1984, 8Bokros1969, 9Shi1997*], the PAHs can associate so that to form liquid droplets within the gas phase. However, in the literature, this theory is not unanimously admitted [*10Hu2002*]. There is also a not clear consensus about the carbon species responsible for the nucleation taking place within the gas phase or onto the substrate surface, respectively [*4Huttinger1998*].

The active gas phase specie characteristics (diffusivity, reactivity, composition) and those of the substrate (reactivity, wetting) play an important role in the deposition process [*10Hu2002*]. Going further the early hypothesis by Diefendorf [*11Diefendorf1960*] who first discriminated between two different mechanisms, namely (i) the growing at the graphene edges and (ii) the direct deposition of new layers, Hu *et al.* claimed that as radicals are more

diffusive and reactive than PAHs species, in the absence of active sites to chemisorb on, they are the only species responsible for the homogeneous nucleation, whereas PAHs are mostly responsible for the heterogeneous one [*10Hu2002*]. According to this, the PyC deposition was considered to be driven by two independent mechanisms, which are either the chemisorption of molecules onto active sites (*e.g.* graphene edges) or the physisorption of polyaromatic hydrocarbons (PAHs) onto less active surfaces (*e.g.* graphene faces). However, based on experimental evidences, Monthioux *et al.* [*12Monthioux2006*] proposed a PyC deposition model involving a transient formation of PAH-containing droplets within the gas phase as suggested by Grisdale [*6Grisdale1953*], however while allowing the concomitant nucleation and growth from radicals as well. In summary, the composition of the more or less active species, either primary or secondary, within the gas phase (prevalence of radicals or PAHs), which is determined by the synthesis conditions, is a very important parameter influencing the final carbon deposit.

Based on [*8Brokos1969*], the pyrolytic carbon deposition mechanisms involve both thermodynamic and kinetic parameters such as:

- Gas composition: is a complex parameter, to which corresponds an overall H/C atomic ratio of the gas phase. The nature of the hydrocarbon precursor, particularly its stability and own H/C ratio, as well as its partial pressure can influence the type of nucleation and the final characteristics of the deposited carbon. For instance, a highly stable hydrocarbon precursor as methane (as opposed to acetylene for instance) slows down the cracking and recombination processes, which favours heterogeneous nucleation.
- The dilution of the carbon source with reactive (H_2, N_2) or non-reactive gas (Ar) can oppose recombination reactions, and delays the nucleation process. In the particular case of adding H_2 to the carbon source, the H/C ratio increases, as well as the dilution of the active species, and a delay in the cracking and recombination processes is evidenced. A better control of the resulting solid is achieved by slowing down the reaction this way.
- The residence time: is the time allowed to the pyrolysis to occur at a given temperature (isothermal conditions). The shortest residence times favour small radicals whereas large residence times favour PAHs and homogeneous nucleation. The residence time increases the deposition down the length of the furnace. Of course, long residence time also allows secondary products still in the gas phase to crack again, hence radicals are always produced, yet in decreasing proportion as the residence time increases. The residence time may involve a static atmosphere.
- Temperature of pyrolysis: is the temperature provided at a given position of the furnace and corresponding at least to the needed energy to decompose the feedstock carbon source. Once the cracking temperature is reached, a higher temperature increases the concentration of reactive species. This, in turn, is favourable to homogeneous nucleation (leading sometimes to the formation of soot), instead of heterogeneous nucleation onto the surface, inducing a situation of competition between the mechanisms. A temperature gradient can exist between the pyrolysis temperature and that reached at the substrate surface.

- Pressure: allows controlling the recombination rate between species. A low pressure of hydrocarbons can give low rate surface carbon growth [*11Diefendorf1960*]. The pressure of the system can be reduced either by reducing the total pressure or by reducing the partial pressure of one of the contributing gases. Overall reduced pressure is a condition used in chemical vapour infiltration conditions, where the PyC is intended to fill-in the inner open porosity of a 3D substrate (e.g., a carbon fiber fabric). On the other hand, high pressure opposes the dissociation of the precursor, but favours recombination.
- In addition to these factors, which are valid to all CVD systems, further parameters can also be considered for hot-wall, piston-type CVD systems:
- The location of the substrate in the furnace: the given position of the substrate in the furnace can be of an utmost importance. This depends on the geometry and temperature profile of the furnace. In the case of a furnace with a long isothermal zone as described in [*13Allouche2003*], the location of the substrate is closely influenced, thermodynamically by the local temperature, and kinetically by the time of flight of the species.
- The time of flight: corresponds to the time given to the species issued from the precursor (e.g., methane) cracking to recombine within the gas phase (i.e., before reaching the substrate surface). It could be evaluated as a function of the linear flow velocity of the carbon species across the reactor at standard conditions [*13Allouche2003*]. Therefore, the time of flight depends closely on the reactor dimensions and geometry, and the gas flow rate. Unlike the time of residence, the time of flight implies that the gas phase is not static, and takes into account not only the isothermal zone but all the thermal gradient of the furnace.
- Flow pattern: whether the gas flow remains laminar or becomes turbulent may have a significant influence on the texture of the deposited carbon. For a given incoming gas phase composition, it depends on the geometry of the solid parts (supports, substrates, etc.) present into the furnace tube on the path of the gas flow, and on the gas flow rate. It is characterized by the so-called Reynolds number, whose calculation includes parameters such as fluid density, viscosity and velocity, in addition to the tube diameter. Below a Reynolds number of 2100, a laminar flow is assumed (considering a somewhat constant viscosity, i.e. the case of a Newtonian fluid) [*14LaNasa2014*].

When involving a catalyst, as for growing carbon nanotubes, CVD is designated as CCVD (catalytic-CVD). Two methods of synthesis concerning the catalytic thermal decomposition of hydrocarbons are described in the literature [*2Tibbetts1989, 15Tibbetts1993*]:

- floating catalyst method (the catalyst resides in the gas phase)
- fixed-bed catalyst method (the catalyst is supported onto a substrate)

The floating-catalyst method is characterized by the fact that the catalyst is introduced along with the gaseous feedstock, for instance as a vaporized, liquid catalyst-precursor such as ferrocene, and usually the CNT growth also occurs in the gas phase. As the CNTs are more or less rapidly pushed away from the hot zone by the gas flow, the subsequent catalyst-free carbon deposition onto the primarily-grown CNTs is quite limited. This is a process more favorable to

continuous production, as the CNTs can be continuously collected at the downstream end of the reactor. For instance, this is how the Pyrograf-III® CNT grade by Applied Sciences Inc. (Ohio, USA) is prepared [*16Lake*]. It is not the process used in this work.

On the other hand, the fixed-bed method allows carrying-out a process involving two-step named lengthening and thickening [*17Dresselhaus1988*]. During the lengthening step, the gaseous carbon source (methane, acetylene, benzene, etc.) is first diluted (most of the time) in hydrogen gas to prevent the deposition of any amorphous carbon by reducing the formation of unsaturated species [*18Billaud1989*]. Under high temperature, the mixture of gases is then decomposed over the catalyst (most often a transition metal, Fe, Ni, Co) deposited (most of the time) onto planar substrates (carbon, silicon, quartz) leading thus to the growth of carbon nanotubes onto a substrate surface [*19Baker1973*]. Afterwards, the second step is related to a direct, catalyst-free, pyrolytic decomposition of the gaseous mixture leading to the deposition of PyC onto the surface of the CNTs previously formed and their subsequent thickening [*3Delhaes2002, 5Oberlin2002, 20Endo1995*].

The following *Section* is a summary of the data reported in [*12Monthioux2006, 13Allouche2003, 21Allouche2005*].

1.2. Description of the morphologies obtained

As reported in *Chapter 1* (*Section 2*), conical morphologies can be obtained in a single-step CCVD, but they can also be obtained by a two-step CVD process, from CH_4 and H_2 mixture and using carbon nanotubes as substrates (**Fig.1**).

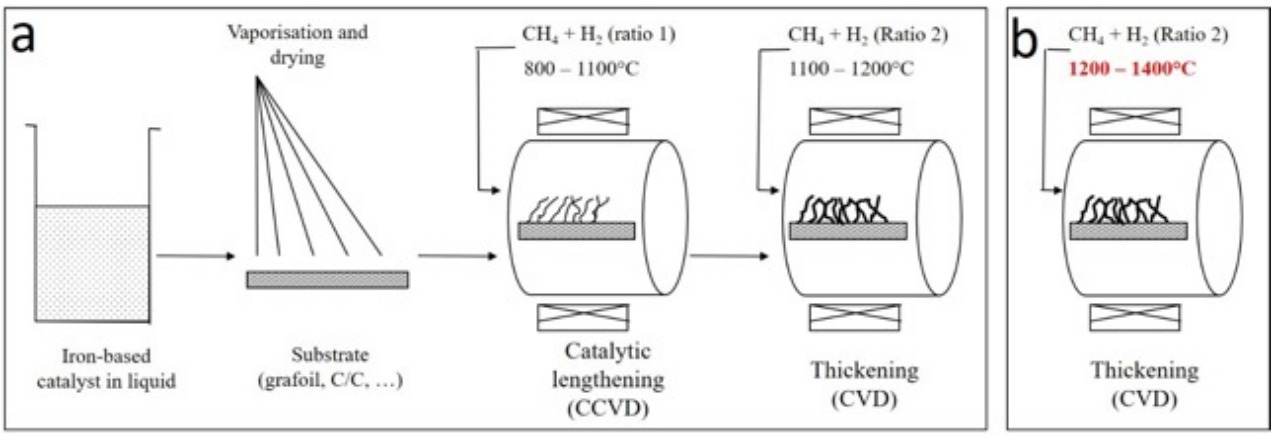

Figure 1: *Sketch of the two-step (C)CVD process.* ***(a)*** *Synthesis conditions for growing VGCFs.* ***(b)*** *synthesis conditions for growing non -standard morphologies, all of them including more or less developed conical forms. Dwell times are 1-2.5 hours at the ultimate deposition temperature in step 2.*

The lengthening corresponds to a linear temperature ramp (10°C/minute) up to about 1100°C. During this step, carbon nanotubes (5-10 nm) were formed by a catalytic process from CH_4 and H_2 (ratio 1), using a suspension of iron-based catalyst nanoparticles in liquid sprayed onto a carbon (Grafoil®) substrate. Then, during the second step, the gas phase was enriched in carbon source (ratio 2) while temperature was also increased (up to 1200°C-1400°C), allowing the thickening of either Vapor Grown Carbon Fibers (VGCFs) or more or less extended VGCF-

related morphologies combined with conical morphologies through a pyrolytic deposition process onto the surface of the nanotube (see **Fig.2**). From the gas phase composition and flow, and furnace geometry, a Reynolds number of 1.1 was calculated, indicating that the flow pattern is in the laminar regime.

Aside morphologies bearing carbon conical forms, other filamentous morphologies were obtained (see **Fig.2**):

(i) standard VGCFs, from slightly distorted to straight, with diameters between 7-35 μm. According to their surface roughness (smooth or rough texture), they were named as $VGCF_S$ or $VGCF_R$, respectively.

(ii) non-standard morphologies: slightly distorted as the VGCFs but more or less segmented, always with a rough surface (bead, short fiber segments), and combined with nano- to micro-sized cone-related shapes, from short truncated cones to fully developed cones, always with a smooth surface. According to the presence of either bead-related or fiber-segment-related rough surface morphologies and their development, and the more or less high prevalence of the conical parts with smooth surface, the non-standard morphologies were named as:

- Beaded Fiber (BF): made of rough-surface beads associated side by side, with no conical parts, and with diameters in the range of 5-10 μm.
- Long Grain Chaplet Fiber (LGCF): of 4 μm in diameter, made of rough-surface fiber-segments attached to each other by more or less developed, smooth-surface truncated conical parts.
- Pearl-Necklace Beaded-Fiber (PNBF): of 3-5 μm in diameter, made of rough-surface beads attached to each other by more or less developed, smooth-surface truncated conical parts.
- Spiky Short Fibers (SSF): of 1-2 μm in diameter, made of rough-surface short fiber-segments associated with a fully-developed smooth-surface cone at both ends. Each SSF is attached to the neighboring one by a carbon nanofilament which is assumed to a naked (or barely thickened) primary CNT grown during the first step.
- Spiky Beads (SB): of 3 μm in diameter, made of rough-surface beads associated with a fully-developed smooth-surface cone on two opposed sides. Each SB is attached to the neighboring one by a carbon nanofilament, as for the SSF morphology.

Depending on the temperature at which the isothermal zone is set, it may happen that all these varieties of morphologies could be found at different positions along the furnace, from the same synthesis experiment. In consequence, the above-given indicative diameters are relative to that obtained within a same experiment, for a set temperature (isothermal zone) of 1260-1295°C and 150 min step 2 duration. However, diameters can vary significantly from an experiment to another, depending on the CH_4/H_2 ratio, location in the furnace, and set temperature.

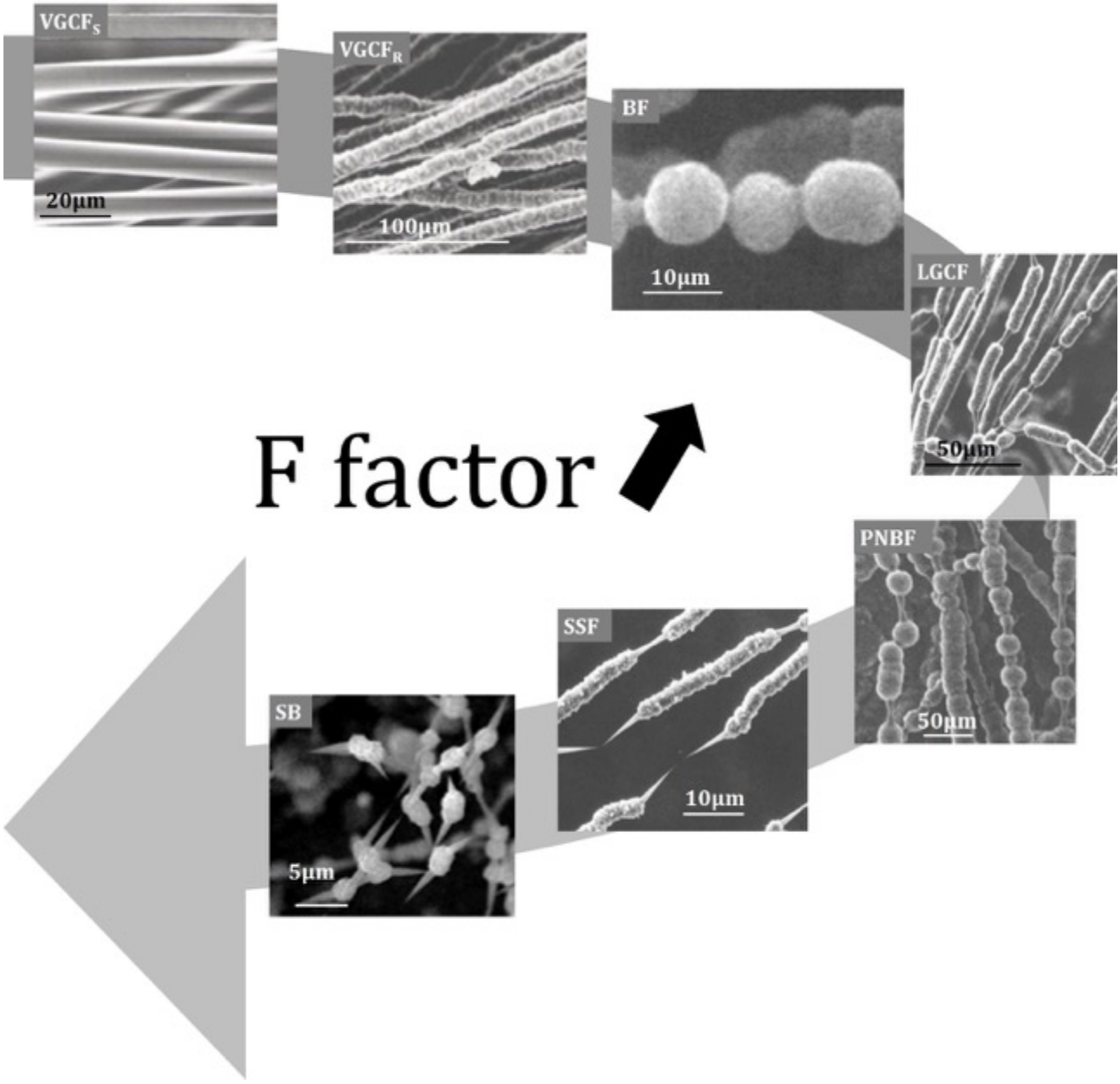

***Figure 2**: The various carbon morphologies obtained by the two-step (C)CVD process in Allouche's experiments ranked according to their* F factor *degree, from standard carbon vapor grown fibers (VGCF$_S$ and VGCF$_R$) to non-standard carbon morphologies (BF, PNBF, LGCF, SSF, SB, respectively).*

Therefore, all the synthesized non-standard morphologies involve sub-morphologies related to VGCF (rough-surface fiber-segments and beads) and smooth conical morphologies (cones fully or partially developed). The more the cone-related sub-morphologies are developed, the less the VGCF-related sub-morphologies are present. For a better understanding of these variations, a factor of morphological complexity, the *F factor,* was defined. The latter consists of the ratio of the proportion of cone-related sub-morphologies over the proportion of the VGCF-related sub-morphologies. For the morphologies where no cone was present (*e.g.* VGCF$_S$, VGCF$_R$, BF), F = 0, therefore the surface roughness degree was considered instead. The *F factor* was found to increase from 0 to 1 as follows:

(F = 0)* VGCF$_S$ < VGCF$_R$ << BF < LGCF < PNBF < SSF < SB *(F = 1)

1.3. Pyrolysis conditions *vs* morphology type

The pyrolysis conditions driving the *F factor* value are presented in **Table1**, in which 4 zones of possible growth are considered (represented by the columns), regularly displayed from upstream (-42.5 cm) to downstream locations (0 cm), the latter corresponding to the middle of the isothermal one.

	Gas phase composition CH_4/H_2)	Position of substrates within the furnace relative to the center (position'0 cm'), and related temperature and products obtained, for a thickening time of 150 minutes							
		- 42.5 cm		- 35 cm		- 17.5 cm		0 cm	
		T °C	Products	T °C	Products	T °C	Products	T °C	Products
1	1/2	1000	*No thickened morphologies*	1050	VGCF-S	1100	VGCF-S	1100	VGCF-S
2	1/4		*No thickened morphologies*		*No thickened morphologies*		VGCF-S		VGCF-S
3	1/2	1170	VGCF-S	1210	VGCF-S	1260	VGCF-S + BF	1260	VGCF-R + LGCF
4	1/2	1220	VGCF-S	1260	VGCF-R + BF	1295	PNBF + BF	1295	PNBF + SB
5	1/4		VGCF-S		VGCF-S + BF		VGCF-R + LGCF		SSF
6	1/2	1315	VGCF-S	1355	LGCF +VGCF-R	1390	LGCF	1390	SSF
7	1/4		VGCF-S		VGCF-R		LGCF		SSF
		1		2		3		4	

Direction of gas flow

Domain 1 Domain 2 Domain 3 Domain 4 Domain 5

Table 1: *Synthesis conditions vs obtained morphologies for a thickening time of 150 minutes, as a function of the isothermal (1100°, 1260°,1295°, 1390°C) and local temperatures, the substrate position in the furnace (with 0 cm as the center of the isothermal zone), and different gas mixtures (CH_4/H_2 = 1/2 and 1/4, by decreasing CH_4 while keeping H_2 unchanged). It is worth noting that, in most of the case, the morphologies formed are a mixture of several types. Only the prevalent ones are mentioned for clarity. Domain 1: no thickening; Domain 2: domain where* F factor *= 0 prevails with all the VGCFs exhibiting a smooth surface; Domain 3: domain where* F factors *are intermediate, including VGCFs with a rough surface; Domain 4: domain where the SSF morphology occurs; Domain 5: domain where the highest* F factor *(F = 1, for SB) prevails. The Table is modified from the original as published in [*12Monthioux2006*], with a fifth domain added for better clarity.*

Standard morphologies (VGCF) were obtained at different positions of the substrate in a temperature range of 1000-1100°C (set temperature for the isothermal zone), and a CH_4/H_2 gas mixture (CH_4/H_2 (flow rate) = 1/2 or 1/4). Under the tested conditions, only the diameters of the fibers but not their global morphology and roughness (smooth surface) were affected by the location of the substrate in the furnace and the local temperature. The deposit thickening

appears to depend on the local temperature. No fibers were formed at -42.5 cm, then fibers with small diameters (~1 μm) were formed at -35 cm, which culminated at ~15 μm at -17,5 cm, then diameters started to decrease (~10 μm) in the middle of the furnace (because of the massive consumption of the carbon feedstock in the upstream zones). All of this was attributed to the low isothermal temperature (1100°C) which was enough to initiate the cracking process, hence to generate radicals, but not enough to generate the secondary species involved in the droplet composition. Therefore, the pyrocarbon deposition is slowed down. On the other hand, when adding further hydrogen to the gas mixture (CH_4/H_2 (flow rate) = 1/4), the moment of actual thickening of the primary CNTs into VGCFs is delayed, and starts to occur at -17,5 cm only with slightly distorted $VGCF_S$ of very low diameters (0.7 μm), which culminates at ~1 μm only at the 0 cm location (against 10 μm for CH_4/H_2 (flow rate) = 1/2).

Non-standard morphologies (BF, PNBF, LGCF, SSF SB) were obtained as soon as higher isothermal temperatures were used (1260°C, 1295°C et 1390°C respectively). At such temperatures, cracking and then subsequent carbon deposition are expected everywhere in the furnace, however, as for the regular conditions above-mentioned, the diameter distribution of the morphologies obtained did not increase monotonously with the temperature but reached a maximum at some local temperature for a given time of flight (position in the furnace) which was always located far before the middle of the isothermal zone (0 cm). Afterwards, diameters kept decreasing throughout the downstream part of the furnace. According to this, the extent of thickening of non-standard morphologies closely depends on both the temperature and time of flight parameters.

Concerning the morphology type, the highest *F factor* morphologies (SSF and SB) were obtained at the highest temperatures and in the middle of the isothermal zone, hence with long times of flight. The latter implies a high degree of "maturation" of the gas phase, where "maturation" may be defined as the overall effect generated by all the reactions taking place in the gas phase until the formation of PAH species, which are driven by both the temperature and the time of flight. Both parameters somehow play an antagonist role, as an increase of temperature tends to promote cracking, whereas an extent of time of flight tends to promote recombination. The chemical composition of the droplets, which can be represented by their H/C ratio, varies so that the droplet physical properties (surface tension and viscosity) are governed by the maturation degree. Such an effect was claimed to play a dominant role on determining the structure and morphology type of the deposited carbon. For conditions where the time of flight (not considering the downstream half of the furnace) and the temperature are the highest, the gas phase maturation is assumed to be the highest, but the combination of increasing both parameters did not show a monotonous impact on the morphologies obtained (see the *F factor* domains reported in **Table1:** comparing lines 4 and 6 in column 4). This is because the effect of temperature and that of time of flight on the maturation are somehow antagonist. For the former, cracking reactions prevail, promoting smaller molecules and ultimately radicals, while recombinations prevail for the latter, promoting larger molecules and ultimately PAHs. The latter can explain the backward evolution of the *F factor* observed when SSFs are formed preferably to SBs (highest *F factor* of 1) at the highest maturation degree (**Table1**, column 4, lines 6 and 7).

The enrichment in H_2 proportion in the incoming gas phase was also considered at play as it was shown to decrease the *F factor*. It seemed logical as adding H_2 opposes to both the cracking reactions of methane and the recombination reactions (such as polycondensation and polyaromatization). However, doubling the hydrogen proportion was made by reducing the CH_4 flow, hence the total gas flow was also reduced meanwhile, resulting in an increase of the time of flight. Therefore, evaluating the impact of the H-enriched atmosphere was not easy to achieve in Allouche's experiments because it is difficult to distinguish whether the decreasing *F factor* is due to the hydrogen proportion variation or is actually due to the lower flow rate as well (**Table1**: compare lines 4 and 5 in columns 3 or 4). It was thus suggested that decreasing the time of flight and increasing the H_2 proportion have a similar decreasing effect on the *F factor*. But It would be interesting to test the impact of these two parameters independently.

For the highest maturation degree of the gas phase (by combining the highest temperature and the highest time of flight, lines 6 and 7 column 4 in **Table1**), adding H_2 to the gas mixture did not change the morphology type but increased slightly their diameter (from 1 to 2 µm). However, this affirmation is based on the results of only one experiment type. More experiments of this kind are needed in order to ascertain this point.

In summary, based on **Table1,** it was concluded that the time of flight of the species issued from the methane cracking plays a primordial role on controlling the morphological complexity of the *F factor*. However, it is the maturation degree of the gas phase (resulting from the combination of the time of flight and local temperature effects in various proportions) that really determines the type of morphologies obtained. Because the maturation therefore depends on two parameters whose effects on the gas phase composition are antagonistic, its relationship with the *F factor* is not straightforward, and the highest *F factor* is obtained for a maturation optimum (line 4, column 4), not for a maturation maximum (which occurs for lines 6 and 7, column 4). Finally, regarding the yield of solid carbon deposit, a similar antagonistic role between the time of flight and the local temperature is revealed. On the other hand, at a given location in the furnace, adding H_2 can either decrease the PyC deposition by delaying the cracking and the recombination processes, and/or increase it by maintaining the gas phase enriched in carbon species over longer times of flight at the same time.

1.4. Detailed description of the conical sub-morphology: the Spiky-Bead case (SB)

For the interest of our work, we will focus our attention on the characterization parameters (texture, nanotexture, and structure) of the peculiar bead/fiber-cone morphologies.

As most of the graphenic materials are anisotropic, aside of their morphology and structure, knowing their texture and nanotexture is essential for understanding their growth mechanism as well as their potential properties and applications.

As seen in *Chapter 1*, here, **structure** relates to crystallography, which means, for graphenic materials, it is related to the way graphenes are piled up within a crystallite, i.e. a coherent domain in which graphenes are perfect whatever their in-plane dimension. Several configurations are possible: turbostratic, graphitic, partially graphitic, commensurate, and rhombohedral (as stacking faults). According to the structure type, a graphenic material can

exhibit a high degree of crystallinity or coherence (as in the graphitic structure, which is periodic in the three directions of space), or a low degree of crystallinity (as in the turbostratic structure, which makes the crystal to be biperiodic only).

However, most of the properties of a bulk graphenic carbon material are not determined by its structure type but by the proportion of defects (which relates to nanotexture) and the degree of anisotropy (which relates to texture). It is well-known, for example, that based on the orientation of graphene layers (parallel or perpendicular) with respect to the growth axis, carbon nanofibers can exhibit good or poor mechanical strength and modulus, and conductive or insulating properties respectively. In consequence, given the importance of the texture and nanotexture for describing carbon materials, some explanations about these concepts will be given.

In the scope of this work, the **texture** can then be understood as the orientation and arrangement of the graphene layers with respect to each other or relative to a specific direction, e.g. the growth axis, regardless of the graphene dimensions and perfection. Typically, isotropy and anisotropy are textural terms.

On the other hand, the **nanotexture** describes the face-to-face stacking and side-to-side association of the crystallites within areas of overall similar graphene orientation (SGO), whatever the texture. However, crystallites within SGO areas are more or less extended, and slightly disoriented with respect to each other and separated from the neighbouring ones by defect lines (removable upon thermal annealing). On the other hand, SGO areas are spatially limited and separated from each other by grain boundaries which gather a variety of structural defects, resulting in large, disorientations (non-removable upon thermal annealing) [*22Monthioux2002, 23Ouzilleau2019*]. The average in-plane dimension of the straight parts of the graphene layers within a SGO relates to the average width L_a of the crystallites, and the average number of graphenes stacked strictly parallel relates to the average height L_c of the crystallites, as depicted in **Fig.3.**

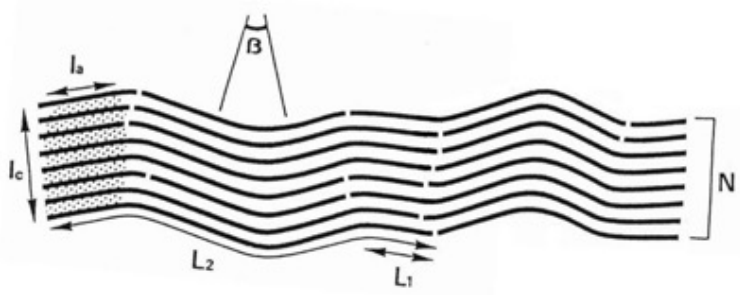

Figure 3: *Sketch of a SGO area (or a portion of) and nanotexture parameters. The shaded region illustrates what a single crystallite of L_a and L_c dimensions is, as seen by diffraction methods (X-rays or electrons). N = the average number of graphenes within a coherent stack (crystallite). β is the misorientation angle, L_1 is the length of rectilinear fringes (dimensions of perfect graphenes, equal to L_a), L_2 is the average length of continuous fringes,* a priori *a single graphene yet distorted due to in-plane defects or bond angle deformations. Therefore, a same graphene may contribute to several crystallites. [*26Monthioux2017*].*

Therefore, structure, texture, and nanotexture are strictly independent parameters. In particular, the term "nanotexture" is preferred instead of "nanostructure" because the parameters involved do not relate to crystallography but to crystallite sizes only. As the term

"texture" indeed, it also relates to the mutual display of graphenes but observed at nanoscale, but it is NOT to designate a nanosized texture (e.g., a nanosized concentric arrangement of graphenes). "Nanotexture" is also preferred instead of "microtexture" once used [*24Rouzaud1983, 25Rouzaud1989*] because the parameters involved are actually in the nanometer range.

The overall constitution of a spiky bead morphology (a bead of 3-4 µm in diameter, sided by two opposed sharp cones), was studied by Transmission Electron Microscopy (TEM). The whole morphology grows onto a CNT previously formed during the lengthening step. Therefore, the primary CNT is still present in the core of the bead, and in the core of the cone as well (see **Fig.4b and 5** for instance). This makes that a primary CNT naturally links the successive spiky-bead morphologies (or others) (**Fig.4c**) which appear to be periodically dispatched along the CNT (see examples provided later on). The beads exhibited a coarsely concentric, microporous texture and a turbostratic structure with a core with a different, dense texture of a diameter of up to 250 nm. A medium range nanotexture was also revealed, with coherent domains with a number N of graphenes up to 30 and *L1* up to 10 nm, and average length of continuous fringes *(L2)* up to 15 nm.

As seen in cross-section, the cones are made of concentric graphenes. It was demonstrated that the cones emerge from inside the bead instead of growing from its surface, as the primary carbon nanotube is still present as the core of the bead, yet thickened by a dense carbon deposit, i.e., different from the rest of the bead, and whose thickness increases from the bead center to the bead surface, hence forming a reversed cone. As depicted in **Fig.4a**, the bead overlaps the cone as a confirmation that they both grow somehow independently. No metal particle was ever found associated to the cones, confirming that the conical shape has not a catalytic origin, contrarily to the primary nanotubes, and relates to specific pyrolytic carbon deposition mechanisms.

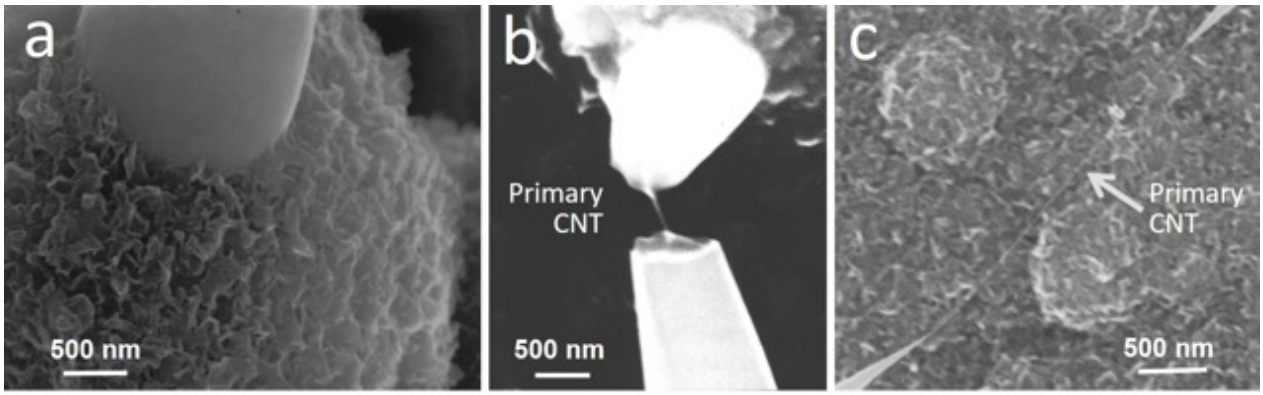

Figure 4: *Scanning electron microscopy image of cone-related sub-morphologies.* ***(a)*** *The bead (rough surface) cone (smooth surface) interface showing that the former overlaps the latter.* ***(b)*** *Evidence for the presence of a primary CNT as the axial core of the cone sub-morphology, made visible upon the incidental breaking of a cone-to-cone junction.* ***(c)*** *From the presence of the primary carbon nanotube joining two opposed cones from two different aligned SBs (out of the picture frame), it is also demonstrated that the cones grow onto the CNT. From [*21Allouche2005*].*

As deduced from **Fig.5**, the conical shape is made of perfectly concentric graphene cylinders that become larger and shorter the closer they are to the cone surface. Concerning the nanotexture of the cones, it is more perfect than it looks from **Fig.5c** but it was altered by the imaging conditions in the TEM (operated at 300 kV). **Fig.5b**, chronologically taken before **Fig.5c** during the same TEM investigation, confirms this at it shows better aligned graphenes. **Figs.5a** and **5b** also show that the graphenes are parallel to the main growth axis (indicated by the hollow core of the primary CNT). Unlike the microporous texture of the beads, the cones show a dense texture, very similar to that of high-nanotexture multiwalled carbon nanotubes (e.g., as prepared by the electric arc process).

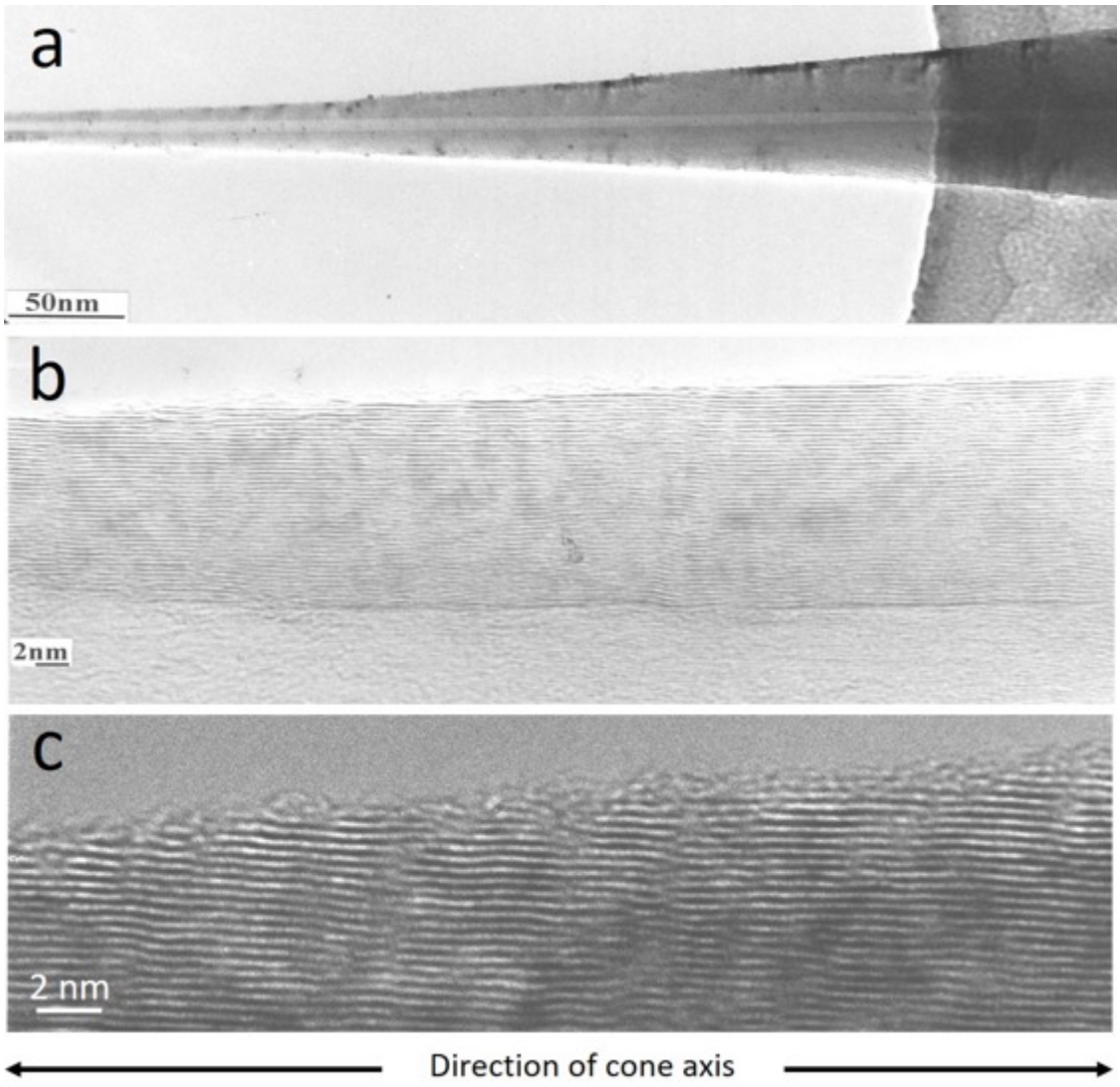

Figure 5: *TEM images of a carbon cone.* ***(a)*** *Low magnification TEM image close the cone apex.* ***(b)*** *HRTEM image (lattice fringe mode) of the upper part of the cone longitudinal section in (a); the hollow core is at the bottom.* ***(c)*** *Enlarge HRTEM image of the cone surface. The nanotexture appears to be high, specifically in (b), but graphenes are not perfect, as many defects have been generated upon the electron irradiation at high energy (Philips CM30, LaB_6 electron source, 300 kV).*

Finally, combining all the observations on the beads and the cones obtained from TEM and SEM on such morphologies and bead cross-sections ended up with the overall texture which is sketched in **Fig.6** below.

A turbostratic structure was revealed for the beads in SB morphology (**Fig.7a**), which implies that graphenes are piled up parallel to each other, however exhibiting mutual, random rotational and/or translational disorder (two-dimensional – or biperiodic – structure) [*27Biscoe1942*]. On the other hand, the cone structure was shown to vary from turbostratic to graphitic (or partially graphitic) from the center to the surface close to the cone base, see **Fig.7**.

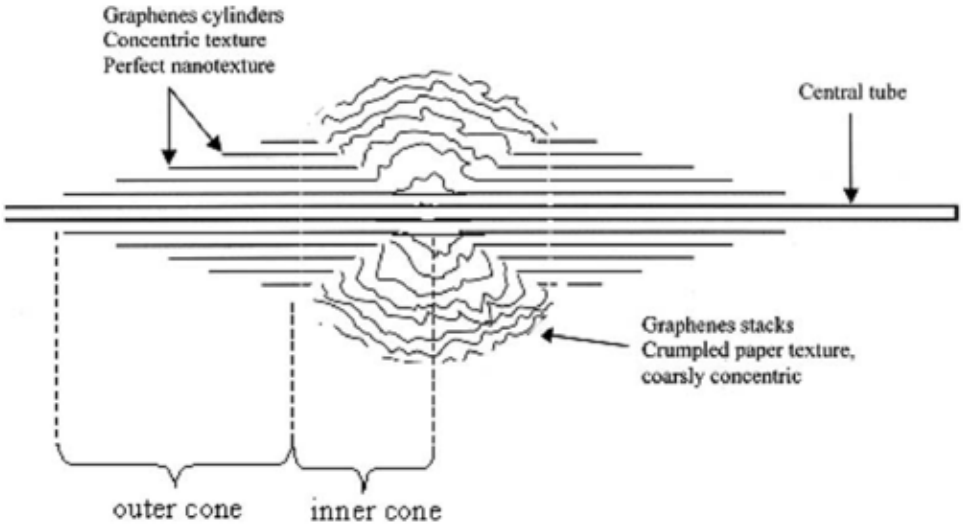

Figure 6: *schematic representation of the SB texture in cross-section. It shows the central nanotube (main axis), the concentric, high-nanotexture graphene layers which make the inner and outer conical part with smooth surface, and finally the microporous carbon deposit which composes the bead with rough surface. From [*21Allouche2005*].*

The partially graphitic structure revealed at the cone-base surface suggests that graphene layers are piled up according to a combination of a graphitic sequence (i.e., the ABAB stacking sequence typical of the three-dimensional graphite structure first revealed by Bernal [*28Bernal1924*]) and turbostratic stacking. This structural variation of the cones was related to their curvature radius. For short curvature radii, successive concentric layers are not commensurate because the difference of radius from a layer to the neighboring one does not allow the atoms of both layers to dispose according to the ABA sequence. However, when the curvature radius is long enough, graphene can be locally equivalent to a plane over areas large enough for inducing some commensurability of the layers on limited extended domains. Obviously, the longest curvature radii are found close to the cone base and for the outermost layers. Importantly, this phenomenon of partial graphitization suggests a same helicity of the concentric graphene layers because, in the absence of polygonization, this is the only way ABAB stacking can take place. This is confirmed from the diffraction pattern on **Fig.7b**, which shows intensity reinforcements all around the *100* ring displayed according to a hexagonal symmetry and also symmetrically displayed with respect to the cone axis. According to the described structure, texture and nanotexture, the SB, especially the conical part, could exhibit excellent properties for applications requiring good mechanical strength and modulus, as well as a good thermal and electrical conductivities, similar to that of perfect concentric-type CNTs [*29Monthioux2006b*]. In addition, as the cone surface is mostly made of graphene faces and steps that are one-atom thick only, we understand why the cones exhibit such a smooth surface since its roughness is at the atom scale. On the other hand, as steps actually are free graphene edges, they can play the role of active sites during the growth process. One could also anticipate

that such a manipulatable conical surface with well-located, one-atom-thick reactive sites might be useful to some applications (*e.g*. chemical sensing applications).

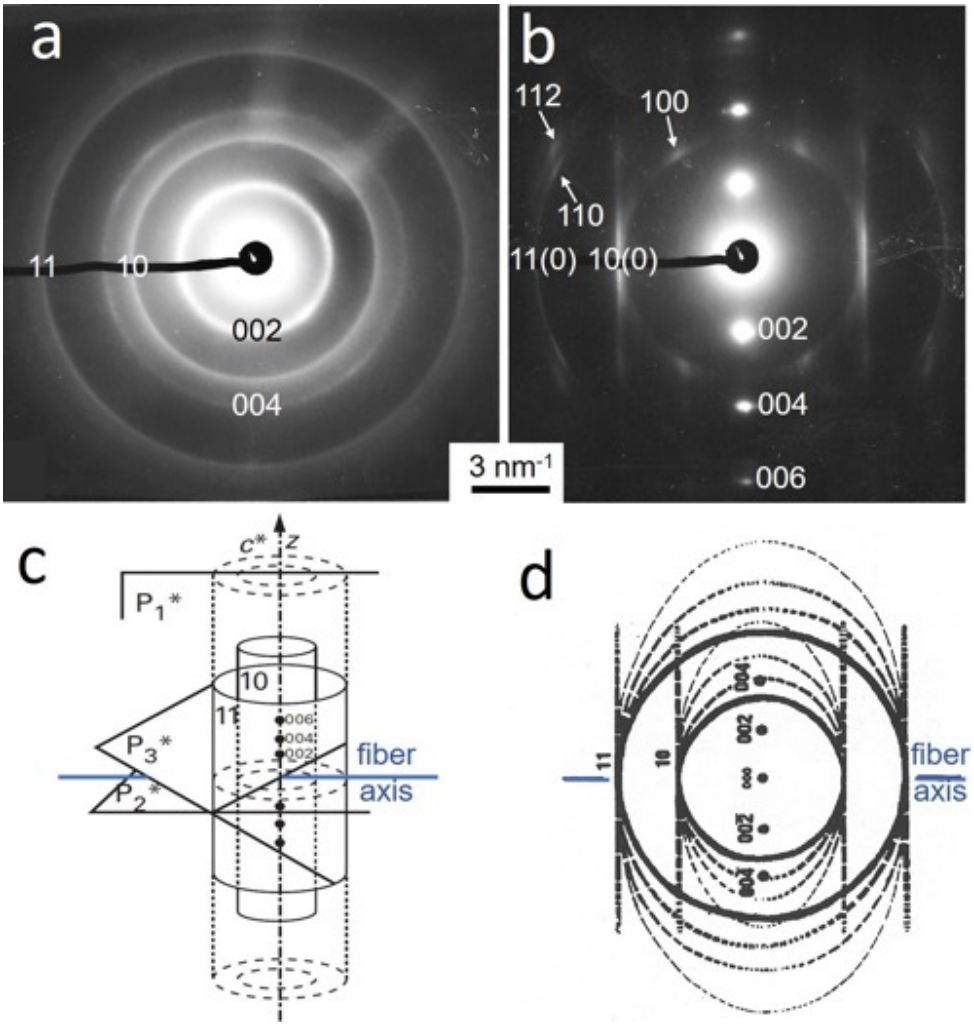

Figure 7: (a) *Electron diffraction pattern from a bead portion: the structure is turbostratic (randomly stacked graphenes), since providing only* 00l *(due to the graphene periodic stacking) and* hk *(because each graphene behaves like an individual, bidimensional crystal in the in-plane direction) reciprocal elements;* 00l *and* hk *show up as full circles and full circular asymmetric bands respectively, which is a consequence of both the concentric texture and the turbostratic structure.* ***(b)*** *Electron diffraction pattern of a cone seen longitudinally showing a combination of rings and spots; full rings indicate the turbostratic structure;* hk0 *spots (arrowed) indicates that many of the concentric graphenes exhibit the same helicity (zigzag type (n,0), here);* 112 *spots (arrowed) indicate that graphitic structure is also present. The cone axis is in-plane and perpendicular to the [00l] direction. The peculiar aspect of the pattern is typical of a fibrous texture (i.e., all the graphenes are parallel to the fiber axis, whereas they are oriented in all directions of space in cross-section, because of the concentricity),* ***(c)*** *Sketch of the reciprocal image of a turbostratic graphene stack;* hk *reciprocal elements appear as elongated cylinders because all the possible in-plane orientations are found in the stack, and each graphene is considered as a one-atom-thick crystal by the incoming coherent electron wave. The only reciprocal elements for which all the graphenes contribute altogether as a single crystal are the* 00l *ones, hence they are not elongated but spots.* ***(d)*** *Sketch of the diffraction pattern resulting from an ensemble of graphene stacks displayed according to a fibrous texture. It is obtained by rotating the reciprocal cylinders in (c) around the fiber axis. The diffraction pattern results from the intersection of the concentric cylinders by various planes such as P1*, P2*, and P3* and all the planes in-between. (a) and (b) from [*21Allouche2005*], (c) from [*30Oberlin1986*], (d) from [*22Monthioux2002*].*

1.5. Growth mechanisms

Based on a scanning electron microscopy investigation of samples from early stages of thickening (**Fig.8**) as well as the SB texture revealed (**Fig.6**), a growth chronology of the carbon conical forms was established: a carbon nanotube (5-10 nm Ø) is produced by catalytic growth at the early step (so-called lengthening step). Then, during the catalyst-free thickening step, an ordered deposition occurs first, forming a double cone onto the primary carbon nanotube, according to a spindle-like shape (**Fig.8a**); then, a more disordered deposition occurs, at the place where the thickening is maximum, i.e., at the middle of the spindle corresponding to the junction of the opposed cone bases (**Fig.8b**); afterwards, the disordered deposit turns into forming a bead at the base of the double cone, see **Fig.8c**.

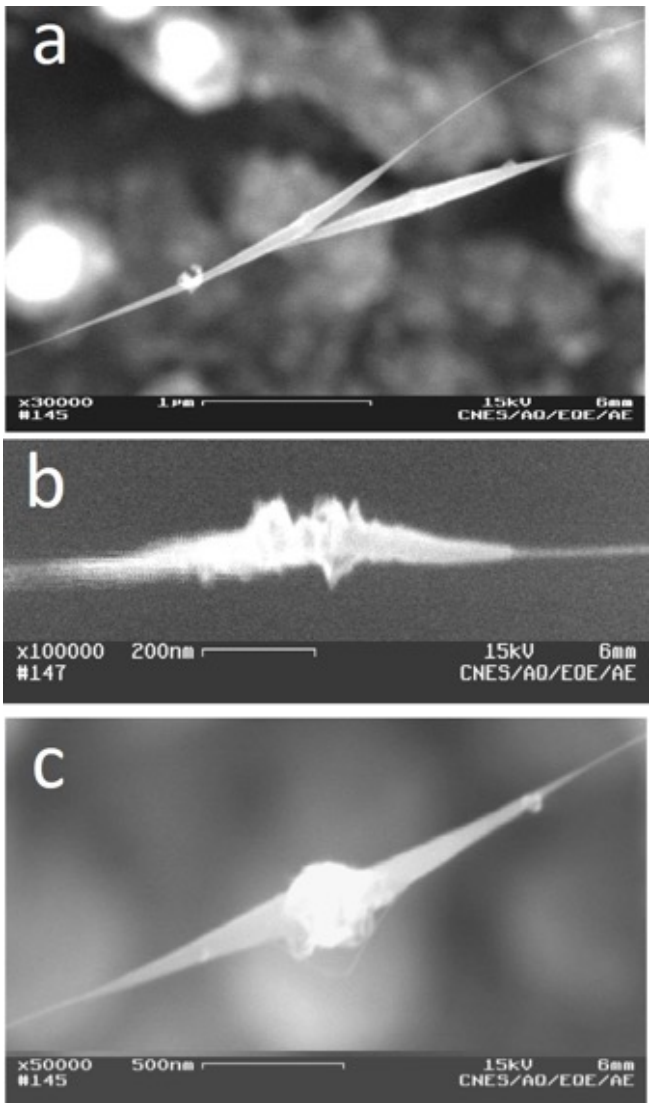

Figure 8: *SEM images showing the chronological formation of the SB morphology.* ***(a)*** *Formation of a spindle-like double cone onto a nanotube surface;* ***(b)*** *Disordered deposition onto the thickest part of the double cone once it reaches a threshold value of 100 nm;* ***(c)*** *A bead starts to form. Images (a) and (b) correspond to a 5-minute thickening time experiment. Image (c) corresponds to 15-minute thickening time experiment. From [*12Monthioux2006*].*

Then beads and cones keep growing simultaneously (**Fig.9a**). The whole process actually occurs many times all along the CNT, distributed somehow periodically (**Figs.9a and 9b**). The local thickening conditions (overall thickening time, time-of-flight, temperature, CH_4/H_2 ratio) govern the thickness ultimately reached by the smooth surface cones and the rough surface sub-morphologies (beads or fiber segments). They also govern the occurrence frequency of the formation of the primary spindle-shape double cones along the CNTs. If they are many and form close to each other, cones growing from neighboring sites may happen to meet without fully developing, hence forming the PNBF (or the LGCF) morphologies (see **Fig.2**).

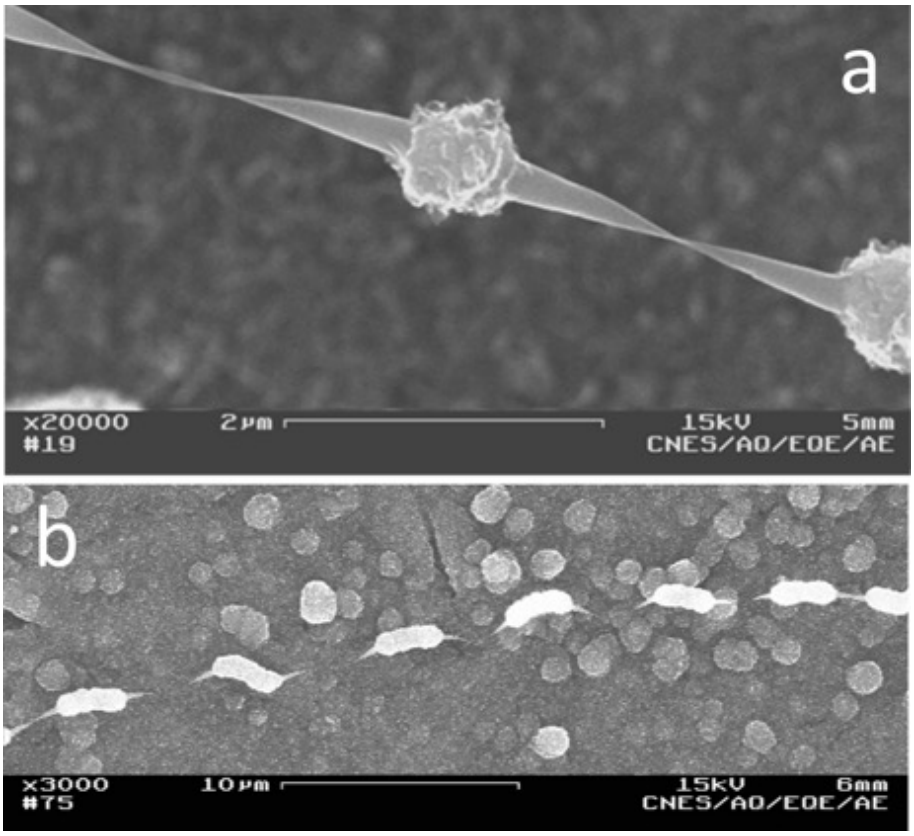

Figure 9: *SEM images showing* ***(a)*** *A SB morphology on the way to turn into a PNBF morphology (30-minute thickening-time experiment), and* ***(b)*** *SSF morphologies whose fiber segment sub-morphology is oversized with respect to the reference SSF morphology shown in Figure 2b (150-minute thickening-time experiment). In both cases, the periodic character of the deposit is obvious. Image (a) from [*12Monthioux2006*], image (b) is unpublished from Allouche's work.*

In order to account for the periodicity of the deposition event, a pyrolytic carbon deposition model was proposed. This model is a combination of the droplet nucleation model initially proposed by [*6Grisdale1953*] and supported by several observations since then [*8Bokros1969, 9Shi1997, 31Koizlik1974, 32Ford1976, 33Je1984, 34Bouchard2001*], and the particle/filler model later on proposed by Hüttinger's group [*35Dong2002, 36Hu2003*] and subsequently accepted by a major part of the community as a preferred alternative to the droplet model. The particle/filler model assumes that polyaromatic (PAHs) species originating from polycondensation reactions of previously formed moieties [*35Dong2002*] are the particles, whereas lighter, linear hydrocarbon molecules are the filler, all of them resulting from the cracking and subsequent recombination events at various extent, and that the various

pyrocarbon textures observed in the literature result from the various proportions of both. However, because the particle/filler model could barely explain the primary formation of the spindle-like double cone and the cone *vs* bead/fiber-segment differentiation if not liquid at some point, Allouche *et al.* supposed the existence of pitch-like droplets, i.e. alike colloids in which the micelles are the PAHs and the suspensive medium are the lighter hydrocarbons, thereby somehow reminding the particle/filler hypothesis. In addition, they considered that radicals are present in the gas phase along with the droplets. The droplet characteristics (number, size, aromaticity, viscosity) are determined by the local conditions previously defined, such as temperature, time of flight and gas composition. Unlike radicals, which need active sites to deposit, droplets deposit randomly on any surface.

A whole scenario was then able to be proposed to account for the growth chronology as deduced from the SEM images. Starting from the co-existence of droplets and radicals, the proposed mechanism is based on the wettability, by the PAH-containing droplets, of the substrate (the primary nanotube surface) where the deposition and carbonization processes take place. According to the substrate geometry (non-planar), two conditions of partial wetting can define the way droplets are deposited onto the nanofilament [*37Dujardin1999*]. These conditions depend on the nanotube over droplet diameter ratio (**Fig.10**).

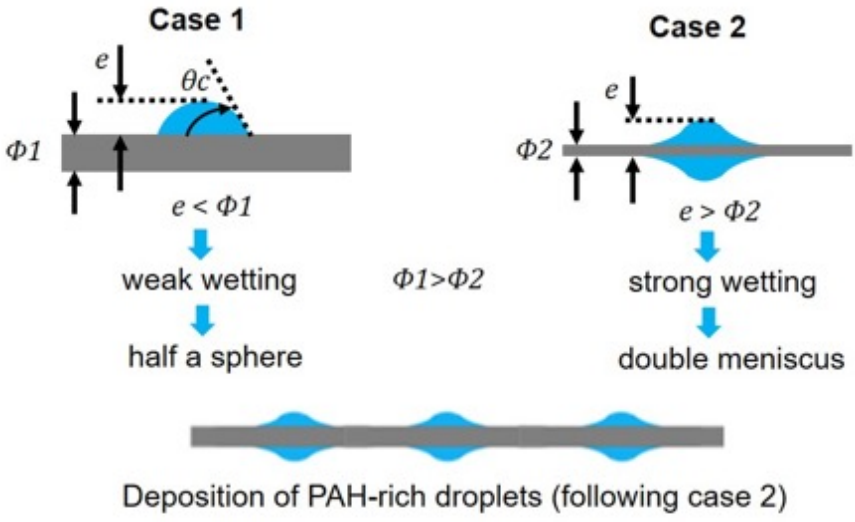

Figure 10: *Two conditions of partial wetting between nanofilaments and PAHs droplets.* ***(a)*** *Weak wetting scenario (case 1): the diameter of the nanofilament is larger than the diameter of the deposited droplets;* ***(b)*** *Strong wetting scenario (case 2): the diameter of the nanofilament is smaller than that of the deposited droplets. Adapted from [*37Dujardin1999*].*

Finally, a whole scenario was able to be proposed, which is summarized in **Fig.11**. First, CNTs are formed by CCVD, corresponding to **Fig.11a** during which thickening may possibly occur but is limited. As long as carbon nanotubes have smaller diameters than droplets, PAH-rich droplets are deposited on the carbon nanotubes surface forming a double meniscus (case 2 in **Fig.10**). The primary deposition event is assumed to be somewhat periodic because driven by the statistical occurrence of the droplets in the gas phase. This double meniscus is responsible for forming the first double cones observed in the SB morphology (see **Fig.8a**), corresponding to

Fig.11b. The PAHs from the droplets align parallel to the nanotube because of the capillary forces and surface tensions that develop at both interfaces (CNT surface/droplet and droplet/atmosphere) and then carbonize as concentric graphenes. The cones continue growing the same way until a threshold value of ~100 nm for the diameter at the cone base is reached.

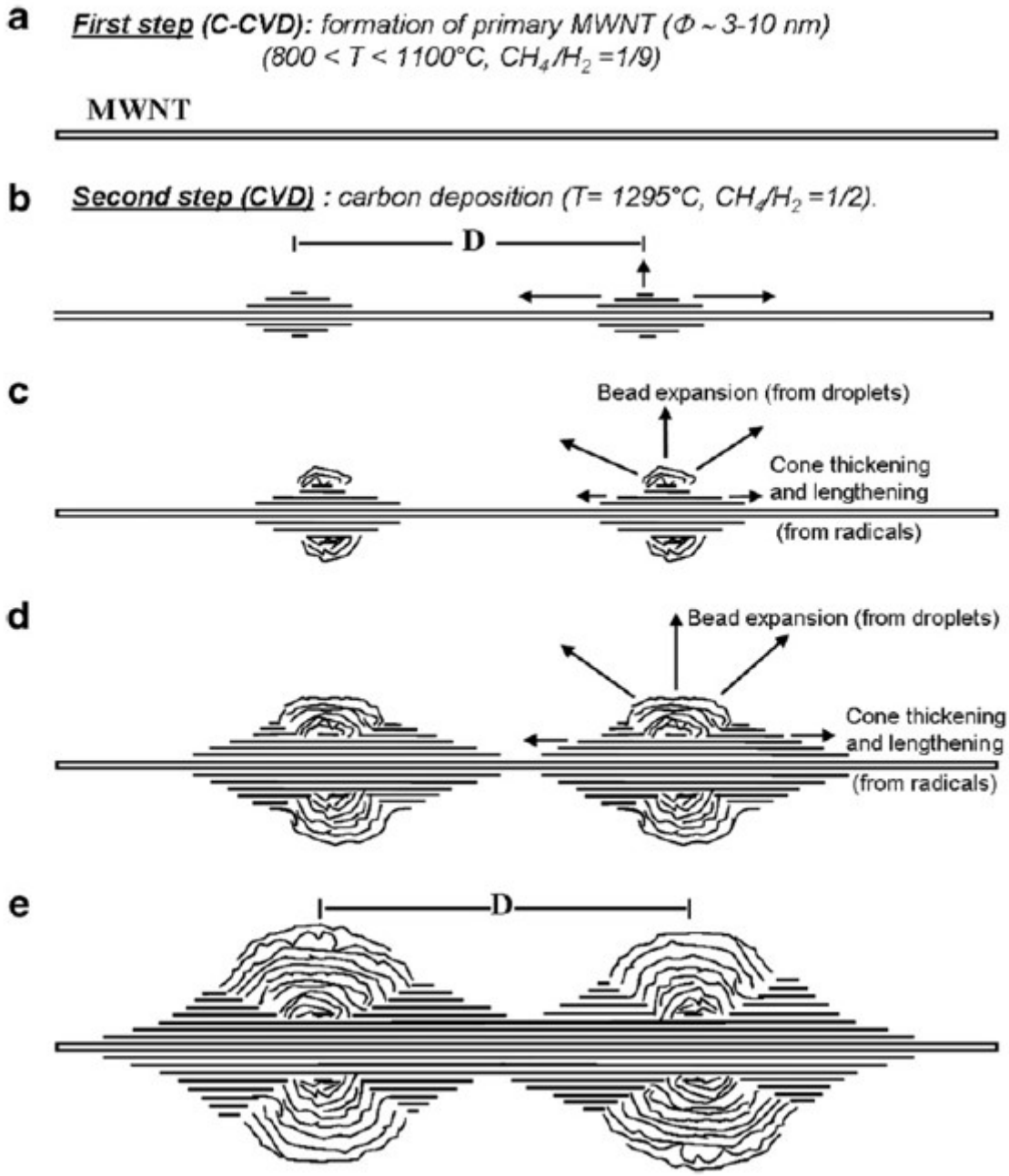

Figure 11: *Chronology of the formation of the spiky-bead and pearl-necklace-beaded-fiber morphologies. From [*12Monthioux2006*].*

Once the threshold value is reached, the deposition from the droplets continues at the common base of the double cones now in a more disordered manner and starts to form a bead (case 1 in **Fig.10)** because, at that time, the radius of curvature of the substrate surface has become long

enough for the droplets to deposit on it as they would onto a flat substrate. This step corresponds to **Fig.11c.**

Once this step is reached, the cones and the beads continue to grow simultaneously (**Fig.11d-e**), but now driven by a competition between the two carbon deposition modes, i.e. radical chemisorption and PAH-droplet physisorption respectively. Radicals will thus deposit on the active sites (typically graphene edges, which are mostly present at the cone surface and were created by the carbonization of the double liquid meniscus) and the physisorption of PAHs will occur presumably on any surface, i.e. on the beads, the cones, and even on the parts of the nanotubes yet to cover. The faster kinetic growth of the beads with respect to that of the cones, which makes that the beads partly overlap the cones thereby leaving inner cones oriented in the opposed direction from the outer cones, was explained by two main factors: (*i*) beads are formed from PAHs, which are larger entities and then contain more carbon atoms than radicals; (*ii*) PAHs forming the beads are not well aligned because they result from a weak wetting interaction with the substrate surface. The latter is responsible for the textural differences between the bead (microporous texture) and the cones (dense texture). If the primarily deposited droplets at the step of **Fig.11b** are far enough apart from each other, or if the growth is stopped by turning the heating off, the cones can fully develop or remain so, and the SB morphology is formed (**Fig.11d**), otherwise cones growing in opposed directions meet by their tip and the PNBF morphology is formed (**Fig.11e**).

1.6 Questions and remarks

It is important to point out that the previous work was performed using a specific reactor from the experimental laboratory of Applied Science Inc. (API, Cedarville, Ohio, USA). It was stated that the know-how regarding how to grow the peculiar morphologies described in Allouche's work is now lost at API. Therefore, a furnace whose characteristics were as close as possible from the API furnace was bought and installed at CEMES. In consequence, for the scope of this work, we had to retrieve the growth conditions and ascertain the reproducibility of the synthesis process with our own set-up at CEMES, in particular regarding one of the most interesting morphology: the spiky-short-fiber (SSF). Considering that

(i) the related know-how by API was able to be lost;

(ii) no one in the world has ever reported the synthesis of similar morphologies in spite some of them have aimed at studying the deposition of graphene onto CNTs [*38Zheng2013, 39Li2013*], to which should be added all the work on VGCFs that was carried-out for 40 years, the synthesis of which is based on the same two lengthening and then thickening steps as for growing cone-bearing morphologies ([*2Tibbetts1989, 15Tibbetts1993, 17Dresselhaus1988, 20Endo1995*] among many others),

(iii) the only attempt of deliberately growing similar morphologies (by a researcher formerly at post at API once back to his lab) has failed in forming anything else but some rare, beaded morphologies with no fully developed cones along with wrong interpretation of the structure and formation mechanisms, in spite of several years of attempts [*40Ting1999, 41Ting2000, 42Ting2001*],

…it was anticipated that this part of the work would not be straightforward.

The proposed growth model can explain many aspects concerning the texture of the synthesized morphologies (*e.g*. the presence of a carbon nanotube at the center of all morphologies, the occurrence of inverted inner cones in the beads of the SB morphology, the difference in texture for the cones and the beads/fiber-segments respectively). However, important issues can be further developed. For instance:

- the inner texture revealed for the SB morphology can barely apply to the SSF morphology as such. It would be interesting to find out about the SSF inner texture and see in which extent it would affect the overall growth mechanism proposed.
- On the other hand, even under the hypothesis that droplets are formed in sub-micrometer gas phase volumes of average local temperature far below the experimental one (1200°C-1390°C), knowing better about the formation and lifetime of liquid hydrocarbon droplets in such environment would help ascertaining their existence.
- Furthermore, some experimental support accounting for the periodicity of the early step deposits as well as the actual formation of the double meniscus is still needed.
- It also remains unclear how the proposed model can explain the same helicity of the successive cylindric graphenes forming the cones as revealed by their partially graphitic structure. The latter should be further exploited in order to deeply understand cone nucleation and growth process modes.
- Finally, moreover because of our targeted application, it is essential to know what the cone apex looks like, as the previous work does not give any information on the cone apex main characteristics (dimensions, structure, nanotexture, etc.).

2. The synthesis of carbon-cone-bearing morphologies at CEMES

2.1. Introduction

The micro/nanosized conical parts along with the micrometer-sized carbon beads or fibre segments are key morphological components for allowing handling and mounting the carbon cones and then using them for various applications. In the particular context of our work, their textural and nanotextural characteristics allow interesting physical properties such as electrical and thermal conductivities and mechanical strength to be expected, that could make them excellent candidates for various applications (see *Chapter 1*), among them probes for Near Field Microscopy (also designated as Scanning Probe Microscopy - SPM).

One objective of the thesis work was to reproduce the synthesis of these morphologies in our reactor at CEMES by finding the most suitable conditions in temperature, gradient

temperature, gas ratio[7], and to validate the growth mechanism described in the previous *Section*. We will also try to answer the different questions presented in the previous part.

From our knowledge, aside from the API team in the USA (which is no longer able to reproduce the synthesis process), the only reported attempts for reproducing the API process were published by Ting *et al.* [*40Ting1999, 41Ting2000, 42Ting2001*], and were not fully successful. So, we are conscious of tackling a high-sensitivity synthesis process, typical of mechanisms in which all the driving reactions are out of equilibrium, and for which key-parameters have not all been identified yet.

2.2. Description of the process[8]

2.2.1. Furnace description

The reactor employed is a horizontal, piston-type furnace from *Lindberg,* with a heating source able to reach a maximal temperature of 1500°C. The furnace is monitored by an *Eurotherm* controller allowing adjusting the heating-up parameters. The synthesis process takes place in a ceramic tube from *Anderman Ceramics.* The synthesis is operated at atmospheric pressure. The furnace is placed into a special (explosion-proof) room, which consists of concrete bunker-type walls, and a light roof. This configuration allows the trajectory of any possible shock wave to be redirected upwards to the room ceiling and then outside, so that to prevent any lateral damage in case of incident. On the other hand, the gas flow is conducted to the furnace through stainless steel tubes, and each gas flow is monitored by a flowmeter system. The gases are blended before entering the furnace. The exiting gas flow goes to an extractor towards the outside of the room after passing by a small water tank so that to trap the solid particles that could possibly be carried by the gas. It is also important to point out the existence of CH_4 and H_2 leak detectors able to close the valves at the very exit of the gas bottles, for protecting both the people and the room from any possible incident.

2.2.2. Preparation of substrate

The catalyst consists of commercial suspension in water of iron nanoparticles of about 10 nm in diameter (**Fig.12a**). Centimetric coupons of Papyex® material (exfoliated and then high-pressure laminated graphite from MERSEN, otherwise designated as "flexible graphite") are used as substrates to support the catalyst nanoparticles (**Fig.13**). The Papyex coupons are soaked in the suspension and then placed in an ultrasonic bath. Then, the coupons are dried in air, and ten of them are displayed separated from each other on a refractory support.

[7] This work has benefited from the thorough preliminary work carried-out by Mathieu Delmas within the ANR projects HD-Strain and then CANAC, and then the help of Aurélien Masseboeuf. It would have been impossible to reach the results here-presented if we had to start the work from scratch.
[8] We are sorry that some information about the set-up and synthesis conditions are not provided so that to protect the know-how.

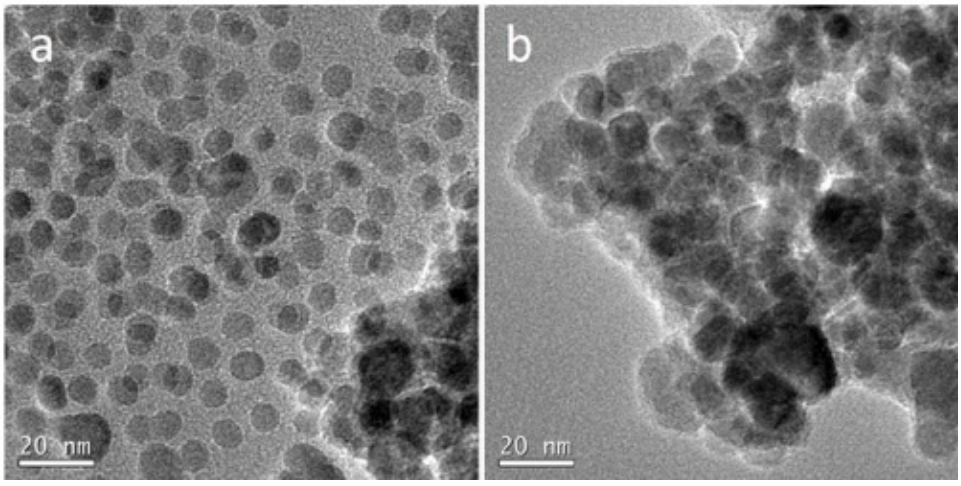

Figure 12: *Morphology of the catalyst nanoparticles from the suspension. The suspension was sprayed onto a TEM Cu grid coated with a plain amorphous carbon film. Because the suspension had aged, the image in* ***(a)*** *is a rare one where the nanoparticles are still individualized. However, in most of the places they are found agglomerated as in* ***(b)****. (Image credit: L. Noé, CEMES).*

Finally, the support is introduced inside the furnace so that the coupon numbered #10 is placed at the middle of the isothermal zone. Coupons #10 down to #6 are in the isothermal zone, which is quite long, ~30 cm (see the furnace temperature profile in inset of **Fig.15**). The other coupons are aligned in the upstream part of the temperature gradient (see **Fig.13**).

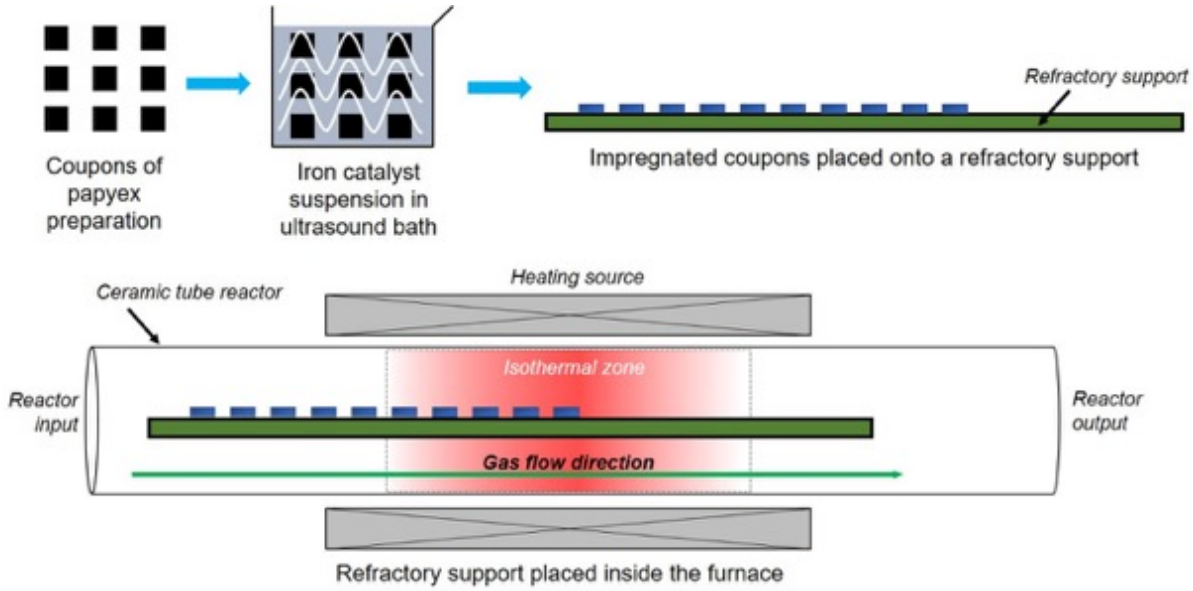

Figure 13: *Substrate preparation and placement in the furnace.*

The substrate preparation and placement in the furnace are slightly different from those used in the original experiments [*13Allouche2003*]. Instead of using a spraying and subsequent heat-drying process for the substrate preparation as depicted in (**Fig.1**), an impregnation method [*43Komiyama2006*] is chosen in order to tentatively enhance the reproducibility of the catalyst dispersion onto the substrates, otherwise too much dependent on the spraying conditions (spraying angle, distance, and duration). The coupon dimensions and separation distances onto

the support, as well as their placement in the furnace are adapted to the set-up dimensions, which are somewhat different from those described in [*13Allouche2003*]. Also, no substrates are placed beyond the middle of the isothermal zone in the downstream part as we had no intent to carry-out the related study. Indeed, in Allouche's work, morphologies formed in the downstream part were found to correspond to much more complex mixtures than in the upstream part, making difficult to use them to support any conclusion regarding the mechanisms [*13Allouche2003*].

It is worth noting that the protocol above-mentioned for the substrate preparation is the optimized one. Actually, after some time (few months to few years), iron particles tend to agglomerate in the suspension (**Fig.12b**), which could result in lowering the primary CNT yield significantly. We carried-out a study using various probe-sonication conditions and Dynamic Light Scattering which has shown that the agglomerates can be dismantled in some extent, but the initial status of suspended individual nanoparticles was never able to be recovered. Therefore, although working with fresh suspension and then substrates soaked in it was preferred at some point, the various experiments include different solution qualities (we have worked with (i) an "old" suspension; (ii) a sonicated "old" suspension; (iii) a "fresh" suspension), and the substrates were either sprayed with the suspension, or soaked in it and bath-sonicated. These variations are assumed to affect the lengthening step but not significantly the thickening step, as they were found to have a direct consequence on the overall yield in CNTs but not on the type of morphologies formed, thereby meaning that only individual catalyst particles do form CNTs whereas agglomerates do not. Therefore, observations regarding the comparison of the quantity of the morphologies produced are not significant, and we only will comment on the type of morphologies and thickness deposited.

2.2.3. Process conditions

The furnace is set up as follows: temperature ramp 10°/minute, starting from room temperature up to 1390°C[9]. From room temperature to 500°C, 200 sccm argon flow is established, in order to clean up the reactor for residual gases and water, and remove surfactants from the iron particles. Then the Ar flow is replaced by 1000 sccm of H_2 until 800°C is reached; the H_2 flow is remained constant during 30 minutes at 800°C (this step is mostly to reduce the iron nanoparticles which turned to iron oxides once in the suspension and/or once in air). After that, a CH_4/H_2 = 1/9 ratio is established during the 800°-1100°C ramp and the same gas flow remains for 22 minutes at 1100°C to allow the primary MWCNTs to grow (lengthening step). These CNTs will then be the substrates for the CVD deposition of both the standard and non-standard carbon morphologies. It is important to point out that, when the CNT growth was maintained for more than 22 minutes, no cone-related sub-morphologies are formed during the following thickening step (**Fig.14**). This suggests that CNTs not only grow with a diameter somehow driven by the catalyst particle size during this first step, but also thicken in some extent. Long dwell times may favor carbon filaments with diameters too large

[9] All temperatures values provided in the text and figures are that given to the main controller, which is driven by a thermocouple located outside the reactor tube. A slight temperature difference exists with respect to the actual temperature in the reactor tube axis. For instance, a 1390°C set-up temperature corresponds to a 1395°C ± 5°C.

for allowing the overall droplet-driven deposition mechanisms that generate the cone-related sub-morphologies (see **Fig.10** and the related comments).

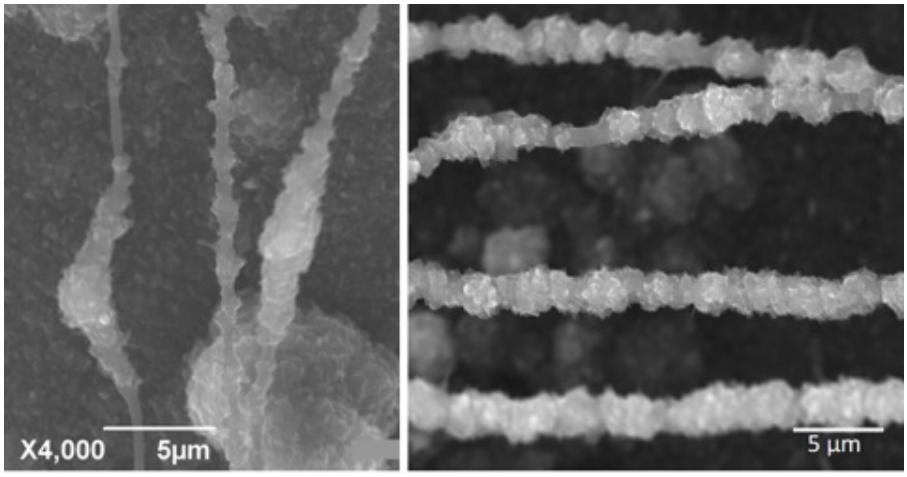

Figure 14: *Examples of cone-free morphologies obtained after thickening, when the lengthening step at 1100°C was maintained for more than 22 minutes (here: 50 minutes), whereas cone-related sub-morphologies are obtained in the same thickening conditions when the regular duration of 22 minutes is used (see* ***Table2a****)*

The temperature is then increased from 1100 to 1390°C under a 200 sccm argon flow only, in order to avoid carbon oxidation and prevent the deposition of unwanted pyrolytic carbon. Finally, a flow of CH_4/H_2=1/2, or 1/4 is established at 1390°C for the thickening process during 2 hours. Then the furnace is turned-off, and the cooling process is ballistic, i.e. natural, and conducted under inert atmosphere. The whole operating procedure is summarized in **Fig.15.**

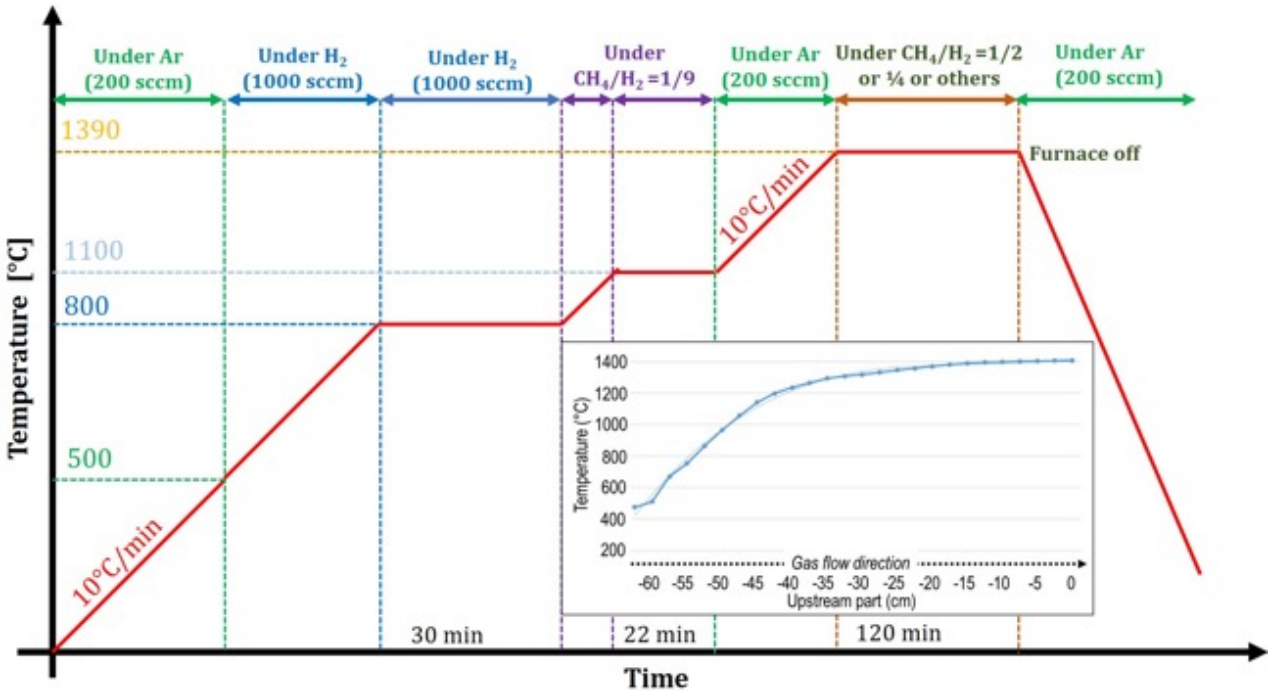

Figure 15*: Diagram of the synthesis conditions concerning the gas flow concentration, temperature, heating ramp, and time. In inset is the temperature profile of the upstream part of the furnace (0 = middle of the isothermal zone) for a set-up temperature of 1390°C under Ar flow.*

2.3. Towards the synthesis of Spiky Short-Fibers (SSF)

Our experiments are based on the previous synthesis conditions established in [*12Monthioux2006, 13Allouche2003*] and summarized in **Table1**. We will report only on the final experiments, i.e. those that were successful in growing cone-related sub-morphologies, and more specifically corresponding to the conditions expected to form the wanted morphologies, namely the SSF. Basically, a sufficiently high maturation degree of the gas phase (high temperature and long time-of-flight) was desired in order to promote the formation of PAH-rich droplets within the gas phase in addition to the formation of radicals. In consequence, our starting experimental conditions, which will be used as reference ones, are as follows: CH_4/H_2 (flow rate) = 1/2 for a total flow rate FLOW3, set-up temperature (isothermal zone) of 1390°C, thickening time of 120 minutes (**Table2a**). Other flow rate values FLOW*i* used are reported in the following as FLOW1 to FLOW8, for which the flow rate value increases along with the incremental number *i*.

Meanwhile, our goal is to verify whether the results from varying the synthesis conditions follow the same trends predicted by the mechanisms proposed in Allouche's work.

2.3.1 Reference conditions (1390°C, CH_4/H_2 = 1/2, total flow rate = FLOW3)

SSFs were not obtained under the conditions expected to do so based on Allouches's previous results. As shown in **(a)** of **Table2** (afterwards referred to as experiment **Tab2a**), we have obtained beads combined with well-developed cones far before the center of the isothermal zone already (substrate #5), which had never happened in Allouche's experiments. Nevertheless, our results tend to globally agree with those of [*13Allouche2003*] for some aspects: (*i*) substrates are never representative of a single morphology but of a mixture of several, yet with a prevalent one; (*ii*) the morphological *F factor* increases from substrates #1 to #10, i.e., as the gas phase maturation increases.

On the other hand, unlike in Allouche's results, the deposited thickness is found to continuously decrease from substrates #1 to #10 instead of reaching a maximum somewhere in-between. As Allouche's result is however a common observation in CVD processes, it is assumed that the maximum of thickness is reached before, somewhere in the upstream part between the gas injector and the location of substrate #1.

For instance, $VGCF_R$s of ~10 µm and ~8 µm diameter are obtained at positions #1 and #2 respectively; a majority of BFs (diameter ~5 µm) is formed at positions #3 et #4; PNBFs of diameters decreasing from ~4 to ~3 µm are obtained at positions #5 to #7; at positions #8 to #10 SB morphologies with fully developed cones are formed, however, the diameter of the morphologies decreases from ~3 to ~0.5 µm so that, in position #10, cones are still well developed but beads may even be absent from the nanotube surface.

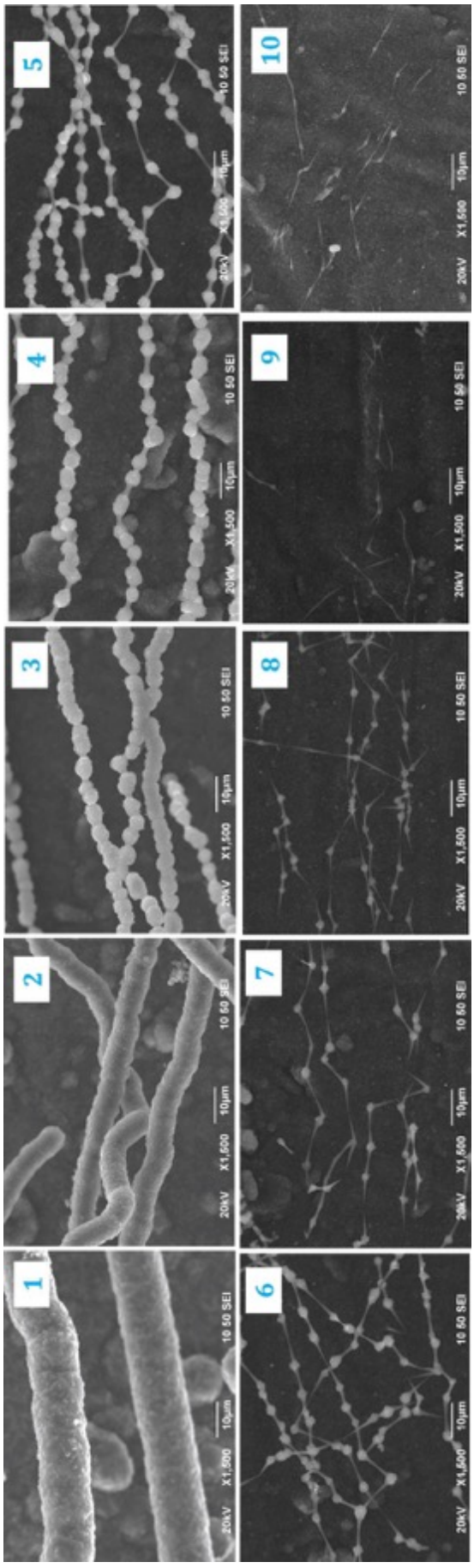

(a) *CH_4/H_2 = 1/2; total flow rate FLOW3 (reference conditions).*

Table 2: (a) *to* ***(c)*** *Scanning electron microscopy images of the morphologies obtained for a set-up temperature of 1390°C. Positions 1, 2… 10 correspond to the positions of the substrates (from which the images were taken) aligned in the furnace from the most upstream position (#1) to the center of the isothermal zone (#10). The specific conditions for each experiment are provided below the image series:*

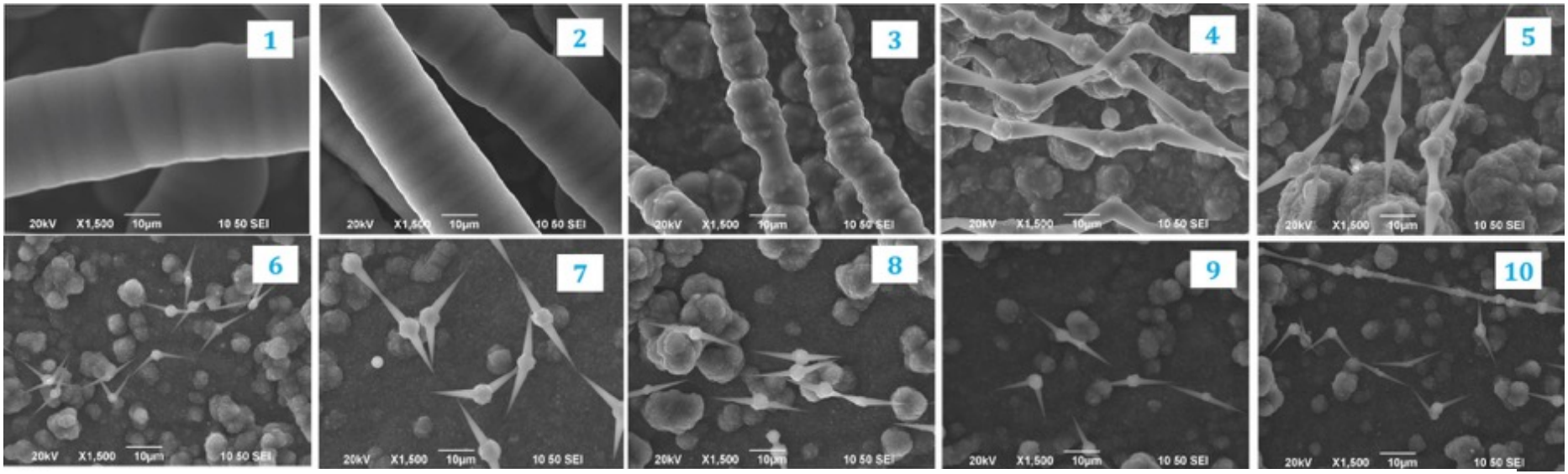

(b) *CH_4/H_2 = 1/4, both by decreasing CH_4 and increasing H_2 with respect to the reference conditions in (a), hence with a total flow rate FLOW5 > FLOW3*

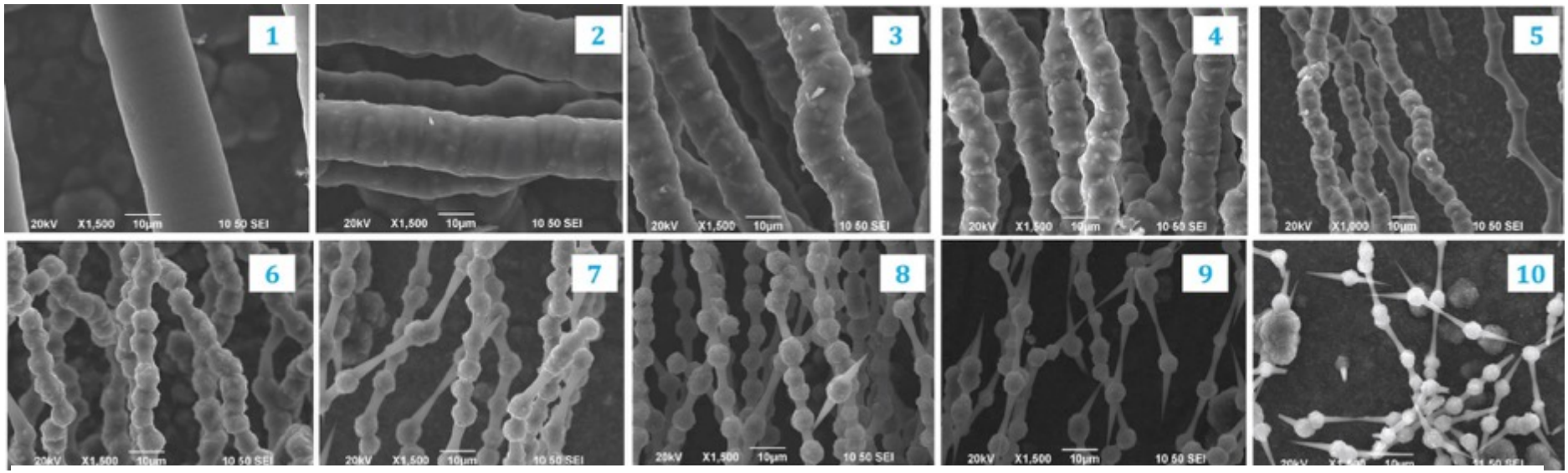

(c) *CH_4/H_2 = 1/4, by increasing H_2 while keeping CH_4 unchanged with respect to reference conditions, resulting in a total flow rate FLOW8, with FLOW8 > FLOW5*

A major difference with Allouche's results (**Table1**) is that SBs were only obtained at the ultimate time of flight and for the isothermal temperature of 1295°C in his experiments, against 1390°C and for a large range of times of flight here. It is assumed, according to **Table1**, that the SSF morphology requires ultimate maturation conditions (highest temperature and longest time of flight) to be formed, but those were already reached in our furnace yet resulting in producing SBs only. Therefore, the nature of the species in the gas phase has to be modified otherwise, and we decided to focus on changing the gas phase composition.

Two examples are provided in **(b)** and **(c)** of **Table2** (afterwards referred to as experiments **Tab2b** and **Tab2c**) both corresponding to CH_4/H_2 (flow rate) = 1/4, but obtained differently: referring to conditions for **Tab2a, Tab2b** is obtained by both decreasing CH_4 and increasing H_2 resulting in a higher total flow rate FLOW5, whereas Tab2c is obtained by only increasing H_2 resulting in a total flow rate FLOW8 (with FLOW8 > FLOW5 > FLOW3). Clearly, they both resulted in higher thickening for all the positions shown, from #1 to #10 compared to the reference conditions (**Tab2a**): morphology diameters range from ~10 down to 0.5 µm in **Tab2a,** whereas they range from ~32 down to ~3 µm in **Tab2b** and from ~24 to 5 µm in **Tab2c.** This looks like a paradox, since the gaseous feedstock was not enriched in carbon but enriched in H_2 (CH_4 was decreased for **Tab2b**, and remained unchanged for **Tab2c**). Also, as both experiments used total flow rates higher than for the reference conditions, the related times of flight were shorter (because of the higher velocity of the gas phase), hence it cannot be said that the higher deposited thickness at the center of the furnace is due to a higher maturation effect. Therefore, this effect is only due to the enrichment of the gas phase in H_2. As reminded in *Section 1.1*, adding H_2 has the effect of opposing (delaying) the thermal cracking of CH_4 because it is one of the products from the cracking reaction, but it also may oppose the recombination reactions and the nucleation because of its dilution effect for the molecules active in these processes. What is observed for **Tab2b** and **Tab2c** with respect to **Tab2a** is consistent with this: the increase in the H_2 concentration has delayed the cracking in the early steps of the deposition, leaving the gas phase enriched in carbon species for longer time of flight and inducing thicker deposits at the other positions further downstream. Following the logic of the mechanisms previously deduced from Allouche's experiments, the almost vanishing of the bead sub-morphology in #10 of **Tab2a** would come from a depletion in PAH-rich droplets of the gas phase because of the lack of carbon species. On the other hand, in **Tab2b** and **Tab2c**, the concentration in carbon species at these positions has increased, hence allowing an increased formation of PAHs and a subsequent higher thickness of the bead sub-morphologies.

The consequences of modifying the gas phase by increasing the H_2 proportion was then investigated further.

2.3.2. Decreasing CH_4/H_2 by decreasing CH_4 and leaving H_2 unchanged (hence reducing the total flow rate)

Table3 gathers a series of experiments for which the CH_4/H_2 concentration ratio is progressively decreased from 1/2 (top) down to 1/3 (bottom) by decreasing the CH_4 concentration only while leaving the H_2 concentration unchanged, resulting in meanwhile decreasing the total flow rate.

(a) CH_4/H_2 = 1/2 FLOW3 (Reference conditions, same as Tab2a)	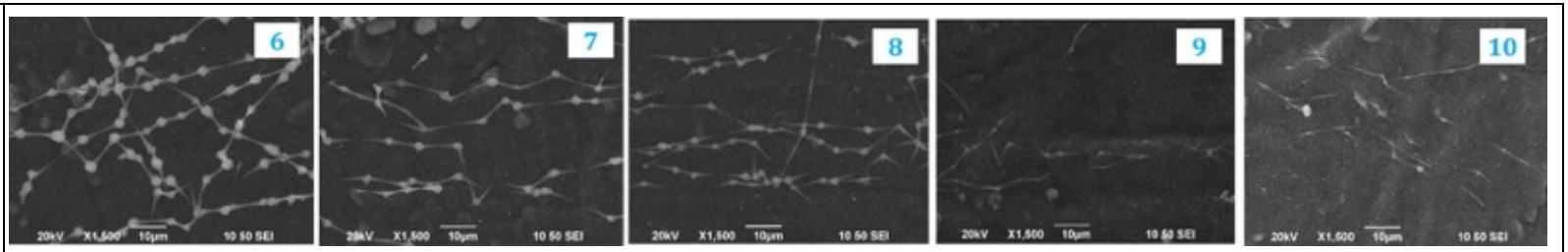 PNBF present on #6 and #7, then SB present and prevalent from #8 to #10 with the beads barely developed in #10
(b) CH_4/H_2 = 1/2.2 FLOW2	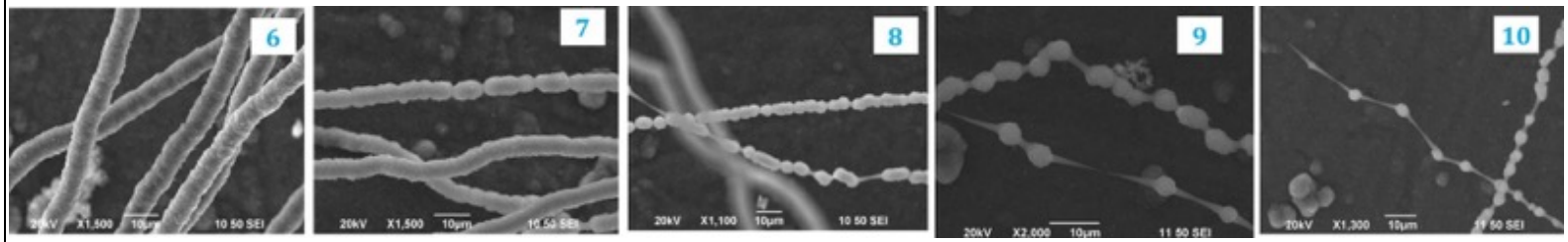 VGCF and SB until #8, and then mostly PNBF and few SB from #9.
(c) CH_4/H_2 = 1/3 FLOW1	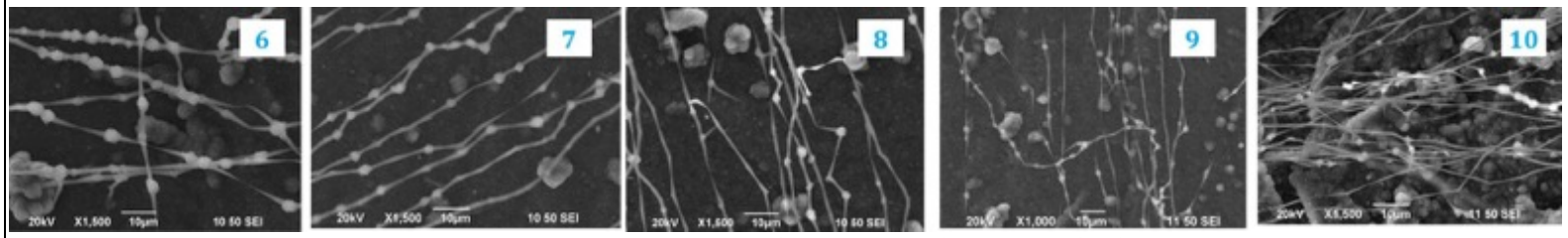 PNBF prevalent all along, however with an increasing prevalence of cone-related (smooth surface) sub-morphologies while bead-related (rough surface) sub-morphologies vanish.

Table 3: *Effect of the decreasing CH_4/H_2 ratio of the gas phase on the morphologies grown in the isothermal zone, by decreasing the CH_4 flow and keeping the H_2 flow constant (hence decreasing the total gas flow rate).*

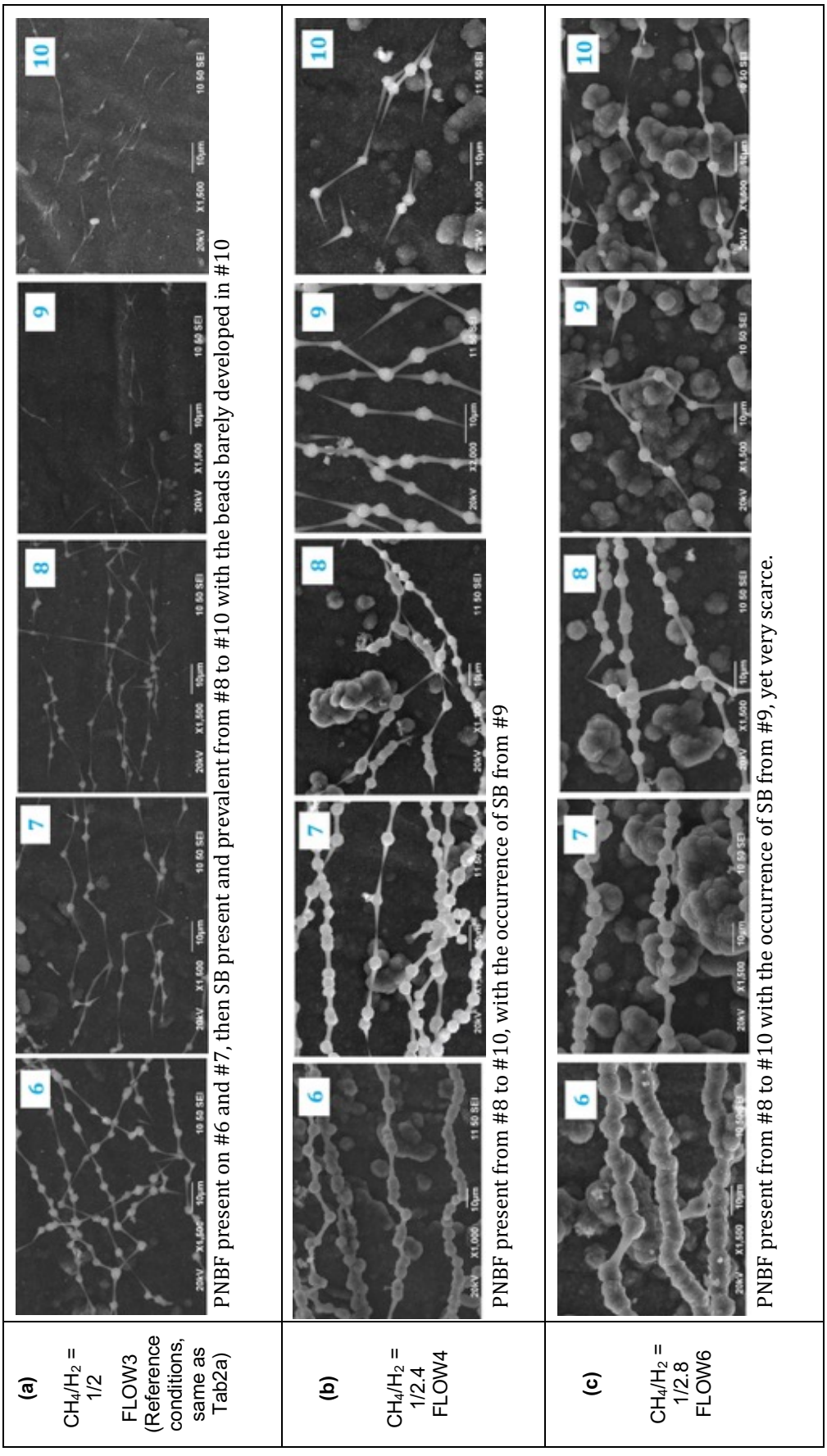
(a)
CH_4/H_2 = 1/2
FLOW3
(Reference conditions, same as Tab2a)
PNBF present on #6 and #7, then SB present and prevalent from #8 to #10 with the beads barely developed in #10
(b)
CH_4/H_2 = 1/2.4
FLOW4
PNBF present from #8 to #10, with the occurrence of SB from #9
(c)
CH_4/H_2 = 1/2.8
FLOW6
PNBF present from #8 to #10 with the occurrence of SB from #9, yet very scarce.
6
7
8
9
10

(d) CH_4/H_2 = 1/3 FLOW7	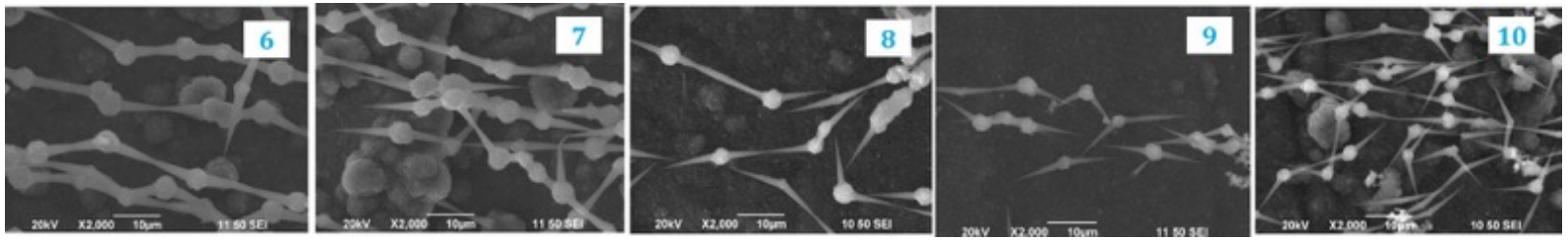 PNBF prevalent at #8, then SB prevalent at #9 and #10.
(e) CH_4/H_2 = 1/4 FLOW8 (same as Tab2c)	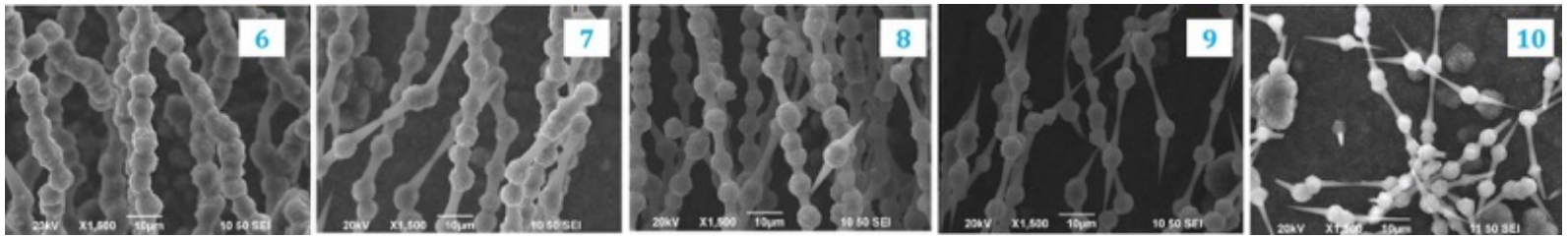 PNBF prevalent at #8 and #9, then SB significantly present at #10.

Table 4: *Effect of the decreasing CH_4/H_2 ratio of the gas phase on the morphologies grown in the isothermal zone, by increasing the H_2 flow while maintaining the CH_4 flow constant (hence increasing the total gas flow).*

Considering **Tab3a** and **Tab3b** in this experiment series, changing the concentration ratio from 1/2 to 1/2.2 does not change much the type of morphologies found on the ultimate substrates #9 and 10, i.e. SBs and PNBFs with well-developed cones are formed. However, it is enough for the tendency previously observed to be confirmed: increasing the H_2 proportion by decreasing the CH_4 proportion results in larger beads (~4 µm diameters are observed at position #10 for **Tab3b** against ~0.5-1 µm for **Tab3a**), hence higher thickness is deposited. On the other hand, increasing further the H_2 proportion by decreasing further the CH_4 concentration resulting in a concentration ratio of 1/3 no longer follows the trend: almost no beads are formed, and the filaments no longer exhibit any rough surface deposit instead (see **Tab3c**). Therefore, the deposited thickness increases from **Tab3a** to **Tab3b** and then decreases from **Tab3b** to **Tab3c**, while the CH_4/H_2 concentration ratio decreases all along. This might look surprising, but it may be explained by the fact that the CH_4 concentration for **Tab3c** is the lowest of all the experiments reported here while the H_2 concentration is lower than for **Tab2b** and **Tab2c.** Because of this, the concentration of carbon species at positions #9 and #10 is no longer enough for allowing significant amounts of PAHs to form. As a consequence, the deposit mainly occurs from radical species, which is consistent with the smooth surface aspect.

2.3.3. Decreasing CH_4/H_2 by increasing H_2 and leaving CH_4 unchanged (hence increasing the total flow rate)

Table4 gathers a series of experiments for which the CH_4/H_2 concentration ratio was progressively decreased from 1/2 (top) down to 1/4 (bottom) by increasing the H_2 concentration only while leaving the CH_4 concentration unchanged, resulting in meanwhile increasing the total flow rate.

Because the CH_4 concentration is sufficient (1.5 times that for **Tab3c**), PAH-related sub-morphologies (e.g., beads) are always present even at position #10 whatever the H_2 concentration (from **Tab4a** to **Tab4d**). Likewise, the SB morphology is always present, although in various proportions with respect to the PNBF morphology. It is present as early as at position #8 for **Tab4a** even if the beads are barely developed. However, for higher H_2 flow rates (**Tab4b** to **Tab4d**), SBs appear only from position #9, and then only at position #10 for **Tab4e**. Therefore, the higher the H_2 flow rate, the more delayed is the formation of the SB morphology as the main effect, whereas the incidence on the thickness deposited is subordinate as soon as the concentration ratio is lower than 1/2. This might be due to the effect of the increasing total flow rate, whose consequence is to increase the gas velocity, hence to decrease the time of flight for a given distance in the furnace, which means lowering the formation of PAHs.

It is worth noting that LGCF morphology was also formed as a minor phase (**Fig.16**) at position #10 for an experiment with a similar CH_4 flow ratio as that of **Tab3b**, but a total flow rate in-between FLOW7 (**Tab 4d**) and FLOW8 (**Tab 4e**) instead. This is quite promising, because it appears to be one of the rare experiments approaching the formation of the desired SSF morphology.

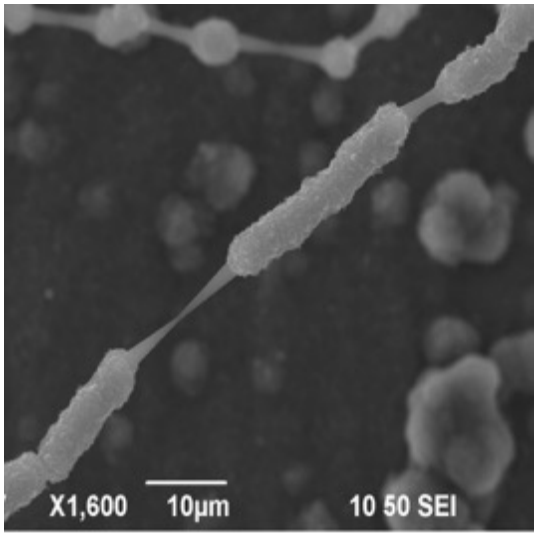

***Figure 16**: Example of the LGCF morphology formed as a secondary phase at position #10 in the experiment with a similar CH_4 as for **Tab3b**, but with a total flow rate in-between FLOW7 (**Tab 4d**) and FLOW8 (**Tab 4e**).*

2.3.4. Defining the conditions for the synthesis of the SSF morphology

From the observations above, few important statements can be made:

- Despite a large range of CH_4 and H_2 concentrations was investigated, it tends to mostly affect the deposited thickness, and not so much the type of morphology formed, especially at the center of the isothermal zone.
- Lowering CH_4/H_2 ratio by lowering CH_4 is possible until some bottom limit is reached, below which it has a dramatic consequence on the morphology formed, because the gas phase is too much depleted in carbon species.
- Increasing the total gas flow rate, hence the gas velocity, is able to shift downstream the time of formation of the morphologies (specifically SB).
- None of our experiments have succeeded in synthesizing the SSF morphology yet

Well-developed cones are then obtained over a large range of CH_4 and H_2 concentrations, combined with beads often well developed as well, but combining the cones with short fiber segments is missing. Referring to **Table1** again, we see that the prevalent formation of the SB morphology (line 4 column 4, corresponding to the highest *F factor*) occurred at the middle of the isothermal zone, hence at the longest time of flight with respect to the furnace portion considered, but does not correspond to the highest maturation conditions since the temperature was only 1295°C. Synthesizing SSF required to reach a higher maturation than the one used for SB, which was achieved by either slowing down the total flow rate (by decreasing CH_4) hence increasing the time of flight (line 5 column 4), or increasing the temperature (line 6 column 4) or both (line 7 column 4). However, with our set-up, SB are formed at the center of the isothermal zone and for the highest temperature available (1390°C). The only way to increase the maturation further and possibly reach the needed conditions to form SSF could then be to increase the time of flight by (i) **considering the downstream part of the isothermal zone**, so far ignored based on Allouche's results; (ii) **slowing down the gas velocity** by lowering the total flow rate by lowering both CH_4 and H_2.

Because, considering **Table1,** the formation of LGCFs (which occurred column 3, lines 5, 6, and 7) seems to precede that of SSF (which occurred column 4, same lines), the new series of experiments could **start with the conditions** that were able to form the LGCF morphology at position #10 (**Fig.16**). If low CH_4 concentrations have to be used, resulting in limiting too much the formation of PAHs, **longer dwell times** could be used (e.g., 150 minutes or more, instead of 120).

2.4. Understanding further the growth mechanisms

Validating the formation mechanisms of the peculiar cone-bearing morphologies previously proposed (see *Section 1.5*) supposes to confirm the hypothesis of the formation and co-presence of PAH-containing droplets in addition to radicals at some moment during the time of flight and in variable proportions within the gas phase. One question is then whether there is any observation in our experiments that might not be consistent with this scenario, another one is whether another scenario is possible. Then, after questioning whether the first step of the deposition onto the carbon nanotube surface is driven by the droplet behavior and the competition between droplets and radicals, another important issue to consider to better understand the growth mechanism of these morphologies is to characterize the cone-apex texture and nanotexture, which was missing in Allouche's work, and evaluate whether the observations can be ascribed or not to the initially-proposed growth model.

2.4.1. The deposition process

Several models for the deposition of thin films from a vapor phase can be found in the literature. When considering the growth on "flat" (i.e., without steps) surface, three growth modes can be distinguished [*44Reichelt1988, 45Ratsch2003*]:

- the layer-by-layer growth, so-called Frank-van der Merve (FM) growth, in which the interaction between the substrate and the depositing species (adhesion) is much higher than the cohesion between the depositing species. A next layer will grow only once the first layer is completed.
- the 3D-island-based growth, so-called Volmer-Weber (VW) growth, in which small clusters are nucleated directly on the substrate surface and then grow into islands as a condensed phase. The formation of islands takes place from the beginning of condensation, if the interaction energy between the depositing species (cohesion) is larger than that between the deposit and the substrate (adhesion)
- A mixture of both, so-called Stranski-Krastanov growth, in which a first layer-by-layer growth step is followed by the formation of 3D islands. The reason for switching the growth mode could be that the interaction of the second layer with the first layer is not as strong as it was between the first layer and the substrate. But many other reasons are possible [*46Venable1983*].

Such growth models are able to be applied to a large variety of materials. However, they are often discussed in terms of atoms, i.e. the depositing species are by far less large and complex than those involved in our gas phase at high maturation level. In addition, two major differences makes us think that such models may barely apply to our system: one is the substrate nature, i.e., a nanosized filament, which has little to do with the kind of surfaces usually considered when discussing these growth models; another is the fact that the chemical composition of the depositing species (hydrocarbons) evolves during the formation of the deposit which may affect the adhesion *vs* cohesion competition which seems to be the main driving factor. However, based on their observation that the deposition of pyrolytic carbon starts with the formation of islands, consistently with the literature [*34Bouchard2001, 47Soutric1998*], Lee *et al.* [*48Lee2012*] have convincingly shown that the deposition of PyC may follow the Volmer-Weber model. But the formation of our complex morphologies, which comprise both a smooth and a rough surface sub-morphologies growing at the same time, constitutes a main objection to Lee *et al.*'s statement, as there is no way that the Volmer-Weber model may account for it. Therefore, other scenarios will be considered.

Because both smooth surface and rough surface sub-morphologies are formed in the same time onto the same CNT as substrate, the species involved in growing both should be different. Therefore, there are no other alternative than hypothesizing that two very different species should be responsible for the formation of each of the sub-morphologies, respectively. Hence, the hypothesis of the co-existence of PAHs and radicals is believed to be robust.

This said, the next question to answer is whether the PAH deposit on the CNTs as such or as a liquid, wherever it forms. In addition to the support of the literature previously cited [*6Grisdale1953, 8Bokros1984, 9Shi1997, 31Koizlik1974, 32Ford1976, 33Je1984, 34Bouchard2001*] for naming just a few, Allouche *et al.* hypothesized the existence of a PAH-rich liquid phase to account for several experimental observations: (*i*) the aspect of condensed droplets of the pyrocarbon islands found in the early step of pyrolytic carbon deposition onto planar surfaces [*34Bouchard2001, 47Soutric1998, 48Lee2012*]; (*ii*) the meniscus morphology of the cones (yet solid) [*12Monthioux2006*]; (*iii*) the axisymmetric geometry of the primarily formed double cones (**Fig.8a**). Therefore, the occurrence of a liquid phase, even transitory, seems to be likely. Even Hüttinger and coll., whose particle-filler model originally did not consider the existence of a liquid phase [*35Dong2002*], admitted it once as a possibility: "*Due to the slow rate of condensation reactions, the life-time of the polycyclic aromatic hydrocarbons should be sufficient to permit the formation of a transient liquid and, in particular, a mesogenic film in which orientation processes are possible before carbon is formed*" [*10Hu2002*]. Meanwhile, they considered as "*relatively unimportant whether or not nucleation is based on the physisorption of individual species or on the physical condensation of aggregated species (droplets)*".

Obviously, such a statement of unimportance regarding the actual existence of liquid droplets is irrelevant when investigating the early step of the deposition mechanisms of pyrolytic carbon onto nanosized filaments. Whether the PAHs exist as such in the gas phase, which would then be a mixture of various species of various sizes and reactivities (hence making the gas phase a monophasic medium), or gather into liquid droplets formed within the gas phase (hence

making the gas phase a biphasic medium), is the next question that is worth addressing: in the former case, a liquid film could form onto the substrate once the PAHs reach it; in the latter case, the liquid phase pre-exists and merely spread over the substrate surface when meeting with it. According to both our observations and the previous ones by Allouche (see **Fig.9** for example), under the conditions favorable for the formation of beads, the beads display more or less periodically along the supporting CNTs. However, it is interesting to notice that, in many cases, the nanotube length is not completely covered by the deposition of beads, and some parts may remain uncovered between the successive, neighboring beads.

To explain this, the hypothesis made in Allouche's work was that the periodicity of the bead display (or that of the other cone-bearing morphologies) merely reflects the statistical distribution of the droplets in the gas phase. The higher the concentration in droplets, the closer to each other the morphologies along the CNT. However, considering the physical phenomena that may occur when a liquid film covers a filament provides another alternative. Indeed, the formation of beads more or less spaced along the carbon nanotubes could be explained by the Plateau-Rayleigh instability (PRI) phenomenon.

Back in the XIXth Century, such an instability was first used to explain the spontaneous deformation of a falling-down liquid cylinder by forming droplets once the fluctuation deformation wavelength (λ) is superior to the liquid cylinder perimeter [*48deGennes2005*]. The size of the droplets being formed is determined by the fastest deformation mode (i.e., the mode that takes the shortest time to develop). The PRI phenomenon is based on the liquid surface tension, whose main objective is to reduce the surface energy for the system to gain in stability while maintaining the same liquid volume [4*9deGennes2005*]. It may surely apply to PAH-rich liquids whatever their rheological properties as, according to [*50Mora2010*], the same phenomenon can be also predicted to occur even with soft solids (polymers, colloids, gels) provided capillarity forces are more important than elastic shear forces.

The Plateau-Rayleigh instability can also explain different natural phenomena occurring when liquid films are in contact with strings, such as the pearls of water on a spider web due to morning dew, as well as in some industrial applications such as fiber manufacturing, coating of optical fibers, surgical textile fibers, etc. [*49deGennes2005*]. However, for the PRI to play a role in such systems, gravity should be negligible, which is achieved as soon as the so-called Bond number *Bo* or the Goucher number *Go* (where $Bo = Go^2$, with *Go* = fiber radius/capillary length[10]) is small ($Bo << 1$), which, in practical, occurs as soon as the filament radius is lower than ~50 µm [*51Carroll1976*], or even lower than a fraction of a millimeter according to Quéré [*52Quéré1999*]. In such conditions, when considering physical systems involving droplets deposited onto fibers (which is assumed to occur with PHA-containing droplets deposited onto a CNT), the PRI can explain common observations concerning the shape of the deposited droplets and their periodicity and regularity (**Fig.17**) in various systems, from microscale [*53Haefner2015*] down to sub-microscale [*54Dolado2019*] and nanoscale [*55Kolb2005*] (referring to the fiber radius). In particular, Dolado *et al.* reported the formation of micron-sized bead-like SnO_2 particles onto Zn_2GeO_4 nanowires with diameters of 100-300 nm, forming

[10] The capillary length is half the droplet height when the surface tension balances gravity, and is equal to $(\gamma/\rho g)^{1/2}$ where γ is the surface tension, ρ the density of the liquid, and g the gravitational acceleration.

a necklace-like morphology [*54Dolado2019*]. Even if the precursors were very different than ours, the similarity in the resulting morphologies with ours is striking.

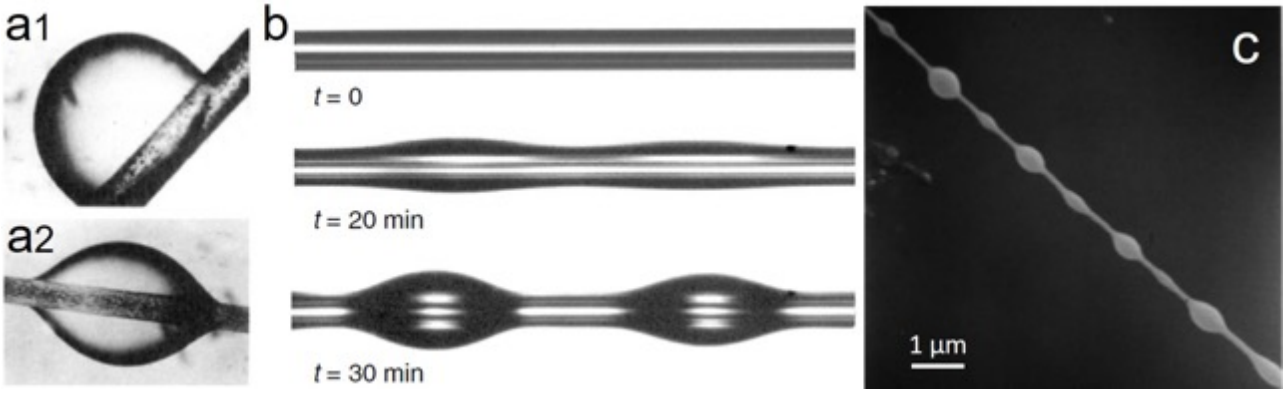

Figure 17: *Effect of surface tension on the shape of a liquid phase deposited onto a filament.* ***(a1)*** *Case of a liquid phase deposited as droplets: non-symmetrical shape;* ***(a2)*** *axisymmetrical shape; the liquid volume is the same but the fiber diameter is larger in (a1); from [*56Carroll1986*].* ***(b)*** *Case of a liquid phase deposited as a film: effect of the PRI, for the example of a liquid polystyrene film wetting a glass fiber (fiber radius ~10 µm); at t = 0, initial film thickness was ~13 µm, and at t = 30 min, equilibrium is reached after the film has broken into axisymmetrical droplets periodically spaced; from [*53Haefner2015*]. (c) Carbonized carbon morphologies periodically displayed along a CNT as obtained by Ting and Lan during their attempts to obtain carbon-cone-bearing morphologies [*41Ting2000*].*

When a liquid droplet deposits onto a filament (due to actual physical contact, or condensation effect), the surface tension drives the shape and configuration of the droplet which either adopts a non-symmetrical shape (**Fig.17a1**) or an axisymmetrical shape (**Fig.17a2**), depending on the droplet volume and the fiber radius [*56Carroll1986*]. This is the basis of the discrimination between the two cases of partial wetting mentioned by Dujardin [*37Dujardin1999*] and already illustrated in **Fig.10.**

On the other hand, when a continuous liquid film – instead of pre-formed droplets - is deposited onto a filament so that to cover the whole surface, the PRI enforces the film to break into axisymmetrical droplets (otherwise designated as "onduloidal" [*49deGennes2005*]) at a speed that depends on the liquid rheology and the fiber surface energetics (**Fig.17b**).

The key-parameters to considerer are the original thickness of the liquid film h, the wavelength λ of the onduloidal droplet display once the PRI effect has played, and the diameter $2r$ of the fiber. These parameters are related in equation (1) providing the film thickness is "moderate or thin" [*57Goren1964*]:

$$\lambda = 2\pi(r + h)\sqrt{2} \qquad (1)$$

Some wettability considerations can also intervene in order to define the configuration of the deposited film: for instance, the higher the surface energetics of the fiber, the more elongated the axisymmetric droplets [*58Chen2017*]. Also, changing the rheological properties of the liquid film such as the shear modulus can modify significantly the shape of the onduloidal droplets (**Fig.18**) [*50Mora2010*].

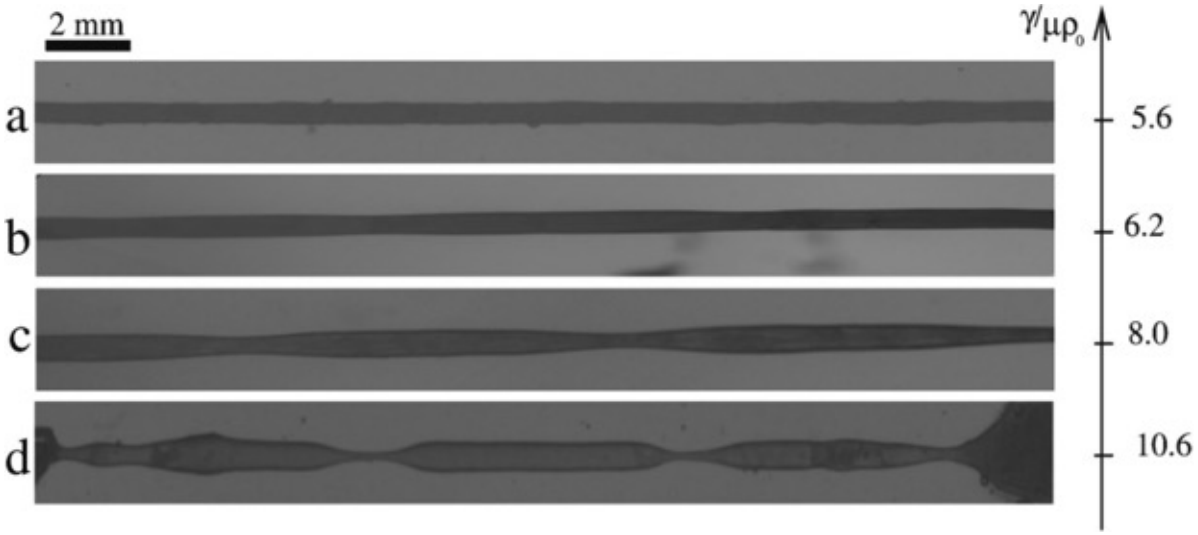

Figure 18: *Equilibrium shape of agar gel cylinders in toluene whose shear modulus was varied from 12 to 27 Pa from (a) to (d) by changing the proportion of water in the gel. Surface tension* γ *= 36.5 mN/m.* μ *= shear modulus.* ρ_0 *= initial cylinder radius. From [*50Mora2010*].*

A key question, in order for the PRI to occur in our system, is whether our PAH-rich liquid phase is able to wet the carbon nanotube surface. Dujardin *et al.* [*59Dujardin1994*] determined that a liquid may wet carbon nanotubes until a cut-off value of its surface tension in the 100-200 mN/m range is reached. A pitch-like nature of the droplets was hypothesized in Allouche's work. This is a reasonable assumption as the recombination reactions combined with secondary cracking in the gas phase certainly produce a variety of cyclic and non-cyclic hydrocarbons in their path to forming PAHs. Therefore, the droplets are a mixture of PAHs and lighter molecular weight hydrocarbons, as pitches are. Pitches, on the other hand, exhibit a large variety of chemical composition, as they are solid residues of coal tar or petroleum distillation, but with melting or softening temperatures in the ~40-300°C range [*60Wagner1988, 61Mochida2000*]. As a consequence, they also exhibit a large range of surface tension values at molten state, from 27 to 320 mN/m [*62Rocha2005, 63Shornikova2012*]. The lifetime of the species in the furnace is probably too short for allowing the formation of heavy molecular weight PAHs, hence the droplets formed should exhibit viscosity and surface tension values corresponding to that of light molecular weight pitches, i.e. in the range of below 1000 cp[11] and below 50 mN/m, respectively [*62Rocha2005*]. Those are values at the softening temperature, and might be lower in the local conditions, which are out of equilibrium as shown by the fact that liquid PAH-containing droplets exist at temperatures at which only a carbonized solid is supposed to be stable. Therefore, the PRI may apply to our droplet/CNT system, which is fully consistent with the axisymmetric shape of the primarily deposited double-cones as illustrated in **Fig.8a**. Several experimental evidences support this statement: in their attempts to reproduce the work carried-out at API, Ting and Lan [*41Ting2000*] have obtained an all-carbon morphology that definitely looks like a series of axisymmetrical droplets periodically dispatched along a string (**Fig.17c**) as predicted by the PRI effect. Moreover, smaller, subsidiary

[11] As more familiar examples, the viscosity of water is 1 cp at 20°C, that of fuels goes up to ~200 cp (at 15°C) [*64Atteia2011*].

"droplets" (actually carbon) are seen between the large ones, which is also typical of a PRI-driven behavior of a liquid covering a string. Indeed, the PRI breaks the primary, large liquid cylinder into onduloidal droplets linked to each other by a thinner cylinder segment of liquid. These thinner cylinder segments may also be subjected to the PRI effect, and generate new, smaller droplets [*57Goren1964*]. Also, it is striking how close the PNBF morphology (**Fig.2**) resembles the onduloidal broken film morphology illustrated in **Fig.17b-bottom**, and the LGCF morphology (**Figs.2 and 14**) resembles that illustrated in **Fig.18d**. As both correspond to different maturation conditions in the furnace, the rheology of the droplets formed could be different, hence generating either the LGCF or the PNBF morphology as a result from the PRI.

Finally, the liquid phase does not need to first deposit as a film onto the CNT to break and adopt one of the various onduloidal shapes illustrated in **Figs.17 and 18**. Preformed isolated droplets meeting the CNT would do the same (statistical effect) as previously hypothesized in Allouche's work. As the periodicity of the deposits can be explained by either the PRI effect or the mere statistical effect, the occurrence of such a periodicity is not enough for ascertaining which of both possibilities occurs, i.e. whether the PAH-rich liquid first deposits as a film or as droplets.

Thanks to equation (1), we may write:

$$h = [\lambda / (2.\pi.\sqrt{2})] - r \qquad (2)$$

Considering images such as **Fig.9b**, the periodicity observed between the cone-bearing morphologies along the CNT that supports them is about 5-6 µm, which can be taken equal to the onduloidal wavelength λ if we assume that the morphology display initially results from the PRI phenomenon. Considering a CNT radius r of ~5 nm, which is a maximum, equation (2) tells that the film thickness h of the PAH-rich liquid film which should have covered the CNT for being able to generate the periodicity seen in **Fig.9b** thanks to the PRI should have been about 560-670 nm. Although no theory is going against such a hypothesis, that the furnace conditions would allow the PAH-containing phase to deposit onto a CNT over such a large thickness as a liquid phase all at once before it carbonizes sounds unlikely. Moreover, the subsequent PRI-driven breaking of the liquid film would have induced micron size onduloidal droplets to form, which is out of range of the observations made in Allouche's work regarding the early steps of the deposition event (**Fig.8**), in particular with respect to the dimensions of the primary spindle-shape double-cones (**Fig.8a**).

Because of this statement, the control of the periodicity of the cone-bearing morphologies along the CNTs by the statistical distribution of preformed droplets in the gas phase seems to be likely, instead of the breaking of a thin liquid film, at least to account for observations such as in **Fig.9b**. However, it cannot be excluded that both possibilities occur, depending on the local conditions and temperature set-up, hence depending on whether PAHs have time to form droplets, and if they do, depending on their number and size. Considering the PRI as effective in certain deposition conditions is suggested by the similarity between **Fig.18d**, and images of the SSF morphologies such as given in **Figs.2** and **16**.

Finally, the above discussion can be summarized by the following sketch (**Fig.19**), as a tentative scenario to account for all the morphologies observed:

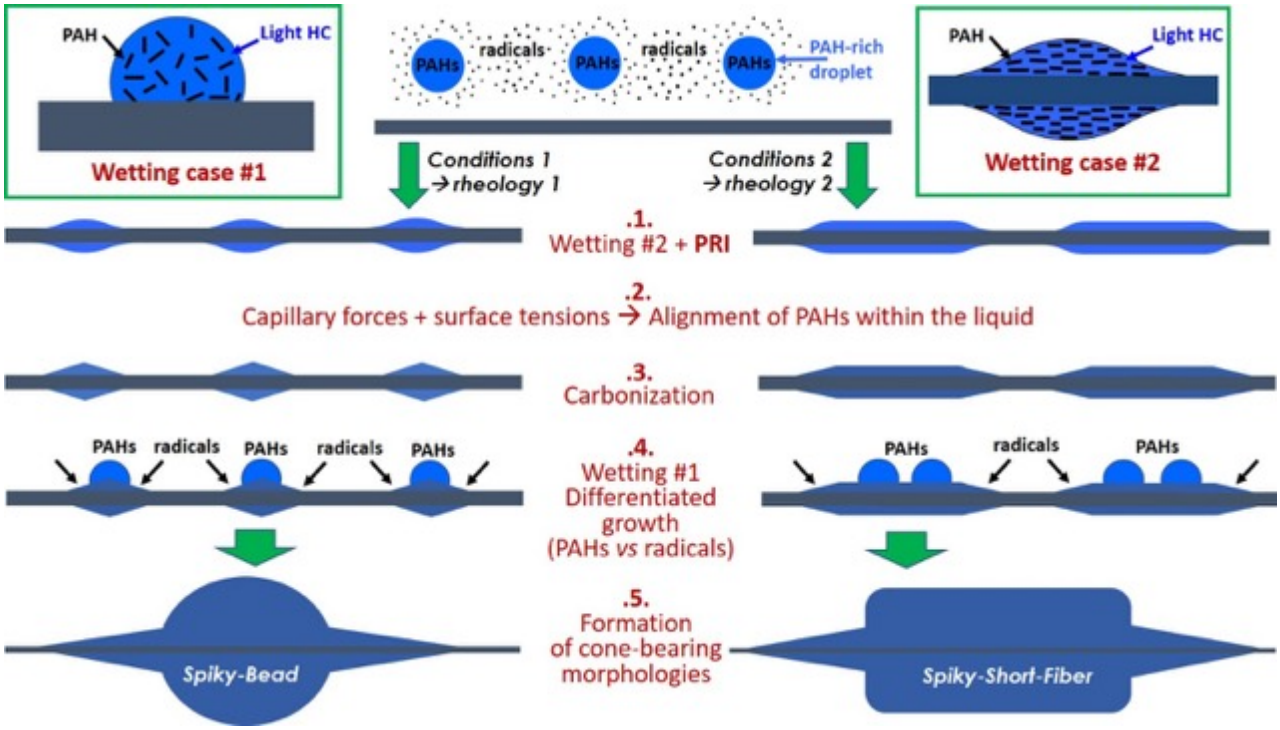

Figure 19: *Sketch of a possible scenario accounting for the various morphologies formed as illustrated in* ***Fig.2****. The two wetting cases refer to* ***Figs.10*** *and* ***17a****. The sketches focus on the formation of SB (left) and SSF (right) morphologies, but starting from closer "droplets" at step 1 would result in the PNBF (left), and LGCF (right) morphologies. Finally, starting from even closer droplets would results in the BF morphology.*

2.4 2. The cone description (SEM, TEM, Raman) and growth

The cone and the cone apex of the SSF morphologies (samples from previous Allouche's work) were studied by SEM, High Resolution Transmission Electron Microscopy (HRTEM)[12] and Raman spectroscopy.

Most of the SEM images of the carbon nanocones do not show any other specific features than the high aspect ratio and very smooth surface (e.g., **Figs.5a, 20c, 20d,** and others throughout the text). However, one was found to clearly exhibit the very same helicoidal feature already shown in **Ch1-Figs.13c** and **15e** as for other carbon cones from the literature. Although this was observed only once, it does not mean that the helicoidal feature should be rare as well. Other cones actually exhibit a surface topography where spiral-like features can be guessed, either suggested by periodically displayed bumps (**Figs.20a-b**), or by faint linear contrasts as arrowed in **Fig.20d1** or framed in **Figs.20c and 20d2**. Therefore, the helical wrapping of the graphenes making the cones could be a general reality, but the evidence of it by SEM usually cannot show-up in the SEM images because the steps are one-atom-high (see **Figs.22-23** to come), which is beyond the resolution power of the SEM. Therefore, to be seen in SEM images,

[12] All the HRTEM images shown here (but **Fig.24b)** are unpublished data and were obtained from Rongrong Wang (CEMES) who has studied the carbon cones for their emission properties [*65Wang2016*]. The TEM used was a Cs-corrected FEI TITAN, FEG source, operated at 80 kV, from the Instituto de Nanociencia de Aragon (Zaragoza, Spain) allowing atomic resolution.

steps should be higher and then made by larger number of graphenes (> 5, i.e. > 1.4 nm high), which may happen once in a while.

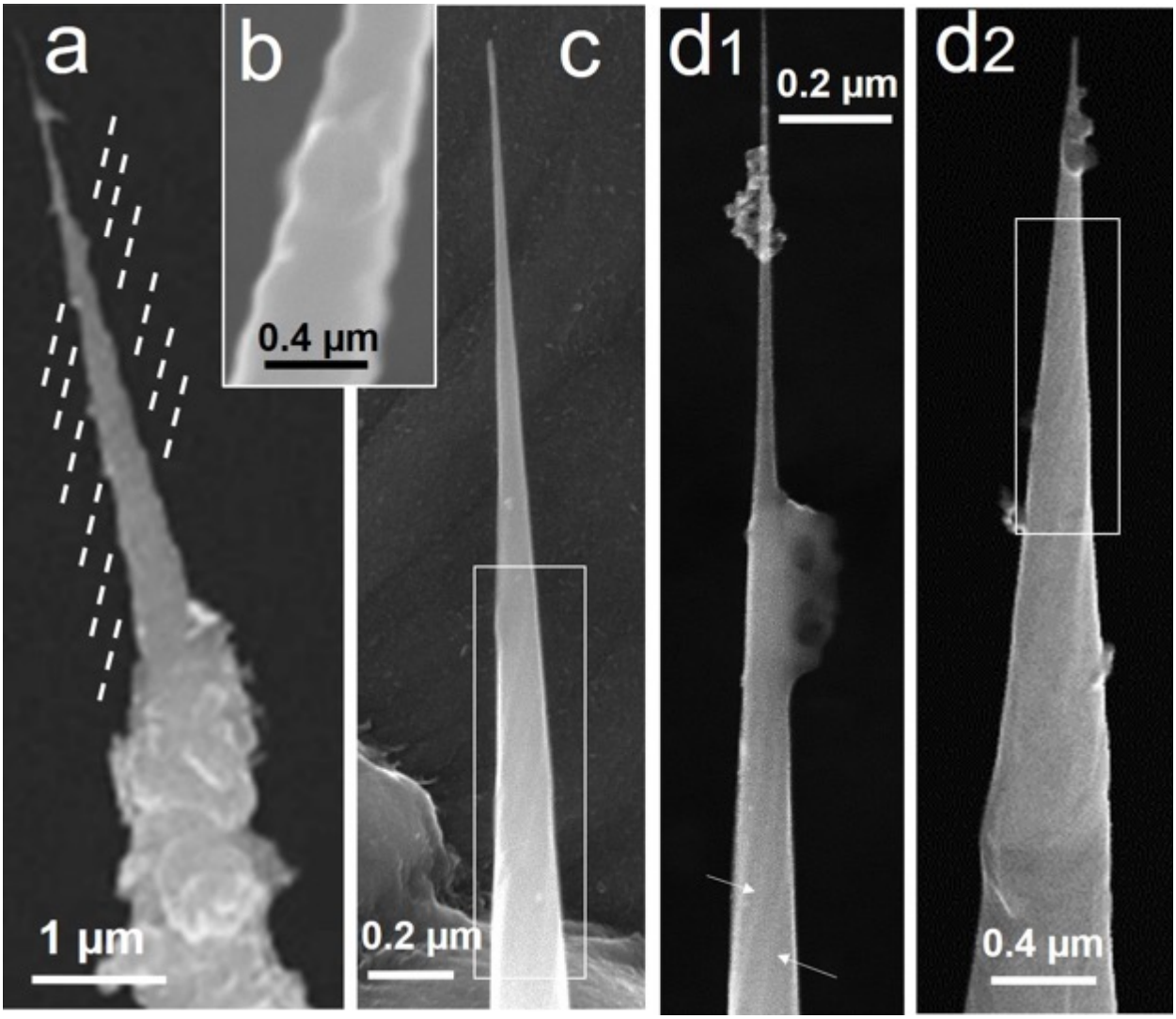

***Figure 20**. Nanocone morphologies with surface features suggesting a spiral wrapping of the graphene making the cones, as seen in other carbon cones from the literature such as those presented in **Ch1-Figs.13c** and **15e**. **(a)** shows a nanocone with a bumpy surface whose bump locations and directions suggest a helicoidal pattern. **(b)** another cone with a bumpy surface. **(c)** detail of the nanocone probe **HiR03-C20** surface; spiral-like feature can be guessed in the framed area. **(d1)** Details of the nanocone probe **HiR02-C22-4** surface; helical lines can be guessed (arrows). **(d2)** the same cone as in (d1), but after KFM testing; spiral-like feature can also be guessed in the framed area; the fact that the helical feature can be guessed in both images supports that it is a reality, not an image artifact. (Photo credits: (a) R. Wang, CEMES; (c), (d1) and (d2) R. Cours, CEMES).*

Several other hints are consistent with the actual helicoidal display of the graphene(s) making the cones. One is that, as stated in Allouche's work (See **Fig.7**) the concentric graphenes were found to exhibit the same helicity, which does make sense if they actually are a single graphene helically wrapped according to the model first proposed by Bacon [*66Bacon1960*] for carbon whiskers (**Ch1-Fig.11a**).

Another hint, very strong we believe, is brought by the behavior of the cones when subjected to a high current flow during various experiments. **Fig.21a** shows a carbon tip to be

used for testing it as STM probe. The cone surface in **Fig.21a** looks like quite smooth as usual, but interestingly it exhibits a step (arrowed) suggesting a helical wrapping. After having been subjected to two sets of *I*/*V* conditions successively (2 nA/1,1 V and 5 nA/0.25 V) during the STM testing, the topography of the cone was found to have become somehow exfoliated as shown in **Fig.21b**, looking like the graphenes have unwrapped. This is exactly how Bacon [*66Bacon1960*] actually demonstrated that the carbon whiskers he had discovered were actually built up from a limited numbers of helicoidally wrapped graphene layers, as illustrated in **Ch1-Fig.11b**. Such a behavior is supported by calculations which demonstrated the spontaneous unwinding of spiral wrapped graphene upon charge injection [*67Braga2004*].

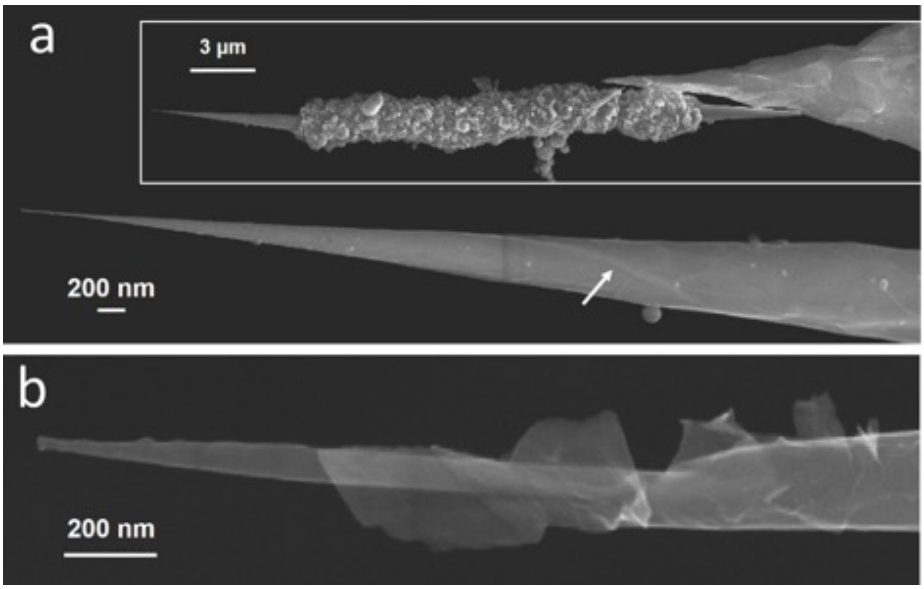

Figure 21*: SEM images showing some degree of graphene exfoliation of the nanocone after having been subjected to two sets of I/V conditions (2 nA/1,1 V and 5 nA/0.25 V) when tested as a STM probe (**Probe #Au-e-002**). **(a)** Enlarged view of the cone tip before testing, showing a step (arrowed) suggesting a helical wrapping of graphene; in inset, a low magnification view of the whole SSF morphology welded onto an electrochemically tapered Au wire (more details in Section3.2.3. in Chapter 3); **(b)** After testing, the cone tip exhibits unwrapped graphenes, consistently with a former helicoidal arrangement of the graphenes making the cones (see text).*

It may be wondered, then, why the unwrapping phenomenon induced at the cone apex by subjecting the cone to some current or voltage has not prevented the carbon cones to make excellent electron emitters with high beam coherence [*68Houdellier2012*] as reported in *Chapter 1* (*Section 3.2.1*). Indeed, cones were shown to be able to withstand emission currents as high as 30 µA and extraction voltage as high as ~1.3 kV [*68Houdellier2012, 69Houdellier2015, 70Mamishin2017]* which is far beyond the range used during the STM testing. The reason might be that all the cones mounted as electron emitters were welded by Focused Ion Beam induced Deposition (FIBID) which will be shown in *Chapter 3* to be responsible for an extensive amorphization of the cone surface over an unknown thickness, and of the cone apex. Because of the amorphization, the graphene free edges at the cone surface no longer exist and the related carbon atoms are welded to the bulk, hence hindering any unwrapping of the graphenes.

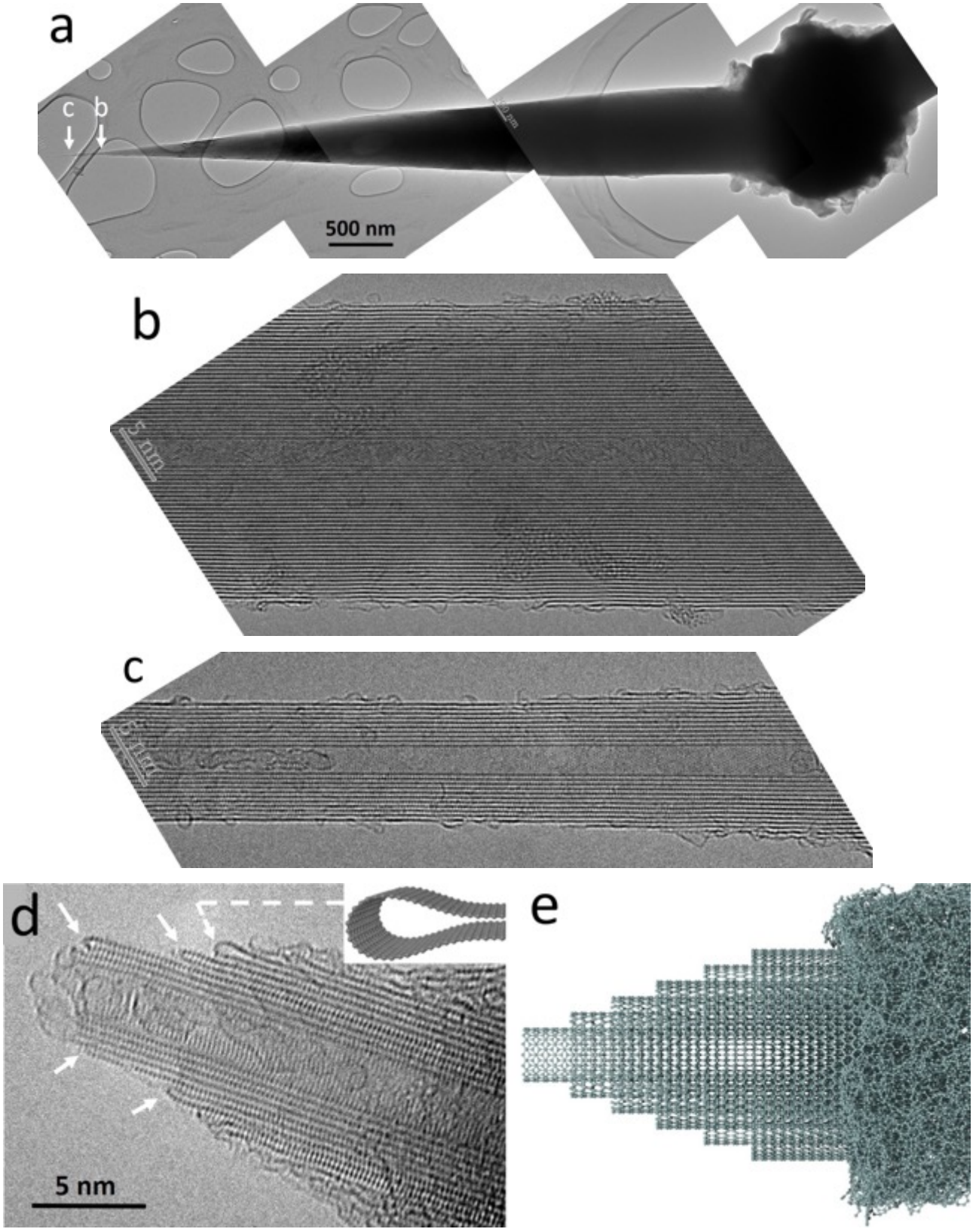

***Figure 22**: **(a)** Photo-montage of low-magnification TEM images showing a whole cone. **(b)** and **(c)** Atomic resolution HRTEM images of segments of the cone, as designated in (a), showing how the graphenes are perfect. **(d)** Atomic resolution HRTEM image of the nano-sized cone apex. Dots are carbon atoms. Several examples of graphenes edges zipped together are arrowed (solid arrows); the dashed arrow designates a different, loop-like, termination. (image credit for (a) to (d): R. Wang, CEMES). **(e)** Atomistic model of the cone texture for the concentric graphene cylinder hypothesis (kindly obtained from I. Suarez-Martinez, Curtin University, Australia).*

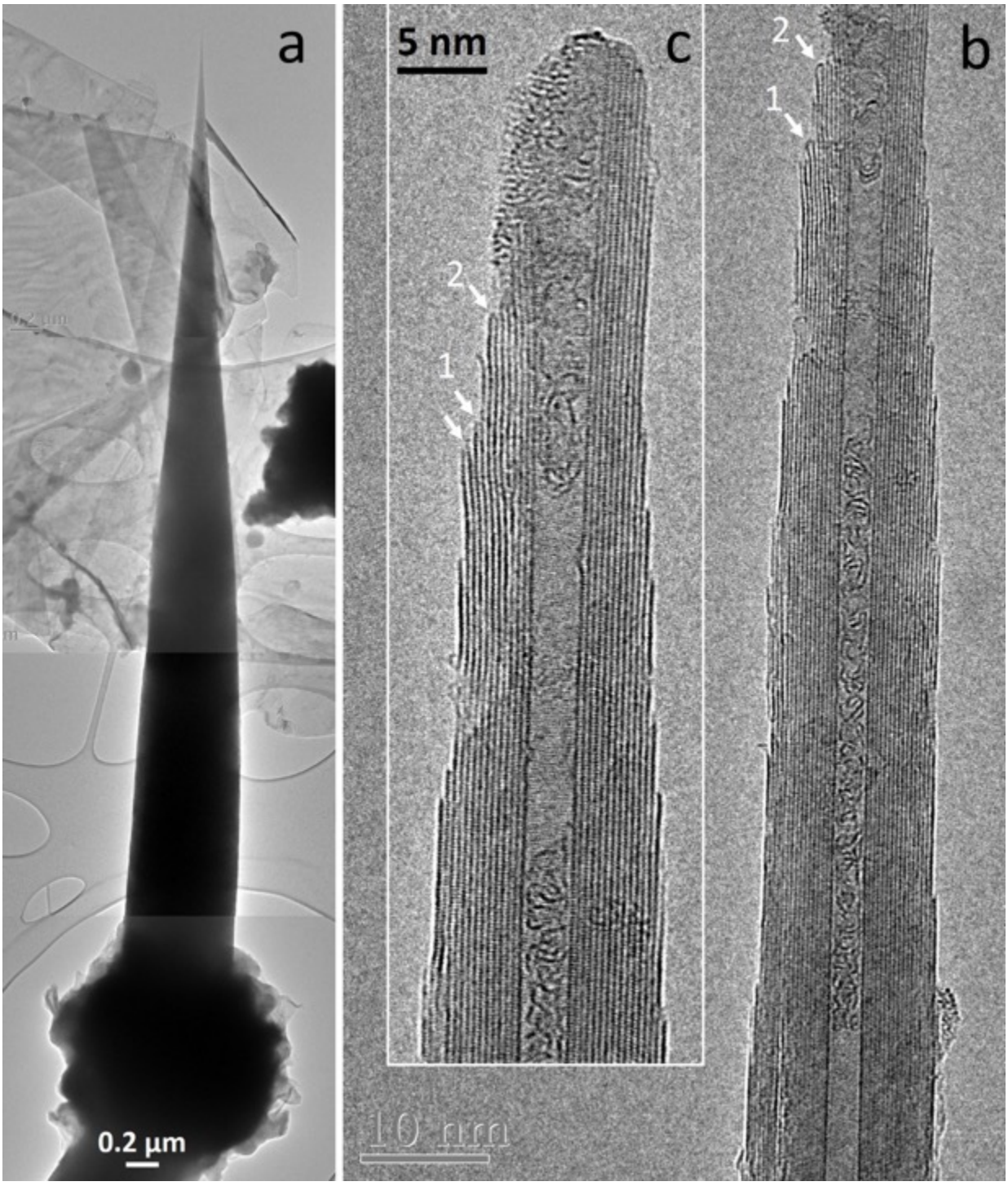

***Figure 23**: **(a)** photo-montage of low-magnification TEM images showing a whole cone, actually the other cone from the same bead as shown in **Fig.22a**. **(b)** and **(c)** Atomic resolution HRTEM images of the end part of the cone. Both images overlap: zipped terminations numbered 1 and 2 are the same in both images. It may be seen that the aspect of the graphene terminations arrowed is slightly different between (b) and (c), indicating that they evolve under the electron beam. The image chronology is not known. (Image credit: R. Wang, CEMES).*

Finally, another hint is that, in the projected HRTEM images of carbon cones (**Figs.22 and 23**), a graphene edge on one side barely corresponds to a graphene edge on the other side at the

same height along the cone, as it should happen if the concentric graphenes were genuine cylinders (refer to the model in **Fig.22e** for example).

Therefore, as opposed to what was described in Allouche's work (see *Section 1.4*), the conical shape is likely to be constituted by a graphene (possibly multilayers) or a limited number of graphenes helicoidally wrapped, instead of concentric graphene cylinders with heights as shorter as their diameter increases, as modeled in **Fig.22e**. Both hypotheses could not be discriminated by HRTEM, as images are projected from the volume.

On the other hand, HRTEM reveals that the nanotexture is very high (perfect graphenes), which is important because fairly high mechanical and conductivity properties can then be expected. However, The surface of the main cone body is made of steps, each step corresponding to a free graphene edge, hence with the height of a single graphene, ~0.34 nm (**Figs.22b,c** and **Figs.23b,c**). The reactivity of graphene edges with respect to graphene faces is well-known, allowing to predict that each graphene step at the cone surface will be the preferred location for reaction, or adsorption. This is confirmed by images such as in **Fig.24a**.

It must be noted that the nanotexture shown in **Figs.22-23** is much higher than the one shown in **Fig.5c**. This is because the image in **Fig.5c** was taken with a TEM (Philips CM30) operated at 300 kV, inducing rapid damaging to the nanotexture, as opposed to 80 kV For **Figs.22-23**. However, a prolonged exposure to the 80 keV electron beam can also induce severe damaging (**Fig.24b**) despite this value is supposed to be below the theoretical energy threshold for the knock-on of carbon atoms from the graphene lattice. This will be further discussed in *Chapter 3*.

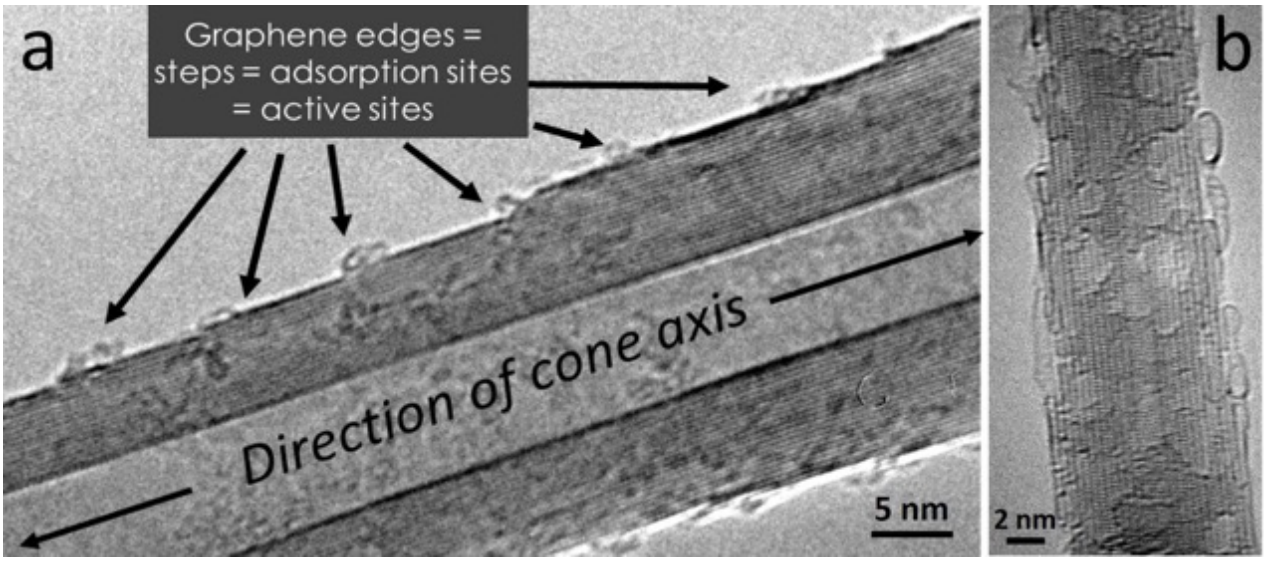

Figure 24: (a) *HRTEM image (lattice fringe mode) of a cone surface showing that each free graphene edge acts as an adsorption site whereas graphene faces do not (Philips CM30 TEM, LaB_6 source, operated at 150 kV. Photo credit: M. Delmas, CEMES).* ***(b)*** *Ongoing damages brought to a cone, close to the apex, due to a prolonged exposure to the 80 keV electron beam (photo credit: R. Wang, CEMES).*

Two apices are shown, in **Fig.22d** and **Fig.23c**, respectively. Their diameter is between 5 to 10 nm. They are quite different from each other, with the one in **Fig.23c** showing partial amorphization. It can be due to either the way the CNT supporting the morphology breaks, or

in-TEM electron irradiation effects, or a combination of both. Indeed, as shown in **Fig.24b**, even a 80 keV electron beam can significantly damage the graphenes if care is not taken of not avoiding long exposure, specifically close to the apex. This sensitivity to electron irradiation may be due to the fact that all the graphenes close to the apex exhibit a defective termination, either as a free edge, or as a zip (see below) joining two adjacent graphenes. Similarly, enhanced irradiation sensitivity was shown for defective CNTs with respect to pristine ones [*71Monthioux2001*].

A closer look at the cone apices shows that graphene terminations are not as simple as at the surface of the main cone body (**Figs.22d** and **Figs.23b-c**). The closer the graphenes to the apex, the higher the chance for having neighboring, superimposed graphene edges. Such a configuration promotes the closure of the graphene pairs with each other without inducing any curvature to the graphenes involved, as they look like they are merely zipped together (solid arrows in **Fig.22d, Figs.23b-c**). This graphene termination is different from the more common loop-like termination which is modelled in inset of **Fig.22d**, and for which an example is also arrowed (dashed arrow in **Fig.22d**). Both closure configurations can be explained by the high stress generated at such a nanosized dimension (as in small-diameter nanotubes). When superimposed graphenes have their edges close to each other, the carbon atoms from both graphenes bond to each other in order to lower the system energy by eliminating the dangling bonds. The event is probably helped by the fact that the graphene layers exhibit the same helicity, as previously demonstrated (**Fig.7**).

It is worth noting that lip-lip interaction between superimposed graphenes that close on each other is a common observation for graphene-based objects grown or annealed at high temperatures, such as polyhedral crystals [*72Gogotsi2000, 73Okuno2005*], platelet nanofibers [*74Yoon2005*], whiskers [*75Saito2007*], graphene nanoribbons [*76CamposDelgado2009*], pyramidal hillocks [*77Glad2014*], among others. But the resulting graphene termination usually adopts the loop-like profile modelled in **Fig.22d-inset** so that to allow the graphene to curve while minimizing the strain on bond angles. But such a configuration is not the preferred one here, and most of the graphenes close without being deformed, or at minima (solid arrows in **Fig.22d** and **Figs.23b-c**). This suggests that the atomic structure of the termination is different from that of a loop, and instead of being a bent graphene involving sp^2-C atoms only, it might be a line of sp^2-C atoms, with a partial sp^3 character because of the strain induced to the non-planar bond angles, joining the incomplete hexagons from both graphene ends. Such a configuration is rarer than the loop one, but is not unique either, see for instance [*74Yoon2005*], and also **Ch1-Fig.9e** [*78Gogotsi2002*] (although the image is less clear that with the cone apex).

The defective termination of the cone apices was also confirmed by Raman Spectroscopy. Indeed, Raman spectra are composed of different Raman emission bands (*G, D*, *D'* and *2D* bands, characterized by their intensity, width, and wavenumber [*79Ferrari2013*]) which provide an accurate characterization of the graphenic carbon structure. Those bands are common features for graphenic materials. For instance, the *D* band (around 1330 cm^{-1}) results from a double resonance process and originates from the inelastic scattering of an electron by a defect (e.g., graphene edge, vacancy) or more generally by a modification of the periodicity; the *G* band (around 1580 cm^{-1}) represents the collective vibration of in-plane C-C bonds in graphene; the

D' band (~1620 cm^{-1}) is not much studied, similar to the D, but using D and D', it is possible to discriminate the type of defects [*80Eckmann2012*]; the *2D* band (~2700 cm^{-1}) is both related to the number of graphenes and stacking type.

Probing the cone apices was made possible by using the accurate piezo-driven displacement of the probe stage of a tip-enhanced Raman spectrometer equipment TERS, which usually allows an accurate positioning of the plasmonic tip with respect to the laser beam. This way, it was expected to make sure to probe the whole cone down to its apex. A SSF morphology was then mounted as a SPM probe following the gluing methodology (See *Chapter 3*) and then was placed instead of a standard Ag tip currently used for TERS. Therefore, the Raman signal obtained was not an enhanced one using the TERS principle, but it was a regular one. In such a configuration, a laser wavelength of 632.8 nm (red) with a power of 0.7mW and a spot size of ~0.5 µm were used to move accurately down along the carbon nanocone from the microfiber segment (A), then to the cone base part (B), then close to the cone apex (C) (**Fig.25**). Very useful information, partly unexpected, about the structural organization and defect types present at different parts of the conical morphology were obtained by analyzing the I_D/I_G and the $I_D/I_{D'}$ ratio from the Raman spectra (**Fig.25**).

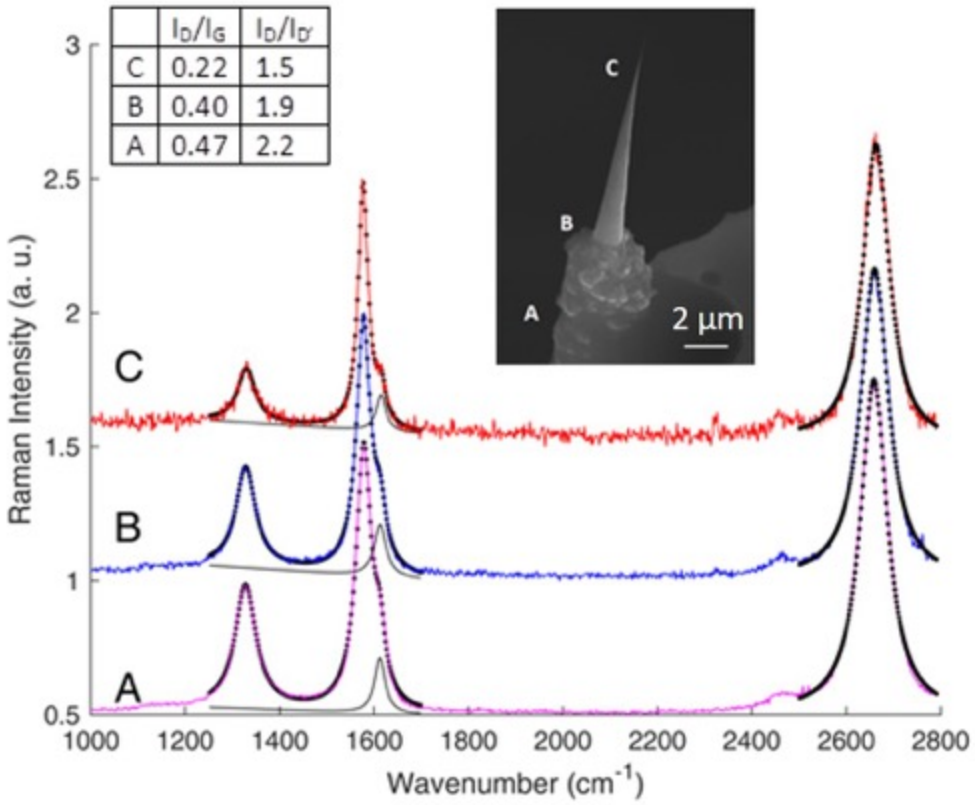

Figure 25. *Raman spectra (recording time: 200 s) on a carbon cone at the various positions indicated on the image in inset. Colored lines are the experimental spectra; heavy lines are the fits; the D' contribution to the fit is also plotted as the thin, solid black line. Top left table: band intensity ratios for each spectrum.*

The highest I_D/I_G ratio (0.47) obtained at location *A* confirms the relatively low structural organization of the microfiber part as previously reported in *Section 1.4*, whereas the lowest I_D/I_G ratio (0.22) at the cone apex (*C*) also confirms the quality and integrity of the graphenes

at the cone apex as previously shown by TEM images. On the other hand, the $I_D/I_{D'}$ ratio showed a continuous decrease from the microfiber part to the cone tip indicating a variation of the defect type present along the morphology (insets in **Fig.25**): for the microfiber part (*A*) and the cone base part (*B*), the $I_D/I_{D'}$ ratios were 2.2 and 1.9 respectively, whereas the cone apex showed a very low value of 1.5. In the case of the microfiber part (*A*), the value 2.2 can be in part associated with graphene stacks with small L_a. On the other hand, the lowest $I_D/I_{D'}$ ratio of 1.5 at the cone apex is unprecedented, hence does not correspond to any predicted defect type (vacancy, boundary, or sp^3 defects) reported in the literature (**Table 5**).

Type of defects	$I_D/I_{D'}$
sp^3	13*
Vacancy	7*
Boundary	3.5*
Zip	1.5 (our result)

Table 5: *$I_D/I_{D'}$ ratio value as a function of the type of defects. Values marked with* correspond to the work by Eckmann et al. [*80Eckmann2012*].*

As a very small volume of matter is analyzed by the laser probe, the contribution of graphene surface and termination defects are enhanced in the Raman signal. We know from the HRTEM images that a quite specific defect at the cone apex is the zipped graphene termination of graphene pair edges (solid arrows in **Figs.22d** and **23c**). Consequently, we associate the quite low value (1.5) of the $I_D/I_{D'}$ ratio - actually the lowest ever reported (to our knowledge) - to this type of zip-like defect. Indeed, it was checked recently that the loop-like defect, in which the graphenes involved are curved (see the model in **Fig.22d**) generates a $I_D/I_{D'}$ ratio value in the range of 10 [*81Picheau2021*].

The reason why $I_D/I_{D'}$ ratio reaches such a low value because of the specific zip-like defect may relate to charge effects. Calculations showed that even moderate buckling of a graphenic structure may induce a flexoelectric behavior able to generate dipole-dipole interactions at the nanoscale [*82Kothari2018*]. From the point of view of Raman emission, it was calculated that polarizing a graphene structure may lower significantly the D band intensity, without affecting the D' band [*83Venezuela2011*]. Therefore, the extreme deformation enforced to the bond angles of the carbon atoms joining the two graphene edges could result in such a strong polarization by concentrating charges at the zip-like termination, hence the unprecedentedly low $I_D/I_{D'}$ ratio value.

3. Conclusions

Synthesis of cone-bearing morphologies: well-developed, micron-size, all-graphenic cones with a very high nanotexture degree are now able to be prepared at CEMES on a routine basis. However, we were able to synthesize the so-called spiky-bead (SB) morphology, i.e., exhibiting the highest *F factor*, but we have not been able to prepare the so-called spiky-short-fiber (SSF)

morphology. Nevertheless, based upon the statement that forming SSF requires the gas phase to reach a higher maturation degree than for forming the SB morphology, several ways to do so were identified, as a roadmap for a forthcoming work.

Deposition mechanisms: Our observations confirm and strengthen the previous statement made by Allouche's work regarding the need for the gas phase to contain two types of species contributing differently to the growth of the carbon solid, namely polyaromatic hydrocarbons (PAHs) and small carbon or hydrocarbon radicals. They also strengthen the hypothesis made in Allouche's work of the gathering of the PAHs into a liquid phase that forms before depositing onto the primary carbon nanotubes (CNTs), which play the role of deposition substrate. We have considered Allouche's hypothesis about the existence of the liquid phase as preformed droplets within the frame of the overall understanding of wetting phenomena, specifically regarding the wetting of strings by liquids, which involves the so-called Plateau-Rayleigh instability (PRI) as a driving phenomenon. This has generated two important conclusions: (i) there are strong evidences for the liquid phase to deposit as a cylindrical film around the primary CNTs, which subsequently breaks into periodically displayed droplets due to the effect of the PRI. This might be the discrimination mechanism between the SB and SSF morphologies in relation with the deposition of liquid phases with different rheological characteristics, the latter being governed by the synthesis conditions; (ii) however, in some conditions, because of the incompatibility between the theoretical onduloidal wavelength value deduced from the equations related to the PRI and the actual periodicity observed between the final morphologies, the direct deposition of preformed droplets onto the primary CNTs should be considered as well.

A valuable side-benefit is the enhanced understanding of the overall deposition mechanisms of pyrolytic carbon. Indeed, the composition of the gas phase in a CVD reactor as ours is independent of the substrate type. In that sense, using carbon nanotubes as deposition substrate has revealed the coexistence of both liquid droplets and radicals in the gas phase, which the deposition of pyrolytic carbon onto "regular" (planar, or fibrous with micron-sized curvature radii) substrates has not been able to reveal with so much evidence.

Growth mechanism of the cone: It was confirmed – but it was expected so - that the cones are built up from concentrically displayed graphenes. However, several observations have converged to oppose the former hypothesis of a cone texture based on concentrically displayed graphene cylinders, and instead strongly suggest a helicoidal display of a limited number of graphenes (possibly multilayered) making the cones to adopt the same texture as the known-for-long Bacon whiskers. At the cone apex, which is the most important part regarding the possible use of carbon cones as SPM probes that will be investigated in *Chapter 4*, the way cones grow leave free graphene edges that tend to close onto each other by pairs as a probable behavior to minimize the free energy, specifically for graphenes with short radii of curvature. It was found that such zip-like graphene terminations are associated with the lowest (1.5) Raman $I_D/I_{D'}$ ratio ever reported in the literature, that we proposed to be the specific signature of this type of graphene termination, which is seen as a defect by Raman spectroscopy.

Results from this *Chapter* were partially published as [*84Puech2019, 85Paredes2020*].

References

1. Carlsson J.-O., Martin P. M. *Chemical Vapor Deposition*. In: **Handbook of Deposition Technologies for Films and Coatings***, 3rd edition* (ed. Martin P. M.), Elsevier (2010) pp.314-363.
2. Tibbetts G. G. *Vapor grown carbon fibers: status and prospects*. **Carbon** 27 (1989) 745-747.
3. Delhaès P. *Chemical vapor deposition and infiltration processes of carbon materials.* **Carbon** 40 (2002) 641–657.
4. Hüttinger K. J. *CVD in hot wall reactors - The interaction between homogeneous gas-phase and heterogeneous surface reactions*. **Chem. Vap. Dep.** 4 (1998) 151-158.
5. Oberlin A. *Pyrocarbons*. **Carbon** (2002) 7-24.
6. Grisdale R. O. *The formation of black carbon*. **J. Appl. Phys.** 24 (1953)1082-1091.
7. Tesner P.A. *Kinetics of pyrolytic carbon formation*. In: **Chemistry and Physics of Carbon** vol. 19 (ed. Thrower P.A.), Marcel Dekker (1984) pp.65-161
8. Bokros J. C. *Deposition, structure and properties of pyrolytic carbon*. In: **Chemistry and Physics of Carbon** vol. 5 (eds. Walker J. M., Thrower P. A.), Marcel Dekker (1969) pp.1-118.
9. Shi R., Li H. J., Yang Z., Kang M. K. *Deposition mechanism of pyrolytic carbons at temperature between 800-1200°C.* **Carbon** 35 (1997)1789-1792.
10. Hu Z. T., Huttinger K. J. *Mechanism of carbon deposition – a kinetic approach*. **Carbon** 40 (2002) 624-628.
11. Diefendorf R. *The deposition of pyrolytic graphite.* **J. Chim. Phys.** 57 (1960) 815–821.
12. Monthioux M., Allouche H., Jacobsen R. L. *Chemical vapour deposition of pyrolytic carbon on carbon nanotubes. Part 3: Growth mechanism*. **Carbon** 44 (2006) 3183-3194.
13. Allouche H., Monthioux M., Jacobsen R. L. *Chemical vapour deposition of pyrolytic carbon on carbon nanotubes. Part 1: Synthesis and morphology.* **Carbon** 41 (2003) 2897-2912.
14. LaNasa P. J., Loy Upp E. *Basic flow measurement laws.* In: **Fluid Flow Measurement** (Third Edition), Elsevier (2014) pp.19-29.
15. Tibbetts G. G., Gorkiewicz D. W., Ali R. L. *A new reactor for growing carbon fibers from liquid- and vapor-phase hydrocarbons*. **Carbon** 31 (1993) 809-814.
16. Lake M., Jacobsen R., Monthioux M. **Private communication**.
17. Dresselhaus M. S., Dresselhaus G., Sugihara K., Spain I. L., Goldberg H. A. *Graphite fibers and filaments.* In: **Springer series in materials sciences**, vol. 5, Springer-Verlag, New York (1988).
18. Billaud F., Baronnet F., Freund E., Busson C., Weill J. *Thermal decomposition of methane.* **Rev. Inst. Franc. Pétr.** 44 (1989) 813-823.
19. Baker R. T. K., Harris P. S., Thomas R. B.; Waite R. J. *Formation of filamentous carbon from iron, cobalt and chromium catalyzed decomposition.* **J. Catal.** 30 (1973) 86-95.
20. Endo M., Takeuchi K., Kobori K., Takahashi K. Kroto H. W., Sarkar A. *Pyrolytic carbon nanotubes from vapor-grown carbon fibers*. **Carbon** 33 (1995) 873-881.
21. Allouche H., Monthioux M. *Chemical vapour deposition of pyrolytic carbon on carbon nanotubes*. *Part 2: Texture and Structure*. **Carbon** 43 (2005) 1265-1278.
22. Monthioux M. *Structures, textures, and thermal behaviour of polyaromatic solids*. In **Carbon Molecules and Materials** (editors: R. Setton, P. Bernier, S. Lefrant), Taylor & Francis, London (2002) pp. 127-177.
23. Ouzilleau P., Gheribi A. E., Chartrand P., Soucy G., Monthioux M. *Why some carbons may or may not graphitize? The point of view of thermodynamics*. **Carbon** 149 (2019) 419-435.
24. Rouzaud J.-N., Oberlin A., Bény-Bassez C. *Carbon films: Structure and microtexture (optical and electron microscopy, Raman spectroscopy).* **Thin Sol. Films** 105 (1983) 75-96.
25. Rouzaud J.-N., Oberlin A. *Structure, microtexture, and optical properties of anthracene and saccharose-based carbons*. **Carbon** 27 (1989) 517-529.
26. Monthioux M., Serp P., Caussat B., Flahaut E., Razafinimanana M., Valensi F., Laurent C., Peigney A., Mesguich D., Weibel A., Bacsa W., Broto J.-M. *Carbon nanotubes*. In: **Nanotechnology Handbook** (editor: B. Bhushan), 4th Edition, revised. Springer-Verlag, Heidelberg, Germany (2017) pp. 193-247.
27. Biscoe J., Warren B. E. *An X-ray study of carbon black*. **J. Appl. Phys.** 13 (1942) 364-371.
28. Bernal J. D. *The structure of graphite*. **Proc. R. Soc. Lond. A** 106 (1924) 749-773.

29. Monthioux M. *Nanotubes et nanofilaments de carbone*. **L'Actual. Chim.** 295-296 (2006) 109-114.
30. Oberlin A. *High-resolution TEM studies of carbonization and graphitization*. In: **Chemistry and Physics of Carbon** vol. 22 (ed. Thrower P. A.). Marcel Dekker, New York (1989) pp. 1-143.
31. Koizlik K., Linke J., Luhleich H., Nickel H., Pflaum P. *Contribution to the pyroaggregate hypothesis and the droplet model of pyrocarbon deposition*. In: **Contribution to the development of reactor graphites and pyrocarbons irradiation behavior, model conceptions and characterization** (editor: Koizlik K.). Proc. 4th London Intern. Carbon and Graphite Conf., Sept. 23-27, 1974, Kernforschungsanlage, Jülich (1974), pp.34-46.
32. Ford L. H., Bilsby C. F. *Porosity related to structure for low temperature propylene pyrocarbons*. **J. Nucl. Mater.** 60 (1976) 79-88.
33. Je J. H., Lee J. Y. *A study of the deposition of pyrolytic carbons from hydrocarbons*. **Carbon** 22 (1984) 563-570.
34. Bouchard E., Lavenac, J. Roux J.-C., Langlais F., Delhaès P. *Pyrocarbon deposits on a graphite surface observed by STM*. **Chem. Vap. Depos.** 7 (2001) 125-130.
35. Dong G. L., Hüttinger K. J. *Consideration of reaction mechanisms leading to pyrolytic carbon of different textures*. **Carbon** 40 (2002) 2515-2528.
36. Hu Z. J., Reznik B., Zhang W. G., Gerthsen D., Huttinger K. J. *Influence of pressure, temperature and surface area/volume ratio on the texture of pyrolytic carbon deposited from methane.* **Carbon** 41 (2003) 749-758.
37. Dujardin E. *Disques, cônes et nanotubes graphitiques : synthèse, propriétés et système mésoscopique*. **PhD Dissertation**, University of Paris-VI, France (1999).
38. Zheng G.-B., Sano H., Uchiyama Y. *A layer-by-layer deposition mechanism for producing a pyrolytic carbon coating on carbon nanotubes*. **Carbon** 57 (2013) 267-273.
39. Li K., Eres G., Howe J., Chuang Y.-J., Li X., Gu Z., Zhang L., Xie S., Pan Z. *Self-assembly of graphene on carbon nanotube surfaces.* **Scient. Rep.** 3 (2013) 2353.
40. Ting J.-M., Lan J. B. C. *Beaded carbon tubes*. **Appl. Phys. Lett.** 75 (1999) 3309-3311.
41. Ting J.-M., Lan B. C. *Formation of nodulated vapor grown carbon fiber.* **Carbon** 38 (2000) 1917-1923.
42. Ting J.-M., Chen Y. M. *Growth of tubular carbon from vapor phase*. **Mater. Chem. Phys.** 72 (2001) 228-231.
43. Komiyama M. *Design and Preparation of Impregnated Catalysts,* **Catalysis Review** 27 (1985) 341-372.
44. Reichelt K. *Nucleation and growth of thin films*. **Vacuum** 38 (1988) 1083-1099.
45. Ratsch C., Venables J. A. *Nucleation theory and the early stages of thin film growth*. **J. Vac. Sci. Technol. A** 21 (2003) S96-S109.
46. Venables J. A., Spiller G. D. T. *Nucleation and growth of thin films*. In "**Surface Mobilities on Solid Materials: Fundamental Concepts and Applications**", Vu Thien Binh ed., Springer-Verlag (1983) pp.341-403.
47. Soutric F., Monthioux M., Musset E., Després J.-F. *Low temperature pyrolytic carbon films: preparation and TEM investigations*. **Proc. Eurocarbon Conf.** (Strasbourg, France) Extend. abstr. 2 (1998) 653-654.
48. Lee W. J., Li C., Gunning J., Burke N., Patel J. *Is the structure of anisotropic pyrolytic carbon a consequence of growth by the Volmer-Weber island growth mechanism?* **Carbon** 50 (2012) 4773-4780.
49. de Gennes P.-G., Brochart-Wyart F., Quéré D. ***Gouttes, Bulles, Perles, et Ondes***. Belin (Paris, France), Collection Echelles (2005).
50. Mora S., Phou T., Fromental J.-M., Pismen L. M., Pomeau Y. *Capillarity driven instability of a soft solid*. **Phys. Rev. Lett.** 105 (2010) 21401.
51. Carroll B. J. *The accurate measurement of contact angle, phase contact areas, drop volume, and Laplace excess pressure in drop-on-fiber systems.* **J. Colloid. Interf. Sci.** 57 (1976) 488-495.
52. Quéré D. *Fluid coating on a fiber*. **Ann. Rev. Fluid Mech.** 31 (1999) 247-384.
53. Haefner S., Benzaquen M., Bäumchen O., SalezT., Peters R., McGraw J. D., Jacobs K., Raphaël E., Veress K. D. *Influence of slip on the Plateau–Rayleigh instability on a fibre*. **Nature Comm.** 6 (2015) 7409.
54. Dolado J., Renforth K. L., Nunn J. E., Hindsmarsh S. A., Hidalgo P., Sanchez A. M., Méndez B. *Zn_2GeO_4/SnO_2 nanowire heterostructures driven by Plateau-Rayleigh instability*. **Cryst. Growth Des.** 20 (2020) 506-513.
55. Kolb F. M., Hofmeister H., Zacharias M., Gösele U. *On the morphological instability of silicon/silicon dioxide nanowires*. **Appl. Phys. A** 80 (2005) 1405-1408.
56. Carroll B. J. *Equilibrium conformations of liquid drops on thin cylinders under forces of capillarity*. A theory for the roll-up process. **Langmuir** 2 (1986) 248-250.
57. Goren S. L. *The shape of a thread of liquid undergoing break-up*. **J. Colloid. Sci.** 19 (1964) 81-86.

58. Chen S., Feng Y., Qin M., Ji T., Feng W. *Improving thermal conductivity in the through-thickness direction of carbon fibre/SiC composites by growing vertically aligned carbon nanotubes*. **Carbon** 116 (2017) 84-93.
59. Dujardin E., Ebbessen T. W., Hiura H., Tanigaki K. *Capillarity and wetting of carbon nanotubes*. **Science** 265 (1994) 1850-1852.
60. Wagner M. H., Jäger H., Letizia I., Wilhelmi G. *Quality assessment of binder pitches for carbon and graphite electrodes*. **Fuel** 67 (1988) 792-797.
61. Mochida I., Korai Y., Ku C.-H., Watanabe W., Sakai Y. *Chemistry of synthesis, structure, preparation and application of aromatic-derived mesophase pitch*. **Carbon** 38 (2000) 305–328.
62. Rocha V. G., Blanco C., Santamaria R., Diestre E. I., Menendez R., Granda M. *Pitch/coke wetting behaviour*. **Fuel** 84 (2005) 1550-1556.
63. Shornikova O. N., Malakho A. P., Kenigfest A. M., Kulakov V. V., Seleznev A. N., Avdeev V. V. *Wetting of carbon fibers by coal-tar pitch melts*. **Fibre Chem.** 44 (2012) 259-264.
64. Atteia O. *Modélisation du devenir des composés organiques dans les aquifères*. Lavoisier, Paris, France (2011).
65. Wang R. *Dopage de nanostructures de carbone pour l'émission de champ*. **PhD Dissertation**, University of Toulouse (France), December 20 (2016).
66. Bacon R. *Growth, structure, and properties of graphite whiskers*. **J. Appl. Phys.** 31 (1960) 283-290.
67. Braga S. F., Coluci V. R., Legoas S. B., Giro R., Galvão D. S., Baughman R. H. *Structure and dynamics of carbon nanoscrolls*. **Nanolett**. 4 (2004) 881-884.
68. Houdellier F. Masseboeuf A., Monthioux M., Hÿtch M. J. *New carbon cone nanotip for use in a highly coherent cold field emission electron microscope*. **Carbon** 50 (2012) 2037-2044.
69. Houdellier F., de Knoop L., Gatel C., Masseboeuf A., Mamishin S., Taniguchi Y., Delmas M., Monthioux M., Hÿtch M. J., Snoeck E. *Development of TEM and SEM high brightness electron guns using cold-field emission from a carbon nanotip*. **Ultramicrosc**. 151 (2015) 107-115.
70. Mamishin S., Kubo Y., Cours R., Monthioux M., Houdellier F. *200 keV cold field emission source using carbon cone nanotip: Application to scanning transmission electron microscopy*. **Ultramicrosc**. 182 (2017) 303-307.
71. Monthioux M., Smith B. W., Burteaux B., Claye A., Fischer J. E., Luzzi D. E. *Sensitivity of single-wall carbon nanotubes to chemical processing: an electron microscopy investigation.* **Carbon** 39 (2001) 1251-1272.
72. Gogotsi Y., Libera J. A.,1 Kalashnikov N., Yoshimura M. *Graphite polyhedral crystals*. **Science** 290 (2000) 317-320.
73. Okuno H., Palnichenko A., Després J.-F., Issi J.-P., Charlier J.-C. *Synthesis of graphite polyhedral crystals using a combustion flame method*. **Carbon** 43 (2005) 692–697.
74. Yoon S.-H., Lim S., Hong S.-H., Qiao W., Whitehurst D. D., Mochida I., An B., Yokogawa K. *A conceptual model for the structure of catalytically grown carbon nano-fibers*. **Carbon** 43 (2005) 1828-1838.
75. Saito Y., Arima T. *Features of vapor-grown cone-shaped graphitic whiskers deposited in the cavities of wood cells*. **Carbon** 45 (2007) 248–255.
76. Campos-Delgado J., Kim Y. A., Hayashi T., Morelos-Gómez A., Hofmann M., Muramatsu H., Endo M., Terrones H., Shull R. D., Dresselhaus M. S., Terrones M. *Thermal stability studies of CVD-grown graphene nanoribbons: Defect annealing and loop formation*. **Chem. Phys. Lett.** 469 (2009) 177–182.
77. Glad X., de Poucques L., Jaszczak J. A., Belmahi M., Ghanbaja J., Bougdira J. *Plasma synthesis of hexagonal-pyramidal graphite hillocks*. **Carbon** 76 (2014) 330-340.
78. Gogotsi Y., Dimovski S., Libera J. A. *Conical crystals of graphite*. **Carbon** 40 (2002) 2263-2284.
79. Ferrari A. C., Basko, D. M. *Raman spectroscopy as a versatile tool for studying the properties of graphene*. **Nature Nanotechnol.** 8 (2013) 235-246.
80. Eckmann A.; Felten A.; Mishchenko A.; Britnell L.; Krupke R.; Novoselov K. S.; Casiraghi C. *Probing the nature of defects in graphene by Raman spectroscopy*. **Nano Lett.** 12 (2012) 3925–3930.
81. Picheau E., Impellizzeri A., Rybkovskiy D., Bayle M., Mevellec J.-Y., Hof F., Saadaoui H., Noé L., Torres Dias A. C., Duvail J.-L., Monthioux M., Humbert B., Puech P., Ewels C. P., Pénicaud A. *Intense Raman D band without disorder in flattened carbon nanotubes*. **ACS nano** 15 (2021) 596-603.
82. Kothari M., Cha M.-H., Kim K.-S. *Critical curvature localization in graphene. I. Quantum-flexoelectricity effect*. **Proc. R. Soc. A** 474 (2018) 20180054.
83. Venezuela P., Lazzeri M., Mauri F. *Theory of double-resonant Raman spectra in graphene: Intensity and line shape of defect-induced and two-phonon bands*. **Phys. Rev. B** 84 (2011) 035433.

84. Puech P., Kandara M., Paredes G., Moulin L., Weiss-Hortola E., Kundu A., Ratel-Ramond N., Plewa J.-M., Pellenq R., Monthioux M. *Analysing the Raman spectra of graphenic carbon materials from kerogens to nanotubes: what type of information can be extracted from defect bands*. **J. Carbon Res.** 5 (2019) 69.
85. Paredes G., Seine G., Cours R., Houdellier F., Allouche H., Ondarçuhu T., Piazza F., Monthioux M. *Synthesis and (some) applications of carbon-nanotube-supported pyrolytic carbon nanocones*. **Indian J. Eng. Mater. Sci.** (2020) in print.

-Chapter 3 -

Fabrication and mounting process of carbon nanocones as scanning microscopy probes

« Continuous improvement is better than delayed perfection »

Mark Twain

Chapter 3: Fabrication and mounting process of carbon nanocones as scanning microscopy probes

1. Scanning Probe Microscopy (SPM) techniques

Scanning Probes Microscopy (SPM) is among the most important advances in material science in the last two decades [*1Eaton2010, 2Wilson2009*]. It corresponds to a family of techniques developed by G. Binning and H. Rohrer in the 80's, allowing to map the surface topography and to measure the material properties at nanoscale by using a scanning probe as sketched in **Fig.1** [*1Eaton2010, 2Wilson2009*]. The main SPM techniques are Atomic Force Microscopy (AFM), Scanning Tunnelling Microscopy (STM), Scanning Near Optical Microscopy (SNOM) etc. The AFM consists in recording the topography of a wide range of materials thanks to the electrostatic interactions between a probe and the specimen surface regardless of their electrical properties (conductive or insulating) or physical state (liquid or solid), whereas the STM is used only for conductive surfaces. Despite their own specificities, these techniques share a common important point: the need of a probe able to detect atomic-scale interactions. The probe characteristics determine the resolution as well as the analytical scope of the SPM [*3futuremarket2011*, *4Bhushan2010, 5Nguyen2005*].]. Therefore, the development of a technological process able to shape the right material, with the required geometric characteristics is one of the big challenges for scanning probes as nanometrology tools in many fields including nanotechnology research and industrial manufacturing process [*3futuremarket2011*]. Such a challenge involves the consideration of physical properties such as mechanical ones (wear resistance, brittleness) and chemical inertness [*5Nguyen2005*], which play a key role on AFM measurements. [*6Stevens2009, 7Marsaudon2008*]. A high electrical conductivity is also needed in the case of SPM conductive modes [*4Bhushan2010*].

AFM-related mode probes consist basically of a tip-cantilever system as depicted in **Fig.1.** The cantilever serves as tip-support. Tip-sample interactions are then measured either by a direct determination of the cantilever deflection by a laser in the case of a contact mode, or by monitoring the amplitude or vibration frequency changes of the cantilever in so-called tapping mode during which the cantilever is put in oscillation [*1Eaton2010*, *4Bhushan2010*]. For this reason, cantilevers are, most of the time, metal-coated to enhance the reflectivity for the laser. Cantilevers are defined by their geometry such as length, width, thickness and mechanical properties such as the constant force (otherwise named "spring constant") and resonance frequency. The constant force and resonance frequency parameters define the quality factor Q *($Q= f_0/\Delta f$),* which is the ratio between the resonance frequency of the maximum amplitude over the bandwidth Δf at the half of the maximum amplitude. The latter defines the range of sensitivity allowed during the measurement [*4Bhushan2010*]. According to the AFM operation

mode (described in *chapter 4*), and the nature of the sample, a specific range of spring constant and resonance frequency values are used.

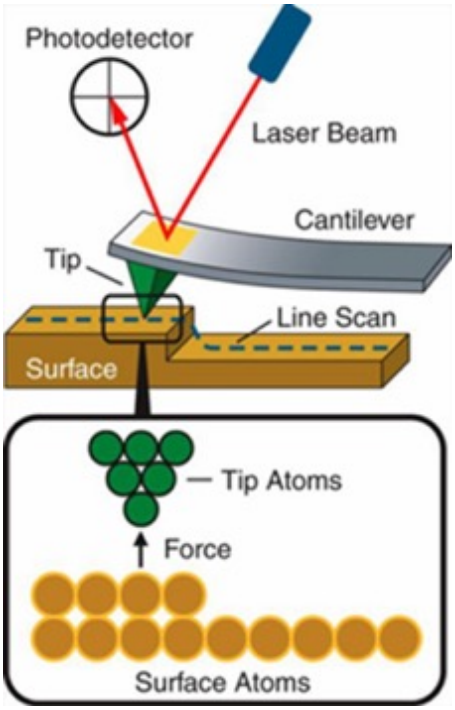

Figure 1: *Schematic representation of a SPM system. A surface is scanned by a probe (tip-cantilever). Tip-sample interaction forces created are sensed by the cantilever through a detector system (a laser beam and a four-quadrants photodetector in this case, usually that for AFM). A deviation of the laser beam reflected on the back of the cantilever represents a cantilever position (deflection) movement. The latter produces a disproportion on a signal (voltage) arriving into each photodiode quadrants. Then, the total output signal coming from the photodiode allows measuring either the interaction forces due to the cantilever deflection (up-down photodiode direction) or friction (left to right photodiode direction) of the system. From [*8Agrawal2012*]*

The tip is defined by several parameters: its apex radius or apex half-angle, length, and the so-called aspect ratio corresponding to the ratio of the tip length over the apex radius. One of the biggest challenges for AFM is to obtain a faithful representation of the sample surface when high roughness is present [*6Stevens2009, 7marsaudon2008*]. For such a purpose, a tip with a small apex radius is necessary. However, a trade-off on the tip length must be found: a short length will limit the analysis of deep roughness, whereas a long length will impact on the mechanical rigidity of the tip (hence likely to generate breaking, deformation, thermal vibrations). This trade-off is strongly dependent on the tip material. According to [*3futuremarket2011*, *9Hu2009*] a tip length between 500 nm and 1µm is suitable in order to reduce excessive lateral flexibility (causing thermal vibrations) and so the image artefacts.

2. Fabrication and mounting process of SPM probes

The first probes were fabricated by gluing a diamond shard onto a hand-cut gold foil cantilever [*2Wilson2009*]. Since then, improvements on innovative materials and process approaches

have been developed [*2Wilson2009, 3futuremarket2011, 5Nguyen2005*]. According to the material type and technological processes, top-down-micromachining or bottom-up fabrication and mounting processes can be employed.

2.1. Top-down micromachining process

Commercial ceramics (i.e. silicon, silicon nitride) tips and cantilevers are both made by top-down micromachining based on lithography processes [*2Wilson2009, 10Rusell2018*], which allows a scaled-up and single-step integrated-fabrication of commercial probes [*10Rusell2018*] as-well as reproducibility. However, for most commercial cantilevers as depicted on **Fig.2**, most of the silicon probes are pyramid-shaped, exhibiting a relatively large apex radius (**Fig.3c**).

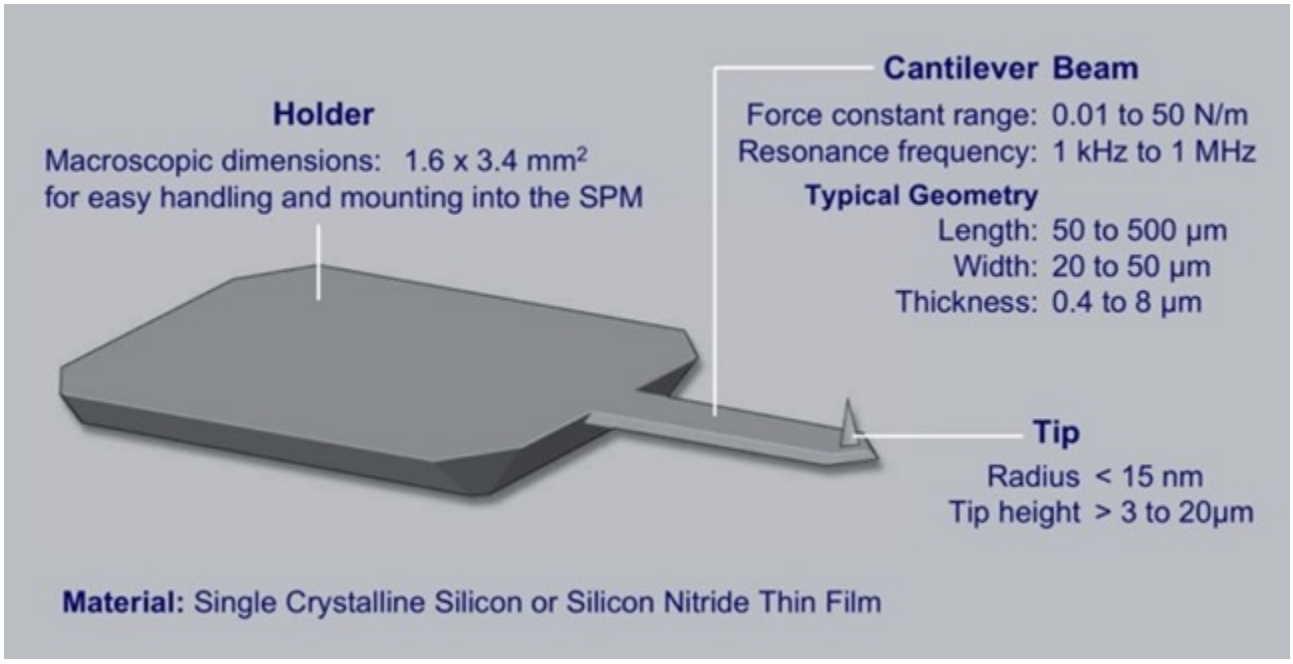

Figure 2: *Main characteristics of a silicon probe manufactured by a micromachining process.* [10Rusell2018].

For obtaining sharper silicon tips (i.e. with an apex radius below 5 nm), additional and cost-adding fabrication steps such as ion-milling or (electro)chemical etching are required [*1Eaton2010, 5Nguyen2005*]. Examples of such probes from the market are provided in **Fig.3a** and **3b**. Tips sharpened by these methods show an unstable mechanical behavior [*5Nguyen2005*] by a change in the tip morphology and some undesirable tip-sample interactions. These facts impact drastically their performances for high resolution imaging [*2Wilson 2009*, *5Nguyen2005*, *6Stevens2009*]. As a ceramic material, silicon is brittle [*5Nguyen2005, 11Guo2005*], affecting the wear resistance and durability of the probes, and tend to break easily. Furthermore, even if silicon can behave as a conducting material thanks to doping processes, metal (e.g. gold) coating steps are needed to enhance the electrical conductance of SPM silicon probes. Conductive probes combining silicon cantilevers and metal tips (tungsten or platinum) have also been reported in the literature [*12Rodriguez2007, 13Brown2013*]. For STM however, probe are usually tapered metal wires (Pt-Ir, W, Au…).

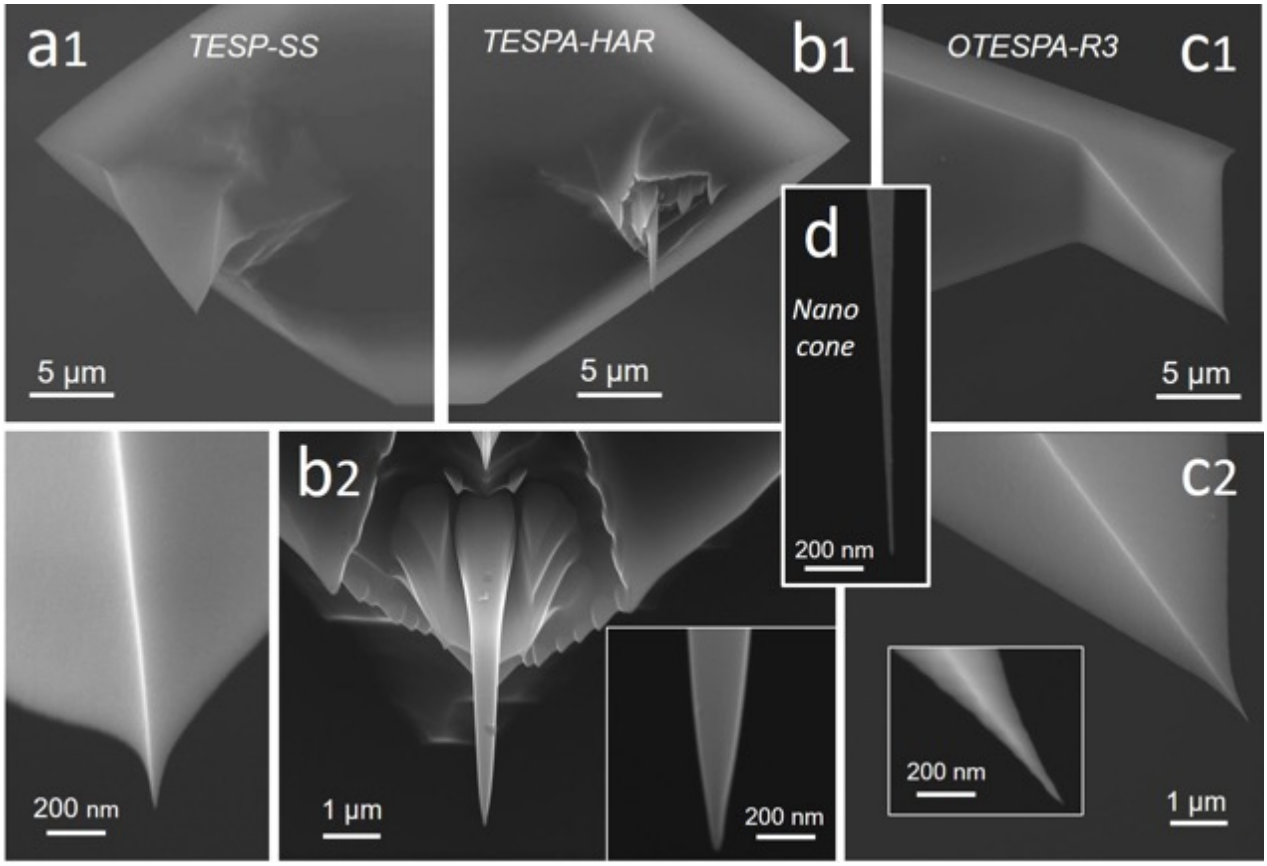

Figure 3: *SEM images showing the morphology and the apex of different silicon probes from the market (from (a) to (c)) compared with a carbon nanocone in (d).* ***(a)*** *A "Super-sharp" Sb-doped silicon probe with a 2-5 nm apex radius, sharpened by electrochemical etching (TESP-SS).* ***(b)*** *A "high-aspect-ratio" sb-doped silicon probe with a 10-15 nm apex radius, sharpened with ion milling (TESPA-HAR).* ***(c)*** *A standard silicon probe of 7-10 nm apex radius (OTESPA-R3).* ***(d)*** *the tip of a carbon nanocone.*

2.2. Bottom up manufacturing process

For overcoming the limitations of silicon, low dimensional carbon tips have been proposed, starting with CNTs [*7Marsaudon2008, 14Ye2004, 15Dai1996, 16Bernard 2008*]. This material exhibits excellent physical properties: high mechanical strength and Young modulus [*17Treacy1996, 18Wong1997*], good wear resistance [*5Nguyen2005*, *6Stevens2009*, 1*0Guo2005*], and good electrical conductivity [*15Dai1996*]. Then, diamond has also been used for specific modes [*3futuremarket2011, 19Hantschel2016*]. However, since these carbon materials are developed through bottom-up methods like CVD, their integration on cantilevers requires the combination of microfabrication and nanofabrication processes [*3futuremarket2011*, *6Stevens2009*]. In the particular case of tips based on CNTs, several methods ranging from direct manipulation to direct-CCVD growth of a CNT onto a cantilever have been proposed [*2Wilson2009, 5Nguyen2005, 7Marsaudon2008*]. However, all of them present limitations regarding:

- the growth of individual CNTs with tailored geometric characteristics (length, alignment, apex radius);

- the integration of a hybrid micro-nanomechanical system (firmly mounting a nanosized carbon tip onto a micromachined silicon cantilever)

Even if multiwalled and single walled carbon nanotubes exhibit suitably small diameters and a high aspect ratio cylindrical shape, they grow most of the time as bundles with random curvatures and not a well-controlled length and growth direction, which limit tip alignment (**Fig.4**) [*6Stevens2009, 20Stevens2006, 21Martinez2005*].

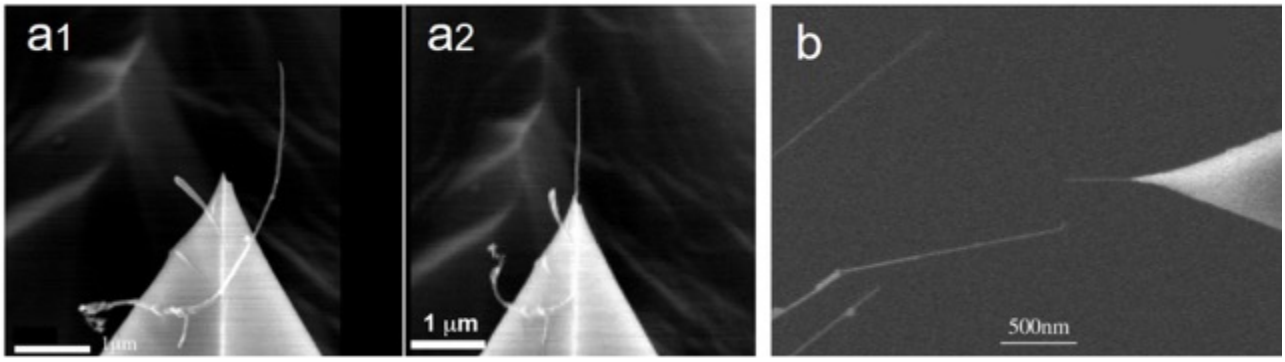

Figure 4: *SEM images of CNT probes modified by ion and electron beam techniques.* ***(a)*** *Before (a1) and after (a2) CNT alignment [*20Stevens2006*].* ***(b)*** *A 300 nm-long CNT tip obtained from shortening by FIB [*21Martinez2005*].*

Controlling the nanotube length is a strong issue since it is related to the high aspect ratio on the one hand, and a large lateral flexibility on the other hand [*22Liu2004*]. In consequence, microfabrication and micromanipulation techniques are used to perform after-growth modifications (i.e. shortening, alignments) while mounting the tips onto the cantilever [*15Dai1996, 20Stevens2006, 23Xu2009*]. The first-developed micromanipulation technique consisted in fixing the nanotube tip onto a pyramidal silicon probe under an optical microscope [*15Dai1996*]. Then, Xu *et al.* proposed an improvement of that method using a dc electrical current between the nanotube tip and a metal-coated silicon one to reduce the undesirable excess length of the protruding tip [*23Xu2009*]. However, probes cut by this method exhibited an open-ended tip, which could tend to generate artefacts during imaging. To remediate this, more sophisticated methods, for example the use of a Scanning Electron Microscope (SEM) equipped by a dual ion/electron beam facility have also been developed [*21Martinez2005, 24Yuzvinsky2005, 25Strus2005, 26Slattery2013*] Cross- or dual-beam methods are claimed to allow both good alignment and close-ended cut tips, while positioning and fixing the tip on the cantilever [*20Stevens2006, 23Xu2009*]. However, controlling the tip position means a good bonding of the tip on the cantilever so that the angle φ made by the tip axis with respect to the normal to sample surface is as close as possible to 0°, which means that the tip axis should make an angle of 11° to compensate the cantilever angle enforced by the AFM probe-holder configuration, which also exhibits a tilt angle of 11-13° (see **Fig.5**). This requires a highly-reproducible process. Furthermore, when using ion or electron beam irradiation, a special attention should be paid to avoid possible damages to the nano-micro "structures" [*24Yuzvinsky2005, 27Raghuveer2004, 28DeTeresa2009*], as they are likely to modify the tip in all aspects, i.e. the apex geometry, dimensions, material structure and properties (amorphization is likely to induce changes in the electrical conductivity, and wear resistance…).

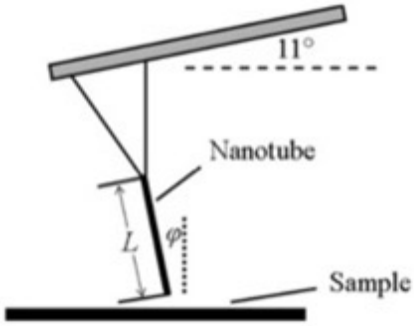

Figure 5: *Schematic representation of the key parameters for the alignment of a nanotube tip on a pyramidal silicon probe [*23Xu2009*].* L *and* φ *represent the nanotube length and the tilt angle between the tip axis and the normal to the sample surface, respectively.*

Others methods based on dielectrophoresis [*8Hu2019*, *29Dremov2015*], or electrochemical processes [*30Hafner1999, 31deJonge2003*] are also used for ensuring tip alignment and geometric shape without inducing further modifications. However, growing individual CNT tips with an adequate control of length and radius has not been reproducibly achieved yet [*32Rius2012*]. Considering this, CNTs with tip curvature radius below 3 nm can be produced by directly depositing a catalyst nanoparticle and then growing a CNT on commercial AFM tips [*30Hafner2012, 33Hafner1999*]. Marsaudon *et al.* reported on the use of SWCNT tips grown by a Hot filament-CVD process, where the deposition of individualized SWCNTs is controlled by dosing the cobalt catalyst pattern thickness [*7Marsaudon2008, 34Marty2006*]. As a result from the difference in the number of walls, SWCNTs showed smaller stiffness as compared to MWCNTs [*16Bernard2008*]. Other approaches combining silicon micromachining and bottom-up manufacturing of tip-like morphologies have been investigated in the literature (*14Ye2004, 5Nguyen2005*]. In particular, Nguyen *et al.* reported the fabrication of CNT-based individual tips with lengths of 3-5 µm without the need for a shortening step and a curvature radius below 30 nm by using e-beam lithography and controlling the tip alignment by PECVD. However, even if these kinds of processes are able of a high yield of tips, they also face some limitations on fabricating sharp and stable (i.e. with good mechanical rigidity) tips.

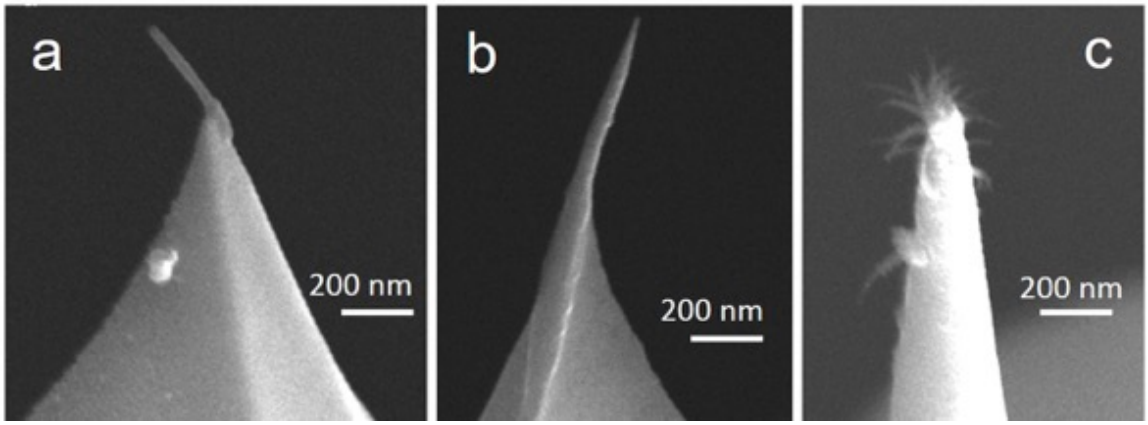

Figure 6*:* ***(a)*** *and* ***(b)*** *SEM images showing two commercial high-resolution carbon nanotube tips coated with a polymer for enhancing the rigidity, (a) from CDI company, (b) from NanoScience company.* ***(c)*** *Diamond-like carbon probe from NT-MDT company. All show poor alignment (image credit: M. Delmas, CEMES).*

For improving the mechanical stability, some authors and suppliers [*6Stevens2009, 35CDI*] proposed hybrid silicon-carbon technology processes. For instance, carbon nanotube probes are coated with silicon material or polymer (**Fig.6a, 6b**) in order to enhance rigidity without shortening the tip. Nevertheless, the polymer coating can provoke excessive rigidity and not well aligned tips, which can lead to tip-sample damages or imaging artifacts for some SPM applications, as well as coarsening of the apex. Gaining in rigidity can also be achieved by changing the type of carbon, i.e. switching from C(sp^2)-based tips (such as CNTs) to C(sp^3)-based tips (diamond-like carbon, single-crystal diamond). But again, this comes with some drawbacks such as alignment difficulty (**Fig.6c**) and/or enhanced brittleness.

Table1 below gathers basic characteristics of some carbon-based SPM probes on market, compared to silicon-based ones.

Supplier	Material	Tip curvature radius (nm)	Useful length (nm)	Unit price (€)
NT-MDT	Diamond-like Carbon	1 à 3	< 20	60#
Bruker	EBD Carbon	30	120	485#
Bruker*	MWCNT	10 à 15	350	1750#
CDI	Polymer-coated MWCNT	20 à 25	200	150#
NanoScience*	MWCNT	10 à 30	500	320#
NanoSensors	SWCNT/DWCNT	1,2 ou 2,4	< 750	465#
Bruker, OTESPA-R3	Silicon	10	n. a.	30
Bruker, TESPA-HAR	Silicon	10-15	4000-5000	78
Bruker, TESP-SS	Silicon	2-5	~200	64
Bruker, TESPA-V2	Silicon	10	n. d.	31
Micromash HQNSC15	(Si+ 30nm Pt coating)	8 (before coating) and 30 (after coating)	n. d.	24
NanoWorld Arrow NCR-10	Silicon	10	12-18	28

**No longer on market. Market prices (right-hand column) marked with # are from ~2013.*
n. a. = not appropriate – n.d. = not determined.

Table 1: *Comparison of carbon-based and silicon-based SPM probes on market. Prices are indicative, as they also vary along with the package type. Completed from [*36Delmas2015*]*

3. Carbon nanocones as SPM probes

As shown in *Chapter 1* (*Section 3.2.2*), very few carbon conical SPM probes have been reported. Since the methods used are similar to that for preparing CNT-based probes, individual growth and controlled geometrical characteristics of conical carbon probes are not fully controlled yet. The most outstanding results was obtained from an e-beam-induced deposition (EBID) process (see **Ch.1-Fig.21a** [*37Chen2006*]). In our work, we evaluate the feasibility and possible added value of using the SSF morphology as SPM probes considering its geometrical shape and

physical properties, and whose obtention is well-defined by a unique CVD synthesis process as described in *Chapter 2*. Comparing with the CNT-based probes, the only additional fabrication step of the nanocone-based probe concerns the mounting process, hence fabricating a carbon cone-based SPM probe is a two-step process only. The spiky-short-fiber (SSF) morphology is presumably easy to handle as the cones grow as individual objects at both ends of a microfiber part, allowing a mechanically stable structure and a much better positioning control than with CNTs during the mounting process onto the tip support. The whole fabrication and qualification process (presented in **Fig.7**) starts with the selection of the synthesized cone sample, then, mounting the cone tip on the cantilever, characterization of the mounted probes and finally the application tests (*Chapter 4*) for different non- conductive and conductive SPM modes.

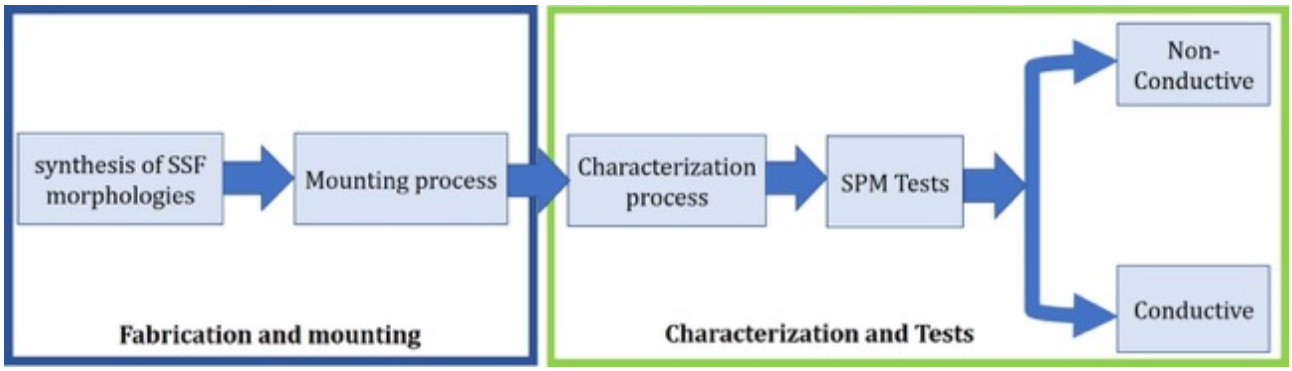

Figure 7: *Schematic flow of the manufacturing and qualification process of the nanocones morphologies as SPM probes. SSF stands for Spiky Short Fiber.*

3.1. SSF carbon nanocone tips: description and characteristics

As presented in *Chapter 2,* SSF morphologies are all graphene-based. It consists of a rough surface microfiber extended at both ends by sharp cones with smooth surface (see **Fig.8a**). The microfiber length in the range of 7-10 µm allows the cone to be easily handled and positioned during the mounting process on the cantilevers. The cone length L is in the range of 2-7 µm and the width W at the base can reach 700 nm-1 µm. Furthermore, the very sharp apex is characterized by an angle noted 2α. This angle can be estimated by the following equation (1):

$$Tan\ \alpha = \frac{W}{2L} \quad (1)$$

Considering a very small 2α angle, (1) can be expressed as follows:

$$2\alpha = \frac{W}{L} \quad (2)$$

Consequently, considering a cone with a 700 nm width and a 6 µm length as depicted in **Fig.8b,** the cone angle 2α is equal to 0.12°.

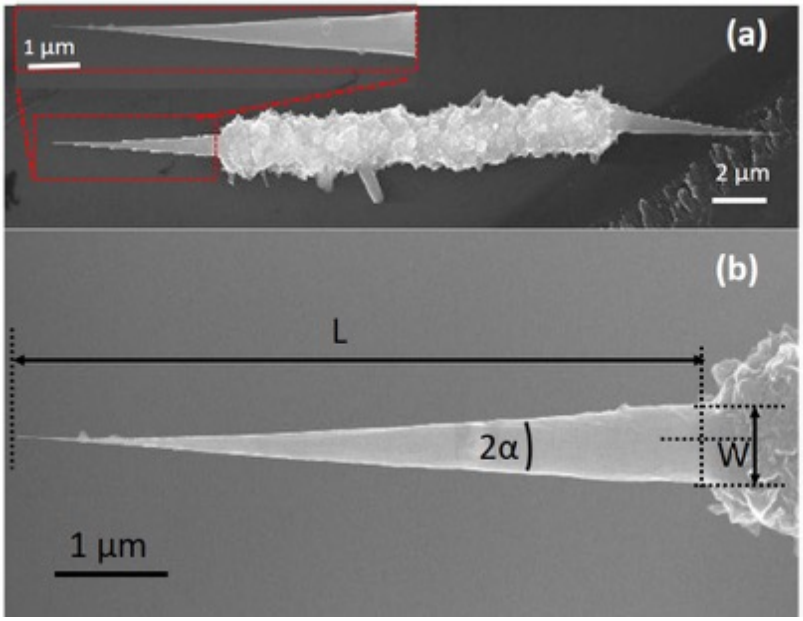

Figure 8: *Geometrical characteristics of a cone tip.* ***(a)*** *SEM image of a whole SSF morphology.* ***(b)*** *SEM image of a cone showing the length (*L*), width (*W*) and apex angle (*2α*) parameters of the cone tip.*

3.2. Mounting process

Three after-growth mounting methods were used to place and fix the tip onto the support: *(i)* gluing (ii) welding through metal deposition using a HELIOS Scanning Probe Microscope (SEM) equipped with a crossed dual ion/electron beam facility, allowing Focused Ion Beam Induced Deposition (FIBID) to be carried-out, and *(iii)* welding through metal deposition using a ZEISS SEM equipped with a crossed dual ion/electron beam facility, allowing Focused Electron Beam Induced Deposition (FEBID) to be carried-out.

In order to account for these three different mounting procedures, in the following, the probes will be designated by a nomenclature number such as <*H(or Z, or G)i(or e)Rxx-Cxx-n*>, where *H* or *Z* are for indicating the equipment used (Helios or Zeiss) whereas *G* is for indicating the gluing method instead, *i* or *e* are for indicating ion- or electron-induced welding i.e., FIBID or FEBID), *Rxx-Cxx* is the ID number of the cantilever, and *n* is the order number in the fabrication chronology.

For SPM methods using cantilevers, the choice of the mounting method (either gluing or BIDing) was based mainly on the kind of test required (conductive or non-conductive) as well as on the know-how and instrumentation available at CEMES.

For STM probes, only FIBID first, and then only FEBID were used to attach the cone tips to the end of a metallic wire (either a PtIr alloy, or Au). Hence, the related probe nomenclature will be <*PtIr(or Au)i(or e)-n*>.

3.2.1. Cantilever specifications

Unlike nanotube probes that are mounted onto the surface of commercial silicon probes (most of the time pyramidal shaped), cantilevers without tip and wearing a cylindrical part of ~10 µm

in height carved out with a groove of few µm in both width and depth were designed by us and then fabricated by *AppNano,* USA (see **Fig.9**). This design was developed to improve the control on both the orientation angle and the tip protruding length during the mounting process of the SSF morphology. The cantilevers are made of silicon doped with antimony without any coating and beam dimensions of 125 µm in length and 35 µm in width.

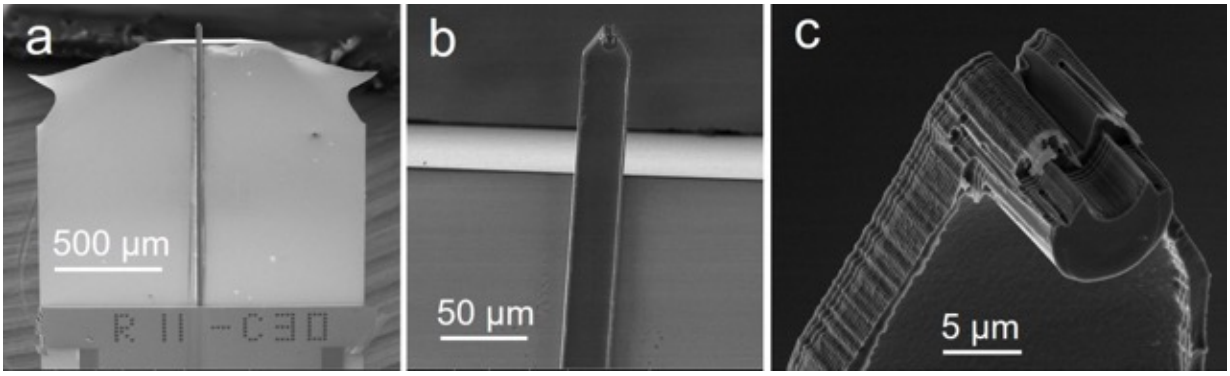

Figure 9: *Cantilever purposely designed at CEMES and manufactured by Appnano company[13], for AFM-related tests.* ***(a)*** *overall view of the whole device.* ***(b)*** *Closer view of the "beam" part (i.e., the cantilever, refer to* ***Fig.2****).* ***(c)*** *View of one example of cantilever termination (Type1), with the groove dedicated to receiving the SSF morphology.*

Two different cantilever batches were manufactured. The two types differ on their nominal thickness values: 4.5 µm for one batch (Type1), and 0.5-1 µm for the other (Type2). In consequence, they also exhibit different nominal spring constant and resonance frequency ranges: 40N/m, 200-400 kHz for Type1 cantilevers; and 25N/m, 90-180 kHz for Type2 cantilevers. The quality factor (Q) was directly measured in the range of 700-800 for Type1 cantilevers[14], and estimated (See **Fig.14a**) at about 275 for Type2 cantilevers. Electrical resistivity of both cantilevers is 0.01-0.025 ohm-cm.

3.2.2. Gluing process

In this process, a synthesized SSF morphology is attached onto the cantilever with an ultraviolet (UV)-curable Norland (NOA 68) optical adhesive resin. The mounting steps are sketched in **Fig.10**. The assembling is conducted by means of a three-axis micromanipulator (from Micromanipulator, Inc.) under an optical microscope. SSF morphologies are scrapped from the Papyex® substrate so that they fall down onto a few-centimeter-large piece of silicon wafer in order to easily handle the SSF substrate in the microscope plate and make easier the subsequent grabbing of the morphologies with the micromanipulator. Then, the cantilever is attached to the micromanipulator rod by using a tiny piece of adhesive film. After that, a small-UV curable resin droplet is deposited onto a glass plate. Some quantity of resin is transferred by capillarity into the cantilever groove by using the micromanipulator for gently touching the droplet surface with it, and will allow attaching the SSF morphology. Few minutes are needed to search, choose, pick a well-aligned (with respect to the morphology axis) cone morphology

[13] Upon funding by the ANR project CANAC.
[14] Type1 Cantilevers were the most used for conducting our tests.

and grab it on the cantilever groove, thanks to the sticking force of the resin glue. The whole operation is monitored under a CCD camera visualizing the micromanipulator rod tip through the x100 objective lens of the optical microscope. The resin is then cured under an ultraviolet lamp (24 W, specimen at ~5 cm distance) with a 350-380 nm wavelength range. Such a wavelength is not in the range of adsorption of CNTs [*38Berd2012*][15], hence we assumed that it is not harmful to the concentric graphenes making the cones either. The whole mounting process takes 15-20 min to be performed by a trained operator. Finally, SEM characterization is conducted to verify the alignment and orientation of the cone tip with respect to the cantilever groove. The in-plane angle named θ and to the out-of-plane angle named φ represent the lateral and vertical orientation of the cone tip with respect to symmetrical plan of the cantilever as depicted in **Figure 17**. Since the UV resin employed is not electrically conductive, the probes made by this method are used for non-conductive SPM mode tests.

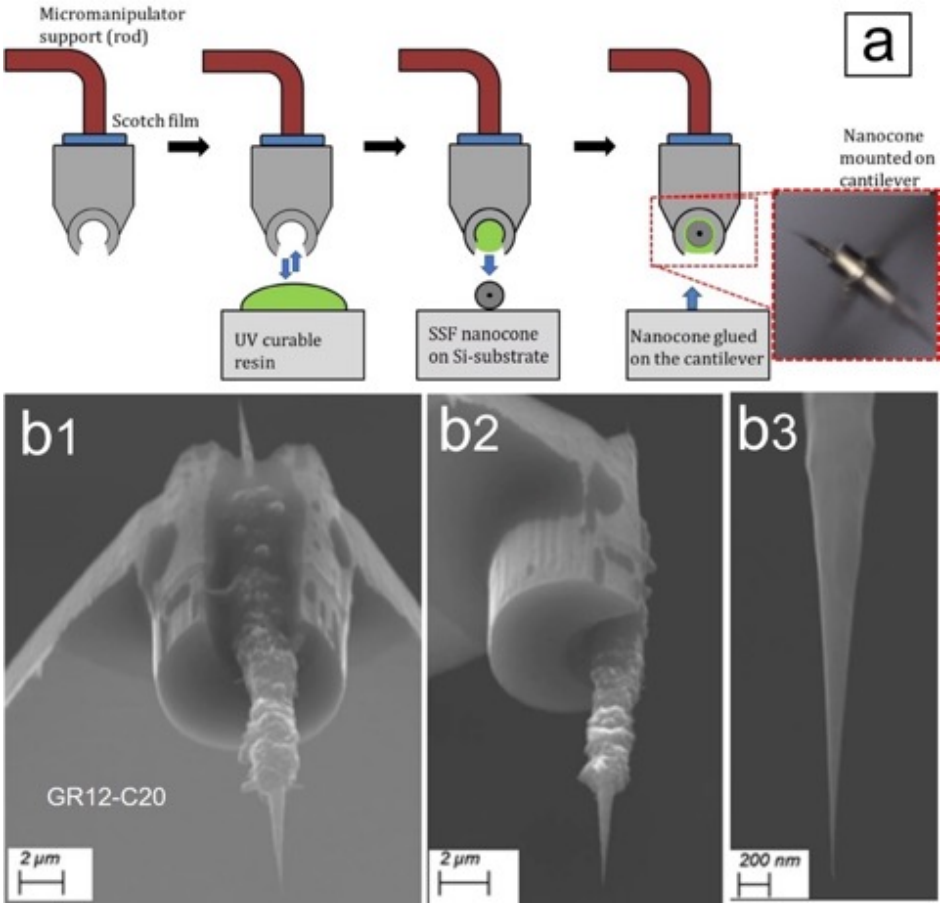

***Figure 10**. **(a)** Schematic of the gluing mounting process of a SSF morphology onto a cantilever. As the morphology always exhibits two cones, the one oriented towards the cantilever backside is useless; in inset is an optical image of a nanocone while being mounted on a cantilever by this method. **(b1)** to **(b3)** SEM images of a carbon probe (**#GR12-C20**) right after the gluing mounting method. In this example, the cone is fairly well aligned with respect to both the short-fiber-part axis and the groove axis.*

[15] Indeed, [*38Berd2012*] observed that single-wall carbon nanotubes were not found to exhibit any absorption in the UV wavelength range used for curing the resin. As, in the graphene cylinders making the cones, C-C bond lengths are similar and radii of curvature are longer (inducing less strained graphene lattices) with respect to SWCNTs, it is assumed that the UV irradiation could not affect them either.

The interest of the process is its rapidity, and the relatively low cost of the equipment involved. On the other hand, because of the limited magnification power of the optical microscope, the lack of 3D view, and the "capturing" effect of the SSF morphology by the resin once both are put in contact, it is not possible to correct any misalignment of the cone axis with respect to the cantilever, either intrinsic to the morphology selected or resulting from the gluing. However, once getting trained with the procedure, only few carbon-cone-equipped cantilevers revealed to be non-usable.

3.2.3. Welding process[16]

The first tests were conducted on a Thermo Fisher HELIOS NanoLab 600i FIB equipped with a micromanipulator (Omniprobe), following the nanocone displacement and welding protocol previously developed at CEMES to cut a SSF morphology by half and then to fix it onto an electron emitter W tip for field emission application [*39Houdellier2012, 40Houdellier2015*]. Thanks to the presence of the terminating cantilever groove, this protocol was adjusted here by welding the whole SSF morphology (instead of half of it) to the cantilever instead. A selected SSF morphology is grabbed by the micromanipulator, moved to the cantilever, placed in the groove and then released from the micromanipulator, and then welded by metal deposition (Pt, or W). This metal deposition is generated by a gas injection system (GIS, similar to that in **Fig.11b**) which spreads organometallic precursor molecules which are decomposed and ionized by a Ga ion beam, whose resulting ions are somewhat focused on the area to cut or weld. The metal atoms released by the interaction of the precursor and the Ga ion beam thereby deposit on the part of the substrate onto which the Ga ion beam is focused, as the principle of FIBID.

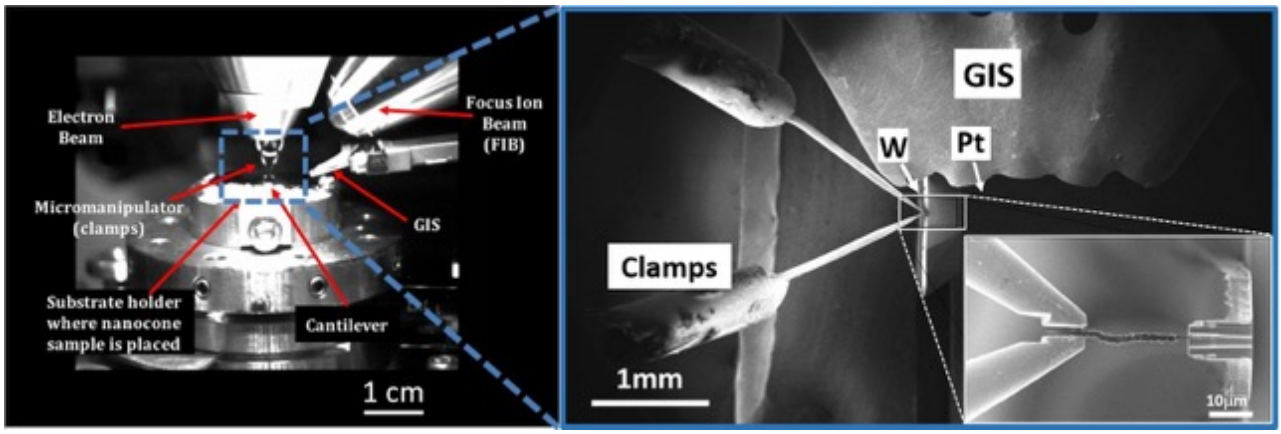

Figure 11: *Configuration of the ZEISS SEM equipped with a cross beam system used for the nanocone probe mounting process.*

However, the micromanipulator in the Helios SEM-FIB is a mere single rod. Grabbing the SSF morphology and then releasing it required a multiple use of the Ga ion beam, for welding the morphology onto the micromanipulator rod first, and then for cutting the metal welding and

[16] All the FIB work was carried-out by the engineer in charge of the equipment at CEMES, Robin COURS.

releasing the morphology in the cantilever groove, and finally to weld the morphology to the cantilever. As reported in forthcoming *Sections 4.1 and 4.2*, a variable degree of amorphization of the carbon cone tip was confirmed by SEM, TEM, and Raman spectroscopy characterization partly presumably as a result from the Ga ion irradiation, despite the ion beam was supposed to be focused on spots far (about 10 µm away) from the cone apex (see **Fig.12** for example). This statement urged us to improve our protocol by:

(1) using FEBID only instead of FIBID. The procedure is the same (see above) but the organometallic precursor is decomposed under an electron beam instead of an ion beam. One inconvenient is that the metal deposition rate is much lower.

(2) using another cross-beam microscope, a ZEISS 1540XB FIB, where the micromanipulator consists of clamps that allow the SSF morphology to be grabbed, moved and then released merely by actioning the tweezers without requiring any use of the electron beam but once (for welding the morphology in the cantilever groove).

By adopting this new protocol, a single metal deposition process using electron beam just once, and no ion beam, was sufficient to mount the SSF morphology onto the cantilever.

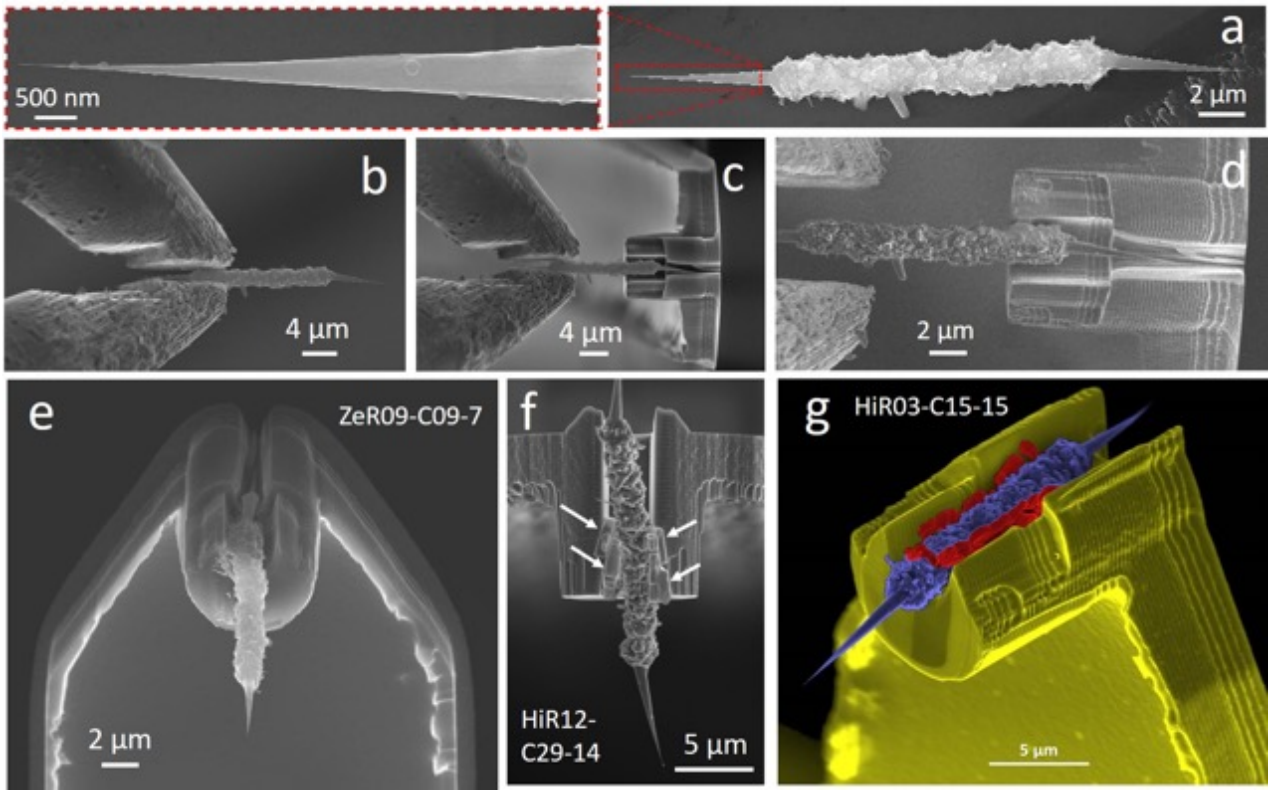

Figure 12: *From* ***(a)*** *to* ***(e)*** *sequence of SEM images showing the chronology of the AFM probe mounting process (probe #**ZeR09-C09-7**): a SSF morphology is placed and weld onto a cantilever (Sb-doped Si) by using Focused Electron Beam Induced Deposition (FEBID).* ***(f)*** *Another example of welded probe (probe #**HiR12-C29-14**) prepared by FIBID, showing the facetted morphology (arrows) of the deposited metal (Pt).* ***(g)*** *another example of welded probe (probe #**HiR03-C15-15**) prepared by FIBID (Pt). Colors were added for better recognition of the various materials: Sb-doped Si (yellow), C (blue), and Pt welding (red). The probes from this mounting process were used for AFM-related mode tests.*

Defined protocol: a SSF morphology is selected (**Fig.12a**) and then grabbed (either directly from the growth substrate or after having scratched the growth substrate above a silicon substrate so that the free morphologies can fall down onto it) with micromanipulator clamps (**Fig.12b**) to be positioned into the cantilever groove (**Fig.12c**) and then deposited there by releasing the clamps (**Fig.12d**). Then, a metal deposit from an organometallic precursor (*$(CH_3)_3Pt(CpCH_3)$* for platinum *or* *$W(CO)_6$* (55% W, 30% C, 15% O) for tungsten) decomposed and ionized by an electron beam is used to weld the local interface between the short-fiber part and the cantilever (**Fig.12e**). The metal deposition is conducted in a volume of few cubic micrometers and an electron beam energy of 2 keV and a 200 pA current during few seconds. Although the deposited metal exhibits facetted shapes suggesting it is crystallized (arrows in **Fig.12f**), it also contains a significant amount of carbon (from the precursor) which may affect the conductivity. Therefore, W was finally preferred over Pt because the electrical conductivity was expected to be better [*41DeTereza2013*]. Obviously, the whole operation is facilitated by the existence of the short-microfiber part in the SSF morphology, which allows it to be "easily" grabbed, manipulated, positioned, and welded while preventing to directly affect the nanocone part.

The whole mounting process takes about 3h to be performed. The presence of several elements (the GIS, the clamps of the micromanipulator, the ion beam line, the electron beam line) in a narrow space (**Fig.11a**) makes the process difficult and time-consuming. Besides, a know-how needs to be acquired to optimize the metal deposition process in order to avoid (or minimize) the irradiation and degradation of the carbon cone tip (for instance, an insufficient time of exposure to the electron beam may impact the bonding strength between the microfibre and the cantilever). This may explain the incidental loss of the probe that has happened sometimes, or unusual features in the resonance frequency curve for some carbon cone-equipped cantilevers, which might reveal a loose welding (see forthcoming **Fig.14**).

As can be seen by comparing **Fig.12** with **Fig.10**, the contact surface and the vertical alignment tend to be better in the case of the gluing process, after which the microfiber part is firmly fixed by being fully embedded in the resin, than for the welding assembling. Nevertheless, as opposed to the gluing bonding process, an in-situ characterization using the high-resolution SEM microscopy mode while conducting the mounting process is possible. However, the SSF morphology cannot be seen under different view angles while being positioned, hence, as for the gluing process, it is nearly impossible to compensate for any intrinsic misalignment between the cone axis and the short-fiber axis. Finally, the main advantage of this process is the possibility to manufacture probes usable in both conductive and non-conductive SPM modes.

For STM probes, FIBID first, and then FEBID were used to attach a SSF morphology to the end of a metallic wire of diameter ~220 µm. The metallic wire was first a Pt-Ir wire merely cut with cutting pliers (**Fig.13a1**). This is a regular procedure for using such a Pt-Ir wire directly as STM probe. But the resulting geometry and dimension of the wire apex thus obtained were not well suitable for subsequently welding a SSF morphology onto it and was making the probe positioning not easy (**Figs.13a2-13a3**). This was then abandoned and replaced by a gold wire, which was tapered by electrochemical etching (**Fig.13b1**) following a similar procedure as sketched in **Ch.1-Fig.19a** before a SSF morphology was welded on it by FEBID (**Fig.13b2**).

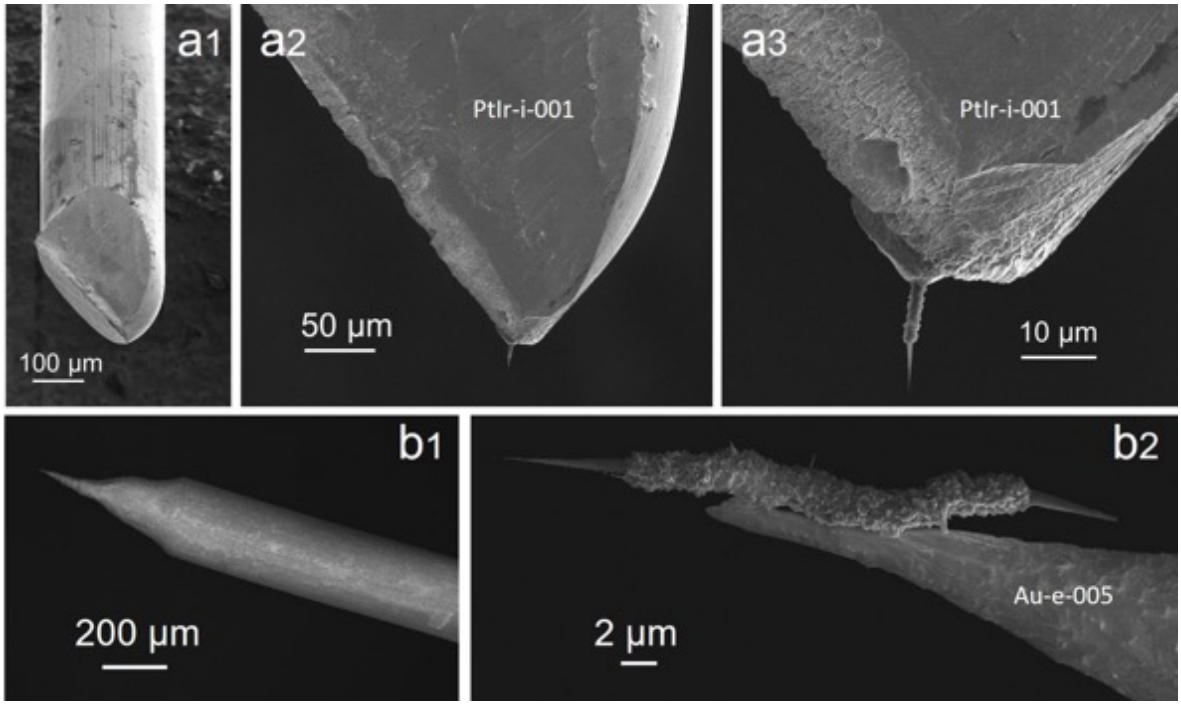

Figure 13. *SEM images of SSF-based STM probes prepared following the same procedure as described by* ***Fig.12****.* ***(a)*** *Welding with Pt by FIBID onto a mechanically cut Pt-Ir wire (Probe #****PtIr-i-001****).* ***(b)*** *Welding with W by FEBID onto an electrochemically tapered Au wire (Probe #****Au-e-005****).*

4. Characterization of the carbon nanocone probes

4.1. Resonance frequency

The effect of the mass possibly induced by the addition of the SSF morphology to the cantilever was evaluated by measuring the resonance frequency of the cantilever with and without a SSF morphology mounted. The mass added by the morphology results to be negligible since no significant change is observed on the resonance frequencies (**Fig.14a**), which remained in the range 250-350 kHz for Type1 cantilevers and 90-180 kHz for Type2 cantilevers (see *Section 3.2.1*).

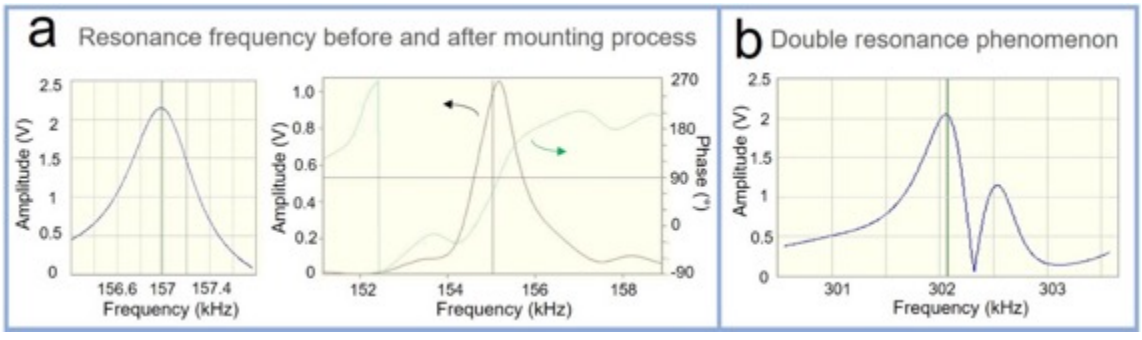

Figure 14: (a) *Example of cantilever resonance frequency recorded before (left) and after (right) mounting a SSF morphology.* ***(b)*** *Example of a double resonance phenomenon evidenced sometimes after mounting a SSF morphology.*

An experimental feature of the resonance curves, which was observed several times for the carbon cone-equipped cantilevers but was unusual for regular Si probes, is the occurrence of an effect of resonance oscillation as a double peak (**Fig.14b**). No clear explanation was found, but a possible consequence of a loose mounting of the SSF morphology, which may happen due to some lack of sufficient adhesion or quantity of the fixing material (resin or welding).

4.2. Tip geometry

Different methods exist for characterizing a SPM probe [*42Wade2004, 43Fujita2007, 44Tian2008*]. One of the most used is SEM in order to observe directly the shape and determine the alignment and position of the cone on the cantilever. However, as SEM is a 2D characterisation technique, it remains a very hard task to accurately measure the tip apex radius. Other authors [*45Han2011*] refer to an indirect characterization based on the measurements drawn from the imaging of a calibration sample by AFM using the probe. A whole measurement campaign was then performed this way.

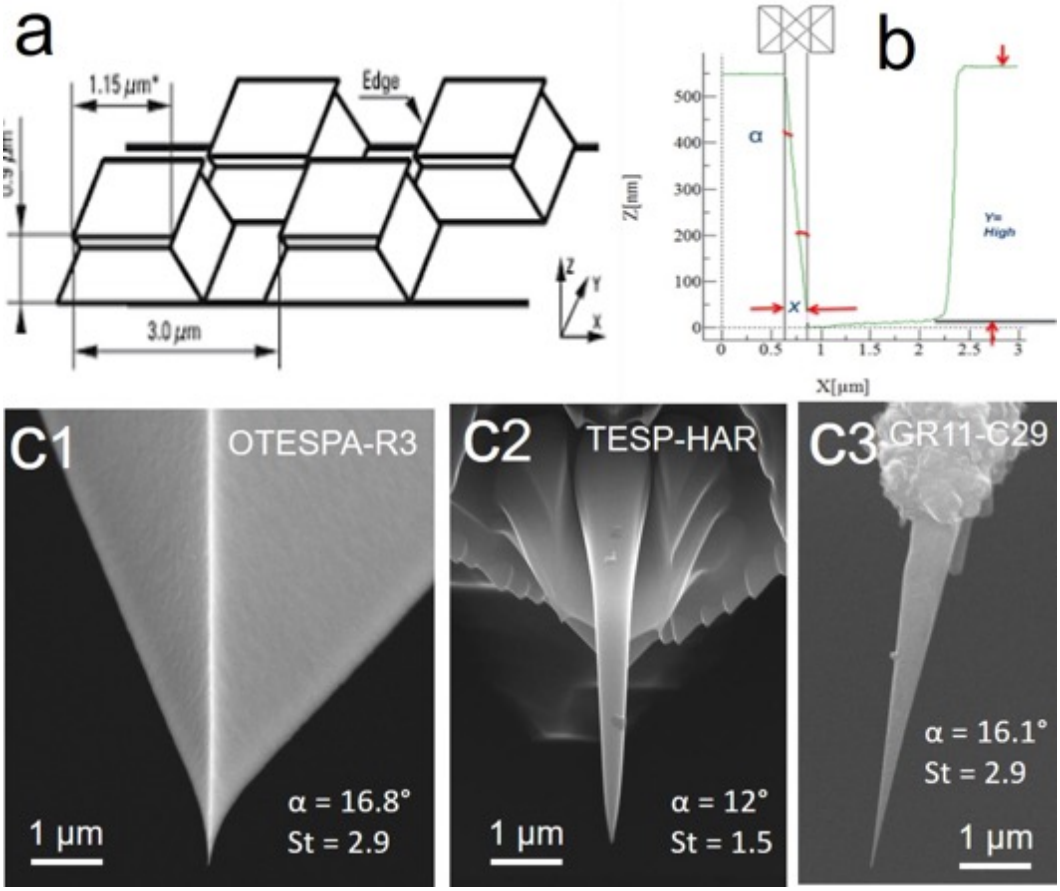

Figure 15: *Methodology to obtain the apex angle of the probe tip from imaging a calibration substrate.* ***(a)*** *sketch of the calibration substrate used (TGX1 from NT-MDT).* ***(b)*** *measurements can be drawn from the AFM profile.* ***(c)*** *Examples of three AFM probes tested, and parameter values obtained from the AFM profiles of the calibration substrate (α = half apex angle. st = standard deviation). Considering the visual, it was expected that the geometric characteristics obtained for the carbon nanocone (c3) would be similar to that of the commercial TESP-HAR probe (c2), but it appeared to be similar to that of a commercial, standard probe (c1) instead.*

However, the recurrent misalignment of the cone axis with respect to the desired direction along with the variability of the misalignment extent generated imaging artifacts which prevented a reliable geometric description of the carbon probes to be obtained (**Fig.15**). This has induced that, in spite of the obvious high aspect ratio of the carbon cones, this characteristic was not exploited during our work.

A deeper analysis using a tool (Tip Qualification) from the Nanoscope Analysis software[17] was supposed to allow making a reconstruction of the shape and apex of the probe from AFM images produced by the tip. However, the reproducibility is not always as obvious as illustrated in **Figs.16b-16c**, and moreover, the reconstructed apex images are difficult to interpret.

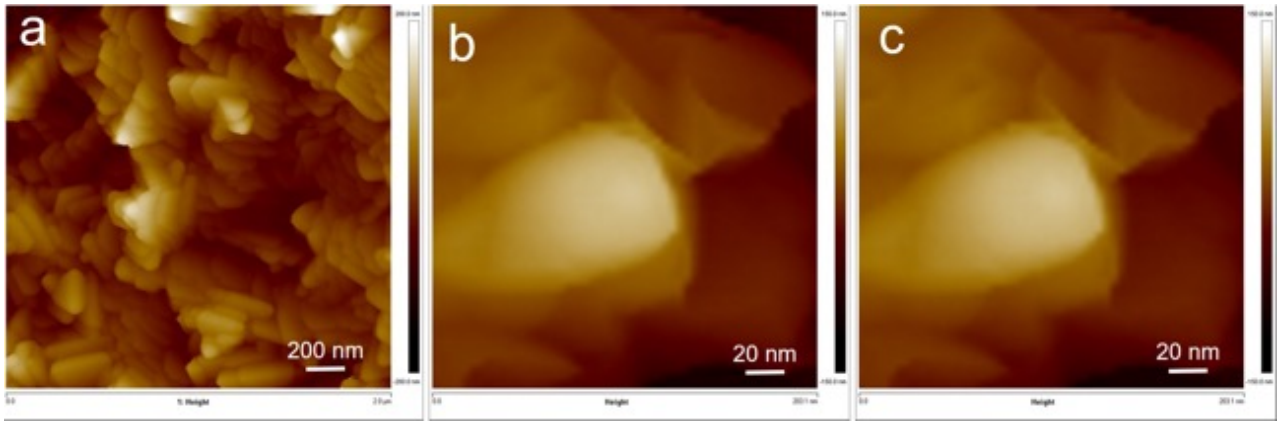

Figure 16. (a) *Example of an AFM image (width = 2 µm) of a titanium substrate obtained with a commercial OTESPA tip (see* ***Fig.15c1****).* ***(b)*** *Reconstructed image of the probe tip as obtained from the software analysis of the image in (a).* ***(c)*** *Reconstructed image of the same probe tip as obtained from the software analysis of another image similar to that in (a), but at a different location on the substrate. Both reconstructed tip images are identical, showing the reproducibility of the method. Photo credit: T. Ondarçuhu, IMFT.*

Consequently, it was chosen to monitor the probe state at different steps, from the moment right after the mounting process and then after their use for the different SPM technique tests, mostly by high resolution SEM. Additional characterization techniques such as High-Resolution Transmission Electron Microscopy (HRTEM) and Raman spectroscopy were also used to check on the structural integrity and apex dimensions of the probes before and after being used in different SPM tests. The HRTEM images already reported in *Chapter 2* (**Ch.2-Figs.22 and 23**) allow roughly estimating the apex radius of the cone tips. Apex radii *R1* and *R2* for the as-synthesized carbon tips shown in **Figs.17a-17b** are 2.2 and 3 nm, respectively. However, depending on the surface characteristics to be investigated (for instance, a surface with a roughness below 1 nm) smaller morphological features of the apex surface other than the overall cone shape may prevail in the interaction with the substrate, such as the protruding detail arrowed in **Fig.17a**. Such an apex is likely to be efficient in revealing atom-scale details in flat substrate surface. Therefore, the tip performances are fairly dependent on the way the cone apex or the supporting nanotube breaks, which is not controlled so far.

[17] Attempts carried-out by T. Ondarçuhu (IMFT, Toulouse)

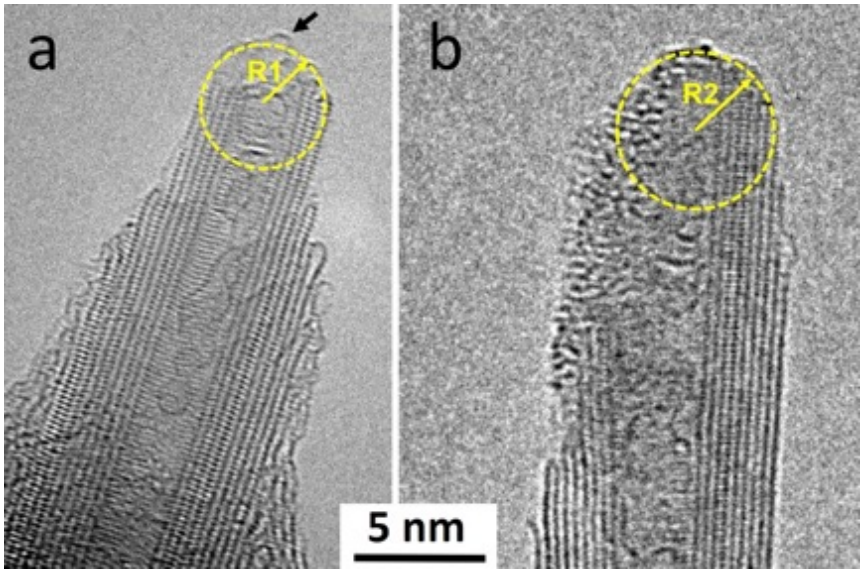

Figure 17. (a) *and* ***(b)*** *Estimating the apex radius of the two different as-synthesized carbon nanocone tips shown in* ***Ch.2-Figs.22 and 23****, respectively. It is reminded that the images are considered to be reasonably reliable and representative of the pristine cone apices as the TEM was operated at 80 keV.*

4.3. Tip alignment

Secondary electron images from the SEM Zeiss 1540 XB were systematically used to characterize the geometrical aspects (length, angle orientation) of the mounted probes, and several examples were provided in the previous figures. The objective was to image the general shape of the probes (before conducting the SPM tests) and then evaluate any change brought by the test type and conditions. Particular attention was paid to the alignment of the cone axis with respect to the symmetry plane of the cantilever (which contains the groove axis). This alignment can be defined by two deviation angles, i.e. the out-of-plane angle θ and the in-plane angle φ between the cone axis and the groove axis, depicted in the red and blue square respectively (see **Figs.18a-18b**).

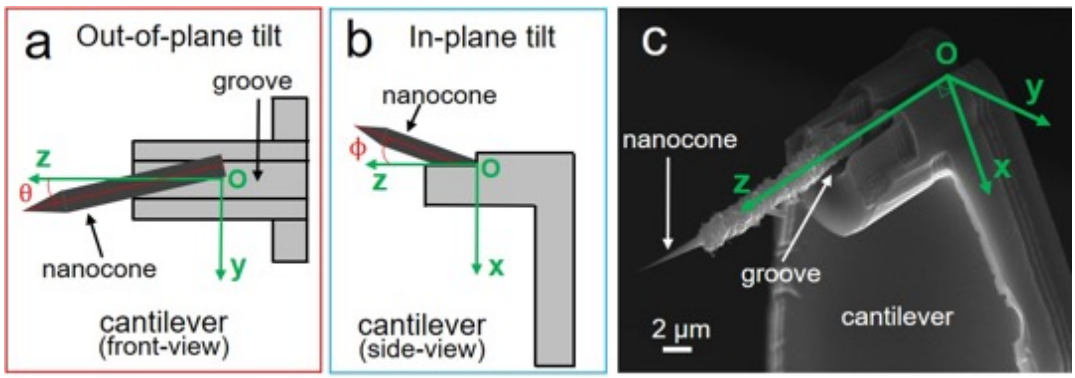

Figure 18. *Illustration of the geometric angles of interest using the example of a probe already mounted onto a cantilever. The scheme within the red and blue squares show the front and side views of the cone alignment as a function of spherical coordinates ((θ, φ) respectively). φ corresponds to the in-plane angle (with the reference plane being the symmetry plane of the cantilever, which contains the groove axis) formed by the cone morphology axis and the Z axis (i.e. the groove axis, perpendicular to the cantilever). θ is the out-of-plane angle (with respect to the cantilever groove axis) formed by the cone morphology axis and the Z axis (the groove axis).*

To achieve the best imaging performances, θ should be as low as possible, tending to zero, while φ should ideally tends to 11-13° in order to compensate the tilt angle of the cantilever holder (see **Fig.5**). As it was previously showed, the mounting procedures, either by gluing or welding, allow a limited control of those angles, with a poor accuracy. Therefore, based on qualitative criteria only, the SEM characterization was mostly similar to a quality-control step in order to qualify or not the carbon probes for being used for subsequent SPM tests and which ones, and also to build an SEM image bank to which we could refer in order to possibly relate any anomaly in the SPM images obtained to any specific geometric of the probe used.

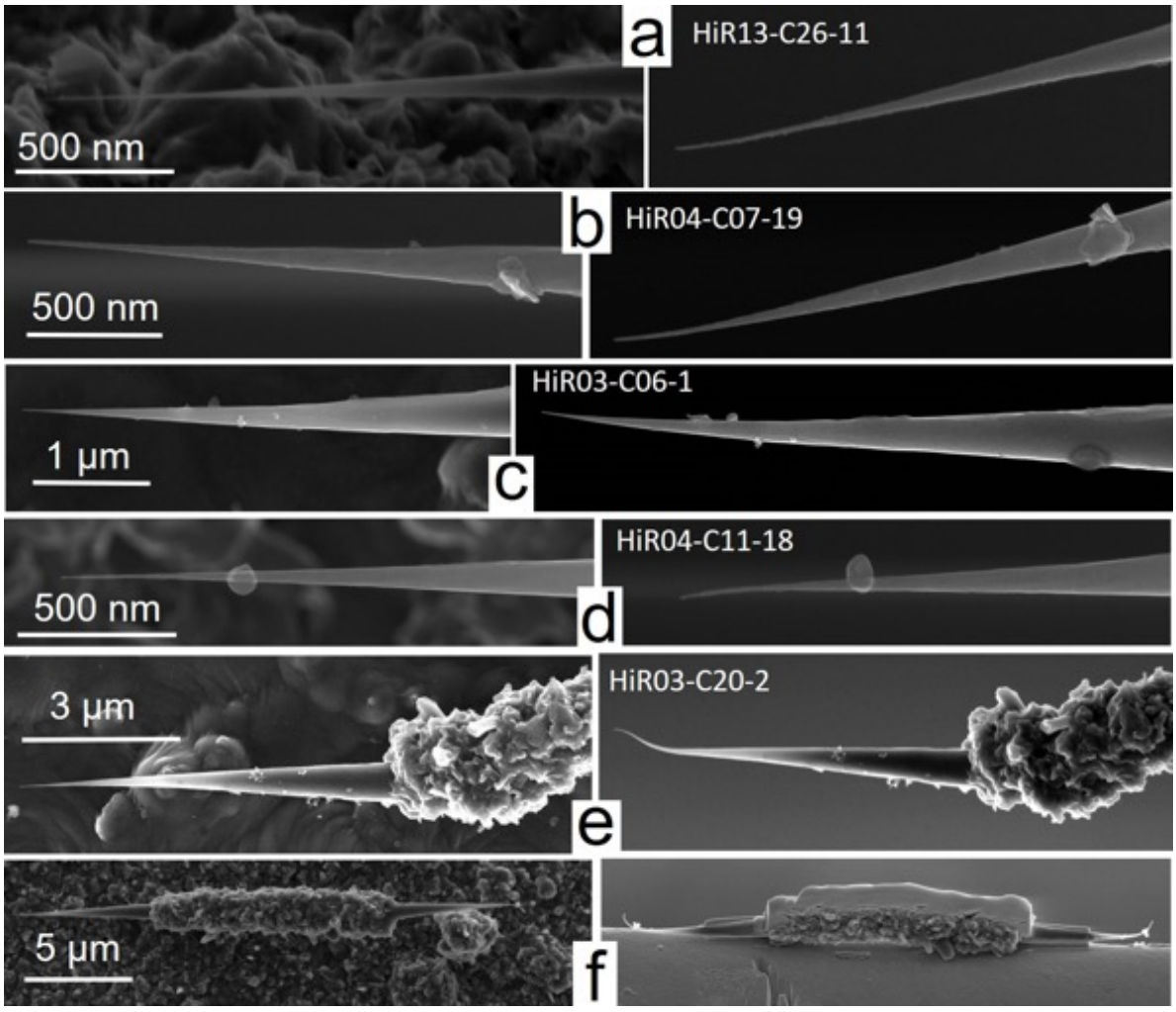

Figure 19. *From* ***(a)*** *to* ***(f)****: Examples of increasing curvatures induced to the cone due to the presumably increasing effect of the Ga ion beam in the HELIOS dual Beam SEM-FIB. Left images: as-prepared, on the growth substrate, before grabbing with the micromanipulator. Right images: after mounting onto the cantilever. Probe numbers are embedded.* ***(f)*** *morphology selected and then extensively welded onto a Cu support prior to preparing a longitudinal cross-section of it by FIB ablation.*

As said in *Section 3.2.3*, we first followed the mounting procedure previously established for mounting the cones as electron emitters at the apex of a W tip [*39Houdellier2012, 40Houdellier2015*]. This procedure was using the HELIOS Dual beam SEM-FIB and was including three times the use of the Ga ion beam: (*i*) for welding the morphology onto the single

rod micromanipulator (FIBID); (*ii*) for releasing the morphology from the rod and depositing it in the cantilever groove; (*iii*) for welding the morphology to the cantilever (FIBID). It was often observed that, as a result, the cone tip ended as being more or less curved (**Figs.19a to 19e**). Moreover, the curvature seemed to be proportional to the total dose received (i.e., the number of ions received over the cumulated exposure time) (**Figs.19a to 19f**). This was confirmed to result from the effect of the ion beam, as it did not happen – with very seldom exceptions - when using an ion-free mounting procedure (see **Fig.12e** for instance).

The mounting procedure finally adopted the ZEISS cross beam SEM-FIB, which allows the FEBID instead of FIBID, and is equipped with a genuine tweezer manipulator which is able to grab and release the morphology without any welding step (see *Section 3.2.3*).

4.4. Structural integrity of the carbon cone once mounted as a probe

SEM images such as that in **Fig.19** suggested some damage brought to the cone structure. The apex radius of some tips as well as the structure integrity of the carbon cone probes were then tentatively evaluated by High Resolution Transmission Electron Microscopy (HRTEM) and/or Raman spectroscopy.

4.4.1. High Resolution Transmission Electron Microscopy (HRTEM)

TEM uses a source of electrons focused on the sample by means of electromagnetic lenses. The TEM electron source is very energetic (60 to 300 keV) relatively speaking, which allows the electrons to pass through the sample volume (provided it is less than few-hundred-nanometer thick) and taking real time projected images of the structure, texture, and nanotexture. A thin sample is required in order to favor the elastic sample-electron interactions responsible for generating the images. Most of the time, the samples are deposited onto a copper grid to be introduced in the microscope (this is how images from **Ch.2-Figs.5, 7,** and **Ch.2-Figs.22 to 24** were obtained, for example). As the cones were mounted on cantilevers, a special TEM specimen holder previously modified at CEMES for this purpose was used to put a whole cantilever into the microscope (**Fig.20b**). HRTEM was used mainly to study the cone apex of probes as depicted in **Fig.20**. The structure and nanotexture of the cone apices right after the synthesis process (**Fig.20a**) were taken as reference for evaluating the possible evolution of the carbon integrity once the cones are mounted on the cantilevers and/or tested as probes. As depicted in **Figs.20c** to **20e**, the structural integrity of the tips appeared to be systematically affected whatever the probe mounting process.

Probes mounted by FIBID were investigated by a TEM (FEI Titan SACTEM FEG) operated at 80 kV. An extensive yet variable degree of amorphization of the carbon material over lengths of several hundred nanometers up to 1-2 micrometers away from the apex, and a significant increase of the apex radius of the tip were observed (**Figs.20c-d**). Rapidly, for cone diameters above ~100 nm, it cannot be said whether the amorphization affects the bulk or only the cone surface, and if so, how deep, because of the 2D-projection effect and the penetration limit of the electron beam. In some cases (**Fig.20c**), the amorphization of the cone tip appears to be surface only, but this is only what remains from the tip.

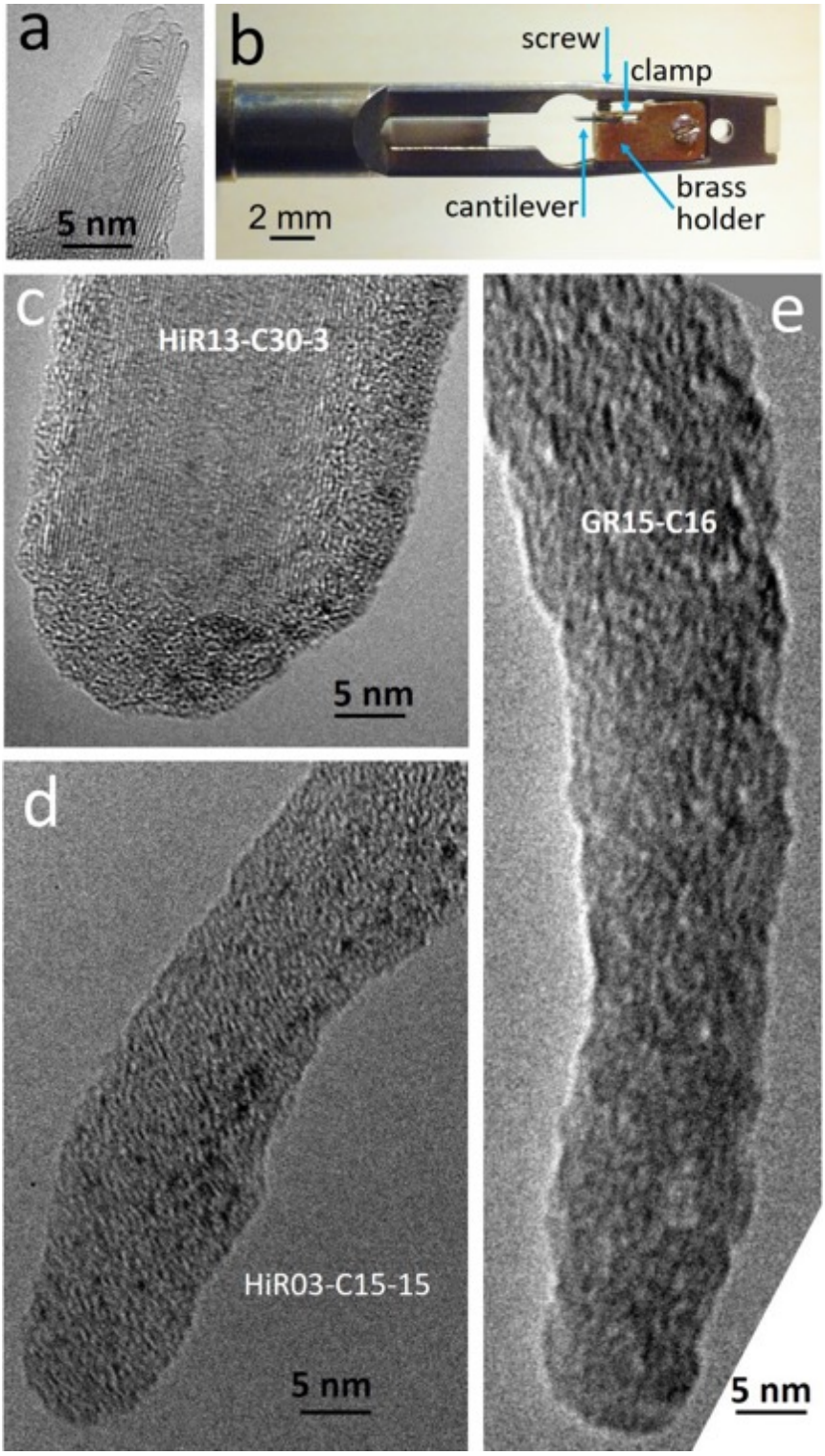

Figure 20. (a) *HRTEM image of the apex of an as-synthesized carbon cone, for comparison with images (c) to (e) at the same scale; an enlarged version is provided in* ***Ch.2-Fig.22d. (b)*** *Detail of the modified TEM holder used to investigate carbon cones when mounted as SPM probes.* ***(c)*** *to* ***(e)*** *Examples of HRTEM images of carbon probe apices when mounted:* ***(c)*** *and* ***(d)*** *using the FIBID process in the HELIOS SEM-FIB; dark spots in both images are assumed to be gallium atoms or clusters, preferably to Pt or W (the welding materials);* ***(e)*** *using the gluing process. Images in (a), (c), and (d) were taken with a FEI TITAN FEG-SACTEM operated at 80 kV (INA, Saragoza. Image credit: R. Arenal). Images in (d) and (e) were taken with a FEI TECNAI F20 FEG-SACTEM operated at 100kV (image credit: S. Joulié, CEMES).*

It is very likely that the large increase of the tip radius was mostly due to the shortening of the thinnest portion of the cone end rather than to a swelling effect resulting from the structure change. This is somehow consistent with the literature, as FIBID Pt deposition was acknowledged to provoke higher disorder and impurity content than FEBID by the presence of a higher concentration of Pt grains in the material as well as possible Ga ion implantation [*28DeTereza2009*]. Furthermore, ion beam was found to be able to break C-C bonds and change the structural properties of carbon materials at least when elevated voltages are used [*27Raghuveer2004, 46Krasheninnikov2010*][18]. An important statement is that, in spite of the relatively low voltage, it was observed that the carbon material from the tips was quite sensitive and amorphized rapidly under the electron beam, so that it was impossible to determine which extent of the amorphization was due to the mounting process and to the TEM observation, respectively.

More surprisingly, probes mounted by gluing (**Fig.20e**), which were also investigated later on by TEM (FEI Tecnai F20 SACTEM FEG), this time operated at 100 kV, also appeared quite sensitive to the electron beam and amorphized quite rapidly while their apices were investigated. Therefore, the final amorphization observed in the image of **Fig.20e** is the result of the in-TEM electron irradiation, not the result from the mounting process, which would have been unlikely anyway as the gluing does not include any step of irradiation by electrons or ions.

A consequence of the observations above is that the TEM technique was found to be useless for assessing the extent of damages brought by the irradiation episodes during the mounting processes because it is itself destructive, even when operated at voltages in the range 80-100 kV, i.e., around the limit or below the energy needed to promote C-C bond breaking and knock-on atom displacements [*47Banhart1999, 48Smith2001*]. TEM is also useless for merely characterizing probe apices before use since, as the result from the TEM investigation, the probes would be subsequently too damaged to be used.

This high sensitivity of the carbon cones, especially at their apex, to electron irradiation in the energy range used (80 or 100 keV) during our TEM investigation was unexpected, as it is atypical for carbon nano-objects with very similar texture and nanotexture such as arc-prepared concentric MWCNTs, and even for SWCNTs. For instance, an electron energy threshold of 86 keV was calculated for a safe TEM investigation of SWCNTs [*48Smith2001*], although they are even more sensitive to electron irradiation than MWCNTs [*47Banhart1999*]. There might be two reasons, both related to the occurrence of structural defects. One is the presence of graphene edges and other defective terminations such as loops and "zips" in our carbon cones (as evidenced in *Chapter 2* and further discussed in the next *Section)* while there is none in MWCNTs. Another is the increased sensitivity of defective carbon lattices to irradiation. This was observed for instance in SWCNTs increasingly altered by chemical treatments [*49Monthioux2001*]. In both cases – defective structure and graphene edges - undercoordinated carbon atoms are involved, which generate a higher sensitivity to irradiation as compared to fully coordinated carbon atoms [*50Krasheninnikov2005*]. This might then

[18] However, for FEBID, in our case, an acceleration voltage as low as 2 kV along with quite short exposition times (few seconds) were employed.

explain why cones with full structural integrity (represented by as-synthesized cones, and also presumably by cones mounted as SPM probes by gluing) withstand a TEM 80 keV electron beam (**Fig.20a** for instance, and other examples in *Chapter 2*) but not a TEM 100 keV electron beam (**Fig.20e**), whereas cones previously damaged by the FIBID welding process cannot even withstand a TEM 80 keV electron beam (**Figs.20c-d**).

Raman spectroscopy investigation was then attempted.

4.4.2. Raman spectrometry

For comparing with TEM results, various carbon cones mounted as SPM probes were placed instead of the Ag standard probe on a TERS equipment for studying their structural integrity, as already reported in *Chapter 2*, where it was used to obtain the Raman signature of the as-synthetized carbon cones (*Section 2.4.2* in *Chapter 2*). Thus, the obtained Raman spectra of the nanocone probes were also used to evaluate the effect of each mounting technique described in *Section 3.2* (i.e., gluing, FIBID, FEBID) on the final structural and nanotextural quality of the probes, as depicted in **Fig.21**.

The statement made above that the occurrence of defects in a graphenic structure is able to enhance its sensitivity to irradiation effects could have questioned the assumption we made earlier (*Section 3.2.2*) that carbon cones mounted as probes by gluing with the UV-curable resin maintain their structural integrity because the power and wavelength of the UV irradiation lamp used is not in the range of absorption of graphene cylinders. But the latter is right for CNTs, which exhibit no defective graphene terminations as opposed to cones, which exhibit many. Would it be possible that those defective terminations might make the cones, at least the cone surface, also likely to be somewhat damaged by the UV conditions? As the TEM investigation is not always able to provide reliable structural information of our carbon cones, the Raman investigation reported at the end of *Chapter 2* (*Section 2.4.2*) fortunately provided structural information on glued cones that is reasonably consistent with the structural information obtained by 80 kV-TEM on as-synthetized cones. Therefore, a SSF morphology mounted by the gluing technique was taken as the reference material (top spectrum) to compare with the cones mounted with the welding procedures which are suspected to affect the graphenic structure in various extent, based on the TEM study.

In this set of experiments, conditions were similar to that used in *Chapter 2* for producing **Ch.2-Fig.25**. The laser probe was focused far from the apex, on the junction between the fiber segment and the cone base, thereby partly overlapping both. This experimental choice was preferred because the apices left after each of the mounting processes are not really comparable, since the TEM investigation showed that they have been shortened in various extent, hence, from a carbon cone to another, the Raman laser would have probed different volumes with variable and non-significant contribution from the material surface. **Fig.21** shows significant differences between the SSF morphology welded by FIBID (bottom spectrum), that welded by FEBID (middle spectrum), and that merely glued by the UV-curing resin, hence not subjected to any ion or electron irradiation step:

- For the gluing-prepared probe, the spectrum is consistent with those already shown in **Ch.2-Fig.25**. The I_D/I_G ratio (0.45) is in the same range as spectra A or B in **Ch.2-Fig.25** (0.47 and 0.40, respectively), probably in accordance with the proportion of short-fiber part probed by the laser spot in each spectrum. Same for the $I_D/I_{D'}$ ratio which equals 1.95 (to be compared with 2.2 and 1.9 for spectra A and B, respectively, again referring to **Ch.2-Fig.25**).
- For the FEBID-prepared probe (middle), the graphenic nature is obviously maintained as the G, D', and 2D band intensities remain unchanged, as well as the G band linewidth (~20 cm^{-1}), but an increase of defects is observed as revealed by the significant increase of the D band relative intensity (I_D/I_G ratio up to 0.85), and of the $I_D/I_{D'}$ ratio which reaches a value of 3.75 now corresponding to a prevalence of other defects in defective graphenic materials (see **Ch.2-Table5** and the related discussion).
- Finally, for the FIBID-prepared probe (bottom), the spectrum typical of graphenic materials was replaced by a spectrum typical of amorphous carbon, where the D and G bands merge to form a broad band, and where the 2D band is no longer observed.

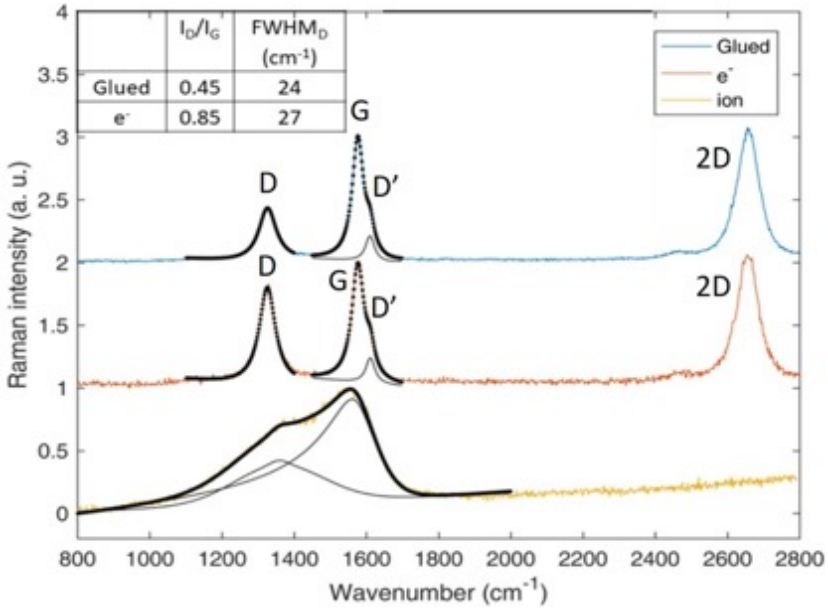

Figure 21. *Raman spectra (with the fitting as the heavy, black solid line) recorded on the cone/short-fiber junction of three different SSF morphologies mounted onto cantilevers as AFM probes by the three different procedures described in Section 3.2: bottom (yellow line): Pt deposition induced by focused ions (FIBID); middle (red line): Pt deposition induced by focused electrons (FEBID); top (blue line): gluing with a UV-curable resin. In the top-left inset are provided the I_D/I_G height ratio, as well as the linewidth of the D band for the two carbon probes exhibiting the regular D + G (+ 2D) bands typical of graphenic carbon materials.*

This experiment provides useful information in a more reliable way than the previous TEM results. Considering that the laser probe only penetrates over ~20 nm[19] in the carbon material, the spectra obtained are mostly representative of the surface state, not of the bulk. Only the use

[19] The Raman probe penetration depth can be calculated as $\lambda/(8\ \pi.\kappa)$ = ~18 nm, where λ is the incoming wavelength, and κ is the extinction coefficient [*51Blake2007, 52Weber2010*].

of focused ions (FIBID) heavily amorphizes the carbon material surface, whereas the use of focused electrons (FEBID) only increases the surface concentration of defects. For the cone mounted using focused electrons (FEBID), the linewidth of the D band (24-27 cm^{-1}) as well as that of the G band (19.3 and 20.8 cm^{-1}) remain nearly constant while only the I_D/I_G ratio strongly increases. According to Cançado *et al*., this reveals an increase of point defect concentration (e.g., interstitial atom, substitutional atom, vacancy) preferably to line defects (e.g., screw or edge dislocation) [*53Cançado2017*], which is consistent with an effect of irradiation damages.

Interestingly then, this set of experiments (including the Raman study reported in *Chapter 2*, around **Ch.2-Fig.25** and **Ch.2-Table5**) provides another evidence, in addition to the work by Eckmann *et al*. [*54Eckmann2012*], for the statement that the D' band is not merely a subsidiary of the D band, and why.

5. Conclusions

The feasibility and limitation of preparing carbon-cone-based SPM probes: Diverse techniques of mounting SSF morphologies on purposely designed Sb-doped Si support-cantilevers as SPM probes have been tried, namely gluing, FIBID, and FEBID. More than 130 probes of the various kinds (non-conductive AFM type, conductive AFM-type, and STM type) were fabricated in total.

The accurate, controlled positioning and alignment of the carbon cones with respect to SPM standards and compared to regular Si-probes could not be achieved. Although using the micromanipulators was actually not a reproducible process indeed, the main reason for the frequent misalignment is the intrinsically poor alignment of the cone axis with respect to the short-fiber axis in the as-prepared SSF morphology. This will prevent to exploit the high aspect ratio of the carbon cones in their application as SPM probes so far, until this problem is fixed.

The role of carbon cone surface defects in their processability: The carbon cones morphologies appeared to be very sensitive to irradiation effects, either by means of electrons or Ga ions, actually more sensitive than carbon nanotubes. Because the irradiation-promoted amorphization starts with the surface, it may affect the whole carbon cone tips over variable cone length, because of their dimensions in the nanometer range. Such a sensitivity was attributed to the presence of a large amount of defective graphene terminations (free edges, loop-like defects, zip-like defects) at the cone surface, as compared to carbon nanotubes. This prevents any reliable structural and nanotextural investigation of the as-prepared carbon cones to be carried-out by HRTEM operated at 100kV, for which a maximum of 80 kV is required.

Furthermore, the sensitivity to electron beam irradiation increases as the number of defects increases. This makes that carbon probes prepared by FIBID could not even withstand a 80 keV HRTEM investigation because of the severe structural damages (at least at the cone surface) induced by the FIBID process, which appeared to be highly destructive.

On the contrary, based on Raman results combined with those reported in *Chapter2*, carbon cones mounted using FEBID appeared to be only slightly affected by the process, whereas the gluing process appeared not to affect the cone structure at all (which, however, would benefit

from a confirmation of it by a 80 kV-HRTEM investigation yet to carry-out). Overall, the observations taught us to give-up with the FIBID process as a possible mounting procedure, and to prefer the gluing process in first place, and then possibly the FEBID process as an acceptable alternative.

The choice and limitation of the mounting processes: For optimizing the processing cost, the gluing method appeared to be the most effective as it is much faster than FIB-based methods (~20 minutes as opposed to 2 hours, for the fastest) and only requires a micromanipulator operated under an optical microscope (as opposed to the need of a micromanipulator operated under a Dual-beam FEG-SEM/FIB, which is an expensive equipment). In addition, it leaves the carbon structure presumably unaffected.

However, a significant drawback is that the SPM probes obtained this way are only valid for non-conductive modes because of the insulating role of the resin as an interphase between the carbon probe body and the doped-Si support-cantilever. On the other hand, the benefit of the FEBID mounting process is that the SPM probes obtained this way can be truly multimodes, i.e., operable with either conductive or non-conductive SPM modes provided enough electrical conductivity is maintained despite the surface amorphization. Consequently, FEBID-prepared carbon probes will also be used in the results reported in the next *Chapter*, in which the wear resistance characteristics of the nanocone probes mounted by the different mounting methods as well as their performances for imaging different substrate samples following conductive and non-conductive SPM techniques will be reported.

Results from this *Chapter* were partially published as [*55Puech2019*].

References

1. Eaton P., West P**.** ***Atomic Force Microscopy*****.** *(*Hbk) Oxford University press (2010). *ISBN 978–0–19–957045–4*
2. Wilson N., Macpherson J. V. *Carbon nanotube tips for atomic force microscopy*. **Nature Nanotechnol.** 4 (2009) 483-491.
3. *The world market for Atomic Force Microscopies and AFM probes*. **Future Markets, Inc**. www.futuremarketsinc.com (2011).
4. Bhushan B., Marti O., *Scanning Probe Microscopy - Principle of operation, instrumentation, and probes.* In: **Handbook of Nanotechnology** (ed. Bhushan B.), Chapter 21, Springer-Verlag, Heidelberg, Germany (2010) pp.573-617.
5. Nguyen C. V., Ye Q., Meyyappan M. *Carbon nanotube tips for scanning probe microscopy: fabrication and high aspect ratio nanometrology*. **Sci. Technol.** 16 (2005) 2138-2146.
6. Stevens R. M. *New carbon nanotube AFM probe technology.* **Mater. Today** 12 (2009) 42-45.
7. Marsaudon S., Bernard C., Dietzel D., Nguyen C. V., Bonnot A.-M., Aimé J.-P., Boisgard R. *Carbon nanotubes as SPM tips: mechanical properties of nanotube tips and imaging*. In: **Applied Scanning Probe Methods VIII, Nano Science and Technology** (Bhushan B., Fuchs H., Tomitori M., eds.), Springer, Berlin, Heidelberg (2008).
8. Agrawal D. H., Bhatt P.M. Pathan A. M. *A portable experimental set-up for AFM to work at cryogenic temperature*. Conference on Recent Trends in Engineering Technology, **AIP Conf. Proc. 1447** (2012) 531.
9. Hu X., Wei H., Deng Y., Chi X., Liu J., Yue J., Peng Z., Cai J., Jiang P., Sun L. *Amplitude response of conical multiwalled carbon nanotube probes for atomic force microscopy*. **Roy. Soc. Chem. Adv.** 9 (2019) 429-434.
10. Rusell P. *AFM Probe Manufacturing Nanoworld_Tip_Technology*. Appalachian State Univ. Slides obtained by Courtesy of: O. Krause, NanoWorld Services GmbH, Webinar November 2018.

11. Guo L., Wang R., Xu H., Liang J. *Wear-resistance comparison of carbon nanotubes and conventional silicon-probes for atomic force microscopy*. **Wear** 258 (2005) 1836–1839.
12. Rodriguez B. J., Jesse S., Seal K., Baddorf A. P., Kalinin S. V., Rack P. D. *Fabrication, dynamics, and electrical properties of insulated scanning probe microscopy probes for electrical and electromechanical imaging in liquids*. **Appl. Phys. Lett.** 91 (2007) 093130.
13. Brown J., Kocher P., Ramanujan C. S., Sharp D. N., Torimitsu K., Ryan J. F. *Electrically conducting, ultra-sharp, high aspect-ratio probes for AFM fabricated by electron-beam-induced deposition of platinum.* **Ultramicrosc.** 133 (2013) 62–66.
14. Ye Q., Cassell A. M., Liu H., Chao K.-J., Han J., Meyyappan M. *Large-scale fabrication of carbon nanotube probe tips for atomic force microscopy critical dimension imaging applications*. **Nano Lett.** 4 (2004) 1301-1308.
15. Dai H., Hafner J. H., Rinzler A. G., Colbert D. T., Smalley R. *Nanotubes as nanoprobes in scanning probe microscopy*. **Nature** 384 (1996) 147-150.
16. Bernard C., Marsaudon S., Boisgard R., Aimé J.-P. *Competition of elastic and adhesive properties of carbon nanotubes anchored to atomic force microscopy tips*. **Nanotechnol.** 19 (2008) 035709.
17. Treacy M M J., Ebbesen T W., Gibson J.M. *Exceptionally high Young's modulus observed for individual carbon nanotubes.* **Nature** 381 (1996) 678-680.
18. Wong E. W., Sheehan P. E., Lieber C. M. *Nanobeam mechanics: elasticity, strength, and toughness of nanorods and nanotubes*. **Science** 277 (1997) 1971-1975.
19. Hantschel T., Tsigkourakos M., Zha L., Nuytten T., Paredis K., Majeed B., Vandervorst W. *Diamond scanning probes with sub-nanometer resolution for advanced nanoelectronics device characterization*. **Microelectron. Eng.** 159 (2016) 46–50.
20. Stevens R., Nguyen C., Meyyappan M. *Nanomanipulation and fabrication by ion beam molding.* **IEEE Trans. Nanotechnol.** 5 (2006) 255-25.
21. Martinez J., Yuzvinsky T. D., Fennimore A. M., Zettl A., Garcia R., Bustamante C. *Length control and sharpening of atomic force microscope carbon nanotube tips assisted by an electron beam*. **Nanotechnol.** 16 (2005) 2493–2496.
22. Liu P, Zhang Y. W., Lu C. *Molecular dynamics simulations of bending behavior of tubular graphite cones.* **Appl. Phys. Lett.** 85 (2004) 1778-1780.
23. Xu Z. W., Fang F. Z. *Configuration control of carbon nanotube probe in atomic force microscopy*. **J. Vac. Sci. Technol**. 27 (2009) 1388-1393.
24. Yuzvinsky T. D., Fennimore A. M., Mickelson W., Esquivias C., Zettl A. *Precision cutting of nanotubes with a low-energy electron beam*. **Appl. Phys. Lett.** 86 (2005) 053109.
25. Strus M. C., Raman A., Han C.-S., Nguyen C. V. *Imaging artefacts in atomic force microscopy with carbon nanotube tips.* **Nanotechnol.** 16 (2005) 2482-2492.
26. Slattery A., Blanch A. J., Quinton J. S., Gibson C. T. *Efficient attachment of carbon nanotubes to conventional and high-frequency AFM probes enhanced by electron beam processes*. **Nanotechnol.** 24 (2013) 235705.
27. Raghuveer M. S., Ganesan P. G., d'Arcy-Gall J., Ramanath G. *Nanomachining carbon nanotubes with ion beams.* **Appl. Phys. Lett.** 84 (2004) 4484-4486.
28. De Teresa J. M., Córdoba R., Fernández-Pacheco A., Montero O., Strichovanec P., Ibarra M. R. *Origin of the difference in the resistivity of as-grown focused-ion-and focused-electron-beam-induced Pt deposit*. **J. Mater.** (2009) 936863.
29. Dremov V., Fedoseev V., Fedorov P., Grebenko A. *Fast and reliable method of conductive carbon nanotube-probe fabrication for scanning probe microscopy.* **Rev. Scientif. Instr.** 86 (2015) 053703.
30. Hafner, J. H., Cheung, C. L. & Lieber, C. M. *Growth of nanotubes for probe microscopy tips*. **Nature** 398 (1999) 761–762.
31. de Jonge N., Lamy Y., Kaiser M. *Controlled Mounting of Individual Multiwalled Carbon Nanotubes on Support Tips.* **Nano Lett.** 3 (2003) 1622-1624.
32. Rius G., Yoshimura M. *Cooperative multiwalled carbon nanotubes for enhanced force spectroscopy*. **J. Surf. Sci. Nanotechnol.** 10 (2012) 341-345.
33. Hafner J. H., Cheung C. L., Lieber C. M. *Direct growth of single-walled carbon nanotube scanning probe microscopy tips.* **J. Am. Chem. Soc**.121 (1999) 9750–9751.

34. Marty L., Iaia A., Faucher M., Bouchiat V., Naud, C. Chaumont M., Fournier T., Bonnot. A.M. *Self-assembled single wall carbon nanotube field effect transistors and AFM tips prepared by hot filament assisted CVD***. Thin Solid Films** 501 (2006) 299-302.
35. *https://www.carbondesigninnovations.com/*
36. Delmas M., Monthioux M. CANAC project. Final report to ANR (2015).
37. Chen I.-C., Chen L.-H., Ye X.-R., Daraio C., Jin S., Orme C. A., Quist A., Lal R. *Extremely sharp carbon nanocone probes for atomic force microscopy imaging*, **Appl. Phys. Lett.** 88 (2006) 153102.
38. Berd M., Puech P., Righi A., Benfdila A., Monthioux M. *Resonant laser-induced formation of double-walled carbon nanotubes from peapods under ambient conditions*. **Small** 8 (2012) 2045–2052.
39. Houdellier F. Masseboeuf A., Monthioux M., Hÿtch M. J. *New carbon cone nanotip for use in a highly coherent cold field emission electron microscope*. **Carbon** 50 (2012) 2037-2044.
40. Houdellier F., de Knoop L., Gatel C., Masseboeuf A., Mamishin S., Taniguchi Y., Delmas M., Monthioux M., Hÿtch M. J., Snoeck E. *Development of TEM and SEM high brightness electron guns using cold-field emission from a carbon nanotip*. **Ultramicrosc**. 151 (2015) 107-115.
41. De Teresa J. M., Córdoba R., Fernández-Pacheco A., Sangiao S., Ibarra M. R. *Nanoscale Electrical Contacts Grown by Focused Ion Beam (FIB)-Induced Deposition*. In: **FIB Nanostructures** (Wang Z. M., ed.), Chapter 5, Lecture Notes in Nanoscale Science and Technology Series, vol.20, Springer International Publishing Switzerland (2013) pp.95-122.
42. Wade L. A., Shapiro I. R., Ma Z., Quake S. R., Collier C. P. *Correlating AFM probe morphology to image resolution for single-wall carbon nanotube tips*. **Nano Lett.** 4 (2004) 725-731.
43. Fujita D., Itoh H., Ichimura S., Kurosawa T. *Global standardization of scanning probe microscopy*. **Nanotechnol.**18 (2007) 084002.
44. Tian F., Qian X. P., Villarrubia J. S. *Blind estimation of general tip shape in AFM imaging*. **Ultramicrosc.** 109 (2008) 44-53.
45. Han G., Jian Z., Jing W., Prewett P. D., Jiang K. *Estimation of AFM tip shape and status in linewidth and profile measurement.* **J. Nanosci. Nanotechnol.** 11 (2011) 11041-11044.
46. Krasheninnikov A. V., Nordlund K. Ion and electron irradiation-induced effects in nanostructured materials. **J. Appl. Phys.** 107 (2010) 0701301.
47. Banhart F. *Irradiation effects in carbon nanostructures*. **Rep. Prog. Phys.** 62 (1999) 1181–1221.
48. Smith B. E., Luzzi D. E. *Electron irradiation effects in single wall carbon nanotubes.* **J. Appl. Phys.** 90 (2001) 3509-3515.
49. Monthioux M., Smith B. W., Burteaux B., Claye A., Fischer J. E., Luzzi D. E. *Sensitivity of single-wall carbon nanotubes to chemical processing: an electron microscopy investigation*. **Carbon** 39 (2001) 1251–1272.
50. Krasheninnikov A. V., Banhart F., Li J. X., Foster A. S., Nieminen R. M. *Stability of carbon nanotubes under electron irradiation: Role of tube diameter and chirality*. **Phys. Rev. B** 72 (2005) 125428.
51. Blake P., Hill E. W., Castro Neto A. H., Novoselov K. S., Jiang D., Yang R., Geim, A. K. *Making graphene visible*. **Appl. Phys. Lett**. 91 (2007) 063124.
52. Weber J. W., Calado V. E., Van De Sanden M. C. M. *Optical constants of graphene measured by spectroscopic ellipsometry*. **Appl. Phys. Lett.** 97 (2010) 091904.
53. Cançado L.G., Da Silva M.G., Ferreira E.H.M., Hof F., Kampioti K., Huang K., Pénicaud A., Achete C.A., Capaz R.B., Jorio A. *Disentangling contributions of point and line defects in the Raman spectra of graphene-related materials*. **2D Mater.** 4 (2017) 025039.
54. Eckmann A.; Felten A.; Mishchenko A.; Britnell L.; Krupke R.; Novoselov K. S.; Casiraghi C. *Probing the nature of defects in graphene by Raman spectroscopy*. **Nano Lett.** 12 (2012) 3925–3930.
55. Puech P., Kandara M., Paredes G., Moulin L., Weiss-Hortola E., Kundu A., Ratel-Ramond N., Plewa J.-M., Pellenq R., Monthioux M. *Analysing the Raman spectra of graphenic carbon materials from kerogens to nanotubes: what type of information can be extracted from defect bands*. **Journal of Carbon Research** 5 (2019) 69.

-Chapter 4 -

Application tests of carbon nanocone probes for different SPM modes

« ... No te rindas que la vida es eso,
continuar el viaje,
perseguir tus sueños,
destrabar el tiempo,
correr los escombros y destapar el
cielo... »

Mario Benedetti

Chapter 4: Application tests of nanocone probes for different SPM modes

1. Introduction

At the early beginning of the SPM developments, only the conductive STM mode existed [*1Eaton2010*]. Then, the need of studying more kinds of samples has motivated the development of the AFM technique. At that time, AFM was mainly used for topographic studies. However, thanks to the rapid technological evolution, more than 20 SPM modes (most of them AFM-related) are now currently used[*1Eaton2010*], allowing to combine both topographical images and spectroscopy measurements on a variety of samples [*1Eaton2010*]. Consequently, probes with suitable geometrical characteristics and physical properties (*i.e.* electrical conductivity, magnetic or mechanical properties) are more and more required. In such a landscape, multimode probes should be highly preferred, but they are quite seldom on market, and dedicated probes are more frequent by far. This chapter deals with testing the use of carbon cone-based probes for some of the possible modes, that we chose to classify in two main categories:

(i) non-electrical modes such as "regular" (topographical) AFM and Peak-Force Quantitative Nanomechanical AFM (PFQNM AFM),

(ii) electrical modes such as Conductive AFM (C-AFM), Scanning Tunnel Microscopy (STM), and Kelvin Force Microscopy (KFM).

2. Non-electrical modes

In this section, we refer as non-electrical SPM modes those which do not require electrically conductive probes. In this case, the interaction forces studied between the probe and the surface involves very short- and short-range forces such as interaction repulsive and contact forces as well as van der Waals and capillary forces.

Most of those modes are dedicated to the study of topographic and/or mechanical properties of sample surfaces, for which the trade-off between high aspect ratio and mechanical rigidity of the probes is particularly important.

2.1. Atomic Force Microscopy (AFM)- Topography[20]

2.1.1. Principle and notions

Atomic Force Microscopy (AFM)-Topography can be considered as the basis of all AFM-related techniques. The main objective is to obtain an accurate image of the topology (*i.e.* height mapping) of a sample surface by measuring the force interactions between the surface of the sample and the scanning probe. Depending on the type of physical tip-sample interactions, topographic modes can operate in two main ways: static or dynamic [*1Eaton2010*]. Under the static mode (most known as contact-mode), the probe is in direct contact with the surface as depicted in **Fig.1a**, which induces repulsive forces responsible for a cantilever deflection, friction, or torsion. This cantilever response leads directly to a sample topography. On the other hand, in the dynamic mode (either non- or intermittent-contact mode, most known as tapping mode), a small distance of few nanometers exists between the probe tip and the surface, and a mechanical excitation of the cantilever near to its resonance frequency is set up (**Fig.2**)**.** The force detections are measured from a shift of either the frequency or the amplitude with respect to the cantilever oscillation set-up target value as illustrated in **Fig.1b**.

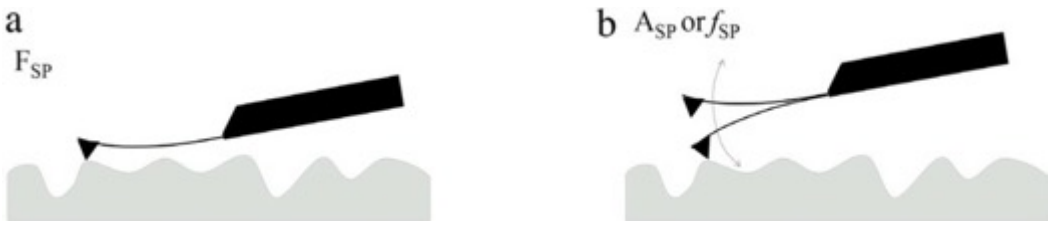

Figure 1: *Different tip-sample interactions.* ***(a)*** *contact mode, where* Fsp *is the contact force trigger value responsible of the cantilever deflection.* ***(b)*** *intermittent contact or tapping mode, where* A_{SP} *and* f_{SP} *(SP stands for set point), correspond to the target amplitude or frequency set point values respectively, allowing the tip-sample interaction detection. From[*2Zhang2018*].*

The choice of the topographic imaging mode is mainly determined by the sample and the goal of the study. For instance, contact mode is currently used for adhesion and friction studies [*2Zhang2018*]; non-contact mode is used for measuring long range forces such as electrostatic and magnetic ones [*2Zhang2018*]; and tapping mode is used for obtaining topography images and carrying-out mechanical studies [*3Strus2005*]. Consequently, all the AFM-topographical tests presented in this section were conducted in tapping mode, in air and room condition (exceptions will be specified).

The tapping mode was developed in the 90's. Its operating conditions are illustrated in **Fig.2a**. The tip-sample interaction forces are detected by a feedback signal (A_s), which controls the Z distance (piezo height). This signal is compared to the set point amplitude (A_o) and allow maintaining a constant cantilever deflection. Thus, a variation (decrease or increase) on the cantilever oscillation amplitude indicates a change on the tip deflection, hence a change on the tip-surface interaction ("contact tap" or not). A topography image of the sample can then be

[20] This part of the work was made in collaboration with G. Seine (CEMES).

obtained from the average of the cantilever oscillation signal A_s (feedback measurements). The AFM-tapping mode is actually the most used for AFM topographical imaging in air condition, because it operates using typical oscillation amplitudes between 1 and 100nm, which allow the probe going from the repulsive to attractive interaction force regimes (depending on the set point amplitude chosen), without entering in contact with the sample [*1Eaton2010, 3Strus2005*] (**Fig.2b**). This allows a large range of properties of a given sample to be probed while using less friction, which consequently reduces lateral forces. Limiting the latter is highly important for avoiding tip-sample damages, which is one of the main drawbacks when imaging in contact mode [*1Eaton 2010*]. Moreover, the tapping mode in air has also its own limitations, mostly related to its sensitivity to the environment conditions that can disturb the measurement (by inducing, e.g., parasitic noise and vibrations) and a slower data acquisition process caused by its feedback system cycle as shown in **Fig.2a**. In order to reduce these effects, other alternatives such as working in vacuum environment or using the "peak force" mode (explained in *Section 2*) can be considered [*2Zhang2018*].

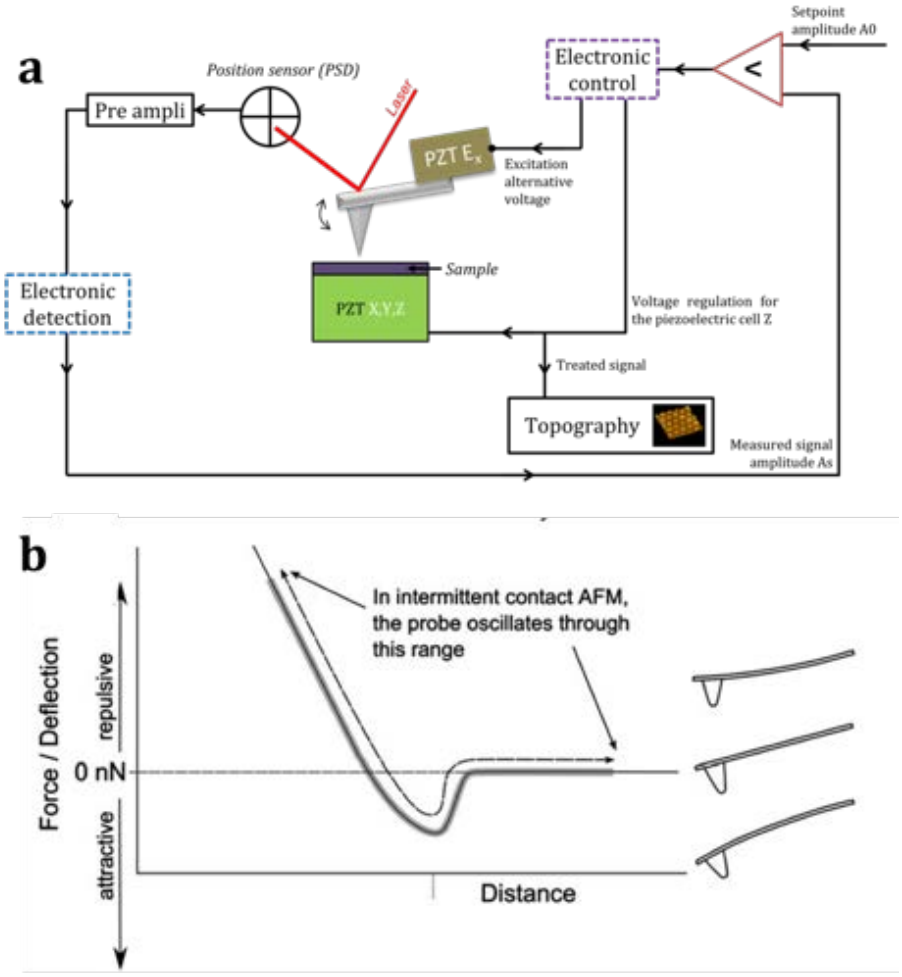

Figure 2: (a) *The operating condition of tapping mode-AFM: the three-dimensional position of the sample is controlled by a piezo-electric cell. The feedback or measured signal (A_s) is responsible for controlling the needed "Z" distance for maintaining the tip in a constant oscillation amplitude or set-point A_0. Finally, a topography image is created at the end of this iterative process.* ***(b)*** *An example of a force-distance curve showing the oscillation range involving the tapping mode AFM. Adapted from [*1Eaton2010, 4Palleau2011*].*

2.1.2. Imaging quality and performances

In topographic-AFM, the quality of the imaging (*i.e.* the most reliable representation of the sample characteristics) can be defined by its vertical and lateral resolution. The vertical resolution "Z" is given by the detection system (piezo) of the probe (**Fig.2**) as well as the electronic signal treatment; and it is estimated to be about 1 Å [*4Palleau2011*]. However, the lateral resolution is more complex to estimate as it involves many aspects. As shown in *Chapter 3*, it depends deeply on the tip (geometry, and tilt angle when mounted onto the cantilever), as well as on the sample nature. **Fig.3** presents a common illustration of the influence of the probe tip geometry on the lateral resolution on AFM tapping imaging. According to this, the ultimate lateral resolution can be defined as the minimal measurable separation distance d_{res} between two particles represented as spheres of radius R (i.e., equal to the probe apex radius)[21] for a Δz_r (i.e. the height of the depression between the two spheres seen in the image, as defined in **Fig.3**) equal for the least to the instrumental noise in the z direction, named Δz_{rmin}, which can be taken as the vertical resolution [*5Hafner2010*]. The lateral resolution limit d_{res} can then be evaluated as a function of the tip apex radius R and Δz_{rmin}, as shown in the expression below:

$$d_{res} = 2\sqrt{2.R.\Delta \mathrm{zr}_{min}} \quad (1)$$

One problem here is to estimate the instrumental noise in the vertical direction, i.e. Δz_{rmin}. A value commonly proposed is 0.1 nm, not considering the thermal noise [*4Palleau2011*].

It is worth noting that the definition above is not valid when reaching magnification range suitable for atomic resolution. In this case, the tip radius is no longer a criterion, and no equation to account for it actually exists as it depends on many other parameters at the atom scale, in addition to the surrounding conditions [*6Gan2009*].

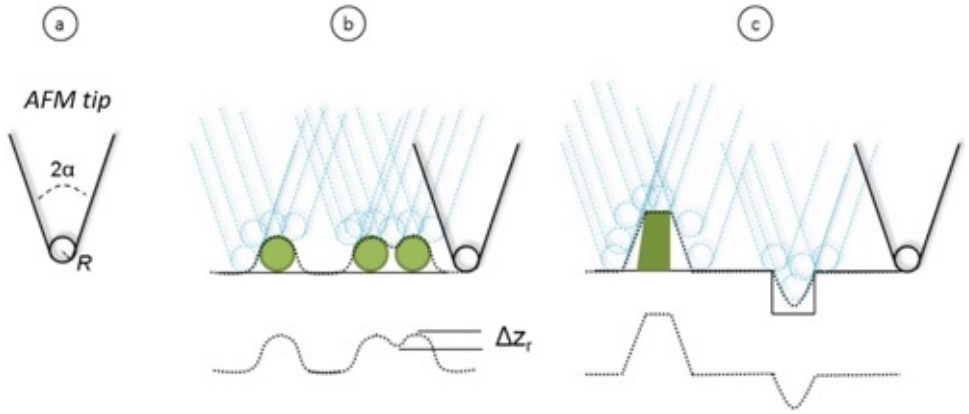

Figure 3: *Influence of the geometry of the probe in the topography resolution.* ***(a)*** *main geometric characteristic of an AFM-tip (R: apex radius, half angle α).* ***(b)*** *impact of the tip apex radius on the definition of nanoscale surface features.* ***(c)*** *Influence of the tip angle on the topographic images of high aspect surface features. From [*4Palleau2011*].*

[21] Indeed, a probe with an apex radius R will not be able to discriminate two adjacent spheres whose radii are smaller than R.

As shown on **Fig.3**, the misleading orientation (with respect to vertical) of the sidewall (half) angle of the tip can induce topographical artefacts that are well-known in the literature as angle artefacts [*3Strus2005*]. For this reason, the tip must be characterized before imaging. Aside from geometric aspects, other artefacts can occur, such as the so-called divot and ringing artefacts [*3Strus2005*]. The divot artefact is found to be linked to high aspect ratio probes, particularly when working on attractive force range. It appears when the transition from attractive to repulsive range is not very distinguishable, allowing two different tip-sample Z-distance to be recorded, yet related to the same probe amplitude. This kind of artefacts occurs mostly when imaging high aspect feature samples [*3Strus2005*]. On the other hand, the ringing artefact is found to occurs mostly in the case of very flexible probes such as carbon nanotube probes and it relates to a lateral bending, adhesion or stiction to trench or protuberance steep-wall surfaces [*3Strus2005*]. Some of these artefacts and other kinds of image distortion can be avoided by controlling the operating conditions from the early beginning of the so-called tip-engagement step (landing of the tip on the surface sample), and during the scanning process [*7Su2003*]. For avoiding tip damaging during engagement, protocols exist according to each AFM technique [*8Strus2009*]. However, controlling damages during the scanning process is a more complex task. In addition to considering the impact of the operating conditions (i.e. ratio of tapping amplitude and oscillation amplitude, scan size, feedback error, etc.), the mechanical properties (i.e. wear resistance, adhesion, stiffness) of the tip- material are supposed to be also considered [*8Strus2009, 9Bernard2008*]. Some adjustments of the acquisition parameters of the imaging can be easily done, for instance, by increasing the number of pixels for each line of the measured image in order to improve the digital resolution [*4Palleau2011*]. Moreover, conducting experimental studies of the mechanical behavior of the probes seems to be a grueling job [*3Strus2005, 9Bernard2008, 10Buchoux2009*]. Hence, few works addressing this subject are reported in the literature and most of them correspond to theoretical studies. Some authors [*11Larsen2002, 12Guo2005*] reported on wear resistance studies by making a qualitative comparison and correlations between the shape of the probes before and after topographic tests by using SEM images. On the other hand, when concerning the tip adhesion or elasticity forces, which can be present at the tip-sample interaction, the combination of theoretical and experimental "force spectroscopy" analysis methods [*8Strus2009, 9Bernard2008, 13Liu2004*] are the most used. These kinds of analysis are very useful for establishing the tip-sample interaction type, for adjusting the imaging protocol, and for globally understanding the performances of the topography imaging. This subject will be addressed in more details in *Section 2.2.*

In this Section, we evaluate the capability of the nanocone tip to resolve the topography of different types of sample surface. The quality, resolution, and reproducibility of the images are evaluated qualitatively by comparing with standard commercial silicon probes and the stability of the tip for long-time scanning is tested by means of a sample roughness measuring protocol.

2.1.3. Capability of the carbon nanocone as AFM probes

Taking as reference the apex radius value of 2-3 nm previously characterized (see **Ch.3-Fig.17**), a high lateral resolution of our nanocone probes was expected. Therefore, a whole set of AFM

imaging on a calibration substrate exhibiting deep trenches was made first, but the variability in the geometrical positioning of the tip with respect to the cantilever and the substrate made that results were not as accurate as expected (see *sections 4.2* and *4.3* in *Chapter 3*). As a consequence, the capability of the carbon nanocone probes for resolving tiny details and clearly separate different features of nanoscale samples was tested on different samples for which the cone misalignment has no or little importance: *(i)* a silicon wafer, *(ii)* Au nanoparticles supported on a doped-Si-wafer; *(iii)* a HOPG substrate. The nanocone probe performances were subsequently compared to those of silicon probes from Bruker whose main characteristics are described in **Ch.3-Fig.3**. The tests were conducted on the same substrates, and using the same operating parameters in a *multimode (Nanoscope IIIa) AFM* microscope from Bruker, operated in tapping mode-amplitude modulation feedback on air. Then, the images were treated by means of the WxSM software.

2.1.4. Sample description and imaging protocol and performances

a) Au nanoparticles deposited on Si wafer

100 µl of a solution of gold nanoparticles (25-100 nm) at 0.05 mg/ml (Tannic Nanoexact Gold JMW1019 from Nanocomposix company) was diluted in 100 µl of deionized water, and put into a sonication bath during 5 minutes. Then, a droplet of this solution was dispersed on a piece of doped-Si wafer of about 1 cm^2, previously cleaned using ethanol, and then dried in air (**Fig.4b**). A same surface of the prepared sample was scanned by one of our nanocone probes (**#GR11-C29-14**, see **Fig.4a**) and by two different silicon probes (**OTESPA-R3**, **TESP-SS**, see **Ch.3-Fig.3**)**.** All the probes were tested under the following conditions: scan size from 5 µm to 250 nm wide, scan speed of 2 Hz, and scan pixels of 256x256 points per line. The scanning process showed to be stable all along the acquisition.

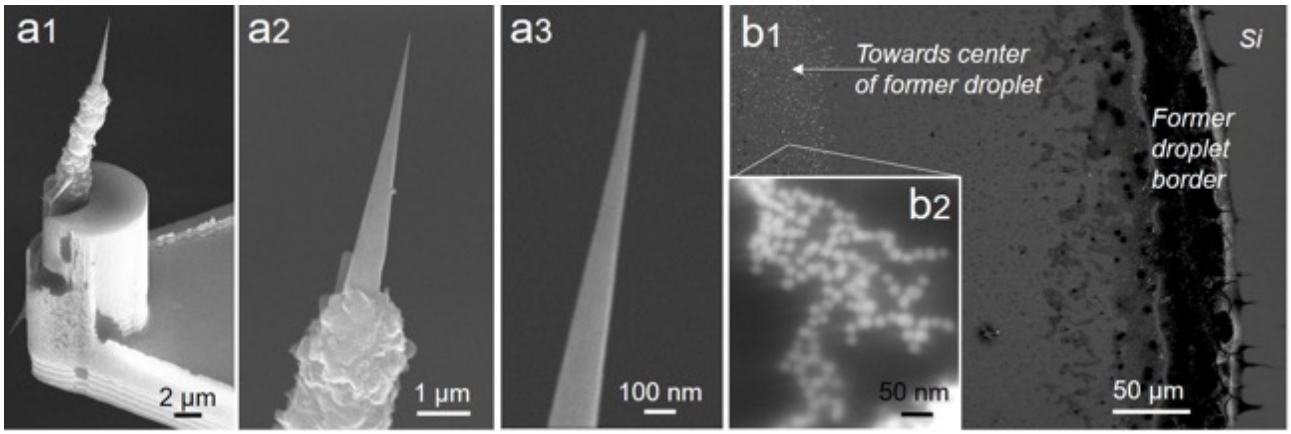

Figure 4: (a) *SEM images of the carbon nanocone probe* ***#GR11-C29-14****, mounted by the gluing process (photo credit: A. C. Torres-Dias, CEMES).* ***(b)*** *SEM images (back-scattered electrons) of the Au nanoparticles deposited onto a Si wafer as a droplet of a suspension of Au nanoparticles (image credit: S. Le Blond, UMS Castaing, Toulouse).*

Fig.5 shows the topographic image (left) and the height profile (right) of two neighbouring Au nanoparticles on the silicon substrate respectively obtained by the three different probes above-mentioned. From the image performed by the **Otespa-R3** silicon probe (**Fig.5a**), the two

nanoparticles appear to be merged into a single one with an overall length evaluated at about 165 nm. On the contrary, as an expected result from the differences in the probe characteristics, the **TESP-SS** probe (**Fig.5b**) is able to reveal a separation distance between the two nanoparticles. On the other hand, the topographic image appears more resolved by using the nanocone probe (**Fig.5c**) with respect to the **TESP-SS**, as the two nanoparticles appear more separated in the nanocone probe image.

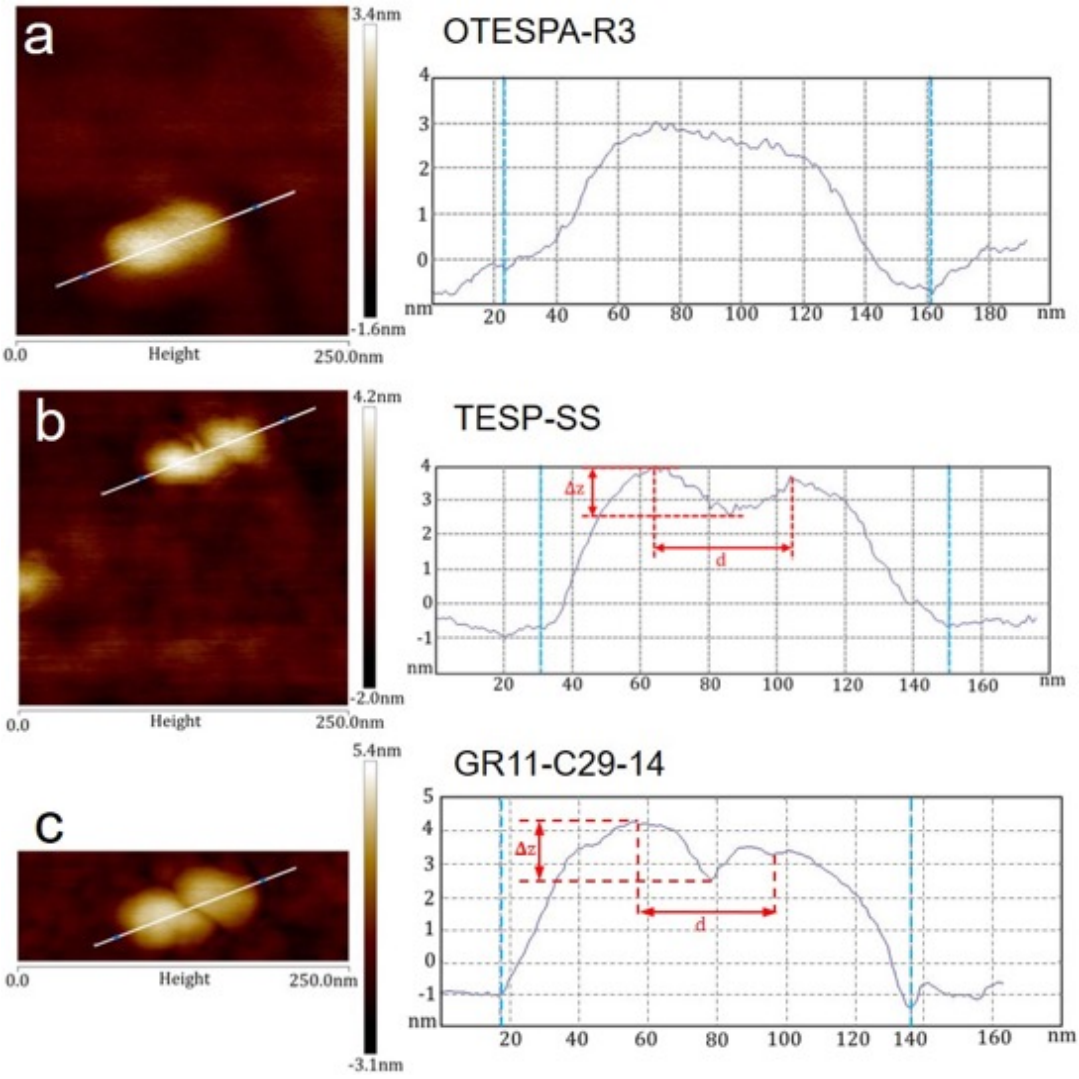

Figure 5: *Comparison of AFM tapping-mode images (left) of the same gold nanoparticles (dispersed on a silicon substrate) and related height profiles (right) obtained from* ***(a)*** *the commercial Si probe* ***OTESPA-R3, (b)*** *the commercial silicon probe* ***TESP-SS****, and* ***(c)*** *the carbon nanocone probe (****GR11-C29-14****).*

The difference in the separation resolution can be evaluated by the measurement of the depth Δz_r between the highest summit and the height of the bottom of the trench between the two nanoparticles. Δz is of about 1.3 nm and 1.8 nm for the **TESP-SS** and the nanocone probes, respectively. Also, these two probes give the same overall length of about 119 nm for the two combined Au nanoparticles, and a similar distance d between the particle centers, estimated at about 40 nm for both probes. It is worth noting that comparing the images in **Fig.5b** and **Fig.5c** with eyes only gives the impression that particles are seen larger with the carbon probe, while

comparing the height profiles tells that it is not so. This can be explained by the scale range provided by the nanocone probe (8.5 nm) with respect to both the other tips (6.2 nm and 5.0 nm, respectively, for the **TESP-SS** and the **Otespa-R3** silicon probes). Overall, the discrepancies in lateral resolution observed between the three probes logically follows the difference in the values of the resolution limit d_{res} as calculated according to equation (1), i.e., 2.8 nm, 1.3-2 nm, and 1.3-1.6 nm for the **Otespa-R3**, **TESP-SS**, and carbon cone probes, respectively (taking R equal to the radius range for each, i.e., 10, 2-5, and 2.3-3 nm, respectively, as reported in *Chapter 3* (**Ch3-Table1** and **Ch3-Fig.17**)and taking Δz_{rmin} equal to 0.1 nm as mentioned in *Section 2.1.2*). These clear differences evidence the impact of the probe apex radius for enhancing image resolution.

b) Highly-Oriented Pyrolytic Graphite (HOPG)

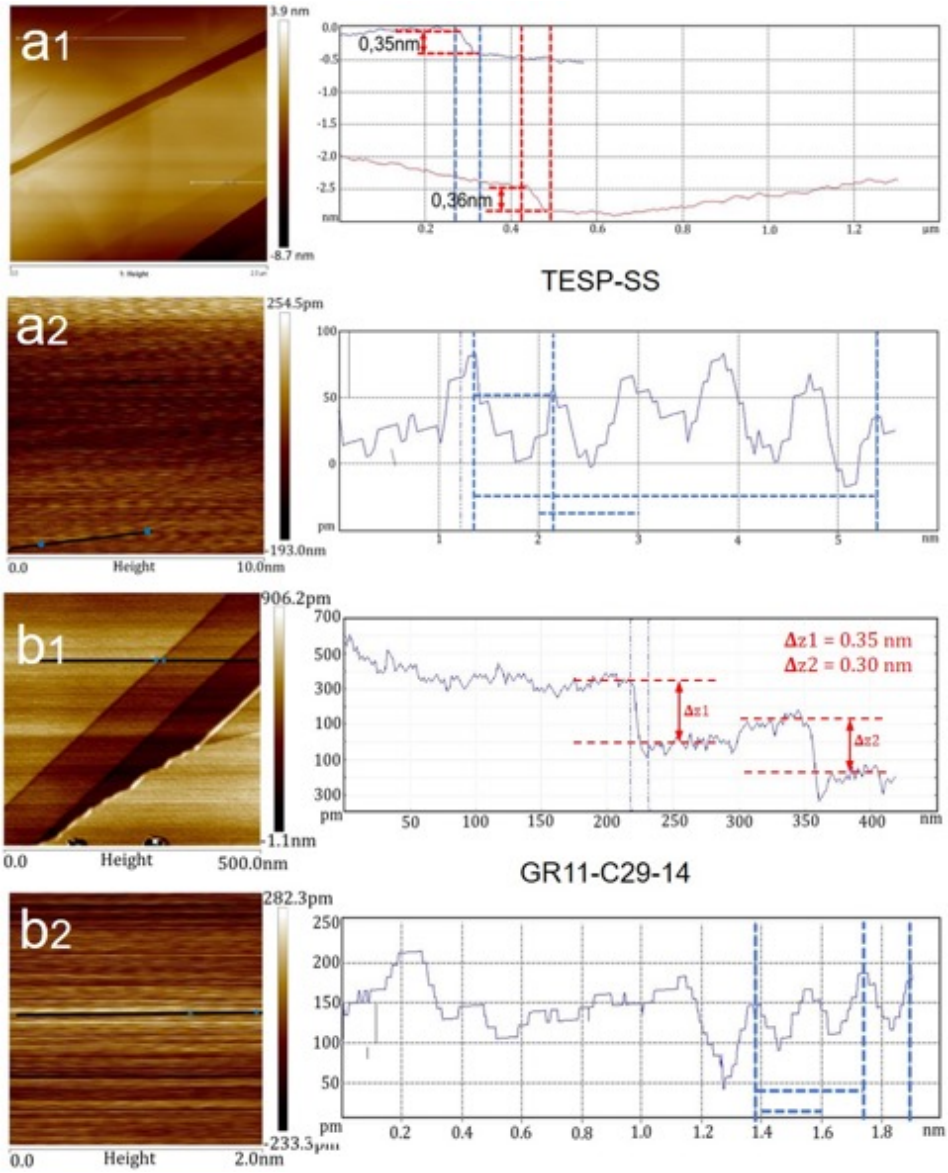

Figure 6: *Comparison of AFM tapping-mode images of a HOPG substrate (left) and related height profiles obtained with* ***(a1)*** *a commercial silicon probe* ***TESP-SS*** *at low (256x256) and* ***(a2)*** *high magnification (256x256), and with* ***(b1)*** *the carbon nanocone probe* ***GR11-C29-14*** *at low (256x256) and* ***(b2)*** *high magnification (512x512).*

Because of its simple preparation, HOPG is a commonly used substrate for studying the resolution in SPM modes. Topographical images on a HOPG substrate from Bruker company were conducted following two configurations: flat graphene planes and several graphene sheet steps measurements to evaluate the capacity of measuring the distance *(i)* between two carbon atoms in the plane of the substrate (measured in the flat zone) and *(ii)* between two superimposed graphene layers (measured on a surface step).

These measurements are performed using the **TESP-SS** silicon probe and the same nanocone tip **GR11-C29-14,** previously used for imaging the Au nanoparticles. The acquisition parameters employed were usually 256x256 points and a scan size of 500x500 nm^2 (scan rate 2 Hz) and 2x2 nm^2 (scan rate 60 Hz) for the nanocone probe, and two different scan sizes of 2x2 μm^2 (scan rate 2 Hz) and 10x10 nm^2 (scan rate 60 Hz) for the Si probe.

Fig.6 represents the topographic images (left) and height profiles (right) of a HOPG substrate in zones including both flat surface areas and several graphene steps (**Figs.6a1** and **6b1**). The topographic images of the flat zone by the two probes present different steps with a similar amplitude. The distance between two superimposed graphene planes, i.e., the step height, determined using the height profiles is evaluated at about 0.30-0.35 nm for the nanocone probe and ~0.35 nm for the **TESP-SS** probe. These values are in the range (with a 5-10% accuracy) of the theoretical value of 0.335 nm as the intergraphene distance for graphenic materials arranged according to the graphite structure [*14Maire1970*]. Since, in AFM measurement, uncertainty is in the range of 20%, these measured values can be considered in good agreement with the theoretical ones.

At high magnification (**Figs.6a2 and 6b2**), the images of flat zones from both the **TESP-SS** and the carbon nanocone probe present periodic oscillations in height, the period of which can be calculated from the distance delimited by the dashed blue lines in the height profiles. The oscillation periods were calculated and evaluated at about 0.18 nm for the nanocone probe, On the other hand, the **TESP-SS** probe image gives a period value of about 0.79 nm. Because of their periodical feature, such oscillations could be expected to relate to the graphite atomic lattice. However, considering this lattice as sketched in **Fig.7**, none of both values are close to any of the lattice constants. Indeed, 0.18 nm makes a 27% deviation with respect to the theoretical value of 0.142 nm corresponding to the in-plane C-C bond. The closest lattice constant from this value could be the 0.213 nm distance (corresponding to the *(10.0)* plane family) with which the deviation is only 15%, but the fact that it was observed that the periodicity did not change in proportion of the magnification range of the image (not shown) makes suspicious that it actually comes from the sample characteristics, and suggests that it might be due to another cause. On the other hand, the 0.8 nm period found with the **TESP-SS** probe was actually found to vary according to the magnification range (not shown), which makes confident that it might be somehow related to the graphite lattice. For instance, it is equal to 4 times the 0.213 nm value (*(10.0)* planes), or 4 times the 0.246 nm value between two α (red) atoms (corresponding to twice the *(11.0)* interplane distance, which is the periodicity of the pseudo-triangular lattice that is more commonly observed in the literature, as mentioned in **Fig.7** caption), accepting a deviation of ~6% and ~19%, respectively. But the reason why such multiple of the actual periods would appear is not clear.

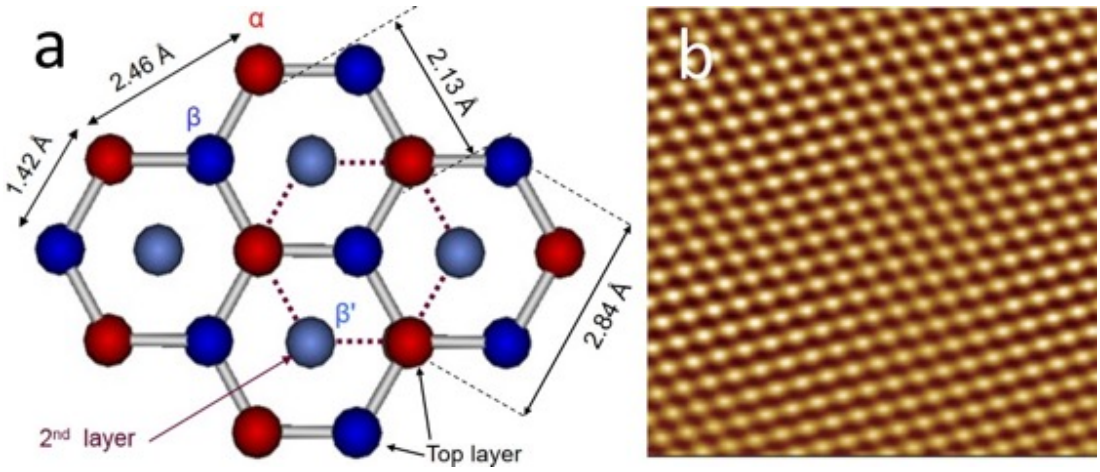

Figure 7: (a) *Sketch of the graphite lattice (top view) here represented by two superimposed layers only. Each α carbon atom (red) is above another carbon atom underneath, whereas each β carbon atom (blue) is facing a hexagon center (light blue atoms are from the second layer underneath). Therefore, carbon atoms from a same graphene layer are not all equal, which makes that it is a common observation in SPM that the graphite lattice (as opposed to single graphene or turbostratic graphenic carbon) has a somewhat triangular appearance in AFM, as in the example provided in* ***(b)*** *(from https://parksystems.com/applications/materials/nano-materials/).*

Generally speaking, the poor quality of the images shown in **Figs.6b and 6d** is not much surprising. Obtaining better images of the HOPG atomic lattice would require to operate in controlled environment (temperature, hygrometry, atmosphere).

A SEM control of the aspect of the carbon probe after being used for imaging the Au nanoparticles and then the HOPG surface did not show any obvious changes, specifically regarding the apex dimensions, at least in the range of the SEM resolution (**Fig.8**).

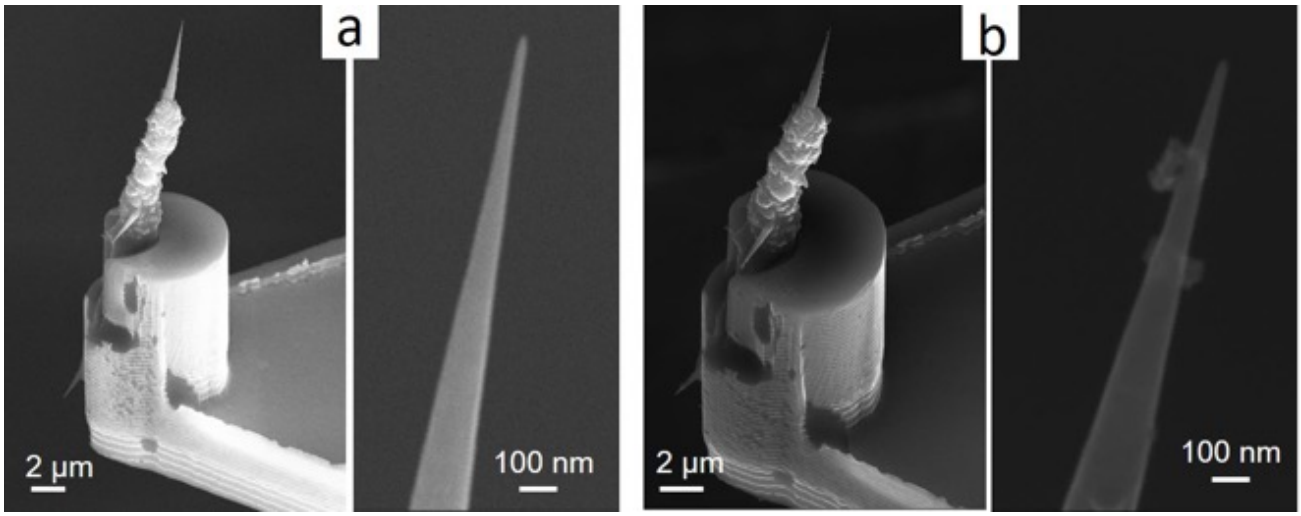

Figure 8: *SEM images of the nanocone probe* ***GR11-C29-14 (a)*** *before being used and* ***(b)*** *after being used for the topographic tests concerning the Au nanoparticles and HOPG samples.*

c) Single silicon crystal surface (wafer)

A flat surface of a cross-sectioned silicon monocrystal of about 1cm x 1cm, actually a piece of a Si wafer, was also studied by using a nanocone probe and a commercial **OTESPA**[22] (#**Si-Otespa-4**) probe. The acquisition parameters employed were: scan size of 2x2 μm^2, 2 hz, and 256x256 points per line. Examples of images obtained are given in **Fig.9**.

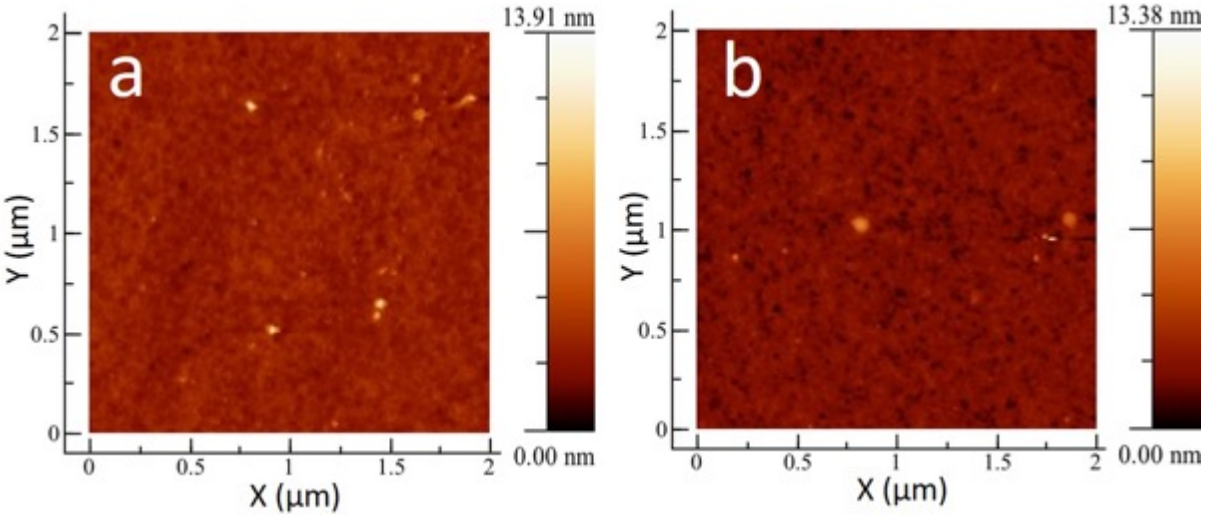

Figure 9: *AFM tapping-mode images of a silicon wafer substrate.* ***(a)*** *With a standard* ***OTESPA*** *silicon probe (****#Si-Otespa-4****).* ***(b)*** *With a nanocone probe (****#GR07-C20-68****). Both images were taken on the same substrate but not at the exact same place.*

At the scale at which the images in **Fig.9** were recorded, both look alike. The roughness of a silicon wafer surface being low, i.e., in the nanometer range, there is not topological detail to see and comment on with which we could detect some difference in performance between both probes. The whole scale of the height variation (provided aside the images) is similar for both. The slight difference in the maximum height is not significant as it may depend on the height of the dust particles lying onto the surface, which appear as bright spots in both images. More significant, maybe, is the number of dark spots on the images which is much higher in the carbon probe image (**Fig.9b**) than in the **OTESPA** image (**Fig.9a**). As the darkest color corresponds to the lowest z value, it may mean that the carbon probe is able to reveal more of the bottom of the deep details of the Si surface, relatively speaking, consistently with the highest sharpness of the carbon probe with respect to the **OTESPA** probe, as previously mentioned (apex radius *R* of 2-3 nm and 7-10 nm, respectively). On such a relatively smooth surface, the role of tiny protrusions that the way the supporting-CNT breaks is able to generate at the cone apex (see arrow in **Ch.3-Fig.17a**) might become important for revealing tiny topological details.

2.1.5. Durability test: wear resistance of the carbon nanocones

The results from *Section 1.1* demonstrate the ability of carbon nanocone as AFM probe for topographic imaging. However, further evaluation of the behavior of the tip along the scanning

[22] OTESPA probe characteristics are quite similar to that of OTESPA-R3 in their geometry and apex dimensions.

process with time is needed in order to assess the stability of the measurements and the durability of the tip. For such purpose, a wear resistance and durability were developed based on the literature [*12Guo2005*] and some recommendations from a Bruker company representative.

a) Description of the wear resistance test protocol

The durability performances of two standard **OTESPA** silicon probes noted **Si-Otespa-3** and **Si-Otespa-4** were compared with three carbon nanocone probes: *(i)* one was mounted by the FEBID welding process noted **ZeR09-C26-25**, and *(ii)* two were mounted by the gluing process noted **GR05-C16-64** and **GR07-C20-68**. These probes were tested on the same silicon wafer substrate for more than 22 hours (up to 40 hours) without interruption. A total surface of 1024 µm was scanned with a 2x2 μm^2 wide scan size, 2 Hz, 256x256 pixels, and an acquisition time of 128 s per image.

The durability performance was evaluated by the evolution of the roughness measurement over time of a same substrate area for each probe. The same area was scanned over 22-40 h for each probe, but the area scanned was different from a probe to another. The roughness was measured by recording the root mean square (*RMS,* or *Rq*) roughness[23], which is expressed as follows:

$$Rq = \sqrt{\frac{1}{l_r}\int_0^{l_r} z(x)^2 dx} \tag{2}$$

Rq was preferred to the roughness average R_a, which is expressed as follows:

$$Ra = \frac{1}{l_r}\int_0^{l_r} |z(x)dx| \tag{3}$$

because the former is more sensitive to the sample height changes[*15DeOliveira2012*]. Thus, it was expected to be more sensitive to revealing the difference in sharpness between two probes, or when a probe has become blunt for being overused and is no longer able to follow as accurately as it was the sharp peaks and deep valleys that can be present on a substrate.

The plots of the absolute RMS roughness values (noted RMS_a^i for the probe *i*) reported in **Fig.10a** show a difference in the first measurement certainly due to roughness differences in the various zones scanned by each probe, i.e., not all zones exhibit the exactly same average height, and not all the probes start from the same height either. Therefore, the relative RMS roughness values (noted RMS_r^i for the probe *i*) were calculated and plotted over time on **Fig.10b** for better comparison. $RMS_r^i(t)$ at a time t is defined below and is calculated with respect to the first measurement of the absolute roughness RMS_a^i performed at t = 0:

$$RMS_r^i(t) = \frac{[RMS_a^i(t) - RMS_a^i(0)]\text{x}100}{RMS_a^i(0)} \tag{4}$$

[23] Expressed in words, the RMS roughness value of a surface is obtained by calculating the mean of the squared distances to the average height plane at every locus of the surface and then taking the square root of it.

b) Comparison of probe performances

Fig.10a shows the variation of *Rq* obtained from the various probes on the already described silicon wafer surface, as a function of the scanning time. In general, nanocone probes show to be stable and maintain a high resolution of the images all along the scanning process, which held 25 hours for the probe **ZeR09-C26-25**, 30 hours for the probe **GR07-C20-68**, and up to 40 hours for the probe **GR05-C16-64.** In the case of **GR07-C20-68**, which performed rather well for a period of 22 hours, an abrupt withdrawal of the tip occurred, but once the tip was put back to the surface, the scanning process continued following the previous normal track until the scanning was purposely stopped 3 hours later. Because the shift in RMS roughness measurement follows a continuous increase until 22 h of measurement, which is different from the behavior of the Si probes which is more erratic, it is believed that this shift, which is not observed for the other carbon probes, is due to the progressive occurrence of the event that has induced the sudden withdrawal of the tip.

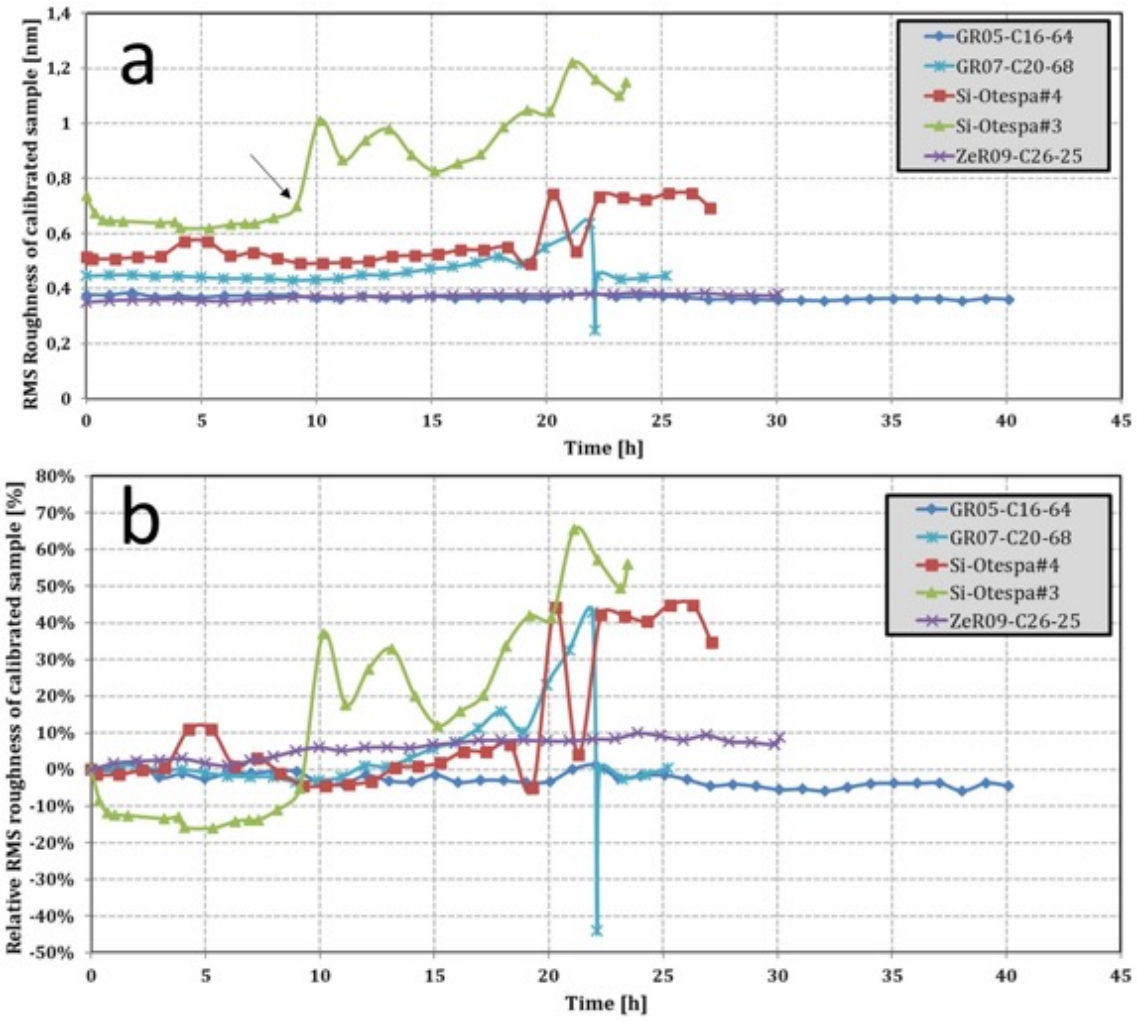

Figure 10: *Variation of the RMS roughness as measured by five different probes (**GR05-C16-64**, **GR07-C20-68**, **ZeR09-C26-25**, **Si-Otespa-3** and **Si-Otespa-4**) as a function of the scanning time. **(a)** shows the absolute RMS roughness. The arrow refers to a comment in the text. **(b)** shows the relative RMS roughness, i.e., the normalization of the variation of roughness with respect to the first measurement for each probe.*

Overall, for the three carbon probes, regardless of the mounting process (gluing, or FEBID welding), the *Rq* is fairly steady over times as long as 40 hours. On the opposite, it can be noted that the RMS roughness variations started being larger and more abrupt for the silicon probes as early as from 9 h and 13 h of scanning time for the **Si-Otespa-3** and **Si-Otespa-4** probes, respectively.

As previously said, the differences observed in **Fig.10a** in the absolute *Rq* values for each probe, even when considering the steady part of the plots only, might be due to differences in the roughness characteristics of the areas scanned by each probe. Hence, considering the relative instead of absolute *Rq* values as explained earlier and reported in **Fig.10b** allows getting rid of the uncertainty about the significance of the absolute *Rq* values. The relative *Rq* variation reaches up to 65% for the **Si- Otespa-4** whereas it barely reaches 10% for the carbon nanocone tips (not considering the relative *Rq* variation of almost 45% for the **GR07-C20-68**, which is visibly affected by the experimental problem that resulted in the tip withdrawal).

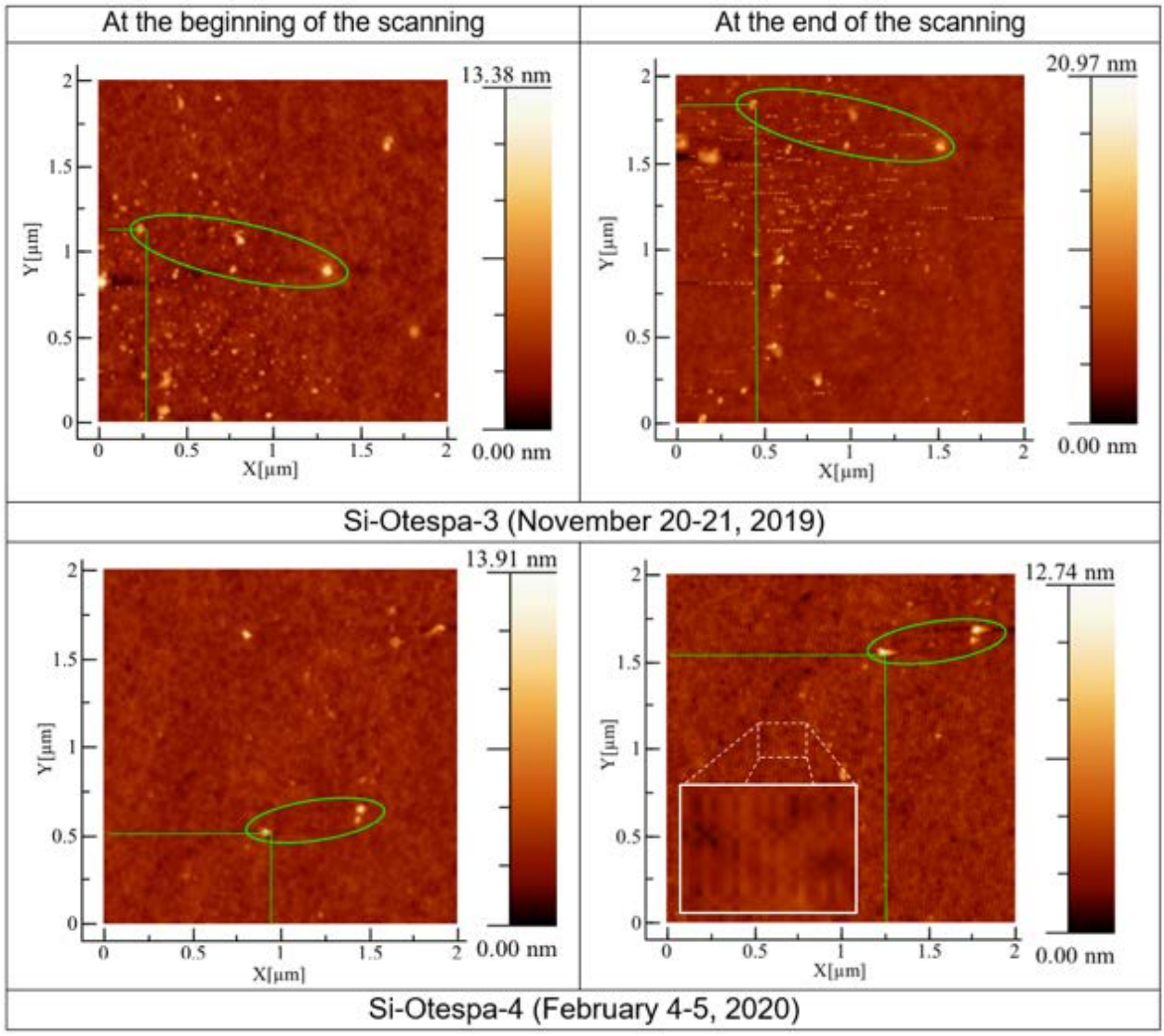

Figure 11: *Comparison of the evolution in resolution of images obtained with* ***OTESPA****-type silicon probes from the early scanning time vs. the end of the scanning period for the same probes having provided the graphs presented in* ***Fig.10.*** *Green marks are to indicate the same surface details in each image couple. The white solid-line frame shows an enlargement of the white dotted-line framed area, to show the occurrence of a periodicity.*

These variations can be further analyzed through the comparison of the topographic images obtained by the probes at the beginning and at the end of the scanning time, starting with the silicon probes (**Fig.11**). The final images related to the probes **Si-Otespa-3** and **Si-Otespa-4** show the presence of artefacts as the presence of spurious dotted white lines for the former, and the deformation of the largest spots as well as periodic oscillations (see the enlarged framed area) for the latter, all related to the scanning direction. These events are likely to be related to a possible damage of the probes, which could not be seen at the magnification range of the SEM (**Fig.12**) because most of the absolute height variations that can be found on such a Si wafer surface is out of the range of the SEM resolution power.

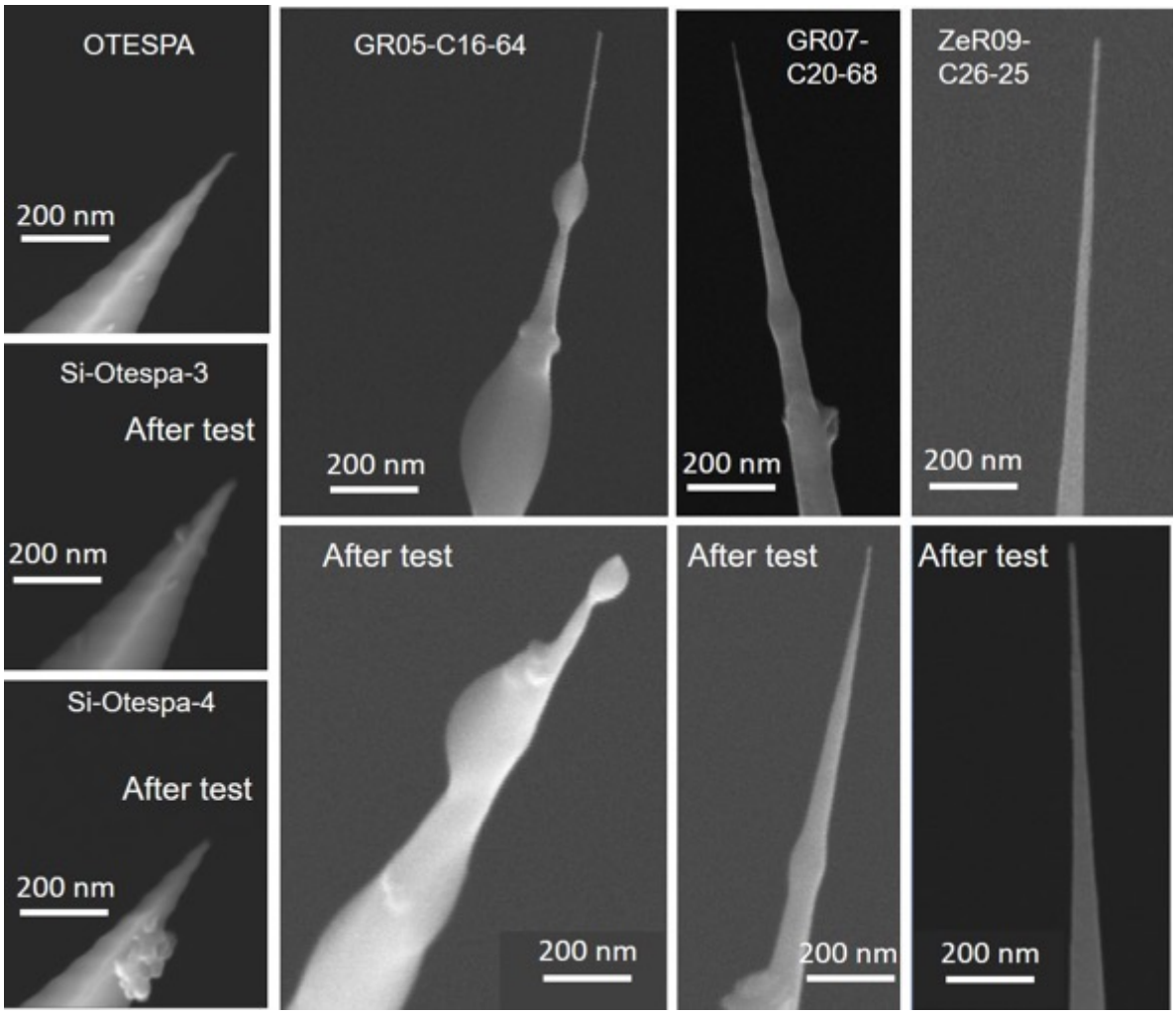

Figure 12: *SEM images of the different probes used for the durability test, before (upper images) and after the test (lower images). The bulges visible along the cones of the* ***GR05-C16-64*** *et* ***GR0 7-C20-68*** *are likely to be resin droplets which have migrated towards the tip while still in liquid state. This can be avoided by better controlling the way the cantilever and the resin are put in contact.*

The same comparison between the starting and the ending images is provided for the carbon nanocone probes in **Fig.13**. No artefact is present in any of the topographic images whatever the probe and the scanning time. The starting and the ending images look alike for all the three probes.

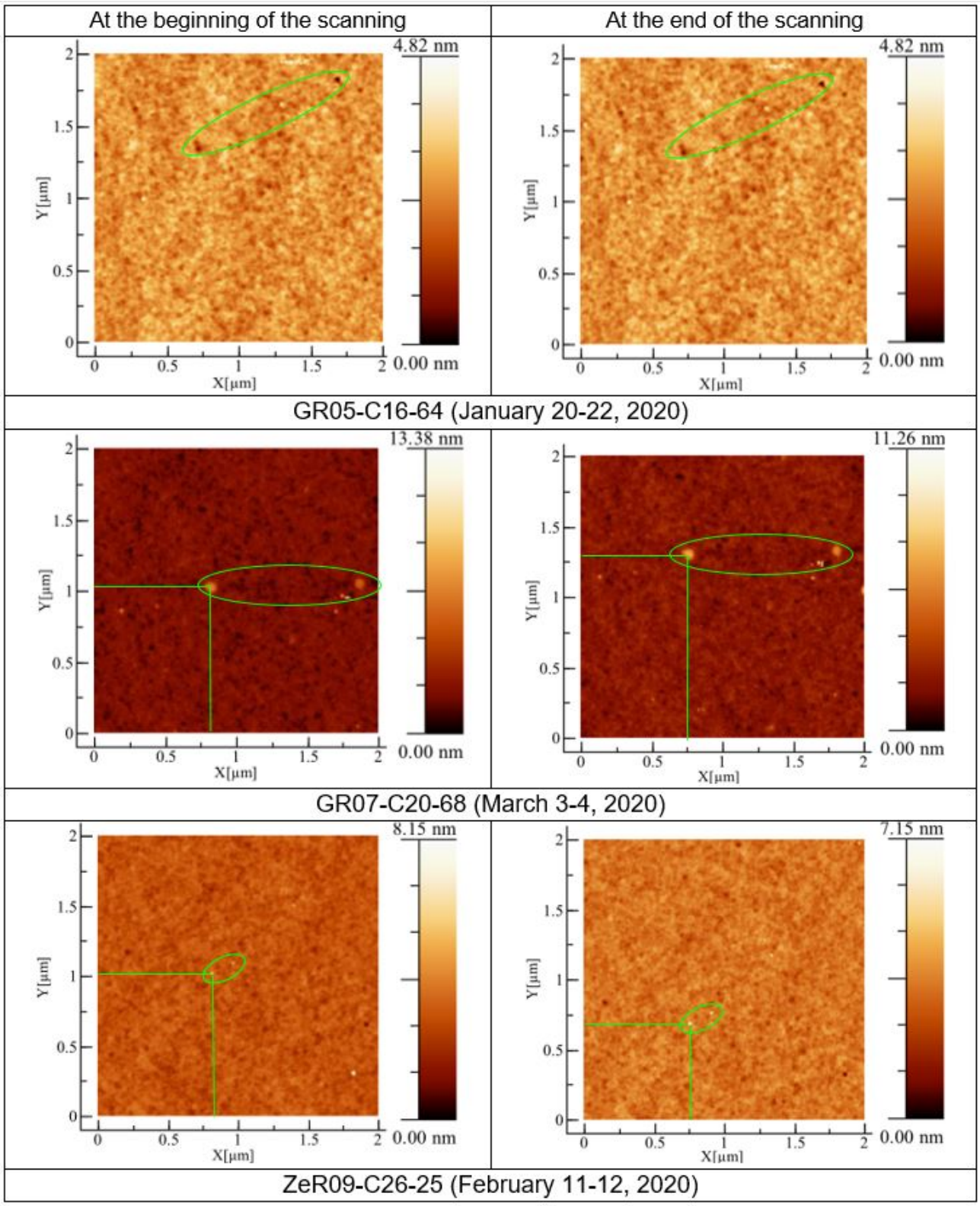

Figure 13: *Comparison of the evolution in resolution of images obtained with carbon nanocone probes from the early scanning time vs. the end of the scanning period for the same probes having provided the graphs presented in* ***Fig.10.*** *Green marks are to indicate the same surface details in each image couple.*

Consistently with the permanence of the image resolution up to scanning times as long as 40 hours, the carbon cone apices do not look affected by the test (**Fig.12**), but for the **GR05-16-64** probe. Obviously, the probe has lost the CNT-like part above the bulge. It is hard to believe that such an apex would have been able to provide a topographic image at the end of the test equivalent to that obtained with the probe apex as it appeared to be at the beginning of the test. One explanation can be the breakage of the probe during the manipulations that have followed the test (when taking back the cantilever from the AFM, or related to the SEM observation).

It is worth noting that a shift in the image position for both silicon probes has occurred, as evidenced by comparing the green marks in both the starting and the ending images, possibly caused by a drift in time of the piezoelectric cell monitoring the substrate position. This drift of the piezoelectric cell can explain the change of the contrast range which passes from 13.38 nm to 20.97nm and from 13.91 nm to 12.74nm, for the **Si-Otespa-3** and **Si-Otespa-4** probes, respectively. On the other hand, a piezoelectric cell drift is not observed for the probe **GR-05-C16-64**, and occurred in a very limited extent for the two other probes. By looking at each of the images that have generated the curves in **Fig.10**, it was verified that the drift observed between the starting and the ending images of the series accounts for the total drift, i.e. drifting was not erratic all along the experiment duration, and once it started, the drift has kept occurring in the same x and y directions until the experiment was stopped.

It is striking to observe that, on the one hand, both the **OTESPA** Si probe experiments have been subjected to a large drift, whereas none of the carbon nanocone probe have, and that, on the other hand, both OTESPA probes exhibit the largest relative *Rq* variations over the whole experiment duration whereas the carbon nanocone probes exhibit the lowest ones (**Table1**), not considering the large variations in relative *Rq* which was actually caused by the episode of probe withdrawal for the **GR07-C20-68.**

	Si-Otespa-3	Si-Otespa-4	GR05-C16-64	GR07-C20-68	ZeR09-C26-25
Total shift (µm)	0.93	1.42	0	0.34	0.39
Mean relative *Rq* (%)	24.6	13.2	2.4	1.5	6.1

Table1: *"Total shift" is, for each probe, the sum of the absolute values of the drift in x and y directions measured between the starting and the ending images provided in* ***Figs.11*** *and* ***13****. "Mean relative Rq" is, for each probe, the calculated mean of the absolute values of the relative Rq measured for each point plotted in the curves of* ***Fig.10b****.*

The reason why both observations should be related is not obvious. It was verified that it is not related to the dates or seasons at which the experiments have taken place, which could have played a role through the hygrometry level for instance, as the experiments have been dispatched from November 2019 to March 2020, and that the experiments with the **Si-Otespa-4** and the **ZeR09-C26-25** were both carried-out within a week in February 2020 (see the experiment dates reported in **Figs.11** and **13**). Another observation supporting such an intriguing correlation is that, although the drift has started immediately for the **Si-Otespa-4** and has kept going at slow rate until the end of the experiment, the drift has started at the very same time as the relative *Rq* has started to jump for the **Si-Otespa-3** (marked by an arrow in **Fig.10a**).

2.2. Peak- Force Quantitative NanoMechanical AFM (PFQNM AFM)[24]

Quantitatively measuring the nanoscale mechanical properties of a sample consists in accurately discriminating between different phases or phase orientations. As opposed to regular AFM, PFQNM AFM studies the mechanical response of the sample subsurface, hence no longer looks at the specimen surface only but characterizes the specimen volume in some extent. For mechanical characterizations across topographic imaging, the volume of the sample being measured depends on the tip geometry and spring constant of the cantilevers [*16Belec2016*]. A smaller tip-curvature radius allows a smaller sample volume to be studied and a better identification of the different phases present on a given sample by discriminating them better, whereas the spring constant determines the range of cantilever deflections and therefore the range of sample deformation [*16Belec2016*]. Various SPM modes operated either in contact mode (e.g., dealing with the so-called volume force) or in tapping mode (e.g., tapping phase imaging) can be considered for assessing mechanical properties [*17Pittenger2012*]. However, most of the tapping-mode-related techniques have limitations regarding quantitatively measuring multiple properties independently as, in such a mode, the phase contrast can also depend on height differences and the acquisition parameters (i.e. amplitude set point, etc.), not on the material property only. On the other hand, the contact mode can be time-consuming since it requires collecting thousands of measured points for mapping the properties of a sample [*17Pittenger2012*]. However, PFQNM can combine mapping of multiple quantitative mechanical properties from real-time data-measurements with a resolution similar of a regular height tapping image [*17Pittenger2012*].

In this work the capability of the geometry and stiffness of our nanocone probes for characterizing mechanical properties of different homogeneous and heterogeneous samples was tested by using peak force quantitative nanomechanical mapping.

2.2.1 PFQNM AFM mapping - principle and notions

Peak force tapping (PFT) is a recently developed non-resonant intermittent contact mode [*2Zhang 2018*]. This technique does not depend on the cantilever mechanical oscillations like some traditional intermittent-tapping modes presented in *Section 2.2.1*, but on the target force (peak force) applied by the probe to the sample. The working principle of this technique is depicted in **Fig.14**, which consists in measuring the interaction between a sample and the scanning probe. This probe is put in contact to the surface while increasing continuously the force applied (*i.e.* by decreasing the distance between the cantilever and the sample) up to a maximum value (peak force). When this value is reached, the probe is removed from the surface. During this process, the detection in real-time of the cantilever deflection allows the measurement of the interaction between the probe and the sample. PFT works at low frequencies from 100Hz to a few kHz [*2Zhang 2018*], and allows the real-time measurement of the forces of the tip at each tap. Thus, the PFQNM mode combines topography and force curve

[24] This part of the work was done in collaboration with C. Villeneuve-Faure (LAPLACE, Toulouse).

mapping measurements of a wide range of samples (*i.e*. hydrogels, polymers, metals, semiconductors, etc.) with a lateral resolution below 5 nm comparable to regular tapping modes described in *Section 2.2.1*, but in a faster way since it does not require collecting any amplitude oscillation feedback as in AFM tapping mode [*2Zhang 2018, 17Pittenger2012*].

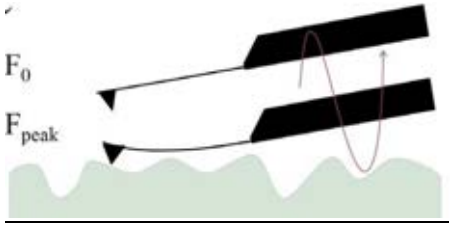

Figure 14: *Schematic representation of a tip-sample interaction during the peak force tapping: F_0 refers the set point of the resonance frequency and F_{peak} to the maximum force reached at each tip-tap on the surface. From [*2Zhang 2018*].*

A force curve is generated during each tip-tap and corresponds to the tip force when approaching and retracting the probe from the surface [*2Zhang 2018*] as depicted in **Fig.15**. In such a curve, the force determined by the cantilever deflection (**Fig.15a**) is plotted either as a function of time (**Fig.15b**), or of the cantilever "*Z*" position (**Fig.15c**), or tip-sample distance (**Fig15d**), and allows the material properties of the tip to be determined. Usually, such a curve as a function of the *Z* position is generated point-by-point using force spectroscopy [*1Eaton2010*].

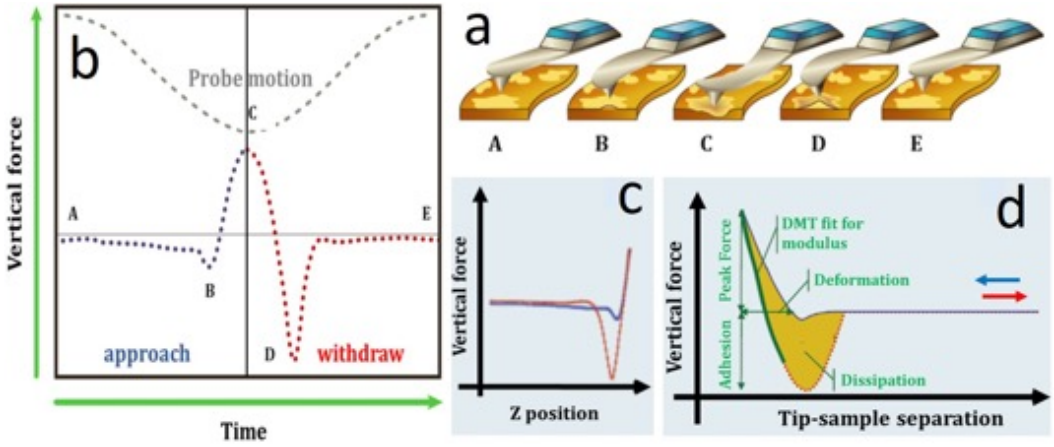

Figure 15: *Different force curve information that can be extracted from a PFQNM AFM process.* ***(a)*** *sketch of the mechanical behavior of both the cantilever and the material; letters A to E stand for the different positions of the cantilever during the PFT process. The force is plotted as a function of* ***(b)*** *time;* ***(c)*** *cantilever position (called Z position);* ***(d)*** *tip sample distance. The blue and red curves correspond to the approach and the withdrawal of the cantilever from the sample, respectively. From [*16Belec2016, 18BrukerSite*].*

Fig.15 shows the different representations used for force curves. As explained before, the force between the sample and the probe is described by the deflection variation of the cantilever in the very same way as a spring constant is related to the spring elongation (deformation):

$$F = k \,.\, \Delta Z \tag{5}$$

Where F is the force applied (here the force on the cantilever), k the spring constant, ΔZ is the elongation of the spring (here the cantilever deflection).

Fig.15b describes the evolution of the tip-sample contact force (*i.e.* the cantilever deflection). The cantilever approaches (goes down) and withdraws (goes up) from the surface respectively between points A to C and between points C to E. Point B corresponds to the moment when attractive forces pull the probe to the sample (jump to contact) while approaching the cantilever to the sample. This induces a sudden increase of the cantilever deflection followed by the tip-sample contact. While the cantilever keeps going down, the deflection decreases until it increases again in the opposite direction until reaching point C which corresponds to the maximum contact force (peak force) between the probe and the sample. After that, the cantilever starts to retract from the surface and the deflection decreases as the contact force decreases. The probe is still in contact with the substrate hence inducing a cantilever deflection in the opposite direction thanks to the attractive forces while the cantilever goes up until point D is reached (minimum force). From point D to point E, the cantilever is no longer in contact with the surface and no deflection variation is measured. The latter can be schematized as function of the Z position and the force (**Fig.15c**) from which the linear deformation of the probe can be extracted when the probe is in contact with the surface corresponding to the zone between C and D in **Fig.15b**. Then, a tip-sample distance curve called also force-distance curve (FDC) (**Fig.15d**) can be calculated from the Z position (the cantilever deflection). Thus, the FDC allows extracting multiple quantitative information such as elastic deformation, adhesion force between probe and sample, Young modulus of the probe etc. The reliability of this quantitative measurement is mostly driven by the characteristics of the probes (spring constant of the cantilever and apex radius of the tip). The tip-sample adhesion force is directly proportional to the tip apex radius. Different models are available for extracting the Young modulus [*19Roa2011*]. The main one is the Derjaguin-Muller-Toporov's (DMT) model, which focuses on apex-surface interaction. In our study, the Young modulus is calculated following the DMT model as indicated in the equation:

$$F - F_a = \frac{4}{3} E^* \sqrt{R_c . \varepsilon^3} \tag{6}$$

In this equation, F_a is the tip-sample adhesion force, F the applied force (peak force), R_c is the curvature radius of the tip, ε the deformation due to the penetration of the tip into the substrate. E^* corresponds to the reduced Young modulus as defined below depending on the Young modulus and Poisson coefficient of the sample (E_s and ν_s) and tip (E_{tip} and ν_{tip}). In the case of a non-deformable probe (*i.e.* a probe with a high Young modulus), the measurement of E^* is directly linked to E_s.

$$E^* = \left[\frac{1-\nu_s^2}{E_s} + \frac{1-\nu_{tip}^2}{E_{tip}} \right]^{-1} \tag{7}$$

Consequently, before conducting PFQNM imaging, a calibration process of the tip is necessary for determining the main mechanical parameters of the probes (*i.e.* deflection sensitivity, cantilever spring constant, and tip apparent apex radius, etc.). For such a purpose, the

calibrations can be performed either with absolute or reference sample methods [*17Pittenger2012*, *20Hutter1993*].

2.2.2. Mechanical properties of the probes used (both nanocone- and Si-based)

The mechanical behavior as well as the tip radius of three nanocone probes were tested and compared with a commercial silicon probe **Tespa-V2**, whose SEM-measured apex radius was ~8 nm (**Fig.16**).

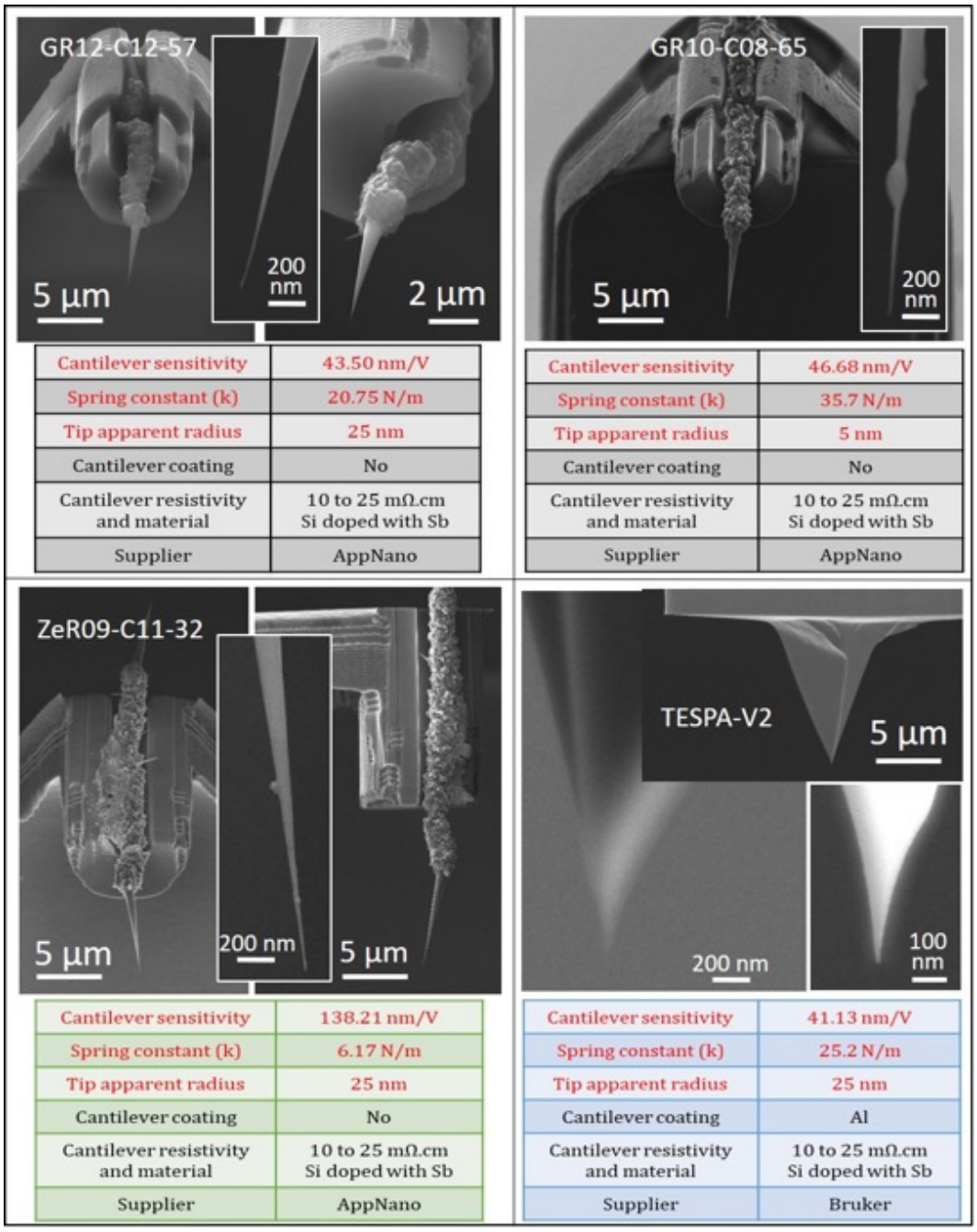

Cantilever sensitivity	43.50 nm/V
Spring constant (k)	20.75 N/m
Tip apparent radius	25 nm
Cantilever coating	No
Cantilever resistivity and material	10 to 25 mΩ.cm Si doped with Sb
Supplier	AppNano

Cantilever sensitivity	46.68 nm/V
Spring constant (k)	35.7 N/m
Tip apparent radius	5 nm
Cantilever coating	No
Cantilever resistivity and material	10 to 25 mΩ.cm Si doped with Sb
Supplier	AppNano

Cantilever sensitivity	138.21 nm/V
Spring constant (k)	6.17 N/m
Tip apparent radius	25 nm
Cantilever coating	No
Cantilever resistivity and material	10 to 25 mΩ.cm Si doped with Sb
Supplier	AppNano

Cantilever sensitivity	41.13 nm/V
Spring constant (k)	25.2 N/m
Tip apparent radius	25 nm
Cantilever coating	Al
Cantilever resistivity and material	10 to 25 mΩ.cm Si doped with Sb
Supplier	Bruker

Figure 16: *Main characteristics and calibrated parameters of the nanocone and commercial silicon (**TESPA-V2**) probes used for the PFQNM AFM tests. Data in red were obtained in this work by means of the various calibration procedures. (Photo credit: A. C. Torres Dias, M. Kandara, R. Cours, CEMES; S. Le Blond, UMS Castaing, Toulouse).*

Two of them were mounted on cantilevers by the gluing process (probes # **GR12-C12-57** and **GR10-C08-65**) while one was assembled by the FEBID welding process (# **ZeR09-C11-32**). Different calibration methods using a Multimode-8 microscope from Bruker were performed on these different probes. These four probes are described in **Fig.16**.

a)Cantilever sensitivity and contact force

The deflection sensitivity was first extracted from a FDC on Si or TiO_2 substrates using force spectroscopy (**Fig.17**). The contact force allowed for each probe was then calculated from the spring constant and deflection of the cantilever. **Figs.17a-b** show the FDCs of the nanocone probe **GR12-C12-57** approaching a Si substrate on two different regions (only the approach is reported). The FDCs were successively performed for several maximum cantilever deflection values (from 30 to 150 nm in **(a)** and from 50 to 700 nm in **(b)**) in order to construct the graphs and to find the cantilever break point. The superposition of the different FDCs shows the reproducibility of the mechanical behaviour of the probe and the interaction between the sample and the probe.

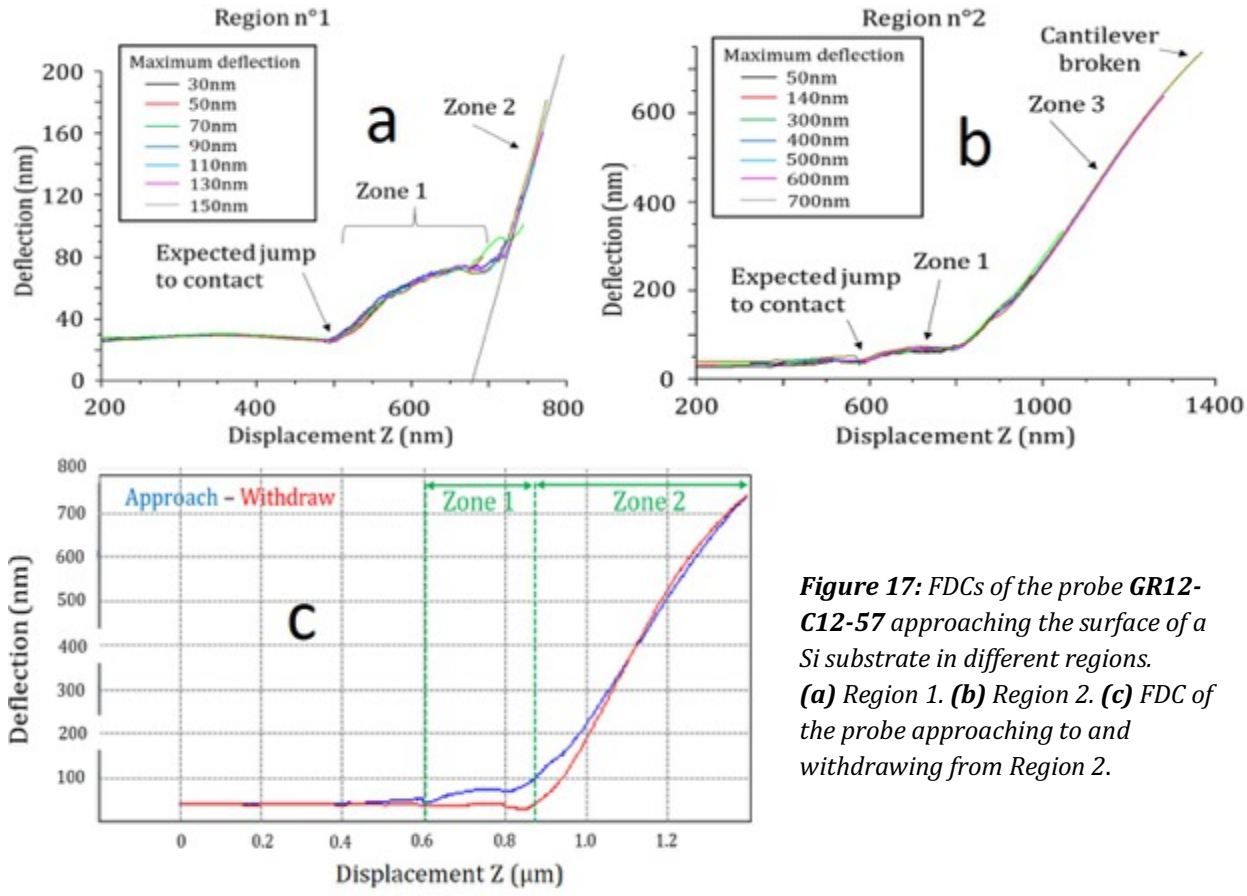

Figure 17: *FDCs of the probe* ***GR12-C12-57*** *approaching the surface of a Si substrate in different regions.* ***(a)*** *Region 1.* ***(b)*** *Region 2.* ***(c)*** *FDC of the probe approaching to and withdrawing from Region 2.*

Fig.17c presents the FDC of the same probe for a maximal deformation of 700 nm when approaching and then withdrawing the probe on Region 2. The graph can be divided into two main zones as indicated in the curve: zone 1 corresponds to the beginning of the interaction between the probe and the substrate surface, and zone 2 corresponds to the linear mechanical

behaviour. A deflection sensitivity of 43.50 nm/V was extracted from zone 1 as the cantilever presents the expected linear mechanical behavior (whose slope is shown by the black line in **Fig.17a**) for a Z displacement above 700 nm. However, for the carbon probes, no or very limited jump-to-contact is evidenced in the zone where it was expected to occur, as designated by point B in **Fig.15b** for instance. The lack of a clear contact jump point could result from a compensation between attractive forces (i.e. van der Waals) and repulsive interactions between the probe and the surface [*7Strus2009*]. Alternatively, the lack of contact jump might also result from *(i)* a too high spring constant preventing the cantilever to bend; *(ii)* the small curvature radii of the carbon probe apex, as the attractive forces are proportional to the surface areas facing each other. On the other hand, the aspect of the hysteresis in zone 1 between the approach and the withdrawal of the probe is different from the theoretical one (see **Fig.15**) as it presents low adhesion forces, which may indicate a possible friction effect induced by the tilt angle made by the cone axis with respect to the ideal, vertical orientation (see **Fig.16**) as discussed later on, or, alternatively, by some viscoelastic deformation of the substrate and/or the probe. However, no hysteresis phenomenon is evidenced in zone 2, indicating that no remaining deformation was present after every full approaching (trace) and retracting (retrace) cycle of the probe, hence a visco-elastic behaviour is unlikely. Other tests are required in order to assess the reproducibility of this mechanical behaviour. For this reason, comparisons of FDCs between different nanocone probes (glued and welded) and with respect to a commercial **TESPA-V2** probe were conducted on a TiO_2 substrate. The results of these tests are presented in **Fig.18.**

b) Spring constant

The spring constant of the cantilevers can be estimated by the AFM-thermal tune [*20Hutter1993*], however this method is not suitable for measuring spring constant higher than 40 N/m. It directly relates to the stiffness of the beam. This method does not require any contact with a sample and consists in evaluating the spring constant of the probe by putting the cantilever into oscillation at its resonance frequency. Such oscillations are driven by the thermal fluctuations. The spring constant were evaluated at 20.75 N/m, 35.7 N/m and 6.17 N/m respectively for the **GR12-C12-57**, **GR10-C08-65**, **ZeR09-C11-32** nanocone probes, and 25.2 N/m for the commercial silicon probe (**Fig.16**). These results agree with the range of values given by the suppliers (19-55 N/m for the silicon probe and 25-40 N/m for the nanocone probes) except for the **ZeR09-C11-32,** which exhibits the lowest value (6.2 N/m). Such a low value was unexpected and questions whether the quality of the welding might not be the cause of it. Indeed, it has been observed several times that the W material of the welding does seem to always well adhere to the carbon-silicon contact.

From these results, it was calculated, using the simple equation (5), that the cantilever associated with the nanocone probe **GR12-C12-57** could support a maximum force of 14 µN inducing a maximum deflection of 700 nm as they are values at which the cantilever has broken (**Fig.17b**). Furthermore, because of its very low calculated spring constant, the reason why the probe **ZeR09-C11-32** does not show any contact jump either (see **Fig.18c** for instance) might relate to the small curvature radius of the carbon cone apex which does not allow enough attractive forces to develop between the sample surface and the tip and bend the cantilever.

The apparent tip radius of the probes was also calibrated along with other peak force imaging parameters. This will be presented ***in section 2.2.4*a.**

2.2.3 Comparison of the mechanical properties of the different probes

Although a FDC presents a global picture of the whole probe, the impact of the geometry and material properties (*i.e.* stiffness) of the tip on the interaction with the substrate can be estimated. Such an estimation is made possible by the comparison of the different FDCs obtained from carbon nanocone and silicon probes approaching and then withdrawing from the surface of a TiO_2 layer with a scan speed of 2 Hz. As shown in **Fig.18**, the different probes exhibit different mechanical behaviour. In such curves, the linear part of the Deflection vs Displacement *Z* allows calculating the sensitivity.

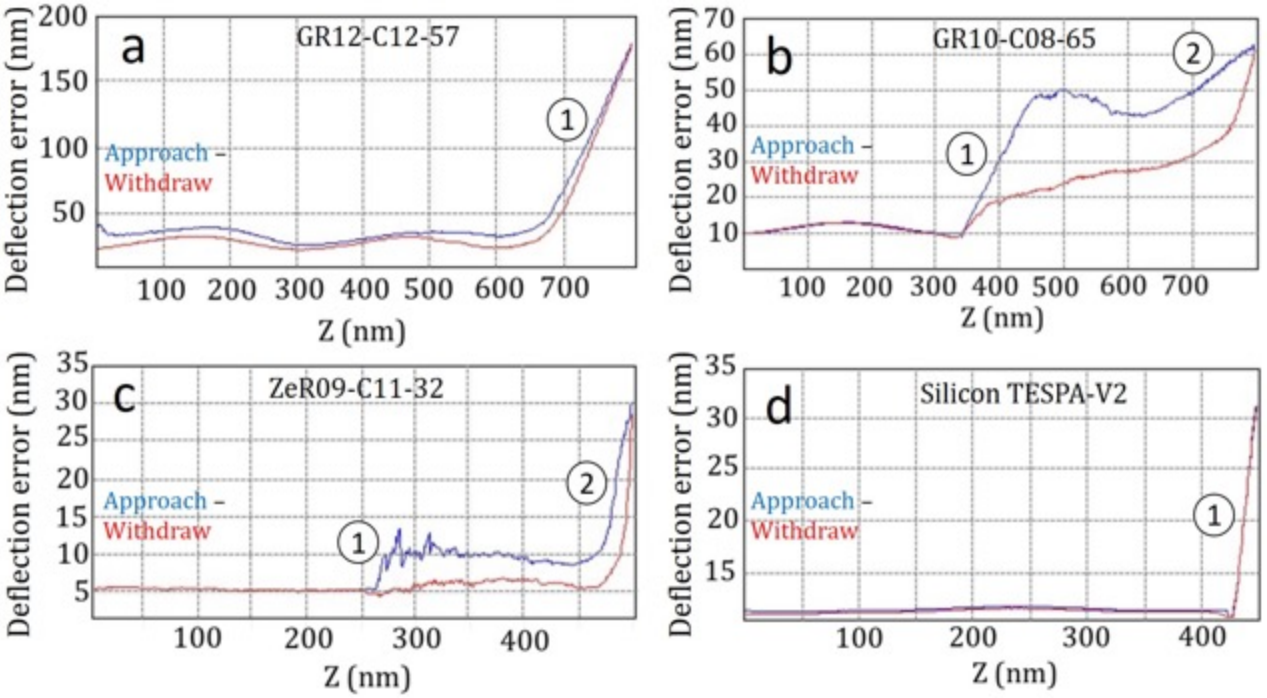

Figure 18. *FDC curves of the different probes approaching and withdrawing the surface of a TiO_2 substrate. The cantilevers sensibility is measured from zone 1 for all the probes except for probe* ***ZeR09-C11-32*** *for which it was measured from zone 2 (its zone 1 corresponds to a too short deflection range for allowing mechanical property measurements).*

The results obtained from the standard silicon probe (**Fig.18d**) shows that an interaction with the surface occurs for a *Z* distance close to 425 nm with a quite small adhesion effect of the probe on the surface corresponding to the jump contact point, with a weak hysteresis between the approaching and the withdrawal curves, then followed by the zone of linear mechanical behavior.

The behavior of the three carbon probes is different. They interact with the surface at different *Z* distances, which may be explained by the different overall lengths of the probes. Indeed, the longer this length is, the smaller should be Z. [*7Strus2009*]. This is consistent with what **Fig.16** shows, i.e., the overall cumulated length of the microfiber part and of the cone

protruding from the cantilever groove is shorter for probe **GR12-C12-57** than for probe **ZeR09-C11-32**, which goes along with an interaction with the substrate occurring for the highest *Z* (~650 nm) for the former, and the lowest *Z* (~250 nm) for the latter. As reported in the previous section, no or a very limited contact jump is reported for the carbon cone probes. A hysteretic feature for the FDCs is shown in **Figs.18b-c,** as already obtained in **Fig.17c**, which could be explained likewise by a friction with the surface due to the probe misalignment (tilt). Indeed, the carbon cones are quite sharp, with a cone angle in the range of few degrees. The conical morphology is likely to make the structure stiffer than a CNT that would exhibit a diameter in the range of the cone apex, but this stiffness improvement may be somehow killed in case the cone is not perpendicular to the surface when the force is applied, hence promoting easier bending. Depending on the extent of the bending, which is not driven by the probe material only but also by the force applied, and the probe/surface interaction, two behaviors may occur depending on whether the probe apex pins or slips onto the surface [*8Strus2009, 10Buchoux2009*] as sketched in **Fig.19**.

The linear behavior observed for the **GR12-C12-57** from 650-700 nm goes up to a cantilever deflection of 155 nm for an applied force of 3. 2 µN (see **Table2**). No hysteresis phenomenon was observed this time contrary to what was reported for the same probe on **Fig.17c**. Maybe this could be related to the difference in the tip-surface interaction due to the difference in the substrate material involved (Si for the **Fig.17c**, TiO_2 for the **Fig.18a**). The nanocone probe **GR10-C08-65** also exhibits a linear behavior (from Z = 350 to 450 nm), but not very prominent as it is subsequently followed by a plateau (for Z between 450 and 600 nm) with a deflection up to 40 nm. A similar plateau is obtained for a lower contact force (around a 12 nm deflection) in the FDC corresponding to the welded nanocone **ZeR09-C11-32**. The presence of such a plateau may be explained by: *(i)* the existence of an overall effective spring constant of the probe which is different from the nominal spring constant of the cantilever only (in the case of the probe **GR10-C08-65**) and *(ii)* a strong tilt of the probe (in the case of the probe **ZeR09-C11-32**) as explained in [*8Strus2009*] whose effect may be enhanced when combined with a long length probe (indeed, probe **GR12-C12-57** shows a similar backward tilt as probe **ZeR09-C11-32**, but does not show such a plateau, which may be related to the shorter probe length). Due to these geometric characteristics, the probe can either slip (**Fig.19a**) or bend (**Fig.19b**) on the surface, thus impacting the performance and the use of the probes for PFQNM microscopy.

Then, for both the probes **GR10-C08-65** and **ZeR09-C11-32**, the plateau is followed by another linear part but with slope variations depending on the probe and whether the approaching or withdrawal paths are considered. There is a clear tendency for the curves in **Figs.18b** and **18c** to both resemble that of **Fig.19b**, i.e. corresponding to a pinning and bending effect. Such a similarity is expected from the fact that the slipping or pinning behavior difference depends on the tip/surface interaction hence in the type of materials involved, which should not differ for these two probes since they are both a carbon cone tip interacting with the same TiO_2 surface.

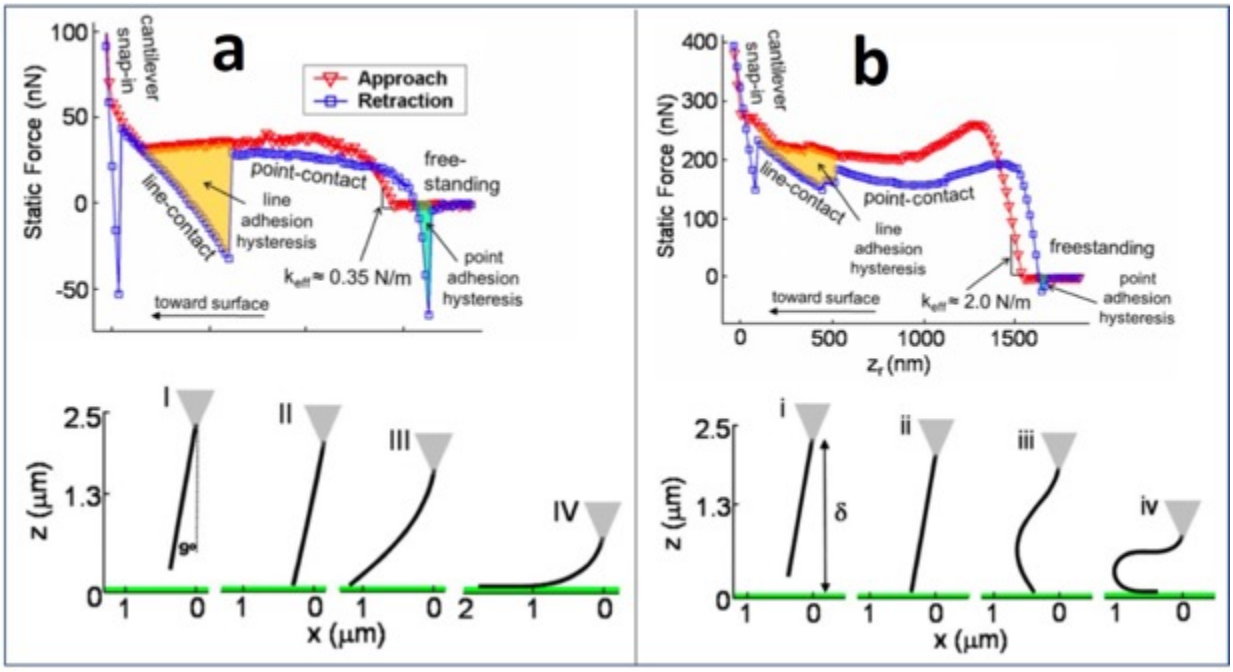

Figure 19: *Schematic representation of the behavior of a high aspect ratio probe (typically a CNT) on a surface* ***(a)*** *slipping (on a HOPG surface).* ***(b)*** *pinning and bending (on a SiO_2 surface). [*8Strus2009*].*

Table2 below reports the ranges of values of the cantilever deflection (ΔW) and of its conversion into an applied force (ΔF) by using the calculated spring constant. These parameters are determined for each probe in the linear behaviour from which the cantilever sensitivity is calculated in **Fig.18,** which constitutes the most optimal working range for PFQNM microscopy. Except for the probe **ZeR09-C11-32**, the minimum force is equal to 0 since the cantilever is not in contact with the sample even if the deflection is non-zero (so-called the deflection error). **Table2** indicates that the glued nanocone probes own the largest working range with the possibility to use forces up to 1.4 and 3. 2 µN for deflections up to 40 and 155 nm for **GR10-C08-65** and **GR12-C12-57,** respectively (considering only the FDCs in **Fig.18** and not the deflection at the cantilever breaking).

Probe name	GR12-C12-57	GR10-C08-65	ZeR09-C11-32	TESPA-V2
Cantilever deflection W_{min}	0	0	5 nm	0
Cantilever deflection W_{max}	155 nm	40 nm	25 nm	31 nm
ΔW	155 nm	40 nm	20 nm	31 nm
Force F_{min}	0	0	30 nN	0
Force F_{max}	3.2 µN	1.4 µN	154.3 nN	0.7 µN
ΔF	3.2 µN	1.4 µN	124.3 nN	0.7 µN

Table 2: *Summary of the main mechanical properties (indicative values extracted from the FDCs in* **Fig.18***) of the different tested probes.*

2.2.4. Capability of the carbon nanocones as PFQNM AFM probes

After the calibration, the capability of each nanocone probe for PFQNM AFM imaging was evaluated by the measurement of the Young modulus of different homogeneous (polystyrene (PS), polyethylene (PE), phenyl-C61-butyric acid methyl ester (PCBM), and polyimide (PI)) and heterogenous (PS/PE) polymer films. Such a technique allows the mapping of both the variations of height and Young modulus of a specified area. All of the measurements were performed with a scan speed of 2 Hz. However, the contact force between the probe and the substrate must be selected before scanning the surface. This force depends on the tip radius and the mechanical properties of the probes, and is chosen for each probe in order to generate a targeted deformation of the substrate. This deformation is selected to be close to 2 nm in order to avoid large tip-sample contact areas, which could limit the resolution [*16Belec2016*]. Besides, as explained in *Section 2.2.1*, the tip radius must be determined for the evaluation of the Young modulus of both the tip and the sample.

a) Apparent tip radius

The apparent radius can be deduced from the force magnitude produced by the cantilever when the tip is in contact with the sample (point B in **Fig.15**). Such evaluation was performed by peak force mode measurement on polystyrene as reference substrate (**Fig.20a**). The contact force for achieving a substrate deformation of 2 nm was targeted for each probe. The corresponding forces were determined at around 15 nN, 20 nN, and 37 nN for the probes **TESPA-V2, GR10-C08-65** and **GR12-C12-57**, respectively. The probe **ZeR09-C11-32** showed a much larger force (120 nN), which is consistent with the lowest spring constant previously measured for this probe. A similar apparent tip radius of 25 nm was determined for each probe except for the **GR10-C08-65** for which the apparent radius was about 5 nm (see Tables in **Fig.16**). This radius difference is not clearly understood, but it could be related to actual differences in the apex dimensions that are beyond the resolution capabilities of the SEM used (see **Fig.16**) and more in the capability of a TEM (see **Ch.3-Fig.17** and **Ch.3-Fig.20**).

b) Young modulus mapping on a homogeneous sample

Figs.20a-b depict the topography and Young modulus imaging of a PS substrate surface performed by the four probes. The statistical distribution of the different Young modulus values is also provided (**Figs.20c**) as calculated from the surface mapping. The value with the highest occurrence (expressed in %) is considered as the Young modulus of the sample. The apparent tip radius and force involving a sample deformation of 2.2 nm for each probe is indicated in **Figs.20c**. As seen on the histogram, the PS Young modulus was found to be in the range of 2-3 GPa by using the nanocone probes, which is close to the theoretical value yet slightly underestimated (3-4 GPa, according to [*21BrukerSiteb*]). The same sample was also studied by using a silicon **TESPA-V2** probe with a sample deformation of 1 nm which was obtained for a contact force of 15 nN, and the Young modulus found (around 4.5 GPa) is also rather consistent with the theoretical value, yet slightly overestimated.

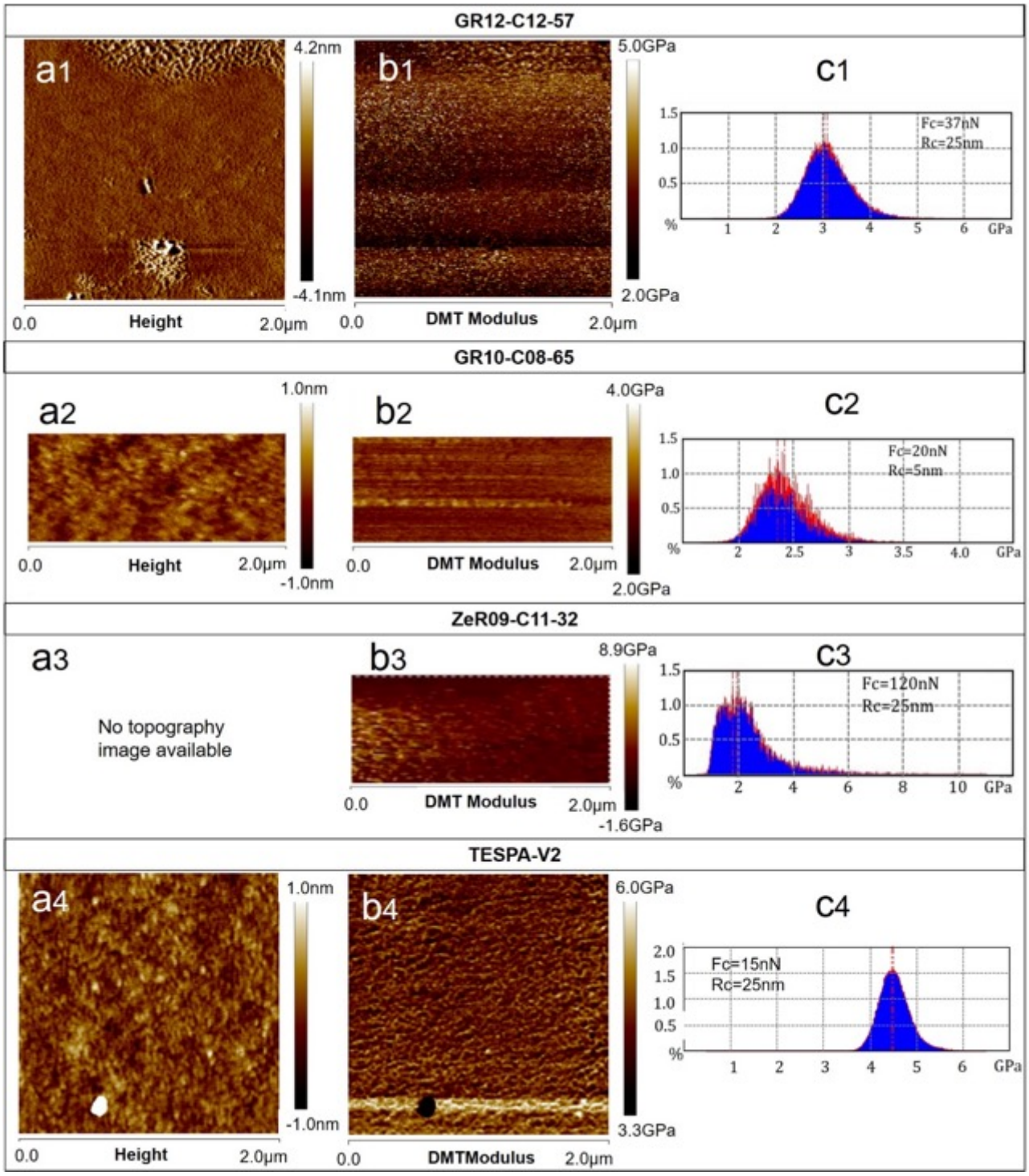

Figure 20: (a) *Topographic and* ***(b)*** *Young modulus mapping of a PS sample surface as obtained by the four probes.* ***(c)*** *represents the statistical distribution of Young modulus values extracted from the mapping. F_c and R_c stands for the contact force and tip radius, respectively.*

c) Young modulus imaging on a heterogeneous sample

Samples composed of several materials with different Young modulus were also studied for comparing the capability of the nanocones for discriminating mechanical property differences

in a multiphase material. A test sample from Bruker[25] based on a mix of polyethylene (PE) and polystyrene (PS) film spin-coated on a silicon substrate was used, as a quite common substrate for demonstration. The choice of the substrate was mainly based on the good contrast it can provide thanks to the two different elastic moduli present, typically 3-4 GPa for PS and 0.2-0.7 GPa for PE. Topography and Young modulus mappings of the surface performed by the different probes are presented in **Fig.21**.

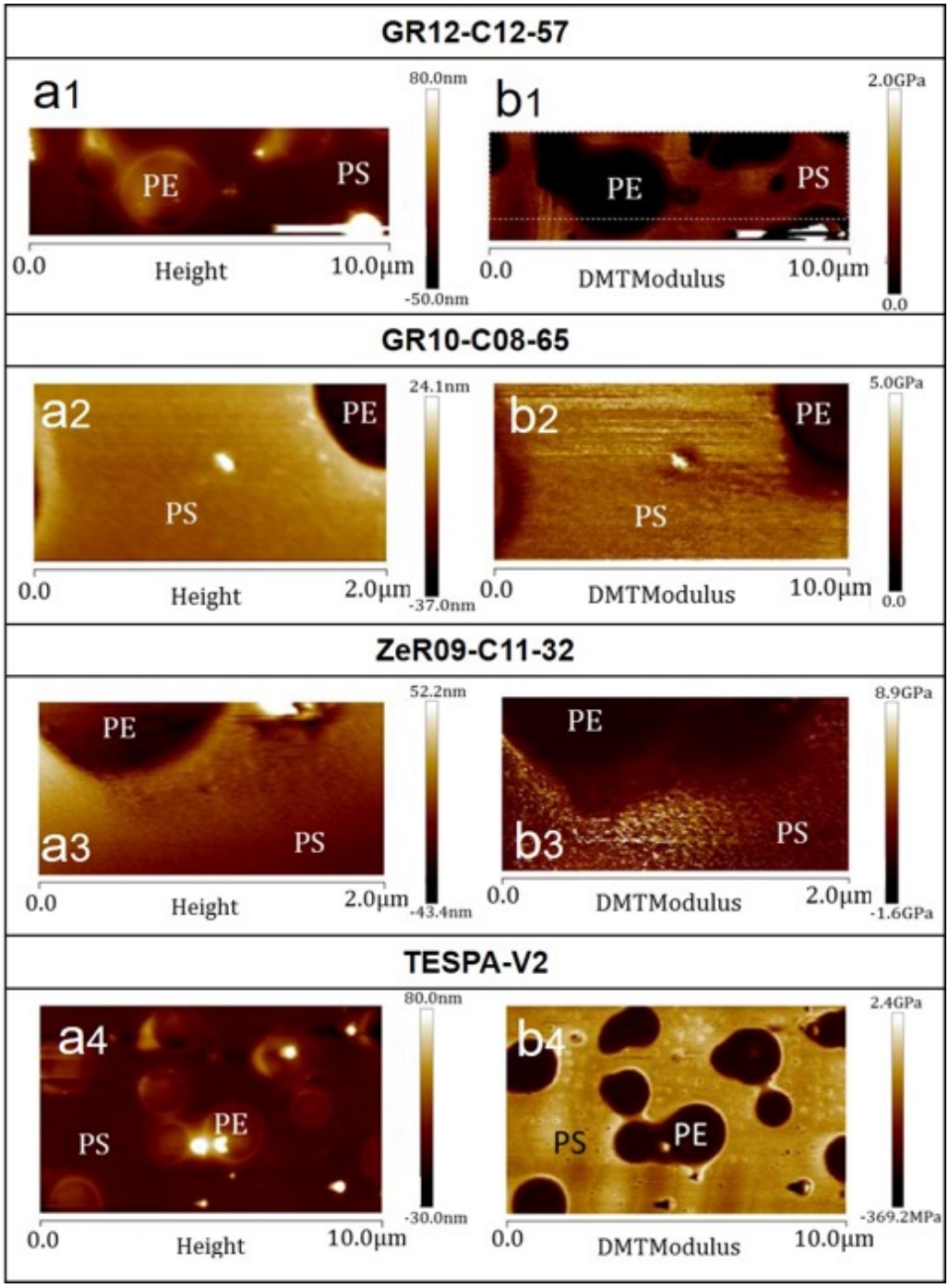

Figure 21: (a) *Topography and* ***(b)*** *Young modulus mappings of the PS-PE composite sample obtained from the different probes.*

[25] (https://www.brukerafmprobes.com/p-3724-ps-ldpe-12m.aspx)

The contact forces used for the mapping are of 25 nN, 50 nN, 120 nN and 30 nN for the probes **GR12-C12-57**, **GR10-C08-65**, **ZeR09-C11-32** and silicon **TESPA-V2**, respectively. The highest contrast in the Young modulus mapping images is provided by the **TESPA-V2.** The different Young moduli determined from these mappings are reported in **Table3** below along with the contact force used and the resulting average deformation of the PE and PS materials. The uncertainties are related to the dispersion of the Young modulus values in the histograms. The modulus values obtained are quasi systematically underestimated whatever the probe, including the reference (Si) one. However, in the average, the carbon cone probes provide values closer to the expected ones than the reference probe, and closer to reality for the PE than for the PS.

Probe name	GR12-C12-57	GR10-C08-65	ZeR09-C11-32	TESPA-V2
Contact force	25 nN	50 nN	120 nN	30 nN
Average deformation of PS	1 nm	1.5 nm	2 nm	1.5 nm
PS Young modulus	0.70 +/-0.10 GPa	2.90 +/-0.27 GPa	2.00 +/-1.00 GPa	1.50 +/-0.20 GPa
Average deformation of PE	25 nm	14 nm	2 nm	25 nm
PE Young modulus	0.10 +/-0.02 GPa	1.00 +/-0.10 GPa	0.18 +/-0.05 GPa	0.1 +/-0.05 GPa

Table 3: *Summary of the performances of the different probes for the Young modulus measurement of the polystyrene (PS) and polyethylene (PE) components of a heterogeneous (composite) sample.*

2.2.5. Evolution of the measurement parameters as a function of the contact force

The possible variation of the targeted deformation fixed at 2 nm during the measurement can induce some variations and uncertainties on the results. For this reason, the Young modulus of the homogeneous (PS, PE) and heterogeneous (PS/PE) substrates are also evaluated as a function of the applied force or sample deformation. **Figs.22a-c** present the Young modulus and deformation variation of PS and PE materials with respect to the contact force of the carbon probes on the surface, which is correlated with a targeted reference deformation in PS. The applied forces are selected according to the working range of the probes as described in **Table2**.

Equation (6) predicted a linear relationship between the Young modulus and the applied force. This is verified by the probe **GR10-C08-65** (**Fig.22b**) and is likely to be verified by the probe **GR12-C12-57** as well (**Fig.22a**), but not for the probe **ZeR09-C11-32**. For this probe, the non-linearity relates to the prevalence of the plateau and the short zone 1 in its FDC (**Fig.18c**). Furthermore, these graphs show the benefit of working at small sample deformation (hence at small contact force) since the Young modulus uncertainties tends to increase with the applied force (although, again, not for the probe **ZeR09-C11-32**). Such graphs allow the determination of the most suitable contact force in order to extract all the Young modulus of the composite sample on a same mapping with the lowest uncertainty possible.

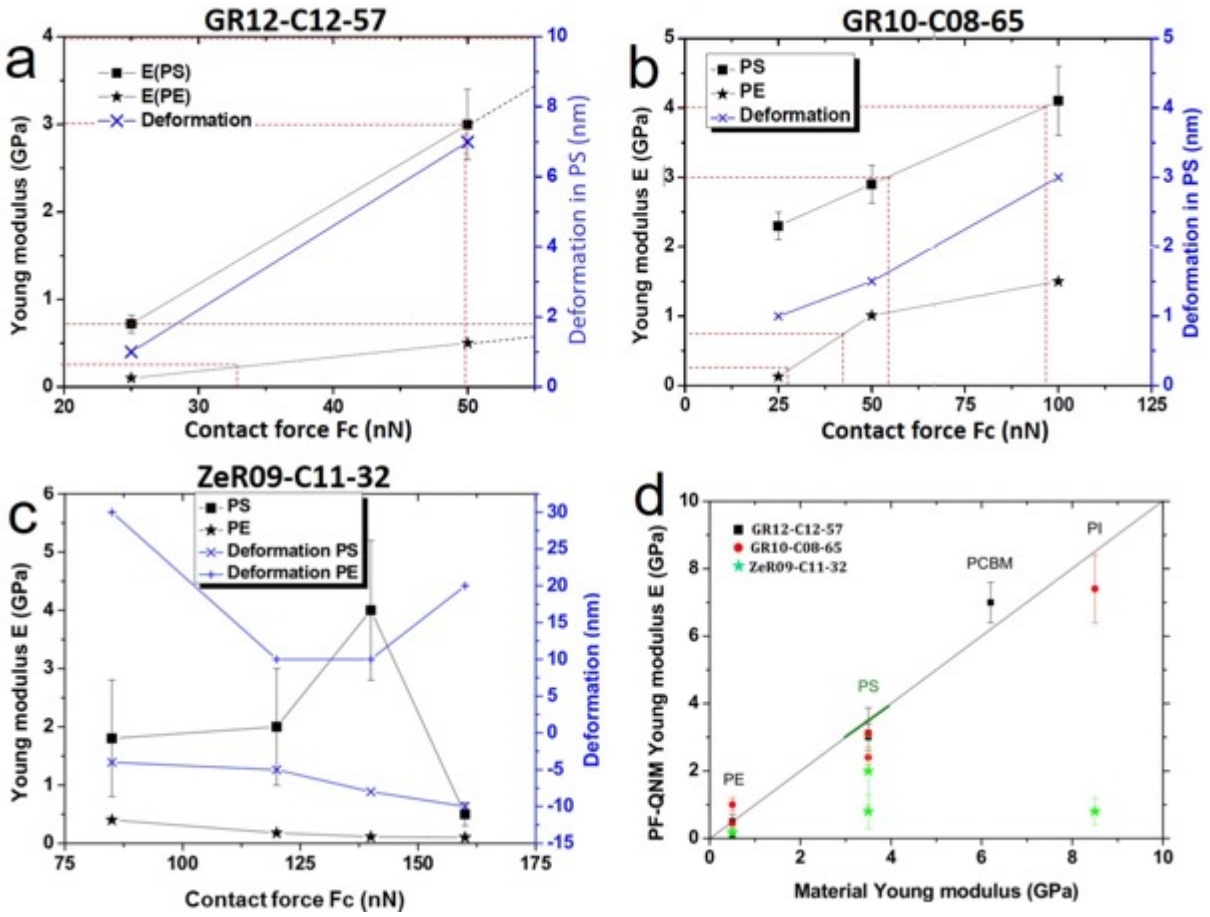

Figure22: (a) to (c) *Young Modulus and polymer deformation variation with respect to the contact force F_c for each carbon probe.* ***(d)*** *represents the Young modulus values of different polymers determined with the nanocone probes through PFQNM compared with the theoretical values.*

By considering the theoretical range values of elasticity modulus given before for each material, **Table4** indicates the suitable contact force range for the PS and PE materials taken from the graphs in **Figs.22a-c.** It appears that a contact force in the 50-60 nN range is suitable for the reliable measurement of the Young modulus of both the polymers at the same time with the probe **GR12-C12-57** while it constitutes an acceptable trade-off for the probe **GR10-C08-65**. The non-consistent results obtained for the probe **ZeR09-C11-32** may be explained by the impact of the plateau of the FDC curve instead of working in the linear behavior zone (**Fig.18c**).

Probe name	$E_{PS\text{-}min}$	$E_{PS\text{-}max}$	$F_{c\text{-}min}$	$F_{c\text{-}max}$	$E_{PE\text{-}min}$	$E_{PE\text{-}max}$	$F_{c\text{-}min}$	$F_{c\text{-}max}$
GR12-C12-57	3 GPa	4 GPa	50 nN	(60 nN)	0.2 GPa	0.7 GPa	33 nN	(50 nN)
GR10-C08-65			56 nN	94 nN			28 nN	43 nN

Table 4: GR12-C12-57 *and* ***GR10-C08-65*** *contact force ranges required for accurately characterizing Young modulus of PS and PE samples respectively. Values between parentheses are extrapolated.*

Finally, different Young modulus measurements were also performed by PFQNM microscopy with the carbon nanocone probes on PCBM and PI materials. Such measurements were compared with the theoretical values in order to evaluate the performance and the capability

of the probes. This comparison is plotted in **Fig.22d**. According to this graph, the probes **GR12-C12-57** and **GR10-C08-65** are well-suited for these measurement since the values found are close to the theoretical value. The elasticity modulus is determined with an uncertainty of 11% and 24% respectively for the probes **GR10-C08-65** and **GR12-C12-57**. Such uncertainties can be compared with that of the commercial silicon probes, which is 14%.

Checking how the probes survived the extensive PFQNM-AFM tests was qualitatively made (**Fig.23**). Only the probes **GR10-C08-65** and **ZeR09-C11-32** were able to be imaged because the probe **GR12-C12-57** was deliberately solicited up to breakage. It appears that the test has been quite stressful for the probe apices, including the reference probe **TESPA-V2**, as their radii have significantly increased (compare a2 to a4 and b2 to b4). Interestingly, image a3 reveals that the probe **GR10-C08-65** exhibits a severe backward angle, which may have contributed to the specific behavior of this probe in the deflection *vs* Z curve (**Fig.18b**) for instance.

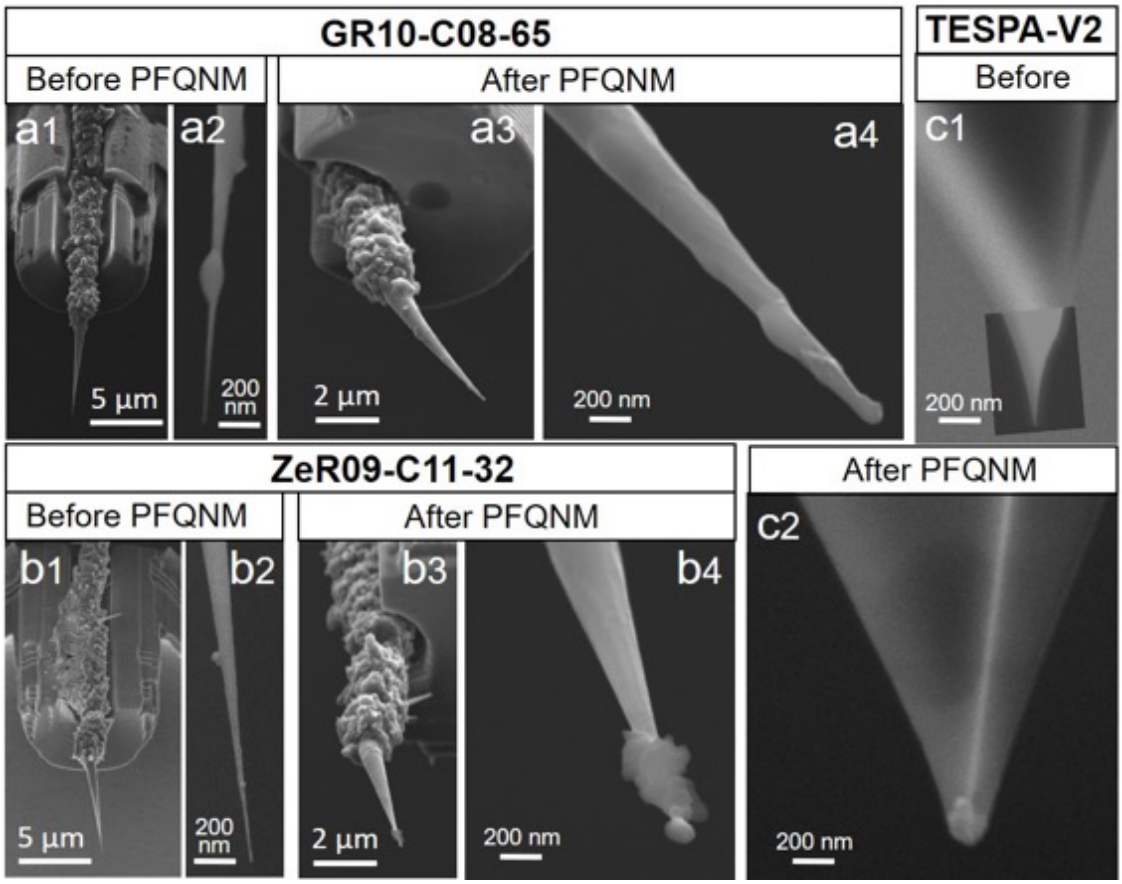

Figure 23: *SEM images of both the carbon cone-based probes* ***GR10-C08-65*** *and* ***ZeR09-C11-32*** *before and after the whole set of PFQNM-AFM experiments (photo credit: R. Cours, CEMES; S. Le Blond, UMS Castaing, Toulouse).*

3. Electrical modes

With the expansion of the SPM techniques, due mainly to their potential as nanometrology tools for research and industries (*e*.g., quality control of semiconductors, etc.), there is an increasing demand for using electrical modes [*22Avila2010, 23Benstetter2017, 24Hantschel2016*]. As the common and long-time-known Scanning Tunnel Microscopy (STM) mode can study a limited

range of samples (i.e. conductive and semiconductors), electrical AFM-related techniques such as Kelvin Force Microscopy (KFM), Scanning Impedance Microscopy (SIM), Scanning Capacitance Microscopy (SCM), Piezoresponse Force (electrical) Microscopy, Conductive AFM (C-AFM), Scanning Spreading Resistance Microscopy (SSRM), and Scanning Capacitance (or Gate) Microscopy (SCM/SGM) have been also developed (**Table4**).

Technique	Mode	Probe oscillating signal added to the DC biased tip	Probe detection signal	Topographic and electrical images sequence	Information provided
Detection at tip					
Scanning Kelvin force microscopy (SKFM)	NCM	AC	F	sep	Surface potential, work function
Scanning impedance microscopy (SIM)	NCM	AC	F	sep	Frequency-dependent potential
Scanning capacitance microscopy (SCM)	CM	AC	C	sim	Capacitance
Piezoresponse force microscopy (PFM)	CM	AC	D	sep	Sample-induced deformation
Conductive atomic Force microscope (CAFM)	CM	—	I	sim	Conductivity
Scanning spreading resistance microscopy (SSRM)	CM	—	I	sim	Spreading resistance
Detection across the sample					
Scanning gate microscopy (SGM)	NCM	—	I	sep	Current across the sample

*NCM = noncontact mode; CM = contact recording mode; AC = alternating current, DC = direct current; F = force harmonic response; C = capacitance gradient; D = deflection; I = current; sep = separated; sim = simultaneously.

Table 5: *Different electrical AFM-related modes and the main information they can provide* [*22Avila2010*].

As shown in **Table5,** all of these AFM-related techniques allow measuring distinctive electrical or electronic properties (i.e., capacitance, conductivity, surface potential, etc.) across topographic images. For achieving this, a sample is scanned with an electrically conductive probe. Unlike STM mode, which is based on the principle of tunneling current, most of the AFM electrical modes imply resistive or capacitive measurement through the tip, either in contact or non-contact (i.e., tapping mode). For this reason, both the electrical and mechanical properties of the tip are crucial aspects to consider.

As shown in **Table6**, most of the current commercial conductive probes are metal-coated (with, e.g., Pt, Au, or Ti) or doped-diamond-coated silicon, or solid metal, or solid doped-diamond probes [*25Hui2017*]. However, they all have limitations regarding mechanical and electrical stability [*26Jiang2019*]. Metal-coated tips, for instance, are fabricated by sputtering and evaporation processes, which can increase the original tip apex radius significantly [*23Benstetter2017*]. On the other hand, these probes frequently degrade during scanning, which can generate morphological changes of the probe and consequently further damages to both tip and sample [*26Jiang2019, 27Jacob1998*]. The latter cannot only affect the topographic image,

but also induce mechanical frictions and electrical instabilities during the measurements [*25Hui2017, 23Benstetter2017, 26Jiang2019, 27Jacob1998*]. The electrical instabilities seem to be reduced by using diamond-doped probes[*24Hantschel2016*], or other alternatives described in the literature, such as Pt-Ir coated probes further coated with a graphene layer [*25Hui2017, 28Lanza2013*]. Among these two latter solutions, graphene-coating seems to be less expensive and a promising durable method preferable to diamond, which has been reported to damage the surface due to its high modulus and hardness [*25Hui2017, 28Lanza2013*]. However, from our knowledge, these graphene-coated probes are not commercially produced yet.
It is also worth to note that aside from tip coating, cantilevers with reflective coating only can be also used for enhancing the laser reflection and sensibility of the cantilever optical detection system [*4Palleau2011*]. Despite all these efforts for improving conductive SPM probes, enhancing both current density and mechanical stability for long-time scanning period has not been achieved yet [*23Benstetter2017, 25Hui2017, 26Jiang2019, 27Jacob1998*].

Type	Model	Tip Coating (nm)	Bulk Materials	Tip Radius (nm)	Spring k (N/m)	Freq (kHz)	Manufacturer	Unit Price ($)
Metal varnished Si tip	SCM-PIC	PtIr	n-doped Si	20 + 5	0.2 (0.1–0.4)	13 (10–16)	Bruker	41.9
	OSCM-PT	Pt (20)	Si	15 + 10	2 (0.6–3.5)	70 (50–90)	Bruker	51.2
	SCM-PTSI	Pt/Si	n-doped Si	15 + 10	2.8 (1–5)	75 (50–100)	Bruker	156.7
	SMIM-150	TiW	Si_3N_4	50 ± 10	8 (7–9)	75 (70–80)	Bruker	139.8
	MESP	Co/Cr	Si	35 + 15	2.8 (1–5)	75 (50–100)	Bruker	116.7
	Arrow CONTPT	Cr/PtIr (5/25)	Si	33 ± 10	0.2 (0.06–0.38)	14 (10–19)	NanoWorld	38
	CONTPT	Cr/PtIr (5/25)	Si	30 ± 10	0.2 (0.07–0.4)	13 (9–17)	NanoWorld	42.98
	ATEC-CONTPT	Cr/PtIr (5/25)	Si	33 ± 10	0.2 (0.02–0.75)	15 (7–25)	Nanosensors	41.39
	PPP-CONTPT	Cr/PtIr (5/25)	Si	30 ± 10	0.2 (0.02–0.77)	13 (6–21)	Nanosensors	46.11
	PtSi-NCH	Pt	Si	30 ± 10	42 (10–130)	330 (204–497)	Nanosensors	152.08
	ACCESSS-NC-GG	Au	Si	30	113	330	App Nano	53.99
	TiN-ACT	TiN	Si	70	37	300	App Nano	39.5
	AC240TM	Ti/Pt (5/20)	Si	28 ± 10	2 (0.3–4.8)	70 (45–95)	Olympus	35.94
	NSC14/Pt	Pt or Au	Si	<30	5 (1.8–13)	160 (110–220)	µ-Masch	40.3
	Electri Tap 190-G	Cr/Pt	Si	<25	48 (20–100)	190 ± 60	Budgetsensors	37.26
Doped diamond varnished Si tip	CDT-FMR	Doped diamond	Si	83 ± 17	2.8 (1.2–5.5)	75 (60–90)	NanoWorld	143.66
	CDT-CONTR	Doped diamond	Si	83 ± 17	0.2 (0.02–0.77)	13 (6–21)	Nanosensors	152.08
	CDT-NCLR	Doped diamond	Si	83 ± 17	48 (21–98)	190 (146–236)	Nanosensors	152.08
	DD-ACCESS-NC	Doped diamond	Si	100–300	93	320	App Nano	154.48
	DDESP-FM	Doped diamond	Si	150 + 50	6.2 (3–11.4)	105 (80–103)	Bruker	132.8
	AD-0.5-AS	Single crystal diamond	Si	10 ± 5	0.5 (0.1–1)	30 (10–50)	Bruker	186.5
	AD-0.5-SS	Single crystal diamond	Si	<5	0.5 (0.1–1)	30 (10–50)	Bruker	279.6
Solid metal AFM tip	RMN-12PT400B	None	Pt	15 ± 5	0.3 (0.18–0.42)	4.5 (3.15-5.85)	Bruker	74.5
Solid doped diamond AFM tip	SSRM-DIA	None	Diamond	5–20	3/11/27	-	Bruker (IMEC)	372.2
	P-CT1T2S	None	Diamond	-	0.71	50	Advanced Creative Solution Technology	1050
	P-CTCR1S	None	Diamond	<10 nm	0.35	35	Advanced Creative Solution Technology	950

Table 6: *Main characteristics of available commercial SPM conductive probes* [*25Hui2017*]. *In this work, a metal varnished Si tip and a Si-doped as depicted in* ***Fig.26*** *are used for comparison with our nanocones probes.*

In this work, the conductive capability (without coating), apex radius and slender shape of our nanocone probes are tested for C-AFM, Scanning Tunnel Microscopy (STM), and Kelvin Force Microscopy (KFM) respectively. Performances are compared with those of commercial conductive probes.

3.1. Conductive AFM (C-AFM)[26]

3.1.1. Principle and notions

The C-AFM technique allows a topographic image and a mapping of local electrical and electronic properties of a variety of materials from insulating thin films, dielectric, 2D materials to soft molecular electronics [*23Benstetter2017*]. The working principle of the C-AFM is based on the application of a bias voltage between a sample surface and a conductive probe (**Fig.24**). Aside from mapping the surface current, it is also possible to record current-voltage (*I-V*) curves of a specific locus on the surface [*23Benstetter2017*]. In C-AFM, the topographic information is detected by a regular optical system (laser and photodiode), whereas the measured current is collected by the tip and redirected to an amplifier which is connected to the tip as sketched in **Fig.24**. The latter allows differentiating whether the performances of the technique are affected by topographic artefacts or by electrical conductivity issues. Concerning the topographic imaging, C-AFM-related techniques works mostly in contact mode, although some type of tapping can be also employed for reducing tip-sample damages caused both lateral and vertical forces when applying high electrical fields.

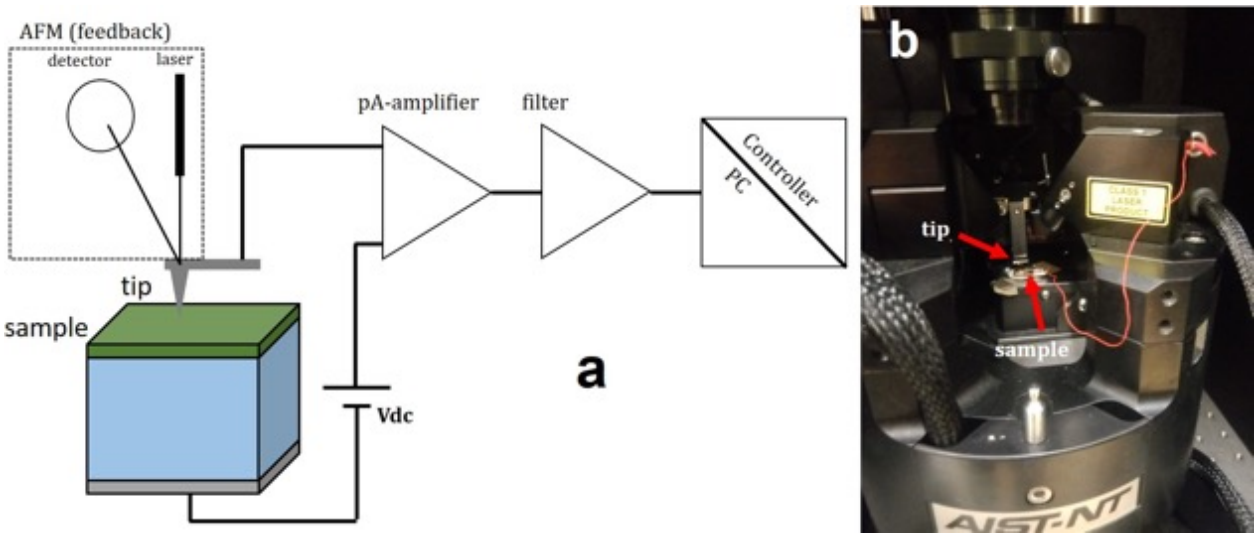

Figure 24: (a) *Schematic of a C-AFM working principle in tapping mode. A bias voltage is applied from the sample to the tip or vice-versa. Then, the analogous current signal is converted into a digital voltage by using the amplifier and a filter.* ***(b)*** *The AIST-NT, SPM 1000 model AFM microscope used for our C-AFM tests. It is operated in tapping mode called point by point (I top mode), allowing current from few pA to µA. The voltage applied for I/V curves can go from -8 to +8 V.*

[26] This part of the work has been carried-out in collaboration with M. Tasse and G. Molnar (LCC, Toulouse).

Tip-sample damage due to mechanical or current-induced wearing during the scanning process is actually the main drawback of C-AFM. Mechanical wear for instance, can increase up 6 times the initial tip-radius of the probes as depicted in **Fig.25** [*23Benstetter2017*]. Therefore, considerations concerning achieving smaller apex radius, as well as good electrical and mechanical properties of the tip are of upmost importance in this mode.

For metal-coated or varnished Si-tips, the radius can reach up 50 nm, whereas the effective emission area can go from 1 nm^2 to 800 nm^2 [*26Jiang2019*]. This effective area response in C-AFM measurements has be shown to be affected by capillary effects (i.e. induced by the nanosized film of water covering the sample surface) [*26Jiang2019*].

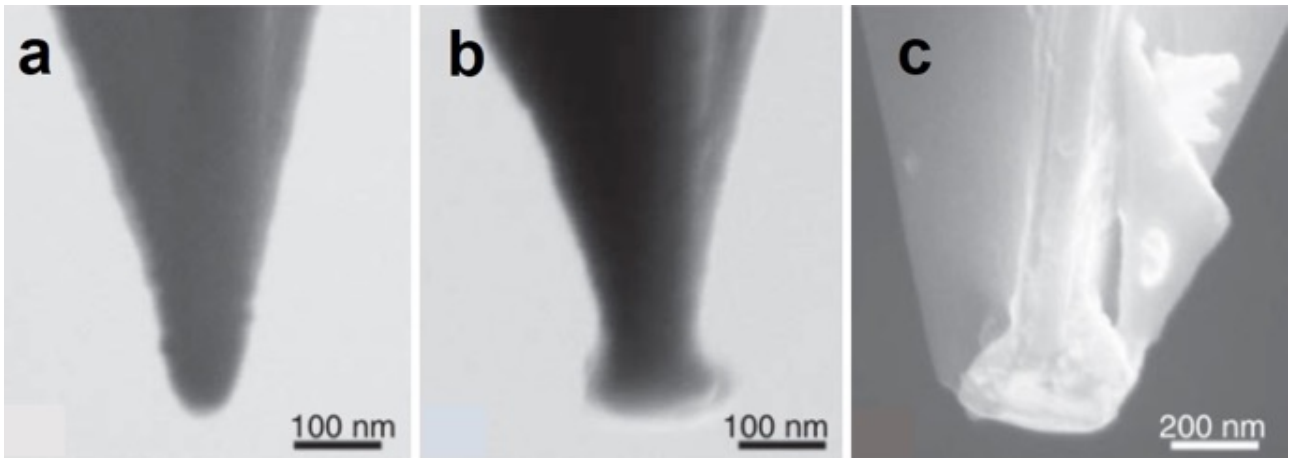

Figure 25: *SEM images showing the evolution of a metal-coated tip (CoCr):* ***(a)*** *Before conducting any C-AFM test.* ***(b)*** *After at least 10 scans and I-V measurements.* ***(c)*** *Example of a worn and damaged tip [23Benstetter2017].*

3.1.2. Capability of the carbon nanocones as C-AFM probes

a) Sample description, imaging protocol and performances

Three carbon nanocones probes noted **ZeR06-C11-14, ZeR07-C07-26** and **ZeR09-C05-23** (all mounted by means of the FEBID process) are tested and compared with two silicon probes **HQNSC15** (Pt-coated, 30 nm radius) from Micromash and a **PPP-NCL A-10** (doped Si, without coating) from Nanosensors. The main characteristics of these probes are presented in **Fig.26**.

Current -voltage (I-V) curves and electrical mapping respectively were conducted on a sample prepared as described in section 2.1.4.a, consisting in gold nanoparticles deposited from a droplet of a suspension in deionized water on a Highly Oriented Pyrolytic Graphite (HOPG) substrate[27] from Bruker company. The sample was cleaned using a Gatan Solaris 950 plasma cleaner (H_2/O_2= 1:00 during 10 minutes) for removing any possible organic species (e.g., surfactants) or water layer formed on the sample surface in order to avoid its impact on the electrical measurements.

[27] https://www.brukerafmprobes.com/p-3516-hopg.aspx

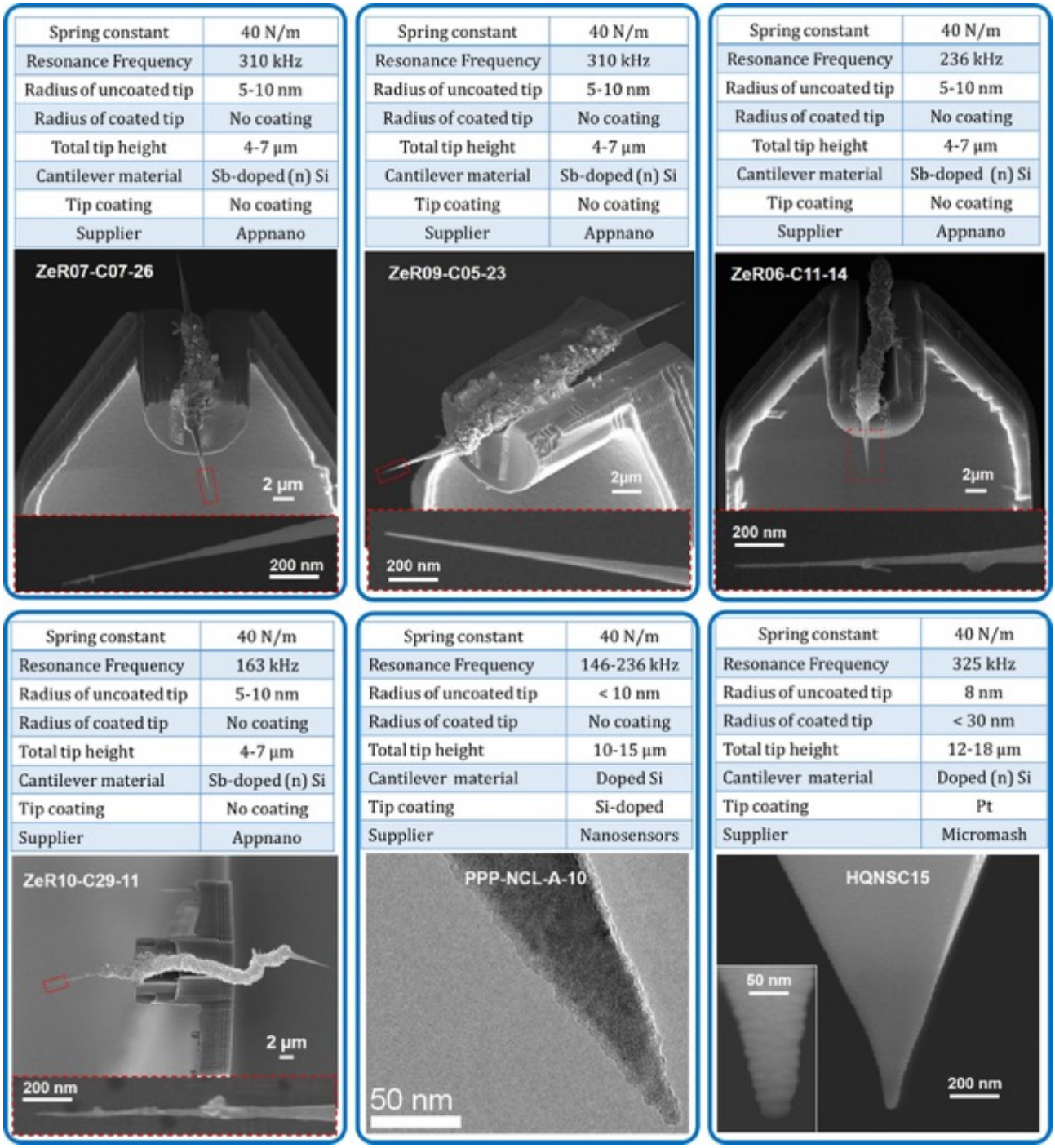

Figure 26: *Main characteristics of the nanocone and silicon probes used for the C-AFM tests. The grainy aspect of the HQNSC15 probe is due to the Pt coating (photo credit: R. Cours, CEMES; S. Le Blond, UMS Castaing, Toulouse).*

The tests were performed on C-AFM in tapping mode (point by point) or I top mode using a microscope AIST-NT, SPM 1000 model as depicted in **Fig.24**. In this mode, local current is measured in contact mode; but the displacement from each scanning point to another is made in semi-contact or tapping mode[28]. For I/V measurements, each curve was generated by the

[28] SPM Smart SPMTM-1000 Instruction Manual

two-pass procedure (trace-retrace)**.** This includes four measurements at each point, for ascertaining the homogeneity and reproducibility (**Fig.27**).

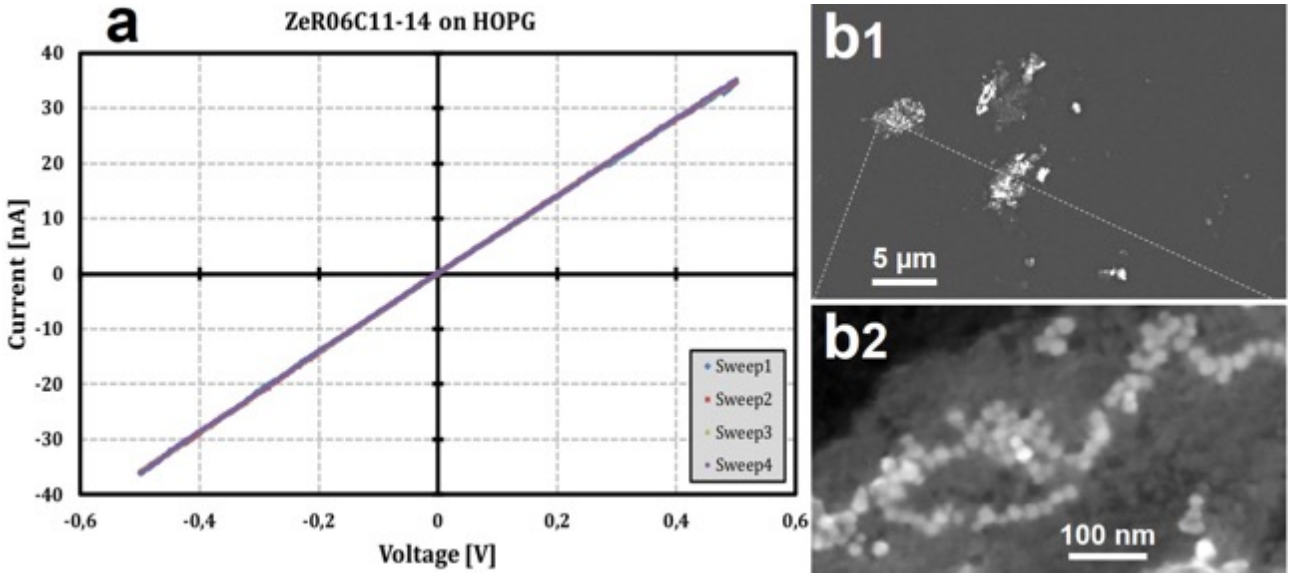

Figure 27: (a) *Example of reproducibility test involving four I-V plots obtained on the same locus on HOPG with the carbon cone probe ZeR06-C11-14. The four plots are exactly superimposed.* ***(b)*** *SEM images of Au nanoparticles onto the HOPG substrate (photo credit: S. Le Blond, UMS Castaing, Toulouse).*

Although, for preliminary tests, bias voltages were conducted up -8 to +8V for assessing the maximum capability of the probes for supporting high voltages, in this work we will present results concerning optimized measurements when a range of voltages in between 0.5-2 V was applied to the sample (exceptionally 5 V), and the tip was grounded. The I-V curves were taken at up to 6 different locations within a topographic image of 5X5µm^2 wide, whereas current mapping of 2x2µm^2 wide scan were also conducted. Current mappings33 were performed in so-called *U-tip* configuration where a positive bias voltage is applied to the tip while the potential of the substrate is maintained at 0 (as opposed to the so-called *U-smpl* configuration, which is the opposite).

b) Current-voltage (I-V) curves and current mapping

Figs.28-29 depict two different topographic images performed by a nanocone probe and a silicon probe respectively, with I-V curves measured on different zones of the sample. Various current variations and behaviors can be seen with respect to the voltage for each probe. The linear current variation on the HOPG substrate (top-right) is typical of an ohmic contact, while the small fluctuations and non-linear S-shape current variations with the Au nanoparticles correspond to a Schottky contact.

In order to verify whether the conductivity behavior could be induced by some specificity of the tip, a new set of experiments was performed with another carbon cone probe, now the **ZeR06-C11-14**. In addition, another reference tip was also tested (the Pt-coated **HQNSC15** from Micromash). Results are reported in **Figs.30-31**, and are consistent with the previous findings.

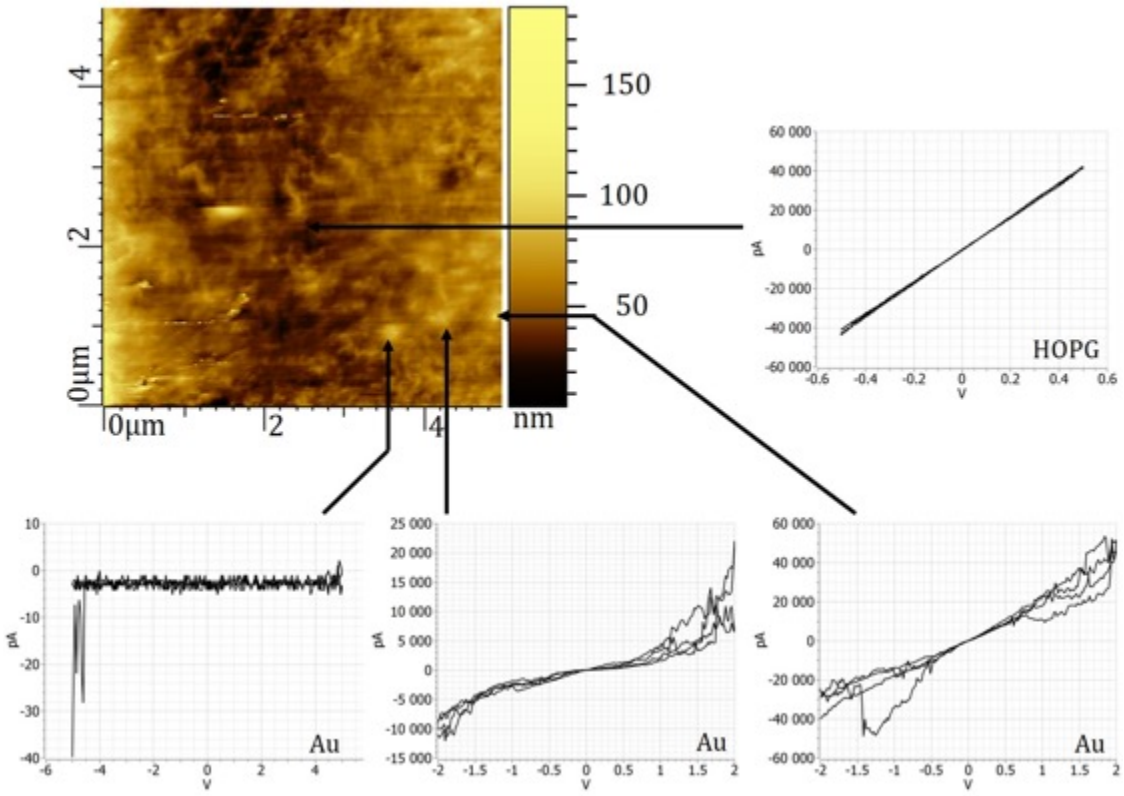

***Figure 28**: Topography image of the HOPG/Au sample performed by the carbon nanocone probe **ZeR10-C29-11**. The different insets correspond to I-V curves on different regions on the sample.*

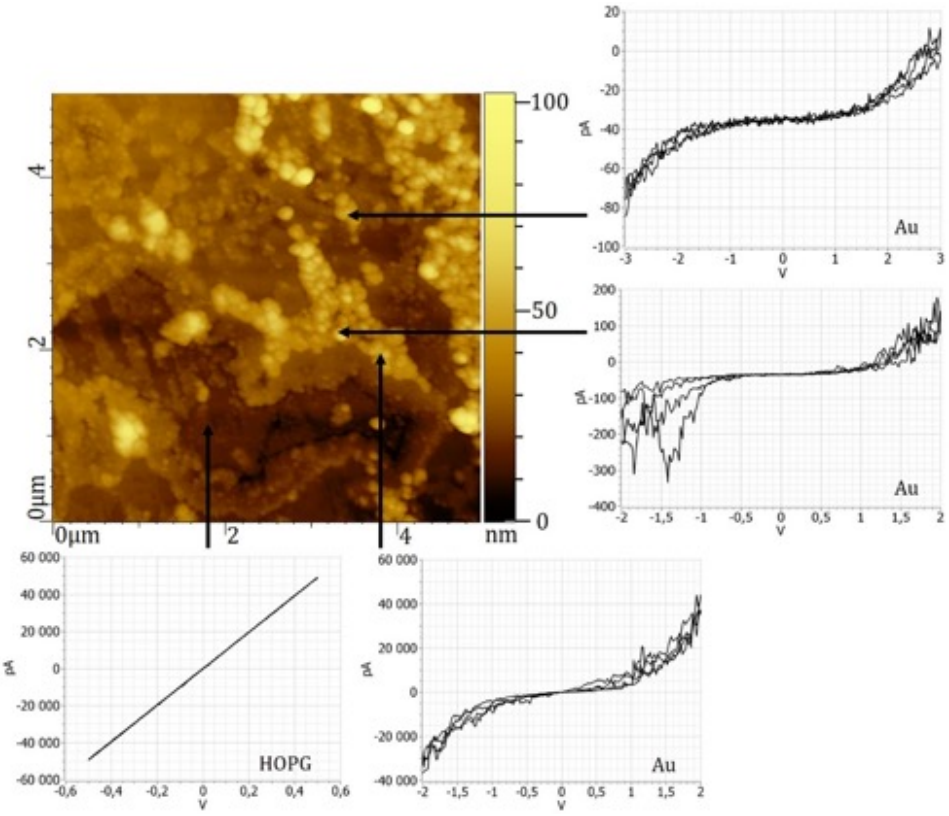

***Figure 29**: Topography image of the HOPG/Au sample performed by the silicon probe **PPP-NCL A-10**. The different insets correspond to I-V curves on different regions on the sample.*

With the carbon cone probe, for an applied voltage of 0.5 V on HOPG, a current around 35 nA is reached (**Fig.30a**). However, when the same probe is placed on an Au nanoparticle, reaching the same current requires almost 2 V due to the Schottky contact (**Fig.30b**). The topographic image showing the region of the sample where the I-V curves were measured is given in **Fig.30c**.

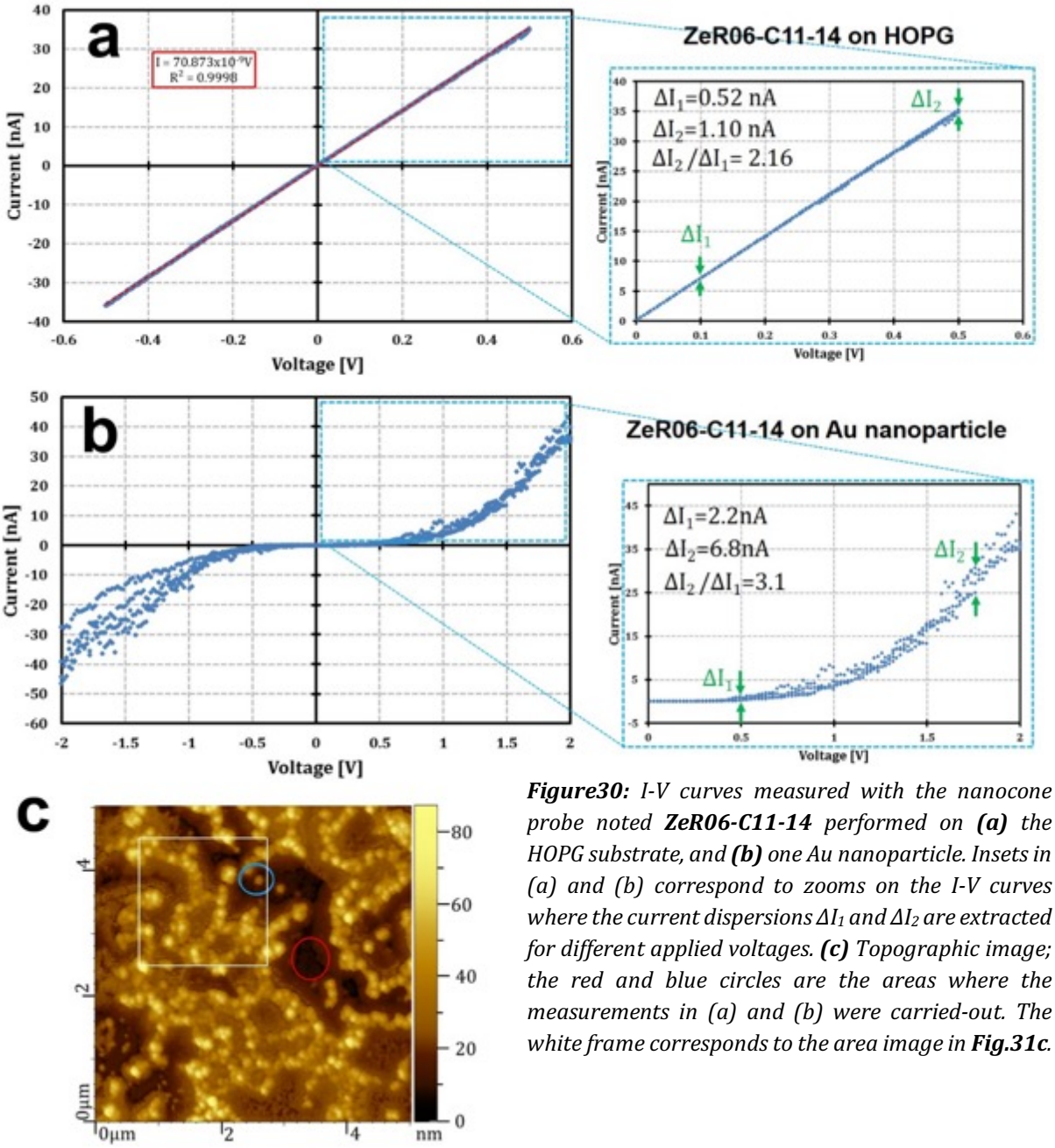

Figure30: *I-V curves measured with the nanocone probe noted* ***ZeR06-C11-14*** *performed on* ***(a)*** *the HOPG substrate, and* ***(b)*** *one Au nanoparticle. Insets in (a) and (b) correspond to zooms on the I-V curves where the current dispersions ΔI_1 and ΔI_2 are extracted for different applied voltages.* ***(c)*** *Topographic image; the red and blue circles are the areas where the measurements in (a) and (b) were carried-out. The white frame corresponds to the area image in* ***Fig.31c****.*

With the **HQNSC15** reference probe, the current obtained on HOPG at 0.5 V is about the same or even lower (~32 nA, **Fig.31a**) as with the carbon probe. On the other hand, 0.5 V is sufficient to reach a current of ~23 nA on the Au nanoparticle tested (**Fig.31b**), whereas 1.7 V was necessary for reaching the same current with the carbon probe (**Fig.30b**).

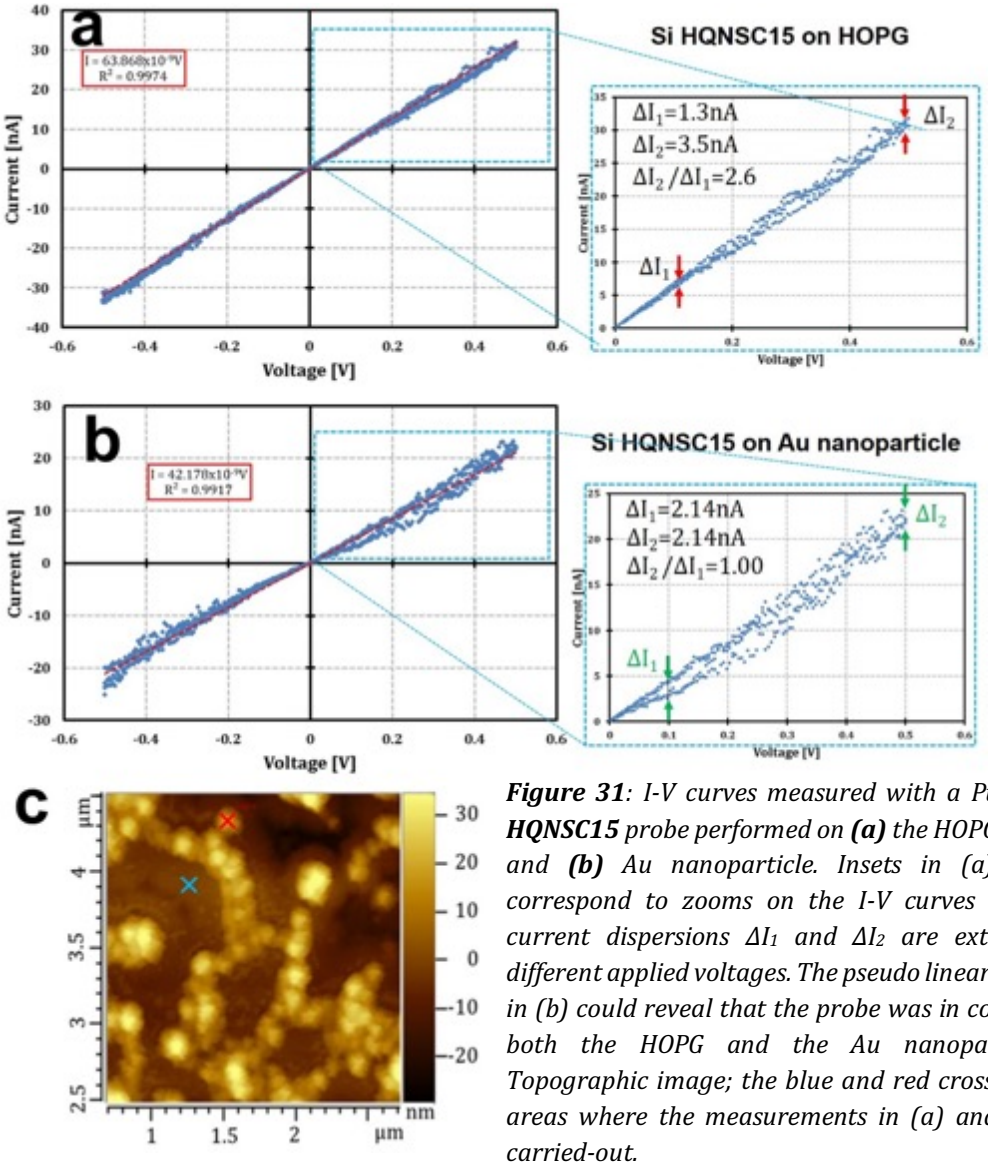

***Figure 31**: I-V curves measured with a Pt-coated Si **HQNSC15** probe performed on **(a)** the HOPG substrate and **(b)** Au nanoparticle. Insets in (a) and (b) correspond to zooms on the I-V curves where the current dispersions ΔI_1 and ΔI_2 are extracted for different applied voltages. The pseudo linear behaviour in (b) could reveal that the probe was in contact with both the HOPG and the Au nanoparticle. **(c)** Topographic image; the blue and red crosses are the areas where the measurements in (a) and (b) were carried-out.*

The similarity in both the carbon cone probe and the reference probe results on the HOPG substrate is good news, as it ascertains that the carbon probes are suitable as C-AFM probes. Indeed, it means that their performances are not altered significantly by the thin amorphous carbon film that possibly exists onto the cone surface, as it was revealed at the end of *Chapter 3* for FEBID-prepared probes by the Raman study. Hence, the discrepancy observed between the carbon cone probe and the reference probe in the current value for a given voltage results from differences between the Au nanoparticles measured, not from the probes or the probe-particle interactions.

From the ohmic behavior of the measurements reported in **Figs.30a and 31a**, an evaluation of the conductance of the whole system constituted by the probe (tip and cantilever), the contact point between the probe and the surface, as well as the contribution of the sample, an estimation of the conductive behavior of the probe can be performed. Hence, by comparing the conductance of the probes given by the slope coefficient of the I-V curves on HOPG, it appears that the nanocone probe has a slightly higher conductance of around 70.9 nS than the

silicon one with a conductance of almost 63.9 nS. This conductivity difference implies that a higher current is achieved for the nanocone probe than for the silicon probe at a given voltage, as already pointed out above. Consequently, as a better imaging contrast is determined by the less resistive probe, the nanocone probe should allow a better phase discrimination that the commercial one.

More in the details, considering the results on HOPG as a reference material obtained with both probes, it can be seen from the different I-V curves (**Figs.30a** and **31a**) that a better resolution in current is obtained when working at lower voltages whatever the probe as the current dispersion increases with the voltage (ΔI = 0.5 nA against 1.6 nA for the carbon probe, and 1.3 nA against 3.5 nA for the reference Pt-coated Si probe, at 0.1 V at 0.5 V respectively). The observation is the same when measuring an Au nanoparticle, yet involving higher dispersions (ΔI = 2.2 nA for the carbon probe and 5 nA for the reference probe, at 0.5 V). Based on this example, the resolution in current is stated to be better for the carbon probe than for the Pt-coated Si probe. This current dispersion variation has an impact on the resolution of the current mapping images, as shown on **Figs.32a-b** where a better resolution is achieved at lower voltage.

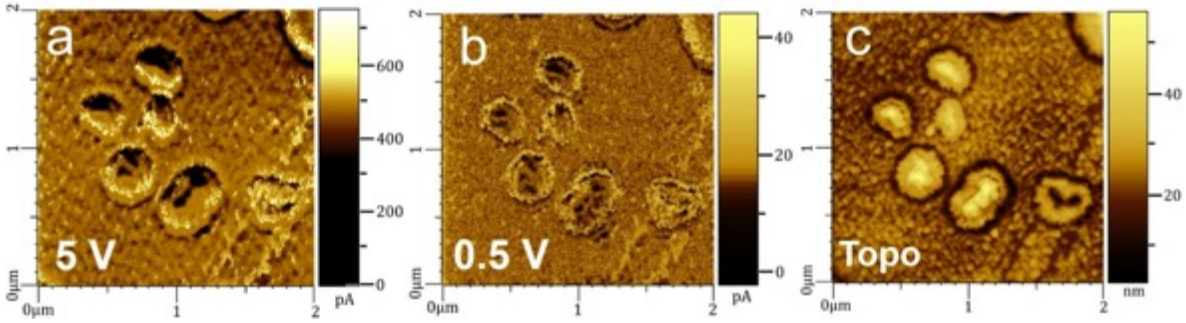

Figure 32: (a) *Current mapping image of the Au/HOPG substrate obtained by the nanocone probe* ***ZeR07-C07-26*** *at 5 V.* ***(b)*** *the same, at 0.5 V.* ***(c)*** *Topographic image.*

For comparison, **Fig.33a** reports a current mapping on another area of the same Au/HOPG sample obtained from the reference probe **HQNSC15** at 0.5 V, along with the corresponding topography image (**Fig.33b**). Details in **Fig.33a** appear less sharp than with the carbon probe for the same bias (**Fig.32b**) indicating a lower resolution, consistently with the lower current dispersion observed for a carbon nanocone probe with respect to a reference Si probe at 0.5 V (**Figs.30a** and **31a**, respectively).

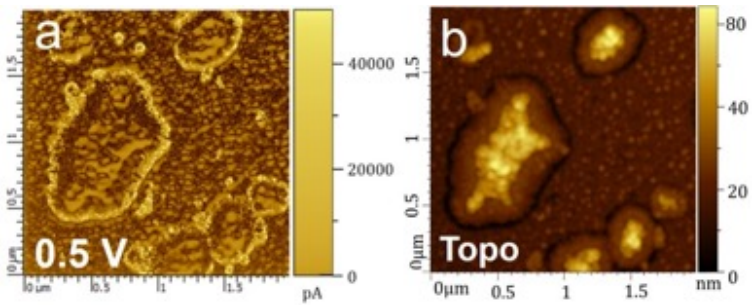

Figure 33: (a) *Current mapping image on the Au/HOPG substrate obtained by the Si reference probe* ***HQNSC15*** *at 0.5 V.* ***(b)*** *Topographic image.*

All these results show the promising properties of carbon nanocone probes for C-AFM imaging. Although our measurements concern the whole system and not only the tip, these are favorable results when considering that a bare nanocone (i.e., without any coating) is used, whereas the silicon commercial probe is coated by 30 nm of Pt.

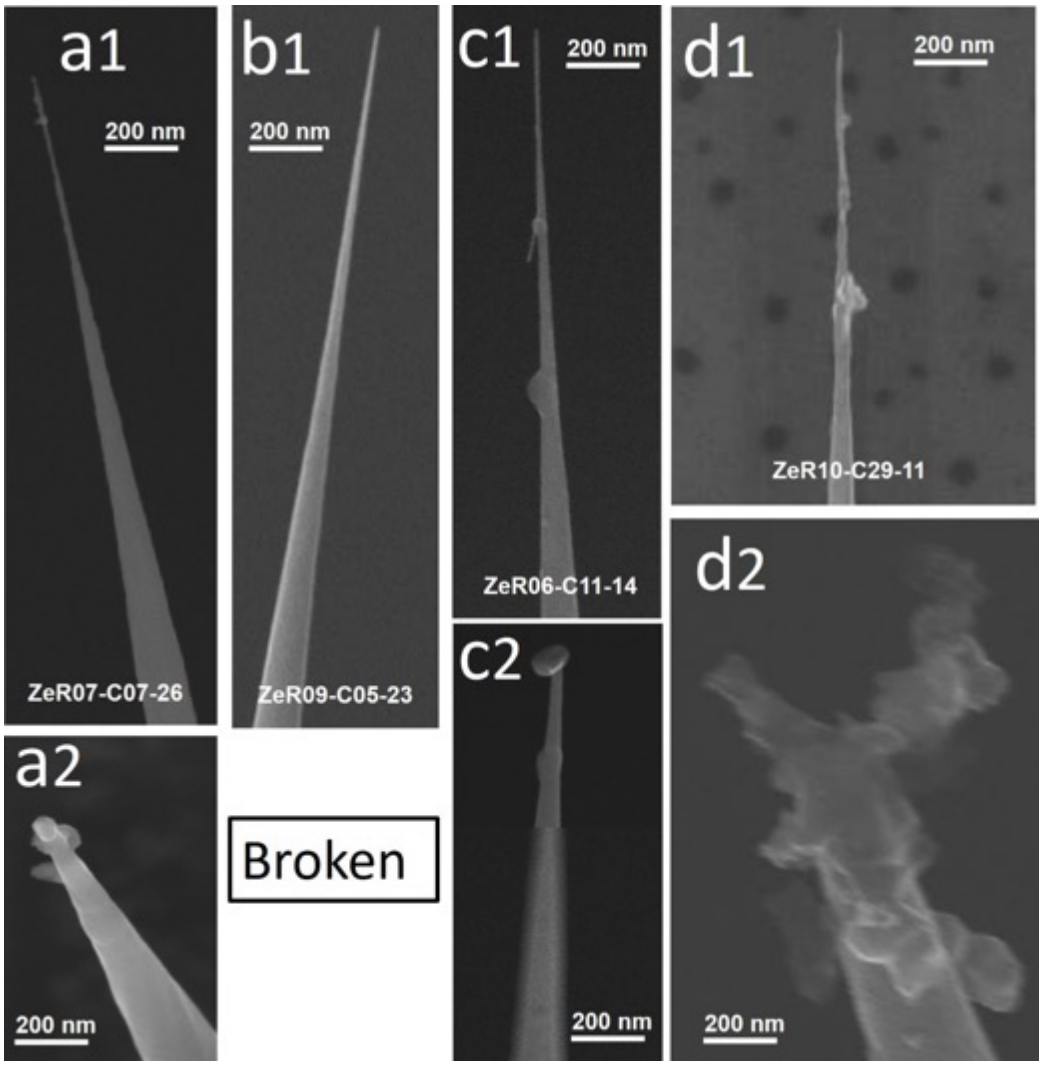

Figure 34: *SEM images of the nanocone probes before (a1 to d1) and after (a2 to d2) the C-AFM tests. From the apex radius of the tips after test, it is estimated that the probe* ***ZeR07-C07-26*** *was shortened by 800 nm, the probe* ***ZeR06-C11-14*** *was shortened by 1 µm, and the probe* ***ZeR10-C29-11*** *was shortened by about 3 µm. (Photo credit: R. Cours, A. C. Torres-Dias, M. Kandara).*

Fig.34 shows SEM images before and after the C-AFM tests. It can be observed a variable degree of wear suffered by the nanocone probes. The tip apices have systematically enlarged, sometimes considerably. This was caused not only by some kind of flattening of the tip (as in **Fig.34c2**) but mostly by a shortening of the cones due to the more or less extensive loss of the thinnest part. The most severe damage was suffered by the probe **ZeR10-C29-11**, which is the one that has shortened the most, and whose remaining apex looks like it has burst or heavily exfoliated (**Fig.34d2**). The latter reminds the unwrapping effect of the graphenes by an excess current that was observed by Bacon on carbon whiskers (see **Ch.1-Fig.11b**) and which was also

suspected on our cones after preliminary STM tests (see **Ch.2-Fig.21**). Correspondingly, the probe **ZeR07-C07-26**, which was actually exposed to a relatively low voltage range (but a single current mapping at 5 V) shows a limited wear, possibly mostly mechanical, whereas the probe **ZeR10-C29-11**, which worked in the highest range of voltage (-6 to 6 V), shows hints of presumably current-induced wear instead.

3.2. Scanning Tunneling Microscopy (STM)[29]

3.2.1. Principles and notions

STM allows three-dimensional surface mapping and atomic resolution imaging of a conductive or semiconductor sample. This is possible by scanning it with a conductive probe. In STM, as soon as the electron orbitals of the atoms from the probe and from the substrate are close enough to overlap, corresponding to a narrow gap of 0.3-1 nm, a tunnel current may flow thanks to a bias voltage applied between the probe tip and the substrate [*5Hafner2010]*. This tunnel current corresponds to the electronic density of states present on the surface, and it varies exponentially with the separation distance between the sample and the probe [*29Hansma1998].* Thus, surface structure information can be extracted from the tunnel current variation as a function of the tip position.

As depicted in **Fig.35**, the position in (X, Y, Z) of the probe is traced by a piezo-electric system. The tip sample distance is controlled, at constant current, by a bias voltage from typically few mV to 2 V, applied to the tip. The lower the voltage, the closer to the surface and vice-versa. Then, a tunnel current, typically in the range of 0.2 to 10 nA, can be generated [*5Hafner2010]*.

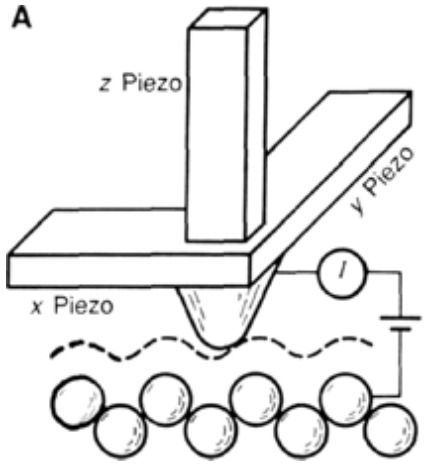

Figure 35*: Schematic representation of the STM working principle [*29Hansma1998*].*

When working in STM, two configurations are possible: either working in constant height or constant current mode, at room conditions (in air) or under vacuum environment. When working at constant height, the current is monitored by a specific height point, whereas in the

[29] This part of the work was carried-out in collaboration with G. Seine and R. Péchou (CEMES).

latter mode, the height is varied in order to maintain a constant current thanks to a feedback loop system. However, constant current mode and vacuum environment are the most recommended conditions for achieving atomic resolution images [*5Hafner2010*]. Whatever the mode chosen, a very sharp ended tip with well-defined atomic structure (crystallinity) is required. The latter is a key point since mostly the last atoms of the tip are in interaction with the sample, being responsible of the generation of the tunnel current effect.

As previously described in *Chapter 3*, different STM tips such as PtIr, Au, or W tapered wires exist. However, PtIr alloy probes are the most currently used because it combines the stiffness of the Ir and the chemical inertness of the Pt (hence preventing the formation of an oxide layer) for ensuring better resolved images [*5Hafner2010*].

In this work, the feasibility of nanocones probes to be used for STM topographic imaging is tested using constant current mode in air condition.

3.2.2. Capability of the carbon nanocones as STM probes

a) Samples description, imaging protocol and performances

Nanocone tips mounted onto either a PtIr wire via the FIBID process or an Au wire by the FEBID process as described previously in *Chapter 3 Section 3.2.3* were tested for obtaining topographical STM images of three different substrates: a piece of Au-coated Si wafer, a indium tin oxide (ITO) surface, and a HOPG (same origin as that used for the AFM tests).

During a first set of experiments, the tests were performed on the HOPG substrate using a Multimode IIIA Nanoscope microscope, however different experimental issues were faced. The carbon nanocones mounted onto a PtIr wire (see an example in **Ch3-Fig.13a1-a3**) were able to allow recording a tunnel current but were not able to provide any contrast. The suitability of the PtIr extremity, which was very coarse because merely cut with a wire cutter as for preparing regular PtIr STM probes, was then questioned because possibly able to generate protruding splinters able to interact with the substrate in parallel with the carbon probe. Therefore, Au wires electrochemically tapered where then preferred (see an example in **Fig.36**). First attempts did not succeed in acquiring any image of the sample either when the same standard conditions (250 mV, 5 nA) as those routinely used for Pt-Ir probes were used. Thanks to the SEM characterization of the carbon probe **Au-e-002** used for these tests, an unwrapping phenomenon of the nanocone was observed, as already shown in *Chapter 2* (**Ch2-Fig.21**). This suggested that, assuming a helical wrapping of the constituting graphenes as discussed in *Chapter2 Section 2.4.2*, the current the nanocone was subjected to was too high, that is to say high enough for inducing the graphenes to unwrap, as previously observed in the literature for graphenic whiskers [*30Bacon1960*] or calculated [*31Braga2004*]. Consequently, other tests were conducted at lower current using a fresh nanocone probe (numbered **Au-e-005**) on an Au film onto a SiO_2 substrate. The STM microscope Dimension D3100 from Bruker was used for allowing small current values down to 300 pA. The idea of this test was to start with the lowest current as possible and then to increase it until an image was obtained in order to establish the most suitable current working range for our nanocone probes.

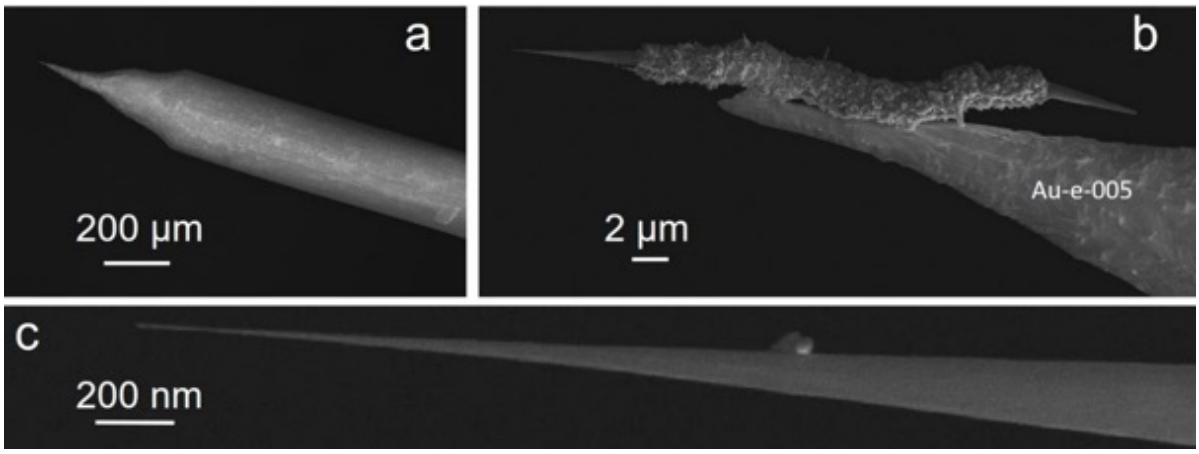

Figure 36: *SEM images of the carbon nanocone probe* ***Au-e-005*** *used for the STM tests.* ***(a)*** *low magnification of the probe mostly showing the Au wire.* ***(b)*** *medium magnification showing the SSF morphology welded (by FEBID) onto the tapered end of the Au wire.* ***(c)*** *high magnification showing the sharp tip and its small apex radius.*

b) Au substrate

Imaging with scan size from 250 to 400 nm was conducted for testing nanocone probes for imaging an Au substrate surface (Renishaw Diagnostics – Klarite, usually used as a SERS substrate), with a voltage range of 200-400 mV and current ranging from 300 pA to 2 nA using the Bruker Dimension D3100 microscope. This is a polygranular film whose grain diameters vary between ~80 and ~120 nm according to the images obtained (**Fig.37a**). An STM image obtained on the same microscope with an **Au** probe is shown in **Fig.37b** for comparison, although conditions were not optimized, inducing the Au grains to somewhat look like lamellae. Few information was available regarding the way the Au substrate was prepared, but the similarity of aspect with a thermo-evaporated Au film, an optimized STM image of which from the literature is shown as **Fig.37c** [*32Govind2011*] suggests that our substrate was prepared the same way. Hence, the carbon nanocone probe allows the Au grains to be visualized and measured, although a higher degree of noise can be observed compared to the images provided as references.

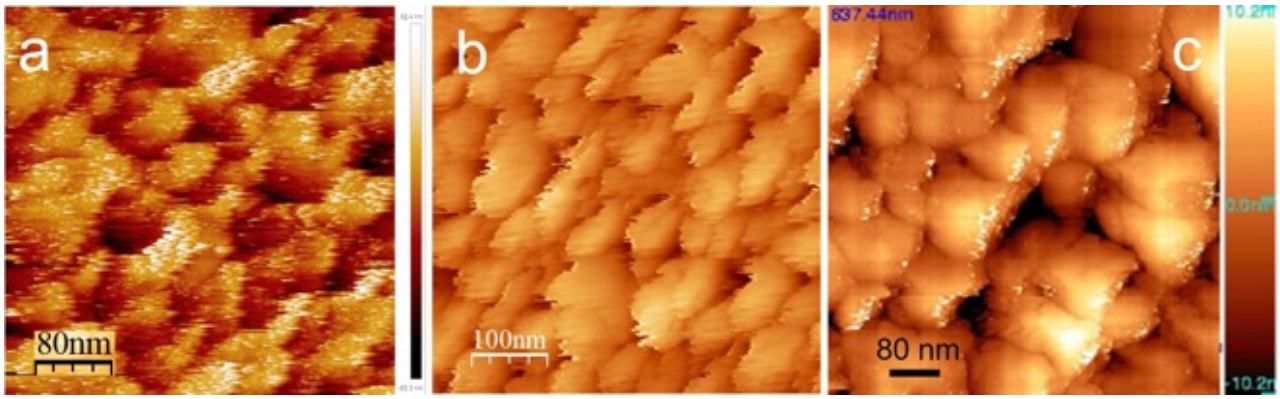

Figure 37: ***(a)*** *400 nm wide STM image of the Au surface obtained at 200 mV and 500 pA with the nanocone probe* ***Au-e-005.*** ***(b)*** *~500 nm wide STM image (non-optimized) obtained with the same microscope with a electrochemically tapered Au wire probe (i.e., similar to that shown in* ***Figs.36a-b*** *without the SSF morphology.* ***(c)*** *637.4 nm wide image (optimized) obtained at -85 mV and 200 pA current on a thermo-evaporated Au surface [*32Govind2012*].*

c) ITO substrate

The same nanocone probe **Au-e-005** was then tested on an indium-tin oxide (ITO) substrate using the Multimode IIIA Nanoscope, hence with voltage in the same range (500 mV), but with higher currents (1800-3000 pA) (**Fig.38a**). The typical grainy aspect of the surface is revealed, although the image is very noisy in an asymmetric way, and barely matches that obtained with the reference **PtIr** probe (**Fig.38b**).

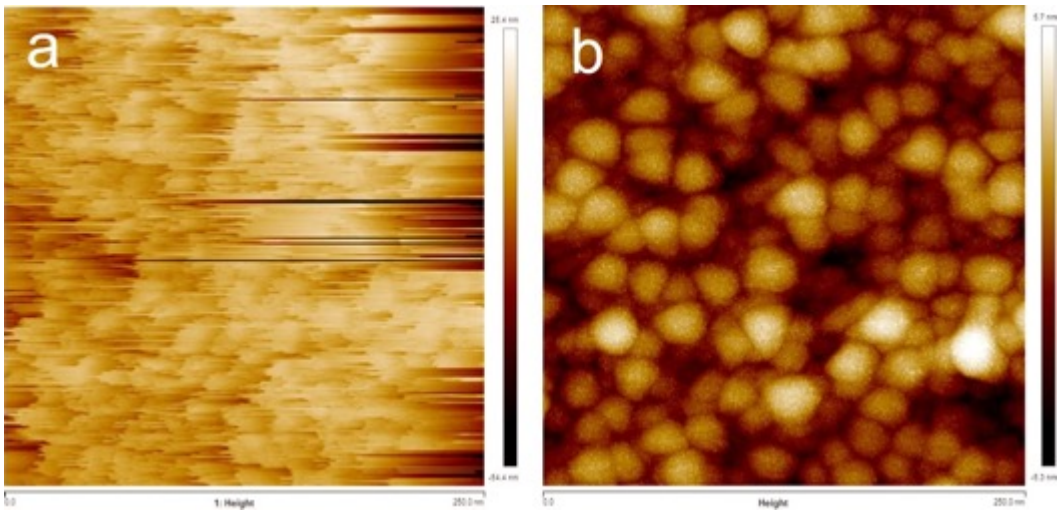

Figure 38: *250 nm wide STM images of the ITO surface obtained by* ***(a)*** *the carbon nanocone probe* ***Au-e-005*** *(500 mV, 1.8 nA, 0.5 Hz scan rate) and* ***(b)*** *the reference PtIr probe (500 mV, 3 nA, 2 Hz scan rate).*

The left part of the image in **Fig.38a** shows the grains looking like lamellae, which they are actually not, considering **Fig.38b**. However, the comparison with the image obtained on an Au substrate with the reference probes in **Figs.37b-c** gives hope that this artifact could be fixed by optimizing the imaging conditions. On the other hand, the right part of the image is highly disturbed, making that the ITO grains are not seen. In this image, only the right-to-left pathways of the scanning probe were recorded. The same effect, but reversed, was observed in the associated image recorded from the left-to-right pathways of the scanning probe (not shown). This suggests that the image perturbance results from some mechanical flexibility of the probe tip, as if the piezo-displacement starts moving leftward while the probe tip remains pinned for a while, and then finally unpins. This "flexibility" could be due to the cone tip, which is so sharp and elongated that it is similar to a CNT over a certain length (~200 nm, see **Fig.36c**), or possibly due to the SSF morphology fixation becoming loose.

d) HOPG substrate

Then, the same nanocone probe **Au-e-005** was tested on a HOPG substrate at the minimum current value (2 nA) allowed by the Multimode IIIA Nanoscope and with an applied voltage in the range 80-100 mV. STM images of medium-range magnification were taken for showing graphene steps, and then, further high magnification was used to attempt revealing the interatomic distances of the graphene structure lattice. Comparisons with a reference **PtIr**

probe were also conducted. The parametric conditions of the reference probe were set up at 350 mV, 3 nA (medium-range magnification) and 50 mV, 2 nA (high magnification).

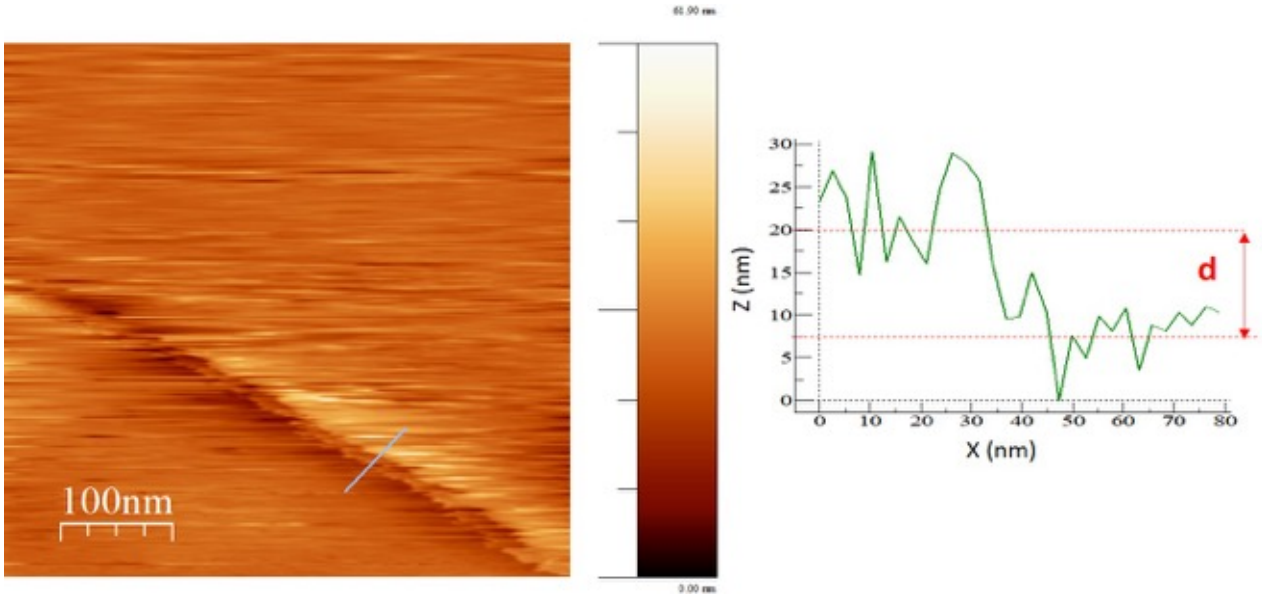

Figure 39a: *STM image (100 mV, 2 nA, 5 Hz scan rate) of the HOPG surface obtained by the carbon nanocone probe* ***Au-e-005*** *(left). One height profile was recorded (right): d = 12.5 nm.*

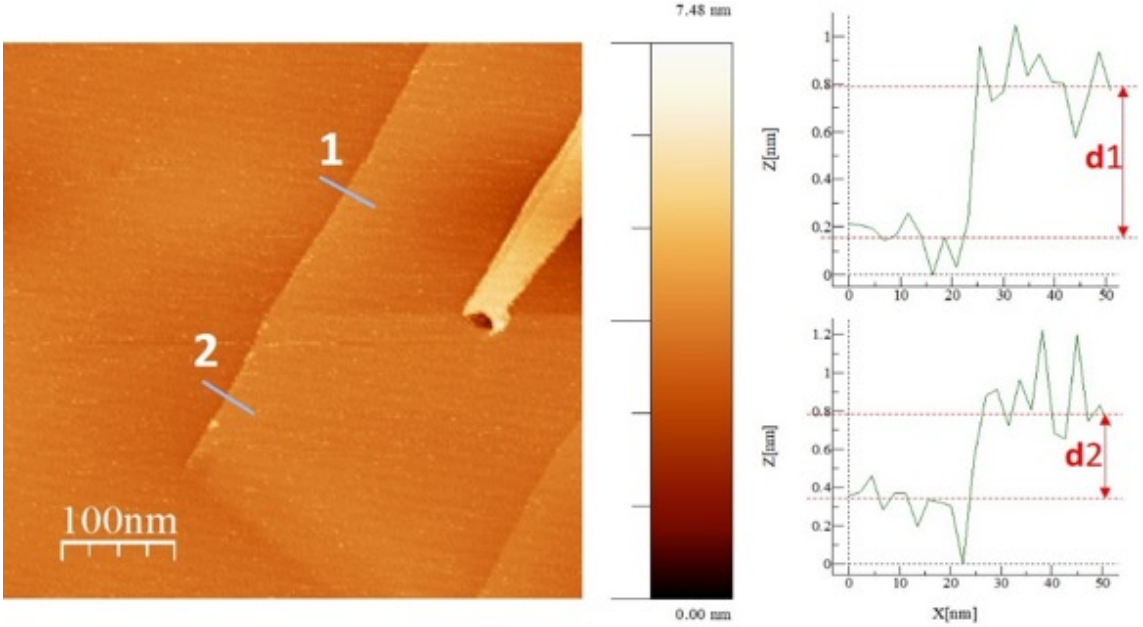

Figure 39b: *STM image (350 mV, 3 nA, 2 Hz scan rate) of the HOPG surface obtained by a* ***PtIr*** *probe (left). Two height profiles (right) were recorded (right): d1 = 0.63 nm, d2 = 0.43 nm.*

Although STM imaging was achieved with both probes, the image obtained with the **Au-e-005** probe (**Fig.39a**) shows a lesser quality than that of the reference probe (**Fig.39b**). The medium-range magnification image obtained by the nanocone probe is able to show a graphene step but it is a very high one, of about 12.5 nm, which means that about 37 graphenes are involved, or possibly much less but partly exfoliated, which could explain the specific aspect of the step. On the other hand, the reference **PtIr** probe allows observing a graphene step from which two

height profiles were taken, providing step heights of 0,63 and 0,43 nm, respectively. The former could correspond to two graphenes (= 2 x 0.335 nm, considering a 6% error), whereas the latter could possibly correspond to a single graphene yet with a high 28% error.

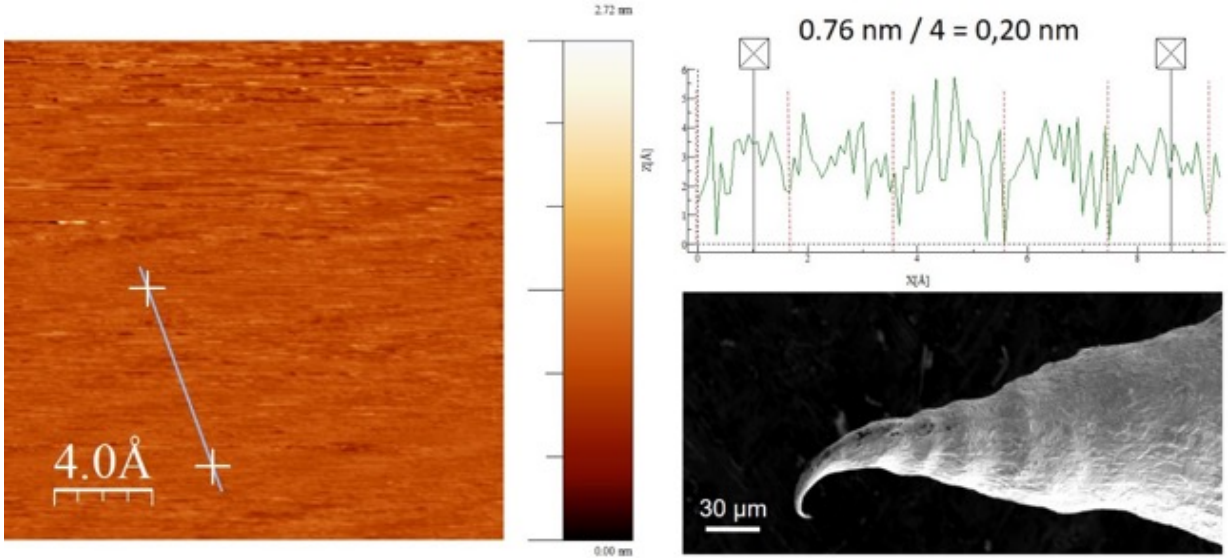

Figure 40: *STM image (81 mV, 2 nA, 5 Hz scan rate) of the HOPG surface at high magnification obtained by the* ***Au-e-005*** *probe. (left). One height profile was taken (right) hardly showing a periodicity of ~0.20 nm. SEM image of the probe after the STEM tests, showing that the SSF morphology is gone and that the Au supporting tip is now bent (photo credit: S. Le Blond, UMS Castaing, Toulouse).*

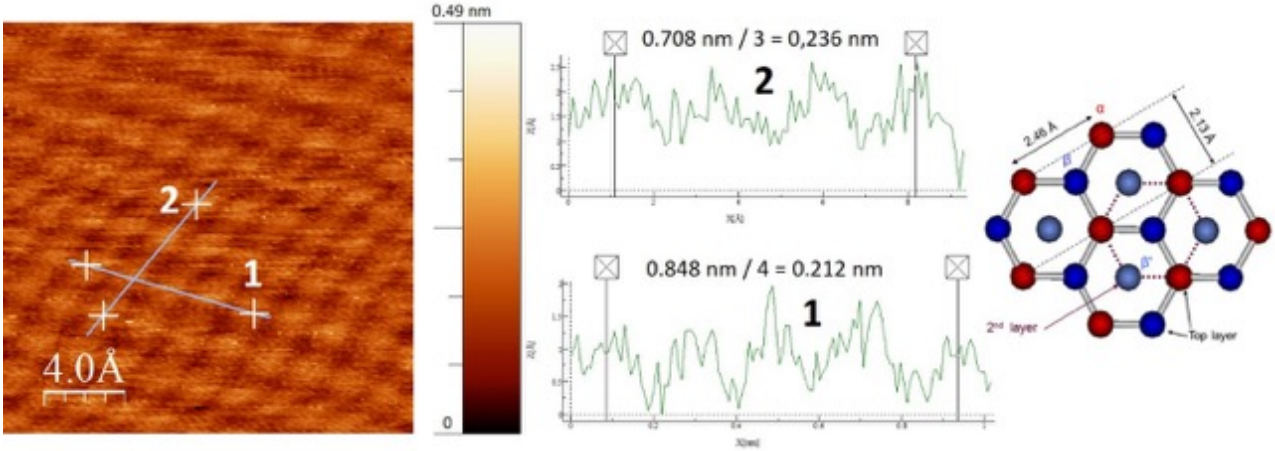

Figure 41: *STM image (50 mV, 2 nA, 5.9 Hz scan rate) of the HOPG surface at high magnification obtained by the* ***PtIr*** *reference probe. (left). Two height profiles were taken (middle): "1" shows a periodicity of 0.212 nm, "2" shows a periodicity of 0.236 nm. The corresponding distances in the graphite lattice are shown on the right hand.*

When considering high magnification images, the carbon nanocone probe was not successful for allowing atomic resolution measurements (**Fig.40**). They show systematically highly noisy images with little contrast as compared to what was obtained with the reference **PtIr** probe (**Fig.41**). For the most, some faint periodical feature can be guessed, measured at ~0.20 nm, that we can slightly estimate (with around 6% uncertainty) to be the atomic periodicity at 0,213 nm corresponding to the *(10.0)* family plane in graphite. On the other hand, the **PtIr** reference probe was able to provide images showing a periodicity of 0.212 nm (profile 1), corresponding exactly to the inter-plane distance of *(10.0)* in graphite, and another periodicity

of 0.236 nm (profile 2) corresponding to twice the inter-plane distance of *(11.0)* in graphite (with a 4 % error). These results are consistent with both the theory and the common observations in the literature, the **PtIr** probe was only able to image one type of atoms, α (red) or β (blue) referring to **Fig.41(right)**, therefore showing a triangular symmetry instead of a hexagonal one.

The image of the **Au-e-005** carbon nanocone probe after having been subjected to the STM tests is striking (**Fig.40**): it is highly damaged, with the carbon cone gone and the gold tip support heavily bent. Therefore, it may be questioned when this happened. It is believed that the probe as such could have not been able of a sufficient spatial (x-y) resolution to catch the grain size of both the Au and the ITO substrates shown in **Figs.37a** and **38a**, respectively. Likewise, it could not be able to image the step at the HOPG surface with such a steep profile as shown in **Fig.39a**. Therefore, damaging the probe was probably done afterwards during the various handlings that have preceded the SEM observation.

This said, considering previous reports on carbon-nanotube-based probes being able to accomplish STM measurements [*33Dai1996, 34Pasquini2005, 35Sripirom2011*], the factors limiting our carbon nanocones for STM atomic resolutions tests are not clearly understood. Carbon nanocones exhibit very small apices in the range of CNT diameters or even lower, and their electrical conductivity was ascertained to be sufficient, for the least, for being suitable probes in C-AFM tests. However, considering the work from [*35Sripirom2011, 36Yoshimoto 2007*] whose carbon cones and CNTs of 25 and 20 nm diameters were respectively used in STM, it seems that, surprisingly, the apex size is not a crucial point to consider. Consequently, we can then suppose a possible variability of the current effect as different materials (Au, W, C), compose the whole nanocone probe device. Yoshimoto *et al.* reported that in the case of CNT probes supported on W wire tips, the junction electrical resistance scattered from 100 kΩ to several MΩ from tip to tip, which was evaluated to be a very high value for conducting STM measurements [*36Yohimoto2007*]. Another possibility can be the pronounced lack of structural integrity at the nanocone apex, as the consequence of the variable amorphization degree observed and discussed in *Chapter 3.* This could explain why our first attempts using FIBID-prepared probes (the most amorphized) were unsuccessful, whereas a reasonable STM signal was obtained when FEBID-prepared probes (slightly amorphized only) were used. As it will be shown in the KFM section coming next, this amorphization could be suspected to cause a broadening of the local charge density around the tip apex. However, we do not have a direct way to evaluate this impact. An element whose low conductivity may be suspected is the quality of the welding, which does not always result in a good contact with the supporting material (i.e. the wire or the cantilever). But this was observed more often with Si cantilevers than with metal wires. Finally, maybe the most limiting factor for achieving atomic resolution is related to the environment conditions. Most of the STM imaging using carbon probes reported in the literature take place in vacuum, after following a degassing process at high temperature (600-800°C) and subsequently annealing of up 1200°C for avoiding any type of contaminants of the probes [34*Pasquini2005, 35Sripirom2011, 36Yoshimoto 2007*]. Here, we worked in room environment and no pretreatment was performed on the nanocone probe prior to the tests.

3.3. Kelvin Force Microscopy (KFM)[30]

3.3.1. Principles and notions

The KFM is an electrical AFM mode, which allows measuring the surface potential of a sample by the detection of electrostatic forces between the tip and the sample (5-100nm tip-sample distance) via tip-sample dc voltages [*37Girard2002, 38Girard2002b, 39Girard2006*]. The signal detection in KFM can be achieved by frequency modulation (single pass method), or amplitude modulation (double-pass method) *[4Palleau2011].* In this work we use the amplitude modulated method by following the so-called double pass lift principle.

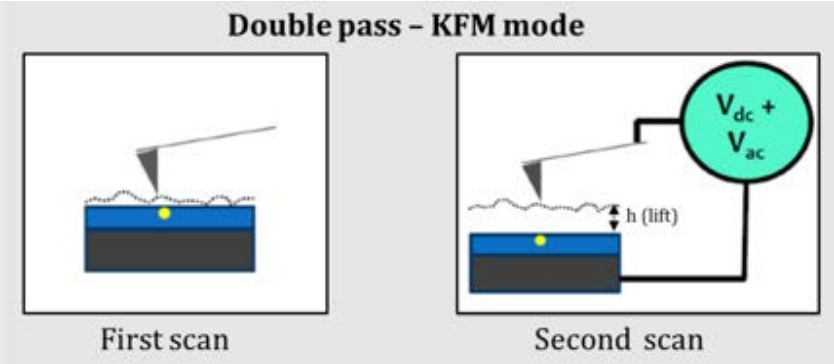

Figure42: *Double pass-KFM mode principle: the first scan (left) corresponds to a mechanical excitation of the probe as for standard tapping mode; in the second scan (right) a lift of the probe is performed from the surface (between 5 and 100 nm) in order to detect electrostatic forces. The surface potential measurement requires also an electrical excitation (V_{dc}+ V_{ac} sinωt) applied between the sample and the probe.*

As shown in **Fig.42.**, the double pass (lift) method consists of two steps. In the first step a topographic image (in tapping mode) of the sample is conducted thanks to a mechanical excitation of the probe near to its resonance frequency. In the second step, the oscillation of the tip is no longer performed via a mechanical excitation but via an electrical one, and the probe is lifted up from the sample at a typical distance in the range of 5-100 nm called "lift height" at which the topography of the sample recorded during the first step is reproduced. This electrical excitation consists of applying an external bias composed by both an alternative V_{ac} and a modulable V_{dc} voltages. During the second step, we look for cancelling the tip oscillations by controlling the V_{dc} component of the system through a so-called lock-in loop. This is achieved once V_{dc} is equal to the surface voltage (sample-probe contact potential difference). Hence, a KFM image is actually a mapping of V_{dc}. This is the way surface potential differences and materials work-functions can be discriminated.

The tip-sample voltage can be simply expressed as follows [*39Girard2002*]:

$$V = V_{dc} + V_{ac}\sin(\omega t) \tag{8}$$

[30] This part of the work was made in collaboration with E. Palleau and L. Ressier (LPCNO, Toulouse)

In this equation, V_{dc} and V_{ac} are the external bias applied to the tip. V_{dc} is a voltage monitored by the microscope, whereas V_{ac} is controlled by the operator. The operation range value of V_{ac} may vary according to the microscope used. In the case of an ICON microscope the range is in-between 250 mV and 2 V. However, for a Multimode 8 microscope V_{ac} may go up to 6 V. The operator must carefully choose this parameter because on the one hand, it has to be high enough to detect weak signals, but not too high (< 10 V) so that to prevent a too early contact with the surface to occur, which can be caused by a phenomenon of parameter amplification [*40Ouisse2006*]. The control of V_{ac}, along with the choice of the probe, the lift, and the feed-back electronic control constitute the key parameters in KFM. In this work, Vac is optimized by increasing it progressively until a parametric amplification is observed.

The electrostatic force between the probe and the sample is given by the expression below, where C and ΔV correspond respectively to the capacitance and the voltage difference between these two elements:

$$F_e = \left|\frac{\partial}{\partial z}\left(\frac{1}{2}C\Delta V^2\right)\right| = \left|\frac{1}{2}\frac{\partial C}{\partial z}\left(V_{probe} - V_{sample}\right)^2\right| \quad (9)$$

This voltage difference can be expressed as follows where $V_{charges}$ is the potential created by the electrical charges present (eventually deliberately injected) on the sample and V_{CPD} correspond to the contact potential difference (hence the work function difference) between the probe and the sample. V_{CPD} can vary with the position of the probe on the sample surface in case of work function variation.

$$\Delta V = V_{dc} + V_{ac}.sin(\omega t) - V_{charges} + V_{CPD} \quad (10)$$

The electrostatic force becomes therefore:

$$F_e = \left|\frac{1}{2}\frac{\partial C}{\partial z}.\left[\left(V_{dc} + V_{CPD} - V_{charges}\right) + V_{ac}.sin(\omega t)\right]^2\right| \quad (11)$$

The development of the equation above is detailed below and show three different components: a first one independent of the excitation frequency ω (in blue), a second one dependent on the frequency ω (in green) and a third one dependent of the frequency 2ω (in red):

$$F_e = \left|\frac{1}{2}\frac{\partial C}{\partial z}.\left[\left(V_{dc} \mp V_{CPD} - V_{charges}\right)^2 + 2.\left(V_{dc} + V_{CPD} - V_{charges}\right)V_{ac}.sin(\omega t) - \frac{{V_{ac}}^2}{2}.cos(2\omega t)\right]\right| \quad (12)$$

This electrostatic force will induce the deflection of the cantilever: the first component will create a constant bending of the cantilever overtime, the second and third a deflection at a frequency ω and 2ω, respectively. These different deflections will generate an electrical output signal. The use of a lock-in amplifier connected to the output of the cantilever allows to selecting and investigating the signal amplitude of one of these components during the KFM measurement. By studying the second component dependent of the frequency ω, the corresponding amplitude signal will be zero for a bias polarization of the probe V_{dc} equal to $V_{charges}$-V_{CPD}. Consequently, the electrical potential mapping can be performed by monitoring the V_{dc} bias voltage during the KFM measurements with respect to the potential V_{CPD}. In the case of homogeneous work-function of the sample all over the surface, this potential is constant and does not depend on the probe position.

3.3.2. KFM signal, contrast, and resolution parameters

A reliable KFM measurement must be consistent with the topography of the sample. A high contrast is required to differentiate the surface potential of the materials composing the sample. Furthermore, the mapping given by KFM must be also consistent with the polarization sign (negative or positive) present on the surface sample. For a highly resolved KFM signal, local electrostatic forces must be higher than non-local ones [*27Jacobs1998*]. For achieving this, a clear discrimination between both topography and electrostatic contributions is required. This is particularly important as KFM is an averaging technique which accounts for all the capacitive contributions that may happen between the probe and the sample (**Fig.43**). When working in amplitude modulation, the tip-sample distance can be controlled by adjusting the set point amplitude, and then, by adjusting the lift of the probe during the second step. The lower the set point amplitude and lift values, the more accurately the topographic image and KFM signal. However, lowering the amplitude implies working closer to the sample, which can induce attractive forces (i.e. van der-Waals, electrostatic) and create an unwanted virtual height on the topographic image, affecting also the accuracy of the KFM signal [*4Palleau2011*]. On the other hand, a lower lift could also induce a mixture of topographic and electrostatics contributions to the KFM measurement, whereas a higher lift can affect the sensitivity of the measurements. According to [*4Palleau2011*], a lift between 10-50 nm is a good trade-off for adequate working conditions. Beyond these parameters, the choice of the probe, cantilever surface and tip geometry appear to be crucial factors for improving the contrast and resolution in KFM [*27Jacob1998*]. A small surface cantilever, and a long and slender tip will favor a constant and close enough tip-sample contact while avoiding the possible parasitic capacitance effects shown in **Fig.43** which affect the reliability of the KFM signal [*27Jacob1998*]. Although the apex radius of the tip seems not be a strong limiting factor since slightly blunt tips were predicted to be more adapted than very smaller one [*27Jacob1998*], anyway, metal-coated tips are definitely not recommended because their degradation during the scanning process was shown to drastically affect the KFM contrast and resolution [*27Jacob1998*].

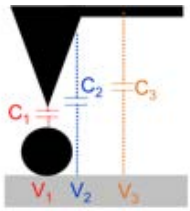

Figure 43: *Possible capacitance side effects induced by the cantilever and the tip shapes and likely to affect the KFM measurements [*41Chevalier2017*].*

Finally, in order to reach an optimal resolution (< 1mV) of the KFM signal, a proper adjustment of the feedback of the lock-in amplifier must be done [*27Jacob1998*]. This adjustment must consider the probe characteristics such as the spring constant and resonance frequency. According to [*4Palleau2011*] working at higher spring constant (around 40 nN/m) and higher resonance frequency (around 200-300 kHz) allows better reproducible measurements to be obtained.

In this section, we evaluate the capability of our nanocone probes as charge injector and for KFM measurements on different substrate samples.

3.3.3. Capability of nanocones probes for KFM

a) Samples and measurement imaging protocol

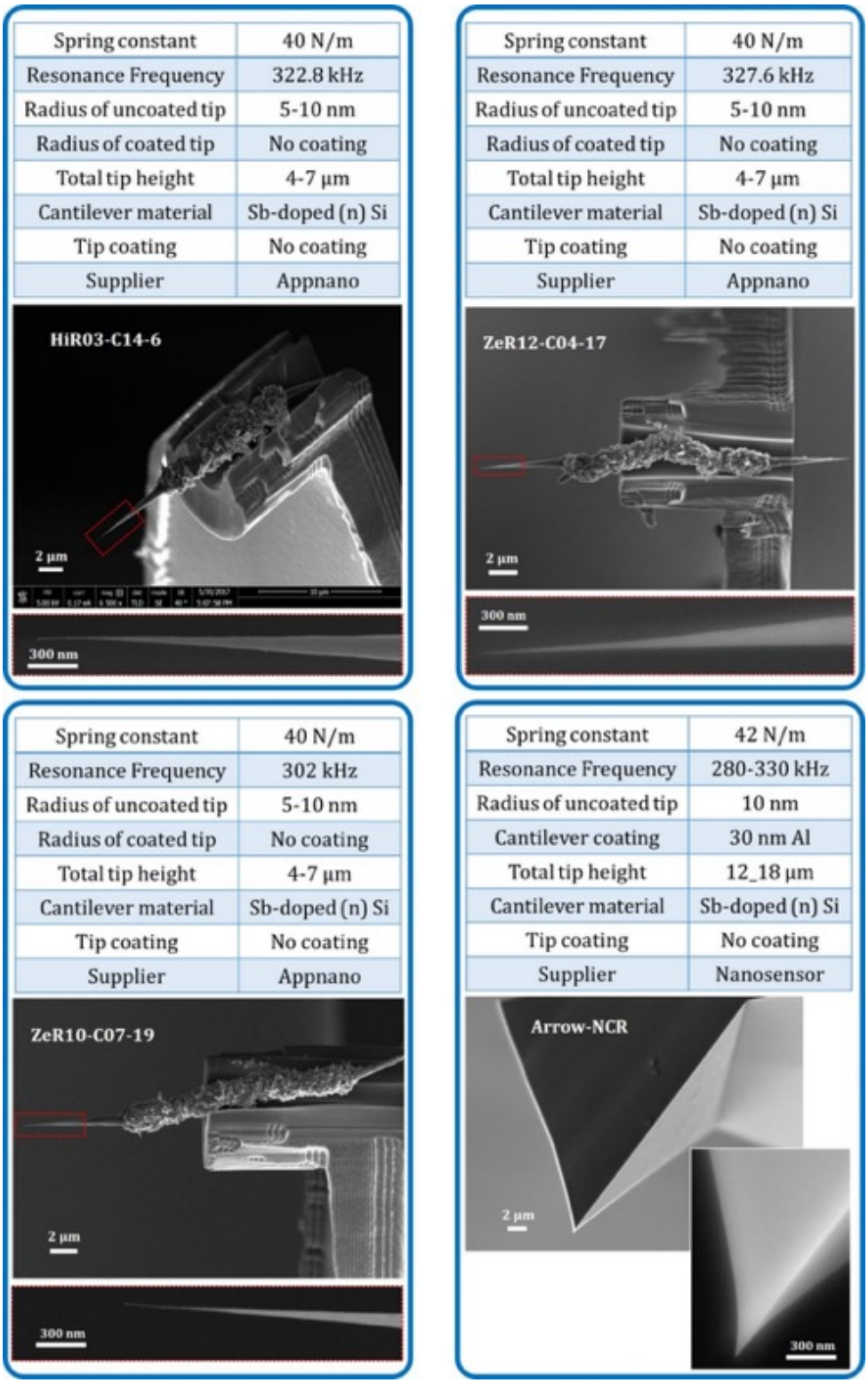

Figure 44: *Main characteristics of the nanocone and silicon (Arrow NCR) probes used for the tests. Both probes have similar characteristic regarding cantilever dimensions and resonance frequency ranges. (Photo credit: R. Cours, CEMES; S. Le Blond, UMS Castaing, Toulouse).*

The conductive performances of carbon nanocone probes were tested with charge writing first, and then the performance of the nanocones for KFM surface potential measurement was investigated on different substrates such as charged latex nanoparticles and Aluminum A2024 alloy.

The tests were conducted in air using two different AFM microscopes from Bruker company *(i)* a Multimode 8, *(ii)* an ICON. The comparisons were systematically made with a reference probe (**Arrow NCR**). This is a commercial silicon N 10^{-19} cm^{-3} doped probe, with a cantilever coated with 30 nm of Al on its upper face able to enhance 2.5 times the laser reflection signal. This probe has a resonance frequency in the range of 280-330 kHz and spring constant of 42 N/m. All the KFM tests were performed using the conditions presented in **Table7.** The features of the different tested probes are described in **Fig.44.**

Target amplitude	500 mV
Amplitude setpoint	355 mV
Drive amplitude (V_{ac})	305 mV
Drive amplitude 2	500 mV
Phase lock-in amplifier	-101°
Scan speed	0.2 Hz
Points per line	256x256
Probe lift	30 nm

Table 7: *Presentation of the KFM measurement parameters.*

b) Charge injection test

The nanocone probe noted **HiR03-C14-6** was used as a conductive tip for charge writing with two different polarization voltages (+ and -50 V) applied to the tip to generate 4 charged lines, following the protocol described in [*4Palleau2011*]. The charge writing process was conducted on a 100 nm-thick poly (methyl methacrylate) (PMMA) film used as electret (i.e., a material that retains its electric polarization after being subjected to a strong electric field) onto a 10^{16} cm^{-3} p-doped Si substrate (**Fig.45a**). The charge distribution on the PMMA surface is then measured by KFM (**Figs.45b-c**). The same microscope ICON was used for both charge injection and KFM measurements. The main interest of this test is *(i)* to ascertain a sufficient conductivity of the [welded nanocone + cantilever] assemblage, and *(ii)* to evaluate the applicability of the carbon nanocones for being used as a nanofabrication tool and of the advantage brought by the cone small apices.

As shown in **Fig.45,** the nanocone probe is conductive since effective charge injection was possible and subsequently visualized by KFM mapping. The KFM shows the charges of same sign as that of the probe polarization. However, the resolution is not optimal since the charge injection seems to be broaden as compared with that obtained from a commercial probe where the lines are narrower and more contrasted. This broadening phenomenon can be understood either by *(i)* a difficulty of the nanocone probe for withstanding the high applied voltage; *(ii)* an increase of the tip apex or an original tip apex larger than expected; *(iii)* a mere deficiency of the probe for enabling a KFM signal. All these three factors are likely, considering that the nanocone probe used in this test was mounted by the FIBID welding process, which was shown in *Chapter 3* to be able of significantly increasing the cone apex as a consequence of the severe

surface amorphization of the carbon material, which also may affect dramatically the electrical conductivity. On the other hand, although the consequences of a larger apex have supposedly a minor impact on the KFM signal according to the literature [*27Jacob1998*], the difficulty we had for assessing reliably the extent of the cone apex broadening does not allow telling whether it might have a significant impact on the signal.

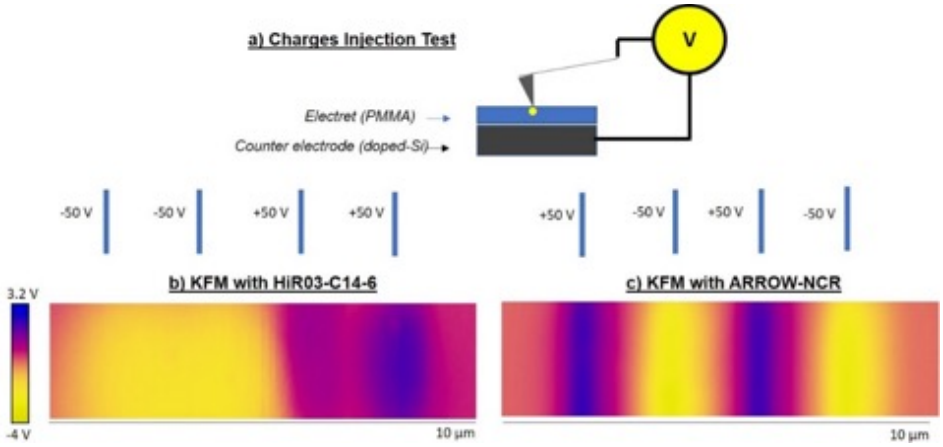

Figure 45: (a) *Schematic representation of the charge injection process. Two KFM images of the charged PMMA surface,* ***(b)*** *from a nanocone probe* ***HiR03-C14-6****;* ***(c)*** *from a doped-silicon (****Arrow-NCR****) probe.*

c) KFM- Negatively-charged latex nanoparticles assembled by nanoxerography onto PMMA substrate

The same nanocone probe noted **HiR03-C14-6** was used for discriminating negatively charged nanoparticles from a non-conductive substrate. **Fig.46a** shows a 5 µm wide topographic image of two lines of negatively-charged 100 nm-large latex[31] nanoparticles which were assembled electrostatically on positively charged lines written on a PMMA substrate (the so-called nanoxerography process described in [*42Palleau2011b*]). **Figs.46b-c** correspond to the KFM images obtained from the nanocone probe and the commercial Arrow-NCR probe respectively.

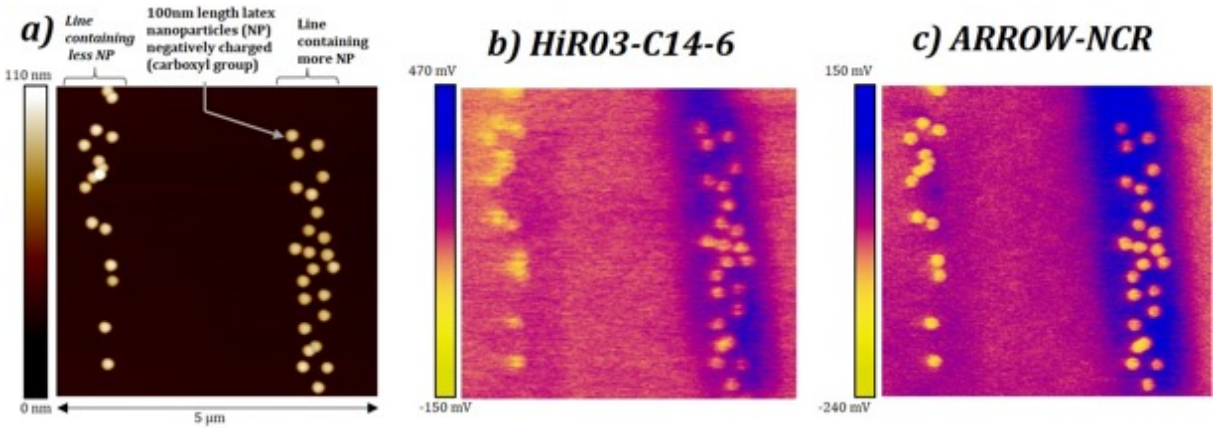

Figure 46: (a) *Topographic image of lines of negatively-charged latex nanoparticles onto a PMMA surface.* ***(b)*** *and* ***(c)*** *The KFM images of the same obtained by a nanocone probe and a silicon arrow-NCR probe respectively.*

[31]The "latex" denomination is commercial (https://www.sigmaaldrich.com/catalog/). The material is actually surface-functionalized polystyrene.

It can be observed that even if the carbon nanocone was able to follow the sample topography and to duly show the adequate actual negative signal of the charged nanoparticles, it shows more blurred contours and a less contrasted signal compared to the commercial probe. Surprisingly, the lateral resolution of both probes is alike, meaning that the cone apex radius was not enlarged beyond that of the silicon reference probe, which answers the question raised at the end of the previous section.

When a nanocone probe noted **ZeR12-C04-17** mounted by the FEBID process was used for KFM images of the same sample, better-contrast images were obtained as shown in **Fig.47.** This time, the nanocone probe shows a similar contrast (even possibly better) as the commercial silicon probe. However, a slightly lower spatial resolution of the nanocone can be observed on the topographic and KFM images.

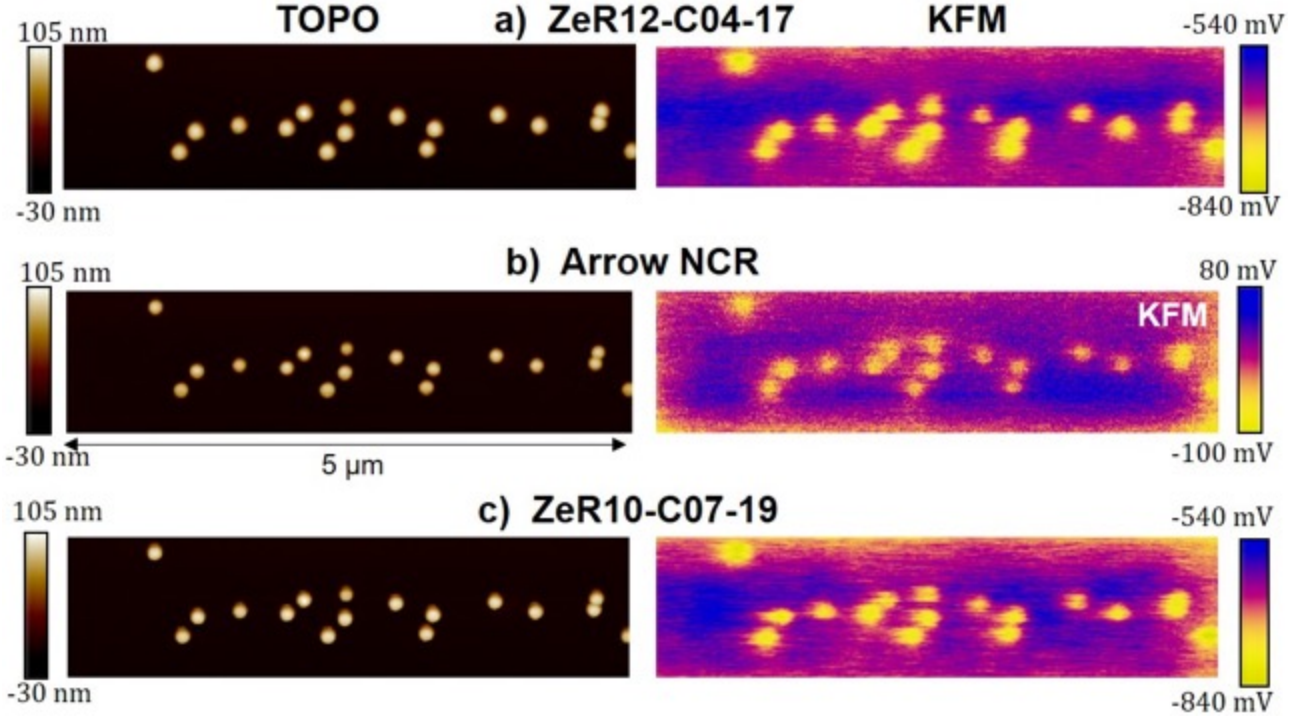

Figure 47: *Negatively-charged latex nanoparticles onto a PMMA surface. Topography and KFM images for* ***(a)*** *the carbon cone probe* ***ZeR12-C04-17. (b)*** *the reference Si probe.* ***(c)*** *the carbon cone probe* ***ZeR10-C07-19.***

Fig.47c also shows the same area imaged by another carbon nanocone probe (**ZeR10-C07-19**, hence mounted by FEBID as well). The results are quite similar to that of the other carbon nanoprobe shown in **Fig.47a**, and even slightly better regarding the spatial resolution, now closer to that of the reference probe. Comparing **Figs.47a** and **47c** illustrates a good reproducibility of the carbon cone probes when they are prepared by the same process.

Comparing either the topography or the KFM images as obtained with a carbon cone probe and the Arrow-NCR probe in **Figs.46 and 47** shows that the lateral resolution of the latter is systematically slightly better with the **Arrow-NCR** probe, which was unexpected considering the small apex radii of the former (**Fig.44**). Interestingly, using a cantilever previously coated with a 5-10 nm film of evaporated gold prior to welding a carbon nanocone onto it by FIBID

(**Fig.48c**) resulted in KFM images of latex nanoparticles with a smaller apparent diameter (**Fig.48a**) than with the **Arrow-NCR** probe (**Fig.48b**).

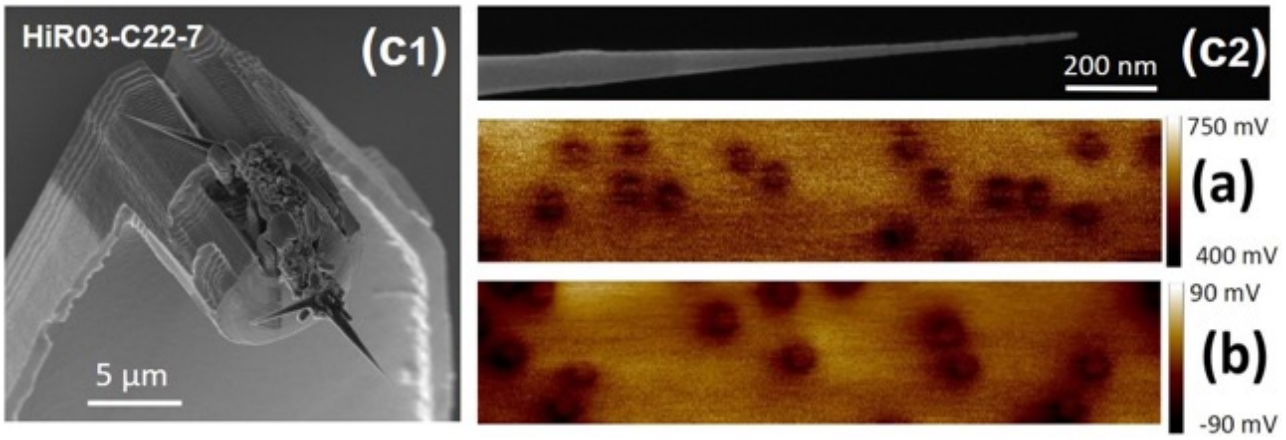

Figure 48: *KFM images of charged latex nanoparticles obtained* ***(a)*** *with the carbon nanocone probe imaged in (c), and* ***(b)*** *with the Si-doped cantilever* ***Arrow-NCR****. (****(c1)*** *SEM micrographs of the carbon cone probe* ***HiR03-C22-7****, along with* ***(c2)*** *a magnified view of its apex. (c1-c2 photo credit: R. Cours).*

This experiment was a preliminary attempt to improve the reflectivity of the cantilever upper face so that for the laser to detect more accurately the cantilever deflection variations. The **Arrow-NCR** probe is actually coated with Al for the very same reason. Therefore, it seems that improving the reflectivity of the cantilever upper face of the carbon probes is beneficial to the lateral resolution.

d) KFM- Aluminum alloy A2024 sample[32]

Fig.49 shows 15 µm wide topology (AFM) and KFM images of intermetallic particles in an aluminum alloy (A2024) surface obtained by the nanocone probe **HiR03-C14-6** and the silicon probe, respectively. KFM images with similar contrast were obtained, revealing the surface potential differences with respect to the Al matrix substrate. The background of the aluminum matrix of the substrate can be clearly distinguished from the intermetallic particles. The white dashed frame shows two nanoparticles, which are better resolved by the nanocone probe than by the commercial one in topographic mode.

Higher magnification images of these two nanoparticles as well as their corresponding KFM images are presented in **Fig.50.** For such a high magnification of 3 µm-wide images, comparable topographic and KFM signals from the nanocone probe and the Arrow-NCR probe are also observed, even with a slightly more intense signal for the carbon probe.

[32] In addition to Al, this alloy contains 0.50 Si, 0.50 Fe, 3.80-4.90 Cu, 0.30-0.90 Mn, 0.10 Cr, 0.25 Zn, 0.15 Ti (at.%)

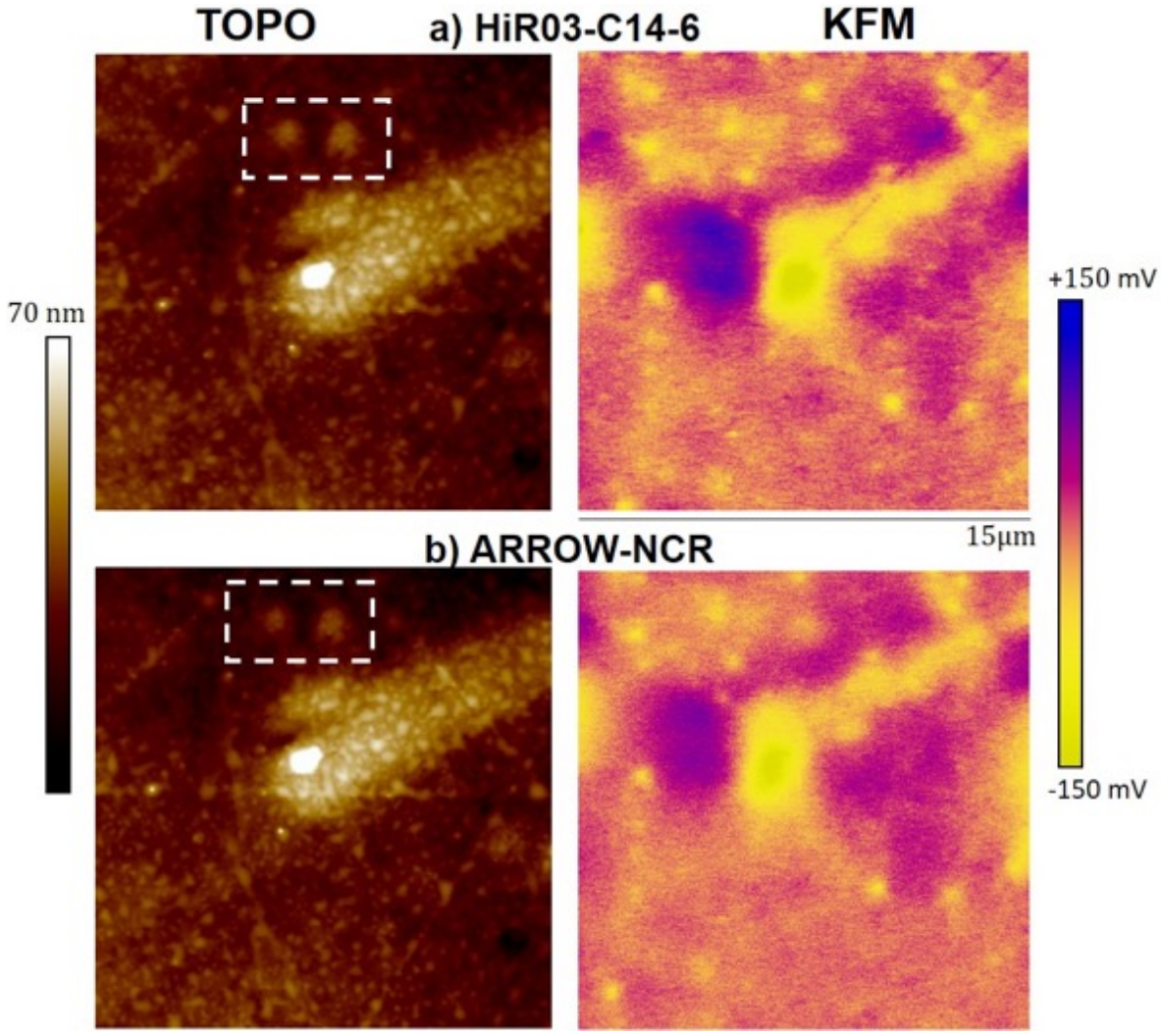

Figure 49: *Intermetallic particles in an aluminum alloy (A2024) matrix surface. Topography (left) and KFM (right) images for* ***(a)*** *the carbon nanocone probe* ***HiR03-C14-6****;* ***(b)*** *the reference Si probe.*

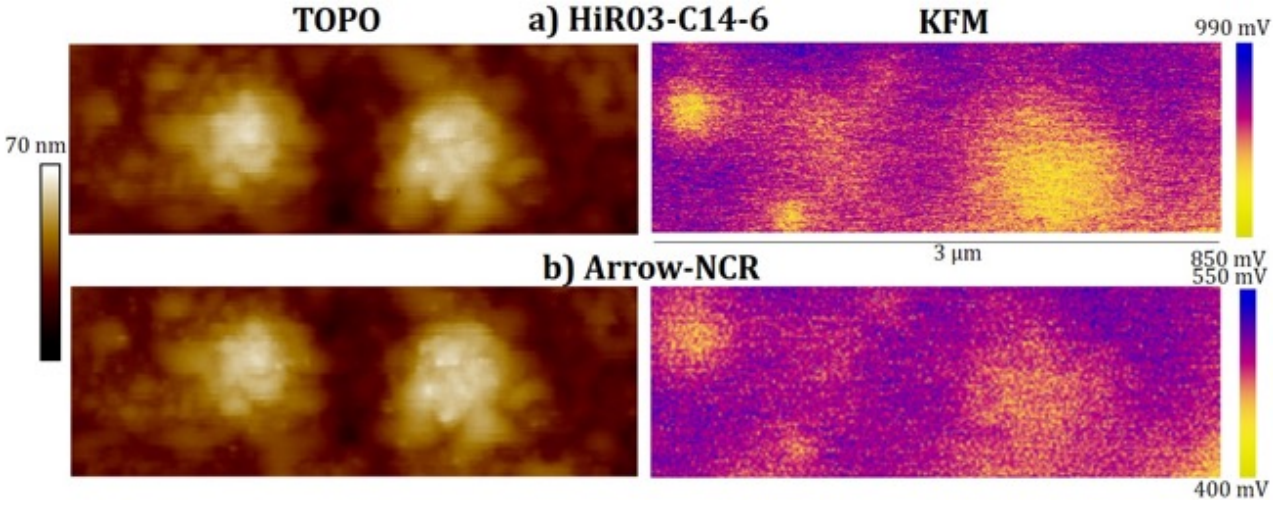

Figure 50: *Higher magnification of the area framed in* ***Fig.49****. Intermetallic particles in an aluminum alloy (A2024) matrix surface. Topography (left) and KFM (right) images for* ***(a)*** *the carbon nanocone probe* ***HiR03-C14-6****;* ***(b)*** *the reference Si probe.*

Figs.51a-b show a topographic and a KFM scan of another zone of the alloy substrate by the nanocone probe **ZeR12-C04-17** prepared by FEBID and the silicon probe, respectively. Both probes depict a very well-defined topography of the intermetallic nanoparticles present in the aluminum matrix. A clear discrimination can be made between the two type of materials. However, the KFM signal obtained by the nanocone probe shows a much better discrimination between the nanoparticles and the substrate compared to the signal obtained by the silicon probe, as well as compared to that of the carbon cone probe prepared by FIBID (**Figs.49-50**).

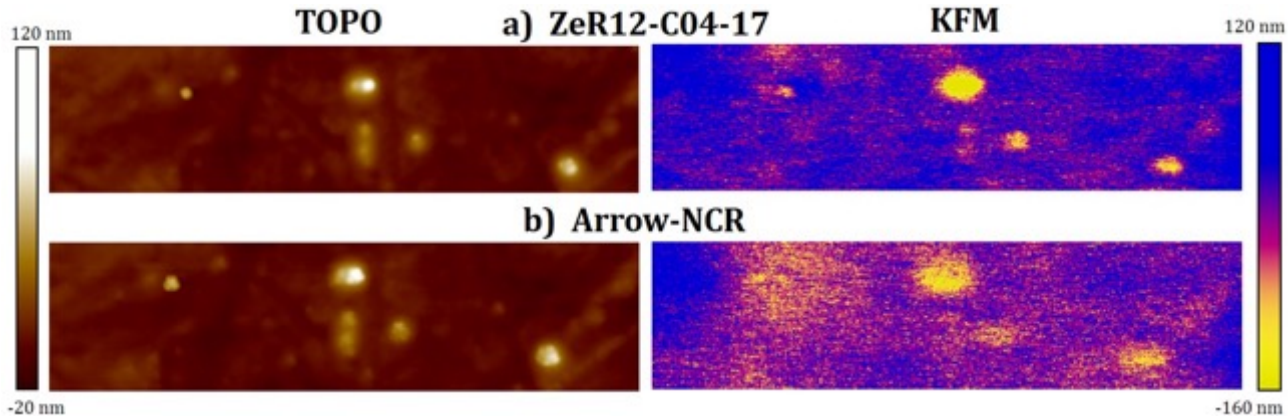

Figure 51: *Intermetallic particles in an aluminum alloy (A2024) matrix surface. Topography (left) and KFM (right) images for* ***(a)*** *the carbon nanocone probe* ***ZeR12-C04-17****;* ***(b)*** *the reference Si probe.*

The various carbon nanocone probes that have been used in this KFM study were investigated by SEM in order to reveal any morphological change. Results are shown in **Fig.52**. For all of them, the carbon cone has been shortened, and the apex radius has been enlarged. The type of morphological modification suggests a wearing effect preferably to an alteration due to an excess of current or voltage.

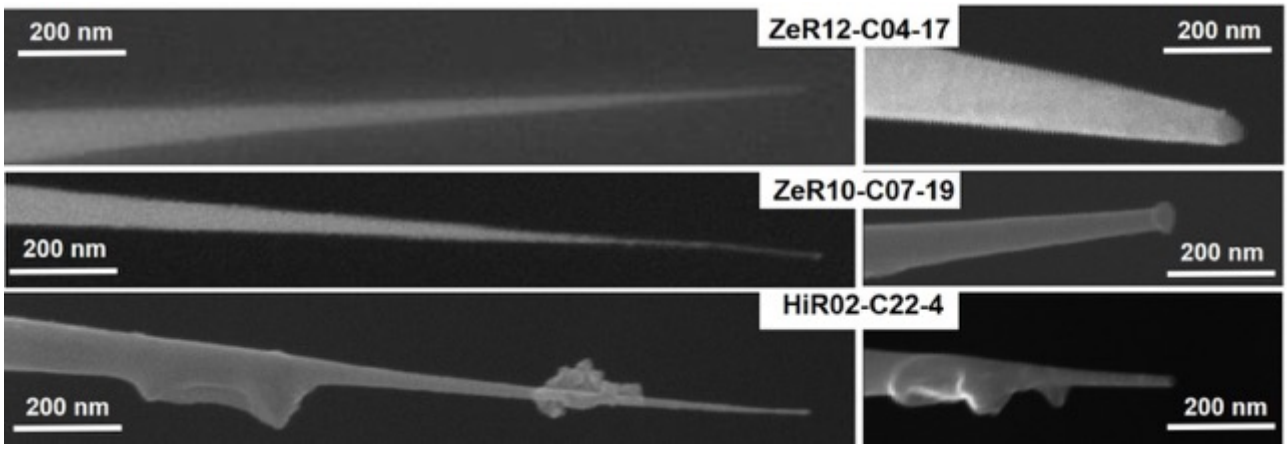

Figure 52: *SEM Micrographs of the tips of the various nanocone probes used for the KFM study. Left: as prepared, before use. Right: after the KFM measurements. Since the probe* ***HiR03-C14-6,*** *whose results are shown in* ***Figs.45****,* ***46****,* ***49*** *and* ***50*** *was lost, no micrograph is presented for this probe. The probe* ***HiR02-C22-4*** *was used in the early days of the KFM experiments, hence its results barely compare with the others and are not reported in any of the Figures. (Photo credit: R. Cours).*

4. Conclusions

Atomic Force Microscopy (AFM): Overall, all the data demonstrate the ability of the carbon nanocones in making AFM probes while providing image resolution equivalent or better than silicon probes, whatever the Si-probe type tested (**OTESPA-R3**/**OTESPA**, and **TESP-SS**). However, carbon nanocone probes have shown a poor ability in ultimate magnification imaging, in the range of atomic resolution. On the other hand, long scanning time tests have demonstrated the robust character of the nanocone probes with respect to the silicon ones, thereby showing a higher wear resistance. This is consistent with both the higher strength of the sp^2 C-C bond (598 kJ/mole) over the Si-Si bond (330 kJ/mole), and the well-known flexibility of the 2D graphenic structure over the 3D tetrahedral silicon structure.

Peak-Force Quantitative NanoMechanical AFM (PFQNM-AFM): Once the needed calibrations are carried-out in order to determine the most appropriate contact force range to apply, the carbon nanocone probes appear to be suitable for PFQNM-AFM. Indeed, they allow Young moduli of a variety of polymer films to be obtained with values reasonably close to the theoretical ones, and within an uncertainty of the same range as the reference Si probe. They are also able to discriminate between the components of a composite material, both in topography and modulus imaging mode. More in the details, the various carbon probes exhibit discrepancies between each other. Such discrepancies possibly originate from the combination of the variations in two geometrical characteristics, i.e., the overall protruding length, and the misalignment of the cone axis with respect to the ideal verticality over the substrate surface. The longer the length and the larger the angle misalignment, and the more the carbon cone would behave like a CNT, for which the excessive flexibility is a drawback that the conical geometry is usually able to prevent in some extent.

Conductive AFM (C-AFM): Carbon nanocone probes can be used for C-AFM measurements without requiring any coating of the cantilever or the tip. Both I/V and mapping current measurements are possible providing the applied voltage does not overpass 2 V. For a voltage range of 0.5-2 V and a force between 100-150 a.u (arbitrary unit of the AIST-NT, SPM 1000 microscope*),* current values up 35 nA can be reached in many different points. Mapping measurements and topographic images are consistent with sample characteristics. Carbon probes also show a similar performance as commercial silicon probes (either doped or Pt-coated) for measuring I/V curves of the studied sample. This is consistent with the finding that nanocone probes show a global conductance similar or even slightly higher to that obtained with a Pt-coated silicon commercial probe. However, as reported for commercial probes (e.g., **Fig.25**), nanocone probes exhibit a variable degree of damaging after the C-AFM tests that might not be due to mechanical wear only, confirming that the carbon cones are sensitive to excess voltage or current conditions.

Scanning tunneling Microscopy (STM): Carbon nanocones can produce more or less correct STM images at medium-range magnification providing low currents are used, but they are unsuccessful in imaging crystal lattices (atomic resolution). We think that the limitation of our

carbon nanocones for these tests is related to either the mounting process and in particularly to the degradation of the crystalline structure of the cone apex caused by the variable degree of amorphization, which adds a barrier to the electron flow in the tunneling process, and the environment conditions. Further investigation must be conducted in order to confirm this, including more carbon probes, and a careful optimization of the current/voltage conditions.

Kelvin Force Microscopy (KFM): The nanocone probes were found to be suitable for both charge injection and KFM measurements whatever the FIBID or FEBID mounting procedure used, showing qualitatively correct signal contrast and image resolution. When comparing to a commercial silicon probe commonly used for such a SPM mode, carbon probes show similar, and in some cases better resolved and more intense signal. However, slightly poorer lateral resolution and noisier images were observed sometimes. The lateral resolution could be improved by using Al-coated cantilevers so that to enhance the upper face reflectivity, as it is commonly made with doped Si probes. Concerning the variability in the signal-noise performances, they seem to affect the FIBID-prepared probes preferably to the FEBID-prepared ones. Hence, it might relate to the presence of the amorphous carbon at the cone surface which is more abundant in the case of the FIBID process, which plays the role of a barrier for the charges to cross, which they could do more or less efficiently depending on the current and voltage conditions. A careful and more thorough study should be carried out to ascertain this. On the other hand, the reason why the carbon probes show better sensitivity sometimes as revealed by a better contrast in the KFM images cannot result from the difference in the work function of the material making the probe, as they are fairly close (in the range of 4.5 eV for n-doped Si [*43Novikov2010*] as compared to 4.8 eV for our carbon cones [*44deKnoop2014*]).

References

1. Eaton P., West P**.** ***Atomic Force Microscopy*****.** *(*Hbk) Oxford University press (2010). *ISBN 978–0–19–957045–4.*
2. Zhang H., Huang J., Wang Y., Liu R., Huai X., Jiang J., Anfuso C. *Atomic force microscopy for two-dimensional materials: A tutorial review*. **Optics Comm.** 406 (2018) 3–17.
3. Strus M. C., Raman A., Han C.-S., Nguyen C.V. *Imaging artefacts in atomic force microscopy with carbon nanotube tips.* **Nanotechnol.** 16 (2005) 2482-2492*.*
4. Palleau E. *Assemblage électrostatique dirigé de nanoparticules colloïdales sur des surfaces par nanoxérographie par microscopie à force atomique.* PhD **Thesis dissertation**, University of Toulouse, (2011).
5. Hafner J., Chen E., Lal R., Jin S. *General and special probes in scanning microscopies*. In **Handbook of Nanotechnology** (Bhushan B., ed.), Springer Verlag (2010) pp. 619–633.
6. Gan Y. *Atomic and subnanometer resolution in ambient conditions by atomic force microscopy*. **Surf. Sci. Rep.** 64 (2009) 99-121.
7. Su C., Huang L., Kjoller K., Babcock K. *Studies of tip wear processes in tapping mode atomic force microscopy.* **Ultramicrosc.** 97 (2003) 135–144.
8. Strus M. C. and Raman A. *Identification of multiple oscillation states of carbon nanotube tipped cantilevers interacting with surfaces in dynamic atomic force microscopy***. Phys. Rev. B** 80 (2009) 224105.
9. Bernard C., Marsaudon S., Boisgard R., Aimé J-P. *Competition of elastic and adhesive properties of carbon nanotubes anchored to atomic force microscopy tips.* **Nanotechnol.** 19 (2008) 035709.
10. Buchoux J., Aimé J.-P., Boisgard R., Nguyen C. V., Buchaillot L., Marsaudon S. *Investigation of the carbon nanotube AFM tip contacts: free sliding versus pinned contact*. **Nanotechnol.** 20 (2009) 475701.

11. Larsen T., Moloni K. Flack F., Eriksson, M. A., Lagally M. G., Black C. T. *Comparison of wear characteristics of etched-silicon and carbon nanotube atomic-force microscopy probes.* **Appl. Phys. Lett.** 80 (2002) 1996-1998.
12. Guo L., Wang R., Xu H., Liang J. *Wear-resistance comparison of carbon nanotubes and conventional silicon-probes for atomic force microscopy*. **Wear** 258 (2005) 1836–1839.
13. Liu P., Zhang Y. W., Lu C. *Molecular dynamics simulations of bending behavior of tubular graphite cones.* **Appl. Phys. Lett.** 85 (2004) 1778-1780.
14. Maire J., Méring J. *Graphitization of soft carbons*. In **Chemistry and Physics of Carbon** vol. 6 (Walker P. L. Jr., Thrower P., A., eds.), Marcel Dekker (1970) pp.125-180.
15. De Oliveira R. R. L., Albuquerque D. A. C., Cruz T. G. S., Yamaji F. M., Leite F. L. *Measurement of the Nanoscale roughness by Atomic Force Microscopy: basic principles and applications. In :* **Atomic Force Microscopy-Imaging, Measuring and Manipulating Surfaces at the Atomic Scale (**Bellitto V., ed.), Intech (Rijeka, Croatia) (2012). ISBN: 978-953-51-0414-8, InTech *https://cdn.intechopen.com/pdfs/33450.pdf.*
16. Belec L., Joliff Y. *Mechanically affected zone in AFM force measurements — Focus on actual probe tip geometry.* **Materials and Design** 104 (2016) 217–226
17. Pittenger B., Erina N, Su C. *Quantitative Mechanical Property Mapping at the Nanoscale with PeakForce QNM.* **Bruker Nano Surfaces Division**. 2012.
18. Peak Force Tapping Quantitative, Highest Resolution Imaging and Property Mapping. Bruker company brochure. https://www.bruker.com/products/surface-and-dimensional-analysis/atomic-force-microscopes/modes/modes/imaging-modes/peakforce-tapping/overview.html.
19. Roa J. J., Ocins G., Diaz J., Sanz F., Segarra M. *Calculation of Young's modulus value by mean of AFM*. **Re. Pat. Nanotechnol.** 5 (2011) 27-36.
20. Hutter J. L., Bechhoefer J. *Calibration of atomic-force microscopy tips*. **Rev. Sci. Instrum.** 64 (1993) 1868-1873.
21. (https://www.brukerafmprobes.com/p-3724-ps-ldpe-12m.aspx)
22. Avila A., Bhushan B*. Electrical measurement techniques in Atomic Force Microscopy.* **Crit. Rev. Sol. State Mater. Sci.**, 35 (2010) 38–51.
23. Benstetter G., Hofer A., Liu D., Frammelsberger W, Lanza M. *Fundamentals of CAFM Operation Modes.* In **Conductive Atomic Force microscopy: Applications in Nanomaterials** (Lanza M., ed.), Wiley-VCG Verlag & Co. (2017), pp_.45-77.
24. Hantschel T., Tsigkourakos M., Zha L., Nuytten T., Paredis K., Majeed B., Vandervorst W. *Diamond scanning probes with sub-nanometer resolution for advanced nanoelectronics device characterization*. **Microelectron. Eng.** 159 (2016) 46–50.
25. Hui F., Chen S., Liang X., Yuan B., Jing X., Shi Y., Lanza M. *Graphene Coated Nanoprobes: A Review*. **Crystals** 7 (2017) 269.
26. Jiang L., Weber J., Puglisi F.M., Pavan P., Larcher L., Frammelsberger W., Benstetter G., Lanza M. *Understanding current instabilities in conductive Atomic Force Microscopy.* **Materials** 12 (2019) 459.
27. Jacobs H. O., Leuchtmann P., Homan O. J., Stemmer A. *Resolution and contrast in Kelvin probe force microscopy.* **J. Appl. Phys.** 84 (1998) 1168-1173.
28. Lanza M., Bayerl A., Gao T., Porti M., Nafria M., Jing G. Y., Zhang Y. F., Liu Z. F., Duan H. L. *Graphene-coated Atomic Force Microscope tips for reliable nanoscale electrical characterization*. **Adv. Mater.** 25 (2013) 1440–1444.
29. Hansma P. K., Elings V. B., Marti O., Bracker C. E. *Scanning Tunneling Microscopy and Atomic Force Microscopy: Application to biology and technology*. **Science** 242 (1988) 209-216.
30. Bacon R. *Growth, structure, and properties of graphite whiskers.* **J. Appl. Phys.** 31 (1960) 283-290.
31. Braga S. F., Coluci V. R., Legoas S. B., Giro R., Galvão D. S., Baughman R. H. *Structure and dynamics of carbon nanoscrolls*. **Nanolett**. 4 (2004) 881-884.
32. Govind M. K., *Temperature-dependent morphological evolution of clustered gold surface*. **J. Nanopart. Res.** 14 (2012) 963.
33. Dai H., Hafner J.H., Rinzler A G., Colbert D T., Smalley R E. *Nanotubes as nanoprobes in scanning probes microscopy*. **Nature** 384 (1996) 147-150.
34. Pasquini A., Picotto G.B., Pisani M. *STM carbon nanotube tips fabrication for critical dimension measurements.* **Sensors Actuat. A** 123–124 (2005) 655–659.
35. Sripirom J., Noor S., Köhler U., Schulte A. *Easily made and handled carbon nanocones for scanning tunneling microscopy and electroanalysis.* **Carbon** 49 (2011) 2402-2412.

36. Yoshimoto S., Murata, Y., Kubo K.., Tomita K.., . Motoyoshi K., Kimura T., Okino H., . Hobara R ., Matsuda., I., Honda S.-i., Katayama M., Hasegawa, S. *Four-Point Probe Resistance Measurements Using PtIr-Coated Carbon Nanotube Tips.* **Nano Letters** 7 (4), (2007). 956-959
37. Girard P., Ramonda M., Saluel D. *Electrical contrast observations and voltage measurements by Kelvin probe force gradient microscopy*. **J. Vac. Sci. Technol. B** 20 (2002) 1348-1355.
38. Girard P., Titkov A. N., Ramonda M., Evtikhiev V. P., Ulin V. P. *Observations of self-organized InAs nanoislands on GaAs (0 0 1) surface by electrostatic force microscopy*. **Appl. Surf. Sci.** 201 (2002) 1-8.
39. Girard P., Titkov A N. *Electrostatic force and force gradient microscopy: principles, point of interest and application to characterisation of semiconductors materials and devices.* In **Applied Scanning Probe Methods II. NanoScience and Technology** (Bhushan B., Fuchs H., eds.), Springer, Berlin (2006) pp.283-320.
40. Ouisse T., Martins F., Stark M., Huant S., Chevrier J. *Signal amplitude and sensitivity of the Kelvin probe force microscopy*. **Appl. Phys. Lett.** 88 (2006) 043102.
41. Chevalier N., Melin T. *Introduction à la Microscopie à Force Electrostatique*. Action Nationale de Formation DFRT KFM. 2017.https://indico.mathrice.fr/event/107/session/1/material/0/0.pdf.
42. Palleau E., Sangeetha N.M., Viau G., Marty J.-D Ressier L. *Coulomb force directed single and binary assembly of nanoparticles from aqueous dispersions by AFM nanoxerography*. **ACS nano** 5 (2011) 4228-4235.
43. Novikov A. *Experimental measurement of work function in doped silicon surfaces*. **Sol. State Electron.** 54 (2010) 8-13.
44. de Knoop L., Houdellier F., Gatel C., Masseboeuf A., Monthioux M., Hÿtch M. *Determining the work function of a carbon-cone cold-field emitter by in situ electron holography*. **Micron** 63 (2014) 2–8.

Conclusions
&
Perspectives

« If you knew how much work went into it,
you would not call it genius »

Michelangelo

A multidisciplinary study was necessary to evaluate the potential of the carbon conical micro-nano form as SPM probes, starting from the synthesis and characterization of such objects. The reproducibility and understanding of the growth process of the so-called Spiky Bead (SB) and Spiky Short Fiber (SSF) morphologies, and the study of the feasibility and fabrication of SSF-based SPM probes for insuring the geometric, mechanical and electrical characteristics required for their use for different SPM modes, as well as conducting the related application tests, constituted the main points investigated.

In *Chapter 1*, an original and extended bibliography study concerning the different ways of generating carbon conical shapes, the properties that have been investigated, and the applications they have been already tested for, is presented, as what we believe to be the most comprehensive review performed to date on the subject. It can be noted that *(i)* the existing carbon conical morphologies have not been studied as thoroughly as other carbon nanoforms such as carbon nanotubes and graphenes, *(ii)* no standard designation of conical carbon forms exists: they are indeed named differently without following any particular criterion or classification. Some authors do a mere qualitative or morphological comparison with conical forms previously reported in the literature while assuming a similarity in texture or structure with their own morphologies, without carrying out the needed characterization to ascertain it. Consequently, it had become difficult to distinguish between the various conical forms and to relate them to their growth mechanisms and properties. Therefore, a classification of three different categories based on the main causes driving the conical shape is proposed: *(i)* structural, *(ii)* textural and *(iii)* process-related. The first type involves the generation of conical forms by the existence of disclination or dislocations in the graphene lattice; the second type corresponds to those generated according to the way graphene layers are arranged with respect to the growth axis although not in relation with a structural defect; and the latter type is mainly generated during or after a particular growth process or conditions whatever the structure and texture. This classification can be used as reference to better describe and understand the intrinsic properties and characteristics exhibited by each carbon conical type, and may help determining the growth process and conditions suitable for obtaining the appropriate conical form to a given application. Overall, it is shown that several papers from the literature should be revisited in order to reach a better consistence with others regarding the type of cones formed and the related growth mechanisms, or even more, to determine the structure of the carbon involved. In this regard, the same confuse situation exists for carbon cones as for carbon nanotubes regarding the actual discrimination between the helically wrapped graphene model and the concentrically displayed graphene model.

In *Chapter 2*, we focused on *(i)* reproducing at CEMES the same cone-bearing morphologies, in particular the so-called SSF morphology, as prepared during a previous thesis work carried-out by H. Allouche with a partner lab in the USA (Applied Science Inc.) by means of CVD deposition of pyrolytic carbon onto individual carbon nanotubes, and *(ii)* confirming the deposition and then growth mechanisms proposed. Consequently, a set of experiments were conducted, starting by a parametric study in order to find the most suitable conditions impacting the gas

phase composition and concentration of species and subsequently the morphology type. Although we deliberately limited the number of parameters to the set-up temperature and to those related to the gaseous feedstock (CH_4 and H_2 concentrations, and total gas flow), determining the actual role of each of the parameters was a quite difficult task as the specific furnace geometry induces an additional parameter, the time-of-flight of species, which generates complex and dynamic events, typically multiple cracking and recombination reactions whose results are barely predictable since corresponding to non-equilibrium conditions. Temperature and time-of-flight both influence the modification of the gas phase and the type of contained carbon species, yet differently (the former tends to promote cracking reactions while the latter tends to promote recombination reactions), the resulting overall evolution being designated as the gas phase maturation. Therefore, the system appears as some kind of black-box from which what happens in it can only be guessed from the characteristics of the resulting material, after the deposited species have carbonized. Accordingly, and after having considered several deposition and growth models from the literature, we stated that, as formerly proposed in Allouche's work, the maturation process should result in the joint formation of radicals and polyaromatic hydrocarbons (PAHs) which both deposit subsequently onto the CNTs (the former chemisorb onto active sites such as graphene edges, the latter physisorb onto any surface). It is actually believed that this is the only way to explain the concomitant formation of sub-morphologies as different as smooth-surface cone with perfectly aligned graphenes and rough-surface beads (or short fiber segments) with barely aligned graphenes.

In this picture, it was confirmed that at high maturation degree of the gas phase (obtained from combined high temperature and long time-of-flight of species), SB morphologies can be produced. From experimental observations, it was also established that, when a high maturation state is reached, the variation of the gas concentration seems to affect the thickness (or volume) of the synthesized morphologies but not the morphology type. On the other hand, SSF were not reproduced under our conditions as they seem to require not only a high maturation degree of the gas phase but also an optimal inflection point allowing a higher PAHs over radicals ratio to be generated with respect to that for forming SBs. For a forthcoming work, we therefore proposed to consider longer times-of-flight at the maximum set-up temperature (1390°C) by investigating the deposits obtained in the downstream part of the furnace beyond the center of the isothermal zone, which was ignored in this study. This will be helped by the fact that, in this work, a minimal threshold for the total flow as well as for the CH_4/H_2 ratio, along with an optimal CH_4 and H_2 concentration range presumably suitable for the SSF synthesis have been identified.

The previous Allouche's hypothesis regarding the existence of a liquid, PAH-rich hydrocarbon phase is maintained, and now demonstrated. This is strongly supported by both considering the literature dealing with the physical phenomena involved when wetting a string with a liquid, and the experimental observations. As a result, it appears very likely that the so-called Plateau-Rayleigh instability (PRI) phenomenon plays a leading role in the deposition mechanism of the PAH-rich liquid phase onto the CNT support. This is the first time that the

existence of this specific physical process is revealed in the overall pyrolytic carbon deposition mechanism. In particular, the PRI could be responsible for the preferred formation of the SSF morphology over the SB morphology once the liquid phase has reached the appropriate rheological properties, whereas the SB morphology might result from the statistical deposition effect of preformed droplets onto the CNTs in a periodic manner that reflects their statistical distribution in the gas phase.

Concerning the inner texture of the cones, which somehow relates to their growth mechanism, we have come to reject the concentric graphene cylinder display proposed in Allouche's work and to prefer the helically wrapped graphene model instead. This new insight is based on the presence of spiral-like steps at the cone surface, the unwrapping behavior of the graphenes upon charge injection, and the offset between the opposed graphene layer edges on both side of the cone with respect to the cone axis revealed by TEM. On the one hand, this is consistent with the literature which shows this graphene display to be a frequent one for carbon cones prepared in related conditions; on the other hand, it is also consistent with the previous findings by Allouche, who observed that the concentric graphenes exhibit a same helicity and are also able to locally exhibit the graphitic structure for long curvature radii. Meanwhile, the TEM characterization allowed the apex diameter of the cone tips to be estimated at ~4-5 nm, and is also confirming a perfect nanotexture, which stresses our prediction for excellent mechanical strength and electrical properties of those cones. The study also came out with the identification of a specific graphene termination type (zipped graphene pair edges) seen as a defect by Raman spectroscopy, which existence is revealed by a specific Raman signature based on an unprecedented low value of 1.5 for the $I_D/I_{D'}$ ratio, which is the lowest ever found in the literature.

Carrying-out application tests for the carbon nanocones as SPM probes required mounting the SSF morphologies onto cantilever-like supports compatible with SPM equipment, which was described in *Chapter 3.* However, this come with its own challenges. First, three mounting processes have been used (focus ion (FIBID) or electron (FEBID) welding, and gluing). Both the Pt or W welding processes have to be used for preparing electrically conductive probes, whereas the gluing method could only be used for non-conductive ones, due to the insulating nature of the gluing, UV-curable polymer. Although, as expected, SSF revealed to be useful for being easy to handle with the micromanipulator during FIBID/FEBID and for being visible under an optical microscope during gluing, both processes cannot be considered as optimized ones as they do not allow the cone to be aligned with respect to the cantilever geometry with high accuracy. The welding process came with several issues, more particularly on *(i)* the quality of the fixation between the cone and the cantilever by the welding material, which does not always show a good adhesion (see the figure below), and *(ii)* the more or less severe surface amorphization of the carbon material caused by either the ion or electron irradiation steps. Both issues are likely to be detrimental to the electrical conductivity (as possibly responsible for, e.g., the variability in the current flow during STM tests), whereas the former one is suspected to induce some mechanical instability (as possibly responsible for, e.g the double resonance curves for some cantilevers, and the incidental loss of the carbon probe from some

cantilever supports). The amorphization problem is actually much reduced by using the FEBID instead of the FIBID protocol, however the mechanical fixation issue remains and is difficult to evaluate. On the other hand, the gluing method is much faster (~20 minutes instead of 2-3 hours /probe), provides a firm mechanical fixation, and seems to be robust and reproducible, with better alignment statistics, possibly due to the guiding role of the groove located at the end of the support-cantilever. Alignment problems remain, though, but are largely generated by the intrinsic poor alignment of the cone with respect to the microfiber part (referring to the SSF morphology), which is an issue to fix at the step of the carbon cone synthesis. This could be fixed by attempting to form the SSF morphologies onto pre-aligned and straight, individual carbon nanotubes.

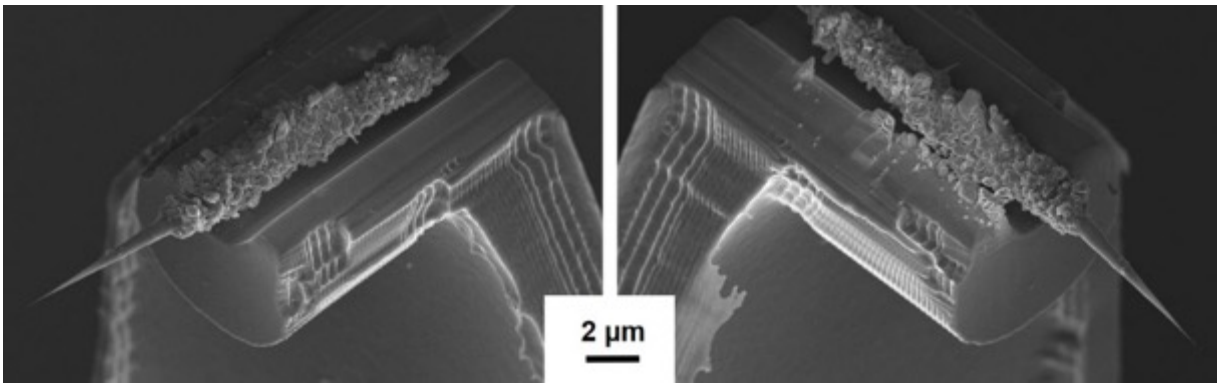

*Example of the probe **ZeR11-C20-35** showing a possibly loose fixation with no welding material on one side, and poorly adhering welding material on the other side.*

Finally, the main drawback of this process is its non-suitability for preparing conductive probes. The latter could then be overcome by using an electrically conductive glue, either based on a conductive polymer (such as polypyrrole) or on an insulating polymer loaded with a conductive filler (e.g., metal particles). However, considering the dimensions of the morphologies to glue, the conductive particle filler should be in the sub-nanometric range, which is not available on the market. Preliminary attempts were conducted (but not presented in this dissertation) to load an epoxy resin with metal nanoparticles of various nature (Cu, Ag, Au) and morphologies (spherical or elongated) including carbon nanotubes, but the tests were not further developed because of other issues to address (presence of surfactants, particle dispersion issues).

Finally, coming to the SPM tests as reported in *Chapter 4*, two choices were possible: *(i)* going deep on a selected, specific SPM technique, or *(ii)* exploring the multimode ability presumably allowed by the carbon probe characteristics. In our case, the second option was preferred because it allows an exploratory study from which the main limits and opportunities could be determined. Forthcoming works could then be identified for a deeper development of selected SPM tests. A qualitative selection of the probes was first performed on a geometric assessment carried-out through SEM characterizations and presumed conductivity performances based on the conducting properties of all the individual materials involved in welded cantilevers (graphenic carbon, doped Si, W or Pt). Although the cone lengths are relatively the same (6-7

µm) for all the carbon probes and the shape is quite homogenous, the carbon probes differed from each other from the misalignment angle with respect to the cantilever geometry, and the variable length of the SSF morphology protruding from the cantilever groove (which depended on the mounting step), which was observed to impact mostly the results with the PF-QNM, STM and KFM tests. The carbon nanocone probes were then evaluated by controlling their performances based on parameters such as resolution, durability and versatility. However, a major drawback of working on a variety of modes is to find the appropriate protocol for assessing the degree of suitability of the probes to each of the SPM modes tested. This work section was quite difficult because there is no specific protocol or probe standardization available in the literature, and the various probe suppliers have not yet developed standardized SPM measurement procedures. Therefore, most of our testing protocols consisted in qualitatively comparing images taken with the carbon probes with respect to commercial ones considered as references, and then to check the possible evolution of the shape/aspect ratio and tip radius of the probes consecutively to the test.

The Table below gathers the main performances, limitations and possible improvements of the carbon nanocone probes for the various modes tested:

SPM mode	**AFM**	**PF-QNM**	**C-AFM**	**STM**	**KFM**
C-probe type	Glued and FEBID	Glued and FEBID	FEBID	FEBID	FEBID
Nanocone performance	✓ Topographic images are possible. ✓ Better resolution than Otespa R3. ✓ Similar resolution than Tesp-SS. ✓ Stable behavior for scanning more than 30h without interruption.	✓ Suitable for quantitative nano-mechanical (i.e. Young modulus) measurements. ✓ Ability of discriminating between different components of a composite material.	✓ A global conductance slightly better than silicon commercial probes.	✓ Mid-range magnification topographic images	✓ Signal with similar resolution and contrast than Arrow probe. ✓ Charge injection is also possible.
Limitations	• Non-suitable for sample with large z variations, due to variability on inclination angles	• Tip wear resistance • Mechanical flexibility of the carbon tip part?	• Sensitivity to high voltage and/or current • Tip wear	• No atomic resolution image is possible in air condition.	• Noisy signal • Low spatial resolution • Tip wear resistance
Proposed improvement	⇒Growing SSF morphologies onto pre-aligned CNTs during synthesis alignment	⇒ Better fixation and integration during mounting process	⇒ Direct measurement of nanocone conductivity	⇒Better fixation and integration during mounting process	⇒ Work under vacuum ⇒ Cantilever reflective coating

Summary of the carbon nanocone performances for the various SPM modes tested. Otespa-R3, Tesp-SS, Arrow are doped-Si commercial probes taken as references.

From this table, it can be summarized that the main drawbacks are related to the cone alignment and the mounting process. About the latter, it would be worth investigating the incidence of the FEBID mounting process on the current or voltage sensitivity behavior observed with the cones. This should come with a direct measurement of the conductivity of a carbon cone, and also of a whole SSF morphology.

In conclusion, this work has demonstrated that the carbon nanocone-bearing SSF morphologies exhibit a good potentiality as probes for a variety of SPM modes. However, improvements are needed which should be achievable by improving the cone/fiber alignment during synthesis, and the quality and conductivity of the mounting material for fixing the SSF morphology on the support cantilever while placing the base of the conical part as close as possible from the cantilever border. Once these limitations will be overcome, the doors will be opened to a niche application as multimode SPM probes allowing the characterization of multi-properties of a same sample surface while keeping the same probe. This could be particularly interesting when considering semiconductors or composite materials. Overall, we believe that this work has contributed to demonstrate that carbon nanocones are worth being investigated as carbon nanoforms of high interest, comparable to that of carbon nanotubes. Meanwhile, we also believe that this study has contributed to carbon material science through the new knowledge it has brought to the mechanisms of pyrolytic carbon deposition at nanoscale.

****

ANNEXES

Sum up table of all the probes prepared and their use in the SPM tests

(N/A = no test was applied; Other = characterization tests)

# Probe	Probe name	Mounting process				Tests performed						Probe - final state	Reference in manuscript
		Technique	Fixation?	Alignment problems?	Other remarks	AFM	KFM	CAFM	PFQNM	STM	Other		
			Strong/Weak	YES/NO								Ok/broken/damage after mounting or test	
Focus Ion Beam Induced Deposition (FIBID)													
1	HiR03-C06-1	FIBID - Pt	Strong	YES	Ion irradiation sensitivity	N/A						Broken (manipulating)	*Ch3-fig.19c*
2	HiR03-C20-2	FIBID - Pt	Strong	YES								Broken (manipulating)	*Ch3-fig.19e*
3	HiR13-C30-3	FIBID - Pt	Strong	YES		X						Broken (manipulating)	*Ch3-fig.20c*
4	HiR02C22-4	FIBID - Pt	Strong	YES		X	X					Damaged	*Ch2-fig.20d1 and Ch4-fig. 52*
5	HiR03-C13-5	FIBID - Pt	Weak	YES		X						Broken (manipulating)	-
6	HiR03-C14-6	FIBID - Pt	Strong	NO		X	X					Broken (manipulating)	*Ch4-fig. 44-46 and 49a-50a*
7	HiR03-C22-7	FIBID - Pt	Strong	NO		X	X					OK.	*Ch4-fig.48C1*
8	HiR03-C24-8	FIBID - Pt	Weak	NO		X		X				Broken (manipulating)	-
9	HiR12-C28-9	FIBID - Pt	Strong	NO		N/A						Broken (manipulating)	-
10	HiR0X-CXX-10	FIBID - Pt	Strong	YES								Broken (manipulating)	-
11	HiR13-C26-11	FIBID - Pt	Strong	YES								Damaged	*Ch3-fig.19a*
12	HiR12-C26-12	FIBID - Pt	Strong	YES		X						Broken (manipulating)	-
13	HiR13-C27-13	FIBID - Pt	Weak	YES		N/A						Damaged (TEM)	-
14	HiR12-C29-14	FIBID - Pt	Weak	YES		X						Damaged (TEM)	*Ch3-fig.12f*
15	HiR03-C15-15	FIBID - Pt	Strong	NO		N/A						Damaged (TEM)	*Ch3-fig.12g*
16	HiR04-C05-16	FIBID - Pt	Weak	NO								Damaged (TEM)	-
17	HiR04-C06-17	FIBID - Pt	Weak	YES								Damaged (TEM)	-
18	HiR04-C11-18	FIBID - Pt	Strong	NO								Damaged (TEM)	*Ch3-fig.19d*
19	HiR04-C07-19	FIBID - Pt	Strong	YES								Damaged (TEM)	*Ch3-fig.19b*
20	ZiR05-C15-1	FIBID - Pt	Weak	NO								Damaged (TEM)	-
21	Pt-Ir-001	FIBID-Pt onto Pt-Ir wire	Strong	NO						X		Damaged	*Ch3-fig.13a1 and a2*
22	Pt-Ir-002	FIBID-Pt onto Pt-Ir wire	Weak	YES						X		Damaged	-

# Probe	Probe name	Mounting process				Tests performed						Probe - final state	Reference in manuscript
		Technique	Fixation?	Alignment problems?	Other remarks	AFM	KFM	CAFM	PFQNM	STM	Other	Ok/broken/damage after mounting or test	
			Strong/Weak	YES/NO									
Focus Electron Beam Induced Deposition (FEBID)													
23	ZeR07-C25-1	FEBID-Pt	Strong	YES			X					Broken (manipulating)	_
24	ZeR07-C26-2	FEBID-Pt	Strong	YES		N/A						Broken (manipulating)	_
25	ZeR07-C27-3	FEBID-Pt	Strong	NO			X					Damaged	_
26	ZeR07-C29-4	FEBID-Pt	Weak	YES				X				Damaged (TEM)	_
27	ZeR08-C28-5	FEBID-Pt	Weak	YES							X	Damaged (TEM)	_
28	ZeR11-C10-6	FEBID-W	Weak	YES							X	Broken during test	_
29	ZeR09-C09-7	FEBID-W	Weak	YES							X	Broken (manipulating)	*Ch3-fig. 12e*
30	ZeR10-C11-8	FEBID-W	Strong	YES				X				Broken (manipulating)	_
31	ZeR08-C27-9	FEBID-W	Strong	YES							X	Broken (manipulating)	_
32	ZeR10-C06-10	FEBID-W	Strong	YES		X					X	Broken (TEM)	_
33	ZeR10-C29-11	FEBID-W	Strong	YES				X			X	Damaged (shortened)	*Ch4-fig. 26, 28 and 34d1*
34	ZeR05-C20-12	FEBID-W	Strong	YES?				X				Broken (manipulating)	_
35	ZeR06-C07-13	FEBID-W	Weak	YES				N/A				Broken (manipulating)	_
36	ZeR06-C11-14	FEBID-W	Strong	NO				X				Damaged (shortened)	*Ch4-fig.26, 27,30 and 34c1*
37	ZeR12-C24-15	FEBID-W	Weak	YES				N/A				Broken (manipulating)	
38	ZeR08-C19-16	FEBID-W	Strong	NO				X				OK	_
39	ZeR12-C04-17	FEBID-W	Strong	NO			X					Damaged	*Ch4-fig. 44, 47a, 51a, and 52*
40	ZeR06-C29-18	FEBID-W	Strong	NO				X				Broken (manipulating)	_
41	ZeR10-C07-19	FEBID-W	Strong	NO			X					Damaged	*Ch4-fig.44, 47c, and 52*
42	ZeR0X-CXX-20	FEBID-W	Strong	NO								Broken during mounting	
43	ZeR0X-CXX-21	FEBID-W	_	_				N/A				Broken during mounting	
44	ZeR0X-CXX-22	FEBID-W	_	_								Broken during mounting	
45	ZeR09-C05-23	FEBID-W	Strong	NO				X				Broken (manipulating)	*Ch4-fig.26 and 34b1*
46	ZeR09-C13-24	FEBID-W	Weak	NO				N/A				New (in stock)	_
47	ZeR09-C26-25	FEBID-W	Strong	NO		X						OK	*Ch4-fig.10, 12, 13*
48	ZeR07-C07-26	FEBID-W	Strong	YES				X				Damaged (shortened)	*Ch4-fig.26, 32, and 34a1*
49	ZeR04-C20-27	FEBID-W	Weak	NO								New (in stock)	_
50	ZeR0X-CXX-28	FEBID-W	Strong	YES								New (in stock)	_
51	ZeR09-C10-29	FEBID-W	Strong	YES				N/A				New (in stock)	
52	ZeR12-C25-30	FEBID-W	Weak	YES								New (in stock)	
53	ZeR0X-CXX-31	FEBID-W	Strong	YES								New (in stock)	_
54	ZeR09-C11-32	FEBID-W	Strong	NO					X			Damaged	*Ch4-fig.16, 18; 20-23*
55	ZeR09-C12-33	FEBID-W	Strong	NO									
56	ZeR11-C21-34	FEBID-W	Weak	YES				N/A					
57	ZeR11-C20-35	FEBID-W	Weak	NO								In stock	_
58	Au-e-001	FEBID-W onto Au wire	Weak	NO						X		Damaged	_
59	Au-e-002	FEBID-W onto Au wire	Weak	NO						X		Damaged	*Ch2-fig.21*
60	Au-e-003	FEBID-W onto Au wire	Strong	NO						X		Damaged	_
61	Au-e-004	FEBID-W onto Au wire	Strong	NO						X		Damaged	_
62	Au-e-005	FEBID-W onto Au wire	Strong	NO						X		Damaged	*Ch3-fig.13b2; Ch4-fig.36*

# Probe	Probe name	Mounting process				Tests performed						Probe - final state	Reference in manuscript
		Technique	Fixation?	Alignment problems?	Other remarks	AFM	KFM	CAFM	PFQNM	STM	Other	Ok/broken/damage after mounting or test	
			Strong/Weak	YES/NO									
Glued-Optical Microscope (part 1)													
63	GR14-C09-1	Glued- UV-resin	_	_	_							Broken during mounting	_
64	GR14-C10-2	Glued- UV-resin	_	_	_							Broken during mounting	_
65	GR15-C19-3	Glued- UV-resin	Weak	YES	Cone glued outside groove							OK	_
66	GR05-C08-4	Glued- UV-resin	Strong	YES	_							Broken (manipulating)	_
67	GR04-C17-5	Glued- UV-resin	_	_								Broken during mounting	_
68	GR05-C14-7	Glued- UV-resin	Strong	NO	_				N/A			Damaged (Chip)	_
69	GR03-C16-8	Glued- UV-resin	Strong	YES	_							Broken (manipulating)	_
70	GR04-C04-9	Glued- UV-resin	Strong	NO	_							Broken (manipulating)	_
71	GR04-C09-10	Glued- UV-resin	Strong	NO	Resin droplets on the cone surface							Broken (manipulating)	_
72	GR04-C27-11	Glued- UV-resin	_	_	_							Damaged during mounting	_
73	GR04-C25-12	Glued- UV-resin	_	_	_							Damaged during mounting	_
74	GR04-C08-13	Glued- UV-resin	Strong	NO	_	X						Damaged	_
75	GR11-C29-14	Glued- UV-resin	Strong	NO	Resin droplets on the cone surface	X						Damaged	*Ch4-fig.4-6 and 8*
76	GR04-C13-15	Glued- UV-resin	Strong	NO	_						X	Broken during test	
77	GR04-C14-16	Glued- UV-resin	Strong	NO	_						X	Broken (manipulating)	_
78	GR12-C20-17	Glued- UV-resin	Strong	NO	_				X			OK (but calibration problems)	*Ch3-fig.10*
79	GR11-C28-18	Glued- UV-resin	Strong	NO	_							Broken (MEB)	_
80	GR11-C24-19	Glued- UV-resin	Strong	NO	_				N/A			Damaged (TEM)	_
81	GR12-C05-20	Glued- UV-resin	Strong	YES	Cone-fiber misalingment							Broken (manipulating)	_
82	GR13-C08-21	Glued- UV-resin	Strong	YES	Cone-fiber misalingment			X				Damaged	_
83	GR13-C29-23	Glued- UV-resin	Strong	NO	_						X	Damaged during test	_
84	GR09-C15-24	Glued- UV-resin	Strong	NO	_						X	Damaged (TEM)	_
85	GR12-C18-25	Glued- UV-resin	Weak	YES	Cone glued outside groove						X	Damaged (TEM)	_
86	GR11-C23-26	Glued- UV-resin	Strong	NO	_				N/A			Broken (manipulating)	_
87	GR04-C23-27	Glued- UV-resin	Strong	YES	Resin droplets on the cone surface						X	Damaged (TEM)	_
88	GR06-C12-28	Glued- UV-resin	Strong	YES	Resin droplets on the cone surface						X	Damaged (TEM)	_
89	GR12-C27-29	Glued- UV-resin	Strong	NO	_							Broken (MEB)	_
90	GR08-C23-30	Glued- UV-resin	Strong	YES	Cone-fiber misalingment						X	Broken (MEB)	_
91	GR08-C22-31	Glued- UV-resin	Strong	YES	Cone-fiber misalingment						X	Broken (manipulating)	_
92	GR06-C13-32	Glued- UV-resin	Strong	YES	Cone-fiber misalingment							Broken (manipulating)	_
93	GR09-C04-33	Glued- UV-resin	Strong	NO							X	Broken during test	_
94	GR09-C02-34	Glued- UV-resin	Strong	NO	_				N/A			Broken (manipulating)	_
95	GR08-C17-35	Glued- UV-resin	Strong	YES	Resin droplets on the cone surface				N/A			OK	_
96	GR15-C12-36	Glued- UV-resin	Strong	YES	Resin droplets on the cone surface- end by nanotube						X	Broken (manipulating)	_
97	GR09-C06-37	Glued- UV-resin	Strong	YES	Resin droplets on the cone surface				N/A			OK	_
98	GR02-C07-38	Glued- UV-resin	_		_							Broken (MEB)	_
99	GR02-C08-39	Glued- UV-resin	Strong	NO	Resonance poblems)	X					X	Damaged	_
100	GR06-C09-40	Glued- UV-resin	Strong	NO	_		X				X	Broken (TEM)	_

# Probe	Probe name	Mounting process				Tests performed						Probe - final state	Reference in manuscript
		Technique	Fixation?	Alignment problems?	Other remarks	AFM	KFM	CAFM	PFQNM	STM	Other		
			Strong/Weak	YES/NO								Ok/broken/damage after mounting or test	
Glued-Optical Microscope (part 2)													
101	GR09-C09-41	Glued- UV-resin	Strong	NO	Resin droplets on the cone surface	N/A						OK	*Ch3-fig.12e*
102	GR11-C04-42	Glued- UV-resin	Strong	YES	_						X	Damaged (TEM)	_
103	GR11-C03-43	Glued- UV-resin	Strong	NO	_	N/A						Broken (manipulating)	_
104	GR11-C08-44	Glued- UV-resin	Strong	YES	Cone glued outside groove	X						Damaged	
105	GR11-C07-45	Glued- UV-resin	Strong	NO	Cone-fiber misalingment/ resin droplets						X	Damaged (TEM)	_
106	GR11-C05-46	Glued- UV-resin	Strong	NO	_		X				X	Damaged (TEM)	_
107	GR09-C13-47	Glued- UV-resin	Strong	YES	Cone-fiber misalingment						X	Damaged (TEM)	_
108	GR08-C05-48	Glued- UV-resin	Strong	NO	_						X	Damaged	_
109	GR10-C23-49	Glued- UV-resin	Strong	YES	_						X	Damaged	_
110	GR05-C17-50	Glued- UV-resin	Strong	YES	_						X	Damaged (TEM)	_
111	GR09-C22-51	Glued- UV-resin	Strong	NO	_						X	Damaged (TEM)	_
112	GR09-C24-52	Glued- UV-resin	Strong	NO	_							Broken (manipulating)	_
113	GR05-C11-53	Glued- UV-resin	Strong	NO	_						X	Broken (TEM)	_
114	GR15-C16-54	Glued- UV-resin	Strong	YES	_	N/A						Damaged (TEM)	*Ch3-fig.20e*
115	GR12-C13-55	Glued- UV-resin	Strong	YES	_						X	Damaged	_
116	GR12-C14-56	Glued- UV-resin	Strong	NO	_						X	Damaged (TEM)	_
117	GR12-C12-57	Glued- UV-resin	Strong	NO	_				X			Broken (intentionally)	*Ch4-fig.16-18a, 20-22*
118	GR15-C14-58	Glued- UV-resin	Strong	YES	Resin droplets on the cone surface							Damaged (TEM)	_
119	GR12-C15-59	Glued- UV-resin	Strong	NO	_							Broken (manipulating)	_
120	GR02-C11-60	Glued- UV-resin	Strong	NO	Resin droplets on the cone surface							Damaged (TEM)	_
121	GR05-C24-61	Glued- UV-resin	Strong	YES	Cone glued outside groove							OK	_
122	GR09-C28-62	Glued- UV-resin	Strong	YES	Resin droplets on the cone surface- end by nanotube							Damaged (TEM)	_
123	GR05-C27-63	Glued- UV-resin	Strong	YES	Resin droplets on the cone surface- end by nanotube	N/A						OK	_
124	GR05-C16-64	Glued- UV-resin	Strong	NO	Resin droplets on the cone surface	X						Damaged (manipulating)	*Ch4-fig.10, 12, 13*
125	GR10-C08-65	Glued- UV-resin	Strong	YES	_	X			X			Damaged	*Ch4-fig.16, 18, 20-23*
126	GR08-C21-66	Glued- UV-resin	Strong	YES	Resin droplets on the cone surface	N/A						OK	_
127	GR02-C26-67	Glued- UV-resin	Strong	NO	Resin droplets on the cone surface							Broken (manipulating)	
128	GR07-C20-68	Glued- UV-resin	Strong	NO	_	X						OK	*Ch4-fig.9, 10, 12, 13*
129	GR12-C23-69	Glued- UV-resin	Weak	YES	Cone glued outside groove	N/A						OK	_
130	GR06-C25-70	Glued- UV-resin	Strong	NO	_							Broken (manipulating)	_
131	GR05-C25-71	Glued- UV-resin	Strong	NO	_							Broken (manipulating)	_
132	GR10-C22-72	Glued- UV-resin	Strong	NO	_							OK	_
133	GR09-C20-73	Glued- UV-resin	Strong	NO	_							OK	_
134	GR09-C21-74	Glued- UV-resin	Strong	NO	_							OK	_
135	GR05-C22-75	Glued- UV-resin	Strong	NO	_							OK	_
136	GR11-C06-76	Glued- UV-resin	Strong	NO	_	N/A						OK	_

Résumé
en
Français

(Extended abstract in French)

Introduction

Les matériaux carbonés conviennent à de nombreuses applications car ils peuvent présenter des propriétés physiques (électriques, thermiques et mécaniques) exceptionnelles et polyvalentes. Celles-ci se sont avérées particulièrement améliorées dans les formes de carbone à l'échelle nanométrique, c'est-à-dire les morphologies de carbone dont au moins une dimension est inférieure à 100 nm. Les représentants emblématiques de ces formes de carbone sont généralement les nanotubes et les graphènes, qui ont tous les deux généré une quantité énorme de travaux et de publications dans le monde entier, le dernier ayant fait l'objet d'un prix Nobel en 2010. Cependant, une autre forme de carbone, conique, mérite d'être prise en considération alors qu'elle n'a pas fait l'objet de la même attention mondiale, en particulier les nanocônes de carbone. Les nanocônes de carbone peuvent présenter des caractéristiques géométriques spécifiques telles qu'une forme en aiguille, un rapport d'aspect élevé, un angle de cône variable, et une base de taille micrométrique, associée à un apex nanométrique. Ils peuvent également présenter la même variété en termes de nombre de parois, de texture et de nanotexture que les nanotubes de carbone (NTC). En conséquence, ils devraient présenter une meilleure stabilité mécanique que la morphologie en cylindre étroit qui est typique de leurs homologues nanotubes. Ils présentent également des propriétés thermiques et électriques intéressantes, à condition que les couches de graphènes soient parfaitement alignées par rapport à l'axe du cône. Tout cela peut faire des formes coniques d'excellents candidats pour toute une série d'applications allant des nanoélectrodes, des matériaux adsorbants à grande surface, des émetteurs d'électrons et des sondes pour les microscopies en champ proche (aussi appelées "microscopies à sonde à balayage" - SPM).

Le CEMES étudie depuis plusieurs années la formation d'une variété de nanocônes de carbone obtenue par le dépôt de carbone pyrolytique sur des NTCs individuels comme support. Bien que les mécanismes de formation puissent encore être débattus, ils ont été testés avec succès comme émetteurs d'électrons dans un travail précédent, permettant en fait de concevoir une source d'électrons à émission de champ froid dotée des meilleures performances jamais obtenues. Ce contexte a été une excellente motivation pour étudier les mêmes nanocônes de carbone en vue d'une autre application prometteuse, à savoir comme sondes pour la SPM. La SPM vise à acquérir des images haute résolution de caractéristiques tridimensionnelles à l'échelle nanométrique et à mesurer les propriétés locales d'une surface. Les morphologies coniques en carbone peuvent combiner la stabilité mécanique d'un cône et le rapport d'aspect élevé d'un cylindre de diamètre étroit, ce qui les rend potentiellement supérieures aux NTCs et aux sondes commerciales en silicium couramment utilisées. Cependant, contrairement aux NTCs qui ont été largement étudiés pour cette application, seuls quelques travaux concernant le potentiel des nanocônes de carbone pour les sondes SPM sont rapportés dans la littérature. Cela peut être lié à de nombreux facteurs relatifs aux processus de synthèse, et aux obstacles techniques. En effet, peu d'études sont rapportées sur la synthèse, les propriétés et les applications des formes coniques de carbone. Les formes coniques en forme d'aiguille peuvent être produites par de nombreuses méthodes telles que le dépôt chimique en phase vapeur (DCPV), le plasma, etc. La plupart de ces procédés sont limités soit au niveau du rendement, du contrôle de la forme géométrique, du contrôle de la structure du matériau et du respect de

l'intégrité structurale, comme dans le cas des techniques assistées par plasma. D'autre part, la manipulation des morphologies coniques en tant qu'objets individuels afin de les monter sur des supports spécifiques à la SPM tels que des cantilevers n'est pas simple et s'accompagne de nombreux problèmes techniques. De même, des tentatives de croissance directe de pointes coniques sur des cantilevers par divers moyens ont également été menées, mais aucune de ces techniques n'a permis d'obtenir une croissance et un contrôle individuels des formes coniques. Par conséquent, la préparation de sondes SPM basées sur des cônes de carbone individuels au moyen de procédés contrôlés, reproductibles, et faciles constituait une perspective très prometteuse mais aussi un défi à relever. En outre, la littérature est assez limitée en ce qui concerne la variété des modes de SPM pour lesquels les sondes coniques en carbone ont été testées.

Dans ce travail, la faisabilité de l'utilisation de nanocônes de carbone préparés par DCPV comme sondes SPM est évaluée depuis la synthèse des cônes de carbone jusqu'à leur test pour différents modes SPM. L'étude est présentée comme suit :

- Le chapitre 1 présente une étude bibliographique exhaustive décrivant les principales formes de cônes de carbone rapportées dans la littérature sous tous les aspects de leur processus de synthèse, de leurs caractéristiques physiques et des applications testées.

- Le **chapitre 2** décrit le procédé original de croissance par DCPV utilisé pour la synthèse à relativement haut rendement de morphologies uniques comportant des cônes de carbone à géométrie et dimensions contrôlées, en particulier celles appelées *Spiky Bead* (SB) et *Spiky Short Fiber* (SSF). La structure interne du cône de carbone, sa texture et sa nanotexture sont étudiées par microscopie électronique à balayage (MEB), microscopie électronique à transmission (MET) et spectroscopie Raman, et les mécanismes de formation sont discutés afin d'apporter, pensons-nous, un nouvel éclairage sur les mécanismes globaux du dépôt pyrolytique de carbone.

- Le **chapitre 3** présente différentes approches techniques pour monter les morphologies SSF pour constituer des sondes SPM. Les cônes de carbone une fois montés comme sondes sont caractérisés par différentes techniques (SEM, TEM, Raman).

- Dans le **chapitre 4**, les sondes SPM à base de nanocônes de carbone sont évaluées pour divers modes SPM électriques et non électriques, en considérant une variété de critères tels que la performance, la durabilité et la polyvalence des sondes. Tout au long de ces tests, des comparaisons avec des sondes commerciales en silicium ou en métal sont également effectuées.

- Enfin, une section consacrée aux **conclusions et aux perspectives** met en évidence les principaux résultats concernant, d'une part, les mécanismes de synthèse des formes coniques présentées dans ce manuscrit, et d'autre part, leurs performances en tant que conseils pour chacun des modes SPM testés. Les améliorations possibles sont également identifiées et des conseils sont donnés pour les mettre en œuvre dans les travaux à venir.

Chapitre 1 : Les (nano)cônes de carbone à base de graphène : un état de l'art

Il existe une grande variété de morphologies coniques du carbone, à parois simple ou multiple, à partir de tailles nanométriques jusqu'à atteindre des dimensions micro-nanométriques. Le monde des (nano)cônes de carbone est aussi vaste que celui des NTCs, et peut-être encore même plus vaste, car ils nécessitent de décrire les mêmes paramètres que les NTCs (diamètre, nombre de parois, angle d'hélicité, nanotexture, texture, structure) mais avec des paramètres spécifiques supplémentaires tels que l'angle du cône, de dislocation éventuelle et, d'une manière générale, le type de défaut structurel (disinclinaison, dislocation) dont ils peuvent être issus.

Les cônes de carbone présentent donc des caractéristiques distinctes, qui dépendent entièrement de leur mécanisme de croissance et de leur processus de synthèse. Malheureusement, les connaissances en la matière sont beaucoup moins avancées que pour les NTCs, dans tous les aspects possibles :

Nomenclature : *graphite/graphitic/graphenic/graphene cones, hexagonal-pyramidal graphite hillocks, nanohorns, fullerene cones, carbon nanocones, graphite whiskers, carbon nanopipettes, cone-shaped graphitic whiskers, Conical crystals of graphite, conical carbon nanotube, conical carbon tubular structures, pointed carbon nanotubes, tubular carbon cones, hollow carbon cones, conical carbon (nano)fibers, tubular graphite cones, conical carbon protrusions*. Dans tous les articles publiés, la nomenclature est très imaginative et figurative, abusivement diverse, et parfois inappropriée, donc généralement trompeuse.

Mécanismes de croissance : la plupart des raisons pour lesquelles les formes coniques sont générées ont été identifiées, soit structurales, (e.g., par dislocation-coin, dislocation-vis, dislocation-coin radiale), soit texturales. Cependant, en raison de la caractérisation globalement médiocre et insuffisante, de la facilité de se référer à des modèles publiés précédemment mais non encore fermement démontrés, et du respect dogmatique de certaines règles géométriques (par exemple, la règle du pentagone, voir **Fig.1**) qui peuvent s'appliquer aux formes moléculaires (cônes de graphène simple, structurellement parfaits, de taille nanométrique) mais pas aux formes coniques défectueuses, plus grandes et à couches multiples, il y a peu de certitude quant à l'arrangement des graphènes et des mécanismes de croissance des cônes de carbone dans une majorité d'articles. Il y a de bonnes raisons à cela ; l'une d'elles est que la MET serait une méthode clé, mais la discrimination entre les différents arrangements de graphène (par exemple, concentrique ou en abat-jour empilés par rapport à un ruban de graphène enroulé en hélice) est rendue difficile parce qu'une image de MET révèle un volume projeté en 2D ; une autre raison est que le nombre d'atomes devient rapidement trop élevé, empêchant l'utilisation de nombreux principes de modélisation.

Il reste donc à comprendre pleinement les mécanismes à l'origine de la formation des différentes morphologies coniques à base de graphène.

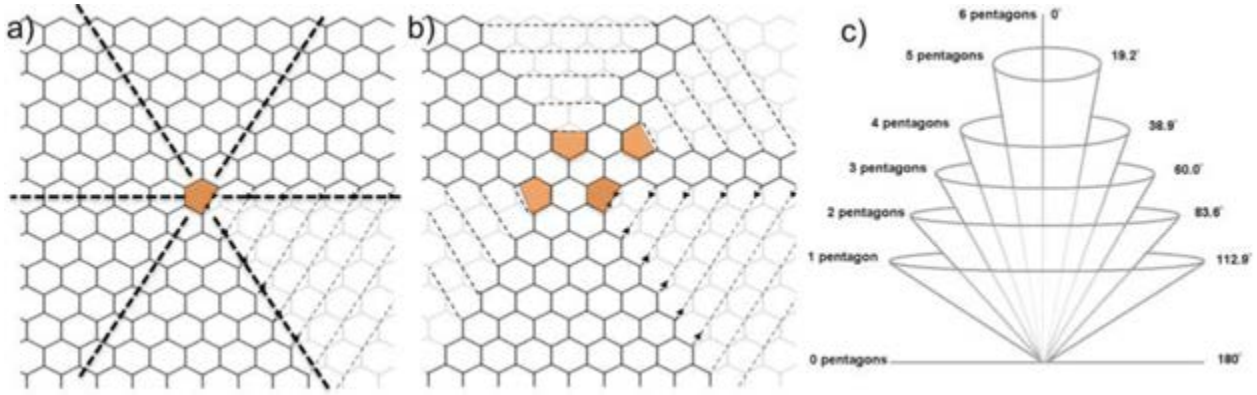

***Figure 1** : Illustration de la création de morphologies coniques par l'incorporation de pentagones dans un réseau de graphène. **(a)** feuille de graphène avec un pentagone dans le réseau. **(b)** Feuille de graphène avec 4 pentagones dans le réseau. **(c)** Relation entre le nombre de pentagones incorporés dans le réseau de graphène et la valeur de l'angle au sommet correspondant du cône formé. De [Karousis et al., Chem. Rev. 116 (2016) 4850].*

Corrélations processus de synthèse *vs* caractéristiques des cônes : Les cônes de carbone basés sur le carbone sp^3, qui n'étaient pas couverts par cette étude, sont certainement mieux compris et contrôlés, en raison de l'isotropie et de la faible polyvalence de l'unité structurale de construction du matériau (le tétraèdre de carbone, par opposition au graphène), et également en raison de l'absence de défauts structuraux (par exemple, disinclinaison, dislocation…) capable d'affecter la morphologie extérieure globale. Par conséquent, la variété des morphologies coniques à base de carbone sp^3 est certainement faible. Cela n'est évidemment pas vrai pour les cônes graphéniques dont la variabilité texturale est grande (**Fig.2**), voire unique dans le monde des matériaux. Bien sûr, on peut trouver des tendances. Par exemple, générer des atomes de carbone individuels ou de petites espèces carbonées (par exemple, des dimères) dans des conditions de vide entraînera la formation de cônes pour lesquels la création de pentagones aura un rôle moteur. De plus, l'utilisation de conditions de DCPV "génériques" (c'est-à-dire non assistées par plasma) peut entraîner des conditions de formation de cônes ressemblant à celles d'autres processus connus tels que la formation de CNT ou le dépôt de carbone pyrolytique.

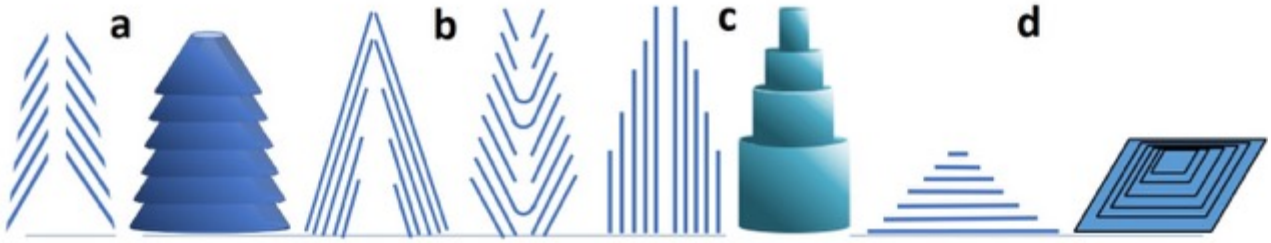

***Figure 2 :** Schéma de morphologies graphéniques dont les formes coniques sont déterminées de trois façons différentes par la texture, c'est-à-dire l'orientation des couches de graphène par rapport à l'axe du cône. **(a)** et **(b)** trois textures différentes pour les feuilles de graphène obliques par rapport à l'axe du cône ; **(c)** feuilles de graphène parallèles à l'axe du cône ; **(d)** feuilles de graphène perpendiculaires à l'axe du cône. Les dessins au trait à côté des modèles 3D schématisent la façon dont la texture interne des morphologies coniques globales est vue sous forme d'images projetées telles qu'obtenues par MET à haute résolution. Bien que les modèles 3D en (a), (c), (d) présentent une configuration en assemblages de graphènes multiples, les textures projetées seraient les mêmes dans le cas d'une configuration à base d'un enroulement hélicoïdal d'un graphène unique.*

Malheureusement, le manque de caractérisation approfondie des cônes de carbone formés empêche encore, dans une large mesure, une approche déterministe de la formation des cônes de carbone, capable de proposer et de prédire les bonnes conditions pour synthétiser des formes coniques présentant les caractéristiques de texture, de nanotexture et de structure souhaitées. Cela est particulièrement vrai pour les procédés assistés par plasma. Même si des travaux concernant les CNTs ont montré que le DCPV assisté par plasma à courant continu tend à induire une texture en chevrons alors que le DCPV assisté par plasma micro-ondes tend à induire une texture concentrique, et que cela semble également vrai pour les cônes, il existe beaucoup d'exemples de synthèse de cônes qui n'ont pas été suivis de la caractérisation nécessaire pour que cette hypothèse soit statistiquement vérifiée. D'autre part, les méthodes assistées par plasma ou par irradiation ne peuvent pas fournir la meilleure qualité structurale et nanotexturale.

Applications : Seuls quelques articles concernant les applications potentielles des morphologies coniques à base de graphène sont signalés dans la littérature. Aucune application commerciale n'a été générée, même dans le domaine où les cônes de graphènes semblent les plus prometteurs, comme l'émission d'électrons et les sondes SPM. Cela peut s'expliquer par plusieurs causes :

(i) Des problèmes de synthèse, puisque pour certains il est encore difficile de contrôler la forme, le rendement et la reproductibilité des formes coniques. Pour les procédés qui permettent un bon rendement et une bonne reproductibilité, comme les procédés assistés par plasma, le matériau est mal contrôlé ou limité en termes de qualité structurale, et ne fournit donc pas les meilleures performances possibles.

(ii) Des problèmes techniques ultérieurs, car pour des utilisations individuelles, il existe une difficulté intrinsèque à contrôler l'emplacement précis et la manipulation d'un cône unique. Soit les cônes doivent pousser à l'endroit même du dispositif où ils doivent se trouver lors de l'utilisation, par exemple à l'extrémité d'un cantilever d'AFM, soit ils doivent être saisis et manipulés après synthèse pour être positionnés au bon endroit. La façon et les dimensions (nanométriques) avec lesquelles les cônes, souvent, se développent empêchent leur manipulation en tant qu'objets uniques. Même si certains auteurs ont réussi à faire pousser *in situ* un seul cône de carbone sur un cantilever sans pointe (**Fig.3**), le processus comporte de nombreuses étapes qui sont à la fois coûteuses et longues.

(iii) La question du coût. En effet, concevoir et réaliser la synthèse adéquate, puis caractériser, et enfin assurer le contrôle de qualité dans la chaîne de fabrication des cônes semblent constituer des procédés coûteux et chronophages.

Il ressort de cette étude, qui s'est efforcée d'être approfondie et complète, que le domaine de recherche des (nano)cônes de carbone est aussi prometteur que celui des CNTs, et pourrait en fait résoudre certains problèmes auxquels les CNTs sont confrontés dans leur utilisation pour certaines applications. Cependant, le domaine des cônes de carbone est injustement négligé car il reste de nombreuses recherches à mener et beaucoup de compréhension à acquérir dans tous les aspects, de la synthèse aux applications. Les chapitres suivants visent à y contribuer.

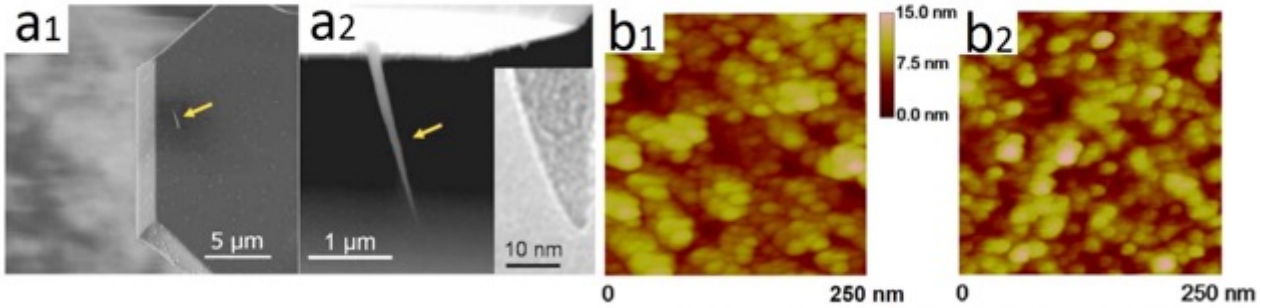

Figure 3 : (a1) *et* ***(a2)*** *image MEB à faible puis fort grossissements d'un cône de carbone (flèche jaune) et de son apex (en encart dans (a2)) sur un cantilever de Si sans pointe. Encadré dans (a2): Image MEB d'un sommet de cône typique (de [Chen et al., Appl. Phys. Lett. 88 (2006) 153102]).* ***(b1)*** *Image AFM (tapping mode) de la surface d'un film de Cu sondée par une pointe de cône en carbone ;* ***(b2)*** *la même surface (zone différente), sondée par une pointe de Si standard (de [Chen et al., Nanotechnol. 17 (2006) 4322]).*

Chapitre 2 : Synthèse et mécanismes de formation des nanocônes de carbone par DCPV

Synthèse des morphologies comportant des cônes : des cônes bien développés, de taille micrométrique, entièrement graphéniques, avec un très haut degré de nanotexture peuvent maintenant être préparés au CEMES de façon routinière. Cependant, nous avons pu synthétiser la morphologie dite "*spiky-bead*" (SB), c'est-à-dire présentant le facteur F le plus élevé (**Fig.4**), mais nous n'avons pas pu préparer la morphologie dite "*spiky-short-fiber*" (SSF). Néanmoins, sur la base de la conviction à laquelle nous sommes parvenus selon laquelle la formation de SSFs nécessite que la phase gazeuse atteigne un degré de maturation plus élevé que pour la formation de la morphologie SB, plusieurs façons de le faire ont été identifiées, comme feuille de route pour un travail à venir.

Mécanismes de dépôt : Nos observations confirment et renforcent les travaux antérieurs du laboratoire concernant la nécessité, pour la phase gazeuse, de contenir deux types d'espèces contribuant différemment à la croissance du solide carboné, à savoir des hydrocarbures aromatiques polycycliques (HAP) et des petites espèces carbonées ou d'hydrocarbonées radicalaires. Elles renforcent également l'hypothèse antérieure de la concentration des HAPs sous la forme d'une phase liquide qui est générée avant de se déposer sur les NTCs primaires, qui jouent le rôle de substrat de dépôt. Nous avons examiné l'hypothèse de l'existence et de la forme adoptée par cette phase liquide en interaction avec les NTCs dans le cadre de la compréhension globale des phénomènes de mouillage, en particulier en ce qui concerne le mouillage des fibres par des liquides qui implique l'instabilité dite de Plateau-Rayleigh comme phénomène moteur (**Fig.5**). Cela a permis de tirer deux conclusions importantes :

(i) Il existe des preuves solides que la phase liquide se condense sous forme de film cylindrique autour des CNTs primaires, qui se brise ensuite en gouttelettes disposées périodiquement en raison de l'effet de l'instabilité de Plateau-Rayleigh. Cela pourrait être

le mécanisme de discrimination entre les morphologies SB et SSF en relation avec le dépôt de phases liquides ayant des caractéristiques rhéologiques différentes, ces dernières étant régies par les conditions de synthèse.

(ii) Cependant, dans certaines conditions, en raison de l'incompatibilité entre la valeur théorique de la longueur d'onde onduloïdale déduite des équations relatives à l'instabilité de Plateau-Rayleigh et la périodicité réelle observée entre les morphologies finales, le dépôt direct de gouttelettes, préformées dans la phase gazeuse, sur les NTCs primaires devrait également être envisagé.

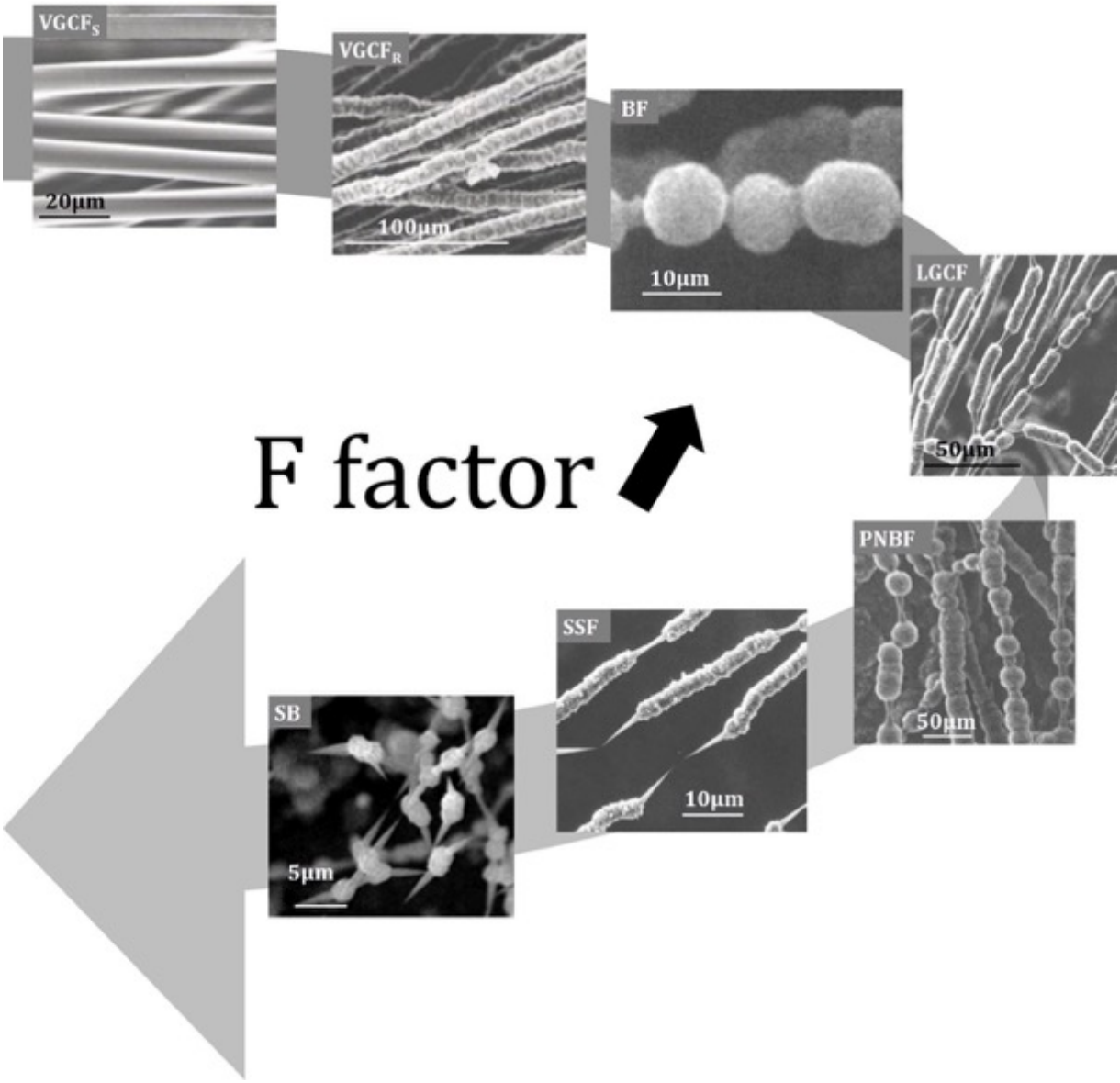

Figure 4 : *Les différentes morphologies de carbone, obtenues par le processus de CVD en deux étapes utilisé dans ce travail, classées selon la valeur du facteur morphologique* F, *qui varie de 0 pour des fibres de carbone standard dites VGCF$_S$ et VGCF$_R$ à 1 pour la morphologie de carbone non standard ultime qu'est la morphologie SB.*

Une conséquence intéressante de l'étude est la meilleure compréhension des mécanismes généraux du dépôt de carbone pyrolytique. En effet, la composition de la phase gazeuse dans

un réacteur de DCPV comme le nôtre est indépendante du type de substrat. En ce sens, l'utilisation de NTCs comme substrat de dépôt a révélé la coexistence de gouttelettes liquides et de radicaux dans la phase gazeuse, ce que le dépôt de carbone pyrolytique sur des substrats macroscopiques (substrats plans, ou fibreux avec des rayons de courbure de l'ordre du micron) n'a pas pu révéler avec autant d'évidences.

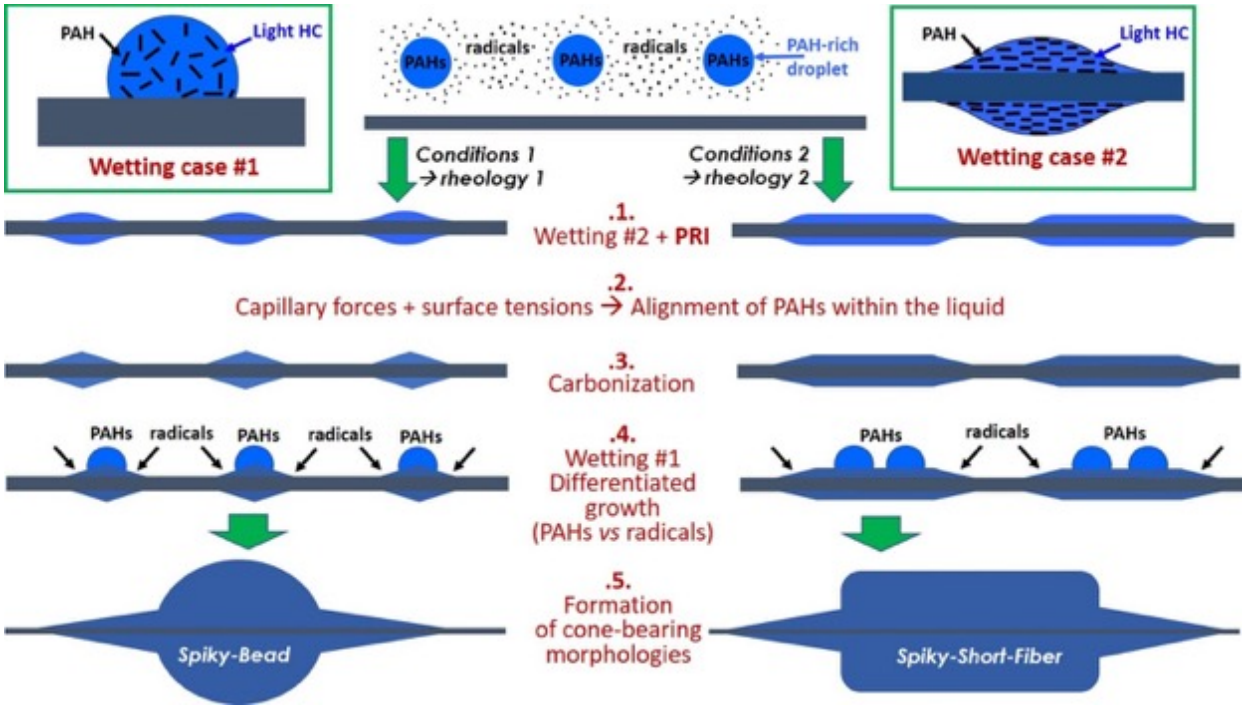

Figure 5 : *Schéma de scénarios possibles rendant compte des différentes morphologies formées comme illustré dans la* ***Fig.4****. Les scénarios se concentrent sur la formation des morphologies SB (à gauche) et SSF (à droite), mais en partant de "gouttelettes" plus proches les unes des autres à l'étape 1, on obtiendrait les morphologies PNBF (à gauche) et LGCF (à droite). Enfin, en partant de gouttelettes encore plus proches, on obtient la morphologie BF.*

Mécanisme de croissance du cône : Il a été confirmé que les cônes sont construits à partir de graphènes disposés concentriquement. Cependant, plusieurs observations ont convergé pour s'opposer à l'ancienne hypothèse d'une texture de cône basée sur des cylindres concentriques de graphènes, et pour, plutôt, suggérer fortement une disposition hélicoïdale d'un nombre limité de graphènes (éventuellement multicouches) faisant que les cônes adoptent la même texture que les *whiskers* de Bacon connus depuis longtemps (**Fig.6**). Au sommet du cône, qui est la partie la plus importante concernant l'utilisation possible des cônes de carbone comme sondes SPM qui sera étudiée au *Chapitre 4*, la façon dont les cônes croissent laisse des bords de graphène libres qui ont tendance à se rapprocher par paires comme un comportement probable pour minimiser l'énergie libre, en particulier pour les graphènes avec des petits rayons de courbure (**Fig.7a**).

Il a été constaté que ces terminaisons de paires de graphènes "zippées" sont associées au plus faible rapport (1,5) des bandes d'émission Raman $I_D/I_{D'}$ jamais rapporté dans la littérature, et que nous avons donc proposé d'être la signature spécifique de ce type de terminaison de graphènes, considéré comme un défaut par la spectroscopie Raman.

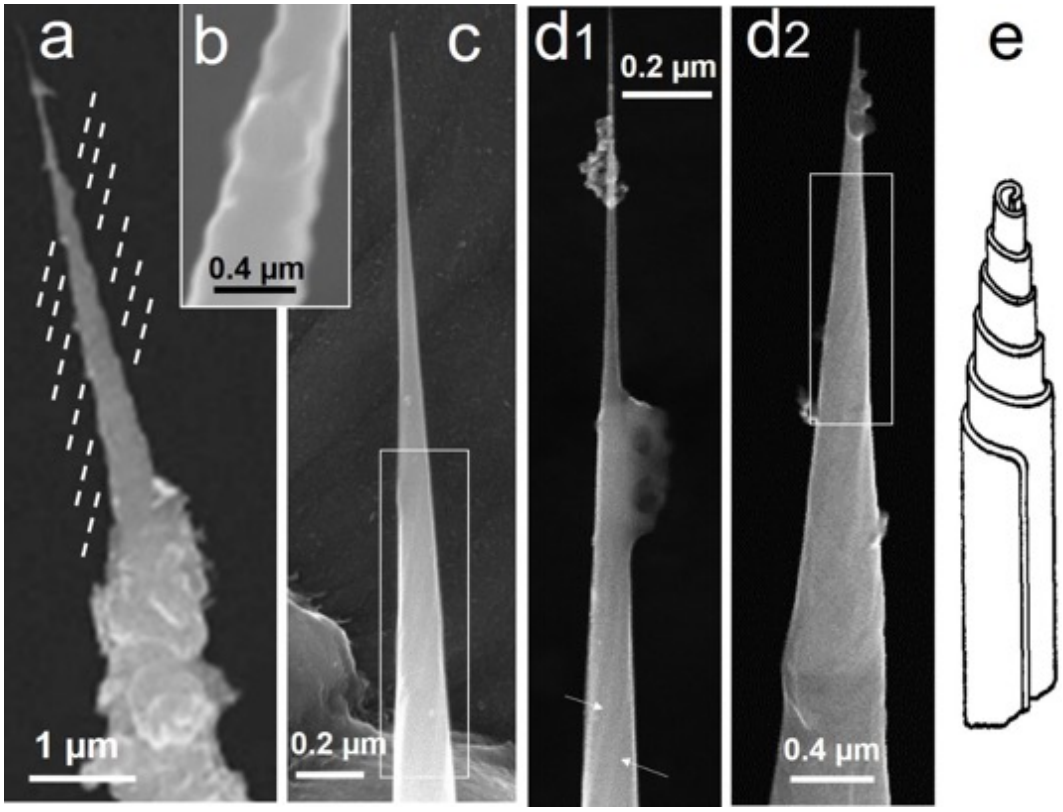

Figure 6 : *Morphologies des nanocônes avec des caractéristiques de surface suggérant un enroulement en spirale des graphènes constituant les cônes.* ***(a)*** *montre un nanocône avec une surface bosselée dont les emplacements et les directions des bosses suggèrent un motif hélicoïdal.* ***(b)*** *un autre cône avec une surface bosselée.* ***(c)*** *détail de la surface de la sonde en nanocône de carbone HiR03-C20 ; on peut deviner un aspect spiralé dans la zone encadrée.* ***(d1)*** *Détails de la surface de la sonde en nanocône de carbone HiR02-C22-4 ; des lignes hélicoïdales peuvent être devinées (flèches).* ***(d2)*** *même cône qu'en* ***(d1)****, mais après le test KFM ; on peut également deviner l'aspect hélicoïdal dans la zone encadrée ; le fait que l'aspect hélicoïdal puisse être deviné dans les deux images montre qu'il s'agit d'une réalité et non d'un artefact (Crédits photographiques : (a) R. Wang, CEMES ; (c), (d1) et (d2) R. Cours, CEMES).* ***(e)*** *modèle d'un whisker de Bacon [Bacon, J. Appl. Phys. 31 (1960) 283].*

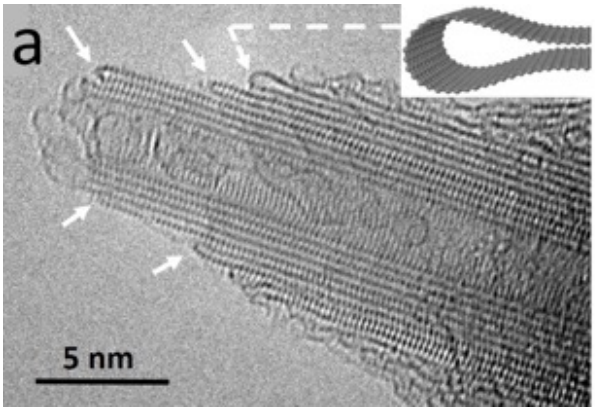

b

Type of defects	$I_D/I_{D'}$
sp^3	13*
Vacancy	7*
Boundary	3.5*
Zip	1.5 (our result)

Figure 7 : (a) *Image MET en résolution atomique de l'apex nanométrique d'un cône de carbone Plusieurs exemple de paires de graphènes refermées l'une sur l'autre ("zippées") sont fléchés. La flèche pointillée désigne un défaut différent (en "boucle"), dont un modèle est donné en encart (Crédit image : R. Wang, CEMES).* ***(b)*** *Rapports des intensités des bandes Raman D et D' pour différents types de défauts, dont le défaut "zip" identifié dans notre travail. Les autres valeurs proviennent de [Eckmann et al., Nanolett. 12 (2012) 3925].*

Les résultats de ce chapitre ont été partiellement publiés dans [*Puech et al, J. Carbon Res. 5 (2019) 69*] et [*Paredes et al., Indian J. Eng. Mater. Sci. (2020) in print*].

Chapitre 3 : Fabrication et montage des nanocones de carbone en tant que sondes pour la microscopie à champ proche

Faisabilité et limites de la préparation de sondes SPM à base de nanocônes de carbone : Diverses techniques de fabrication de sondes SPM par le montage de morphologies dites SSF sur des cantilevers-supports en Si dopé au Sb spécialement conçus pour cela ont été essayées, à savoir le collage (**Fig.8**) et deux modes de soudures, par *Focused Ion Beam Induced Deposition* (FIBID), et par *Focused Electron Beam Induced Deposition* (FEBID). Au total, plus de 130 sondes des différents types (type AFM non conducteur, type AFM conducteur et type STM) ont été fabriquées.

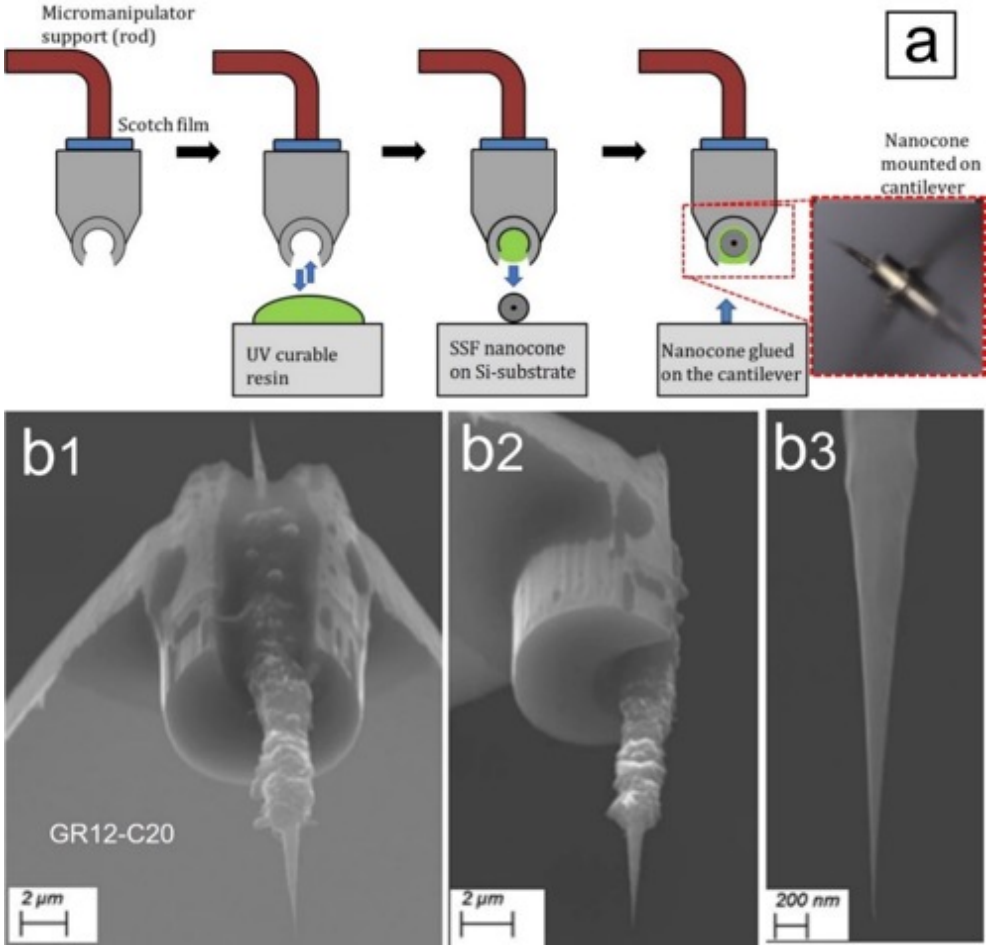

Figure 8 : (a) *Schéma du processus de montage par collage d'une morphologie SSF sur un cantilever-support (c'est-à-dire sans pointe, et comportant une gorge pour accueillir la morphologie).* ***(b1)*** *à* ***(b3)*** *images MEB d'une sonde en carbone (#GR12-C20) juste après la méthode de montage par collage. Comme la morphologie présente toujours deux cônes, celui qui est orienté vers l'arrière du cantilever est inutile ; en encart, on voit une image optique d'un nanocône lors du montage sur un cantilever par cette méthode. Dans cet exemple, le cône est assez bien aligné à la fois par rapport à l'axe de la partie fibre courte et par rapport à l'axe de la gorge.*

Le positionnement et l'alignement précis et contrôlé des cônes de carbone par rapport aux normes de SPM et au niveau des sondes Si standards n'ont pas pu être réalisés. Bien que l'utilisation des micromanipulateurs n'ait en fait pas été un processus reproductible, la principale raison du désalignement fréquent est l'alignement intrinsèquement variable de l'axe du cône par rapport à l'axe de la fibre courte dans la morphologie du SSF lors de la synthèse. Cela empêchera d'exploiter le rapport d'aspect élevé des cônes de carbone dans leur application comme sondes SPM dans la suite du travail, et ce jusqu'à ce que ce problème soit résolu.

Le rôle des défauts de surface des cônes de carbone dans leur mise en œuvre : les morphologies des cônes de carbone semblent être très sensibles aux effets d'irradiation, soit par des électrons ou des ions Ga, voire plus sensibles que les NTCs. Comme l'amorphisation induite par l'irradiation commence par la surface, elle peut affecter tout le volume des extrémités des cônes de carbone sur une longueur variable, en raison de leurs dimensions de l'ordre du nanomètre.

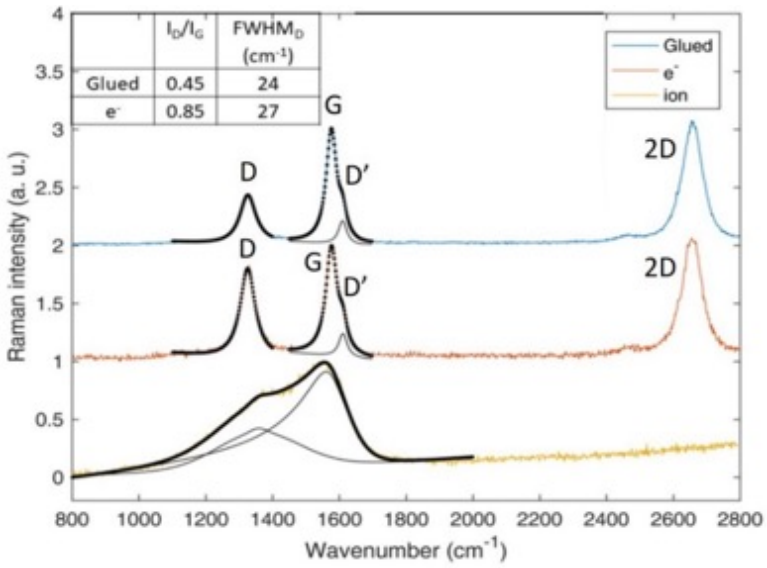

Figure 9 : *Spectres Raman (avec leur ajustement représenté par une ligne noire épaisse continue) enregistrés sur la jonction cône/fibre courte de trois morphologies SSF différentes montées sur des cantilevers en tant que sondes SPM par les trois différentes procédures décrites dans le texte : en bas (spectre jaune) : soudure avec Pt induite par des ions focalisés (FIBID) ; au milieu (spectre rouge : soudure avec Pt induite par des électrons focalisés (FEBID) ; en haut (spectre bleu) : collage avec une résine polymérisable aux UV. Dans l'encart supérieur gauche sont indiqués les rapports d'intensité des bandes Raman D et G ainsi que la largeur à mi-hauteur de la bande D, pour les deux sondes en carbone présentant des spectres avec les bandes D + G (+ 2D) typiques des matériaux graphéniques. Au contraire, le spectre du bas (FIBID) marque une forte amorphisation.*

Une telle sensibilité a été attribuée à la présence d'une grande quantité de terminaisons défectueuses des graphènes (bords libres, défauts de type boucle, défauts en forme de type zip) à la surface du cône, par rapport aux NTCs. Cela empêche toute étude structurale et nanotexturale fiable des cônes de carbone tels que synthétisés par MET haute résolution utilisant des électrons de 100 keV d'énergie, pour lesquels un maximum de 80 keV est sans doute un maximum. En outre, la sensibilité à l'irradiation par faisceau d'électrons augmente avec le nombre de défauts. Cela fait que les sondes en carbone préparées par FIBID ne peuvent

pas résister à une investigation HRTEM à 80 keV en raison des graves dommages structuraux (au moins à la surface du cône) induits par le procédé FIBID, qui semble être très destructeur.

Au contraire, sur la base des résultats Raman combinés à ceux présentés au *Chapitre 2*, les cônes en carbone montés par FEBID semblent n'avoir été que légèrement affectés par le processus, tandis que le processus de collage semble ne pas avoir affecté du tout la structure du cône (cependant, une confirmation de ceci par une étude du en MET à 80 keV est encore à réaliser). Dans l'ensemble, les observations nous ont appris à renoncer au procédé FIBID comme procédure de montage possible, et à préférer le procédé de collage en premier lieu, puis éventuellement le procédé FEBID comme alternative acceptable (**Fig.9**).

Le choix et la limitation des procédés de montage : Pour optimiser le coût de traitement, la méthode de collage est apparue comme la plus efficace car elle est beaucoup plus rapide que les méthodes basées sur le FIB (~20 minutes par pointe contre 2 heures, au plus rapide) et ne nécessite qu'un micromanipulateur fonctionnant sous un microscope optique (contrairement au besoin d'un micromanipulateur fonctionnant sous un FEG-SEM/FIB à double faisceau, qui est un équipement coûteux). En outre, il ne modifie probablement pas la structure du carbone. Cependant, un inconvénient important est que les sondes SPM obtenues de cette manière ne sont valables que pour les modes non conducteurs en raison du rôle isolant de la résine en tant qu'interphase entre le corps de la sonde en carbone et le cantilever-support en Si dopé. D'autre part, l'avantage du procédé de montage FEBID est que les sondes SPM obtenues de cette manière peuvent être véritablement multimodes (**Fig.10**), c'est-à-dire qu'elles peuvent fonctionner avec des modes SPM conducteurs ou non conducteurs à condition que la conductivité électrique demeure suffisante malgré l'amorphisation de la surface.

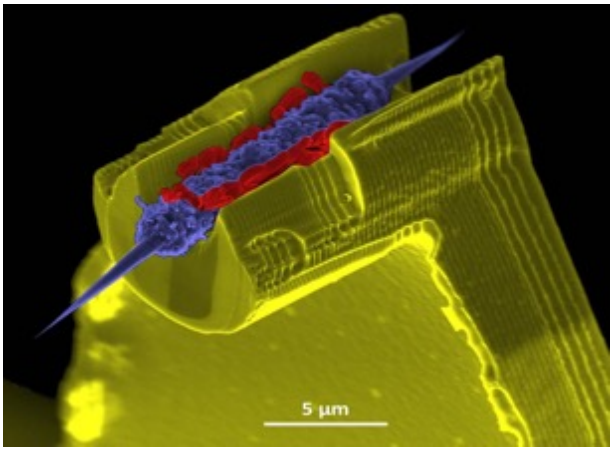

Figure 10 : *Exemple d'une sonde multimode ici soudée par FIBID (une sonde soudée par FEBID a le même aspect). En jaune : le cantilever en Si dopé par Sb ; En bleu : une morphologie en carbone de type SSF déposée dans la gorge du cantilever par le micromanipulateur ; en rouge : la soudure en Pt (qui peut aussi être du W).*

Par conséquent, les sondes en carbone préparées par FEBID seront également utilisées dans les résultats présentés dans le prochain chapitre, qui rapporte les caractéristiques de résistance à l'usure des sondes en nanocônes de carbone montées par les différentes méthodes, ainsi que leurs performances pour l'imagerie de différents types de substrat selon les techniques SPM conductrices et non conductrices.

Les résultats de ce chapitre ont été partiellement publiés dans [*Puech et al, J. Carbon Res. 5 (2019) 69*].

Chapitre 4 : Tests d'application de sondes en nanocônes de carbone pour différents modes SPM

Microscopie à force atomique (AFM) : Dans l'ensemble, toutes les données démontrent la capacité des nanocônes de carbone à constituer des sondes AFM tout en offrant une résolution d'image équivalente ou supérieure à celle des sondes en silicium (**Fig.11**), quel que soit le type de sonde en Si testé (OTESPA-R3/OTESPA, et TESP-SS). Cependant, les sondes en nanocônes de carbone ont montré une faible capacité d'imagerie en résolution atomique. D'autre part, des tests de longues durées de balayage ont démontré la robustesse des sondes en nanocônes de carbone par rapport à celles en silicium, montrant ainsi une plus grande résistance à l'usure (**Fig.12**). Ceci est cohérent avec la résistance plus élevée de la liaison C-C sp^2 (598 kJ/mole) par rapport à la liaison Si-Si (330 kJ/mole), et la flexibilité bien connue de la structure graphénique 2D par rapport à la structure tétraédrique 3D du silicium.

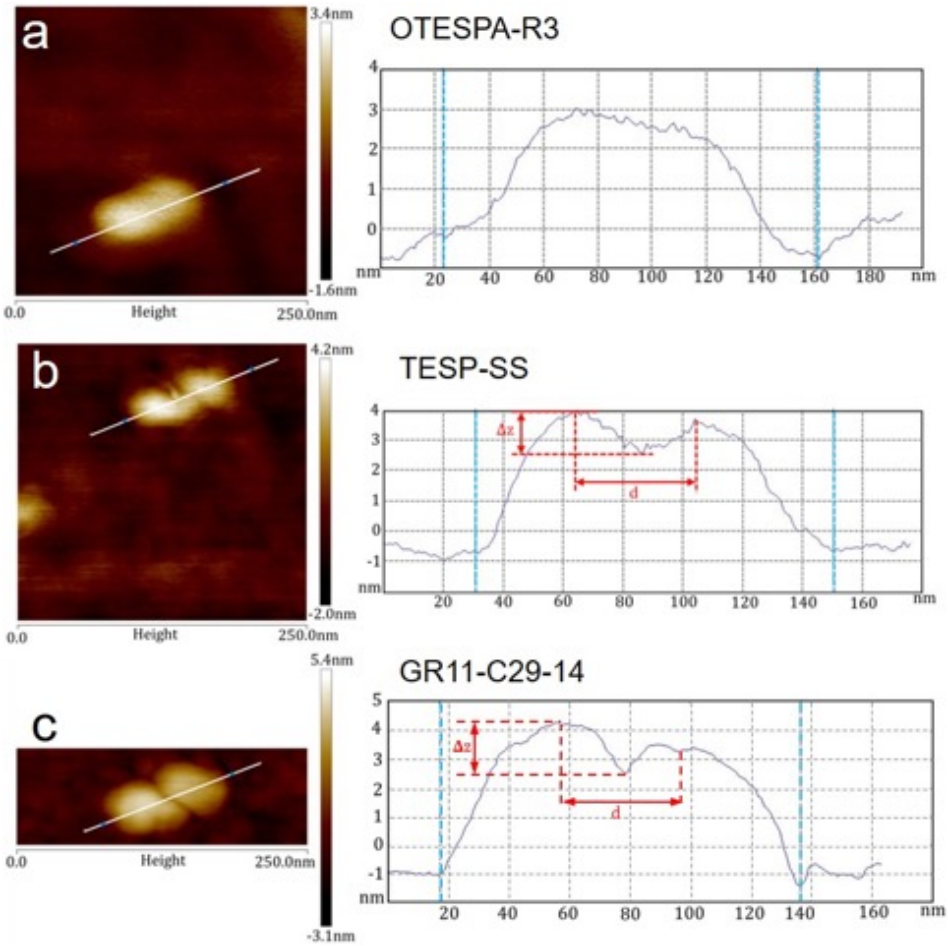

Figure 11 : *Comparaison d'images en mode d'acquisition AFM (à gauche) des mêmes nanoparticules d'or (dispersées sur un substrat de silicium) et des profils de hauteur associés (à droite) obtenus à partir* ***(a)*** *de la sonde en Si commerciale OTESPA-R3,* ***(b)*** *de la sonde en Si commerciale TESP-SS, et* ***(c)*** *de la sonde en nanocone de carbone n°GR11-C29-14.*

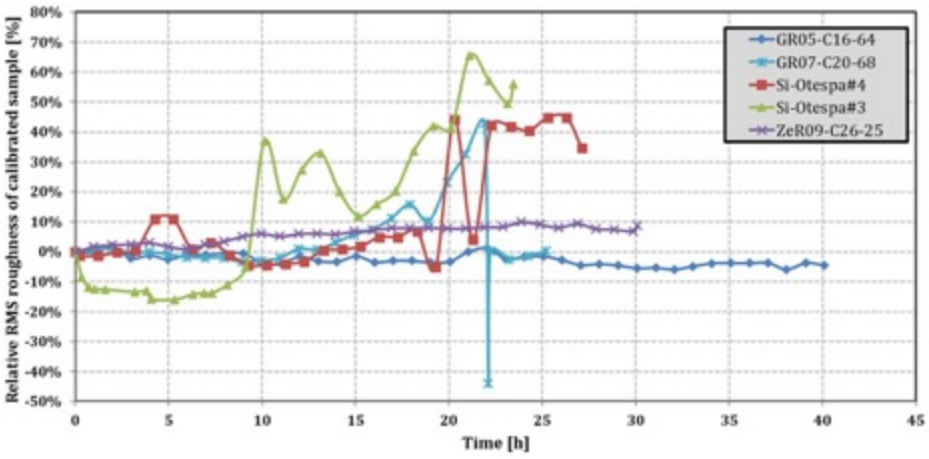

Figure 12 : *Variation de la rugosité RMS relative, c'est-à-dire normalisée par rapport à la première mesure pour chaque sonde, mesurée par cinq sondes différentes (GR05-C16-64, GR07-C20-68, ZeR09-C26-25, Si-Otespa-3 et Si-Otespa-4) en fonction du temps de balayage. Les sondes dont la référence commence par "G" ont été montées par collage, celle dont la référence commence par "Ze" a été montée par FEBID.*

AFM mécanique (Peak-Force Quantitative NanoMechanical AFM) : Une fois les calibrations nécessaires effectuées afin de déterminer la plage de force de contact la plus appropriée à appliquer, les sondes en nanocônes de carbone semblent convenir à la PFQNM-AFM. En effet, elles permettent d'obtenir des modules de Young de divers films polymères avec des valeurs raisonnablement proches des valeurs théoriques, avec une incertitude du même ordre que la sonde de référence en silicium (**Tableau1**).

Nom de la pointe	GR12-C12-57	GR10-C08-65	ZeR09-C11-32	TESPA-V2
Force de contact	25 nN	50 nN	120 nN	30 nN
Déformation moyenne du PS	1 nm	1.5 nm	2 nm	1.5 nm
Module d'Young du PS ***(Valeur théorique : 3-4 GPa)***	0.70 +/-0.10 GPa	2.90 +/-0.27 GPa	2.00 +/-1.00 GPa	1.50 +/-0.20 GPa
Déformation moyenne du PE	25 nm	14 nm	2 nm	25 nm
Module d'Young du PE ***(Valeur théorique : 0.2-0.7 GPa)***	0.10 +/-0.02 GPa	1.00 +/-0.10 GPa	0.18 +/-0.05 GPa	0.1 +/-0.05 GPa

Tableau 1 : *Résumé des performances des différentes sondes pour la mesure des modules de Young des composants polystyrène (PS) et polyéthylène (PE) d'un échantillon hétérogène (composite).*

Elles sont également capables de discriminer entre les composants d'un matériau composite, tant en topographie qu'en mode d'imagerie de module de Young (**Fig.13**). Plus dans les détails, les différentes sondes nanocône présentent des divergences entre elles. Ces divergences proviennent peut-être de la combinaison des variations de deux caractéristiques géométriques, à savoir la longueur totale de la morphologie en carbone dépassant de la gorge du cantilever, et le désalignement de l'axe du cône par rapport à la verticalité idéale vis-à-vis de la surface du substrat. Plus la longueur et le désalignement angulaire sont importants, et plus le cône de carbone se comporte comme un NTC, pour lequel la flexibilité excessive est un inconvénient que la géométrie conique est d'habitude capable d'éviter dans une certaine mesure.

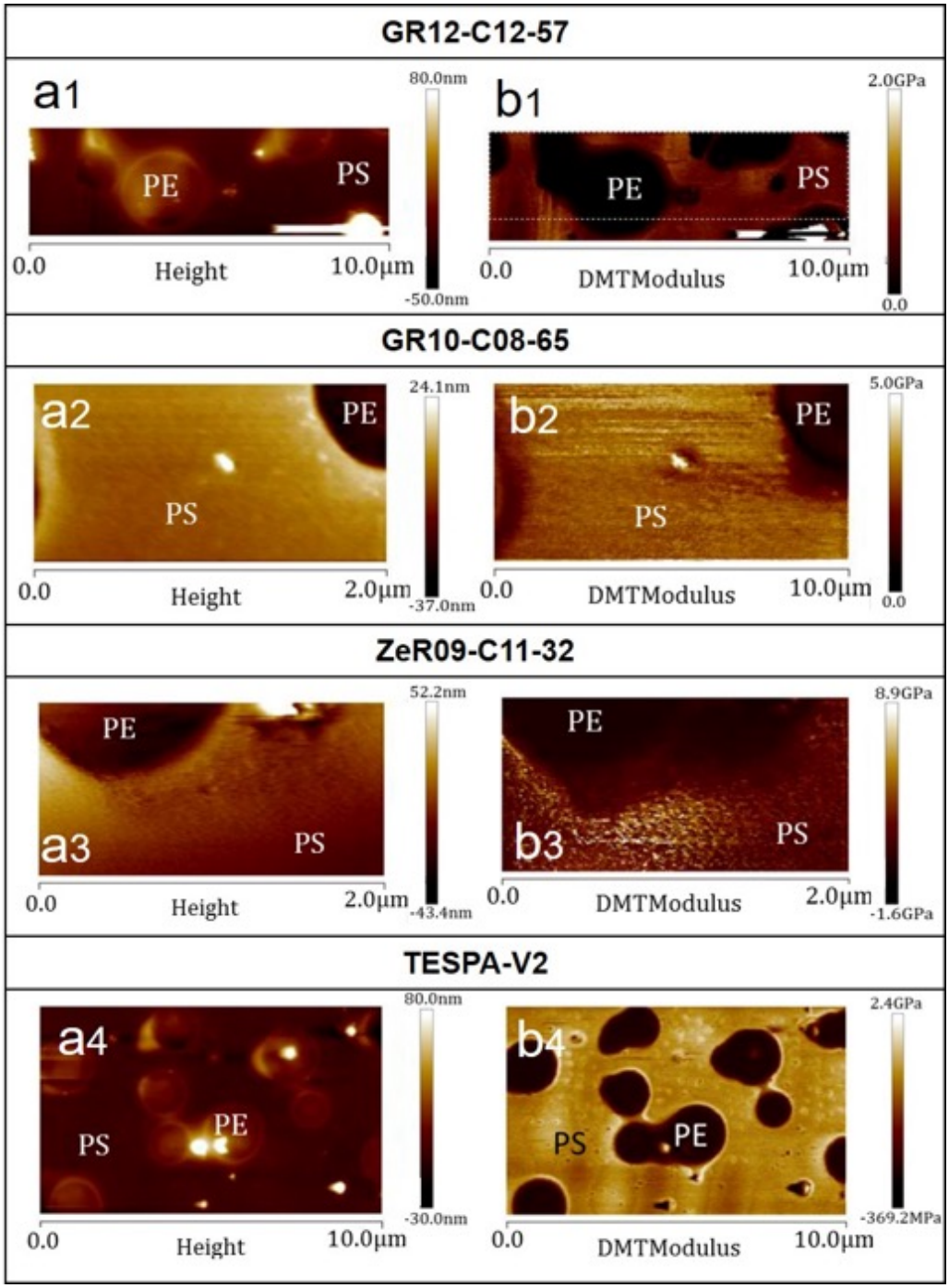

Figure 13 : (a) *Topographies et* ***(b)*** *cartographies des modules de Young d'un échantillon composite polystyrène (PS)-polyéthylène (PE) obtenues par différentes sondes.*

AFM conducteur (C-AFM) : Les sondes en nanocônes de carbone peuvent être utilisées pour les mesures C-AFM sans nécessiter de revêtement (conducteur ou réflecteur) du cantilever ou de la pointe. Les mesures de courant I/V et les cartographies en courant sont possibles à condition que la tension appliquée ne dépasse pas 2 V. Pour une plage de tension de 0.5-2 V et une force comprise entre 100-150 u.a. (unité arbitraire du microscope AIST-NT, SPM 1000), des valeurs de courant allant jusqu'à 35 nA peuvent être atteintes en de nombreux points. Les mesures cartographiques et les images topographiques sont conformes aux caractéristiques de l'échantillon. Les sondes en carbone présentent également des performances similaires à celles

des sondes en silicium du commerce (soit dopées, soit revêtues de Pt) pour mesurer les courbes I/V de l'échantillon étudié. Ceci est cohérent avec la constatation que les sondes nanocônes montrent une conductance globale similaire ou même légèrement supérieure à celle obtenue avec une sonde commerciale en silicium revêtue de Pt. Cependant, comme indiqué pour les sondes commerciales, les sondes nanocônes présentent un degré d'endommagement variable après les tests C-AFM, ce qui confirme que les cônes de carbone sont sensibles aux conditions de surtension ou de courant.

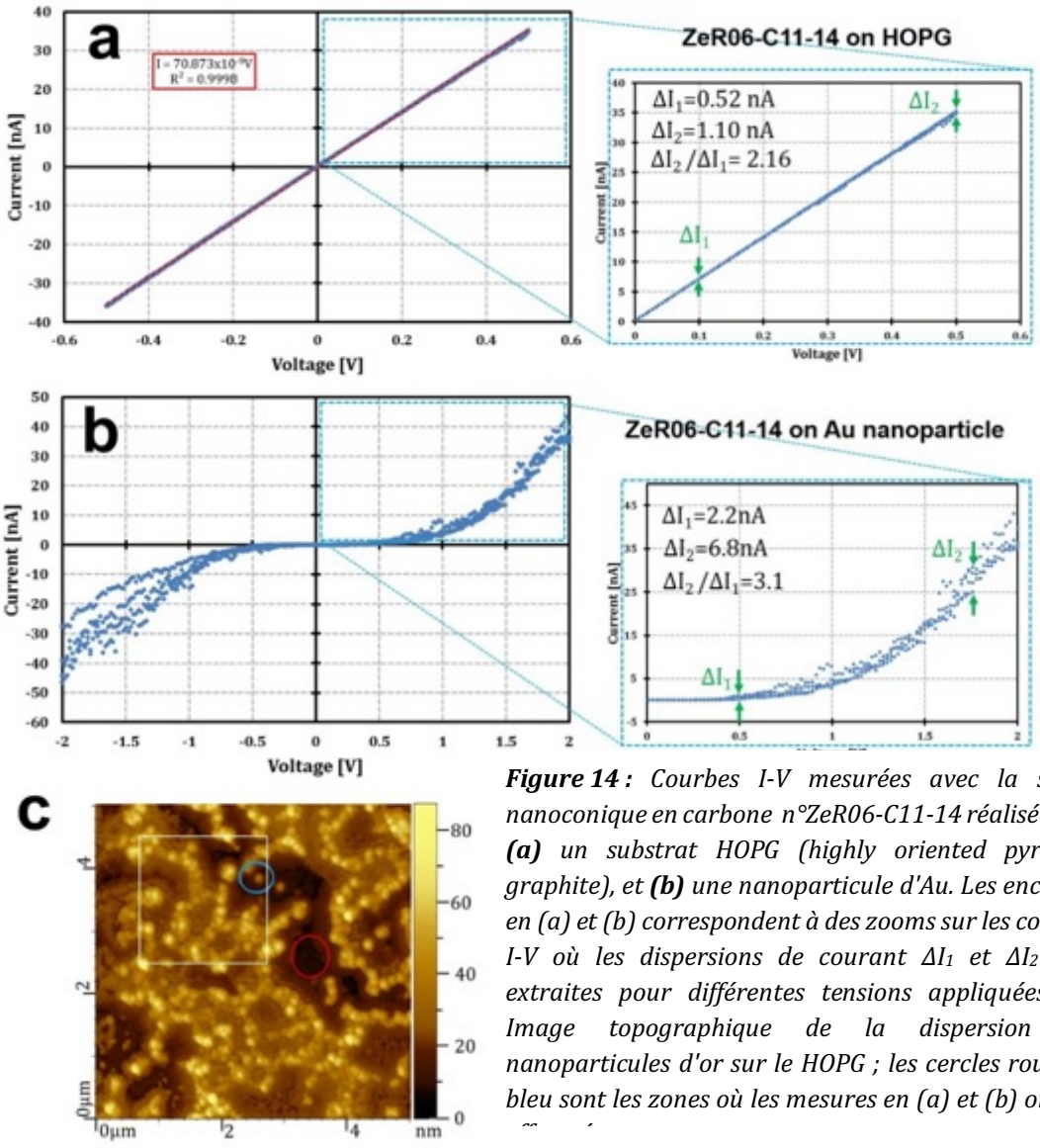

Figure 14 : *Courbes I-V mesurées avec la sonde nanoconique en carbone n°ZeR06-C11-14 réalisées sur* ***(a)*** *un substrat HOPG (highly oriented pyrolytic graphite), et* ***(b)*** *une nanoparticule d'Au. Les encadrés en (a) et (b) correspondent à des zooms sur les courbes I-V où les dispersions de courant ΔI_1 et ΔI_2 sont extraites pour différentes tensions appliquées.* ***(c)*** *Image topographique de la dispersion des nanoparticules d'or sur le HOPG ; les cercles rouge et bleu sont les zones où les mesures en (a) et (b) ont été*

Microscopie à effet tunnel (STM) : Dans les conditions ambiantes, les nanocônes de carbone peuvent produire des images STM plus ou moins correctes à un grossissement moyen (**Figs.15-16**), à condition d'utiliser de faibles courants, mais ils ne réussissent pas à imager les réseaux cristallins. Nous pensons que la limitation de nos nanocônes de carbone pour ces tests est liée au processus de montage et en particulier à la dégradation de la structure cristalline de l'apex du cône causée par le degré variable d'amorphisation, qui ajoute une barrière au flux

d'électrons dans le processus de *tunneling*, et aux conditions environnementales, non optimales. Des recherches supplémentaires doivent être menées afin de confirmer cela.

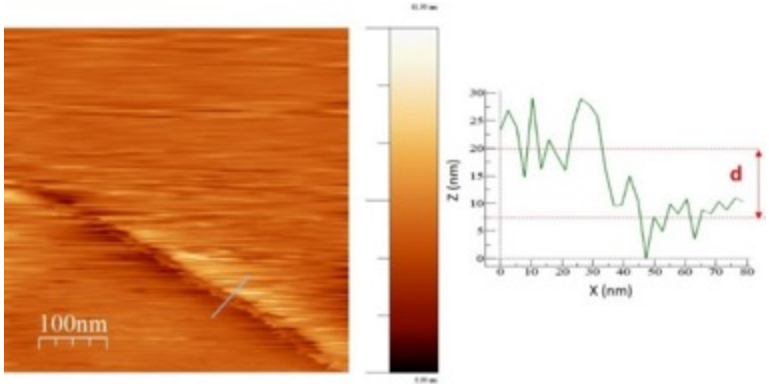

Figure 15 : *Image STM de la surface d'un HOPG obtenue par la sonde nanoconique en carbone n°Au-e-005 (à gauche). Un profil de hauteur a été enregistré sur la marche à l'endroit indiqué (à droite) : d = 12,5nm.*

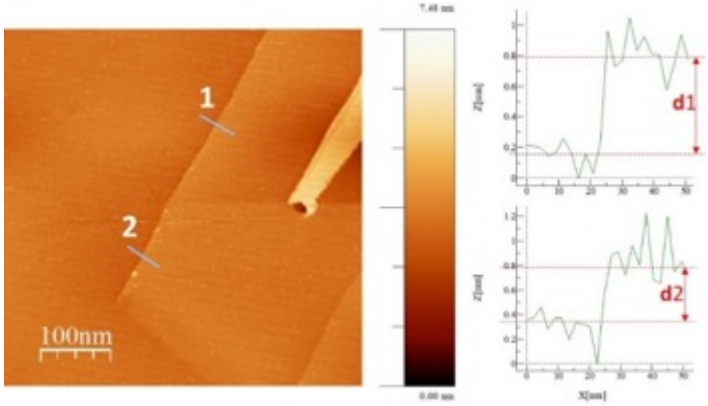

Figure 16 : *Image STM de la surface d'un HOPG obtenue par une sonde PtIr (à gauche). Deux profils de hauteur (à droite) ont été enregistrés sur la marche aux endroits indiqués : d1 = 0,63 nm, d2 = 0,43 nm.*

Microscopie à force Kelvin (KFM) : Les sondes nanocônes se sont avérées adaptées à l'injection de charges et aux mesures par KFM quelle que soit la procédure de montage FIBID ou FEBID utilisée, montrant un contraste de signal et une résolution d'image qualitativement corrects. En comparaison avec une sonde en silicium commerciale couramment utilisée pour un tel mode SPM, les sondes en carbone montrent un signal similaire, et dans certains cas, mieux résolu et plus intense (**Figs.17-18**).

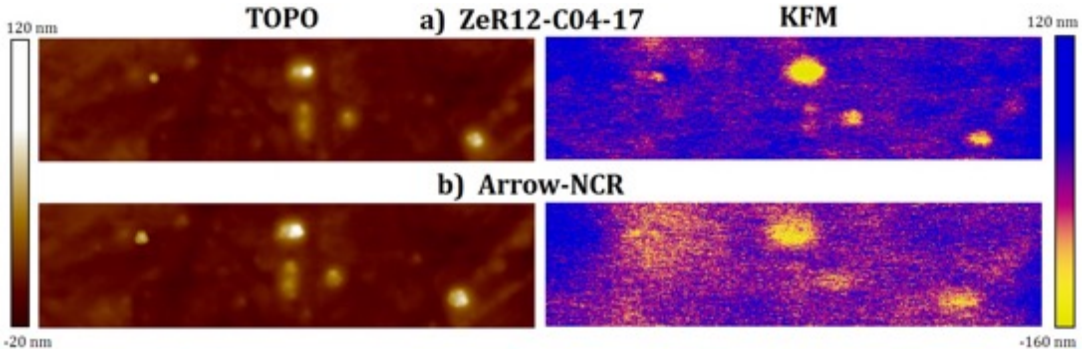

Figure 17 : *Particules intermétalliques dans une surface matricielle en alliage d'aluminium (A2024). Images de topographie (à gauche) et KFM (à droite) pour* ***(a)*** *la sonde nanoconique en carbone n°ZeR12-C04-17 ;* ***(b)*** *la sonde de référence en Si.*

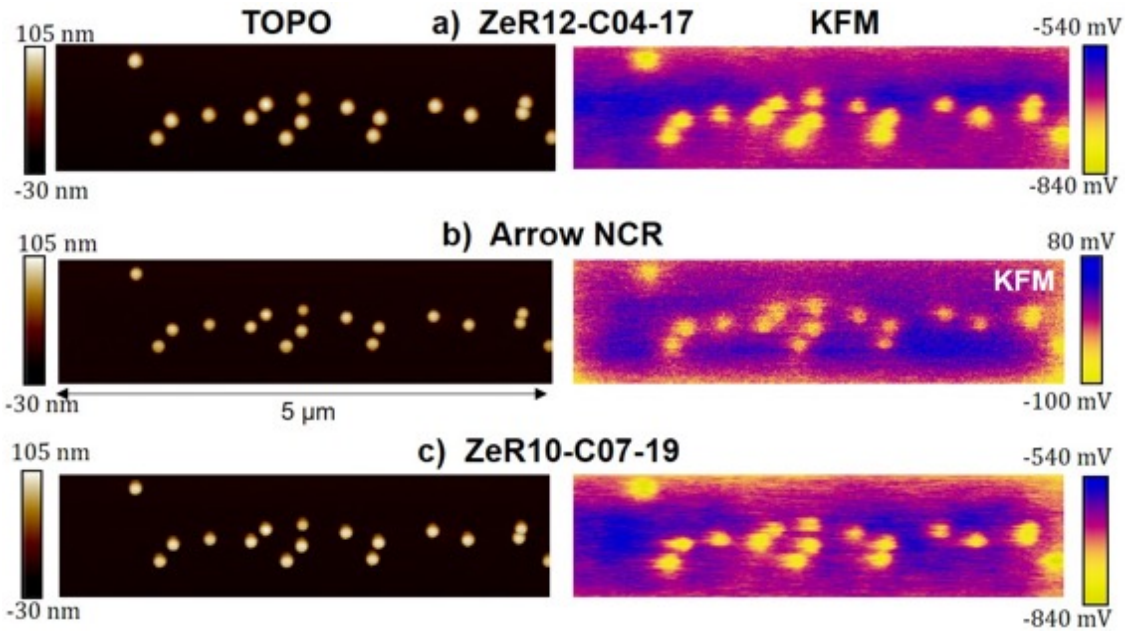

Figure 18 : *Nanoparticules de latex chargées négativement sur une surface de PMMA. Images de topographie et de KFM pour* ***(a)*** *la sonde à cône de carbone n°ZeR12-C04-17.* ***(b)*** *la sonde de référence en Si.* ***(c)*** *la sonde à cône de carbone n°ZeR10-C07-19.*

Cependant, une résolution latérale légèrement plus faible et des images plus bruyantes ont parfois été observées. La résolution latérale pourrait être améliorée en utilisant des cantilevers recouverts d'aluminium afin d'améliorer la réflectivité de la face supérieure, comme c'est souvent le cas avec les sondes en Si dopé. En ce qui concerne la variabilité des performances signal-bruit, elle semble affecter les sondes préparées au FIBID de préférence à celles préparées au FEBID. Ainsi, cela pourrait être lié à la présence de carbone amorphe à la surface du cône, plus abondant dans le cas du procédé FIBID, qui joue le rôle de barrière pour le passage des charges, ce qu'elles pourraient faire plus ou moins efficacement selon les conditions de courant et de tension. Une étude soigneuse et plus approfondie devrait être menée pour le vérifier. D'autre part, la raison pour laquelle les sondes en carbone montrent une meilleure sensibilité parfois comme le révèle un meilleur contraste dans les images KFM ne peut pas résulter de la différence dans la fonction de travail du matériau constituant la sonde, car ils sont assez proches de l'ordre de 4.5 eV pour le Si dopé *n* par rapport à 4.8 eV pour nos cônes de carbone.

Conclusions et perspectives

Une étude multidisciplinaire était nécessaire pour évaluer le potentiel de la forme conique du carbone comme sonde SPM, en partant de la synthèse et de la caractérisation de tels objets. La reproductibilité et la compréhension du processus de croissance de morphologies qui ont été appelées les "Spiky Bead" (SB) et les "Spiky Short Fiber" (SSF), l'étude de la faisabilité et de la fabrication de sondes SPM à base de SSF pour assurer les caractéristiques géométriques, mécaniques et électriques requises pour leur utilisation pour différents modes SPM, et la réalisation des tests d'application correspondants, ont constitué les principaux points étudiés.

Dans le *Chapitre 1*, une étude bibliographique originale et exhaustive concernant les différentes manières de générer des formes coniques en carbone, les propriétés qui ont été étudiées, et les applications pour lesquelles elles ont déjà été testées, est présentée, constituant ce que nous pensons être l'étude la plus complète réalisée à ce jour sur le sujet. On peut noter que (i) les morphologies coniques de carbone existantes n'ont pas été étudiées de manière aussi approfondie que d'autres nanoformes de carbone telles que les nanotubes de carbone et les graphènes, (ii) il n'existe pas de désignation standard des formes coniques de carbone : elles sont en effet nommées différemment sans suivre aucun critère ou classification particuliers. Certains auteurs font une simple comparaison qualitative ou morphologique avec les formes coniques précédemment rapportées dans la littérature tout en supposant une similitude de texture ou de structure avec leurs propres morphologies, sans procéder à la caractérisation nécessaire pour la vérifier. Par conséquent, il est devenu difficile de distinguer les différentes formes coniques et de les relier à leurs mécanismes de croissance et à leurs propriétés. C'est pourquoi une classification en trois catégories différentes, basée sur les principales causes à l'origine de la forme conique, est proposée : (i) structurale, (ii) texturale et (iii) liée aux procédés. Le premier type implique la génération de formes coniques par l'existence de dislocations ou de disinclinaisons dans le réseau de graphène ; le second type correspond à celles générées par la façon dont les couches de graphène sont disposées par rapport à l'axe de croissance, bien que non en relation avec un défaut structural ; et le dernier type est principalement généré pendant ou après un procédé ou des conditions de croissance ou de traitements post-croissance particuliers, quelles que soient la structure et la texture. Cette classification peut être utilisée comme référence pour mieux décrire et comprendre les propriétés et caractéristiques intrinsèques de chaque type de cône de carbone, et peut aider à déterminer le processus et les conditions de croissance permettant d'obtenir la forme conique appropriée à une application donnée. Dans l'ensemble, il est démontré que plusieurs articles de la littérature devraient être revus afin d'atteindre une meilleure cohérence avec d'autres concernant le type de cônes formés et les mécanismes de croissance associés, ou même plus, pour déterminer la structure du carbone impliquée. À cet égard, la même situation de confusion existe pour les cônes de carbone que pour les nanotubes de carbone en ce qui concerne la discrimination réelle entre le modèle de graphènes enroulés de façon hélicoïdale et le modèle en cylindres de graphènes disposés concentriquement.

Dans le *Chapitre 2*, nous nous sommes concentrés sur *(i)* la reproduction au CEMES des mêmes morphologies de cônes, en particulier la morphologie dite SSF, telle que préparée lors d'un précédent travail de thèse réalisé avec un laboratoire partenaire aux Etats-Unis (Applied Science Inc.) au moyen du dépôt DCPV de carbone pyrolytique sur des nanotubes de carbone individuels, et *(ii)* la confirmation des mécanismes de dépôt puis de croissance initialement proposés. En conséquence, une série d'expériences a été menée, en commençant par une étude paramétrique afin de trouver les conditions les plus appropriées ayant un impact sur la composition de la phase gazeuse et la concentration des espèces, puis sur le type de morphologie. Bien que nous ayons délibérément limité le nombre de paramètres à la température de consigne et à ceux liés à la charge gazeuse (concentrations en CH_4 et H_2, et débit total de gaz), déterminer le rôle réel de chacun des paramètres a été une tâche assez difficile

car la géométrie spécifique du four induit un paramètre supplémentaire, le temps de vol des espèces, qui génère des événements complexes et dynamiques, généralement des réactions multiples de craquage et de recombinaison dont les résultats sont difficilement prévisibles puisqu'ils correspondent à des conditions hors équilibre. La température et le temps de vol influencent tous deux la modification de la phase gazeuse et le type d'espèces de carbone contenues, mais différemment (la première tend à favoriser les réactions de craquage tandis que le second tend à favoriser les réactions de recombinaison), l'évolution globale qui en résulte étant désignée comme la maturation de la phase gazeuse. Par conséquent, le système apparaît comme une sorte de boîte noire à partir de laquelle on ne peut qu'essayer de deviner ce qui s'y passe à partir des caractéristiques du matériau résultant, après que les espèces déposées aient carbonisé. En conséquence, et après avoir examiné plusieurs modèles de dépôt et de croissance tirés de la littérature, nous avons conclus que, comme le proposait le travail antérieur, le processus de maturation devait aboutir à la formation conjointe de radicaux et d'hydrocarbures polyaromatiques (HAP) qui se déposent ensuite tous deux sur les NTCs (les premiers se chimisorbent sur des sites actifs tels que les bords du graphène, les seconds se physisorbent sur toute surface). Cette dualité est la seule façon d'expliquer la formation concomitante de sous-morphologies aussi différentes que les cônes à surface lisse constitués de graphènes parfaitement alignés et les boules (ou segments de fibres courtes) à surface rugueuse constitués de graphènes à peine alignés.

Sur la base de ce scénario, il a été confirmé qu'à un degré élevé de maturation de la phase gazeuse (obtenu par la combinaison d'une température élevée et d'un long temps de vol des espèces), des morphologies SB peuvent être produites. A partir d'observations expérimentales, il a également été établi que, lorsqu'un état de maturation élevé est atteint, la variation de la concentration en gaz semble affecter l'épaisseur (ou le volume) des morphologies synthétisées mais pas le type de morphologie. Cependant, les morphologies SSF n'ont pas été reproduites dans nos conditions car leur formation semble exiger non seulement un degré de maturation élevé de la phase gazeuse mais aussi un point d'inflexion optimal permettant de générer un rapport HAP sur radicaux plus élevé que celui nécessaire à la formation des SB. Pour un prochain travail, nous avons donc proposé d'envisager des temps de vol plus longs à la température maximale de consigne (1390°C) en étudiant les dépôts obtenus dans la partie aval du four au-delà du centre de la zone isotherme, ce qui a été ignoré dans cette étude. Cela sera facilité par le fait que, dans ce travail, un seuil minimal pour le débit total ainsi que pour le rapport CH_4/H_2, ainsi qu'une plage de concentrations optimales de CH_4 et de H_2 vraisemblablement adaptée à la synthèse de SSF, ont été identifiés.

L'hypothèse précédente concernant l'existence d'une phase hydrocarbonée liquide riche en HAPs est maintenue, et maintenant démontrée. Cette hypothèse est fortement soutenue par la littérature traitant des phénomènes physiques impliqués lors du mouillage d'un fil par un liquide, et par les observations expérimentales. En conséquence, il semble très probable que le phénomène dit d'instabilité de Plateau-Rayleigh joue un rôle majeur dans le mécanisme de dépôt de la phase liquide riche en HAPs sur le support que sont les NTCs. C'est la première fois que l'existence de ce processus physique spécifique est révélée dans le mécanisme général du dépôt de carbone pyrolytique. En particulier, l'instabilité de Plateau-Rayleigh pourrait être responsable de la formation préférentielle de la morphologie SSF par rapport à la morphologie

SB une fois que la phase liquide a atteint les propriétés rhéologiques appropriées, alors que la morphologie SB pourrait résulter du dépôt statistique des gouttelettes préformées sur les NTCs d'une manière périodique qui reflète leur distribution statistique dans la phase gazeuse.

En ce qui concerne la texture interne des cônes, qui est en quelque sorte liée à leur mécanisme de croissance, nous en sommes venus à rejeter l'arrangement en cylindres de graphènes concentriques proposé dans les travaux antérieurs et à lui préférer le modèle de graphènes enroulés de façon hélicoïdale à la place. Cette nouvelle vision est basée sur la présence de marches en spirale à la surface du cône, le comportement de déroulement des graphènes lors de l'injection de charges, et le décalage entre les bords opposés d'une même couche de graphène de part et d'autre de l'axe du cône révélé par la MET, qui n'évoque pas un cylindre régulier. D'une part, cela est conforme à la littérature qui montre que cette disposition hélicoïdale des graphènes est fréquente pour les cônes de carbone préparés dans des conditions apparentées ; d'autre part, cela est également conforme aux conclusions du travail antérieur, qui a observé que les graphènes concentriques présentent une même hélicité et sont également capables de présenter localement la structure graphitique pour de longs rayons de courbure. Parallèlement, la caractérisation par MET a permis d'estimer le diamètre de l'apex des extrémités des cônes à ~4-5 nm, et confirme également une nanotexture parfaite, ce qui assoie notre prédiction d'excellente résistance mécanique et conductivité électrique de ces cônes. L'étude a également permis d'identifier un type spécifique de terminaison du graphène (bords "zippés" d'une paire de graphènes) considéré comme un défaut par la spectroscopie Raman, dont l'existence est révélée par une signature Raman spécifique basée sur une valeur sans précédent de 1.5 pour le rapport $I_D/I_{D'}$, qui est la plus faible jamais trouvée dans la littérature.

Pour réaliser les tests d'application des nanocones de carbone comme sondes SPM, il a fallu monter les morphologies SSF sur des cantilevers-supports compatibles avec les équipements SPM, ce qui a été décrit au *Chapitre 3*. Cependant, cela s'est accompagné de plusieurs difficultés techniques. Tout d'abord, trois procédés de montage ont été utilisés (soudure par ions focalisés (FIBID) ou par électrons focalisés (FEBID), et collage). Les deux procédés de soudure au Pt ou au W doivent être utilisés pour préparer des sondes électriquement conductrices, alors que la méthode de collage ne pouvait être utilisée que pour les sondes non-conductrices, en raison de la nature isolante du collage, un polymère réticulable aux UV. Bien que, comme prévu, la morphologie SSF se soit révélée utile pour être facile à manipuler avec le micromanipulateur pendant le FIBID/FEBID et pour être visible au microscope optique pendant le collage, les deux procédés ne peuvent être considérés comme optimisés car ils ne permettent pas d'aligner le cône par rapport à la géométrie du cantilever avec une grande précision. Le processus de soudure a posé plusieurs problèmes, plus particulièrement en ce qui concerne (i) la qualité de la fixation entre le cône et le cantilever par le matériau de soudure, qui ne présente pas toujours une bonne adhérence (**Fig.19**), et (ii) l'amorphisation plus ou moins importante de la surface du matériau en carbone causée par les étapes d'irradiation ionique ou électronique. Les deux problèmes sont susceptibles de nuire à la conductivité électrique (qui pourrait être responsables, par exemple, de la variabilité du flux de courant pendant les essais STM), tandis que le premier est soupçonné d'induire une certaine instabilité mécanique (qui pourrait être

responsable, par exemple, des courbes de double résonance de certains cantilevers, et de la perte accidentelle de la sonde en carbone de certains cantilevers-supports). Le problème de l'amorphisation est en fait beaucoup plus réduit en utilisant le protocole FEBID au lieu du protocole FIBID, mais le problème de la fixation mécanique demeure (**Fig.19**) et est difficile à évaluer. D'autre part, la méthode de collage est beaucoup plus rapide (~20 minutes par sonde, au lieu de 2-3 heures par faisceaux focalisés), assure une fixation mécanique ferme, et semble être robuste et reproductible, avec de meilleures statistiques d'alignement, peut-être en raison du rôle de guidage de la gorge située à l'extrémité du cantilever. Des problèmes d'alignement subsistent cependant, mais ils sont largement générés par le mauvais alignement intrinsèque du cône par rapport à la partie en microfibre (en référence à la morphologie SSF), ce qui est un problème à résoudre à l'étape de la synthèse du cône de carbone. Ce problème pourrait être résolu en essayant de former les morphologies SSF sur des nanotubes de carbone individuels pré-alignés et rectilignes.

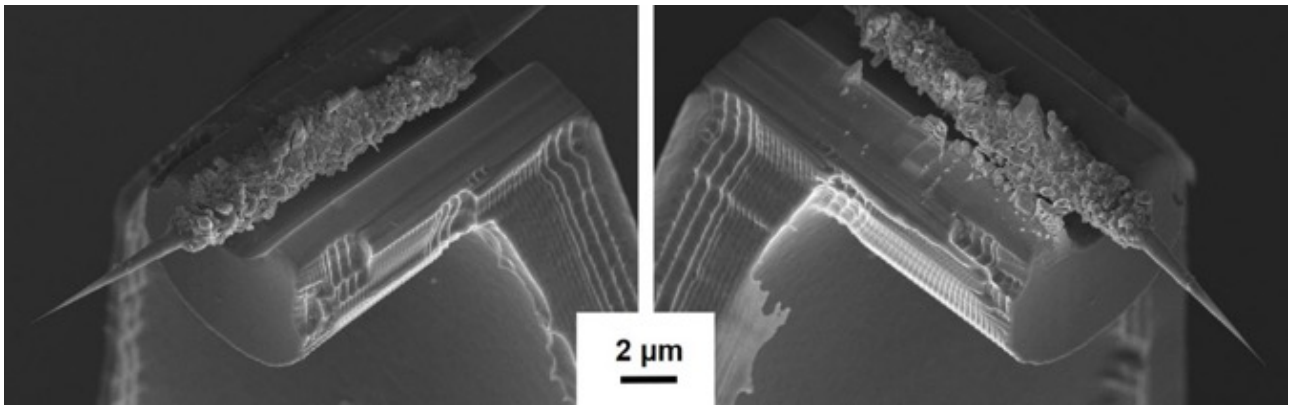

Figure 19 : *Exemple de la sonde n°ZeR11-C20-35 montrant une fixation possiblement faible, sans matériau de soudure d'un côté, et avec du matériau de soudure faiblement adhérent de l'autre côté.*

Enfin, le principal inconvénient de ce procédé est qu'il ne permet pas de préparer des sondes conductrices. Ce dernier pourrait alors être surmonté en utilisant une colle électriquement conductrice, soit à base d'un polymère conducteur (comme le polypyrrole), soit à base d'un polymère isolant mélangé à une charge conductrice (par exemple, des particules métalliques). Toutefois, compte tenu des dimensions des morphologies à coller, le matériau de remplissage à base de particules conductrices devrait se situer dans la gamme sub-nanométrique, ce qui n'est pas disponible sur le marché. Des tentatives préliminaires ont été effectuées (mais non présentées dans cette thèse) pour charger une résine époxy avec des nanoparticules métalliques de nature (Cu, Ag, Au) et de morphologies (sphériques ou allongées) diverses, y compris des nanotubes de carbone, mais les essais n'ont pas été approfondis en raison d'autres problèmes à résoudre (présence de tensioactifs, problèmes de dispersion des particules etc.).

Enfin, en ce qui concerne les tests SPM, comme indiqué au *Chapitre 4*, deux choix étaient possibles : (i) approfondir une technique SPM spécifique sélectionnée, ou (ii) explorer la capacité multimodale vraisemblablement permise par les caractéristiques de la sonde en carbone. Dans notre cas, la deuxième option a été préférée car elle permet une étude exploratoire à partir de laquelle les principales limites et possibilités ont pu être déterminées.

Les travaux à venir pourraient alors être identifiés pour un développement plus approfondi de certains tests SPM. Une sélection qualitative des sondes a d'abord été effectuée sur la base d'une évaluation géométrique réalisée par des caractérisations MEB et des performances présumées de conductivité basées sur les propriétés conductrices de tous les matériaux individuels impliqués dans les cantilevers soudés (carbone graphénique, Si dopé, W ou Pt). Bien que les longueurs des cônes soient relativement les mêmes (6-7 µm) pour toutes les sondes en carbone et que la forme soit assez homogène, les sondes en carbone différaient les unes des autres par l'angle de désalignement par rapport à la géométrie du cantilever, et par la longueur variable de la morphologie du SSF dépassant de la gorge du cantilever (qui dépendait de l'étape de montage), ce qui a été observé comme ayant un impact principalement sur les résultats des tests PF-QNM, STM et KFM.

Les sondes à base de nanocônes de carbone ont ensuite été évaluées en contrôlant leurs performances sur la base de paramètres tels que la résolution, la durabilité et la polyvalence. Toutefois, un inconvénient majeur du travail sur une variété de modes est de trouver le protocole approprié pour évaluer le degré d'adéquation des sondes à chacun des modes SPM testés. Cette partie du travail a été assez difficile car il n'existe pas de protocole spécifique ou de normalisation des sondes disponibles dans la littérature, et les différents fournisseurs de sondes n'ont pas encore développé de procédures de mesure SPM standardisées. Par conséquent, la plupart de nos protocoles d'essai ont consisté à comparer qualitativement les images prises avec les sondes en carbone par rapport à des sondes du commerce considérées comme des références, puis à vérifier l'éventuelle évolution du rapport forme/aspect et du rayon de pointe des sondes consécutivement aux tests SPM.

Le tableau ci-dessous (**Tableau2**) rassemble les principales performances, limites et améliorations possibles des sondes en nanocônes de carbone pour les différents modes testés. A partir de ce tableau, on peut dire que les principaux inconvénients sont liés à l'alignement du cône et au processus de montage. A propos de ce dernier, il serait intéressant d'étudier l'incidence du processus de montage FEBID sur le comportement de la sensibilité au courant ou à la tension observée avec les cônes. Cela devrait s'accompagner d'une mesure directe de la conductivité d'un cône en carbone, et aussi de l'ensemble d'une morphologie SSF.

En conclusion générale, ces travaux ont démontré que les morphologies SSF, grâce aux nanocônes de carbone qu'elles comportent, présentent une bonne potentialité en tant que sondes pour une variété de modes SPM. Toutefois, des améliorations sont nécessaires, qui devraient pouvoir être obtenues par un meilleur alignement cône/fibre pendant la synthèse, ainsi qu'en travaillant sur la qualité et la conductivité du matériau de fixation de la morphologie SSF sur le cantilever-support tout en plaçant la base de la partie conique aussi près que possible du bord de la gorge. Une fois ces limitations surmontées, les portes seront ouvertes à une application de niche en tant que sondes SPM multimodes permettant la caractérisation de plusieurs propriétés d'une même surface d'échantillon tout en gardant la même sonde. Cela pourrait être particulièrement intéressant dans le domaine des semi-conducteurs ou des matériaux composites. Plus généralement, nous pensons que ces travaux ont contribué à démontrer que les nanocônes de carbone méritent d'être étudiés en tant que nanoformes de carbone de grand intérêt, comparable à celui des nanotubes de carbone. Parallèlement, nous

pensons également que cette étude a contribué à la science des matériaux en carbone grâce aux nouvelles connaissances qu'elle a apportées aux mécanismes du dépôt de carbone pyrolytique à l'échelle nanométrique.

Mode SPM	AFM	PF-QNM	C-AFM	STM	KFM
Type C-probe	Collée et FEBID	Collée et FEBID	FEBID	FEBID	FEBID
Performance des nanocônes	✓ Des images topographiques sont possibles. ✓ Meilleure résolution que Otespa R3. ✓ Résolution similaire à celle de Tesp-SS. ✓ Comportement stable pour un balayage de plus de 30h sans interruption	✓ Convient pour les mesures quantitatives nano-mécaniques (c'est-à-dire le module de Young). ✓ Capacité de discrimination entre les différents composants d'un matériau composite.	✓ Une conductance globale légèrement meilleure que celle des sondes commerciales en silicium.	✓ Signal d'images topographiques à grossissement moyen	✓ Une résolution et un contraste similaires à ceux de la sonde Arrow. ✓ L'injection de charge est également possible.
Limitations	• Ne convient pas aux échantillons présentant de grandes variations de z, en raison de la variabilité des angles d'inclinaison	• Résistance à l'usure des pointes • Flexibilité mécanique de la partie en carbone de la pointe ?	• Sensibilité à la haute tension et/ou au courant • Usure des pointes	• Aucune image à résolution atomique n'est possible sous pression atmosphérique	• Signal bruyant • Faible résolution spatiale • Résistance à l'usure des pointes
Amelioration proposée	⇒Des morphologies SSF sur des NTCs pré-alignés pendant l'alignement de synthèse	⇒ Meilleure fixation et intégration pendant le processus de montage	⇒ Mesure directe de la conductivité des nanocones	⇒Meilleure fixation et intégration pendant le processus de montage	⇒ Travail sous vide ⇒ Revêtement réfléchissant en cantiléver

Tableau 2 *: Résumé des performances des nanocônes de carbone pour les différents modes SPM testés. Otespa-R3, Tesp-SS, Arrow sont des sondes commerciales en silicium dopé prises comme références.*

****

Développement de nouvelles sondes à base de nanocônes de carbone pour la microscopie à champ proche

par : Germercy PAREDES GUERRERO

RESUME DE THESE

La microscopie à champ proche permet l'étude topographique et des propriétés physiques (électrique, mécanique, etc.) de la surface d'un matériau à l'échelle nanométrique. Pour ce faire, l'échantillon étudié est balayé en surface par une sonde (ou pointe) dont les caractéristiques géométriques (comme le rayon de courbure de l'apex et le facteur de forme) et les propriétés physiques (mécanique, électrique etc.) doivent être adaptées pour garantir une résolution suffisante et une représentation fidèle de la surface. Cependant, les sondes actuelles présentent des limitations importantes vis-à-vis de la résolution apportée, dans les artefacts possibles d'imagerie, et dans leur adaptabilité concernant leur utilisation dans différents modes (qu'ils soient conducteurs ou non). Ces limitations sont causées principalement par le type de matériau utilisé (par exemple le silicium ou le nitrure de silicium, en standard, ou des nanotubes de carbone), ainsi que par les procédés de fabrication employés pour structurer la géométrie des sondes. Dans ce travail, nous étudions le potentiel de nanocônes de carbone (morphologie carbonée graphénique en forme de cônes à haut facteur de forme et d'apex nanométrique) pour différents modes de microscopie à champ proche. Ces nanocones présentent d'excellentes propriétés mécaniques (forte liaison C-C) et électriques. Ces derniers ont déjà été testés avec succès et brevetés en tant qu'émetteurs d'électrons pour les canons à émission de champ froid équipant les microscopes électroniques par transmission les plus performants. Ces diverses caractéristiques des nanocônes (facteur de forme, apex nanométrique, conductivité, stabilité mécanique, forte cohésion atomique) et d'autres (hydrophobicité, inertie chimique, morphologie multi-échelle micro-nano…) font qu'ils pourraient également constituer une solution prometteuse pour concevoir des sondes potentiellement supérieures aux sondes existantes, qu'elles soient standard ou plus spécifiques comme celles en nanotubes de carbone, pour divers types de microscopie à champ proche, notamment en termes de résolution spatiale et durabilité.

Dans une première partie, cette thèse est dédiée à la synthèse de nanocônes de carbone individuels suivant une méthode originale de synthèse nommée ToF-CVD (*Time of Flight – Chemical Vapor Deposition*). Le travail révèle des mécanismes de formation complexes mettant en jeu d'une part les mécanismes de nucléation en phase hétérogène spécifiques de la CVD du carbone pyrolytique, et d'autre part des mécanismes de mouillabilité impliquant de phénomènes connus du domaine comme l'instabilité de Plateau-Rayleigh. Le montage des nanocônes sur des supports dédiés en tant que sondes pour microscopies à champ proche est ensuite réalisé, suivi par des études de caractérisation (SEM, TEM, spectroscopie RAMAN) pour évaluer leurs caractéristiques initiales du point de vue géométrique et structural et leur évolution vis-à-vis des conditions opératoires requises à la fois lors du montage et pour les différents modes de microscopie à champ proche étudiés.

Dans une seconde partie, le potentiel des nanocônes de carbone en tant que sondes pour des modes de microscopie à champ proche non conducteurs comme le mode topographie (microscopie à force atomique - AFM) et le mode "Peak Force Quantitative Nano Mechanical" (PF-QNM), et pour des modes conducteurs comme pour la microscopie à effet tunnel (STM), la microscopie à force atomique conducteur (c-AFM), la microscopie à force Kelvin (KFM) est évalué. Cette évaluation est faite sur la base de (i) leurs performances ; (ii) leur durabilité ; (iii) leur versatilité. La finalité ultime est de comparer la performance des sondes-nanocônes de carbone par rapport à des sondes commerciales. Les nanocônes de carbone se révèlent être de véritables sondes multimodes avec peu d'équivalents actuels. Des améliorations sont cependant nécessaires et possibles, ce pour quoi des directions sont proposées.

Mots clés : carbone, CVD, nanocônes, champ proche, pointes AFM.

Development of new probes based on carbon nanocones for near field microscopies

by: Germercy PAREDES GUERRERO

THESIS WORK ABSTRACT

Near-field microscopy allows studying the topography and the physical properties (electrical, mechanical, etc.) of a material surface at nanoscale. For such a purpose, the sample surface is scanned by a probe (or tip) which geometric characteristics (such as the apex radius and the aspect ratio) and the physical properties (mechanical, electrical, etc.) must be suitable to ensure a sufficient resolution and a reliable representation of the surface. However, the current probes have significant limitations regarding the resolution, the possible imaging artifacts, as well as their ability to be used in different modes (conductive and non-conductive). These limitations are caused mainly by the type of material used (for example silicon or silicon nitride, for standard probes, or carbon nanotubes), as well as by the manufacturing processes used to structure the geometry of the probes. In this work, we study the potential of carbon nanocones (graphenic carbonaceous morphology with conical shape with high aspect ratio and nanosized apex) for different modes of near-field microscopy. These nanocones exhibit excellent mechanical (strong C-C bond) and electrical properties. They have already been successfully tested and patented as electron emitters for the cold-field-emission guns which equip the most performing transmission electron microscopes. These various characteristics of the nanocones (aspect ratio, nanosized apex, conductivity, mechanical stability, strong atomic cohesion) and others (hydrophobicity, chemical inertia, multiscale micro-nano morphology…), make that they could also constitute a promising solution for designing probes potentially superior to existing probes, either standard or more specific such as those in carbon nanotubes, for various types of near-field microscopy, in particular in terms of spatial resolution and durability.

In the first part, this thesis is dedicated to the synthesis of individual carbon nanocones using an original synthesis method called ToF-CVD (Time of Flight Chemical Vapor Deposition). The work reveals complex formation mechanisms involving the heterogeneous phase nucleation mechanisms specific of the CVD deposition of pyrolytic carbon on the one hand, and well-known wetting mechanisms such the Plateau-Rayleigh instability on the other hand. The mounting of the nanocones on dedicated supports as probes for near-field microscopies is then carried out, followed by characterization studies (SEM, TEM, RAMAN spectroscopy) to assess their starting characteristics from the geometry and structure point of view, and their evolution under the operating conditions required for both the probe fabrication and for the different near-field microscopy modes studied.

In a second part, the potentiality of carbon nanocones as probes for non-conductive modes such as topographic mode (atomic force microscopy – AFM) and "Peak Force Quantitative Nano Mechanical" (PF-QNM) mode, as well as for conductive modes such as scanning tunneling microscopy (STM), conductive atomic force microscopy (c-AFM), and Kelvin force microscopy (KFM) is evaluated. This evaluation is made on the basis of (i) performances; (ii) durability; (iii) versatility. The final goal is to compare the performance of the carbon nanocone probes with other commercial probes. Carbon nanocones reveal to truly be multimode probes with few existing counterparts nowadays. Improvements are needed and possible, for which directions are proposed.

Key words: carbon, CVD, nanocones, near field microscopy, AFM probes.